Improved Simplified Methods for Effective Seismic Analysis and Design of Isolated and Damped Bridges in Western and Eastern North America

by

Viacheslav Koval

A thesis submitted in conformity with the requirements
for the degree of Degree of Doctor of Philosophy

Department of Civil Engineering
University of Toronto

Improved Simplified Methods for Effective Seismic Analysis and Design of Isolated and Damped Bridges in Western and Eastern North America

Viacheslav Koval

Degree of Doctor of Philosophy

Department of Civil Engineering
University of Toronto

2015

Abstract

The seismic design provisions of the CSA-S6 Canadian Highway Bridge Design Code and the AASHTO LRFD Seismic Bridge Design Specifications have been developed primarily based on historical earthquake events that have occurred along the west coast of North America. For the design of seismic isolation systems, these codes include simplified analysis and design methods. The appropriateness and range of application of these methods are investigated through extensive parametric nonlinear time history analyses in this thesis.

It was found that there is a need to adjust existing design guidelines to better capture the expected nonlinear response of isolated bridges. For isolated bridges located in eastern North America, new damping coefficients are proposed. The applicability limits of the code-based simplified methods have been redefined to ensure that the modified method will lead to conservative results and that a wider range of seismically isolated bridges can be covered by this method.

The possibility of further improving current simplified code methods was also examined. By transforming the quantity of allocated energy into a displacement contribution, an idealized analytical solution is proposed as a new simplified design method. This method realistically reflects the effects of ground-motion and system design parameters, including the effects of a

drifted oscillation center. The proposed method is therefore more appropriate than current existing simplified methods and can be applicable to isolation systems exhibiting a wider range of properties.

A multi-level-hazard performance matrix has been adopted by different seismic provisions worldwide and will be incorporated into the new edition of the Canadian CSA-S6-14 Bridge Design code. However, the combined effect and optimal use of isolation and supplemental damping devices in bridges have not been fully exploited yet to achieve enhanced performance under different levels of seismic hazard. A novel Dual-Level Seismic Protection (DLSP) concept is proposed and developed in this thesis which permits to achieve optimum seismic performance with combined isolation and supplemental damping devices in bridges. This concept is shown to represent an attractive design approach for both the upgrade of existing seismically deficient bridges and the design of new isolated bridges.

Acknowledgements

I would like to thank my supervisors Professor Constantin Christopoulos and Professor Robert Tremblay for their valuable guidance and dedication. Their insightful support and steady feedback over the past five years are directly related to the depth of this research. I have learned from their endless enthusiasm and strong practical sense, both vital for the successful completion of this work. It was truly an honor to work with them. I sincerely thank you for giving me this inspiring opportunity.

The financial support for this research program was provided by the Natural Sciences and Engineering Research Council of Canada (NSERC). Scholarship for excellence from the FQRNT (Fonds Québécois de la Recherche sur la Nature et les Technologies) awarded for the highest level of achievement is gratefully acknowledged.

I wish to express my special gratitude to my family, in particular to my wife Kateryna, my son Ihor and my daughter Arianne for their love, understanding and encouragement all through.

Table of Contents

List of Tables

List of Figures

List of Symbols and Abbreviations

ATK – E	artificial time-histories simulated by Atkinson's (2009) for eastern Canada
ATK – W	artificial time-histories simulated by Atkinson's (2009) for western Canada
CEUS	the central-eastern U.S.
DE	design earthquake
DLSP	Dual-Level Seismic Protection
DOF	degree of freedom
EDA	equal displacement approximation
EEA	equal energy approximation
ENA	eastern North America
EQ	earthquake
FPI	friction pendulum isolator
FSI	flat sliding isolator
GM	Ground motion
LB	low bound
LRB	lead rubber bearing
LTH	linear time history
MCG – CEUS	hybrid time histories produced by McGuire (2001) to reproduce the seismicity from the central-eastern U.S.
NA	North America
NLTH	nonlinear time history
OC	oscillation centre
SDOF	single degree of freedom
SE	service earthquake
TH	time history
UB	upper bound
UHS	uniform hazard spectrum
WNA	western North America
WUS	the western U.S.

A	constant spectral acceleration
$A_{\max}$	pulse acceleration amplitude
B	damping coefficient
B_{SA}	damping coefficients defined for spectral acceleration in terms of transmissibility
B_{SD}	damping coefficients defined for spectral displacement using response amplification factor R_d
$[C]$	damping matrix
COV_{EQ}	coefficients of variation for equivalence ratio in statistical analyses
C_v	constant of integration for velocity
C_u	constant of integration for displacement
c	damping coefficient
c_1	damping coefficient for modeling the pier inherent damping or equivalent damping coefficient in Equation (3.21)
c_2	damping coefficient for modeling dampers at the pier
c_3	damping coefficient for modeling dampers at the abutment
c_{cr}	critical damping
D	constant spectral displacement
d	displacement estimate of the bridge deck
d_i	displacement estimate of the bridge deck during iterative step i
d_0	displacement estimate of the bridge deck during iterative step $i-1$
E_{Ab}	absorbed energy
E_{AbL}	energy absorbed by elastic system
E_{AbNL}	energy absorbed by bilinear system
$E_{Ab\ Eq}$	energy absorbed by the equivalent substitute system
E_d	energy dissipated by viscous damping
E_h	amount of energy dissipated in one cycle
E_{in}	relative input energy
E_k	relative kinetic energy

E_p potential energy

F design forces to be resisted by the bridge substructure

F_a site amplification factor for short spectral periods

F_d damping force

$F_{D1}(t), F_{D2}(t), F_{D3}(t)$ damping force at DOF1, DOF2, DOF3 at time t

F_e maximum elastic force

F_i inertia force

Fi_i, Fd_i, Fs_i inertial, damping and spring forces at the i^{th} time step

$Fi_{i+1}, Fd_{i+1}, Fs_{i+1}$ inertial, damping and spring forces at time step $i+1$

$F_{I1}(t), F_{I2}(t), F_{I3}(t)$ inertia forces at DOF1, DOF2, DOF3 at time t

$F_{\max}$ peak force response

F_s spring force

$F_{S1}(t), F_{S2}(t), F_{S3}(t)$ spring force at DOF1, DOF2, DOF3 at time t

F_u ultimate force

F_v site amplification factor for long spectral periods

F_y force at elastic limit or activation force

F_1 forces resisted by the pier structure

F_2 forces resisted by isolators at the pier

F_3 forces resisted by isolators at the abutment

F_{1y} force resisted by the pier structure at elastic limit

F_{2y} activation force for isolation system located at the bridge piers

F_{3y} activation force for isolation system located at the bridge abutment

$\{F_D\}$ damping force vector

$\{F_I\}$ inertia force vector

$\{F_S\}$ spring force vector

f_c' compressive strength of concrete

f_t tensile strength of concrete

f_u ultimate strength of the rebar

f_y yield strength of the rebar

g acceleration of gravity

K_{eff} effective stiffness in Equation (3.24)

k stiffness coefficient

k_{abut} stiffness corresponding to the abutment structure

$k_{abut,j}$ stiffness of abutment j

k_d post-yielding or post-activation stiffness

k_e elastic stiffness

k_{eff} effective stiffness

k_{eq} equivalent stiffness

$k_{eq1}, k_{eq2}, k_{eq2}$ equivalent stiffness ratios for tri-linear hysteresis

k_{eq-e1} equivalent elastic stiffness during DLSP Stage I

k_{eq-e2} equivalent elastic stiffness during DLSP Stage II

k_{isol} stiffness of isolators

$k_{isol,j}$ stiffness of isolator devices installed on a given abutment j

$k_{isol,i}$ stiffness of isolator devices installed on a given pier i

k_{pier} stiffness corresponding to the pier structure

$k_{pier,i}$ stiffness of pier i

k_u initial stiffness of bilinear hysteresis

k_1 stiffness coefficient for modeling pier

k_2 stiffness coefficient for modeling isolators at the pier

k_3 stiffness coefficient for modeling isolators at the abutment

k_{1d} post-yielding stiffness for modeling pier

k_{2d} post-activation stiffness of isolators at the pier

k_{3d} post-activation stiffness of isolators at the abutments

k_{1u} initial stiffness for modeling pier

k_{2u} initial stiffness of isolators at the pier

k_{3u} initial stiffness of isolators at the abutments

$[K]$ stiffness matrix

m mass of SDOF system

m_1 mass of the pier structure or mass at DOF1

m_2 mass of the bridge superstructure or mass at DOF2

$[M]$ mass matrix

NF_1 near-fault-factor-1 (Dicleli and Buddaram, 2007)

NF_2 near-fault-factor-2 (Dicleli and Buddaram, 2007)

n exponential coefficient or number of cycles

P external loading force

PGA peak ground acceleration

PGD peak ground displacement

$P_{\max}$ peak loading force

PS_D spectral pseudo-displacement

$P_1(t), P_2(t), P_3(t)$ external force acting at DOF1, DOF2, DOF3 at time t

$P(t)$ loading force function

p_0 amplitude of loading function

$\{P\}$ loading force vector

Q_d characteristic strength

Q_{2d}, Q_{3d} characteristic strength of isolators at the pier and abutment

R response modification factor

R_{cr} critical value of the response modification

R_d displacement amplification factor

$R_{\min}, R_{\max}$ minimum and maximum response modification factors

$R_{\min 1}, R_{\max 1}$ minimum and maximum response modification factors during DLSP Stage I

$R_{\min 2}, R_{\max 2}$ minimum and maximum response modification factors during DLSP Stage II

S_A spectral acceleration

S_{a-sim} actual acceleration of simulated ground motion used in scaling process

$S_{a-t\arg}$	target acceleration for ground motion scaling
S_D	spectral displacement
SF	ground motion scaling factor
S_V	spectral velocity
T	fundamental vibration period
T_d	post-activation vibration period
T_e	elastic vibration period or initial vibration period of inelastic SDOF system
$T_{eff,inh}$	effective period with inherent damping level
$T_{eff,0\%}$	effective period with 0% of viscous damping
$T_{eff,5\%}$	effective period with 5% of viscous damping
T_{eq-e1}	initial equivalent period during DLSP Stage I
T_{eq-e2}	initial equivalent period during DLSP Stage II
T_g	ground-motion predominant period
$T_{\lim}$	limit of applicability proposed in this thesis for the code simplified method
TR	transmissibility
t	time
t_d	time of fault slip duration
t_i	time step i
t_{i+1}	time step $i+1$
t_r	time of fault rupture propagation
u	relative displacement
u_c	relative displacement of complementary solution
u_{code}	estimate of displacement response using code simplified method
u_e	maximum relative displacement of elastic SDOF system
u_{EEA}	estimate of displacement response using equal energy approximation
u_{EDA}	estimate of displacement response using equal displacement
$u_{ER\mu}$	estimate of displacement response using energy-based *E-R-*μ method
u_g	ground displacement

u_i relative displacement at the i^{th} time step

u_{in} maximum relative displacement of inelastic SDOF system

u_{i+1} relative displacement at time step $i+1$

u_{LTH} maximum displacement response from linear time-history analyses

u_m maximum displacement in development of the energy-based *E-R-μ* method

$u_{\max}$ peak displacement response

u_{NLTH} maximum displacement response from nonlinear time-history analyses

u_p relative displacement of particular solution

u_{st} static displacement

u_{tot} total displacement ($u_m + u_g$)

u_y displacement at elastic limit or activation displacement

u_1, u_2, u_3 relative displacement at DOF1, DOF2, DOF3

u_{1y} pier displacement at elastic limit

u_{1u} pier ultimate displacement

u_{2y} displacement corresponding to the activation of the isolation system located at the bridge piers

u_{3y} displacement corresponding to the activation of the isolation system located at the bridge abutments

$\dot{u}$ relative velocity

$\dot{u}_c$ relative velocity of complementary solution

$\dot{u}_g$ ground velocity

$\dot{u}_i$ relative velocity at the i^{th} time step

$\dot{u}_{i+1}$ relative velocity at time step $i+1$

$\dot{u}_p$ relative velocity of particular solution

$\ddot{u}$ relative acceleration

$\ddot{u}_g$ ground acceleration

$\ddot{u}_i$ relative acceleration at the i^{th} time step

$\ddot{u}_{i+1}$ relative acceleration at time step $i+1$

V constant spectral velocity

V_g peak pulse velocity

$V_{\max}$ maximum velocity

W dead load of the structure

W_c dissipative work

W_D energy dissipated by the structure in a complete cycle in Equation (3.24)

$\bar{x}$ mean value of ratio u_{NLTH}/u_{code} determined in statistical analyses

x upper bound of confidence interval in statistical analyses or horizontal coordinate

$x_1(t), x_2(t), x_3(t)$ horizontal coordinate of DOF1, DOF2, DOF3 at time t

$\dot{x}_1(t), \dot{x}_2(t), \dot{x}_3(t)$ velocity at DOF1, DOF2, DOF3 along the x axis at time t

$\ddot{x}_1(t), \ddot{x}_2(t), \ddot{x}_3(t)$ acceleration at DOF1, DOF2, DOF3 along the x axis at time t

$\{x\}$ displacement vector

$\{\dot{x}\}$ velocity vector

$\{\ddot{x}\}$ acceleration vector

$\{\ddot{x}_g\}$ ground acceleration vector

a post-yielding stiffness ratio or post-activation stiffness ratio

α_{eq1} equivalent post-yielding stiffness ratio during DLSP Stage I

α_{eq2} equivalent post-yielding stiffness ratio during DLSP Stage II

α_{var} azimuthal variability of damage indices

β viscous damping in expression for damping coefficient B

β_e elastic damping ratio defined as proportional to elastic stiffness

β_{eff} effective damping

β_{eq} equivalent damping

$\beta_{eq-\max}$ maximum equivalent damping

β_{inh} inherent damping

β_{inh-e} inherent damping proportional to the elastic stiffness

$\beta_{inh-eff}$ inherent damping proportional to the effective stiffness

β_s equivalent damping in Equation (3.23)

β_v damping ratio of a viscous damper determined at an elastic period T_e in Equation (3.24)

β_0 elastic viscous damping ratio

ΔFi difference between inertia forces at time steps i and $i+1$

ΔFd difference between damping forces at time steps i and $i+1$

ΔFs difference between spring forces at time steps i and $i+1$

Δt time increment

ε_c' strain at compressive strength of concrete

ε_s strain of steel

θ azimuthal direction; direction in which the fault rupture propagates toward the site corresponds to the azimuth $\theta = 0°$

λ system property modification factors

$\lambda_{\min,t}$, $\lambda_{\max,t}$ minimum and maximum system property modification factors - effect of temperature

$\lambda_{\min,a}$, $\lambda_{\max,a}$ minimum and maximum system property modification factors - effect of aging

$\lambda_{\min,c}$, $\lambda_{\max,c}$ minimum and maximum system property modification factors - effect of contamination

$\lambda_{\min,tr}$, $\lambda_{\max,c}$ minimum and maximum system property modification factors - effect of cumulative movement or travel

$\lambda_{\min}$, $\lambda_{\max}$ minimum and maximum system property modification factors

μ ductility ratio

μ_i ductility ratio at iterative step i

μ_1 initial value of ductility used for the iterative step $i = 1$

ξ viscous damping ratio

ξ_e viscous damping ratio proportional to elastic stiffness

ξ_{eff} viscous damping ratio proportional to effective stiffness

ξ_{inh} inherent damping which corresponds to the damping level of the design response spectrum

π dimensionless mathematical constant

σ standard deviation in statistical analyses

τ discrete time

φ phase angle

ω_e angular frequency of elastic SDOF system

ω_{eff} effective circular frequency

ω_d post-activation circular frequency

ω_g ground-motion predominant circular frequency

Chapter 1: Introduction and Research Objectives

1.1 Problem Definition and Background

In North America (NA), the seismic design of bridge structures is regulated by the CAN/CSA-S6-06 Canadian Highway Bridge Design Code (CSA 2006) in Canada and the AASHTO LRFD Seismic Bridge Design Specifications in the United States (AASHTO 2009, 2010). Seismic provisions included in these two codes have been essentially developed for ground motions from historical earthquake events that have occurred along the west coast of North America. One reason for this was the lack of good historical seismic records or simulated ground motion time histories representative of the seismological characteristic of eastern North America. The Eastern North American (ENA) ground motions are very different from those in Western North America (WNA) (Atkinson, 2009). In contrast to WNA, the ENA ground motions are characterized by high-frequency content and most of the seismic energy is transmitted to the system in a shorter period range. This causes concern about the appropriateness of using the same seismic provisions for ENA and WNA and needs to be validated.

As indicated in the Commentary on CAN/CSA-S6-06, Canadian Highway Bridge Design Code (CSA 2006), the seismic provisions currently specified in CAN/CSA-S6-06 are mainly based on the Standard Specifications for Highway Bridges (AASHTO 1994) and mostly reflect state-of-the-art knowledge dating back to the 1980-90. The upcoming CAN/CSA-S6-14 will make use of uniform hazard spectra (UHS) developed based on more recent seismic data. A significant amount of new information has been generated in the last two decades on the characteristics of the ground motions expected in ENA and WNA. The seismic provisions must be validated to reflect this updated seismic data.

Over the last two decades, seismic protection techniques incorporating isolation and damping devices have become increasingly attractive for reducing seismic demand on bridges and achieving more cost effective designs. A simplified method has been adopted in North American codes for the analysis and design of seismic isolation systems for bridges. The method relies on an equivalent effective linearization of the isolated structure and a damping coefficient, or response reduction factor B, that takes into account the energy dissipation capacity of the

nonlinear system assuming equivalent viscous damping. Code-specified damping coefficients have been established essentially based on the effect of viscous damping on the linear response, rather than from nonlinear time history analyses accounting for the actual nonlinear response of actual isolation systems. More specifically, these damping coefficients were estimated from regression analyses by setting average *B* values statistically. For instance, code *B* values vary as a function of the equivalent added damping but do not vary with the characteristics of the anticipated ground motions or the effective period of the linear equivalent system. The accuracy of the approximate simplified method has been extensively investigated worldwide and different factors of influence have been reported. The appropriateness of using the same damping coefficients for both western and eastern North American ground motions has been questioned in past studies (Taylor, 1999; Naumoski et al., 2000). Bommer and Mendis (2005) found that damping effects may also vary with earthquake magnitude and distance as well as with soil types. They stated that magnitude and distance effects can be accounted for by applying different reduction factors. However, there is no consensus on how these parameters can be incorporated in the simplified method to obtain improved response predictions. Due to the large uncertainty on the effect of the different parameters, estimating the response of seismically isolated bridges still represents a challenging task for engineers.

To reduce the parametric uncertainty, the current seismic codes specify limits for the application of their simplified methods. In particular, the equivalent viscous damping is limited to 30% and bridge isolators must be provided with minimum recentring capabilities. Although ensuring the conservative use of the code provisions, these limitations are found to be too restrictive for certain cases of practical applications (Medeot, 2004; Medeot, 2012).

The current code simplified method is based on the steady-state response of an equivalent linear system with viscous damper, which may not be representative of the actual response of bridge isolated structures. In particular, peak displacements are likely to be influenced by transient response under large acceleration pulses or shifting of the oscillation center (Iwan, 1961; Kawashima et al., 1998; Graizer, 2010). It confirms that a more refined method accounting for these effects is needed to improve the accuracy of displacement predictions.

There is a need for an alternative method that could properly take into account the specificity of the expected seismic ground motions and the nonlinear system parameters in the displacement

predictions of isolated and damped bridges such that the current limits can be expanded to allow a greater choice for design engineers.

A design approach based on two levels of seismic hazard has been incorporated in different NA performance-based specifications for the seismic design of bridges. Performance objectives in terms of damage for two hazard levels have been proposed by Huffman et al. (2012) for possible inclusion in the future edition of the CSA-S6 Canadian Highway Bridge Design Code (CSA 2006). Two hazard levels are considered: the Design (DE: upper-level) and the Service (SE: lower-level) earthquakes with a probability of exceedance of 2% and 10% in 50 years, respectively. The use of isolation and damping techniques is an efficient means of achieving the desired level of earthquake performance and safety. However, it is difficult to achieve target design objectives at each of the two seismic hazard levels while taking full advantage of the benefits provided by the isolation and damping systems. When multi-level-hazard performance objectives are considered, the performance criteria may be satisfied for design parameters under an upper-level earthquake (DE) and not satisfied under a more frequent and less intensive event (SE). In practice, the design is carried out for a single-hazard performance level (usually corresponding to the highest seismic hazard) and the consequences of this design on the performance for a lower seismic hazard level are just accepted, without any optimization. Such a design approach usually results in seismic protective solutions that bring no or very limited improvement to the performance of the bridge structure under the SE event where the isolation system is unlikely to be activated and therefore the bridge will have to be designed to respond elastically for this seismic hazard level. If, in contrast, the protection system is designed to fully engage under the lower-level (SE) event, the bridge is likely to experience excessive deformations across the isolation system and, thereby, extensive damage or even the possibility of collapse under a rare, more severe earthquake (DE). Ideally, a bridge protective system based on isolation and damping should positively impact the seismic performance at both hazard levels. However, it is still challenging to meet specific performance objectives under different levels of seismic hazard.

The topic of multi-level hazard design is of growing interest to the scientific and engineering communities. Different researchers worldwide carry out studies on how to efficiently achieve target design objectives at multiple hazard levels (Buckle et al. 2006, Morgan and Mahin 2011, Monzon et al. 2012). Monzon et al. (2012) experimentally studied two different configurations of

protective systems, full isolation and hybrid isolation. The systems were designed at a single level such that the bridge columns remain elastic at a lower-level event which corresponds to more frequent earthquakes. To outline benefits of using the hybrid isolation in achieving the multi-level performance goals, the responses of the bridge with full and hybrid isolations were compared at both lower-level and upper-level events. Morgan and Mahin (2011) have investigated the possibility of achieving the multi-level performance goals in seismic protection of isolated buildings using the triple pendulum isolator. The isolation system was examined through numerical simulations and experiments. The researchers stated that the multi-level-hazard solution obtained with this device may not be general for a wide-class of structural systems and further investigations will be needed. The development of a new multi-hazard protection concept is of significance for achieving optimal designs for the upgrade of existing seismically deficient bridges and for the design of new isolated bridges.

1.2 Project Scope and Goals

The research study presented in this thesis aims to develop enhanced seismic design strategies for isolated and damped bridges in eastern and western North America. The biggest challenges faced by engineers in the seismic design of isolated bridges is a high level of uncertainty related to the seismic randomness (ground-motion parameters) and the effect of nonlinear system parameters. The resulting inaccuracy in response prediction causes concern on the part of researchers and practicing engineers. There is a need for improving our understanding of the sources of the inaccuracy and to provide more reliability for design of isolated and damped bridges. This is the main motivation for this project. The main purpose of this project hinges together threefold objectives as follows.

1) *Verify and enhance the CAN/CSA-S6-06 Simplified Equivalent Method for isolated bridges for eastern and western North American regions.*

   The coefficients B of the CSA-S6 simplified method will be revisited and modified where necessary for both eastern and western North American regions to reflect the design spectra and the seismic data that have been generated in the two decades and that will be used in the upcoming code edition. The limits of application and minimum recentering requirements of the simplified method will also be revisited and adjusted as needed to ensure reliable displacement predictions.

2) *Development of a new simplified method for estimating responses of isolated bridges by considering ground-motion and nonlinear system parameters.*

   A new simplified method that will take into account the differences in ground-motion characteristics and more specific bridge design parameters will be developed with the aim of extending the range of permissible isolation systems beyond the range of applications of the current code simplified method. The development of the method will make use of the concept of *energy allocation* under transient excitation, which can more accurately account for the transient response and possible shifting of the oscillation center of nonlinear isolated bridges, two aspects that are not accounted for in the current code simplified method.

3) *Development of an optimum multi-level-hazard seismic protection concept for bridge structures.*

   The development of a new multi-level-hazard protection concept is the goal of the third phase of this research. The method will provide guidance on the selection, combination and sizing of different isolation and damping systems with the aim of developing a predefined hierarchy of activation of different protective devices exhibiting complementary properties so that specific hazard level performance objectives can be met. The method will be developed such that it can be used for the design of new isolated bridges as well as for the upgrade of existing seismically deficient bridges.

This research will contribute to the development of next-generation techniques and strategies for the design of isolated and damped bridges in both eastern and western North American regions. Satisfying the first two objectives listed above should allow improvement in the accuracy of the simplified method. Satisfying the third objective should allow achievement of more effective protection systems that can be exploited at two different hazard levels.

By implementing these innovative techniques and strategies, bridge owners and designers will be able to determine the optimum bridge protective system in terms of performance and cost-effectiveness. More realistic response estimates will reduce the impact of the uncertainties related to the decision on the implementation of different isolation and damping devices for seismic protection of bridges. The project goals summarized above put in evidence the significance, originality and contribution to knowledge of this research work.

1.3 Project Methodology

The thesis starts with a critical review on the Current Code Analysis and Design Procedures for Isolated Bridges. Then, the project preliminary phase is presented. This phase precedes the primary project framework and is dedicated to the development of 1) a numerical analysis tool and 2) ensembles of ground-motion time histories, both needed to carry out the analyses of the nonlinear structural behaviour of isolated bridges throughout this research project.

To achieve primary goals of this research, this project is organized around three main phases defined by their corresponding objectives as stated in the previous section. Each of these phases can be perceived as an independent work that originally contributes to the main purpose of the project. However, a higher significance level may be expected when these contributions are put together in a complementary way as they are presented in this work.

Overview of Current Code Analysis and Design Procedures for Isolated Bridges

A review on the current methodologies and practices for designing Isolated Bridges is complemented by critical review of the relevant researches. Revising the basic assumptions, made at the time when the method was developed, led to better understanding of the method limitations and related accuracy problems. The critical review of the relevant studies made it possible to select strategies on how to overcome these limitations as well as to establish a project framework with respect to the state of the art.

Preliminary Phase - Analytical Model and Numerical Platform for Nonlinear Time-History Analysis of Isolated and Damped Bridges

A new analytical model and methodology were developed for simulating nonlinear structural behaviour of isolated bridges equipped with different seismic protective devices. The approach aimed at streamlining the modeling assumptions with the purpose of developing a proper and effective, yet simple analytical model that can be used at the preliminary design stages for a fully equipped isolated bridge. The ability of the model to simulate the structural behaviour of deficient bridges equipped with different seismic protective devices was demonstrated through bridge retrofit examples. The model allows engineers to determine optimal seismic protection solution through an iterative optimization design process requiring minimum computational effort. A numerical analysis tool was programmed in MATLAB and may be widely exploited for

teaching-learning process and research purposes due to the possibility of animating seismic response simulations through a graphical user interface.

Preliminary Phase - Ground motion selection and scaling for time-history analysis of isolated bridges in ENA and WNA

Site-specific ensembles of ground-motion time histories are defined and scaled to carry out the analyses of the nonlinear structural behaviour of isolated bridges in eastern and western North America.

The design spectrum in the Canadian CSA-S6-06 code is no longer up to date and it is expected that the Uniform Hazard Spectrum (UHS) currently used in NBCC (NRCC, 2005) for buildings will be adopted as the design spectrum in the next CSA-S6-14. When this study was initiated in 2009, UHS for CSA-S6-14 had not been developed yet and the UHS data specified in NBCC 2005 was adopted as it represented the most recent data available at that time. The UHS data was modified in the 2010 edition of NBCC (NRCC, 2010) but the changes were small and not likely to significantly affect the outcome of the study. Hence, the research was completed using the 2005 seismic data.

The technique and methodology proposed in this study intend to select and scale time histories for dynamic analyses from the perspective of a structural engineer using the available state of the art in seismology. The proposed approach can be summarized in two main steps as follows:

- *Defining a site-specific earthquake scenario from hazard deaggregation;*
- *Selecting and scaling ground motion records using linear scaling process over a period range which is expected to represent the period lengthening during inelastic behaviour of isolated bridges;*

Project Phase 1 - Appropriateness of the CSA-S6-06 code simplified method for design of isolated bridges in ENA and WNA

The first phase of the primary framework aims to examine and enhance the code simplified method currently specified in CAN/CSA-S6-06.

The approach of assessing the *B*-coefficients by using linear time-history analyses (LTHA) is first presented in this study, given that it corresponds well to the state-of-the-art technique of

assessing damping coefficients. The coefficients obtained from LTHA in ENA and WNA are compared to those specified in codes in order to examine the possible influence of the regional characteristics of the seismicity on the reduction effects of damping. The suitability of using the same *B*-coefficient for reducing force and displacement responses is also examined. Based on the results from LTHA, this study also investigates the dependency of *B*-coefficients on the effective period of the structure that has already been identified by other researchers (Atkinson and Pierre, 2004 and Hatzigeorgiou, 2010). The differences observed in the response reduction effects caused by viscous damping are explained by exploiting the concepts of the force transmissibility and response amplification respectively for spectral accelerations S_A and displacements S_D.

Then, an extensive parametric study is carried out using dynamic nonlinear time history analysis (NLTHA) so that the nonlinear response of the bridge isolation systems is properly accounted for. The parametric study was carried out by varying several parameters that may be used to define the system's dynamic properties at the initial design stage. Recommendations are made on possible modifications to improve the accuracy of the code simplified method. To better assess the accuracy of the *B*-coefficients on the seismic displacement response, nonlinear structures were analyzed following the complete iterative procedure prescribed in the CSA-S6-06 simplified method. This study also examines the need for an upper limit on damping for which the *B*-coefficient method can be used in codes.

Given that the sources of the method inaccuracy may be both the local damping reduction effect and the *equivalent linearization method* which is an intrinsic part of the code method, the accuracy of the *equivalent linearization method* is carefully examined and the influence of the nonlinear parameters is outlined. Recommendations are made on how to define the range of parameters for which the *equivalent linearization method* can provide an accurate response estimate. The need for a new simplified method that takes into account the differences in ground-motion characteristics and isolated bridge design parameters is also outlined.

Project Phase 2 - New Energy-Based E-R-μ Simplified Method

In the second phase of this project, a new simplified method that takes into account the differences in ground-motion characteristics and bridge design parameters is proposed.

In order to establish a basis for the development of a new simplified method, two widely adopted methods in earthquake engineering, the Equal Displacement Approximation (EDA) and the Equal Energy Approximation (EEA) are first briefly reviewed. The accuracy is characterized in terms of the relative error in order to determine the limitations that are inherent to the EDA and EEA. The energy concept used in the EEA is then considered for further development. In such a way, different system's properties and ground-motion characteristics can then be taken into account for seismic response prediction.

Special attention is drawn to the effect of the transient phase of loading that occurs at the beginning of the excitation. Based on the principle of conservation of energy, the energy flow is examined within the system's motion in the transient phase of the response before reaching peak displacement. This investigation showed that kinetic energy is a possible key element that must be considered in the new simplified method.

Then, a more detailed insight on the *energy flow*[1] is gained by studying the effect of the response modification factor R and the frequency ratio on the energy allocation. Through this study, it is found that the transition state between *limited-nonlinear* and *highly-nonlinear* responses defines the limit beyond which the kinetic energy has a dominant effect on the response of NL-SDOF systems.

The transient response and possible shifting of the transient oscillation centre, was taken into account by applying the concept of energy allocation under transient excitation. Based on this, a new simplified method is proposed. This method takes into account the differences in ground-motion characteristics and bridge design parameters and can predict the peak displacement of bilinear systems. This new energy-based E-R-μ method was developed purely based on analytical derivations rather than being empirically calibrated. The basis on which the predictions are made assumes that 1) ground motions are represented by a single sine-wave pulse defined by the peak ground acceleration (PGA) and peak ground displacement (PGD) and 2) response to that pulse can be predicted using the E-R-μ method.

1. "Energy flow" refers to the transformation of energy transmitted to the system during a ground motion in different energy forms such as kinetic, absorbed, and dissipated"

Project Phase 3 - New Multi-Level-Hazard Seismic Protection Technique

In the phase 3, a novel Dual-Level Seismic Protection (DLSP) design method that relies on the combination of different isolation and damping systems to achieve a different optimal response for different seismic hazard levels was proposed. The development of the multi-level-hazard performance-based design concept was first reviewed. The proposed methodology was described and an optimization process is then presented.

The DLSP design is based on the selection, combination and sizing of different isolation and damping systems to develop a predefined hierarchy of activation of different protective devices exhibiting complementary properties. Accordingly, isolation devices are introduced at all supports to act as fuses and to control the seismic input in the substructure. At the intermediate pier support, the horizontal resistance offered by the isolators must not exceed the lateral force producing yielding of the pier reinforcements. Supplemental damping devices are combined to the isolation system at the abutments to control the lateral displacement of the superstructure.

A detailed DLSP design was carried out for the structure of deficient bridge with a primary objective of preventing damage to the bridge substructure under both levels of seismic hazard. An optimization process was then used to identify the system properties that best meet the stringent lifeline bridge requirements at these two hazard levels. Results from the optimization process also provided insight into the influence of the response modification factor R on the response of the isolated structure. A further optimization of the system that was achieved by introducing viscous dampers at the abutments was also outlined using new energy-based E-R-μ method and through time-history analyses.

1.4 Organization of the Thesis

The research study presented in this thesis is organized in 11 chapters:

Problem formulation, project scope and detailed methodology are provided in Chapter 1. A critical review of the current methodology and practice for design of Isolated Bridges are described in Chapter 2.

Chapter 3 presents a new analytical model and methodology developed for simulating nonlinear structural behaviour of isolated bridges equipped with different seismic protective devices.

Chapter 4 outlines the process of defining earthquake scenario, records selection and scaling for site-specific suite of time-history records. The importance of considering the effect of seismic directivity is outlined.

In Chapter 5, the appropriateness of the damping coefficient B for western and eastern North American ground motions is investigated. A study on the appropriateness of using an equivalent linear substitute (SDOF system) to estimate responses of NL damped structures is then presented. New damping coefficients are proposed based on these results.

In Chapter 6, the accuracy of the *equivalent linearization method* is carefully examined and the influence of the nonlinear parameters is outlined. This study is used to define the range of parameters for which the *equivalent linearization method* can provide an accurate response estimate.

In Chapter 7, the dynamic behaviour of seismically isolated and damped bridges is studied in depth to gain a better understanding of the physical phenomena involved in the response of isolated bridges. In order to establish a basis for the development of the new simplified method, the energy flow is examined within the system's motion in the transient phase.

In Chapter 8, a new simplified method that takes into account the differences in ground-motion characteristics and bridge design parameters is proposed. This new energy-based E-R-μ method was developed purely based on analytical derivations. The effectiveness and accuracy of this energy-based method for capturing the response of highly-nonlinear systems is then validated.

Chapter 9 summarizes the improvements proposed in this thesis for designing seismically isolated bridge structures and it also concludes with a discussion of their design implications. A detailed insight on the use of the new energy-based E-R-μ method for achieving an optimum isolation solution is provided by studying the effect of the bridge parameters.

Chapter 10 introduces a Dual-Level Seismic Protection (DLSP) design method that relies on the combination of different isolation and damping systems to achieve a different optimal response

under different levels of seismic hazard. The optimal design process of a DLSP is illustrated by using the energy-based *E*-*R*-μ method for the retrofit of actual bridges.

Chapter 11 summarizes the main findings of this study focusing on the contribution to the development of the next-generation techniques and methodologies to mitigate the high seismic risk that exists in both eastern and western North American regions.

Chapter 2: Overview of Current Code Analysis and Design Procedures for Isolated Bridges

2.1 Simplified Method in NA Provisions

Formulation of Equivalent Linearization

Current North American codes include a simplified equivalent static force method to compute the seismic response of isolated bridges and displacements across the isolation bearings. The method is based on the transformation of the actual nonlinear isolated structure into an equivalent linear system. The transformation is illustrated in Figure 2.1(a) for the case of a bridge with isolators exhibiting bilinear response which is representative of numerous isolation systems such as lead-rubber, hysteretic and frictional devices.

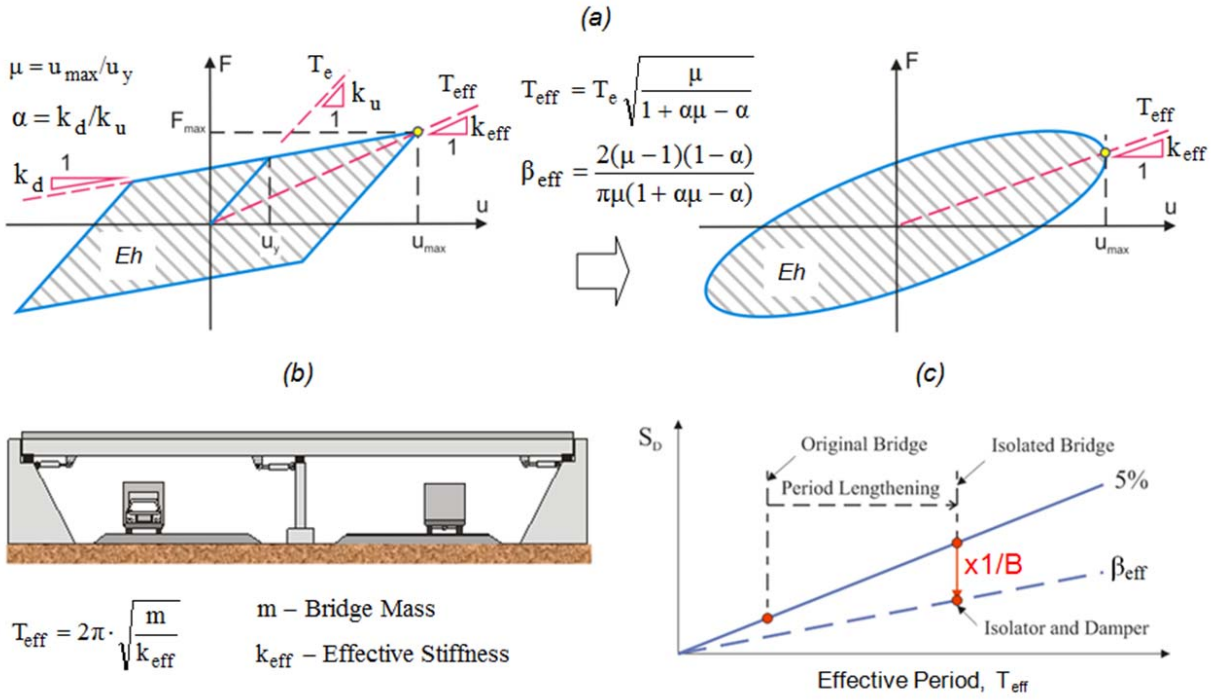

Figure 2.1 Equivalent linearization method: a) transformation of nonlinear system (bilinear response) to equivalent system (viscoelastic response); b) typical isolated bridge - nonlinear system; and c) equivalent linearization method

The equivalent linearized effective system has a stiffness k_{eff}, a period T_{eff} and linear viscous damping ratio β_{eff}. These effective properties are determined at the maximum expected displacement u_{max} and are defined using the geometry of the system hysteretic shape in terms of initial elastic stiffness k_u, post-yielding stiffness ratio α, and ductility demand μ. The resulting effective parameters can be then formulated as follows.

$$k_{eff} = k_u \frac{1+\alpha\mu-\alpha}{\mu} \tag{2.1}$$

$$T_{eff} = T_e \sqrt{\frac{\mu}{1+\alpha\mu-\alpha}} \tag{2.2}$$

where initial elastic period T_e and effective period T_{eff} may be formulated for the oscillatory motion of the linear single-degree-of-freedom (SDOF) system characterized by its mass m and the corresponding stiffness as follows:

$$T_e = 2\pi\sqrt{\frac{m}{k_u}} \quad \text{and} \quad T_{eff} = 2\pi\sqrt{\frac{m}{k_{eff}}} \tag{2.3}$$

The equivalent damping ratio β_{eq} is established so that the equivalent system dissipates the same energy E_h as the actual nonlinear system (Chopra, 1995). The equivalent viscous damping is then formulated through ductility ratio μ and post-yielding stiffness ratio α as:

$$\beta_{eq} = \frac{1}{4\pi}\cdot\frac{Eh}{Es} = \frac{2}{\pi}\cdot\frac{(\mu-1)\cdot(1-\alpha)}{\mu\cdot(1+\alpha\mu-\alpha)} \tag{2.4}$$

In different research studies (Tsopelas et al., 1997; Makris and Chang, 1998), the equivalent damping term is referred to as the effective viscous damping β_{eff}. However, a distinction between these two terms must be made for clarity.

When seismic isolators are the only means available for dissipating energy through the system hysteretic response, the equivalent damping ratio β_{eq} referred to as the effective damping β_{eff} that is assigned as an effective parameter to a linear SDOF system for equivalent linearization.

Otherwise, by considering the energy-dissipation contribution from the hysteretic response of the isolators complemented by the contributions of the viscous dampers and the inherent viscous

damping, the effective damping ratio is defined by three terms as proposed in Tsopelas et al. (1997):

$$\beta_{eff} = \beta_{eq} + \beta_{v,eff} + \beta_{inh} \tag{2.5}$$

North American Code Provisions

In the Canadian Highway Bridge Design Code (CAN/CSA-S6-06), the maximum horizontal seismic force F and the displacement across the isolation bearings u_{max} for an isolated structure are given by:

$$F = \frac{AS_i}{BT_{eff}} W \leq \frac{2.5A}{B} W \tag{2.6}$$

$$u_{\max} = \left(\frac{T_{eff}}{2\pi} \right)^2 \frac{AS_i}{BT_{eff}} g = \frac{250 AS_i T_{eff}}{B} \, (mm) \tag{2.7}$$

where A is the zonal acceleration ratio, S_i is the site coefficient, W is the dead load of the structure and B is the damping coefficient. In these equations, it is implied that the design acceleration spectrum has a maximum value of $2.5A$ and then decreases as a function of the inverse of the period. Both the force and displacement demands are computed by simply dividing the elastic response by the damping coefficient B. This coefficient is therefore defined as the ratio of the demand from 5% damped response spectrum to the demand for the effective damping ratio β_{eff} (Figure 2.1(b)). Values of B vary with β_{eff}, as described later. The code simplified equivalent force method is an iterative procedure which can be summarized in the following three main steps:

1) Determination of spectral quantities associated with the period T_{eff} of the isolated structure.

2) Evaluation of the equivalent damping ratio β_{eff} used to determine B.

3) Evaluation of the structure's force and displacement response using Equations (2.6) and (2.7).

The method is iterative because the values of T_{eff} and β_{eff} in Steps 1 and 2 depend on the displacement response, which, in turn, is evaluated in Step 3. Although the method is considered

a force-based design method, the procedure is in fact used to determine the displacement of the isolated structure (Equation (2.7)) and the design seismic forces for the substructure are subsequently determined from the load-displacement response of the actual nonlinear isolation system.

In the United States, the design procedure in the AASHTO Guide Specification for Seismic Isolation Design (AASHTO 2010) is identical except that the 5% damped elastic design spectrum is constructed using a two-point method depending on the site specific design spectral values S_S and S_1 at periods of 0.2 and 1.0 s, respectively.

The current seismic design philosophy based on the damped elastic response spectra was introduced in North America in the late 1970's. In the early 1980's, seismic protection techniques, incorporating isolation and damping devices, started to draw attention as a possible effective means of reducing the seismic demand and enhancing the seismic response of structures. Guidelines for the design of seismic isolation systems were first published by the Structural Engineers Association of Northern California (SEAONC, 1986). The damping coefficient B, which reflects the energy dissipation capacity as a function of equivalent damping, first appeared in the 1991 UBC (ICBO) provisions for base-isolated buildings (Naeim and Kircher, 2001).

The concept of equivalent damping β_{eff} was introduced by Jacobsen (1930) and formulated as a function of dissipated energy E_h in 1960. Gulkan and Sozen (1974) used it to define a substitute linear structure with a fictitious equivalent damper, as presented in Figure 2.1(a), and the concept was later incorporated in seismic provisions as a simplified design method. The displacement response of the equivalent system is intended to closely reproduce the inelastic response of a real nonlinear structure (Figure 2.1(b)). As illustrated in Figure 2.1(c), the elastic 5% damped spectrum is divided by the damping coefficient $B(\beta_{eff})$ to obtain the resulting reduced response as a function of effective period T_{eff}. The values of B specified in codes have been derived from the work by Newmark and Hall (1982). In these early studies, spectrum amplification factors were computed for different damping levels using the elastic response of a viscously damped single-degree-of-freedom (SDOF) system subjected to the 1940 El Centro earthquake record. These values were then slightly adjusted over the years. Damping coefficients specified in various seismic provisions are presented in Table 2.1.

Table 2-1 Values of the damping coefficient *B*

β	CSA-S6 (2006) AASHTO (1994)	AASHTO (2009)	EC 8: Part 2 (1996)	EC 8: Part 2 (2005)	UBC (1994)	ATC-40 (1996)	Newmark & Hall (1982)	
(%)	B	B	1/η	1/η	B	B1	A[1] Region	V[2] Region
2	0.8	0.76	0.82	0.84			0.77	0.81
5	1.0	1.00	1.00	1.00	1.00	1.00	1.00	1.00
10	1.2	1.23	1.21	1.22	1.19	1.22	1.29	1.20
20	1.5	1.52	1.49	1.58	1.56	1.54	1.81	1.53
30	1.7	1.71	1.70	1.87	1.89	1.82		
40	1.9	1.87	1.87	2.12		2.08		
50	2.0	2.00	2.02	2.35				

1. A Region - Acceleration-sensitive region of the response spectrum
2. V Region - Velocity-sensitive region of the response spectrum

In 1999, values of the damping coefficient were introduced in AASHTO LRFD Guide Specifications for Seismic Isolation Design (AASHTO, 1999). The same values were also incorporated in the 2000 edition of the Canadian code CSA-S6 and are still in force in CSA-S6-06. The third edition of the AASHTO Guide Specification for Seismic Isolation Design (2010) now proposes an exponential equation for the value of B as a function of β_{eff}:

$$B = \left(\frac{\beta_{eff}}{5\%} \right)^{n} \tag{2.8}$$

where the exponent n is set to 0.3. Interpolation between tabulated values is therefore no longer required.

Codes specify limits for the application of this simplified method. In particular, the effective viscous damping β_{eff} is limited to a maximum value of 30% and bridge isolators must be provided with minimum recentring capabilities. The damping limit of 30% was introduced in AASHTO LRFD Guide Specifications for Seismic Isolation Design (AASHTO, 1999) at the same time as the damping coefficients. The changes were adopted based on the development of the NCHRP Project 12-49 provisions (MCEER/ATC-49, 2003). The proposed provisions intended to develop a new set of seismic design specifications which reflect the latest design philosophies (Lee Marsh et al. 2001). However, no explicit scientific basis was provided by the NCHRP Project 12-49 Team to support these changes.

In addition to the damping limits, current CSA-S6 and AASHTO codes also have minimum lateral restoring force criteria to ensure a minimum recentring capability to the system. CSA-S6-06, clause 4.10.10.2 reads: "… The isolation system shall be configured to produce a lateral restoring force such that the lateral force at the design displacement is greater than the lateral force at 50% of the design displacement by at least 0.025W". In AASHTO (2009, 2010), the minimum restoring force at 50% of the design displacement is 0.0125W, which is less stringent than in CSA S6. Unfortunately, the codes do not provide a clear scientific basis for these criteria although it is speculated that these criteria are intended to result in systems with a non-zero post-elastic stiffness. As a result of the difference between both codes, the design of isolated bridges in Canada may be limited more frequently by this requirement when compared to engineering practice in the US.

European Provisions

In Eurocode 8 (EC8), the fundamental mode method corresponds to the equivalent static force method found in NA codes. Although the methods are essentially the same, Eurocode 8 incorporates a displacement-based design approach where performance objectives are explicitly tied to the displacement response. In that approach, the displacement is obtained from the elastic acceleration spectrum using a pseudo-spectral relation, as in the case in NA codes. However, EC8 provides displacement spectral data for long period structures which is more appropriate for the design of seismically isolated structures. The need for a displacement spectrum for long period structures was highlighted by Tolis and Faccioli (1999), and Bommer et al. (2000b) proposed a simple method to obtain the required displacement spectrum.

The method, which was later adopted by EC8, is illustrated in Figure 2.2. Up to the corner period T_D, which defines the beginning of the constant displacement plateau, the elastic displacement is obtained by direct transformation of the elastic acceleration spectrum and the NA codes and EC8 provide identical simplified design approaches.

For the cases where the effective period exceeds 4 s, the plateau of the maximum displacement response is lengthened to the corner period T_E followed by the segment T_E-T_F which links the maximum displacement to the peak ground displacement (PGD) plateau. The PGD value is defined as a function of the peak ground acceleration (PGA). Consequently, the development of

spectral segments beyond T_D, where the spectrum is capped by the constant displacement plateau (T_D-T_E) and PGD, represents a significant difference when compared to the NA codes.

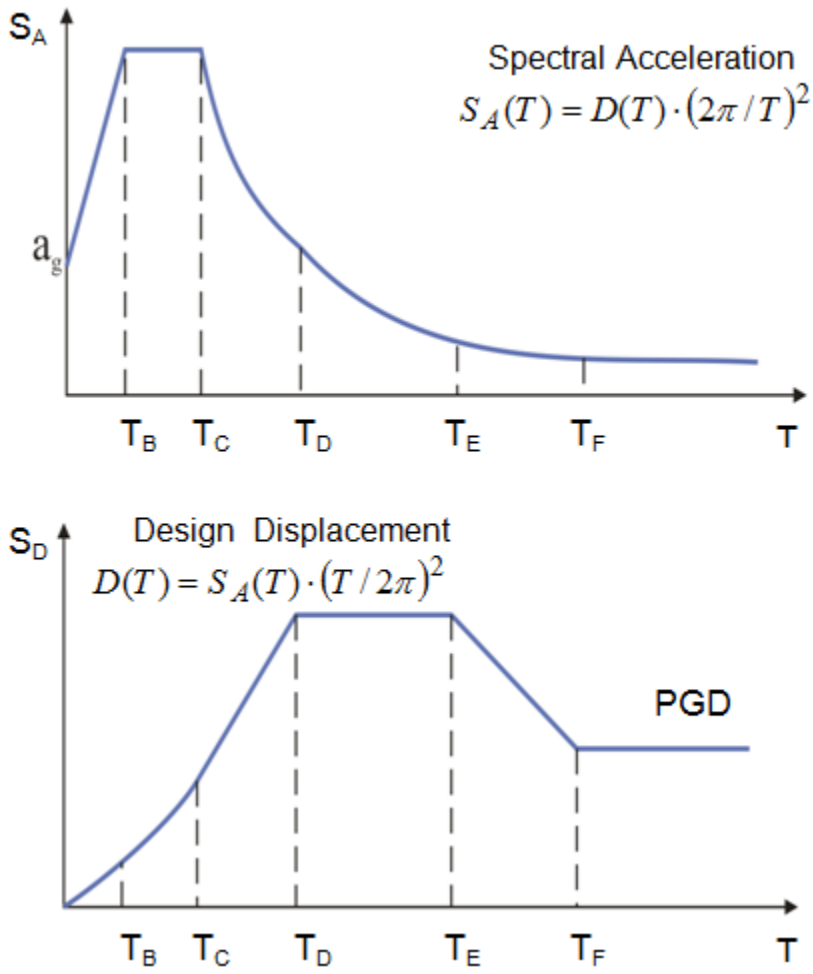

Figure 2.2 Acceleration (S_A) and displacement (S_D) design spectra in Eurocode 8

Accordingly, the EC8 approach produces less conservative displacement predictions compared to AASHTO and CSA-S6 for long period structures. Recently, Bommer and Pinho (2006) emphasized the inconsistency in anchoring T_D to a fixed value and suggested that additional research be performed to consider larger values of T_D. Akkar and Bommer (2007) also confirmed the need to modify the EC8 displacement response spectra because of "a gross underestimation leading to dangerously low spectral displacements at longer periods".

Another difference between the NA and EC8 codes is that EC8 specifies two design spectra to account for the differences in the effects of large and small-to-moderate earthquake events: Type 1 spectrum for surface wave magnitudes $M_S > 5.5$ and Type 2 spectrum for $M_S \leq 5.5$.

Similar to the American codes, Eurocode 8 accounts for the effect of high equivalent damping resulting from the response of seismic isolation systems by using a damping correction factor η . This factor corresponds to the inverse of the damping coefficient B ($\eta = 1/B$). In 1996, the EC8 Part 2 draft (CEN, 1996) incorporated the relationship:

$$\eta = \left(\frac{7\%}{2\% + \beta_{eff}} \right)^{0.35} \tag{2.9}$$

As shown in Figure 2.3, Equation (2.9) (CEN, 1996) produces almost identical reduction effects on spectral values for damping ratios up to 50% damping when compared to Equation (2.8) with $n = 0.3$ (AASHTO).

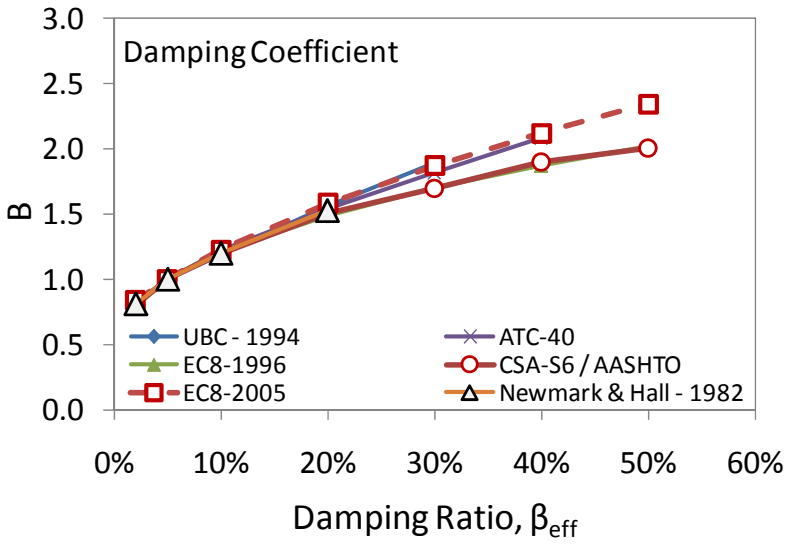

Figure 2.3 Damping coefficient in different seismic codes

In 1999, Tolis and Faccioli, aiming at extending the current code specifications, particularly for the displacement-based approach in EC8, proposed a new less conservative expression for the damping correction factor (Equation 2.4). They realized that for displacement response spectra, specially for periods beyond about 2 s, a larger damping reduction effect may be considered. However, these observations were mainly based on a set of time histories recorded during the

1995 Hyogoken-Nanbu (Kobe, M = 6.9) earthquake where records with fault distances greater than 35 km were excluded. Only five European records with a fault distance ranging between 2 and 20 km and magnitudes $5.3 \leq \text{Ms} \leq 6.7$ were analysed. Tolis and Faccioli (1999) recognized that the results provided by their study had a limited background and were subject to the criticism.

$$\eta = \left(\frac{15\%}{10\% + \beta_{eff}} \right)^{0.5} \tag{2.10}$$

Bommer et al. (2000b) proposed an alternative expression being developed by regression analyses using a much larger dataset of European ground motions, which were previously used by Ambraseys et al. (1996), with surface-wave magnitudes from 4.0 to 7.9 and distances up to 260 km. This expression is specified in the current edition of EC8 Part 2 (CEN, 2005):

$$\eta = \left(\frac{10\%}{5\% + \beta_{eff}} \right)^{0.5} \tag{2.11}$$

The intent of Equation (2.11) was to provide values that were more representative of the European seismicity. With respect to the previous EC8 draft edition (CEN, 1996), these factors offer more of a reduction effect for damping ratios of 20% and greater. In EC8, Equation (2.11) is used for both spectra. However, Bommer and Mendis (2005) indicated that damping response reduction effects for Type 2 spectra could be significantly lower than for Type 1 spectra.

In contrast, in spite of having been recently reexamined, the factors prescribed in both the AASHTO and CSA-S6 remain unchanged and are the same for all North American regions. They are also defined as independent of the structure's natural period. However, Atkinson and Pierre (2002) demonstrated that for a period range of 0.05 - 2.0 s the damping coefficient decreases with the period of structures. Hatzigeorgiou (2010) drew special attention to flexible structures with longer periods for which damping coefficients decrease significantly and may equal almost unity (no reduction effect). These observations are in overall agreement with the explanation given by Chopra (2007) that spectral values in ranges approaching the peak ground acceleration and the peak ground displacement are irrespective of damping given that for $T \to 0$, the structure moves rigidly with the ground and for $T \to \infty$, the structural mass stays still while

the ground underneath moves. It is clear that such an explanation has a scarce scientific basis what confirms the need for a more comprehensive study of the period dependant nature of damping coefficients.

Bommer and Mendis (2005) demonstrated that the influence of damping on spectral values increases with increasing earthquake magnitude and distance and decreases for softer site conditions, also suggesting an increase with ground motion duration. Dependency of the damping coefficient on seismic characteristics has also been observed in other studies (e.g., Atkinson and Pierre, 2004; Cameron and Green, 2007; and Stafford et al., 2008).

These observations suggest that damping coefficients may vary across North America due to the differences in ground motions from earthquakes occurring in western North America (WNA) and eastern North America (ENA). In the more active WNA seismic regions, earthquakes occur more frequently than in the stable continental region of ENA where, accordingly, more energy is released per unit area (stress drop) when an earthquake occurs. Due to the stiffer, denser, and less fractured bedrock in ENA, high-frequency seismic waves generated from earthquakes attenuate more slowly with distance than in WNA. Consequently, seismic records from earthquakes at same magnitude and distance (M-R) in WNA and ENA exhibit different amplitudes, frequency content, predominant periods and durations. These differences may impact on structural response, as observed by Taylor (1999) and Naumoski (2000).

The above discussion demonstrates that there is a need to carefully review the proposed damping coefficients B for western and eastern North American regions in order to better address the spectral shape, and different ground-motion characteristics.

2.2 Critical Review of Limitations of the Equivalent Linearization Method

As discussed in the previous section, the coefficients B on which the code simplified analysis method relies are derived empirically using the elastic response of a viscously damped SDOF system. The coefficients B are calibrated so the accuracy of the simplified method is enhanced by reducing errors in response prediction. The sources of the method inaccuracy may be both the local damping reduction effect and the *equivalent linearization method* which is an intrinsic part

of the code method. A better understanding of the source of these inaccuracies can be reached by investigating solely the *equivalent linearization method.*

Over time various studies have been carried out in order to validate and enhance the method of equivalent linearization or the substitute-structure method. The technique of defining a linear system through effective linear parameters as currently specified in AASHTO and CSA-S6-06 (presented previously in this section (Equations 2.1 to 2.4)) has been questioned because of a limited understanding of the actual sources of errors produced during response estimates. The accuracy problems related to this method were attributed to different physical phenomena and various empirical formulae have been proposed to better approximate the inelastic response of bilinear systems.

Iwan and Gates (1979) proposed an empirical method of linearization for inelastic response spectra. Their research aimed to address the effects of deterioration, stiffness degradation, cracking and ductility. The equivalent linear system was defined by equivalent damping and effective linear period found by optimizing a root mean square (RMS) error between the elastic and inelastic responses. In 1980, Iwan presented an improved empirical formulation for response approximation of structures within the mid-period range of 0.4-4.0 s and ductility range of 2-8. Although the ductility range up to 8 represents severe damage for conventional structures, the response of seismically isolated structures may be characterized much larger ductility ratios.

Hwang and Sheng (1994) examined the formulation specified in 1991 by AASHTO (same as in the current AASHTO and CSA S6-06 provisions) for simplified equivalent analyses of isolated bridges. They claimed that these provisions may not be appropriate given that for higher ductility ratios, the expression of equivalent damping (Equation 2.4)) results in low damping values. As shown in Figure 2.4 for post-yielding ratio $\alpha > 0$, the equivalent damping ratio (Equation 2.4) decreases with the ductility ratio after the curve peak is reached. Researchers presumed that the energy dissipated by the isolators becomes larger with increase of the inelastic response and considering a smaller damping ratio for this case is unrealistic. They used data obtained by Iwan and Gates (1979) to carry out comparative analyses and proposed an alternate formulation for the effective period (effective stiffness). With respect to Iwan's model, an exponential function instead of a power function was adopted.

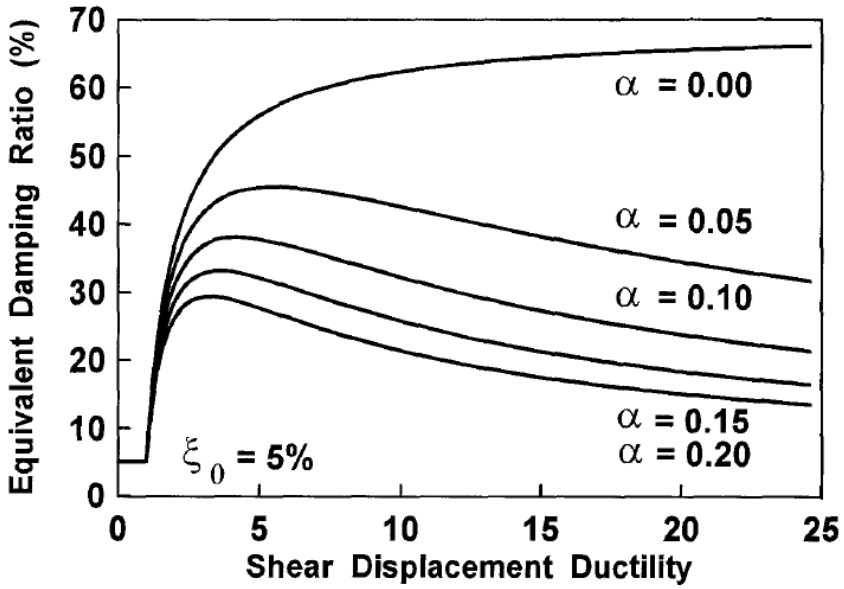

Figure 2.4 AASHTO equivalent damping ratio as a function of shear displacement ductility ratio (Hwang and Sheng, 1993)

In 1996, Hwang and Chiou proposed an equivalent model formulation for analyzing isolated bridges with an extended ductility range up to 50. The empirical formulation was established by modifying the AASHTO specifications for the analyses of bridge structures isolated with lead-rubber bearings.

Aiming to extend the displacement-based design procedure for bridges isolated with LRB, Jara and Casas (2006) proposed a logarithmic expression for the effective damping. These researchers concluded that for LRB bridge isolation, the empirical expression improves the displacement estimate of the equivalent linear model providing a lower data scatter.

Dicleli and Buddaram (2007) assessed the accuracy of equivalent linear analyses methods for the design of seismically isolated bridges subjected to near-fault ground motions with forward directivity effects. The researchers stated that to improve the accuracy, the effective damping expression must incorporate ground-motion parameters: magnitude and fault distance as well as the system parameters: post-yielding stiffness and yield strength. To consider these parameters, they proposed an equivalent damping expression by multiplying the current AASHTO formulation by two empirically obtained functions. However, a large dispersion was observed in the results obtained by using the proposed expression and researchers suggested the use of equivalent analyses only for the preliminary design of bridges located in near-fault zones.

In 2011, Mavronicola and Komodromos assessed the suitability of the equivalent linear analyses by comparing different equivalent models proposed in the literature and previously discussed in this chapter. The six equivalent methods compared by researchers are presented in Table 2-2.

Table 2-2 Effective formulations for equivalent linearization (compared in Mavronicola and Komodromos, 2011)

Method	Effective Formulation for Equivalent Linearization
AASHTO (1991)	$k_{eff} = k_u \dfrac{1+\alpha\mu-\alpha}{\mu}$ $\beta_{eff} = \dfrac{2}{\pi}\cdot\dfrac{(\mu-1)\cdot(1-\alpha)}{\mu\cdot(1+\alpha\mu-\alpha)}$
Iwan (1980)	$k_{eff} = k_e \cdot \left[1+0.121\cdot(\mu-1)^{0.939}\right]^{-2}$ $\beta_{eff} = \beta_0 + \cdot 0.0587\cdot(\mu-1)^{0.371}$
Hwang and Sheng (1993)	$k_{eff} = k_e \cdot \left\{1+\ln\left[1+0.13\cdot(\mu-1)^{1.137}\right]\right\}^{-2}$ $\beta_{eff} = \beta_0 + \cdot 0.0587\cdot(\mu-1)^{0.371}$
Hwang and Chiou (1996)	$k_{eff} = k_u \cdot \left[\dfrac{\mu}{1+0.15\cdot(\mu-1)}\right]^{-1} \cdot \left(1-0.737\cdot\dfrac{\mu-1}{\mu^2}\right)^{-2}$ $\beta_{eff} = \dfrac{1.7\cdot\left(1-\dfrac{1}{\mu}\right)}{\pi\cdot\left[1+0.15\cdot(\mu-1)\right]}\cdot\dfrac{\mu^{0.58}}{4.5}$
Jara and Casas (2006)	$k_{eff} = k_u \dfrac{1+\alpha\mu-\alpha}{\mu}$ $\beta_{eff} = 0.05 + \cdot 0.05\cdot\ln(\mu)$
Dicleli and Buddaram (2007)	$k_{eff} = k_u \dfrac{1+\alpha\mu-\alpha}{\mu}$ $\beta_{eff} = NF_1\cdot NF_2\cdot\dfrac{2}{\pi}\cdot\dfrac{(\mu-1)\cdot(1-\alpha)}{\mu\cdot(1+\alpha\mu-\alpha)}$

Mavronicola and Komodromos stated that the peak responses computed by the six linearized models may differ significantly with respect to the "exact" response from NL THA. However, the researchers observed generally conservative response estimates and they suggested the use of the equivalent linear analyses only in the preliminary design stages. Figure 2.5 presents partial results from these comparative analyses.

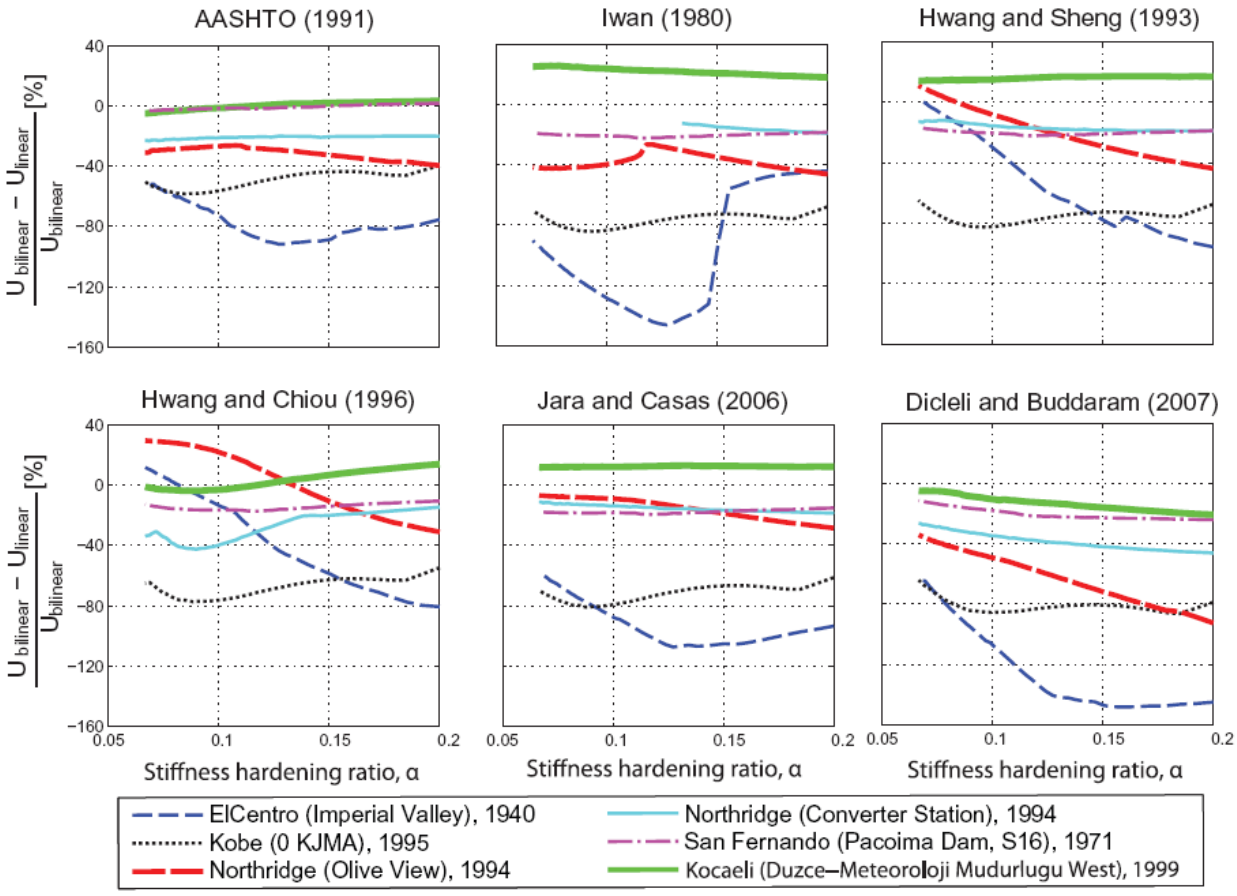

Figure 2.5 Relative errors of the maximum relative displacements at the isolation level considering the proposed linearized models, varying the post-yielding ratio, under the selected earthquake excitations scaled to PGA = 0.8 g (Mavronicola and Komodromos, 2011).

Two other simplified methods that use an equivalent SDOF (single-degree-of-freedom) model are specified in the FEMA 356 (2000) Prestandard and Commentary for the Seismic Rehabilitation of Buildings and the ATC-40 (ATC, 1996c) report, Seismic Evaluation and Retrofit of Concrete Buildings. The method specified in FEMA 356 is termed Displacement Coefficient Method. This method relies on the use of empirically derived factors to modify the displacement response of an elastic SDOF system. The Capacity-Spectrum Method of ATC-40 is

another linearization method alternative. In this method, an equivalent linear SDOF system is formed based on the relationships for the effective period and damping that were empirically derived as a function of ductility. However, the estimates of maximum displacement obtained with these two methods can diverge significantly from one another.

To improve the practical application of these two methods (FEMA 356 and ATC-40), the procedures were revised by the ATC-55 Project. The results of these efforts were summarized in the report FEMA 440 (2005), Improvement of Nonlinear Static Seismic Analyses Procedures. For FEMA 356, the resulting suggestions concern adjustments of the relationships that define the method coefficients. For ATC-40, it was proposed to improve formulation of the effective period and damping. The results obtained using improved methods were compared to results from the NLTHA (Nonlinear Time-History Analyses). The NLTH analyses were carried out using ten ground motion records from two Californian earthquakes (Imperial Valley 1979/10/15 23:16 and Landers 1992/06/28 11:58) on each SDOF system. Nine bilinear SDOF systems were configured using three initial period T = [0.2, 0.5, and 1.0 s], three response modification factors R = [2, 4, and 8] and a post-yielding ratio α=0.05.

It was recognized that these results do not represent a large statistical sample and to draw broad general conclusions. However, they provide an insight into the variations among the methods. Figure 2.6 presents three graphs plotted for each of the three initial periods: 0.2, 0.5, and 1.0 s. The maximum displacement estimates resulting from different method are compared in the FEMA 440 report as a function of the response modification factor R. The authors observed that in some cases, the results obtained from these methods differ by as much as a factor of two. Also, they suggested that this simplified methods should not be used for ductility ratios greater than μ = 10. In addition, it was concluded that the dispersion of displacement responses from NLTHA was relatively large and to reach a relatively meaningful conclusions a larger number of NLTHA may be required.

The above discussions suggest that different methods of equivalent linearization may result in response estimates which can differ significantly from one another. Although being developed on an empirical basis, these methods can significantly underpredict the response of actual inelastic structures, in particular for ductility ratios greater than μ = 10. This can cause concern to the practical application of these methods for design of isolated bridges which are expected to

be prone to large inelastic excursions (or large ductility responses). This indicates that there is a need in more comprehensive study to improve our understanding of the sources of the inaccuracy.

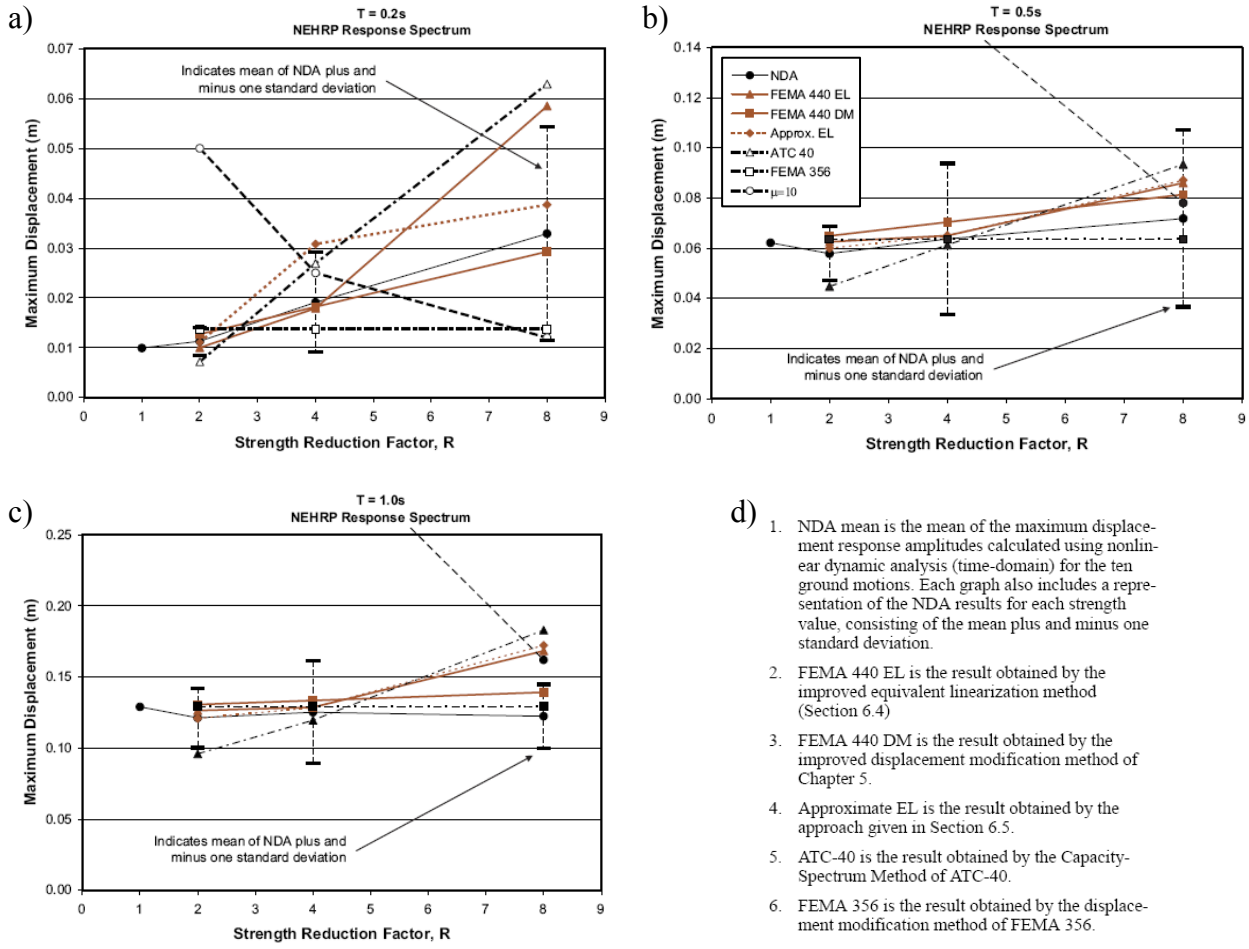

Figure 2.6 Comparison of responses calculated using various methods, response spectra scaled to the NEHRP spectrum, and values calculated for the NEHRP spectrum (FEMA 440): a) SDOF with $T = 0.2$ s; b) SDOF with $T = 0.5$ s; SDOF with $T = 1.0$ s; and d) methods description

2.3 Seismic Protection Mechanism and Devices

The design of isolated bridges using current seismic code provisions (CSA-S6-06 and AASHTO) implies the use of different seismic protection mechanism and devices. The majority of the seismic isolators used to protect bridges in North America are either elastomeric or sliding bearings. A common elastomeric isolator is the lead-rubber bearing (LRB) which is comprised of thin layers of rubber vulcanized onto steel shims and with a lead core installed in the centre

(Figure 2.7). The low lateral stiffness (post-yield slope, k_d) is provided by the rubber material, while the isolator strength (F_y) and the energy dissipation capacity are obtained through the inelastic response of the lead core under lateral seismic motion. Commonly used sliding isolators are either the friction-pendulum isolator (FPI) or the flat sliding isolator (FSI). In both systems, energy dissipation is provided through sliding friction between a stainless steel interface and a compound slider surface.

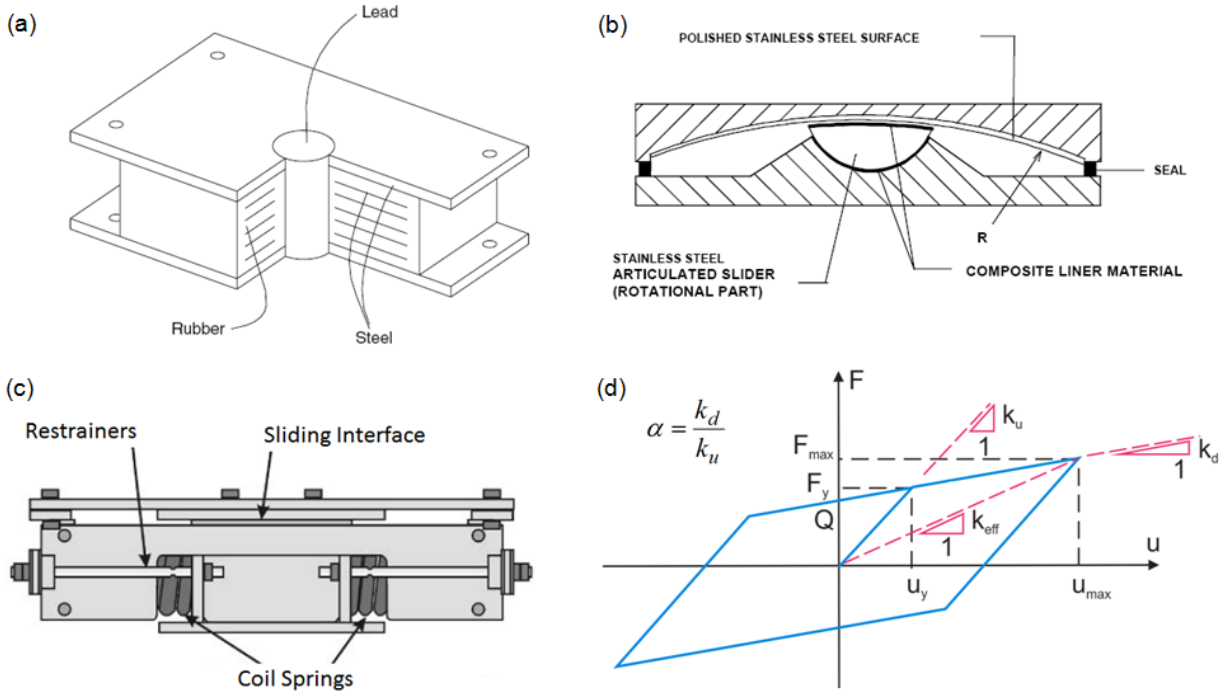

Figure 2.7 Seismic isolators with restoring force: a) LRB (Buckle et al., 2006); b) FPI (Buckle et al., 2006); c) FSI with restoring force (Dion et al., 2012); and d) bilinear force-displacement relationship, $0 < \alpha < 1$.

The restoring force capacity is ensured by the pendulum mechanism on a concave dish for the FPIs and by supplemental lateral spring elements that are installed in parallel with the sliding surface for FSI devices. The horizontal force-displacement response for these three isolators can be idealized by a bilinear hysteretic shape as illustrated in Figure 2.7(d) (Skinner et al. 1993; Constantinou et al. 1993; Naeim and Kelly 1999; and Dion et al. 2012). It is understood that the actual nonlinear response of isolated devices may deviate from the perfectly bilinear response

assumed in this research. The effects of such deviations are not considered in this thesis and could be examined in a separate study.

FSI devices with no or limited recentring capacity are typically used as fuse elements to limit the seismic forces transmitted to substructure elements. They are particularly effective when inserted between the superstructure and the bridge piers, especially in the case of existing bridge columns having limited lateral capacity. Sliding isolators also usually have a very small activation displacement u_y due to a high pre-yielding stiffness, k_u (Zhang et Huo, 2009). However, this very short range of elastic displacements can be lengthened when the sliding interface is combined in series with an elastomeric pad as illustrated in Figure 2.8. The added flexibility can be adjusted as a function of the height of the elastomeric pad.

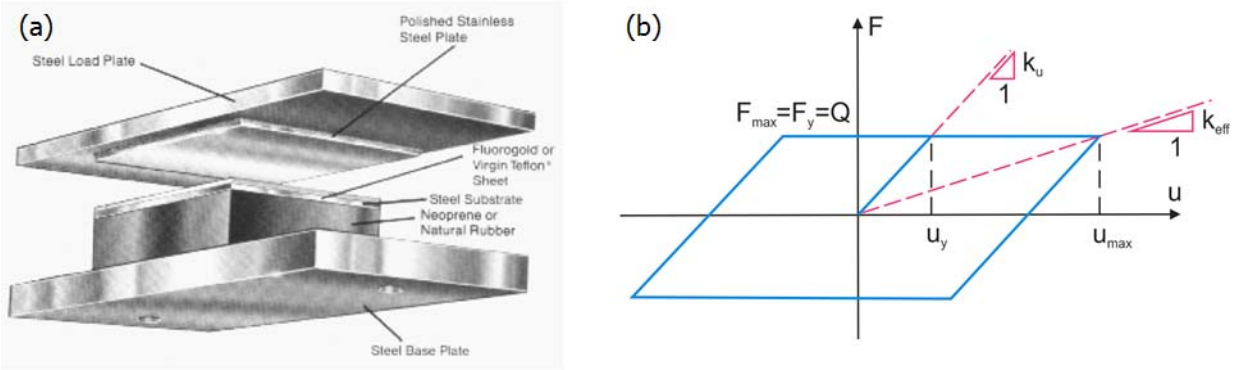

Figure 2.8 Flat sliding seismic isolator without restoring force: a) seismic energy products (www.sepbearings.com); b) bilinear force-displacement relationship, α = 0

LRBs inherently exhibit higher restoring forces upon yielding and the system is therefore more suitable at the abutments where greater lateral resistance can be more easily developed. The typical post-yielding stiffness ratio is $\alpha = 0.1$ (http://www.dis-inc.com/technical.html). While isolators are mainly used to control seismic induced forces, their energy dissipation capacity contributes in reducing the structure's relative displacements across the isolation layer. In design, the effect of this damping is considered in terms of equivalent damping which is added to the inherent damping of the structure.

The addition of velocity dependent viscous dampers can further enhance the damping of the system and contribute to the response control of the isolated structure. Both linear ($n = 1$) or nonlinear ($n < 1$) viscous dampers can be used for this purpose (Figure 2.9). Maximum forces

from viscous dampers and isolators can occur nearly simultaneously in the inelastic range and it is more practical to locate dampers at the abutments, rather than at the piers, to limit the forces on the bridge piers.

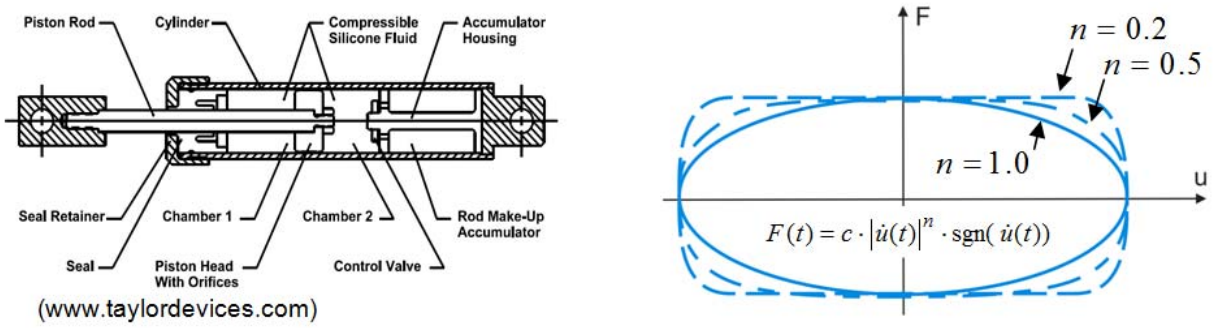

Figure 2.9 Viscous damper

2.4 Summary

In this chapter, a review of the simplified code methods for seismic design of isolated bridges in North American regions was presented. The simplified methods are currently specified in the CAN/CSA-S6-06 Canadian Highway Bridge Design Code (CSA 2006) in Canada and the AASHTO LRFD Seismic Bridge Design Specifications in the United States (AASHTO 2009, 2010). These methods rely on damping coefficients B and the technique of equivalent linearization. The discussion demonstrated that there is a need to carefully review the proposed damping coefficients B for western and eastern North American regions in order to better address the spectral shape, and different ground-motion characteristics.

It was also shown that the sources of the method's inaccuracy may be both the local damping reduction effect and the *equivalent linearization method*. Different equivalent linearization methods were then discussed. These discussions suggest that methods of equivalent linearization may result in response estimates which can differ significantly from one another.

The reviewed studies confirm that the equivalent linearization methods are subject to limitations that may affect the accuracy in predicting the peak displacement response. These observations emphasize the concern to cover a broad range of practical applications when bridges are

retrofitted using different isolation and damping devices. This indicates that there is a need in a more comprehensive study to improve our understanding of the sources of the inaccuracy and how to extend the method's applicability limits.

Finally, isolation and damping devices which are commonly used in North American practice for seismic protection of bridges are reviewed. The main characteristics and expected performance of the isolation and damping devices were outlined. These seismic protection devices are further considered in this research for developing different configurations of isolated bridges.

Chapter 3: Analytical Model and Numerical Platform for Nonlinear Time-History Analysis of Isolated and Damped Bridges

3.1 Introduction

In this chapter, a new analytical model and a methodology to carry out nonlinear simplified isolated bridge analysis are presented. The approach aims at streamlining the modeling assumptions with the purpose of developing a proper and effective, yet simple analytical model that can be used at the preliminary design stages for a fully equipped isolated bridge. The 2-DOF model proposed in this study represents a simple two-span bridge in its longitudinal direction. This is a simplified layout that can be expanded for bridges with more than two spans by making a few additional assumptions. This 2-DOF model can represent a wide range of bridge configurations that are typical of thousands of older bridges in North America that need to be upgraded to meet requirements of current seismic provisions.

Based on this analytical model, a computer program IS-Bridge was written in MATLAB code. This numerical analysis tool was developed in order to simulate the nonlinear structural behaviour of isolated bridges equipped with different seismic protective devices. The main motivation for developing this program was the need to carry out extensive parametric analyses in the framework of the present research study. While SDOF models were adopted to examine and enhance the code simplified method currently specified in CAN/CSA-S6-06 (Chapters 5 to 8), the 2-DOF models were employed for developing and validating the dual-level seismic protection concept (Chapter 10).

After introducing the modelling assumptions and model formulation, a non-iterative direct solution is proposed to analytically solve this model at each discrete step of time-history analysis (THA). A less time-consuming computational process makes the program IS-Bridge much more advantageous with respect to numerous programs which rely on iterative schemes. An important aspect to be considered in the simulation of nonlinear structural behaviour of isolated bridges is the modelling of inherent damping. Different techniques of modelling the inherent damping for

nonlinear THA are discussed. An alternative approach for considering the inherent damping ratio proportional to the effective stiffness is presented. The ability of the model to simulate the structural behaviour of isolated bridges was validated through a bridge retrofit example. The IS-Bridge results from a nonlinear time-history analysis were compared to those obtained using a SAP2000 (CSI, 2009) model of the same structure.

3.2 Analytical Model for Isolated Bridges

With the exponential increase in computing power over the last two decades, a variety of numerical models have been developed and implemented for simulating the nonlinear response of isolated bridges. Increasingly complex and detailed structural models have been developed and have greatly enhanced our understanding of the response of such structures. Commercial software used for structural analysis such as, ETABS, SAP2000 and CSiBridge include elements for modeling damping and isolation devices. Detailed 3-D structural models have been adopted for a variety of projects (e.g., Zhang et al., 2004; Dicleli, 2006; Zhang and Huo, 2009). By analyzing a typical highway bridge having no skew, Zhang and Huo concluded that 2-D and 3-D models yield comparable results while 2-D models are significantly less computationally expensive. It is also arguable whether the extensive amount of information resulting from sophisticated 3-D analyses is necessary at the preliminary design stage of a project. The approach presented in this chapter is therefore aimed at streamlining the modeling assumptions with the purpose of developing a proper and effective, yet simple analytical model that can be used at the preliminary design stages. However, this approach can also be adopted for the final design stage when the code-prescribed criteria are met to use the simplified modeling assumptions.

3.3 Model Assumptions for Reference Bridge

The use of simple equivalent SDOF (single-degree-of-freedom) systems has been recognized for many decades as the simplest means of obtaining information on the dynamic response of isolated structures subjected to seismic excitations. For the analysis of bridge structures in the longitudinal direction, it is common practice to divide the structure into two model elements: the substructure and the superstructure. Most of the bridge mass is located at the level of the deck (superstructure), and the effect of the substructure mass is neglected when computing the dynamic response. Conversely, the stiffness of the substructure has a significant effect on the

structural behaviour and must be taken into account accurately. The superstructure is modelled as a rigid body with an infinite axial stiffness. In the case of straight bridges, the motion of the superstructure in the longitudinal and transverse directions can be considered as uncoupled. Making use of these simplifying assumptions, SDOF analyses can be used for the seismic analysis of most isolated highway overpass bridges. Thus, the entire bridge is represented as a simple oscillator that consists of the total mass lumped at the upper end of a single pole having the equivalent stiffness and damping properties of the bridge substructure. SDOF bridge models have typically been represented by the simple Kelvin-Voigt solid model shown in Figure 3.1, where k_1 and c_1 are the coefficients of lateral stiffness and viscous damping. Both coefficients represent the contribution of the substructure elements including piers, abutments, isolation and damping devices.

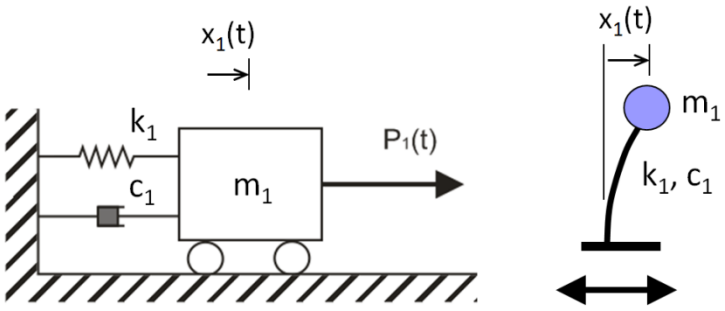

Figure 3.1 Kelvin-Voigt solid model and simple oscillator SDOF system

Accordingly, the lateral equivalent stiffness ($k_1 = k_{eq}$) of the entire substructure is determined for different bridge configurations by considering the contribution of all of the system's elements as shown in Figure 3.2. The figure presents only a few typical cases while other possible configurations also exist and can be represented by adopting the lateral equivalent stiffness k_{eq}.

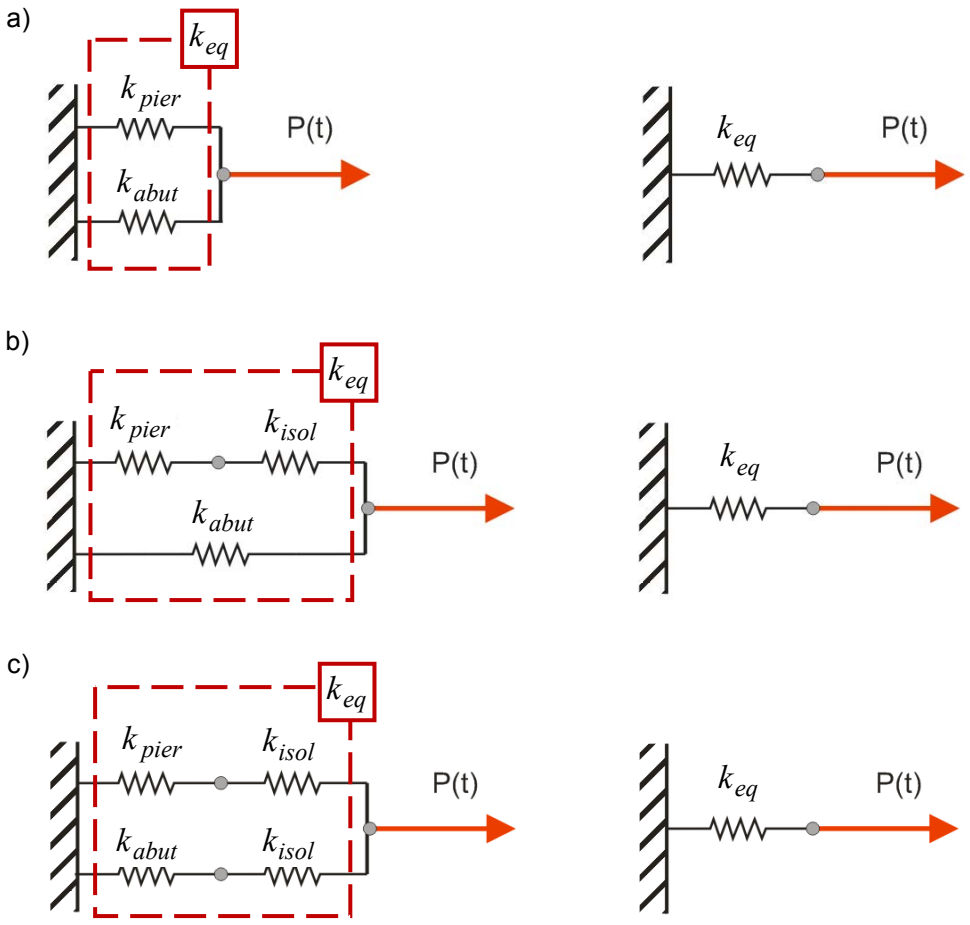

Figure 3.2 Equivalent stiffness for different bridge configurations: a) non-isolated bridge, b) bridge with isolation atop the piers and c) bridge with isolation atop the piers and abutments

For a simple non-isolated bridge model, the equivalent stiffness is determined as a sum of the total stiffness of all piers k_{pier} and the total stiffness of the two abutments k_{abut} (Equation (3.1). This bridge configuration is presented as two parallel springs in Figure 3.2(a).

$$k_{eq} = k_{pier} + k_{abut} \tag{3.1}$$

For a bridge model with isolation atop the piers, the equivalent stiffness is determined following Equation (3.2). In this expression, the first term represents two springs placed in series and it corresponds to the contribution of the piers and their isolators to the global system stiffness. The parameter $k_{isol,i}$ is the stiffness of all isolator devices installed on a given pier i and n is the number of piers. This bridge configuration is illustrated in Figure 3.2(b).

$$k_{eq} = \sum_{i=1}^{n} \frac{k_{pier,i} \cdot k_{isol,i}}{k_{pier,i} + k_{isol,i}} + k_{abut} \tag{3.2}$$

For a bridge model with isolation atop the piers and abutments, the equivalent stiffness is determined following Equation (3.3). Both terms of this expression represent two springs placed in series as shown in Figure 3.2(c). The first term corresponds to the stiffness contribution of the piers and their isolators while the second term represents the two abutments and their isolators. The parameter $k_{isol,j}$ is the stiffness of all isolator devices installed on the same abutment j .

$$k_{eq} = \sum_{i=1}^{n} \frac{k_{pier,i} \cdot k_{isol,i}}{k_{pier,i} + k_{isol,i}} + \sum_{j=1}^{2} \frac{k_{abut,j} \cdot k_{isol,j}}{k_{abut,j} + k_{isol,j}} \tag{3.3}$$

The use of equivalent viscous damping is also a widely accepted approximation in dynamic analysis: the different physical mechanisms contributing to seismic energy dissipation are numerically accounted for by means of a basic velocity-dependant damping mechanism. Given that the real damping of the structure is rarely known and its true properties can be assessed accurately only through testing, a damping coefficient proportional to the stiffness and mass of the structure, referred to as Rayleigh damping, is commonly used for numerical simulations. When SDOF bridge models are represented by the Kelvin-Voigt model, the damping dashpot can be associated only to the overall bridge inherent damping or dampers installed between the abutments and the deck. However, the use of the Kelvin-Voigt model is inappropriate when viscous dampers are acting between the piers and the deck or when different levels of inherent damping are adopted for the pier and its isolators. Tsopelas et al. (1996) used a simplified 2-DOF pier-deck model. This model takes into account different damping and stiffness configurations for an isolated pier as shown in Figure 3.3. It can be noted from this figure that viscoelastic behaviour of the pier is modeled using the Kelvin-Voigt solid model. For modeling isolators atop the piers, the Kelvin-Voigt solid model is extended by introducing a frictional element. As a result, the hysteretic behaviour of isolation and damping devices installed at the pier can be modelled in details.

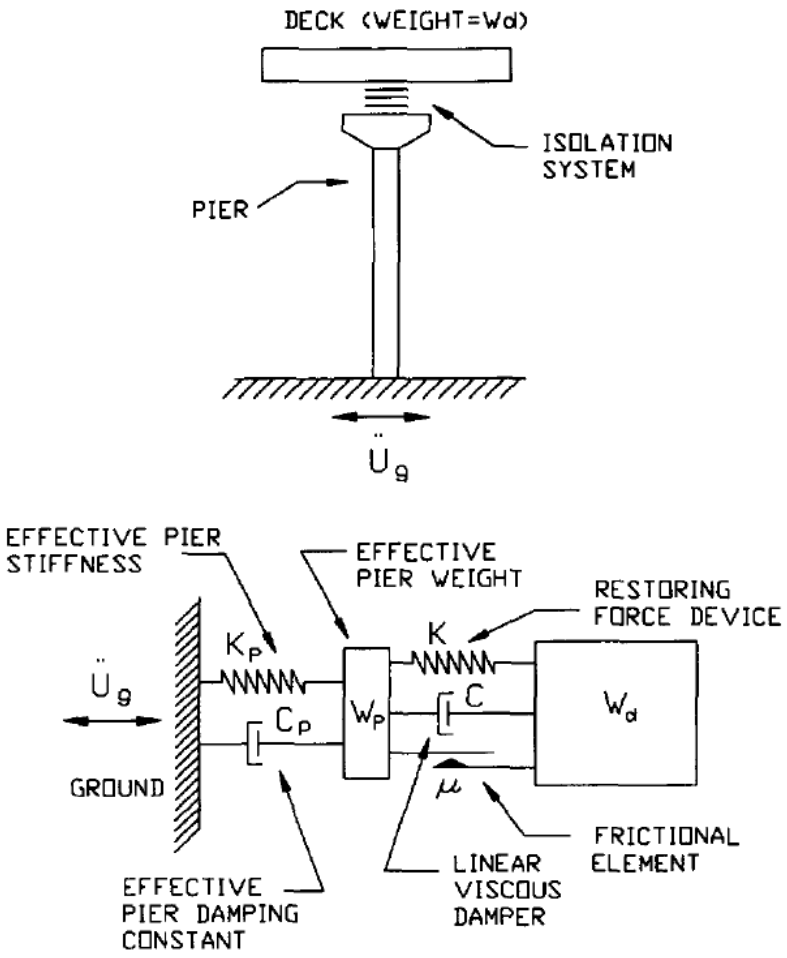

Figure 3.3 Pier-deck model (Tsopelas et al., 1996)

In the present study, the possibility of using seismic protective devices at any strategic location of the structure is investigated. Figure 3.4 presents an example for a reference bridge with isolation and damping devices installed at the abutments and at the piers. The corresponding analytical model is illustrated in Figure 3.5. It can be noted that complementing the pier-deck model proposed by Tsopelas et al. (1996), the model applied in the present study makes it possible to take into account properties of the protective devices at any location between the bridge substructure and superstructure.

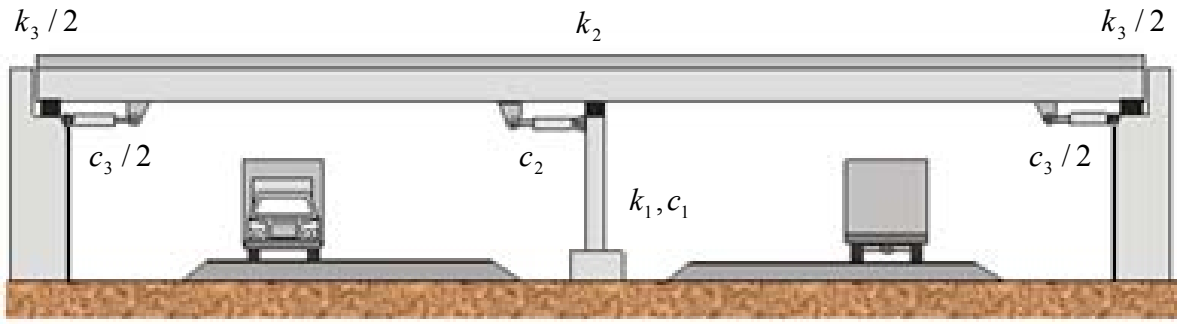

Figure 3.4 Example of fully equipped bridge

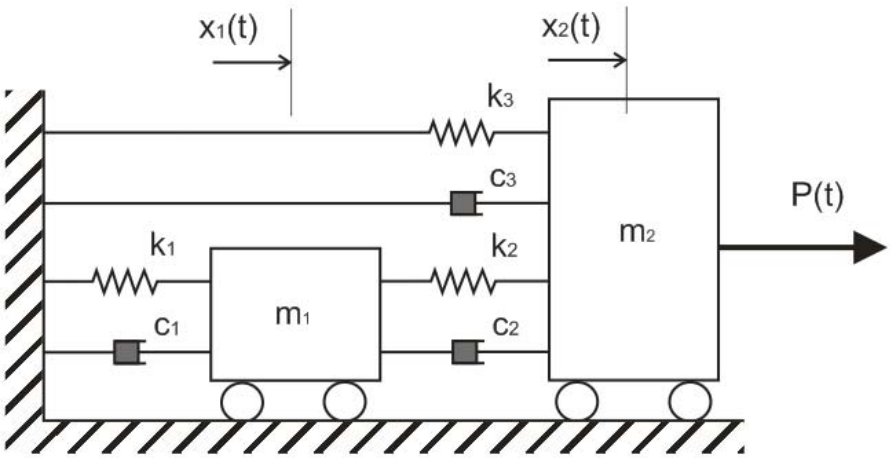

Figure 3.5 Bridge 2-DOF equivalent model

As a result, the analytical model adopted in this study is a further extension of the model proposed by Tsopelas et al. (1996) and consists of two masses linked to each another and to the ground level by standard parallel spring-dashpot systems as previously described for the Kelvin-Voigt model. This model can be described as an equivalent 2-DOF system with effective nonlinear properties assigned to the spring and dashpot elements. Consequently, a wide range of bridge configurations can be represented with this model by making a few assumptions as presented above.

3.4 Closed Form Solution and Computation Process

The dynamic equilibrium for a nonlinear SDOF system is formulated by using Newton's second law equation of motions (Equation (3.4)) which represents the sum of the forces acting on the system mass m_1 at the time t. The solution for the response of this system is obtained by solving the equation of motion for the displacement x_1 defined as a function of time t.

$$m_1\ddot{x}_1(t) + c_1\dot{x}_1(t) + k_1x_1(t) = -m_1\ddot{x}_g(t) \tag{3.4}$$

where $\ddot{x}_g(t)$ is the ground-motion acceleration time history. Consequently, the seismic force induced in the structure is given by $P_1(t) = -m_1\ddot{x}_g(t)$. Accordingly, the force balance resulting from interaction of inertial, damping, spring and induced forces is presented as:

$$F_{I1}(t) + F_{D1}(t) + F_{S1}(t) = P_1(t) \tag{3.5}$$

In spite of the attractive simplicity of the Kelvin-Voigt solid model, such a model can only be applied as far as the bridge model incorporates an overall effective level of damping represented by a dashpot c_1. In the case where different levels of damping must be considered for a more accurate simulation, the use of a 2-DOF model is essential and the corresponding damping properties are assigned to dashpots denoted as c_1, c_2, and c_3. This model involves the participation of two masses denoted as the mass of the substructure, m_1, and that of the superstructure, m_2. However, the inertial forces generated by the mass of the substructure m_1 are relatively small compared to those generated by the superstructure mass. Therefore, for this model, m_1 is considered to be a fictitious mass and the corresponding inertial forces generated by the pier are assumed to be zero. Nonetheless, the term m_1 is still kept in further analytical developments. The model inelastic behaviour is obtained by assigning nonlinear properties to the springs k_1, k_2, and k_3.

The equations of motion for the 2-DOF model are defined in the following matrix form:

$$[M]\{\ddot{x}\} + [C]\{\dot{x}\} + [K]\{x\} = -[M]\{r\}\ddot{x}_g \tag{3.6}$$

where the dynamic coupling vector, mass matrix, damping matrix and stiffness matrix are defined as follows:

$$\{r\} = \begin{Bmatrix} 1 \\ 1 \end{Bmatrix} \tag{3.7}$$

$$[M] = \begin{bmatrix} m_1 & 0 \\ 0 & m_2 \end{bmatrix} \tag{3.8}$$

$$[C] = \begin{bmatrix} (c_1 + c_2) & -c_2 \\ -c_2 & (c_2 + c_3) \end{bmatrix} \tag{3.9}$$

$$[K] = \begin{bmatrix} (k_1 + k_2) & -k_2 \\ -k_2 & (k_2 + k_3) \end{bmatrix} \tag{3.10}$$

The same equations of motion are rewritten as a force equilibrium matrix:

$$\{F_I\} + \{F_D\} + \{F_S\} = \{P\} \tag{3.11}$$

with inertial forces:

$$\{F_I\} = \begin{bmatrix} m_1 & 0 \\ 0 & m_2 \end{bmatrix} \begin{Bmatrix} \ddot{x}_1 \\ \ddot{x}_2 \end{Bmatrix} = \begin{Bmatrix} m_1 \ddot{x}_1 \\ m_2 \ddot{x}_2 \end{Bmatrix} \tag{3.12}$$

damping forces:

$$\{F_D\} = \begin{bmatrix} (c_1 + c_2) & -c_2 \\ -c_2 & (c_2 + c_3) \end{bmatrix} \begin{Bmatrix} \dot{x}_1 \\ \dot{x}_2 \end{Bmatrix} = \begin{Bmatrix} c_1 \dot{x}_1 - c_2 (\dot{x}_2 - \dot{x}_1) \\ c_2 (\dot{x}_2 - \dot{x}_1) + c_3 \dot{x}_2 \end{Bmatrix} = \begin{Bmatrix} F_{D1} - F_{D2} \\ F_{D2} + F_{D3} \end{Bmatrix} \tag{3.13}$$

and spring forces:

$$\{F_S\} = \begin{bmatrix} (k_1 + k_2) & -k_2 \\ -k_2 & (k_2 + k_3) \end{bmatrix} \begin{Bmatrix} x_1 \\ x_2 \end{Bmatrix} = \begin{Bmatrix} k_1 x_1 - k_2 (x_2 - x_1) \\ k_2 (x_2 - x_1) + k_3 x_2 \end{Bmatrix} = \begin{Bmatrix} F_{S1} - F_{S2} \\ F_{S2} + F_{S3} \end{Bmatrix} \tag{3.14}$$

Substituting the equations defining the forces (3.12), (3.13), and (3.14) in the force equilibrium Equation (3.11), the following solution is obtained:

$$\begin{Bmatrix} F_{I1} \\ F_{I2} \end{Bmatrix} + \begin{Bmatrix} F_{D1} - F_{D2} \\ F_{D2} + F_{D3} \end{Bmatrix} + \begin{Bmatrix} F_{S1} - F_{S2} \\ F_{S2} + F_{S3} \end{Bmatrix} = \begin{Bmatrix} -m_1 \ddot{x}_g \\ -m_2 \ddot{x}_g \end{Bmatrix} \tag{3.15}$$

$$m_1\ddot{x}_1 + c_1\dot{x}_1 - c_2(\dot{x}_2 - \dot{x}_1) + k_1x_1 - k_2(x_2 - x_1) = -m_1\ddot{x}_g$$

$$m_2\ddot{x}_2 + c_2(\dot{x}_2 - \dot{x}_1) + c_3\dot{x}_2 + k_2(x_2 - x_1) + k_3x_2 = -m_2\ddot{x}_g$$

Assuming $m_1 = 0$:

$$c_1\dot{x}_1 - c_2(\dot{x}_2 - \dot{x}_1) + k_1x_1 - k_2(x_2 - x_1) = 0 \tag{3.16}$$

$$m_2\ddot{x}_2 + c_2(\dot{x}_2 - \dot{x}_1) + c_3\dot{x}_2 + k_2(x_2 - x_1) + k_3x_2 = -m_2\ddot{x}_g$$

Using Equations (3.16) instead of (3.15), the 2-DOF model is reduced to a SDOF system or, more precisely, a single-mass 2-DOF system. With this transformation, it is possible to exclude the acceleration term $\ddot{x}_1$. As a result, an exact analytical solution is obtained for each time step by simultaneously solving the two Equations (3.16). In this case, there is no need to approximate the system solution by an iterative method. In turn, the response of DOF 1 (position between the pier and the isolator) is subsequently solved for using the corresponding displacement, velocity and acceleration values obtained for DOF 2.

In the above solution, all three dashpots were defined by the equivalent linear damping mechanism in which the damping force is proportional to the relative velocity. The nonlinear behaviour of viscous dampers is commonly modeled using an equivalent linear damping model. This technique is still broadly accepted today when the actual damper properties are unknown or the dampers are assumed to behave linearly to make the computational process simpler. However, the real damper properties specified by the manufacturer can be incorporated into the computational model to obtain more realistic structural behaviour. For this reason, a nonlinear damping model having damping force F_D proportional to the velocity with a constant exponent is adopted to define the behaviour of viscous dampers in this study:

$$F_D = sign(\dot{u})\, c\, |\dot{u}|^n \tag{3.17}$$

where $\dot{u}$ is the relative velocity between two ends of a damper and α is the velocity exponent ranging from 0.2 to 2. For the exponent $n = 1$, the damping model represents a linear response that is directly proportional to the relative velocity.

In this study, an equivalent linear damping model is assumed for the inherent damping response of the pier, while a nonlinear damping behaviour is adopted for each of the two supplemental dampers located between the piers and the abutments. Consequently, the corresponding damping forces are determined as:

$$F_{D1}(t) = c_1 \dot{u}_1(t)$$

$$F_{D2}(t) = sign(\dot{u}_2(t))\; c_2\; |\dot{u}_2(t)|^{n2} \tag{3.18}$$

$$F_{D3}(t) = sign(\dot{u}_3(t))\; c_3\; |\dot{u}_3(t)|^{n3}$$

where, according to the bridge model configuration that is considered in this model, relative displacements, velocities and accelerations are defined through the corresponding absolute quantities as:

$$u_1 = x_1;\; \dot{u}_1 = \dot{x}_1;\; \ddot{u}_1 = \ddot{x}_1$$

$$u_2 = x_2 - x_1;\; \dot{u}_2 = \dot{x}_2 - \dot{x}_1;\; \ddot{u}_2 = \ddot{x}_2 - \ddot{x}_1 \tag{3.19}$$

$$u_3 = x_2;\; \dot{u}_3 = \dot{x}_2;\; \ddot{u}_3 = \ddot{x}_2$$

By rearranging equations (3.16) using (3.18) and (3.19), a more realistic solution for the single-mass 2-DOF bridge model with added dampers is obtained by solving simultaneously both equations (3.20) and (3.21).

$$c_1 \dot{u}_1 - c_2 sign(\dot{u}_2) |\dot{u}_2|^{n2} + k_1 u_1 - k_2 u_2 = 0 \tag{3.20}$$

$$m_2 (\ddot{u}_3 + \ddot{u}_g) + c_2 sign\,(\dot{u}_2)\, |\dot{u}_2|^{n2} + c_3 sign\,(\dot{u}_3)\, |\dot{u}_3|^{n3} + k_2 u_2 + k_3 u_3 = 0 \tag{3.21}$$

To solve this system of equations, Newmark's constant acceleration method (Newmark, 1959) was adopted as it represents one of the most robust step-by-step integration methods. As illustrated in Figure 3.6, a direct solution is computed for $\ddot{u}_2(t_i)$ as long as the model's equivalent stiffness remains the same during a discrete time step between t_i and t_{i+1}. Otherwise, if the equivalent stiffness of the model changes during the evaluated period of time, a stiffness

correction process is applied until the force equilibrium is established. An example of the iterative stiffness adjustment for a discrete step is illustrated in Figures 3.7 and 3.8. The flow chart of the computation process is presented in Figure 3.9.

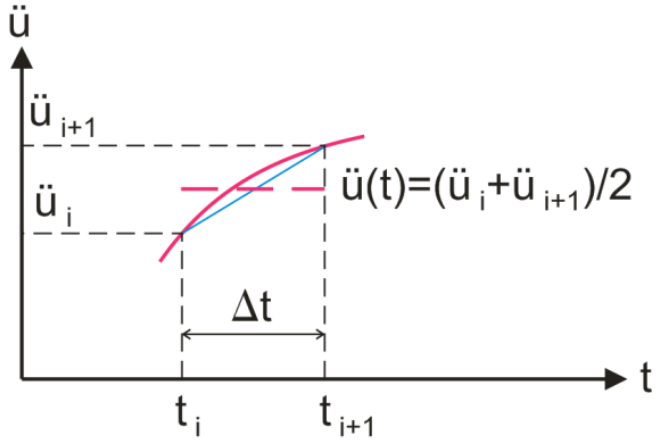

Figure 3.6 Average acceleration assumed for time step Δt

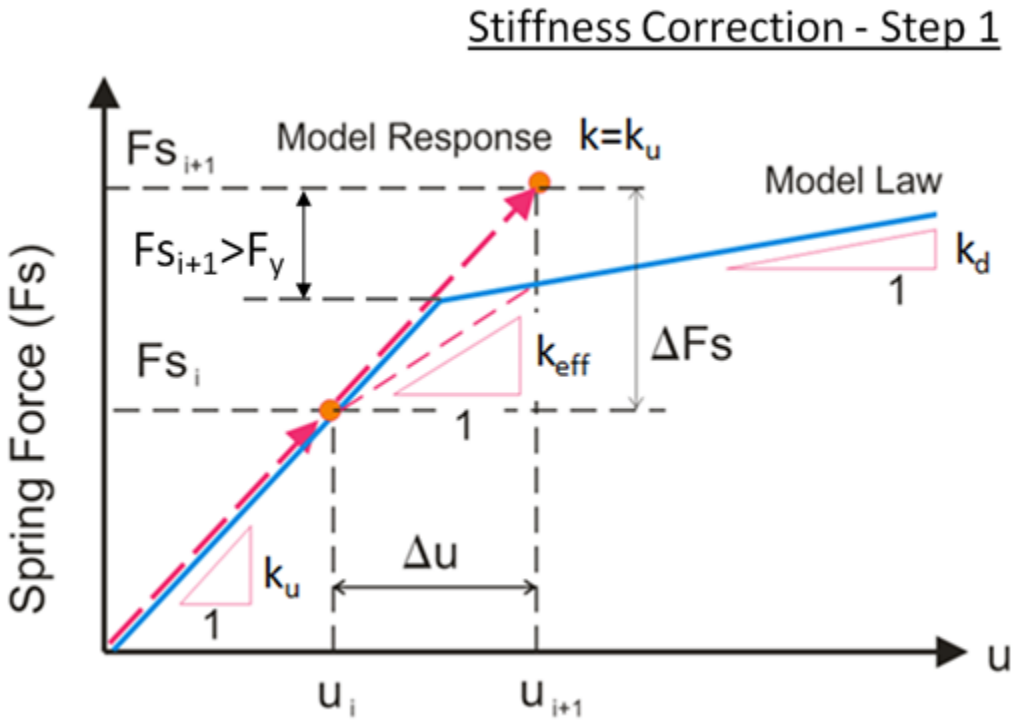

Figure 3.7 Equivalent stiffness correction: Step 1

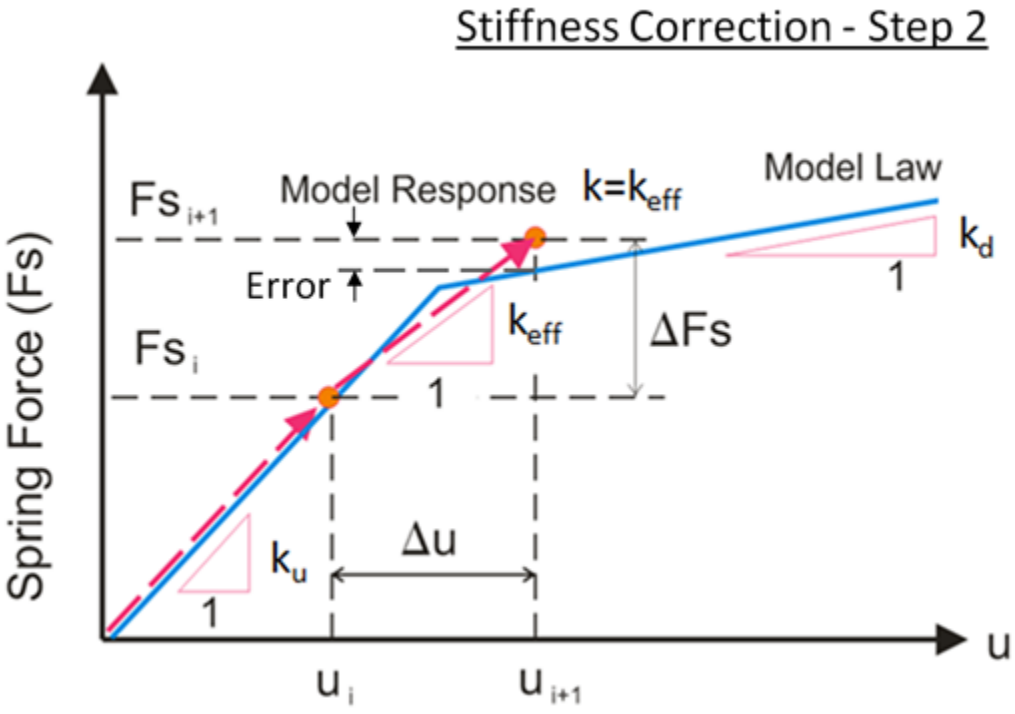

Figure 3.8 Equivalent stiffness correction: Step 2

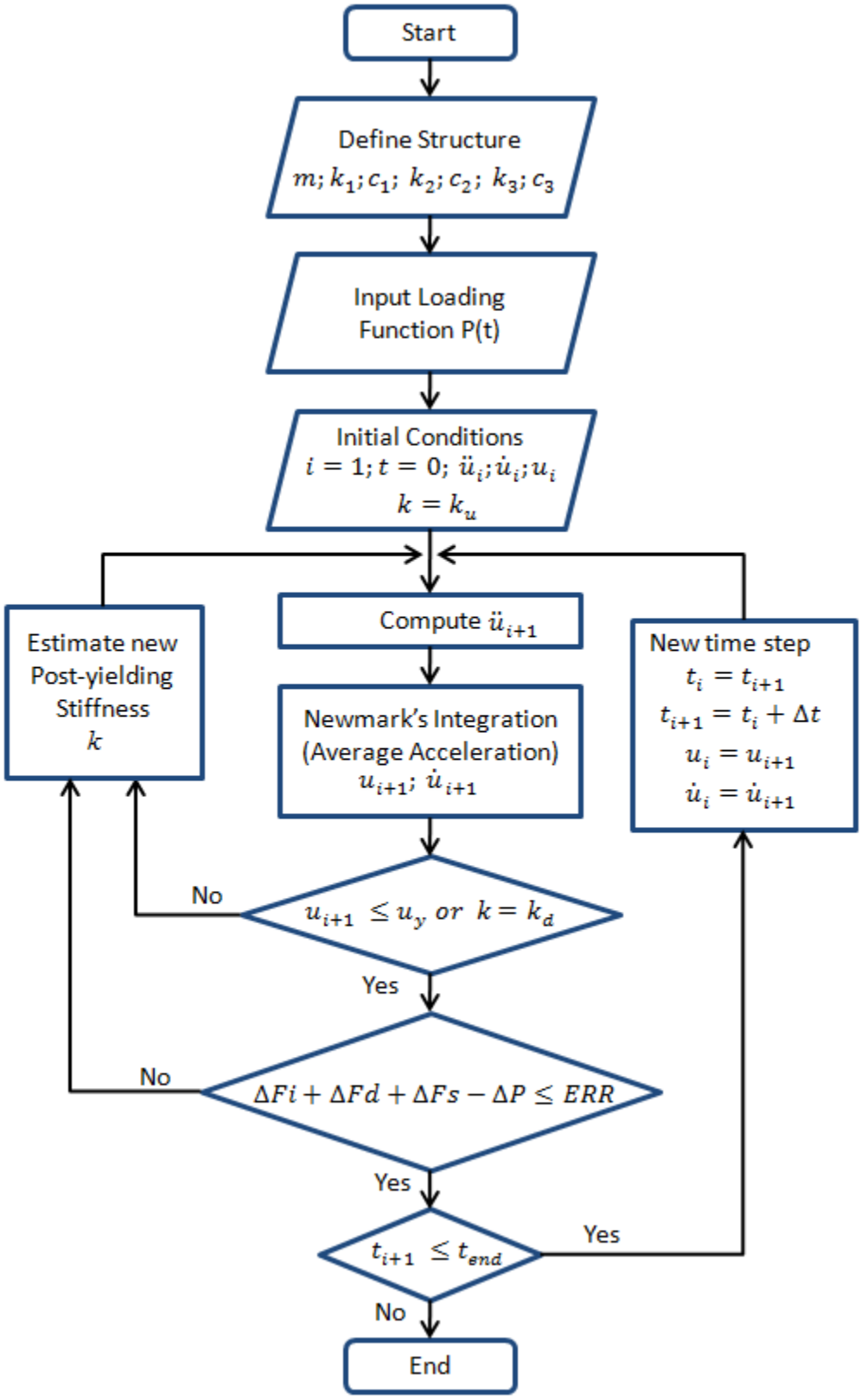

Figure 3.9 Flowchart of the computation process

3.5 Modeling of Inherent Damping

In this subsection, different techniques for modeling the inherent damping for nonlinear THA are presented and discussed. An alternative approach for considering the inherent damping ratio proportional to effective stiffness is then proposed.

3.5.1 Overview of Damping Assumptions

It is usual practice in seismic resistant design to define the earthquake demand by an elastic response spectrum. While the damped linear response of a structure is well understood, the solution for the response of a structure beyond the elastic range is still less well defined due to the assumptions that are made for modeling the inherent damping during the nonlinear response of the system. In an actual bridge structure, diverse sources of inherent damping can be identified: material damping, yielding damping, and interfacial damping. Different physical mechanisms can be associated with the capacity of inherent damping to dissipate seismic energy. The dissipative effect of inherent damping on structural responses can be numerically accounted for by means of an equivalent velocity-dependant damping mechanism.

As discussed earlier in Chapter 2, the concept of equivalent damping was first introduced by Lydik Jacobsen (Jacobsen, 1930) to represent nonlinear damping by an equivalent viscous damping model. In his work, an approximate solution was proposed for a SDOF system undergoing forced steady-state vibration with viscous damping proportional to the first power of the velocity. The velocity term was defined as a product of the maximum displacement and the angular velocity under observation. In his simplified solution, Jacobsen assumed that different damping effects could be reproduced by a linear viscous damping model. His assumptions were generally based on the equality of energy dissipated throughout the work done by the actual and the equivalent damping forces of a system over each cycle as presented in Figure 2.1(a). For the case where the damping force is proportional to the n^{th} power of the velocity, the equivalent damping coefficient, c_1, is determined from the following equality of dissipative work done during a cycle:

$$4c_n \cdot \int_0^{T/4} \left(\frac{dx}{dt}\right)^n dx = 4c_1 \cdot \int_0^{T/4} \left(\frac{dx}{dt}\right)^1 dx \tag{3.22}$$

Jacobsen compared the responses obtained with the simplified approach to the exact analytical solution derived by Den Hartog (1930) for four damping configurations and the results showed close agreement with the minimum error observed at the resonance frequency. Later, in 1960, Jacobsen expressed the equivalent viscous damping ratio for hysteretic behaviour in terms of the dissipative work, W_c, done during one cycle and the maximum potential energy E_p as:

$$\xi = \frac{c}{2\sqrt{k \cdot m}} = \frac{1}{2 \cdot \pi} \cdot \frac{W_c}{E_p} \tag{3.23}$$

where *c, k,* and *m* are the damping coefficient, the initial stiffness and the mass of structure, respectively.

Jacobsen mentioned, however, that his concept becomes almost meaningless when highly nonlinear systems or large values of non-viscous damping are applied.

Gulkan and Sozen (1974) carried out an experimental study of the dynamic response of reinforced concrete structures and concluded that the effective natural frequency decreases when a structure experiences excursions into the inelastic range. They explained this observation by the reduction in stiffness due to degradation of the structure. Additionally, they also found that an increase in energy dissipation capacity contributes, in turn, for reducing the acceleration response below the value expected with constant damping. Thereby, Gulkan and Sozen (1974) proposed to define an equivalent damping ratio, β_s by assuming that the earthquake energy input is entirely dissipated by a fictitious equivalent damper.

$$\beta_s \cdot \left[2m\omega_{eff} \int_0^T u^2 \cdot dt \right] = -m \int_0^T \ddot{u}_g \cdot \dot{u} \cdot dt \tag{3.24}$$

where u is the relative displacement, $\ddot{u}_g$ is the ground acceleration, ω_{eff} is the effective angular frequency and *m* is the mass of the structure.

Iwan and Gates (1979) proposed an empirical method of linearization for inelastic response spectra. The equivalent linear system was defined by equivalent damping and effective linear period found by optimizing a root mean square (RMS) error between elastic and inelastic responses.

In 1997, Tsopelas et al. presented a technical report on the methods suggested by FEMA 273 (1997) and FEMA 274 (ATC/BSSC, 1997) for the use of a simplified linear procedure based on substitute elastic structures with equivalent stiffness and damping properties when the effect of added damping is considered. They suggested to define the effective damping ratio of an equivalent linear system using three terms as:

$$\beta_{eff} = \frac{W_D}{2\pi K_{eff} D^2} + \beta_v \frac{T_{eff}}{T_e} + \beta_{inh-eff} \tag{3.25}$$

where W_D is the energy dissipated by the structure in a complete cycle, β_v is the damping ratio of a viscous damper determined at an elastic period T_e, and $\beta_{inh\text{-}eff}$ is the inherent damping of the structure, usually set equal to 0.05 (5%) unless a different damping level is specified.

Researchers outlined the importance of defining the inherent damping ratio in relation to the effective period T_{eff} and not the elastic period as the effect of improperly modeled inherent damping leads to an unconservative displacement prediction (Tsopelas et al., 1997). As a result, for modelling highly nonlinear systems in this study, a modified Jacobesn's equivalent damping concept has been adopted using the effective period T_{eff} determined by the effective secant stiffness k_{eff} at maximum displacement.

3.5.2 Technique for Modeling Inherent Damping

In engineering practice, the effect of inherent damping is commonly represented by analytical models using a constant damping ratio with respect to the critical damping proportional to the stiffness of the system. In this study to comply with equivalent damping concept, the critical damping proportional to the effective stiffness ($c_{cr} = 2\sqrt{mk_{eff}}$) is adopted. This damping approximation is identical to the one given in Equation (3.29). As a result, the viscous damping coefficient c decreases as the effective period increases.

However, it is understood that the effective period is a function of the maximum displacement and is unknown before the analysis has been completed. For this reason, the effective damping is defined in relation to the elastic damping ratio (proportional to the initial elastic period T_e) and it is determined in three steps. In the first two steps, the effective periods are evaluated for elastic damping ratios $\beta_e = 0\%$ and 5%. The second value corresponds to the assumed inherent

damping $\beta_{inh} = 5\%$. In the third step, the value of the inherent damping of 5% (this example) at the elastic period is determined at the effective period by linear interpolation. The damping ratio β_e and the damping coefficient, c, proportional to elastic stiffness are given in Equations (3.26) and (3.27):

$$\beta_e = \frac{c}{2\sqrt{mk_u}} \tag{3.26}$$

$$c = 2\beta_e \sqrt{mk_u} \tag{3.27}$$

Note that to simplify the step-by-step time-history analysis, the viscous damping coefficient remains unchanged for the entire ground-motion duration and the corresponding equilibrium of forces at each time step is given as:

$$m\ddot{u}(t) + 2\beta_{inh-e}\sqrt{mk_u}\dot{u}(t) + k_t u(t) = -m\ddot{u}_g(t) \tag{3.28}$$

The damping ratio proportional to the effective stiffness $\beta(k_{eff})$ is determined as:

$$\beta(k_{eff}) = \beta(k_u)\frac{T_{eff}}{T_e} = \frac{c}{2\sqrt{mk_{eff}}} \tag{3.29}$$

Once the responses at $\beta(k_u) = 0\%$ and 5% are computed, the value of the elastic damping is transformed into damping that is proportional to the effective stiffness by using Equation (3.29), where the effective period T_{eff} for a bilinear hysteretic behaviour is:

$$T_{eff} = T_e \cdot \sqrt{\frac{\mu}{1 + \alpha\mu - \alpha}} \tag{3.30}$$

The system response is given in terms of the ductility demand μ and α is a the post-yield stiffness ratio. Finally, the inherent damping ratio proportional to the elastic stiffness which is required for the analysis is recalculated using a linear interpolation:

$$T_{eff,inh} = T_{eff,0\%} + \frac{T_{eff,0\%} - T_{eff,5\%}}{0 - \beta_{eff,5\%}}\beta_{inh-eff} \tag{3.31}$$

$$\beta_{inh-e} = \beta_{inh-eff} \frac{T_e}{T_{eff,inh}} \tag{3.32}$$

3.6 Model Validation Example

In order to validate the reliability of the analytical model and the proposed analytical solution, results are compared to those obtained from a corresponding model built with the SAP2000 computer program (CSI, 2009). A concept design bridge located near Montreal was adopted to represent a typical aging bridge that was seismically upgraded using isolation and damping systems in the frame of this validation study. Figure 3.10 present the elevation of the bridge structure arranged across five spans along the total length of 250 m crossing of a river obstacle. The bridge superstructure consists of a single cell concrete box girder with total width of 13.5 m accommodating two lanes and two shoulders as shown in Figure 3.11. The original bridge configuration has all four piers with fixed support conditions, while for an alternative solution, either part of these piers or all piers can be isolated. Two typical isolation devices, the lead-rubber bearing (LRB) and flat sliding isolator (FSI), were adopted in this example to increase the bridge capacity in resisting seismic demand. This is primarily expected due to the capacity of isolators to lengthen the natural period of the structure, thus decreasing the induced seismic forces. A complimentary protection effect is achieved through the seismic energy dissipation which is performed either by friction or inelastic behaviour of the material.

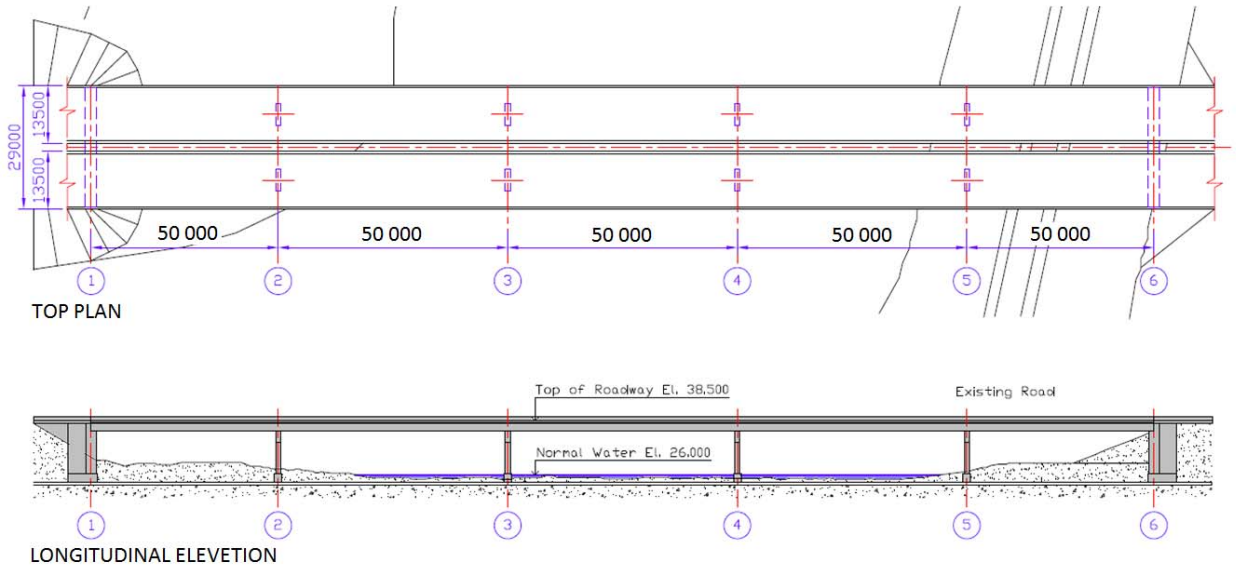

Figure 3.10 Bridge elevation

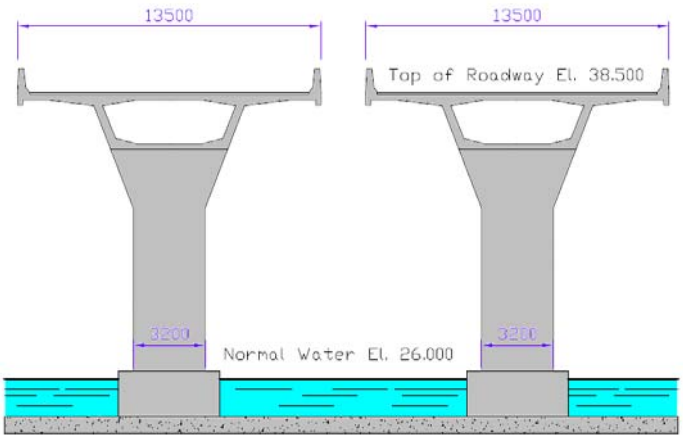

Figure 3.11 Bridge cross-section and pier configuration

3.6.1 Modeling Assumptions

In order to transform the bridge structure into a numerically manageable model, the structure is divided into two model elements: the substructure and the superstructure. As shown in Figure 3.12, most of the bridge mass is located at the level of deck, and the effect of the substructure mass, represented by four piers, is neglected when computing the dynamic response.

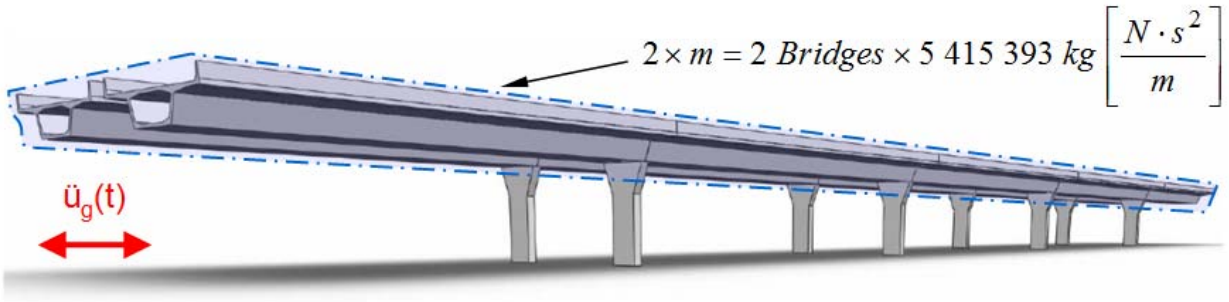

Figure 3.12 Mass assumptions for bridge modelling

Figure 3.13 presents axial loads acting on the abutments (A1 and A6) and the piers (P2, P3, P4, and P5). The pier support conditions are assumed to be fixed-pinned. Accordingly, the pier structure was subjected to shear, moment and axial loads. To evaluate the inelastic response and available ductility capacity of the reinforced concrete cross-section of the pier, the sectional pushover analysis was performed using the program Response 2000 (Bentz, 2000). A typical pier cross-section shown in Figure 3.14 was adopted for this example. The axial load remains constant during the analysis, while the moment and shear loads, which are related through the geometry and support conditions, are increased monotonically up to failure. The pier cross-section, material properties, loading and support conditions used in the pushover analyses are presented in Figure 3.14. The pier elastic limit and lateral stiffness obtained from these analyses are then summarized in Table 3-1 and will be further used in this model validating example.

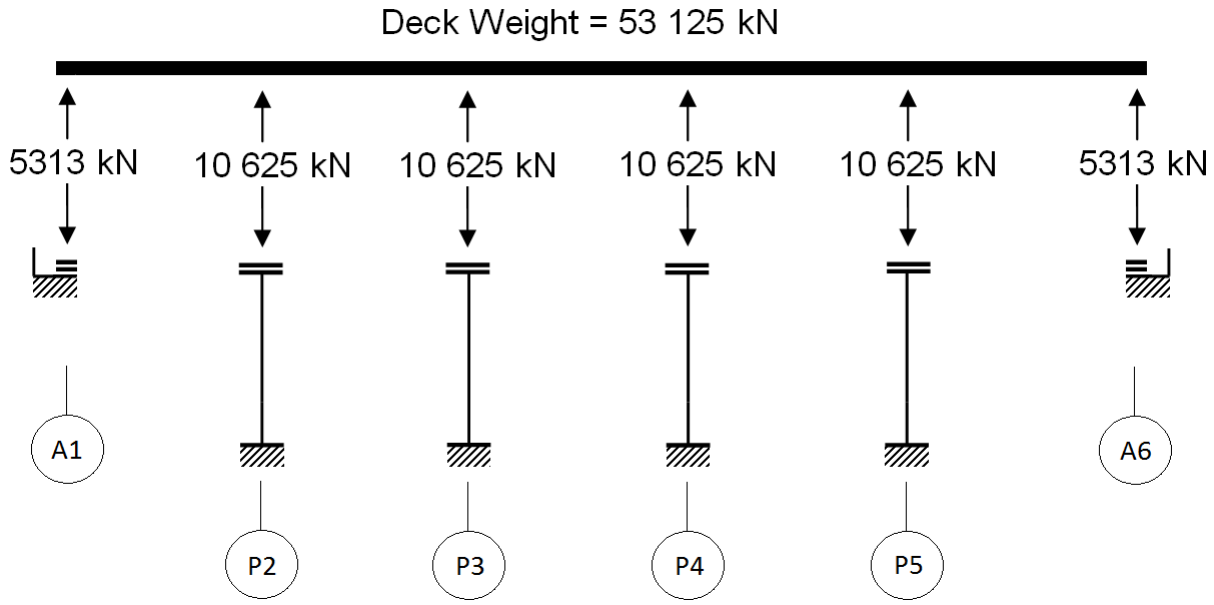

Figure 3.13 Deck weight and axial loads (idealized geometrical distribution)

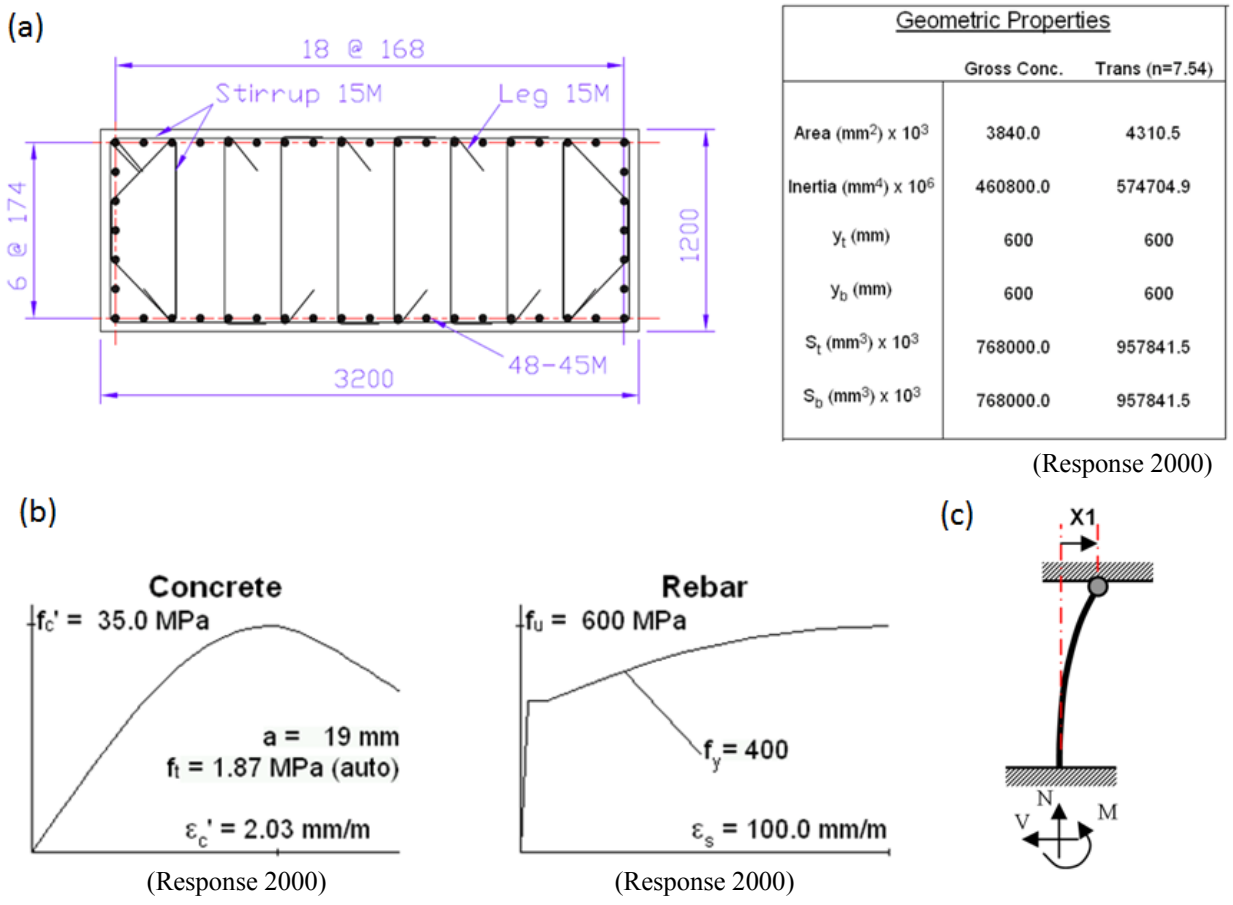

Figure 3.14 Pier modeling assumptions for pushover analyses: a) cross-section and sectional properties, b) material properties, and c) loading and support conditions

Table 3-1 Pier properties for the model validating example

Pier model parameters	P2, P3, P4, and P5
Height of pier without bearing, h (m)	9.70
Axial load (kN)	10 625
Displacement elastic limit, u_y (mm)	57
Ultimate displacement, u_u (mm)	248
Lateral force elastic limit, F_y (kN)	692
Lateral stiffness (kN/m)	12 140

3.6.2 Modeling of Isolation Devices

Two different isolation systems, lead rubber bearing (LRB) and flat sliding isolation (FSI), were chosen for this example. FSI devices without recentring capacity are used as fuse elements to limit the seismic forces transmitted to the piers P2, P3, P4, and P5. LRBs inherently exhibit higher restoring forces upon yielding and the system is therefore installed at the abutments A1 and A6 where greater lateral resistance can be more easily developed. Figure 3.15 presents the bridge protection layout, while isolator's modeling parameters are given in Table 3-2.

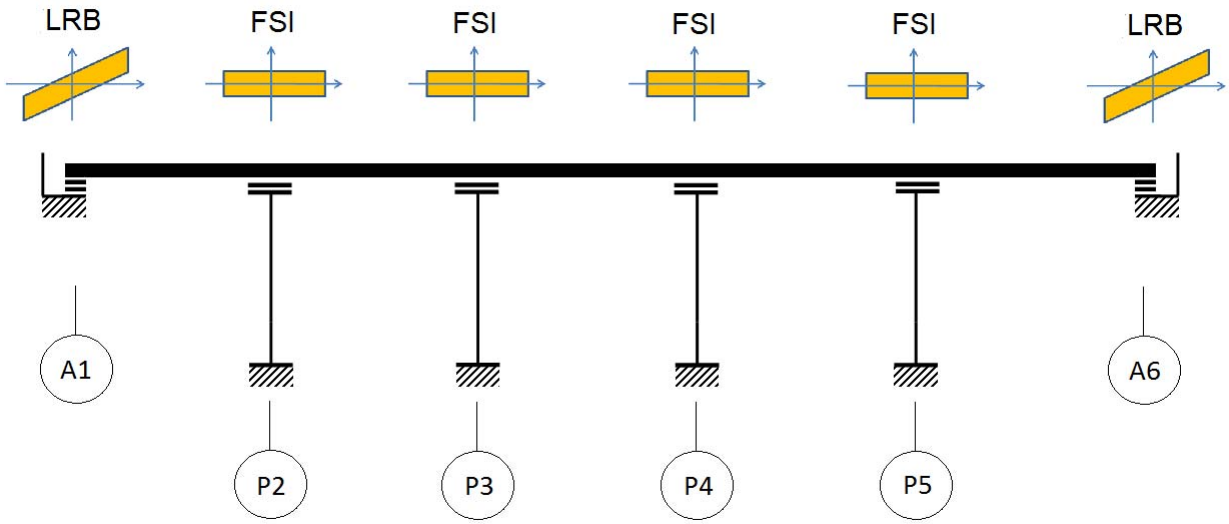

Figure 3.15 Protection axial loads distribution

Table 3-2 Modeling parameters: bilinear hysteretic response

Isolator model parameters	A1 and A6	P2, P3, P4, and P5
Type of Device	LRB (DIS)	FSI
Total Number	4 Isolators	8 Isolators
Coefficient of Friction, μ_s	N/A	2%
Activation Force (kN)	220	106.3
Post-yielding stiffness, k_d (kN/m)	1100	0
Post-yielding stiffness ratio, α	0.1	0

3.6.3 Time-History Ground Motion

A simulated earthquake record corresponding to the moment magnitude of M_w=7.0 and epicentral distance of 70 km was adopted for the example to analyze the bridge located in the region of Montreal, Quebec (Tremblay & Atkinson, 2001). The record was linearly scaled to match the site specific uniform hazard spectra specified in NBCC (NRCC, 2005) for a probability of exceedance of 2% in 50 years. NEHRP site class C was considered. This ground motion is characterized by a total duration of 24.08 s and the peak ground acceleration (PGA) of 0.271 g. The time history of this record is presented in Figure 3.16.

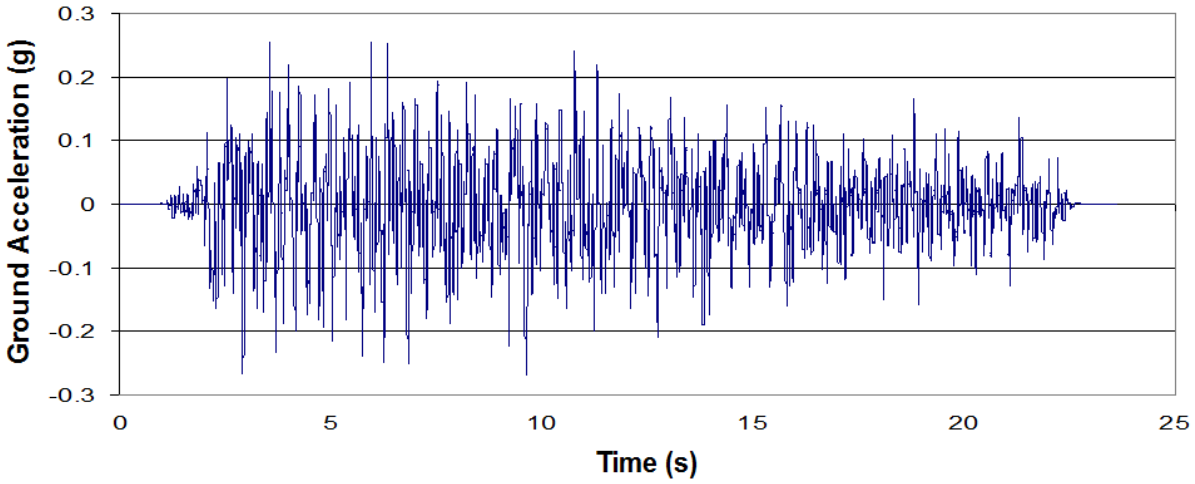

Figure 3.16 Simulated time-history record – M7.0-R70-1

3.6.4 Numerical Modeling with SAP2000

The bridge superstructure is modeled as a rigid body with an infinite axial stiffness. This bridge is straight and uncoupled motions are considered for the longitudinal and transverse directions. In this example, only the longitudinal motion is considered. SAP2000 offers a wide range of link elements that permit to achieve either an effective stiffness or damping through combining different link elements. A "Plastic (WEN)" link element was adopted to represent a combined bilinear effect of an isolation device with a pier. A 5% inherent damping is assumed and modeled by means of mass proportional damping. As a result, a Rayleigh damping element is set to interact directly with the entire bridge structure. To make the computational process less time-consuming, two elements were configured to accordingly represent the contributions of devices installed at the abutments and at the piers. The corresponding numerical model built in the SAP2000 environment is shown in Figure 3.17.

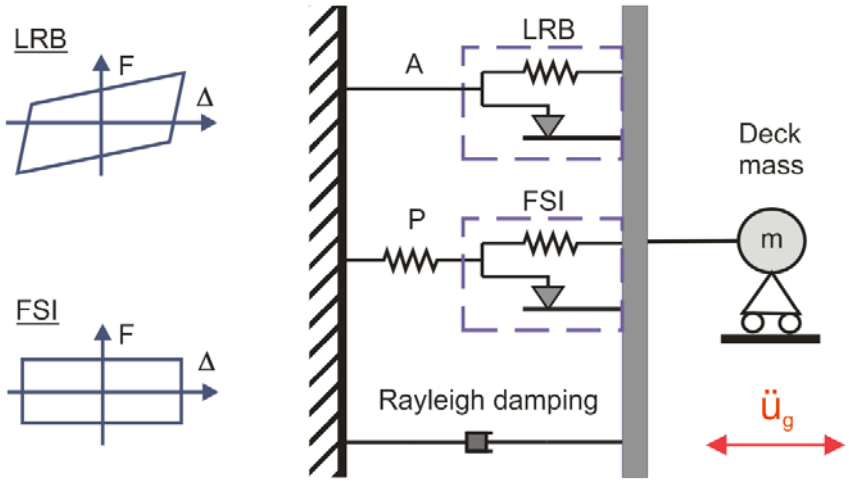

Figure 3.17 Modeling bridge with SAP2000

To facilitate the results interpretation in validating IS-Bridge, in this example, the inherent damping is taken into account as a Rayleigh damping coefficient proportional to the mass of the bridge structure (deck). As a result, the bridge model incorporates an overall level of inherent damping as shown in Figure 3.17. The abutments are considered infinitely stiff with respect to the isolators installed atop. Using such an assumption, the stiffness of the spring k_3 (see Figures 3.4 and 3.5) corresponds only to the contribution of the four abutments' isolators. The elastic and post-activation stiffness parameters of an LRB isolator adopted in this example are 11 kN/mm and 1.1 kN/mm, respectively. The elastic stiffness that represents one abutment with two isolators is 11 kN/mm x 2 Isolators = 22 kN/mm. The bridge elastic stiffness is determined as:

$$k_{u-Bridge} = 12.4 \times 4\ Piers + 22 \times 2\ Abutments = 93.6\ (kN/mm)$$

The bridge initial elastic period (prior to the isolation activation):

$$T_{e-Bridge} = 2\pi \cdot \sqrt{\frac{5\,415\,393}{93.6 \times 10^6}} = 1.51\ (s)$$

The damping coefficient for a 5% inherent damping:

$$C_{e-Bridge} = 2 \cdot 0.05 \cdot \sqrt{5\,415\,393 \cdot 93.6 \times 10^6} = 2251\ (kN \cdot m/s)$$

The mass proportional damping coefficient for modeling Rayleigh damping in SAP2000:

$$\alpha_{dmp} = \frac{C_{e-Bridge}}{m} = \frac{2.251 \times 10^6}{5\,415\,393} = 0.416$$

3.6.5 Results and Comparison

The results obtained from the nonlinear time-history analysis carried out using the SAP2000 model are compared to those from the IS-Bridge model. The time step used for the analyses with both models was set to 0.001 s. The bridge hysteretic responses computed by SAP2000 and by IS-Bridge are presented in Figure 3.18. Similar hysteretic shapes result from both simulations thus indicating that the characteristics of the LRB and FSI devices are properly taken into account by the models (same activation levels, elastic and post-yielding stiffness). The displacement and force time histories are shown in Figure 3.19. An excellent agreement is observed between these responses over the entire record duration. Some slight differences in responses, however, can be noted. The responses from IS-Bridge result in insignificant overshooting generally due to differences in integrating process which is iterative in SAP2000 and is based on direct solution for a discrete time step in IS-Bridge.

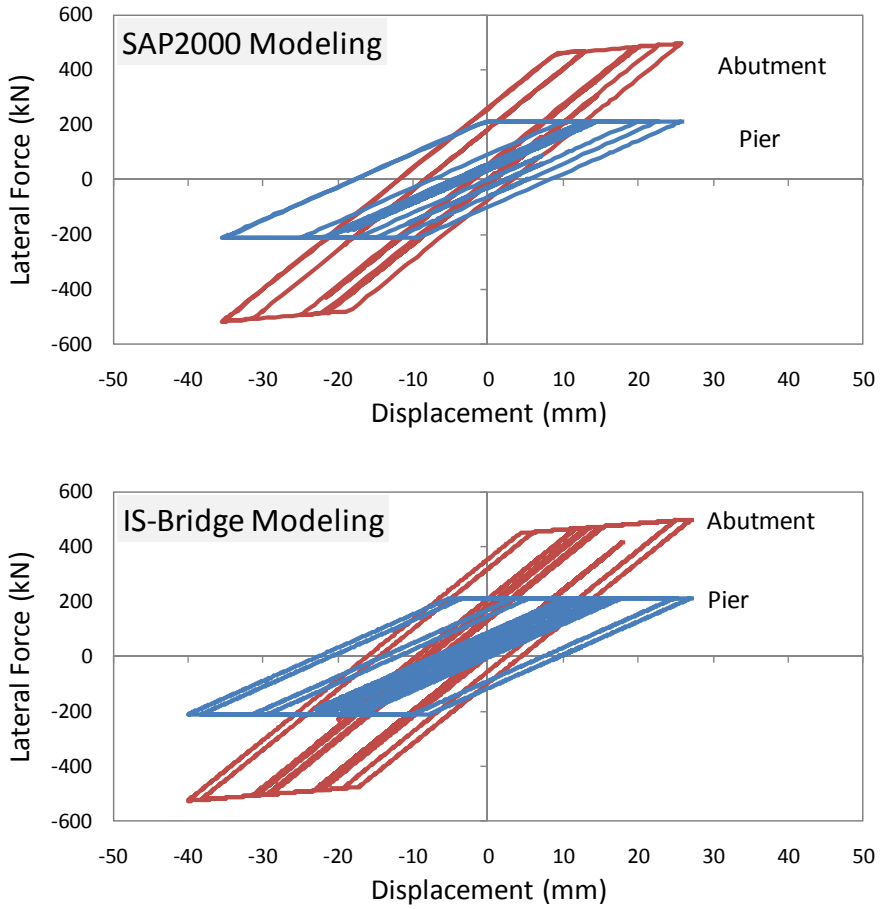

Figure 3.18 Hysteretic bridge response from SAP2000 and IS-Bridge

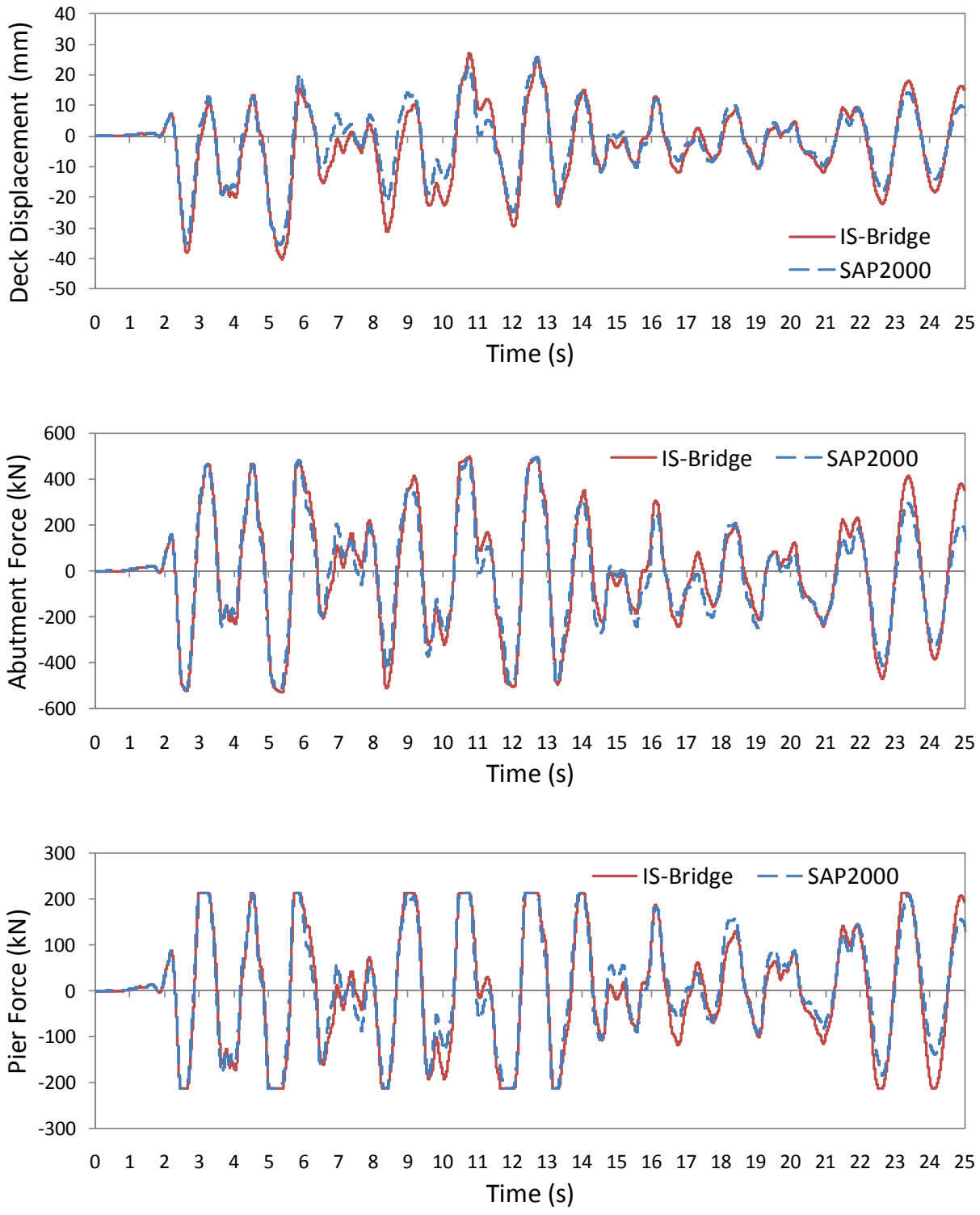

Figure 3.19 Time histories of bridge responses computed by SAP2000 and IS-Bridge

3.7 Conclusions

A new analytical model and methodology to carry out nonlinear simplified isolated bridge analysis are presented and validated in this chapter. The ability of IS-Bridge to accurately simulate the structural behaviour of isolated bridges makes this program an useful tool to carry out the extensive parametric analyses needed to achieve objectives of this research. In addition, this numerical tool can be used at the preliminary design stage of seismically isolated bridges as well as it may be widely exploited for teaching-learning process and research purposes due to the possibility of animating seismic response simulations through a graphical user interface.

Chapter 4: Ground Motion (GM) Selection and Scaling for Time-History Analysis of Isolated Bridges

4.1 Introduction

In this chapter, site-specific ensembles of ground-motion time histories are defined and scaled to carry out the analyses of the nonlinear structural behaviour of isolated bridges in Eastern (ENA) and Western (WNA) North America. In spite of being widely addressed over the last decade by many research studies, the record selection and scaling process is still challenging to structural engineers today. There is a variety of approaches that have been developed for specific design purposes based on either site-specific seismic hazard conditions or properties of structures to be analyzed.

The current seismic code provisions (CSA-S6-06 and AASHTO), however, do not provide an explicit procedure on how to select and scale ground-motion records for nonlinear time-history analyses (THA) of isolated bridges to obtain acceptable response predictions over a wide range of inelastic excursion (related to period lengthening). The technique and methodology proposed in this study intend to select and scale time histories for dynamic analyses from the perspective of a structural engineer using the available state of the art in seismology.

The design spectrum in the Canadian CSA-S6-06 code is no longer up to date and it is expected that the uniform hazard spectrum (UHS) currently used in NBCC (NRCC, 2005) for buildings will be adopted as the design spectrum in the next CSA-S6-14. When this study was initiated in 2009, UHS for CSA-S6-14 had not been developed yet and the UHS data specified in NBCC 2005 was adopted as it represented the most recent data available at that time. The UHS data was modified in the 2010 edition of NBCC (NRCC, 2010) but the changes were small and not likely to significantly affect the outcome of the study. Hence, the research was completed using the 2005 seismic data.

An overview of recent developments in seismology is presented first. The time histories are then selected according to magnitude-distance (M-R) scenarios dominating the seismic hazard for two densely populated Canadian cities: Montreal, Quebec, for ENA, and Vancouver, British

Columbia, for WNA. The amplitude of the ground motions are linearly scaled to match the site specific uniform hazard spectra specified in NBCC (NRCC, 2005). The technique for scaling time histories for a specific period range as proposed by Atkinson (2009) was adopted.

4.2 Overview of Relevant Development in Seismology

Since the 1906 earthquake that devastated San Francisco, scientists and engineers have expressed the need for a better understanding of seismic events and seismic demand on structures. The same year, the Seismological Society of America (SSA) was founded and it marked the beginning of the modern science of seismology in North America. To rebuild San Francisco, the minimum design wind load of 1.4 kPa (30 psf) requirement was adopted to provide structures with the capacity to withstand wind lateral forces. Although there was no direct mention of seismic forces, the increase in structural capacity to resist both wind and earthquakes was intended (Popov, 1994). Learning from the 1925 Santa Barbara and the 1933 Long Beach earthquakes, seismic provisions were progressively introduced into design practice. Seismic forces were then expressed as a percentage of the gravity loads. Several seismological values were specified to account for different seismic zones and soil types. In addition, it is during the 1933 Long Beach earthquake that acceleration time histories were recorded for a strong motion for the first time. Since then, the input based on seismological data were considered by engineers for earthquake resistant design.

During the 1940 El Centro earthquake (Imperial Valley earthquake), sets of detailed strong motion recordings were obtained. These records have been extensively used since by researchers and engineers in time-history analyses to validate the reliability of structural designs and develop new design methods. Through the subsequent decade, seismic design provisions were based on a qualitative evaluation of hazard (Atkinson, 2004). However, it was recognized that even if being scaled to a desired ground-motion intensity, a given ground motion (GM) record may be characterized by magnitude M and distance R parameters that are not necessary representative of the site-specific seismic hazard.

Different seismic models have then been produced to predict and simulate ground-motion activity in the regions of interest. Based on these models, seismic hazard maps could be developed which represented a major improvement for seismic design. In Canada, such a

national probabilistic seismic hazard map was introduced for the first time in 1970 (Atkinson, 2004).

The current building code in Canada is now based on the fourth generation seismic hazard maps that have been proposed by Adams and Halchuk (2003). Significant advances in the understanding of seismicity have been necessary in the development of these maps. Special efforts have also been devoted to the treatment of uncertainty in hazard analyses and this new seismic hazard model incorporates aleatory and epistemic uncertainties. Contrary to the aleatory uncertainty that characterizes inherent physical variability, the epistemic uncertainty results from the lack of knowledge and can be reduced by collecting and analyzing new ground motion data.

In Canada, epistemic uncertainty is reflected by the use of two probabilistic seismic hazard models “H” and “R”. The “H” model was created to represent the hazard based on the historical events that have been observed in the past. It therefore contains only a few seismic sources located in known seismic active areas. To compensate for the short period of seismic observation, the “R” model incorporates a larger number of seismic sources that are based on seismotectonic characteristics reflecting the potential for earthquake activity. For the fourth generation map, the reliability of the seismic hazard in "stable" regions of Canada was improved by introducing a third probabilistic seismic model "F" ("floor"). That model is based on the seismic data obtained worldwide on the earthquake activity in similar continental parts subjected to low seismic activity and was adopted as a "floor" level of seismic hazard across Canada. In addition to the first three probabilistic models, a deterministic model "C" was also developed to include the hazard posed by a realistic scenario generated for a prehistorical great earthquake that occurred on the Cascadia subduction zone in the 18^{th} century. Adams and Halchuk (2003) suggested to choose the highest value of seismic hazard (the more conservative result) from the four models. This approach had been proposed earlier by Adams et al. (1995) and is known as the "robust" model. However, it has been recognized that by using only the "R" model for eastern Canada, the seismic protection could be reduced significantly in regions of high historical seismicity while the protection in other locations would be insignificantly increased (Adams and Atkinson, 2003).

The implementation of the uniform hazard spectrum (UHS) in seismic design is another major development in the seismic hazard methodology. In contrast to the previous code maps, the UHS

provides a constant probability of exceedance for each response spectral ordinates computed at different structure periods. The contribution of earthquake having various magnitude and distance characteristics is considered in the evaluation of the seismic hazard at each specific site. Thus the UHS shape results from the effect of all possible events that can contribute to the site-specific hazard as illustrated in Figure 4.1 for close (local) and distant seismic events.

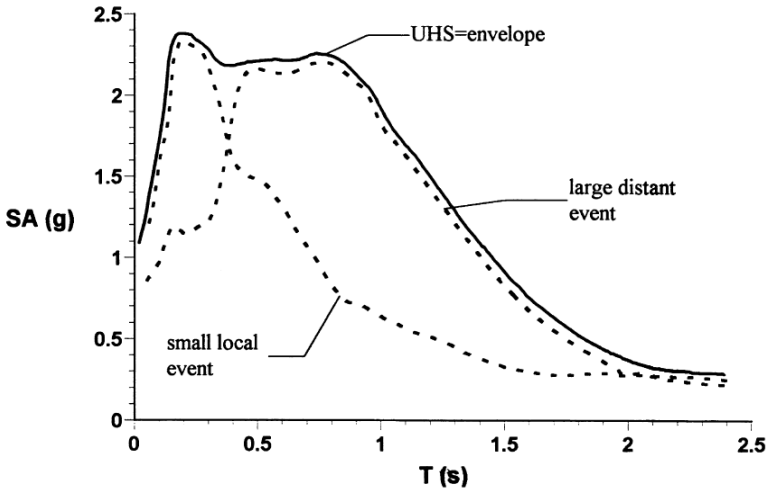

Figure 4.1 The concept of UHS for a location affected by local sources of moderate seismicity and distant sources (Bommer et al., 2000a and Hancock, 2006 after Reiter, 1990)

The fourth generation seismic model (Adams and Halchuk, 2003) provides 5% damped spectral acceleration values at periods of 0.2, 0.5, 1.0, 2.0 s, and PGA (peak ground acceleration). A reference ground condition corresponding to the NEHRP site class C has been adopted to generate the national hazard maps. This ground condition is characterized by an average shear wave velocity of 360 to 760 m/s over the top 30 m of soil, which corresponds to “very dense soil and soft rock” ("firm soil"). The site class C is representative of a large number of well recorded strong ground motions, which minimizes the uncertainty related to site amplification (Adams and Halchuk, 2004). For other site conditions, two site amplification factors F_a and F_v are specified for short and long periods, respectively. The spectral acceleration values for a given site class are obtained by amplifying or de-amplifying the site C value using the corresponding F_a and F_v factors.

For the fourth generation seismic hazard model, the level of probability of exceedance previously specified in the Canadian code as 10% in 50 years (0.0021 per annum) was decreased to 2% in

50 years (0.0004 per annum) (Adams and Halchuk, 2003). This important change aimed to assure a more uniform level of safety against collapse or failure of structures across all regions of Canada (Heidebrecht, 2003). The hazard curves across Canada do not have the same slope, as illustrated in Figure 4.2, and designing for 10% in 50 years hazard level as specified in the current CSA-S6-06 would not result in the same level of protection against stronger earthquakes with lower probability of exceedance. Therefore, a probability of exceedance of 2% in 50 years corresponding to a return period of 2475 years was adopted for the design spectrum in the next CSA-S6-14. Heidebreht (2003) indicated that the design of common structures for events with this lower probability level will provide a uniform level of the target reliability across Canada.

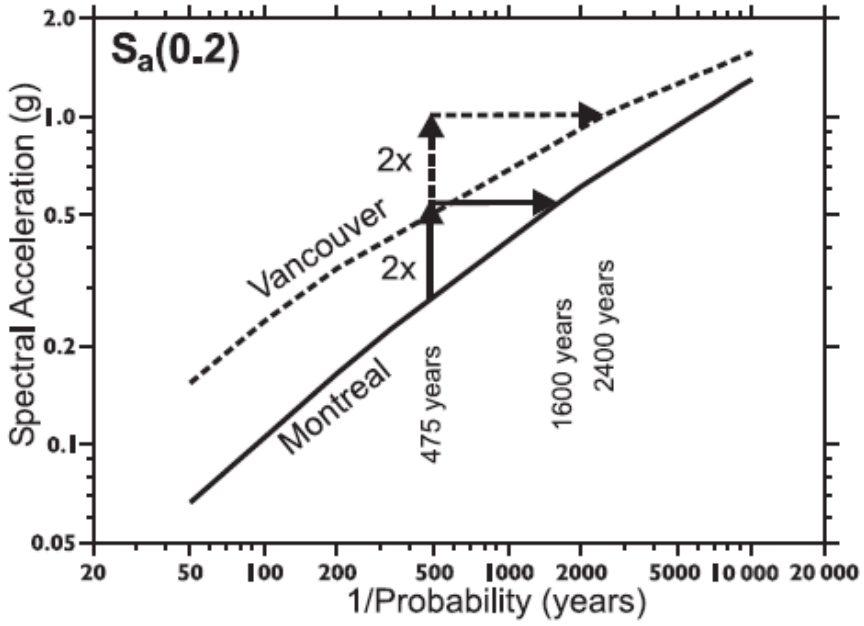

Figure 4.2 Hazard curves for Vancouver and Montréal (Adams and Halchuk 2004)

4.3 Site-Specific Scenarios for ENA and WNA

To define earthquake scenarios and select ground motion time histories for the parametric studies conducted in this project, two locations representative of eastern and western North America were first selected. Two densely populated cities where a large number of bridges are present were chosen: Vancouver, British Columbia, for WNA and Montreal, Quebec, for ENA. As shown in Figure 4.3, these two locations were also selected as they represent the populated regions with the highest seismic risk in western and eastern Canada (Halchuk et Adams, 2004).

These two Canadian cities are representative of other large cities such as Boston or New York in the eastern US and Seattle and Portland in the western US.

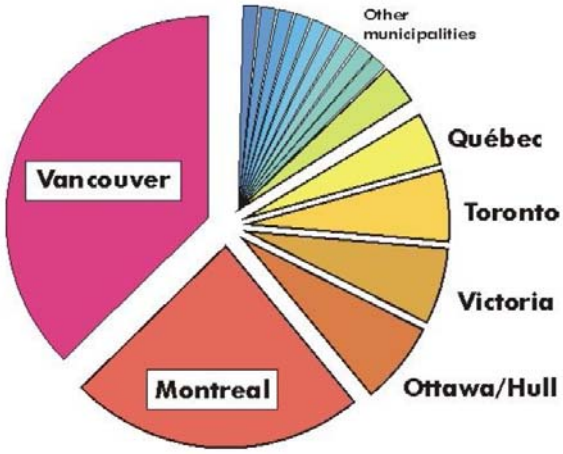

Figure 4.3 Earthquake risk distribution in Canada (Adams, 2011)

For reducing epistemic uncertainty that results from the lack of knowledge, the commonly adopted practice consists in processing a large number of time-history records. However, this technique provides statistically poor results for regions with scarcity in well-recorded historical ground motions as in the case of eastern North America. Significant advances in seismology research made recently suggest the possibility of reducing the number of required records by considering site-specific records which are selected in terms of magnitude and distance (M-R) according to the dominant earthquake scenario.

4.4 Dominant Earthquake Scenarios

In this study, the earthquake scenarios are determined from site-specific hazard deaggregations produced in terms of magnitude and distance (*M-R*) for a probability of exceedance of 2% in 50 years and NBCC site class C (Halchuk and Adams, 2004, Halchuk, 2009 and Halchuk, 2010). The deaggregation of seismic hazard is commonly defined as the *M-R* distribution of the annual rate of exceedance of a target spectral amplitude $S_A(T)$ at a period T. The annual rate of exceedance accumulated by *M-R* bins that represent the relative contribution of each of the earthquake *M-R* scenarios to the hazard. The deaggregated results are generally presented on the form of a binned plot from which one can easily determine which earthquake scenario contributes most to the site-specific seismic hazard at the structure period of interest. The

dominant earthquakes are then used to select the ground-motion records with comparable seismic magnitude and source-to-site distance. These records are applied for inelastic time-histories analyses of structures so that the distribution of delivered energy with time is realistically represented (McGuire et al. 2001b; McGuire et al. 2002).

Deaggregated hazard plots for the 5% damped spectral acceleration *Sa(T)* computed at the four periods T = 0.2, 0.5, 1.0 and 2.0 s are presented in Figures 4.4 to 4.7 for Montreal and in Figures 4.8 to 4.11 for Vancouver. These plots are provided for a probability of exceedance 2% in 50 years (probability of 0.000404 per annum). In these figures, the size of the bins is 20 km in distance and 0.25 in magnitude.

When examining the plots for Montreal, it is clear that for this probability level, more than one *M-R* earthquake scenario may significantly contribute to the hazard. It is also evident that the dominant scenarios also vary with the period T. For instance, two bins with the maximum contribution to the hazard of 68/1000 correspond to the events M5.875 at 10 km and M5.875 at 30 km for the period T=0.2 s. For periods of 0.5 and 1.0 s, the hazard is dominated by events with a greater magnitude M6.875 at 30 km. For period T=2.0 s the maximum contribution to the hazard comes from the event M6.625 at 30 km, which magnitude is greater than that from T=0.25 s and smaller than those from T=0.5 and 1.0 s. Moreover, it can be noted that the contribution to the hazard from distant earthquakes increases with period as those of 1/1000, 4/1000, 11/1000, and 27/1000 for T=0.2 s, 0.5 s, 1.0 s, and 2.0 s, respectively. In contrast to Montreal, the deaggregation plots for Vancouver present mostly similar shape so that the maximum contributions correspond to the same event for periods of 0.2 and 0.5 s (M6.875at 70 km) and for periods of 1.0 and 2.0 s (M7.125 at 70 km).

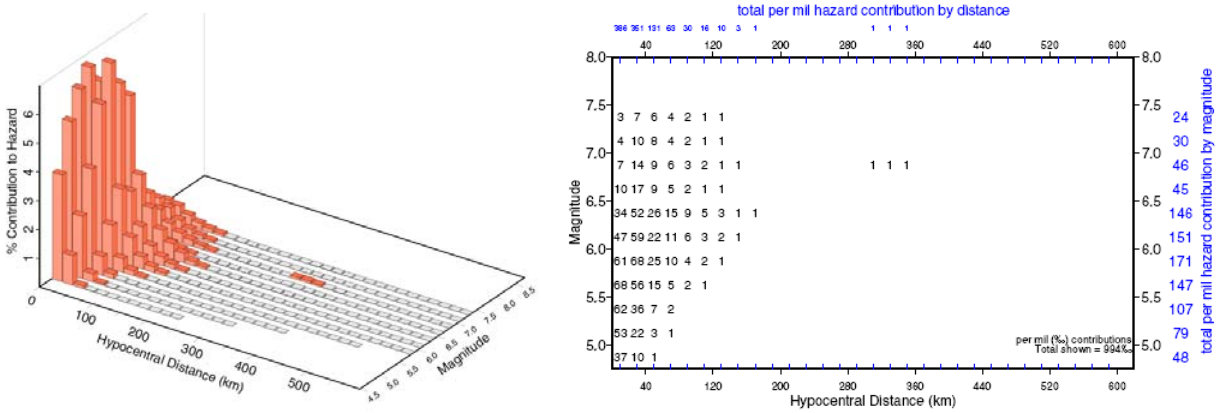

Figure 4.4 Hazard deaggregation for $S_A(0.2)$ = 0.584 g in Montreal for a probability of exceedance 2% in 50 years (Halchuk, 2010)

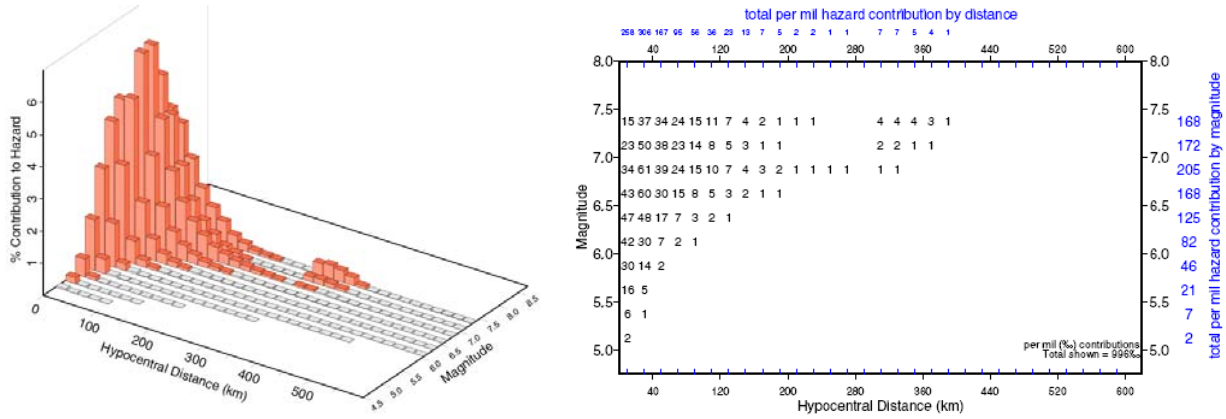

Figure 4.5 Hazard deaggregation for $S_A(0.5)$ = 0.289 g in Montreal for a probability of exceedance 2% in 50 years (Halchuk, 2010)

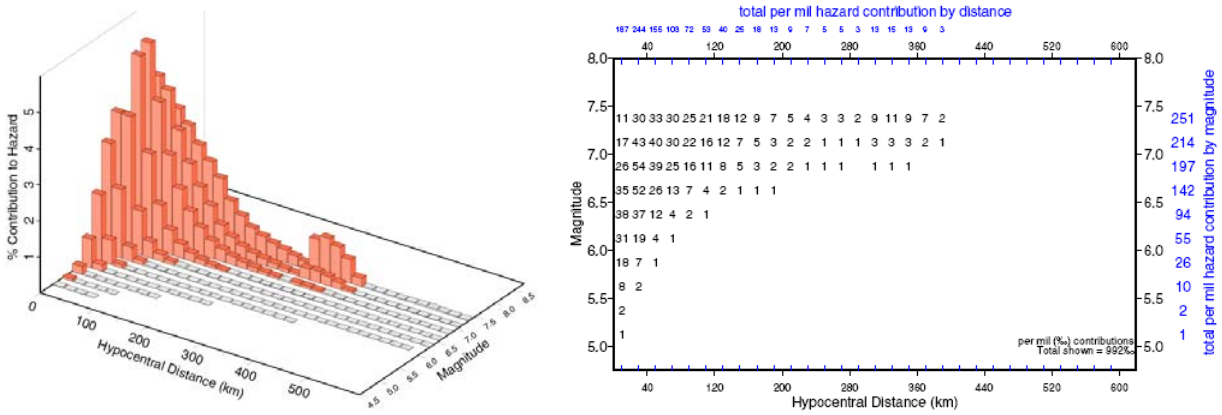

Figure 4.6 Hazard deaggregation for $S_A(1.0)$ = 0.123 g in Montreal for a probability of exceedance 2% in 50 years (Halchuk, 2010)

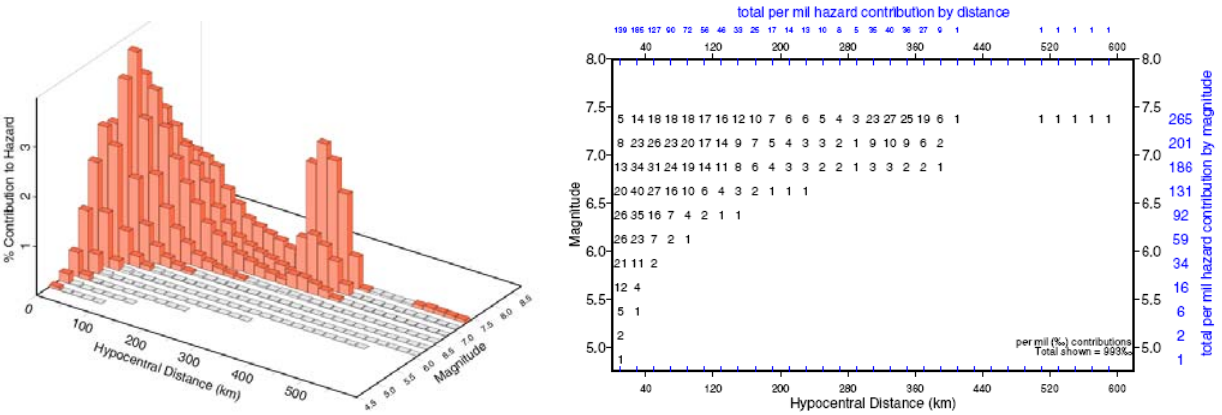

Figure 4.7 Hazard deaggregation for $S_A(2.0)$ = 0.031 g in Montreal for a probability of exceedance 2% in 50 years (Halchuk, 2010)

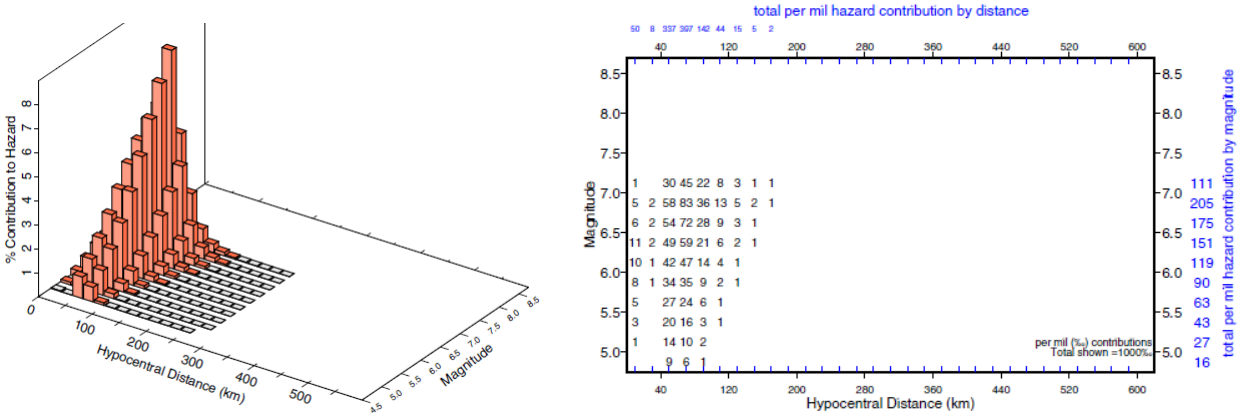

Figure 4.8 Hazard deaggregation for $S_A(0.2)$ = 0.931 g in Vancouver for a probability of exceedance 2% in 50 years (Halchuk, 2010)

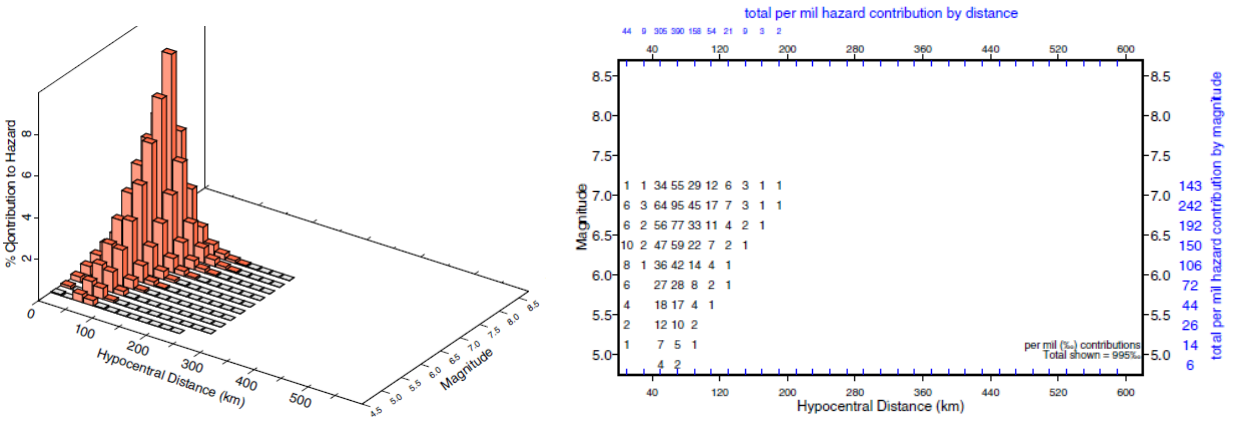

Figure 4.9 Hazard deaggregation for $S_A(0.5)$ = 0.622 g in Vancouver for a probability of exceedance 2% in 50 years (Halchuk, 2010)

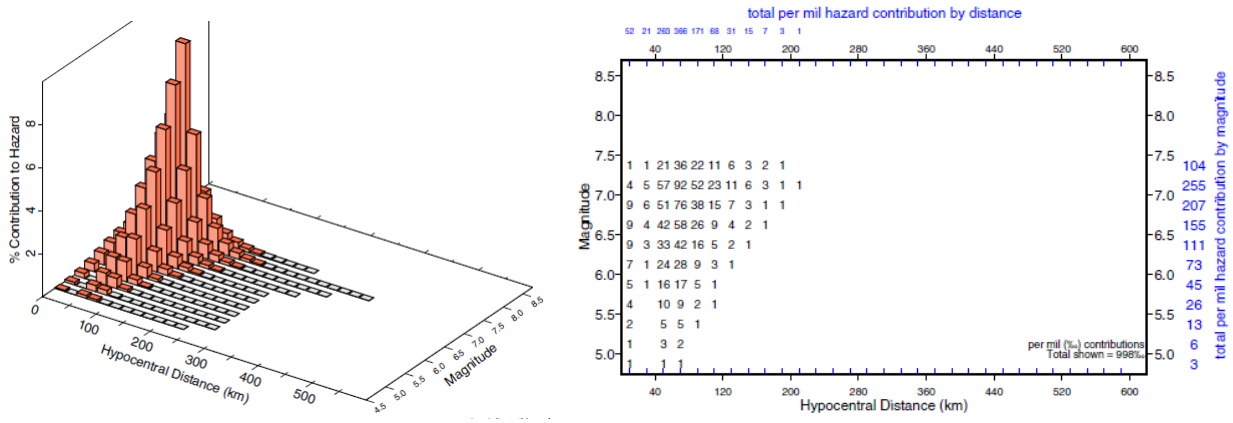

Figure 4.10 Hazard deaggregation for $S_A(1.0)$ = 0.291 g in Vancouver for a probability of exceedance 2% in 50 years (Halchuk, 2010)

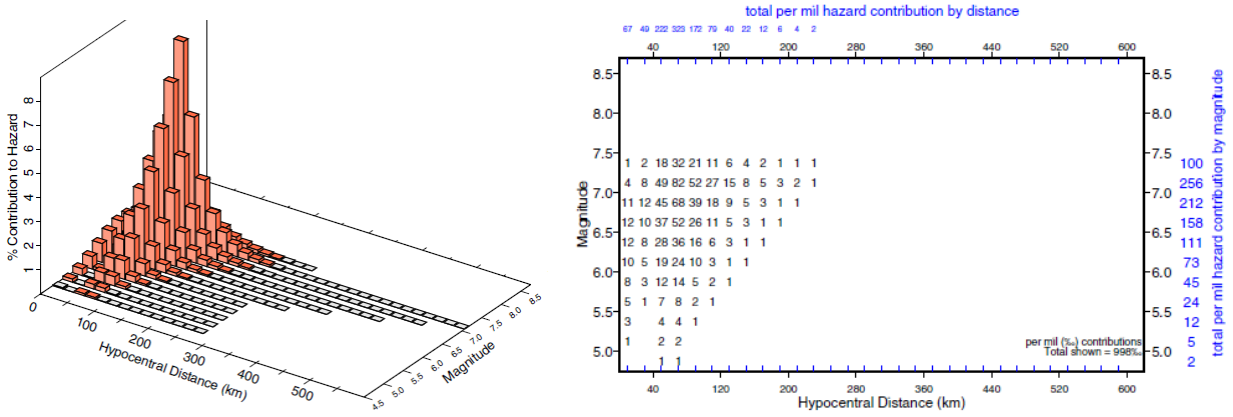

Figure 4.11 Hazard deaggregation for $S_A(2.0)$ = 0.132 g in Vancouver for a probability of exceedance 2% in 50 years (Halchuk, 2010)

Different methods for mathematically deriving a dominant M-R scenario from hazard deaggregation have been proposed over the last two decades. Among them, the methods based on adopting the modal and mean M-R values of *the contribution to the hazard* are commonly chosen for determining the dominant earthquake scenario. The mean magnitude and distance are determined as a weighted average using the *contributions to the hazard* as the weight. In such a way, primarily one dominant earthquake will represent the entire *M-R* range of the plot.

The modal magnitude and distance correspond to the greatest peak *contribution to the hazard*. The deaggregation plot with more than one peak are commonly termed multimodal and more than one dominant earthquake may be then selected adopting modal values (values at peak). The modal and mean M-R values are generally provided with deaggregation results and those parameters can be used to define dominant M-R scenarios for a given deaggregation plot as summarized in Tables 4-1 and 4-2 for four periods in Montreal and Vancouver, respectively (see Figures 4.4 to 4.7 and Figures 4.8 to 4.11).

Table 4-1 Dominant M-R scenarios determined by using the mean and modal techniques for Montreal, for a probability of exceedance 2% in 50 years (summarized form Halchuk, 2010)

$S_A(T)$	Mean Magnitude	Mean Distance	Modal Magnitude	Modal Distance
$S_A(0.2)$	5.95	34 km	5.875	30 km
$S_A(0.5)$	6.75	54 km	6.875	30 km
$S_A(1.0)$	6.89	79 km	6.875	30 km
$S_A(2.0)$	6.87	120 km	6.625	30 km

Table 4-2 Dominant M-R scenarios determined by using the mean and modal techniques for Vancouver, for a probability of exceedance 2% in 50 years (summarized form Halchuk, 2010)

$S_A(T)$	Mean Magnitude	Mean Distance	Modal Magnitude	Modal Distance
$S_A(0.2)$	6.38	66 km	6.875	70 km
$S_A(0.5)$	6.50	69 km	6.875	70 km
$S_A(1.0)$	6.73	72 km	7.125	70 km
$S_A(2.0)$	6.73	74 km	7.125	70 km

The dominant scenarios obtained for Vancouver using the mean and modal values of the *contribution to the hazard*, are in close agreement for all four periods. All four deaggregation plots present a single-mode hazard (single peak) and respective modal and mean values will correspond to a similar dominant earthquake scenario and the corresponding damage potentiality.

In contrast, by comparing the dominant earthquakes summarized in Table 4.1 (modal and mean values) for Montreal, it can be noted that the differences in magnitude and distance between the dominant earthquakes may significantly increase with period. This is primarily because of the influence of distant earthquakes whose effects increase with periods. For instance in Figure 4.7 (T = 2.0 s), the deaggregation plot clearly presents two modes due to the close and distant earthquakes.

As it can be observed in Figure 4.12, if only the earthquake with the maximum *contribution to the hazard* was selected (as that indicated in Table 4.1 for modal earthquake: M=6.625 and R=30 km), the effect of the close event will be "fairly" taken into account while from the distant earthquake will be ignored completely. In contrast, the mean value of the hazard makes it possible to take into account the contribution of all earthquakes. However, in the case of a multi-modal hazard, the mean values of the magnitude and distance may point out an event with a lower hazard and the resulting seismic demand may be non-realistically estimated.

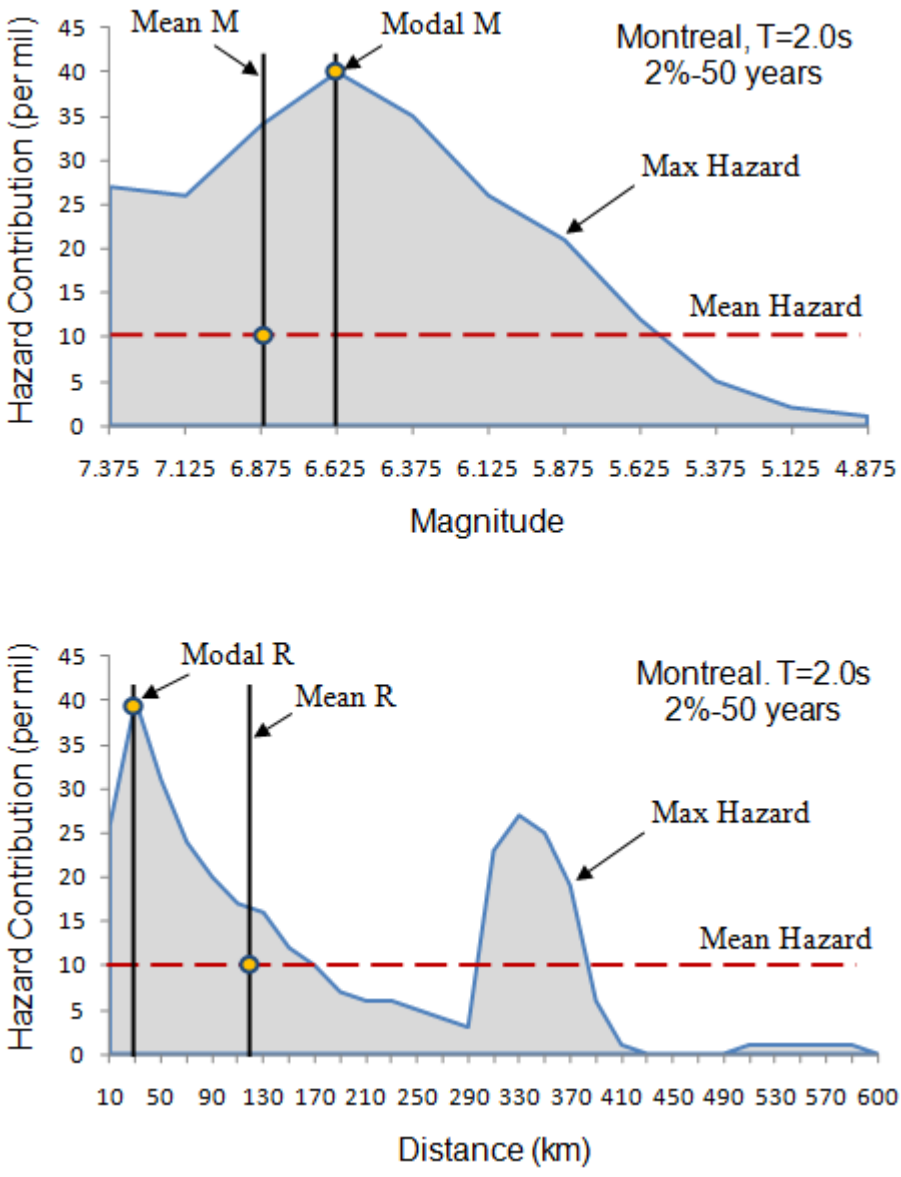

Figure 4.12 Modal and mean earthquakes for Montreal, T=2.0 s, 2%-50 years (mean hazard level is determined over all hazard contributions)

The differences in the dominant scenarios between Vancouver and Montreal may be explained by the effect of different sources that influence the site-specific seismic hazard. For the Western Canadian shore (Vancouver), the high (quick) attenuation of seismic waves reduces significantly the effect of distant earthquakes. In contrast, for Eastern Canada (Montreal), due to the low attenuation, close and distant earthquakes may affect significantly the site-specific hazard.

McGuire (1995) suggested to keep separate modal *M-R* scenarios rather than a mean $\overline{M}$ - $\overline{R}$ earthquake whether different seismic sources dominate the hazard at different periods. This technique makes it possible to reflect different damaging aspects brought by events from different seismic sources. Aiming at exploring the physical meaning of earthquake scenarios, McGuire et al. (2001a) has shown that high-frequency responses (around 10Hz) are dominated by small-magnitude earthquakes occurring at close distances to the site, while low-frequency responses (around 1Hz) are dominated by larger earthquakes at longer distances.

While such an approach would be appropriate for structures characterized by elastic responses, several engineers and researchers raise the question whether this technique will realistically reveal the earthquakes' damage potential for structures that behave within the inelastic range (Tremblay and Atkinson, 2001; Leger and Tremblay, 2009).

In this study, the results from the deaggregation analyses are used to carry out deterministic time-history analyses of the nonlinear structural behaviour of isolated bridges. Accordingly, from the perspective of structural engineering, an earthquake scenario is expected to simulate closely the damage potential of the earthquakes contributing to the hazard.

Several studies have investigated the effect of different ground-motion characteristic on the seismic inelastic response and capacity of structures (Jeong and Iwan, 1988; Tremblay, 1998; Tremblay and Atkinson, 2001; Hancock and Bommer, 2005 and Leger and Tremblay, 2009). These previous studies suggest that the ultimate capacity can be reached through different inelastic behaviors. Structures may fail due to excessive peak deformations or as a result of excessive cumulated inelastic demand (Tremblay and Atkinson, 2001; Hancock, 2006).

In order to account for different damageable effects and evaluate the range of possible responses of various isolated bridge structures, an ensemble of seismic ground motions is used for each site. These ground motions result from multiple likely M-R scenarios.

The approach proposed in this chapter consists in considering earthquakes with the greatest values of the *contribution to the hazard* referred as modal values or bins. The modal values are considered within M-R ranges that are likely prone of producing a large demand to structures (damage to structures).

This however, requires that the M-R ranges with likely damage potential be established beforehand. Because of the inherent physical variability of the earthquakes, these M-R ranges may be individually defined for each of the earthquakes. However, to produce a generalized strategy that could "robustly" take into account damage potential of different earthquakes, the proposed technique is primarily based on the extended M-R ranges. The M-R ranges were proposed by Atkinson (2009) for generating artificial ground-motion records that are compatible with an UHS determined through probabilistic seismic hazard analyses (PSHA). These M-R ranges have been primarily defined to make these artificial records easily match the target UHS from the NBCC 2005 (NRCC, 2005).

The selection of the proper design earthquakes is still challenging given that dynamic characteristic of the ground motions can vary significantly from one site to another (Anderson and Bertero, 1987). By considering several possible ground motions makes it possible to reduce the effect of uncertainty in revealing earthquakes damaging potentiality. In this study, in addition to the Atkinson's M-R ranges, boundaries that delimitate hazard contributions are considered. In this way, the Atkinson's M-R ranges are complemented so that the damaging earthquakes that are not necessary covered by them would be definitely considered for time-history analyses. As a result, a more "robust" technique is adopted as shown in Figure 4.13. It can be seen that in addition to the Atkinson's M-R ranges, the boundary ranges are considered. The M-R boundary ranges cover earthquakes in ranges of the closest distance, greatest magnitude and those from a group of distant events.

The influence of distance and magnitude on the earthquake damage potentiality has been widely reported in the past (Anderson and Bertero, 1987; Bommer and Martinez-Pereira, 1999; Liu et al., 2001, Bommer et al. 2001; Hancock, 2006). Bertero et al. (1978) observed that during the San Fernando earthquake, long-duration acceleration pulses rather than the high frequency acceleration spikes were the cause of the most observed structural damages in structures located close to the earthquake fault. The structures subjected to closer ground motions will most likely experience failures at the prescribed peak of inelastic deformation.

The distant earthquakes may also produce damaging long-duration pulses as, for example, during the earthquake at Bucharest, Rumania in 1977 (Anderson and Bertero, 1987). The damaging long-duration acceleration pulses for sites located at large distance are mostly attributable to soil

amplification or topographical features (Yamada, 1988; Somerville and Yoshimura, 1990; Bommer et al., 2001).

The earthquakes from close distances are typically characterized by a wide frequency range and much shorter duration with respect to that from more distant strong ground motions. For these distant earthquakes, damaging potentiality is generally due to the low frequency (long period) seismic waves that attenuate more slowly with distance when compared to the high frequency waves.

The influence of the ground motion duration on the earthquake damaging effect has been also reported by many studies (Ambraseys and Srbulov, 1994; Bommer and Martinez-Pereira 1999; Bommer et al., 2009). Certain studies reported that the ground motion duration may be strongly influenced by magnitude and distance (Rosenblueth and Bustamante, 1962; Esteva and Rosenblueth, 1964; Trifunac and Novikova, 1995). Esteva and Rosenblueth (1964) developed the first equation that expressed duration as a function of magnitude and distance. It was shown that duration increases exponentially with magnitude and linearly with distance. Trifunac and Novikova, (1995) carried out regression analyses on the Californian earthquakes at epicentral distances up to 100 km and with magnitudes in the range $2.5 < M < 7.5$. They also observed that the ground motion duration increases with magnitude. Earthquakes with large magnitude result in wider response spectra (Kalkan and Chopra, 2010). Their predominant period and duration will be also increased compared to those having small magnitude (Somerville et al. 1997b; Somerville, 2000; Bommer et al. 2001).

The damage potential due to accumulation of damage is widely associated with events having larger pulses and long duration (Nassar and Krawinkler,1991; Hancock, 2006). From an engineering viewpoint, the accumulation of damage results in the increased drifting of the seismic protection system and is expected to be accounted in this study by considering the boundary M-R ranges in addition to those defined by Atkinson (2009). It should be noted that this technique does not prevent from taking the same event two times if it results the most critical from the both the Atkinson's M-R and boundary ranges. As expected, the eventuality of the most damaging effect will be reiterated thus providing the dominant earthquake scenario with a certain level of redundancy.

The technique for selecting dominant earthquakes required for time-history analyses is summarized in the three main steps described below. In Step 1 and Step 2, earthquakes are selected using Atkinson's and boundary M-R ranges. In Step 3, the dominant earthquakes are combined and the number of records required for time-history analyses is then defined.

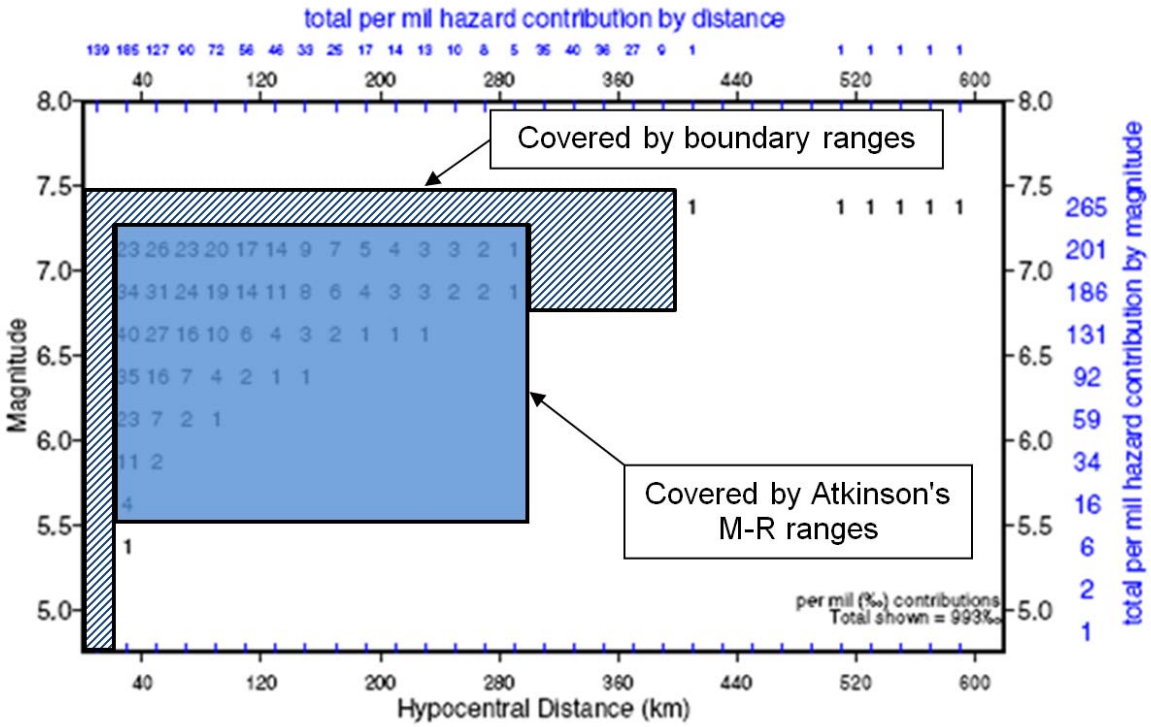

Figure 4.13 Earthquakes covered by Atkinson's M-R ranges and boundary ranges

Step 1. Selection of the dominant GMs from the Atkinson's M-R ranges

For the first step, four *M-R* clusters were segregated from a main deaggregation grid to group events according to their potentially different damaging effects on structures. Two distance ranges and two magnitude ranges define these *M-R* clusters.

Two magnitude ranges were defined as small-to-moderate and moderate-to-large events having, respectively, moment magnitudes M6 and M7 for ENA and M6.5 and M7.5 for WNA. The small-to-moderate events typically match the short-period segment of the UHS, while the moderate-to-large events at longer distances are more appropriate to match the long-period segment of the UHS (Atkinson, 2009). Atkinson generated artificial time histories grouped by two distance ranges of 10-15 km and 20-30 km for small-to-moderate earthquakes and of 15-

25 km and 50-100 km for moderate-to-large earthquakes that result in four subsets defined in terms of magnitude and distance. Adopting these *M-R* ranges for the present study, four suites of earthquakes were defined as presented in Table 4-3.

Table 4-3 Magnitude-distance ranges for Step 2 of scenario definition

Region	UHS Short-Period Range		UHS Long-Period Range	
	Close Events R10 (10-15 km)	Distant Events R30 (20-30 km)	Close Events R10:R30 (15-25 km)	Distant Events R50:R110 (50-100 km)
ENA	**E6C1** M6 at R10 *(5.5<M<6.5)*	**E6C2** M6 at R30 *(5.5<M<6.5)*	**E7C1** M7 R15-R25 *(6.5<M<7.5)*	**E7C2** M7 R50-R110 *(6.5<M<7.5)*
WNA	**W6C1** M6.5 at R10 *(6.0<M<7.0)*	**W6C2** M6.5 at R30 *(6.0<M<7.0)*	**W7C1** M7.5 R10-R30 *(7.0<M<8.0)*	**W7C2** M7.5 R50-R110 *(7.0<M<8.0)*

The corresponding selection process adopted for the second step is presented in Figure 4.14. The bins with the greatest contribution to the hazard are chosen from the deaggregation plots for each of above-defined M-R clusters. As a result, four *M-R* events were selected for each of four periods as summarized in Table 4-4.

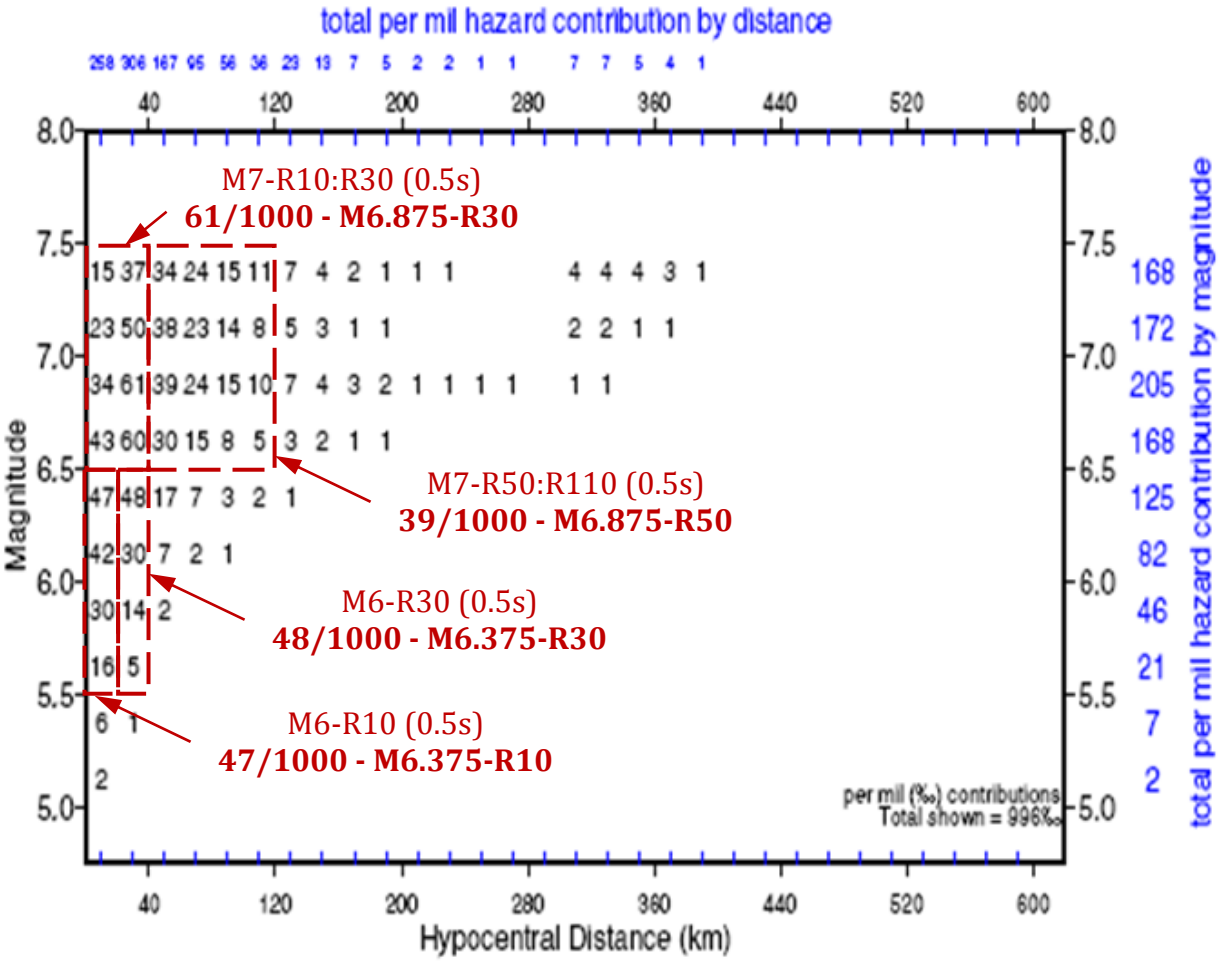

S_A (T)	Short-Period Range M6 (5.5 - 6.5)		Long-Period Range M7 (6.5 - 7.5)	
	R10	R30	R10-R30	R50-R110
S_A(0.5)	47/1000 M6.375-R10	48/1000 M6.375-R30	61/1000 M6.875-R30	39/1000 M6.875-R50

Figure 4.14 Example of selecting earthquake scenarios using Atkinson's M-R ranges (Step 1) from hazard deaggregated for Montreal, $S_A(0.5)$ = 0.289 g, at a probability of exceedance 2% in 50 years (deaggregation by Halchuk, 2010)

Table 4-4 Step 2 - M-R ranges selection approach for Montreal, 2%-50 years

S_A (T)	Short-Period Range M6 (5.5 - 6.5)		Long-Period Range M7 (6.5 - 7.5)	
	R10	R30	R10-R30	R50-R110
S_A(0.2)	68/1000 M5.625-R10	68/1000 M5.875-R30	17/1000 M6.625-R30	8/1000 M6.875-R50
S_A (0.5)	47/1000 M6.375-R10	48/1000 M6.375-R30	61/1000 M6.875-R30	39/1000 M6.875-R50
S_A (1.0)	38/1000 M6.375-R10	37/1000 M6.375-R30	54/1000 M6.875-R30	40/1000 M7.125-R50
S_A (2.0)	26/1000 M6.375-R10	35/1000 M6.375-R30	34/1000 M6.875-R30	31/1000 M6.875-R50

Step 2. Selection of the dominant GMs from the Boundary M-R ranges

In Figure 4.15, the results of the deaggregation are presented in a summary table that is used in the second step of the selection process. In the table, the bins with the greatest *contributions to the hazard* are chosen from the largest magnitude row, from the shortest distance column, and from the separate group if any. In this step, the damage potential of the earthquakes with the closest distance, greatest magnitude and those from a group of distant events is considered for time-history analyses. As a result, three *M-R* events are selected for a given period. The M-R scenarios selected for Montreal using this step are given in Table 4-5 for the four periods.

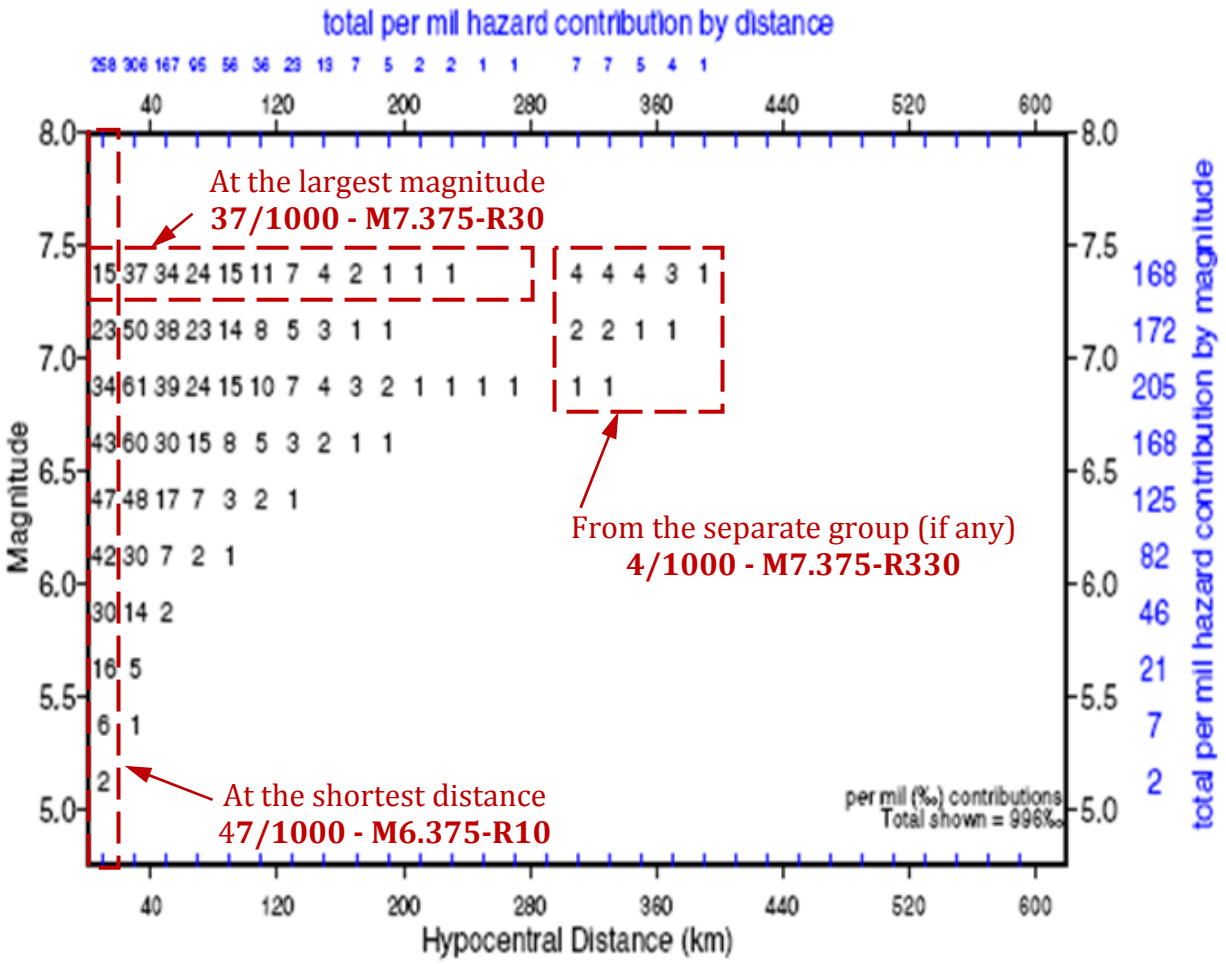

$S_A(T)$	Largest Magnitude M7.375	Shortest Distance R10	Separate Group of Events "Tail" - distant earthquakes
$S_A(0.5)$	37/1000 M7.375-R30	47/1000 M6.375-R10	4/1000 M7.375-R330

Figure 4.15 Example of selecting earthquake scenarios using Boundary M-R ranges (Step 2) from hazard deaggregated for Montreal, $S_A(0.5)$ = 0.289 g, at a probability of exceedance 2% in 50 years (deaggregation by Halchuk, 2010)

Table 4-5 Step 1 - Boundary selection approach for Montreal, 2%-50 years

S_A (T)	Largest Magnitude M7.375	Shortest Distance R10	Separate Group of Events "Tail" - distant earthquakes
S_A (0.2)	7/1000 M7.375-R30	68/1000 M5.625-R10	1/1000 M7.375-R330
S_A (0.5)	37/1000 M7.375-R30	47/1000 M6.375-R10	4/1000 M7.375-R330
S_A (1.0)	33/1000 M7.375-R30	38/1000 M6.375-R10	11/1000 M7.375-R330
S_A (2.0)	18/1000 M7.375-R30	26/1000 M6.375-R10	27/1000 M7.375-R330

Step 3. Target Seismic Scenarios and Number of TH Records

The 28 dominant earthquakes obtained as modal values from the previous two steps are then combined, which resulted in a total number of nine events summarized in Table 4-6. A number of required records, their *M-R* characteristics and the contribution to hazard are given in Table 4-7. Figure 4.16 presents the dominant earthquake scenario obtained by compiling the 28 dominant earthquakes. The nine events were distributed within the four Atkinson's M-R ranges to facilitate the selection of time-history records performed further in this chapter. As presented in Table 4-7, a number of records was assigned to each of the ranges so the least number of alternative records would be a number of two. In this study, the two records correspond to the M-R range with the lowest hazard contribution as that of 161/1000 of E7C2. Note that the level of hazard contribution associated with each of the remaining M-R ranges is not necessary an exact multiple of 161/2 as it could be desired. However, the numbers of records were approximated to be proportionally related to the hazard contribution.

Table 4-6 M-R events selected from Steps 1 and 2 – ENA

M-R Events	Contribution	Earthquake Selection Approach
M5.625-R10 (136/1000)	68/1000	Step 2: *S_A(0.2)-Shortest Distance*
	68/1000	Step 1: *S_A (0.2)-Short-Period Range / R10*
M5.875-R30 (68/1000)	68/1000	Step 1: *S_A (0.2)-Short-Period Range / R30*
M6.375-R10 (222/1000)	47/1000	Step 2: *S_A (0.5)-Shortest Distance*
	38/1000	Step 2: *S_A (1.0)-Shortest Distance*
	26/1000	Step 2: *S_A (2.0)-Shortest Distance*
	47/1000	Step 1: *S_A (0.5)-Short-Period Range / R10*
	38/1000	Step 1: *S_A (1.0)-Short-Period Range / R10*
	26/1000	Step 1: *S_A (2.0)-Short-Period Range / R10*
M6.375-R30 (120/1000)	48/1000	Step 1: *S_A (0.5)-Short-Period Range / R30*
	37/1000	Step 1: *S_A (1.0)-Short-Period Range / R30*
	35/1000	Step 1: *S_A (2.0)-Short-Period Range / R30*
M6.625-R30 (17/1000)	17/1000	Step 1: *S_A (0.2)-Long-Period Range / R10-R30*
M6.875-R30 (149/1000)	61/1000	Step 1: *S_A (0.5)-Long-Period Range / R10-R30*
	54/1000	Step 1: *S_A (1.0)-Long-Period Range / R10-R30*
	34/1000	Step 1: *S_A (2.0)-Long-Period Range / R10-R30*
M6.875-R50 (118/1000)	8/1000	Step 1: *S_A (0.2)-Long-Period Range / R50-R110*
	39/1000	Step 1: *S_A (0.5)-Long-Period Range / R50-R110*
	40/1000	Step 1: *S_A (1.0)-Long-Period Range / R50-R110*
	31/1000	Step 1: *S_A (2.0)-Long-Period Range / R50-R110*
M7.375-R30 (95/1000)	7/1000	Step 2: *S_A (0.2)- Largest Magnitude*
	37/1000	Step 2: *S_A (0.5)- Largest Magnitude*
	33/1000	Step 2: *S_A (1.0)- Largest Magnitude*
	18/1000	Step 2: *S_A (2.0)- Largest Magnitude*
M7.375-R330 (43/1000)	1/1000	Step 2: *S_A (0.2)- Separate Group*
	4/1000	Step 2: *S_A (0.5)- Separate Group*
	11/1000	Step 1: *S_A (1.0)- Separate Group*
	27/1000	Step 1: *S_A (2.0)- Separate Group*

Table 4-7 Distribution and number of records from Step 1 and Step 2 - ENA

E6C1 M6 at R10	**E6C2** M6 at R30	**E7C1** M7 R10:R30	**E7C2** M7 R50:R110
M5.625-R10 (136/1000) *M6.375-R10 (222/1000)*	*M5.875-R30 (68/1000)* *M6.375-R30 (120/1000)*	*M6.625-R30 (17/1000)* *M6.875-R30 (149/1000)* *M7.375-R30 (95/1000)*	*M6.875-R50 (118/1000)* *M7.375-R330 (43/1000)*
358/1000	*188/1000*	*261/1000*	*161/1000*
6 Records	*3 Records*	*3 Records*	*2 Records*

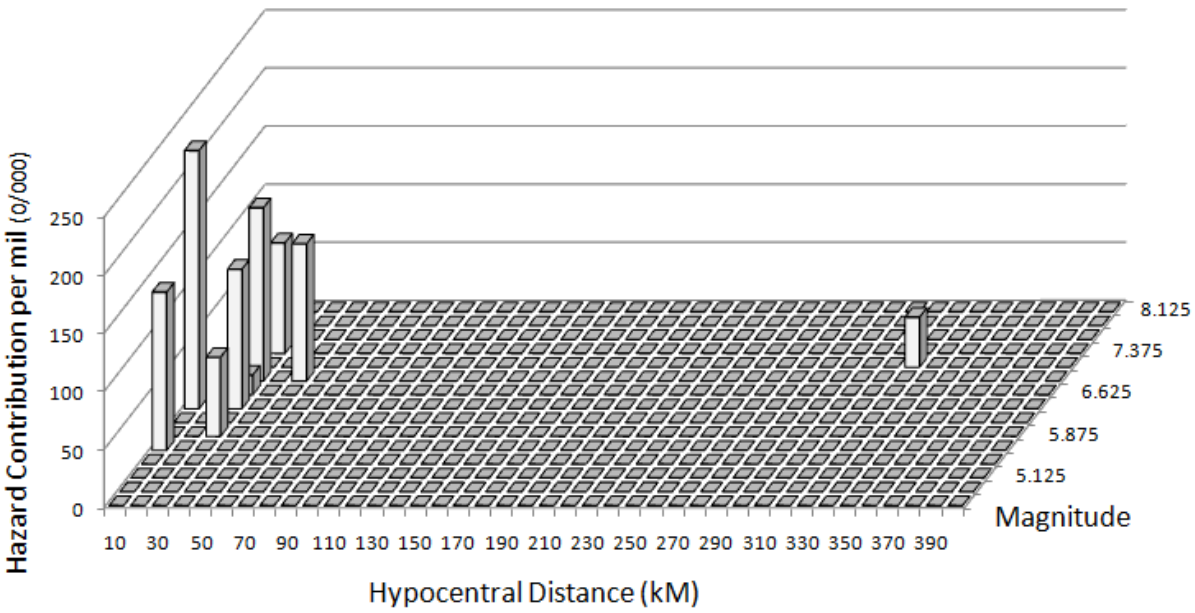

Figure 4.16 Dominant earthquake scenario for montreal at 2% in 50 years (0.2 s to 2.0 s)

This dominant earthquake scenario would be adequate for analyses of structures characterized by a period range for which the deaggregated plots were provided (0.2, 0.5, 1.0, and 2.0 s). However, an extended period range beyond 2.0 s is necessary to cover a large inelastic excursion

of isolated bridges. The hazard deaggregation plots for a longer period range are not available today and there are no studies on how to combine the relative contributions for longer periods. To overcome these limitations and to represent the damage potential for long-period range as for example, 4.0 s and 6.0 s, the earthquakes were arbitrary added to the dominant scenario. The records were added to the suite E7C2 (moderate-to-large events at longer distances) as explained below.

To evaluate the number of records that are needed to complement the seismic scenario derived in previous steps, the distribution of the UHS linear segments as provided by the NBCC (NRCC, 2005) code was adopted. In addition to the periods of 0.2, 0.5, 1.0, and 2.0 s (available deaggregation plots), the period of 4.0 s is specified as a limit beyond which spectral acceleration values are constant. Accordingly, for the cases where the effective period exceeds 4 s, constant annual probability of exceedance of a target spectral amplitude *Sa(T)* are assumed. It has been recognized that for longer periods, more distant earthquakes with larger magnitudes contribute more to the hazard (Adams and Halchuk, 2004).

As discussed in Chapter 2, it was shown by different studies (Tolis and Faccioli, 1999; Bommer et al., 2000b) that acceleration design spectra as specified in the NBCC (2005 and 2010) do not necessary provide engineers with reliable realistic displacement demand in long periods. It raises the question as how to reduce the effect of the uncertainty in response of isolated bridges for which displacement response in long period range is of intrinsic importance.

Aiming to address the effect of the uncertainty in long periods, the extended period range is defined through six periods as 0.2, 0.5, 1.0, 2.0, 4.0, and 6.0 (any longer than 4 s) and for the last two periods, only the contributions from the E7C2 (moderate-to-large events at longer distances) earthquakes are assumed to dominate the contribution to the hazard.

Assuming a proportional distribution of records between the six periods, a number of 14 records was divided by 4 periods and multiplied by 6 records what yields 21 records. The number was rounded down to 20 records for simplicity. The ENA earthquake scenario was then complemented with six records as presented in Table 4-8. Three time histories is a minimum number of records that was attributed to the suites of E6C2 and E7C1. Three records rather than one were intentionally adopted to take into account the record-to-record inherent variability.

The same earthquake selection approach was then performed for developing the WNA target (dominant) scenarios. As a result, a total number of 20 records is adopted for detailed time-history analyses on the nonlinear structural behaviour of isolated bridges in eastern and western North America.

Table 4-8 Distribution and number of records from Step 3 - ENA

E6C1 M6 at R10	**E6C2** M6 at R30	**E7C1** M7 R10:R30	**E7C2** M7 R50:R110
6 Records	*3 Records*	*3 Records*	*8 Records*

4.5 Directivity Effect on Response Variability

The influence of the rupture directivity on the response of structures is another source of uncertainty which effect is frequently omitted during time history selection. The topic of seismic directivity is out of scope of this thesis, however, the effort was done aiming to address the question as how to account for the seismic directivity effect for time-history analyses. The results and details of this particular study are presented in Appendix A.

In this section, the seismic directivity is briefly reviewed and examined to outline its effect on the response variability. The use of a large number of records is suggested to incorporate the record-to-record variability that is in part due to the effect of seismic directivity. However, in daily practice, engineers tend to reduce this number to 1 to 7 aiming at diminishing analysis time and costs (Atkinson, 2010 and 2012 - CSRN). In the new edition of the CAN/CSA-S6-14, the number of records is increased to 11. This makes it possible to better take into account the record-to-record variability when compared to the CAN/CSA-S6-06 specifying only 5 time histories.

The effect of azimuthal position of the site relative to the on the amplitude and duration of ground motion is well-known, as well as the importance to consider the resulting frequency

content and the number of yield reversal in the nonlinear structural analyses (Tremblay and Atkinson 2001; Filiatrault et al., 2013).

The ground motion magnitude is dependent on the finite rupture length. For instance, earthquakes with magnitudes 6 and 8 can have 10 to 300 km fault rupture lengths, respectively (Stein and Wysession, 2003). The phenomenon of seismic directivity and its effects are commonly explained by the fact that earthquakes are generally induced by sudden rupture, or slip initiated at a given point along a fault and it propagates from this point along the fault. Accordingly, it may significantly affect the arrival time of seismic waves that travels from different parts of the fault (Stein and Wysession, 2003). In such a case, the history of the fault rupture can be idealized by a double ramp function with slip duration t_d and time of rupture propagation t_r, the resulting pulse body felt at the site is shown in Figure 4.17. The vertical axis in this plot may indicate the intensity of the energy delivered to a site by shear waves. Spatial variations in amplitude and duration of the ground motion around faults may be a consequence of the fault-rupture directivity (Filiatrault et al., 2013).

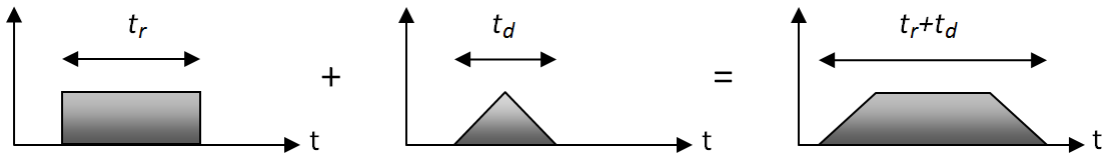

Figure 4.17 Pulse time function

Assuming that energy released during an earthquake by the ground motion is the same at all azimuthal directions from a ruptured fault to a site of interest, the pulse intensity is expected to be increasing as the total time is decreasing. The direction in which the fault rupture propagates toward the site corresponds to the azimuth $\theta = 0°$ and is referred to as a forward directivity. On this basis, Figure 4.18 presents the plan view of the variation of the ground motion amplitude and duration as a function of azimuthal direction where the amount of energy released is idealized by the area of the trapezoid. As shown, the forward directivity can be characterized by the highest

intensity and the shortest duration. The azimuth $\theta = 180°$ or backward directivity corresponds to the case where rupture propagates along the fault in a direction away from the site. For this case, ground motion duration is the longest while the intensity is the lowest.

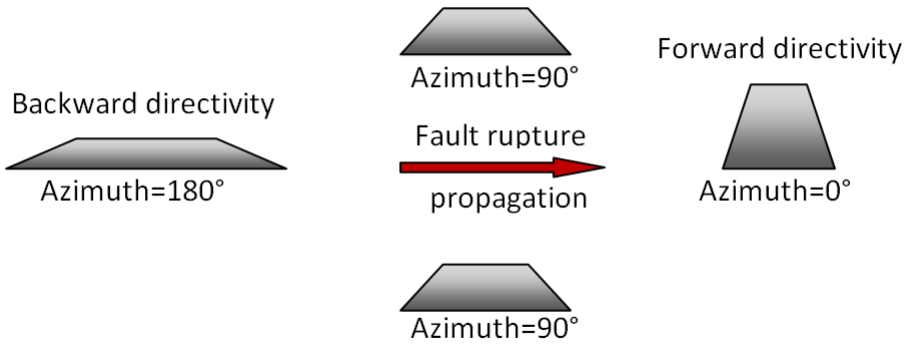

Figure 4.18 Plan view of the directivity effect on the ground motion intensity and duration

The directivity effects have been described theoretically by Ben-Menahem (1961, 1962). Before Somerville's empirical model (1997a), the directivity effects have not been considered as an independent variable such as magnitude and distance, in attenuation relationships. Rather, recordings are used without considering the position of the instrument relative to the direction of wave propagation.

Following the earthquakes that occurred in Loma Prieta (1989), Northridge (1994), and Kobe (1995), the modifications to ground motion attenuation relationship for rupture directivity effects have been incorporated by Sommerville. It was one of the first directivity predictive models that have been derived from the ten real near-fault recordings. Figure 4.19 illustrates the forward and backward rupture directivity effects reported by Somerville (1997a).

Atkinson (2008) generated earthquake time histories that reflect the tectonic conditions prevailing in Canada. The technique of simulation using the stochastic finite-fault (finite-source) method with the code EXSIM (Extended Finite-Fault Simulation, Motazedian and Atkinson, 2005) was applied in this approach. The stochastic finite-source method with respect to the stochastic point-source (Boore, 2005) makes it possible to consider such parameters as faulting geometry, distributed rupture, and rupture inhomogeneity (Atkinson et al., 2009). In the model, the fault-source surface is divided into a number of subsources each of which could be

considered as a small point source of the earthquake ground motion. The entire fault ground motion is then obtained by summing the calculated subsource effects in the time domain, activating the point sources with an appropriate time delay in a predetermined fault direction. On this basis, directivity effects can be taken into consideration by such a finite-fault modeling.

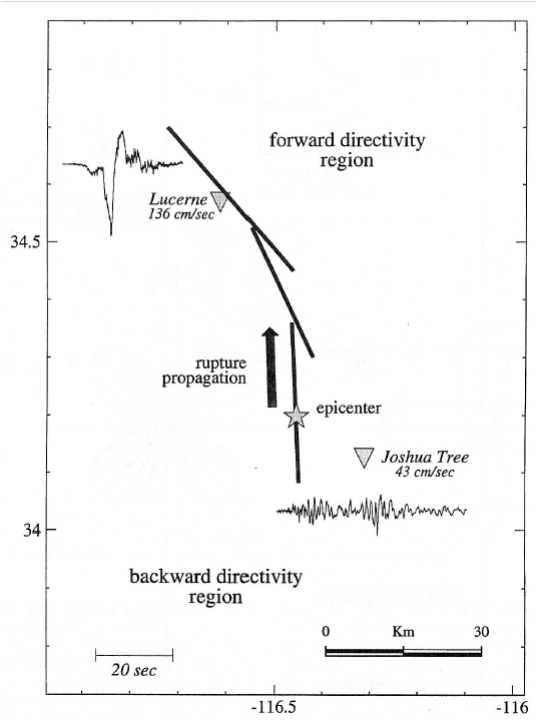

Figure 4.19 Forward and backward rupture directivity from the 1992 Landers earthquake (Somerville, 1997a)

The significance of considering the rupture directivity effect in terms of the response variability may be outlined to justify a larger number of time-history records for nonlinear structural analyses in the time domain. The effect of seismic directivity was investigated to outline its effect on response variability. The study on directivity effects was carried out using Atkinson's 2008 artificial ground motions and consists of two main steps: 1) the characterization of the earthquake records with respect to the ground motion azimuthal direction; and 2) the assessment of the effect of directivity on the inelastic structural responses.

To examine directivity effects, Atkinson's 2008 ground motions were adopted instead of those Atkinson's 2009 scaled in the previous subsection. The reason for using the older sets is that they

formed a complete ensemble in terms of azimuths : 3 different trials x 8 azimuths in 45° increments for each M-R scenario. Accordingly, this particular ground motion set of artificial records were analyzed only in this section of this thesis. Two suites of earthquake time-histories simulated for two moment magnitudes were considered to represent small-to-moderate (short-period) and moderate-to-large (long-period) seismic events for each location: M6.0 and M7.0 for ENA and M6.5 and M7.5 for WNA. To reproduce the effect of close and distant events, two fault-distance ranges were selected. The suites of the small-to-moderate ground motions were analyzed for distances of 10 and 30 km, while those of the moderate-to-large - for distances of 30 and 50 km. Only the records generated for site class C were analyzed in this study.

This thesis is dedicated to methods for predicting the peak response of isolated bridge. The seismic directivity is identified as a possible source of the variability in the response estimates. The details and results of this particular study are presented in Appendix A, while this section presents the resulting conclusion.

The responses from different azimuthal directions were compared with respect that having azimuth $\theta = 0°$ (forward directivity). The index of azimuthal variability α_{var} was examined to identify the maximum amplification effect on the earthquake damage potential. The maximum amplification averaged over the period range 0.5 s - 6.0 s are $\alpha_{\text{var}}(ENA) = 1.45$ and $\alpha_{\text{var}}(WNA) = 1.41$. The largest amplifications correspond to the period range 0.5 - 1.0 s $\alpha_{\text{var}}(ENA) = 1.70$ and $\alpha_{\text{var}}(WNA) = 1.67$.

A particular variability shape was observed for parameters defined as a function of azimuthal distribution for the both steps. There is however no definitive evidence found to establish clear directivity-dependant trends for different M-R suites or hazard-dominant earthquake scenarios. There is likely a limitation in the finite-fault model utilized by Atkinson (2008) for generating artificial ground motions since clear geometric sequences of activating the point sources are not necessary established when rupture effect is simulated.

However, using this available source of time histories generated with azimuthal distribution, the significance of considering the rupture directivity effect in terms of the variability of the damage potential is outlined in this section. To account for this variability during the nonlinear time-

history analyses a large number of time-history records characterized by different azimuthal directions is justified.

4.6 Ground Motion Scaling

Among the numerous approaches that are commonly adopted to make earthquake records matching a target UHS, the amplitude-scaling method is the one that makes possible to preserve the influence of physical characteristics representative of the geological source. The ground-motion parameters as the frequency content and duration do not change when the spectral amplitude is linearly scaled. The ground-motion parameters vary significantly across North America and it was a primary reason for adopting the amplitude-scaling method for investigating nonlinear behaviour of isolated bridges in ENA and WNA. According to the dominant scenario derived above, 20 records are required for each locality (Montreal - ENA and Vancouver - WNA). In this way the site-specific record-to-record variability would be appropriately taken into consideration. Moreover, to account for the effect of seismic directivity, the time-history records having different azimuthal directions will be selected for each of the M-R scenarios.

Due to a scarce number of ground motions corresponding to historical events occurred in ENA, sets of eastern artificial (Atkinson, 2009) and hybrid (McGuire et al., 2001a) ground motions were adopted for the ENA region. To establish the same comparative basis between ENA and WNA, only the set of artificial western records (Atkinson, 2009) was selected for parametric analyses.

The artificial ground motions were generated by Atkinson to match the 2005 NBCC UHS at any generic regions of eastern and western Canada. These records are freely accessible from www.seismotoolbox.ca and are provided for the site classes A, C, D and E. A dataset (catalogue) of 180 records is available for each of these site classes. The records were regrouped by 45 using two magnitude ranges (small-to-moderate and moderate-to-large events) and two fault-distance ranges (close and distant events). This *M*-*R* distribution are summarized in Table 4.3 for ENA and WNA and is adopted for the parametric analyses further presented in this thesis.

The database of hybrid time histories was produced by McGuire et al. (2001a) to reproduce the seismicity from the central-eastern U.S. (CEUS). This database was obtained by processing a range of historic recordings primarily from the western U.S. (WUS). The WUS records have

been then modified using spectral matching approach to reflect appropriately the CEUS ground motion characteristics.

Three ground motions suites were then assembled from records selected from the corresponding databases (Atkinson, 2009 and McGuire et al., 2001a) according to the dominant *M-R* earthquake scenario. Even though the selected time-histories were characteristic of the site-specific seismicity (ENA and WNA) and the required magnitudes and fault distances, these ground motions needed to be scaled to the level of earthquake that corresponds to the probability of exceedance adopted in the NBCC (2005) (2% in 50 years). The scaling process employed in this study is similar to those described in details by Atkinson (2009) and Guilini Charette (2009).

In engineering practice, a challenging part of the selection and scaling process is still to make the records match an entire period range. In this study, each time-history record was scaled with a simple factor so that the area under the response spectrum equals that of the site-specific UHS specified in NBCC (NRCC, 2005) over the same period range. As proposed by Atkinson (2009), the records with the lowest standard deviation of $S_{A\text{-}targ}/S_{A\text{-}sim}$ computed in the 0.2 - 4.0 s period range were then selected. The resulting suites are denoted as ATK-E and MCG-CEUS for ENA and ATK-W for WNA. Spectral values from the UHS NBCC (2005) used for scaling are presented in Table 4-9. Figures from 4.20 to 4.22 present the individual and mean spectra of the scaled ground motions. The records and scaling factors are listed in Tables from 4-10 to 4-12.

Table 4-9 Spectral values from the target UHS NBCC (2005) - 2% in 50 years, site class C

Period	Montreal - ENA		Vancouver - WNA	
T (s)	S_A (g)	PS_D (mm)	S_A (g)	PS_D (mm)
0.0	0.690	0.00	0.940	0.00
0.2	0.690	6.86	0.940	9.30
0.5	0.340	21.1	0.640	39.8
1.0	0.140	34.8	0.330	82.0
2.0	0.048	47.7	0.170	169
4.0	0.024	95.4	0.085	338
6.0	0.024	215	0.085	760

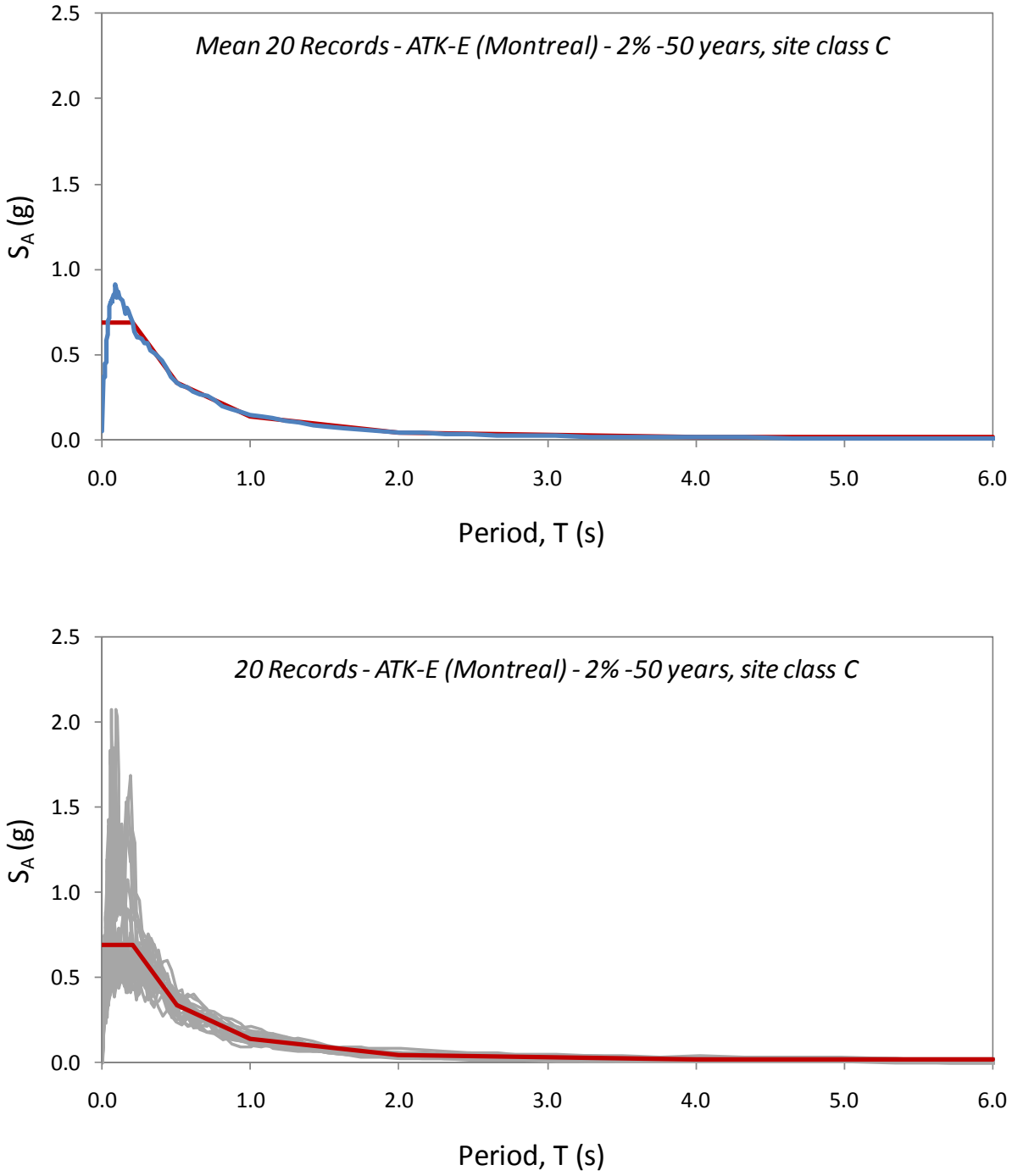

Figure 4.20 ATK-E 20 Records - Mean and individual 5% damped response spectra scaled to the target UHS 2005 NBCC

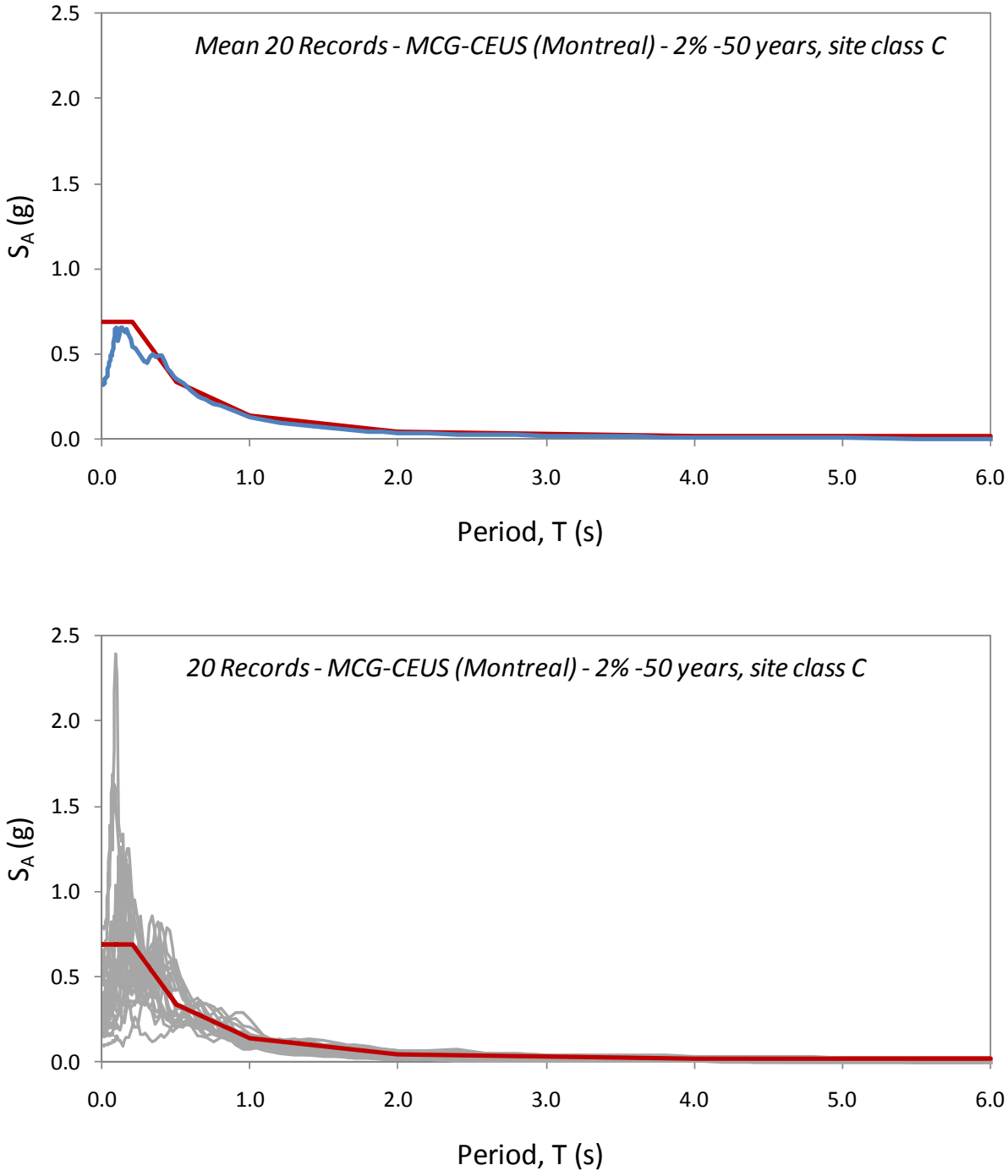

Figure 4.21 MCG-CEUS 20 Records - Mean and individual 5% damped response spectra scaled to the target UHS 2005 NBCC

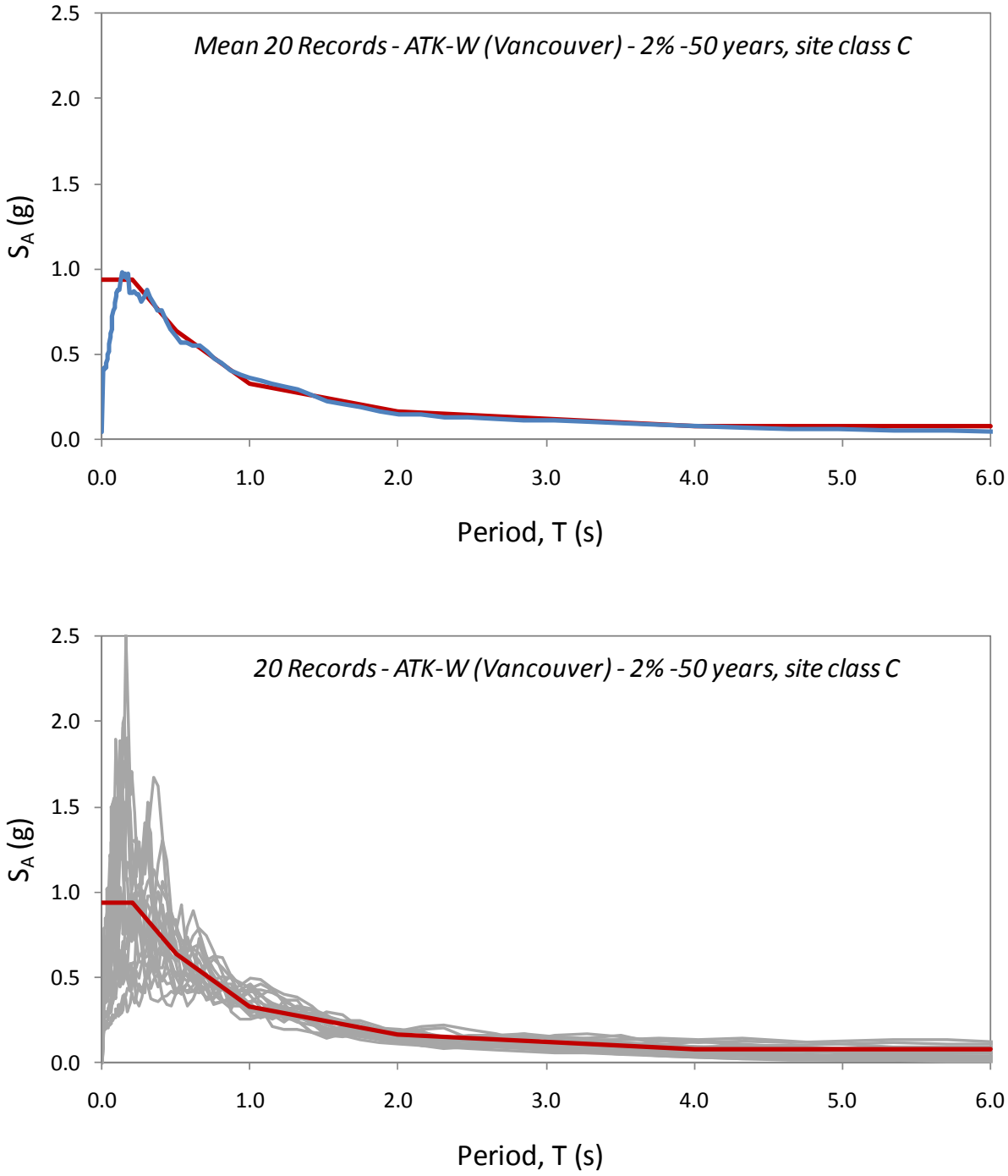

Figure 4.22 ATK-E 20 Records - Mean and individual 5% damped response spectra scaled to the target UHS 2005 NBCC

Table 4-10 ATK-E 20 Records scaled to the target UHS 2005 NBCC, 2%-50 years, site class C, city of Montreal (ENA), $S_{a\text{-}targ}/S_{a\text{-}sim}$ computed over 0.2 - 4.0 s

Record Name	M	R (km)	S.F.	T-Range	$\frac{S_{a-t\arg}}{S_{a-sim}}$	ATK-E Earthquake
E6C1						
E6C1-9	6.0	12.8	1.114	0.2-6.0s	0.366	east6c1-09-2009
E6C1-12	6.0	12.8	1.252	0.2-6.0s	0.462	east6c1-12-2009
E6C1-33	6.0	17	1.360	0.2-6.0s	0.526	east6c1-33-2009
E6C1-34	6.0	16.6	1.075	0.2-6.0s	0.256	east6c1-34-2009
E6C1-42	6.0	17	1.095	0.2-6.0s	0.550	east6c1-42-2009
E6C1-43	6.0	17	1.539	0.2-6.0s	0.325	east6c1-43-2009
E6C2						
E6C2-12	6.0	21.1	2.297	0.2-6.0s	0.763	east6c2-18-2009
E6C2-39	6.0	25.1	2.915	0.2-6.0s	0.966	east6c2-18-2009
E6C2-41	6.0	30.7	3.031	0.2-6.0s	0.568	east6c2-18-2009
E7C1						
E7C1-9	7.0	14.2	0.289	0.2-6.0s	0.260	east7c1-18-2009
E7C1-32	7.0	25.8	0.776	0.2-6.0s	0.227	east7c1-18-2009
E7C1-41	7.0	25.6	0.942	0.2-6.0s	0.200	east7c1-18-2009
E7C2						
E7C2-8	7.0	45.2	1.410	0.2-6.0s	0.304	east7c2-08-2009
E7C2-18	7.0	62.6	2.385	0.2-6.0s	0.211	east7c2-18-2009
E7C2-23	7.0	69.9	2.287	0.2-6.0s	0.275	east7c2-23-2009
E7C2-26	7.0	70.2	2.162	0.5-1.0s	0.162	east7c2-26-2009
E7C2-40	7.0	94.3	2.152	0.2-6.0s	0.184	east7c2-40-2009
E7C2-42	7.0	94.3	2.242	0.2-6.0s	0.240	east7c2-42-2009
E7C2-43	7.0	98.6	2.547	0.2-6.0s	0.262	east7c2-43-2009
E7C2-45	7.0	98.6	2.512	0.2-6.0s	0.195	east7c2-45-2009

Table 4-11 MCG-CEUS 20 Records scaled to the target UHS 2005 NBCC, 2%-50 years, site class C, city of Montreal (ENA) , $S_{A\text{-}targ}/S_{A\text{-}sim}$ computed over 0.2 - 4.0 s

Record Name	M	R (km)	S.F.	T-Range	$\frac{S_{A-t\,\arg}}{S_{A-sim}}$	MCG-CEUS Earthquake
E6C1						
A-CAS270	6.0	16.9	0.648	0.2-1.0s	1.666	Whittier Narrows-1987
H-BRA315	6.5	8.5	0.390	1.0-4.0s	0.546	Imperial Valley-1979
H-CXO225	6.5	10.6	0.451	0.2-1.0s	0.317	Imperial Valley-1979
H-CXO315	6.5	10.6	0.534	1.0-4.0s	0.267	Imperial Valley-1979
A-NHO180	6.0	11.9	1.185	0.2-1.0s	0.247	Whittier Narrows-1987
A-NHO270	6.0	11.9	1.923	0.2-1.0s	1.240	Whittier Narrows-1987
E6C2						
C-FRN224	5.6	30.8	1.262	0.2-1.0s	1.329	Northern California-1967
A-MUL009	6.0	30.3	1.276	0.2-1.0s	1.810	Whittier Narrows-1987
A-MUL279	6.0	30.3	0.824	0.2-1.0s	1.603	Whittier Narrows-1987
E7C1						
CCN090	6.7	25.7	0.320	1.0-4.0s	0.359	Northridge-1994
CHY036-W	7.6	20.3	0.211	1.0-4.0s	1.124	Chi-Chi, Taiwan-1999
HWA006-E	7.6	44.0	1.378	1.0-4.0s	0.309	Chi-Chi, Taiwan-1999
E7C2						
WRP180	6.6	81.6	6.063	1.0-4.0s	0.212	San Fernando-1971
HNT000	6.7	79.6	1.472	0.2-1.0s	0.415	Northridge-1994
WAI200	6.7	57.4	1.440	0.2-1.0s	0.431	Northridge-1994
WAI290	6.7	57.4	1.198	0.2-1.0s	0.295	Northridge-1994
DEL000	6.7	59.3	0.711	0.2-1.0s	0.572	Northridge-1994
DEL090	6.7	59.3	0.814	1.0-4.0s	0.391	Northridge-1994
H05225	6.6	136	2.437	0.2-1.0s	1.368	San Fernando-1971
HOS180	6.7	108	0.962	0.2-1.0s	0.959	Northridge-1994

Table 4-12 ATK-W 20 Records scaled to the target UHS 2005 NBCC, 2%-50 years, site class C, city of Vancouver (WNA) , $S_{A\text{-}targ}/S_{A\text{-}sim}$ computed over 0.2 - 4.0 s

Record Name	M	R (km)	S.F.	T-Range	$\frac{S_{A-t\,\arg}}{S_{A-sim}}$	ATK-W Earthquake
W6C1						
W6C1-19	6.5	10.8	1.024	0.2-6.0s	0.311	west6c1-19-2009
W6C1-21	6.5	10.8	1.347	0.2-6.0s	0.421	west6c1-21-2009
W6C1-25	6.5	11.2	1.806	0.2-6.0s	0.297	west6c1-25-2009
W6C1-34	6.5	12.2	1.299	0.2-6.0s	0.430	west6c1-34-2009
W6C1-38	6.5	13.0	1.765	0.2-6.0s	0.413	west6c1-38-2009
W6C1-44	6.5	13.0	1.885	0.2-6.0s	0.389	west6c1-44-2009
W6C2						
W6C2-1	6.5	19.7	1.652	0.2-6.0s	0.141	west6c2-1-2009
W6C2-7	6.5	13.2	1.292	0.2-6.0s	0.295	west6c2-7-2009
W6C2-25	6.5	26.3	2.170	0.2-6.0s	0.193	west6c2-25-2009
W7C1						
W7C1-11	7.5	17.1	1.051	0.2-6.0s	0.166	west7c1-11-2009
W7C1-17	7.5	21.6	0.973	0.2-6.0s	0.255	west7c1-17-2009
W7C1-26	7.5	18.1	0.725	0.2-6.0s	0.189	west7c1-26-2009
W7C2						
W7C2-10	7.5	50.7	2.785	0.2-6.0s	0.182	west7c2-10-2009
W7C2-13	7.5	30.2	1.032	0.2-6.0s	0.422	west7c2-13-2009
W7C2-14	7.5	30.2	1.335	0.2-6.0s	0.198	west7c2-14-2009
W7C2-19	7.5	70.5	3.500	1.0-2.0s	0.207	west7c2-19-2009
W7C2-25	7.5	68.5	2.273	0.2-6.0s	0.281	west7c2-25-2009
W7C2-33	7.5	100.4	3.194	0.2-6.0s	0.503	west7c2-33-2009
W7C2-39	7.5	100.0	2.841	0.2-6.0s	0.446	west7c2-39-2009
W7C2-40	7.5	100.4	4.767	0.2-1.0s	0.288	west7c2-40-2009

4.7 Conclusions on Records Selection and Scaling

In this chapter, the site-specific ensembles of ground-motion time histories are defined and scaled to carry out the extensive parametric analyses on the nonlinear structural behaviour of isolated bridges in eastern and western North America. In spite of a number of existing approaches that have been developed for specific design purposes, there is no consensus on how to select and scale ground-motion records for nonlinear time-history analyses (THA) of isolated bridges. The technique and methodology were proposed in this study aiming to define time-history records for dynamic analyses from the perspective of a structural engineer using the available state of the art in seismology and where the data is not available adopting conservative approaches rather than those statistically supported. As a result, the hazard-dominant earthquake scenarios were developed for the eastern and western North America. Three suites of 20 time histories each were assembled according the site-specific hazard scenarios. The records were then scaled to match the 2005 NBCC UHS for a wide period range required to accommodate large inelastic excursions prone to the behaviour of isolated bridges. An excellent match was obtained as a result of the records selection and scaling approaches adopted in this study.

In addition, the effect of seismic directivity was outlined. It was emphasized the importance of assembling ground motions suites for different M-R earthquakes that may result in different damage potentials amplified as a function of the azimuthal directivity. The rupture directivity effect is then considered by selecting the time-history records having different azimuthal directions for each of the M-R scenarios.

Chapter 5: Assessment of Damping Coefficients for Seismic Design of Isolated Bridges in Eastern and Western North American Regions

5.1 Introduction

The appropriateness of the damping coefficients *B* that are currently specified in the CAN/CSA-S6-06 Canadian Highway Bridge Design Code (CSA, 2006) in Canada and the AASHTO LRFD Seismic Bridge Design Specifications in the United States (AASHTO, 2009, 2010) for the design of isolated bridges for both western and eastern North American ground motions is investigated in this chapter. The coefficients *B* have been developed based on studying the effects of ground motions from historical earthquake events that have occurred along the North American west coast. The appropriateness of using the same damping coefficients for ENA and WNA has been questioned in past studies (Taylor, 1999; Naumoski, 2000).

The values of *B* specified in codes have been derived from the work by Newmark and Hall (1982). In these early studies, spectrum amplification coefficients were computed for different damping levels using the elastic response of a viscously damped SDOF system to the 1940 El Centro earthquake record. Similar approaches are widely adopted and reported by the majority of studies where *B*-coefficients were evaluated statistically by processing a large number of seismic records (Tolis and Faccioli, 1999; Bommer et al., 2000b; Lin and Chang, 2003; and Hatzigeorgiou, 2010).

The approach of assessing the *B*-coefficients by using linear time-history analyses (LTHA) is first adopted in this study (Section 5.3), given that it corresponds well to the state of the art. The coefficients obtained from LTHA in ENA and WNA are compared to those specified in codes in order to examine the possible influence of the regional characteristics of the seismicity on the reduction effects of damping. The suitability of using the same *B*-coefficient for reducing force and displacement responses is also examined. Based on the results from LTHA, this study also investigates the dependency of *B*-coefficients on the effective period of the structure that has already been identified by other researchers (Atkinson and Pierre, 2004 and Hatzigeorgiou,

2010). The differences observed in the response reduction effects caused by viscous damping are explained by exploiting the concepts of the force transmissibility and response amplification respectively for spectral accelerations S_A and spectral displacements S_D.

Complementary to the earlier studies that were based on LTHA and to accurately address the validity of the damping coefficients for the design of isolated bridges, in Section 5.4, an extensive parametric study is carried out using dynamic nonlinear time history analysis (NLTHA) so that the nonlinear response of the bridge isolation systems is properly accounted for. The parametric study was carried out by varying several parameters that may be used to define the system's dynamic properties at the initial design stage. Based on these results, in Section 5.5, recommendations are made on possible modifications to improve the accuracy of current North American simplified design methods. To better assess the accuracy of the *B*-coefficients on the seismic displacement response, nonlinear structures were analyzed following the complete iterative procedure prescribed in the CSA-S6-06 simplified method (similar to AASHTO 2009, 2010). This study also examines the need for an upper limit on damping for which the *B*-coefficient method can be used in codes.

5.2 Ground Motions Considered for Time-History Analyses

As discussed in details in Chapter 4, because of the scarcity of historical ground motions corresponding to events having occurred in ENA, sets of eastern artificial (Atkinson, 2009) and hybrid (McGuire et al., 2001a) ground motions were adopted for the ENA regions. To establish the same comparative basis between ENA and WNA, only the set of artificial western records (Atkinson, 2009) was analysed. Each of these ground-motion sets were comprised of twenty records that were selected according to site-specific likely earthquakes scenarios. More details in how these scenarios were defined are presented in Chapter 4 (Sections 4.3 and 4.4). For analyses carried out in this parametric study, two densely populated Canadian cities were chosen: Montreal, Quebec, for eastern Canada, and Vancouver, British Columbia, for western Canada. Three suites of twenty ground-motion records, denoted as artificial ENA (ATK-E), hybrid ENA (MCG-CEUS) and artificial WNA (ATK-W), were linearly scaled to the corresponding NBCC design spectrum (NBCC, 2005).

5.3 Linear Time-History Analyses (LTHA)

As a first step in this study, the effect of viscous damping on the response of linear elastic SDOF systems is studied. Such an approach corresponds well to the state of the art in assessing damping coefficients (Newmark and Hall, 1982; Tolis and Faccioli 1999; Bommer et al., 2000b; Lin and Chang, 2003; and Hatzigeorgiou, 2010). In this study, the *B*-coefficients obtained from LTHA are compared to those specified in codes. One of the aspects that is investigated is the influence on *B*-coefficients of the ground motion characteristics such as the ones expected between ENA and WNA records. These analyses are intended to essentially fill a gap in knowledge about differences in how the damping reduction may be affected by western and eastern North American seismicity.

Furthermore, as previously indicated in Equations (2.6) and (2.7) (see Chapter 2), the same damping coefficient *B* is used to determine both the statically equivalent seismic force and the displacement across the isolation bearings as a function of the spectral acceleration S_A and pseudo displacement PS_D, respectively. The validity of using this same *B*-coefficient for both these calculations is verified and discussed in this section.

The response of L-SDOF systems subjected to twenty time-history records, referred to as linear "exact", was mathematically averaged over 20 records for each of the three ground-motion suites. The resulting mean response spectra were constructed for six levels of viscous damping, β = 5%, 10%, 20%, 30%, 40%, and 50% of critical for both spectral acceleration $S_A(\beta)$ and spectral displacement $S_D(\beta)$. These damped response spectra for the three suites of records defined in Chapter 2 (ATK-W, ATK-E, and MCG-CEUS) are presented in Figures 5.1, 5.2, and 5.3, respectively. It can be noted from these figures that the WNA S_D spectra can be approximated by multiple linear segments (period ranges from 0-1.3, 1.3-2.0, 2.0-3.5, and 3.5-4.0 s) corresponding to each respective level of damping. A near constant rate of displacement response indicates that the seismic energy delivered by the WNA ground motions is transmitted to the system at a wide band of frequencies covering a longer period range as it can be noted in Figure 5.4. This figure presents power spectra that was obtained from Fast Fourier Transform (FFT) bringing the amplitude of the ground motion from the time domain to the period (or frequency) domain. In this way, the time function of the ground-motion excitation is simply

decomposed into a series of periodic functions (termed Fourier series) and insight into the seismic energy distribution with respect to period is provided.

In contrast to WNA, the ENA ground motions are characterized by high-frequency content and most of the seismic energy is transmitted to the system in a shorter period range (see Figure 5.4). Structures with fundamental periods close to the ground-motion predominant periods attract more seismic forces because of resonance conditions and structures having longer fundamental periods are less excited by such ground motions and the resulting responses are less prone to dynamic amplification. This is further shown in this chapter. The resulting S_D spectra (ATK-E and MCG-CEUS) present significant changes in the spectral shape which is lower for longer periods.

The damping coefficients B were computed by dividing the site-specific 5% damped response spectrum by the corresponding response of the L-SDOF system for a given level of viscous damping β:

$$B(S_A) = \frac{S_A(5\%)}{S_A(\beta)} \tag{5.1}$$

$$B(S_D) = \frac{S_D(5\%)}{S_D(\beta)} \tag{5.2}$$

Values of $B(S_A)$ and $B(S_D)$ are plotted in Figure 5.5 as a function of β over a period range of 0.2 s to 4.0 s. These values are compared to the damping coefficients specified in the CSA-S6-06 code. It is noted that in CSA-S6-06, the same values are used to determine the statically equivalent seismic force (Equation (2.6)) and the displacement across the isolation bearing (Equation (2.7)) as a function of the spectral acceleration, S_A and pseudo displacement, PS_D, respectively, as both parameters are obtained from the site spectral acceleration reduced by a single B coefficient representing the damping of the isolated system. It is opportune to mention that for a shorter period range (depending on the earthquake characteristics) the pseudo displacement PS_D and displacement S_D spectra may be very close and the use of the code damping coefficients will be accurate. However, for a range of longer periods, the PS_D and S_D spectra diverge given that the PS_D spectrum always increases with period, while the S_D spectrum is bounded by the maximum displacement plateau. In such a case, the damping coefficients

calibrated by using damped S_D spectrum, will result in an underestimation displacement demands on isolated structures.

The results show that the damping coefficients $B(S_D)$, which were assessed using displacement response spectra $S_D(\beta)$ are higher than those specified in CSA-S6-06, indicating that the code values result in conservative displacement predictions for all levels of damping and for all three of the record suites that were considered. Comparing spectral displacements $S_D(\beta)$ rather than spectral accelerations $S_A(\beta)$, agrees well with the original method proposed by Newmark and Hall. Contrary to the results of $B(S_D)$, the $B(S_A)$ values determined from damped spectral accelerations are smaller than the code values, which indicates that the use of the code damping coefficients will result in an underestimation of force demands on isolated structures, which is unconservative.

The code provides two methods to determine seismic forces: 1) by applying directly the damping coefficients in Equation (2.6) and 2) by calculating the forces induced when the isolators reach u_{max} (Equation (2.7)). The results obtained in this study suggest that only the second method should be used for evaluating forces as a function of the maximum displacement.

In addition, it is opportune to mention that both sets of ENA ground motions yield results that are in good agreement with each other. This indicates that these suites have a reasonable level of compatibility, confirming consistency in the record selection and scaling procedures adopted for these time-history analyses.

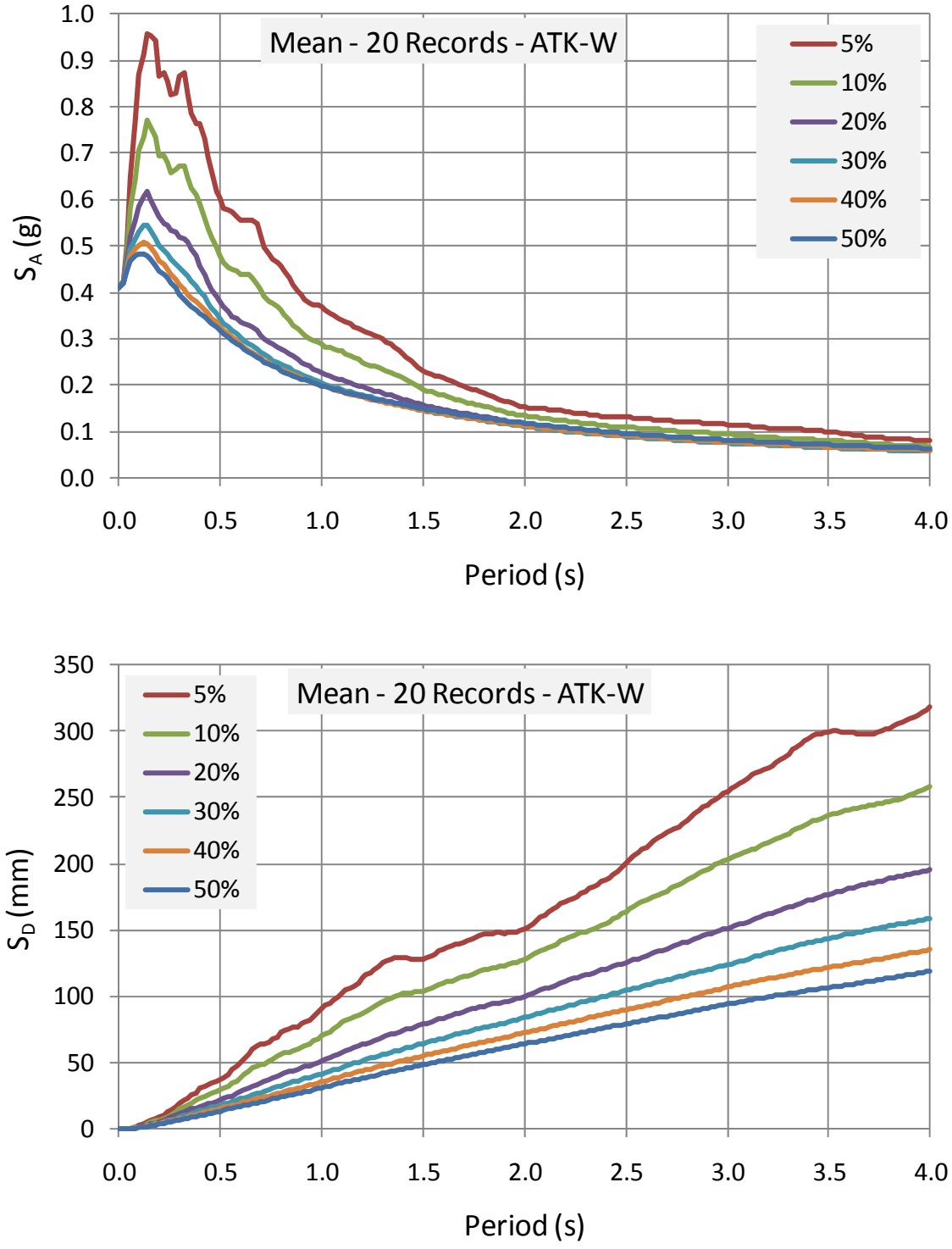

Figure 5.1 Damped response spectra (Mean of 20 Records) - ATK-W

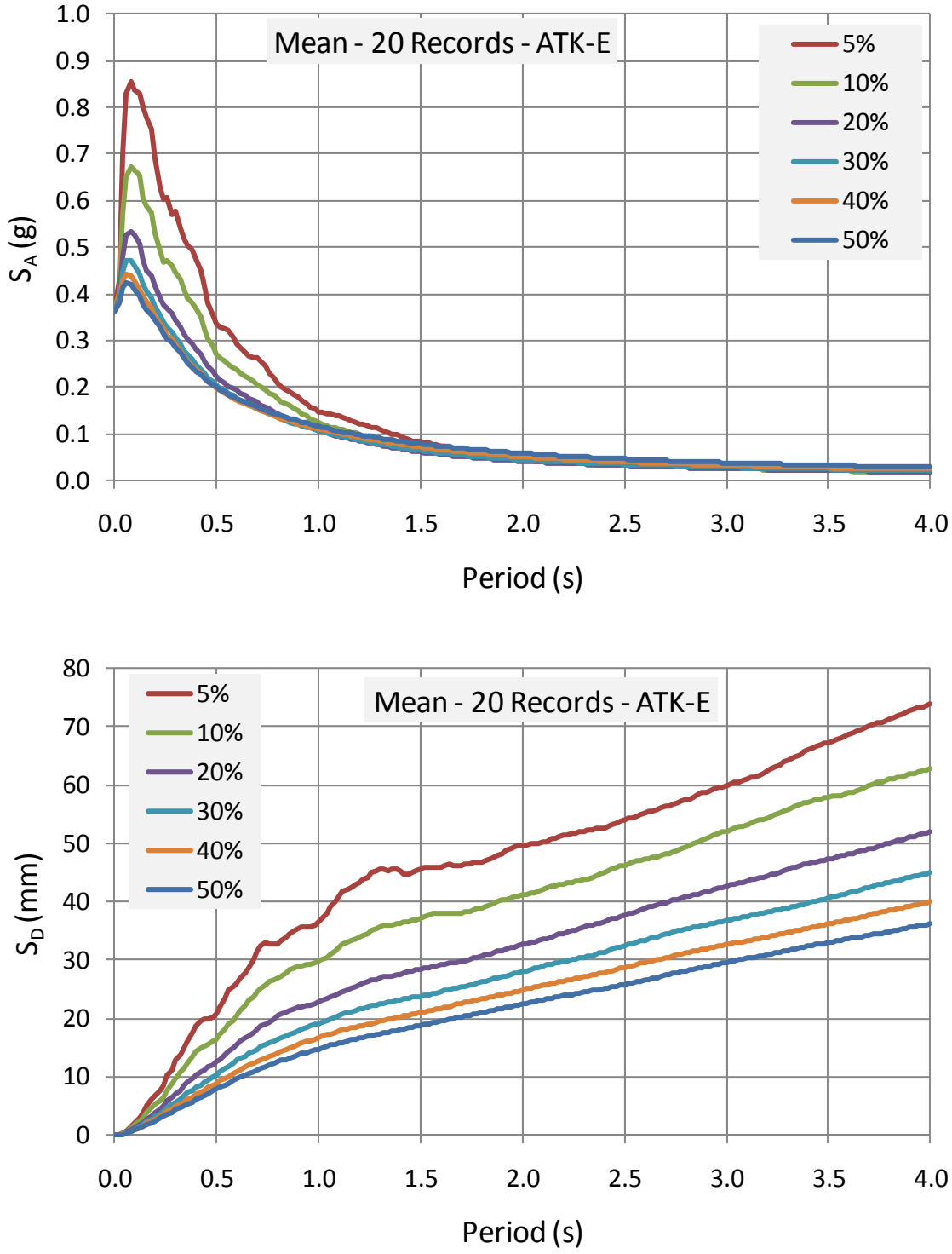

Figure 5.2 Damped response spectra (Mean of 20 Records) - ATK-E

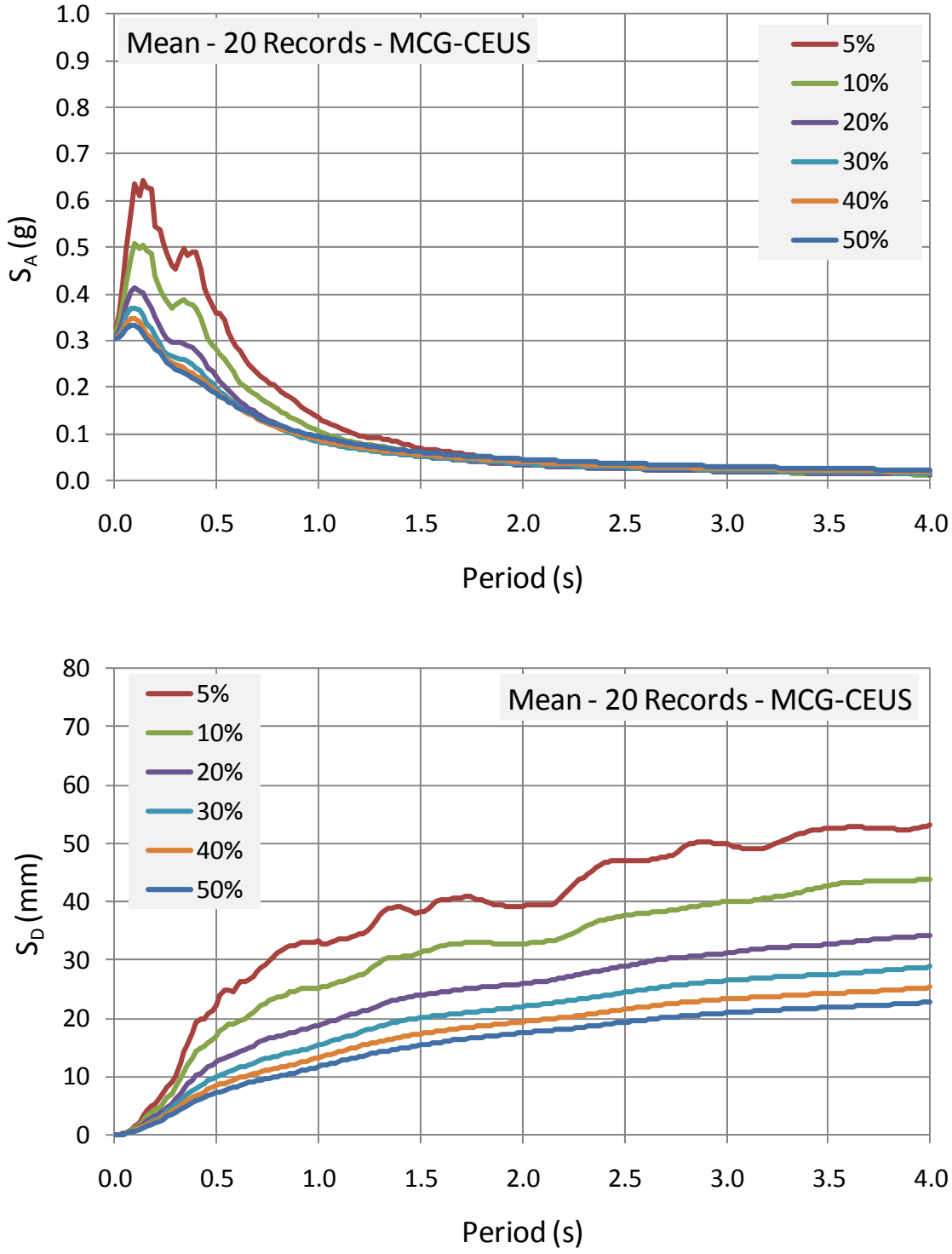

Figure 5.3 Damped response spectra (Mean of 20 Records) - MCG-CEUS

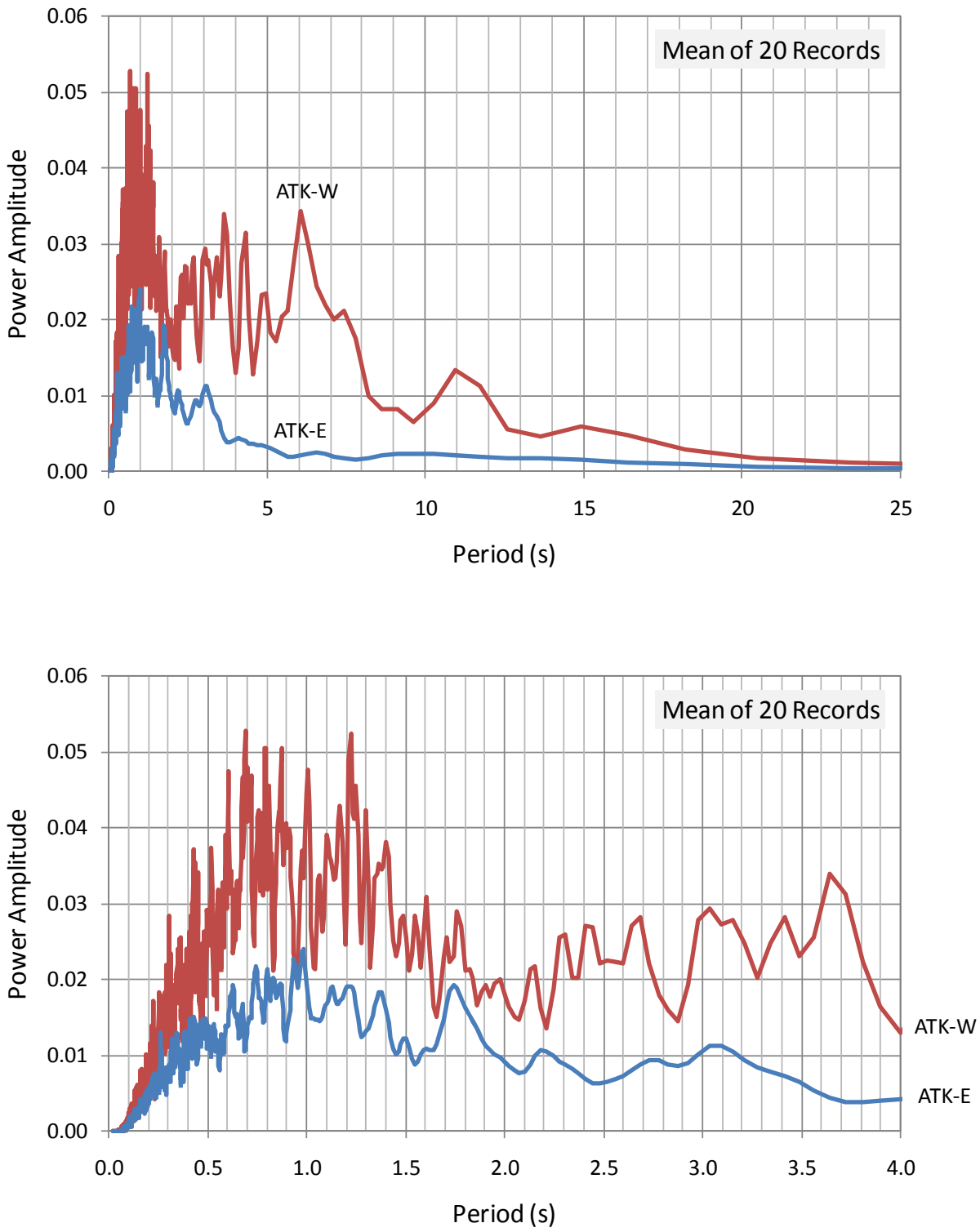

Figure 5.4 Power amplitude with period (Mean of 20 Records) - ATK-W and ATK-E

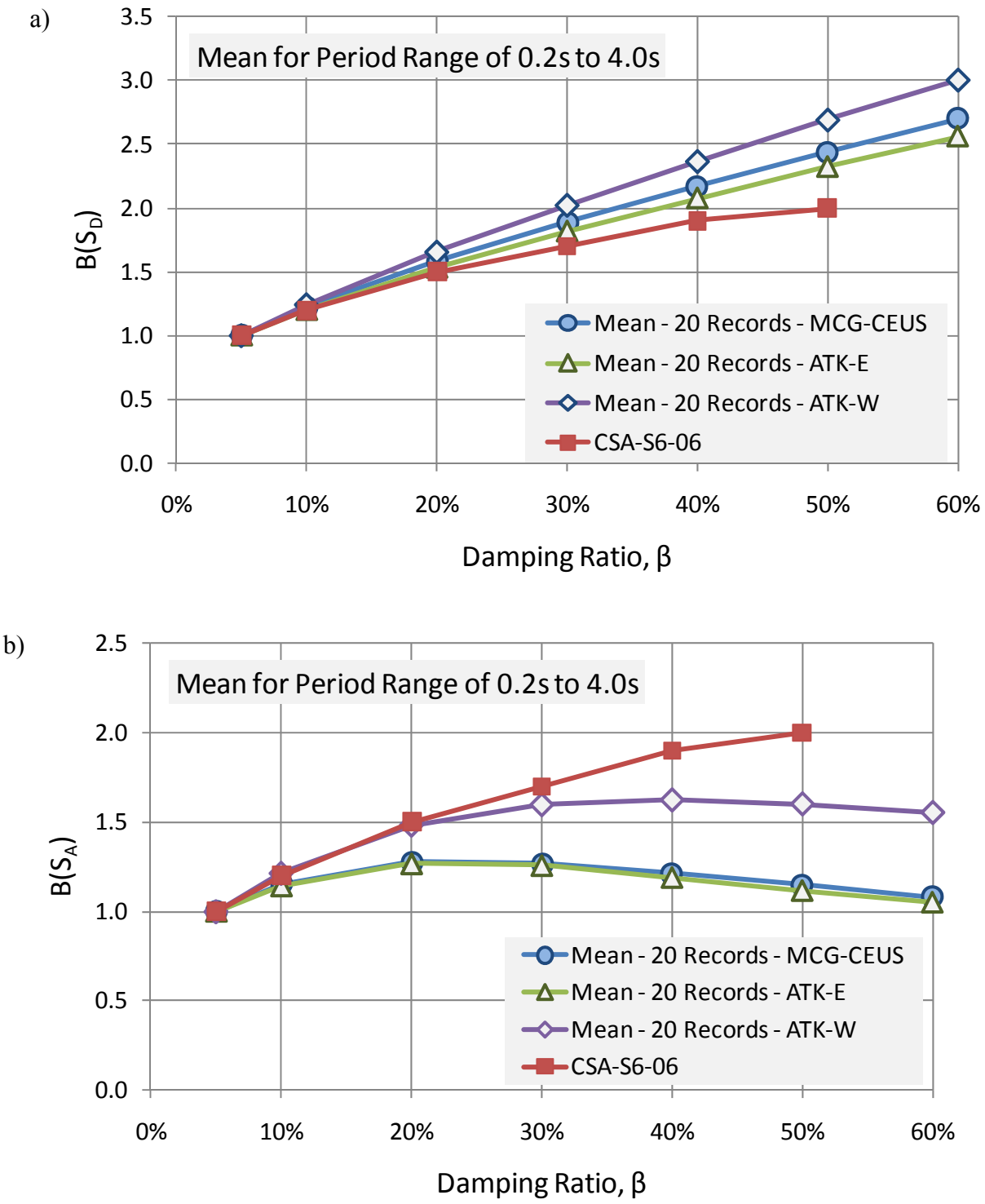

Figure 5.5 Comparison of damping coefficients B for the 0.2 s - 4.0 s period range: a) $B(S_D)$ coefficients and b) $B(S_A)$ coefficients

The *B*-coefficients specified in the current CSA S6 code are assumed independent of the effective period of the linear equivalent system. However, the period-dependant nature of damping coefficients has already been pointed out in past studies (Atkinson and Pierre, 2004 and Hatzigeorgiou, 2010). The analysis results obtained in this study are used to verify this dependency. In Figure 5.6, the average damping coefficients are evaluated separately for five smaller period ranges: 0-0.2 s, 0.2-0.5 s, 0.5-1.0 s, 1.0-2.0 s and 2.0-4.0 s. These period ranges correspond to the linear segments defining the 2005 NBCC design spectrum.

The damping coefficients $B(S_D)$ determined from the spectral displacement responses are examined first on the left-hand side of Figure 5.6. For the very short period range (0-0.2 s), the reduction effect of damping for the WNA records is significantly lower when compared to the longer period ranges which, in turn, are reasonably close to each other. A much more pronounced effect of the period on the damping reduction effect is observed for the ENA suite of records. The reduction effect of damping is the highest between periods of 0.2 s and 1.0 s. In turn, the coefficients computed for the very short period range (0-0.2 s) and the longer period range (2.0-4.0 s) correspond to the lowest contribution of viscous damping. The above-observed differences in damping reduction effect can be primarily explained by different response velocities as shown in Figure 5.7.

The $B(S_A)$ damping coefficients obtained from the acceleration response spectra are presented on the right hand side of Figure 5.6. In Figure 5.6 (b), the code values for WNA are appropriate for values of β up to 30% and for periods ranging from 0.2 s to 2.0 s. For ENA, in Figures 5.6 (d) and (f), the use of the simplified code method appears to be conservative for damping levels of up to approximately 30% and periods ranging from 0.2 s to 1.0 s. These results confirm the upper limit on damping of 30% for which the *B*-coefficient method can be used in codes (CSA-S6-06 and AASHTO).

Figures 5.8, 5.9, and 5.10 illustrate how the damping coefficients *B* obtained for different damping levels vary with the period and clearly show the period-dependant nature of damping coefficients. As shown in these figures, the shape of the $B(S_A)$ and $B(S_D)$ curves are similar only for the short period range. For longer periods, the effect of damping in reducing seismic forces (as given by Equation (2.6) in terms of acceleration) is significantly diminished and may be even inverted. In such case, the added damping could even result in an increase in the

acceleration and seismic force response of the structure as can be seen for the ENA ground motions (see Figures 5.9(a) and 5.10(a)).

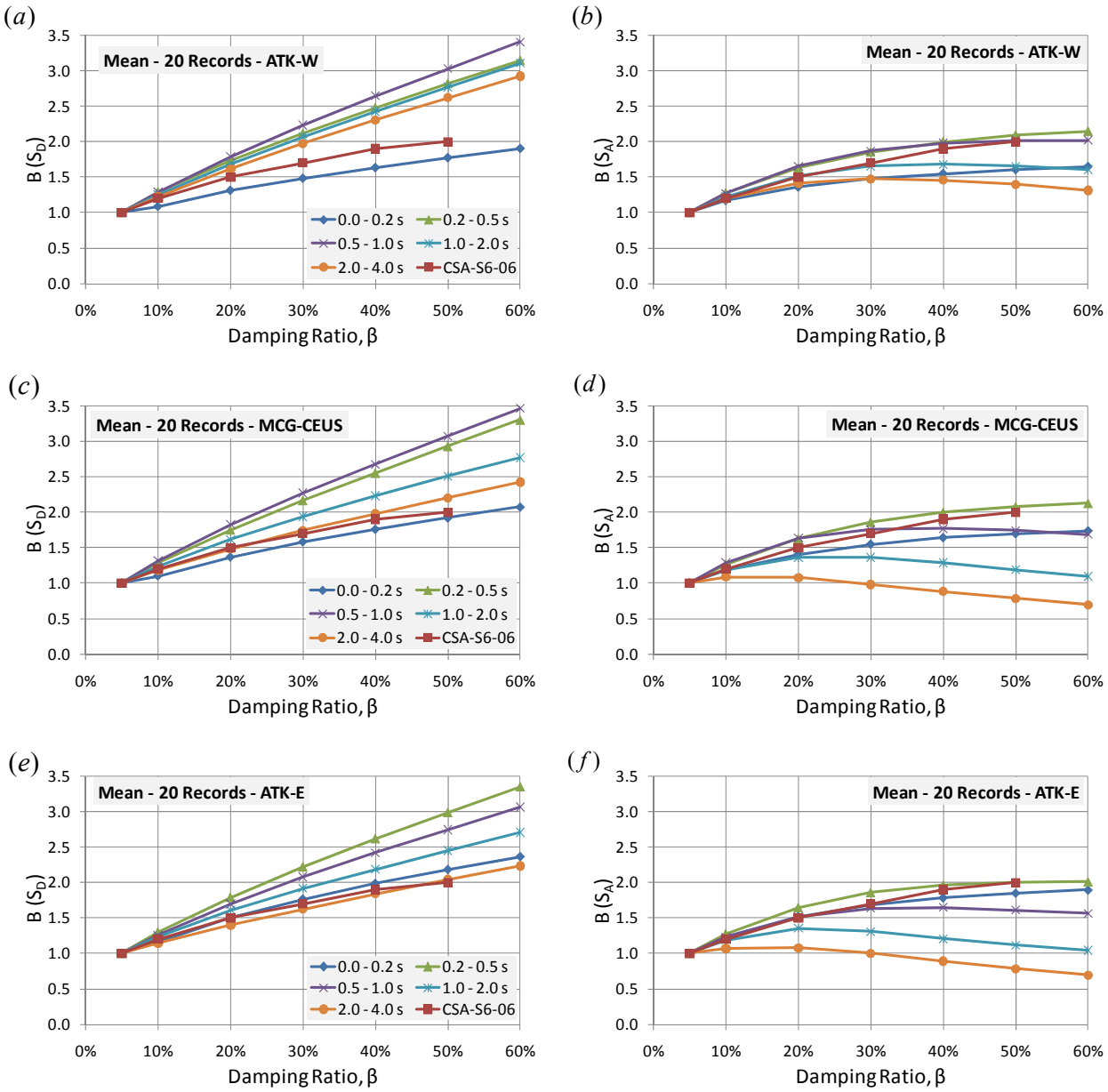

Figure 5.6 Variation of *B*-Coefficient with damping ratio by period range – Mean of 20 Records

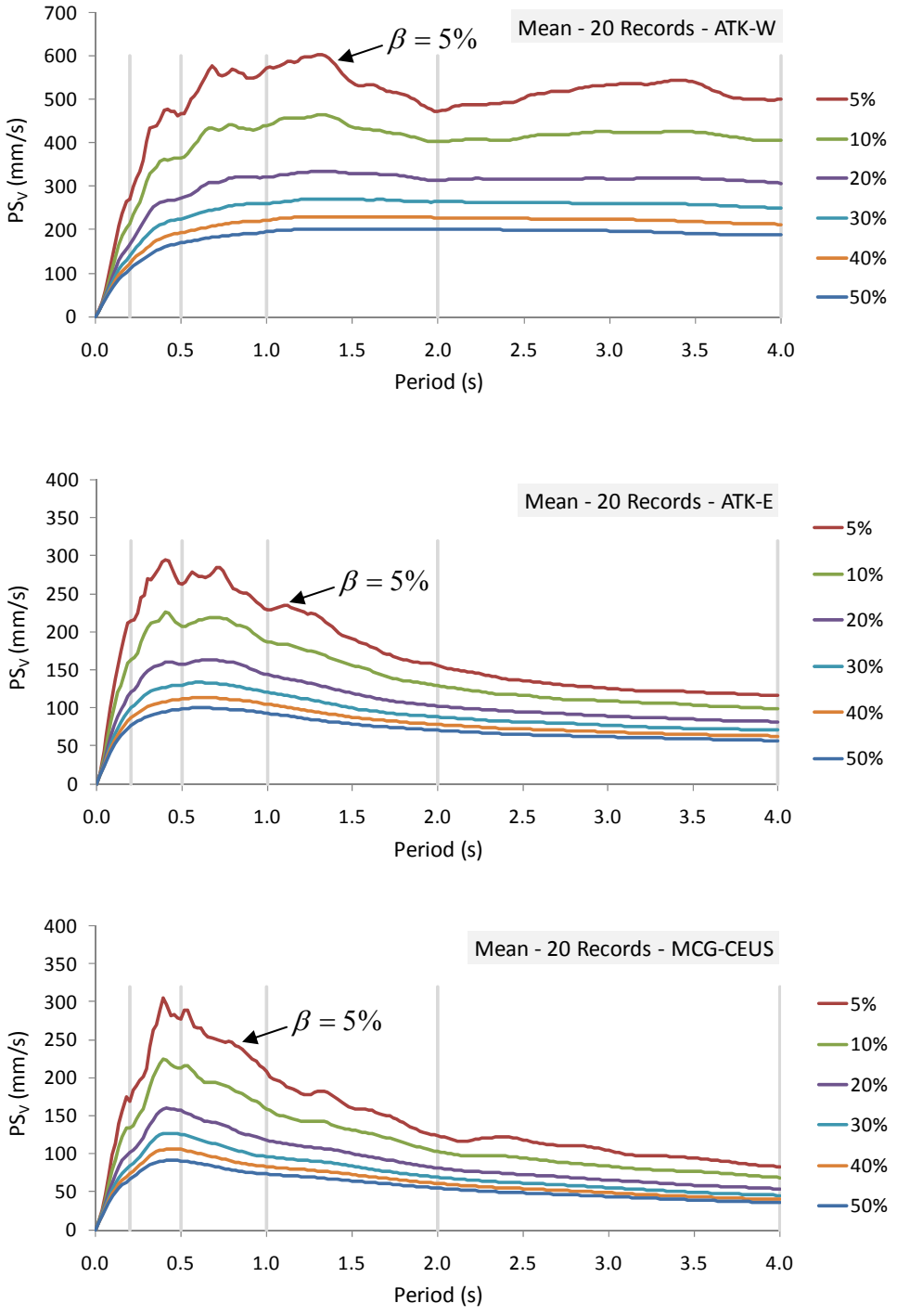

Figure 5.7 Damped pseudo velocity response spectra (Mean of 20 Records)

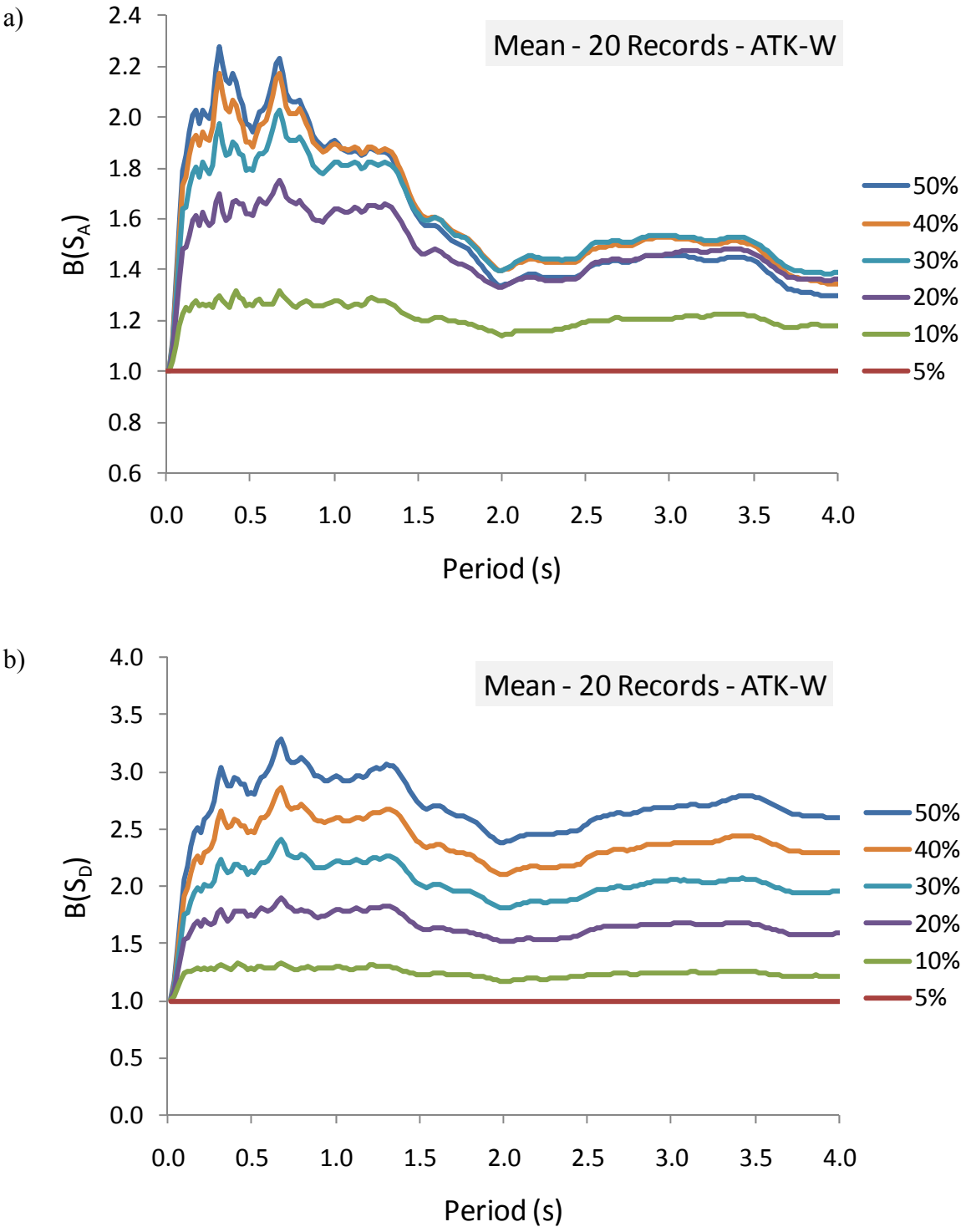

Figure 5.8 Variation of damping coefficients B with period - ATK-W: a) $B(S_A)$ coefficients and b) $B(S_D)$ coefficients

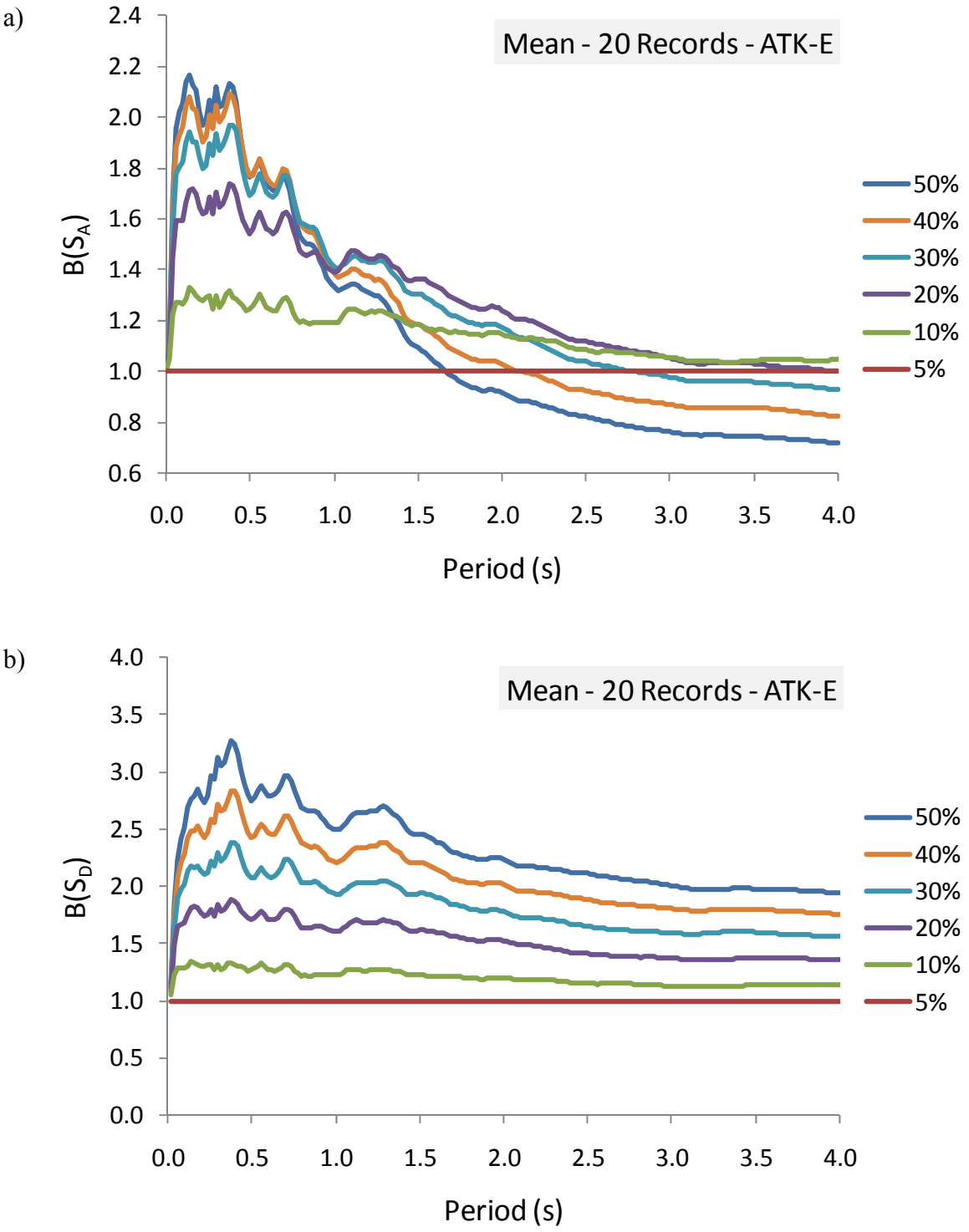

Figure 5.9 Variation of damping coefficients B with period - ATK-E: a) $B(S_A)$ coefficients and b) $B(S_D)$ coefficients

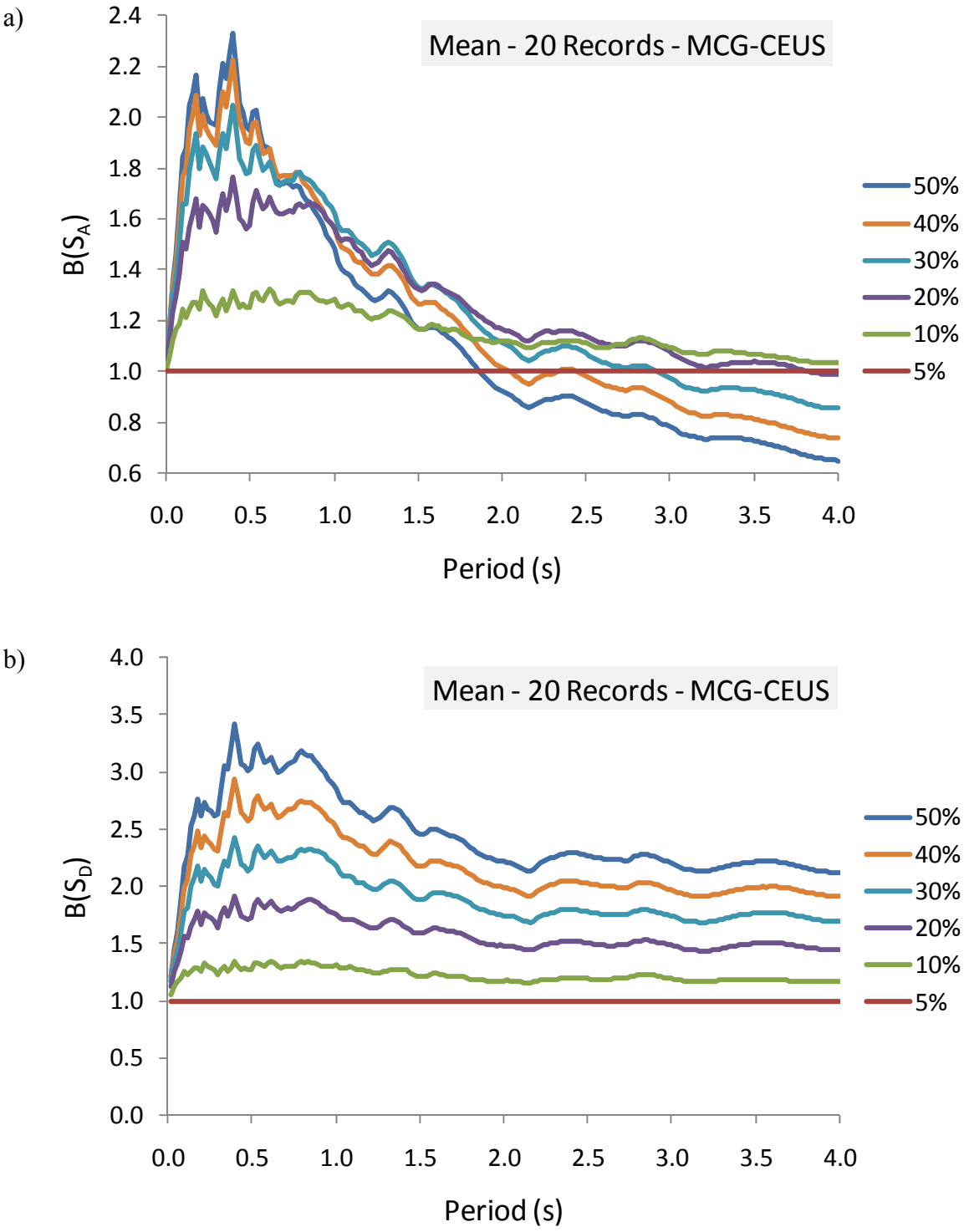

Figure 5.10 Variation of damping coefficients B with period - MCG-CEUS: a) $B(S_A)$ coefficients and b) $B(S_D)$ coefficients

Insight into the observed amplification of the acceleration response (instead of the expected reduction) with increased damping may be gained by studying the damped transmissibility of SDOF systems as a function of the period ratio T / T_g (where T is the structure's fundamental period and T_g is the ground-motion's predominant period). To apply such an analogy, the steady-state response of a SDOF system is assumed to be representative of the one under seismic excitation. This analogy is consistent for this study given that the *equivalent linearization method* is based on an effective stiffness and damping transformation of nonlinear systems derived from the system's steady-state response. Based on Newton's second law, the equation of motion for harmonic base excitation of an SDOF system is defined as:

$$m \cdot \ddot{u}(t) + c \cdot \dot{u}(t) + k \cdot u(t) = -m \cdot \ddot{u}_g \sin\left(\frac{2\pi}{T_g} \cdot t\right) \tag{5.4}$$

where $u(t)$ is the displacement of the system's mass m relative to its base.

Accordingly, the harmonic loading is defined in terms of the ground acceleration as:

$$-m \cdot \ddot{u}_g \sin\left(\frac{2\pi}{T_g} \cdot t\right) = -m \cdot PGA \cdot \sin\left(\frac{2\pi}{T_g} \cdot t\right) \tag{5.5}$$

and the spectral acceleration is determined as:

$$S_A = \max_t \left|\ddot{u}(t) + \ddot{u}_g(t)\right| \tag{5.6}$$

The transmissibility is then defined as a ratio of the transmitted peak acceleration $S_A(T, \beta)$, or the spectral acceleration, to the peak ground acceleration PGA. Using the formulation proposed by Chopra (2011) for the harmonic response of an SDOF system, the transmissibility $TR(T, \beta)$ can be expressed as follows :

$$TR(T, \beta) = \frac{S_A(T, \beta)}{PGA} = \sqrt{\frac{1 + [2\beta \cdot (T / T_g)]^2}{[1 - (T / T_g)^2]^2 + [2\beta \cdot (T / T_g)]^2}} \tag{5.7}$$

The idealized damping coefficient B can be then expressed for harmonic excitation of an SDOF system in terms of the transmissibility ratio as:

$$B_{SA}(T,\beta)=\frac{S_A(5\%)}{S_A(\beta)}=\frac{TR(T,5\%)}{TR(T,\beta)}=\sqrt{\frac{1+[0.1\cdot(T/T_g)]^2}{[1-(T/T_g)^2]^2+[0.1\cdot(T/T_g)]^2}\Bigg/\frac{1+[2\beta\cdot(T/T_g)]^2}{[1-(T/T_g)^2]^2+[2\beta\cdot(T/T_g)]^2}} \tag{5.8}$$

The expression of the damping coefficient B for the acceleration response of an SDOF system under harmonic excitation is presented graphically for different levels of damping in Figure 5.11. It can be noted that for systems having fundamental periods longer than $T_g\sqrt{2}$ and damping ratios higher than 5%, the transmitted force (as given by Equation (2.6) in terms of acceleration) is larger than the force transmitted to the system for the 5% damped case. In addition, for short-periods, the damping reduction effect becomes null as the ratio reduces to unity.

The transmissibility expression for the displacement response is the same as the one given by Equation (5.7). Nevertheless, this formulation expresses the response as a total displacement response (ground displacement added to the relative system displacement), while the spectral value S_D corresponds to the relative system displacement alone. Therefore, to address relative displacement correctly, the displacement amplification factor R_d can be adopted (Chopra, 2011) as follows:

$$R_d(T,\beta)=\frac{1}{\sqrt{[1-(T/T_g)^2]^2+[2\beta\cdot(T/T_g)]^2}} \tag{5.9}$$

The idealized damping coefficient B for the displacement response is then expressed for the harmonic excitation of an SDOF system as:

$$B_{SD}(T,\beta)=\frac{S_D(5\%)}{S_D(\beta)}=\frac{Rd(T,5\%)}{Rd(T,\beta)}=\sqrt{\frac{[1-(T/T_g)^2]^2+[2\beta\cdot(T/T_g)]^2}{[1-(T/T_g)^2]^2+[0.1\cdot(T/T_g)]^2}} \tag{5.10}$$

It can be shown from this expression (see Figure 5.12) that for all $\beta > 5\%$, the corresponding B coefficients will be higher than unity (Equation 5.10). This explains why for systems with damping ratios greater than 5%, the coefficients B result only in a reduction of the displacement response as observed in Figures 5.8 to 5.10. The expression of the damping reduction coefficient B for the displacement response of SDOF systems under harmonic excitation is presented

graphically for different levels of damping in Figure 5.12. For shorter and longer periods, the damping reduction on the displacement response tends to zero effect ($B = 1$).

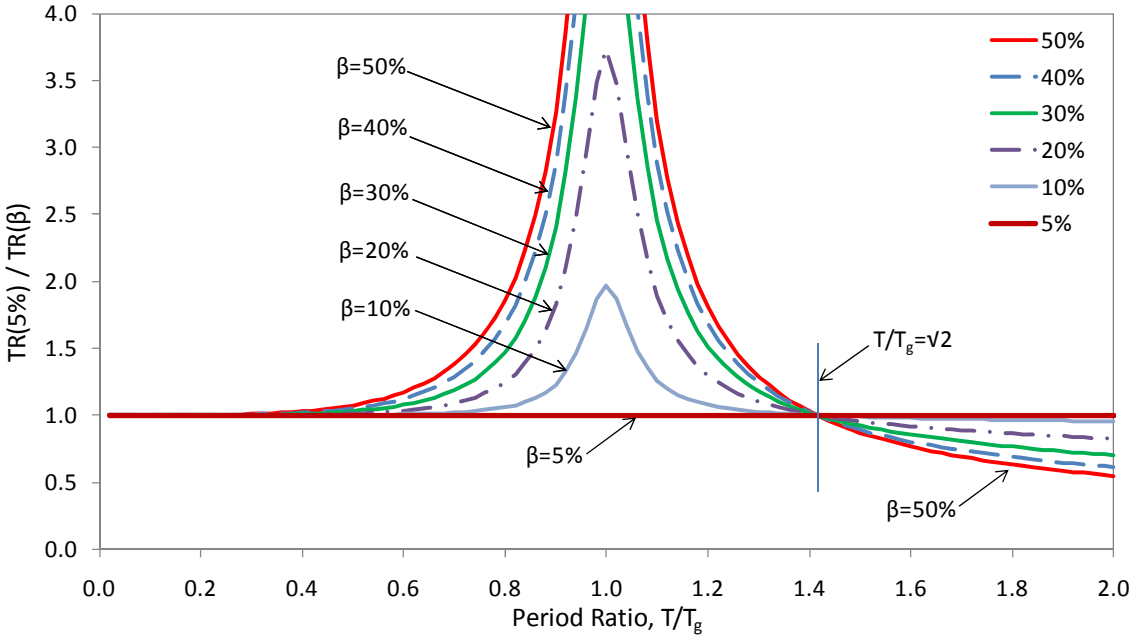

Figure 5.11 Idealized factor $B(S_A)$ for harmonic response of SDOF systems

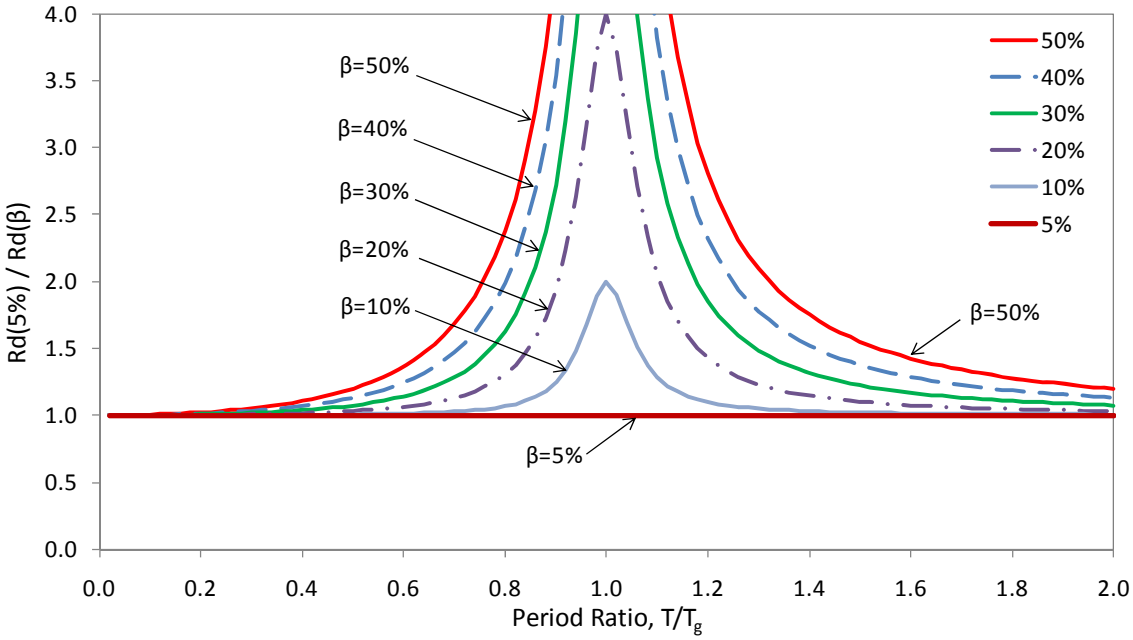

Figure 5.12 Idealized factor $B(S_D)$ for harmonic response of SDOF systems

For seismic ground motion, there is generally more than one predominant period that defines the input ground motion. In addition to this, the random time-distribution of these predominant

periods and the system nonlinear response to non-harmonic ground motion excitations contribute to the complexity of the damping reduction mechanism. Nevertheless, the formulation of the damping coefficients (Equations (5.8) and (5.10)) of a linear SDOF system under harmonic excitations provide an explanation of the physical phenomena leading to the general trends governing the damping reduction effect of isolated bridge structures. Consequently, as shown above, the coefficients $B(S_A)$ and $B(S_D)$ reflect different aspects of the system response (absolute acceleration and relative displacement). As mentioned previously, the coefficients $B(S_A)$ reflect the relation between the pseudo displacement spectra. Even when the pseudo displacement spectrum is close to the displacement response spectrum, the use of the coefficients $B(S_A)$ may not be representative of the "real" damping reduction in displacement response. For this reason, B-coefficients for reducing force and displacement responses must be independently defined and calibrated. In this study, the focus will be set only on the damping coefficients B that relate displacement responses of the system to the 5% damped displacement spectra. The reason for only addressing $B(S_D)$ in detail is that, as explained in Chapter 2, the procedure of the simplified code method (CAN/CSA-S6-06) is used to determine the displacement of the isolated structure. The design seismic forces are subsequently determined from the load-displacement response of the actual nonlinear isolation system.

For a more accurate evaluation of the expected displacement across isolation bearings, the analysis results suggest that the simplified code method should be used to predict displacements rather than accelerations or forces. For assessing the statically equivalent seismic force using Equation 2.6 (see Chapter 2), limitations on the effective period range and the effective damping ratio should also be specified. Otherwise, the use of current code provisions could result in unconservative response estimates.

5.4 Nonlinear Time-History Analyses (NLTHA)

The results presented in the previous section are applicable to the response of linear systems for which the response reduction effect is solely due to velocity-dependant viscous damping. For isolated bridge structures responding nonlinearly, however, the amount of equivalent damping depends on the hysteretic nature and the maximum displacement response, and the equivalent damping is no longer a direct function of the velocity. For this reason, a series of nonlinear time-history (NLTH) analyses were performed for an ensemble of bilinear SDOF systems covering a

wide range of isolated and damped bridge configurations. The same suites of artificial ground-motion records (ATK-E and ATK-W) that were used for the study on linear systems were also adopted for this parametric study.

5.4.1 Structural Parameters for Nonlinear Time-History Analyses

The study was performed on SDOF systems exhibiting the bilinear hysteretic response shown in Figure 5.13. This response is representative of bridge structures protected with a variety of seismic isolators commonly used in practice. For such isolated bridge structures, the equivalent effective period T_{eff} and damping ratio β_{eff} depend on the hysteretic shape and the maximum displacement (see Equations (2.2) and (2.4), Chapter 2). A wide range of effective parameters was considered by varying the following system properties: the response modification factor R, which corresponds to the ratio between the activation lateral force of the isolation system and the elastic force demand, $S_A(T_e,5\%)W$, the initial (elastic) structure period, T_e, the ratio α between the post-elastic k_d and the initial (elastic) k_u structure stiffness, and different levels of viscous damping related to both the elastic period T_e and the effective period T_{eff}.

These parameters were adopted for the present parametric study given that they make it possible to define the hysteretic properties of the system at the initial design stage. Accordingly, the structure-earthquake interaction may be characterized through the period ratio T_e / T_g and the response modification factor R. The response modification factor R has a direct implication in the design process because it relates the isolation activation limit, u_y to the UHS spectral value through the relation:

$$u_y = u_e / R = S_D(5\%, T_e) / R. \tag{5.11}$$

The resulting system configuration, which is defined by u_y as a function of R, is constant for all of the analyses carried out for a given set of 20 records.

Different levels of inherent damping were defined in relation to the elastic and effective periods. Both are frequently adopted by researchers for NLTH analyses and yield comparable results for low-ductility responses. However, the use of inherent damping related to the elastic period may lead to unconservative displacement response for highly nonlinear systems (Jacobsen, 1960). In this study, the results obtained with inherent damping which is defined in relation to the elastic

period are nonetheless included as they are relevant in cases where supplemental damping devices are used in bridges.

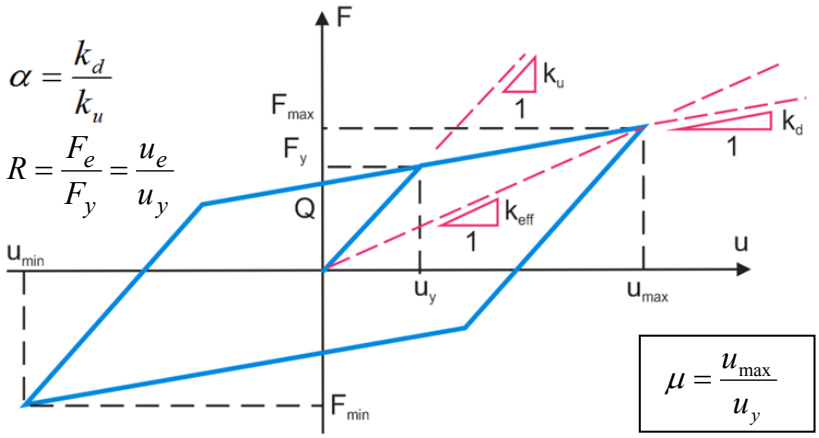

Figure 5.13 Structure nonlinear parameters - Bilinear hysteretic

Table 5-1 presents the parameters used for defining the properties of the nonlinear SDOF systems that were analyzed in this study which resulted in a total of 12 000 time-history analyses (THA). The parameters were changed one at the time, resulting in 300 isolated bridge configurations (5 (R) x 4 (T_e) x 5 (β) x 3 (α)). These parameters and their respective ranges were chosen such that an extensive range of isolated and damped bridge configurations was covered. Each of these isolation systems were analyzed under 20 time-history records for each of the WNA and ENA regions.

Table 5-1 Structural parameters for nonlinear time-history analyses

Analysis Parameters	Eastern North America	Western North America
Response modification factor	R=[4, 16, 28, 40, 52]	R=[4, 16, 28, 40, 52]
Elastic period	T_e=[0.25, 0.5, 0.75, 1.0 s]	T_e=[0.25, 0.5, 0.75 1.0 s]
Inherent damping ratio	β(T_e)= [0%, 2%, 5%]; β(T_{eff})=[2%, 5%]	β(T_e)= [0%, 2%, 5%]; β(T_{eff})=[2%, 5%]
Post-yield stiffness ratio	α=[0.01, 0.05, 0.1]	α=[0.01, 0.05, 0.1]
Ground-motions records	20 Atkinson's 2009 (ATK-E)	20 Atkinson's 2009 (ATK-W)

Values of the damping coefficients B and the corresponding effective parameters were determined from the NLTHA response of each individual system for every record in four steps:

1) The displacement ductility ratio μ was determined as a function of the maximum displacement response u_{max}, that was obtained in each individual NLTHA. The ductility demand is not a common parameter in the evaluation of the response of isolated bridges since it does not relate directly to any physical property of the structural elements. However, μ defined as a function of the design parameter u_y, is a practical measure of the inelastic demand on the structure.

2) Using Equation (2.2), the effective period T_{eff} was computed at the maximum displacement, u_{max} as a function of the ratio μ that was assessed in Step 1 for each individual NLTHA response.

3) The B coefficient was determined by dividing the 5% damped elastic spectral displacement $S_D(5\%,T_{eff})$, by the maximum displacement u_{max} from the NLTHA.

4) The effective damping β_{eff}, which corresponds to the bilinear hysteretic response at the maximum displacement u_{max}, was determined from Equations (2.4) and (2.5).

As a result, the coefficients B were computed for individual responses of 300 isolated bridges subjected to each individual ground motion demand. The damping coefficients B, individual responses u_{max}, effective damping β_{eff}, and effective periods T_{eff} were averaged over the 20 records for the two ground-motion suites (ENA and WNA) and the resulting mean values are then compared to assess the appropriateness of the damping coefficients B.

5.4.2 General Results from NLTHA

In Figures 5.14 and 5.15, both, the mean and individual values of the damping coefficients B obtained from NLTHA are compared to those specified in the NA codes (CSA-06-06 and AASHTO) as a function of the effective damping β_{eff}. Values given by Equation (2.8) with n = 0.3 represent the values obtained using recently adopted NA codes (CSA-06-06 and AASHTO 2009, 2010).

By observing the mean values of the damping coefficients *B*, presented in Figure 5.14(a) for WNA, it can be noted that the majority of the plotted dots are above the curve representing the code-specified damping coefficients, which shows that current code provisions generally result in conservative (larger) response estimates. Damping coefficients are however underestimated for β_{eff} values greater than 20% and this aspect is discussed in further details later.

In contrast, for the ENA records in Figure 5.15(a), a considerable number of points are situated below the curve representing the code prescribed values indicating unconservative predictions when using the code-defined *B* coefficients for all damping levels. Therefore, there is a need to adjust these factors to better predict the expected response of isolated bridges under ENA earthquake records. The different damping coefficients observed for WNA and ENA responses are primarily attributed to the differences in the ground motion characteristics that are expected for seismicity in WNA and in ENA as discussed previously in this chapter.

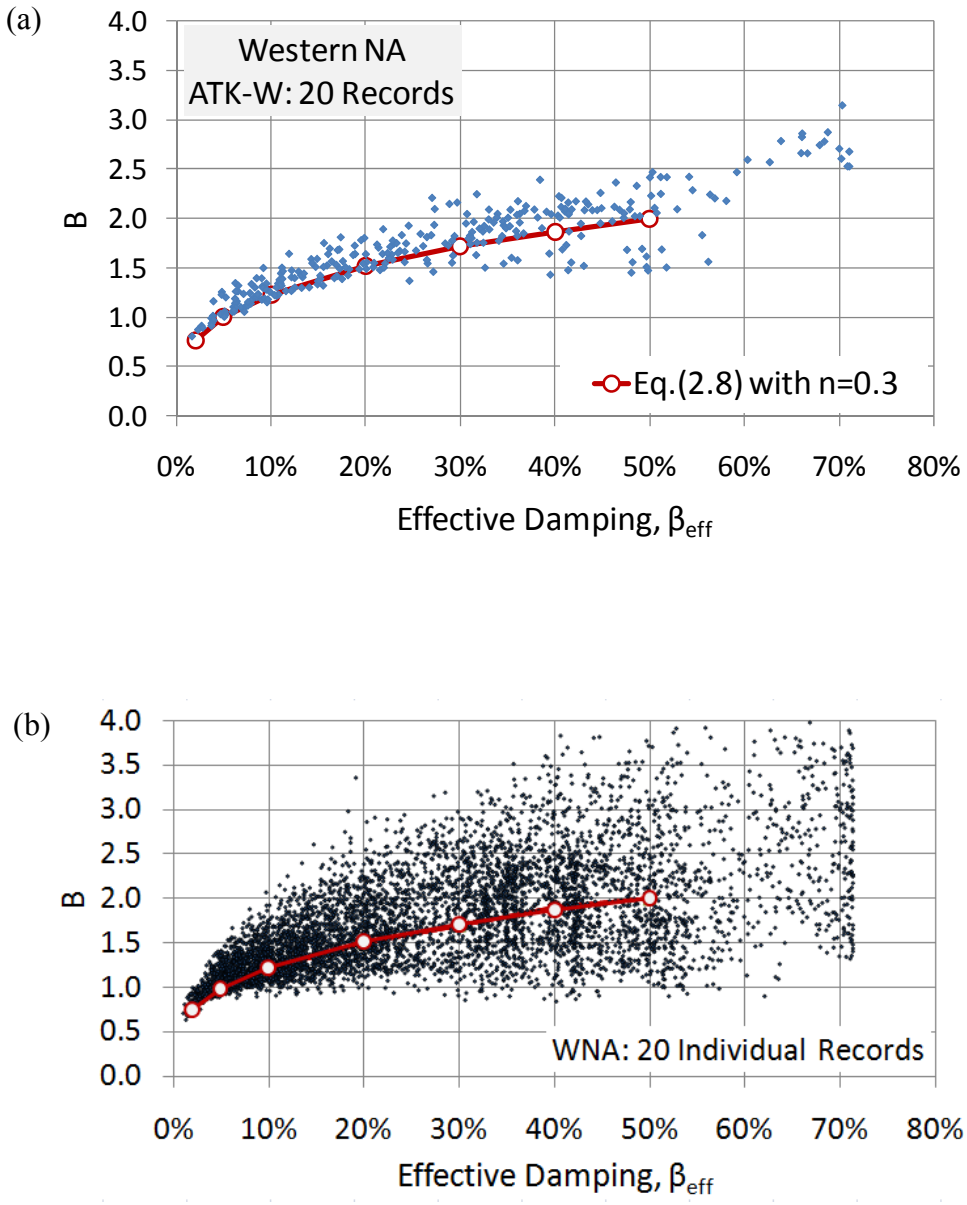

Figure 5.14 Comparison of *B* computed for WNA with those specified in the CSA-S6-06 Code (AASHTO): (a) mean of 20 records, (b) individual records

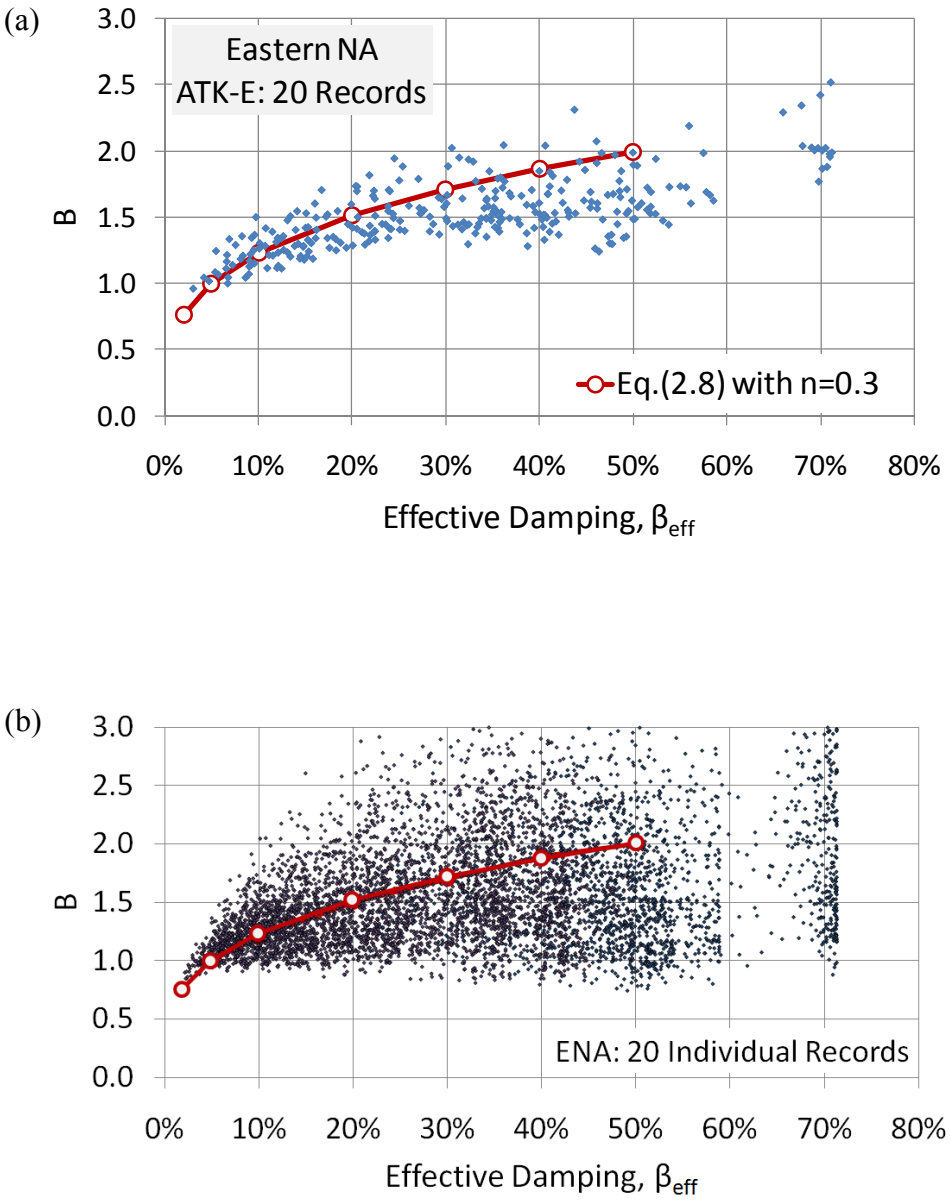

Figure 5.15 Comparison of *B* computed for ENA with those specified in the CSA-S6-06 Code (AASHTO): (a) mean of 20 records, (b) individual records

Figures 5.14(b) and 5.15(b) present individual values of the damping coefficients *B*, which are scattered out over the 20 records when compared to the plot of the mean values. These results provide an overall insight into the variability of the coefficients *B* within a suite of 20 ground motions. Despite a very large scatter in the individual points, the same tendencies as for averaged assessment (Figures 5.14(a) and 5.15(a)) can be easily distinguished from these figures.

To explain the variability of the coefficients *B*, it should be recalled that the damping coefficient method is an approximation and it cannot take into account the effect of the record-to-record variability that may reflect the true random character of the real earthquakes.

5.4.3 Effects of Ground-Motion Characteristics on Damping Coefficients

To gain a better understanding on the variability of the coefficients *B*, the effects of the ground motion characteristics on this parameter are further studied by examining damping coefficients obtained from four different ground motion subsets each representing the ENA suite. These four subsets are divided by grouping earthquake scenarios in terms of magnitude and distance: E6C1 (M6, 10 to 15 km), E6C2 (M6, 20 to 30 km), E7C1 (M7, 15 to 25 km) and E7C2 (M7, 50 to 100 km) (see for more details Chapter 4). Mean 5% damped displacement spectra are given for each subset in Figure 5.16. As expected, for longer periods, the smaller earthquakes E6C1 and E6C2 induce smaller elastic displacement demands when compared to those from the greater earthquakes E7C1 and E7C2. For a given magnitude range, closer earthquakes E6C1 and E7C1 produce larger elastic displacements.

It can be noted from these figures that the spectra from individual records may deviate significantly from each other. The reason for this, as explained in Chapter 4, is that the 20 records (ENA or WNA) were scaled over a certain period range so the mean response spectrum matches the UHS closely (for Montreal and Vancouver). These observations shed light on the mechanisms contributing to the variability of the coefficients *B* within a suite of 20 ground motions.

Figure 5.17 gives the mean damping coefficients computed for each subset. Damping coefficients that are much smaller than the code-specified values (the code predictions are unconservative in this case) are obtained for the M6 events. For the two subsets of larger M7

earthquakes, the code-defined B coefficients generally result in conservative estimates, except for high β_{eff} values (β_{eff} greater than 30%).

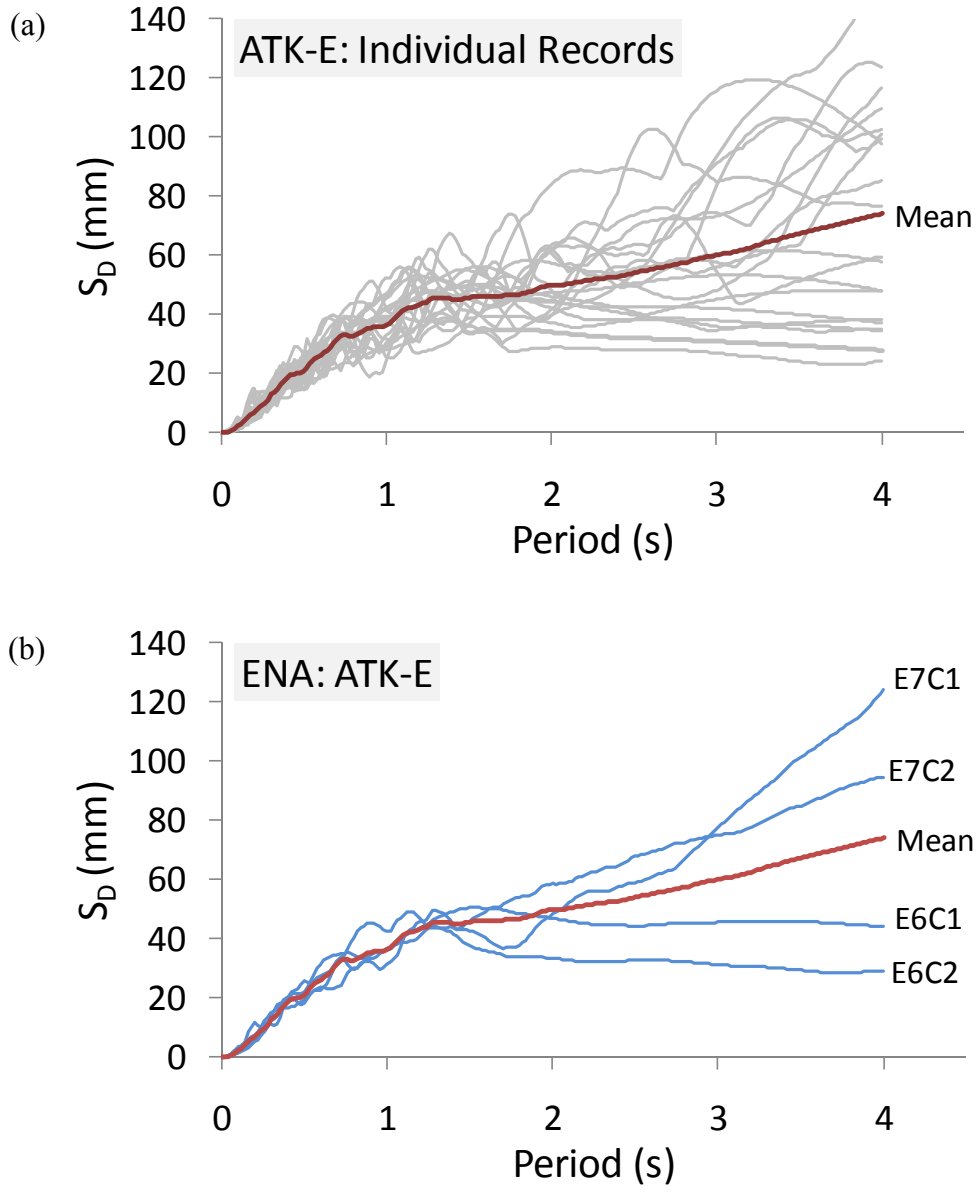

Figure 5.16 ENA response spectra for 20 ATK-E records: (a) individual spectra and (b) mean spectra regrouped according to M-R subsets: E6C1 (6 records), E6C2 (3 records), E7C1 (3 Records), and E7C2 (8 Records)

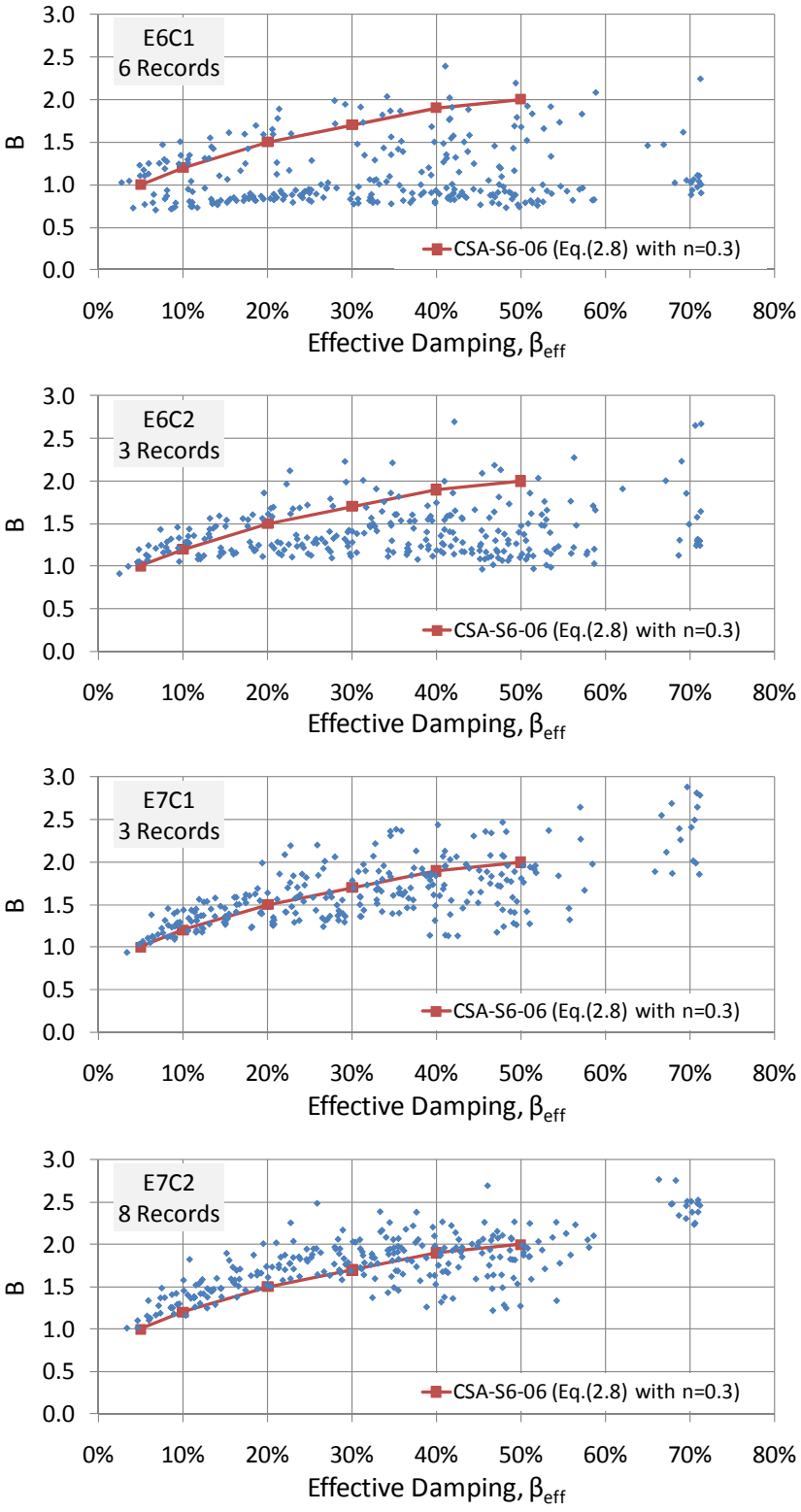

Figure 5.17 Effect of ENA M-R distribution on damping coefficients

5.4.4 Comparison of CSA-S6-06 Design Estimates with Results from NLTHA

To better assess the accuracy of code-specified *B*-coefficients on the seismic displacement response, a number of 180 isolated bridge structures (5 (R) x 4 (T_e) x 3 (β) x 3 (α)) were analyzed following the complete iterative procedure prescribed in the CSA-S6-06 simplified method (similar to AASHTO).

The displacement response was calculated by dividing the 5% damped pseudo-displacement by the damping coefficient as $u_{code} = PS_D(5\%, T_{eff}) / B(\beta_{eff})$. The $PS_D\ (5\%, T_{eff})$ value is determined by transforming the $S_A\ (5\%, T_{eff})$ value from the UHS acceleration spectrum represented by the 20-records mean acceleration response spectrum. The $B(\beta_{eff})$ value is determined as a function of the effective damping β_{eff} using Equation (2.8) with n=0.3 (as specified in AASHTO), As stated in Chapter 2, this expression accurately represents the damping coefficients tabulated in the CSA-S6-06 code and will be further exploited to enhance the accuracy of the simplified method.

The displacement response is however defined as a function of the effective period T_{eff} and effective damping β_{eff}. As a result, the response estimate is obtained by successive iterations because the values of T_{eff} and β_{eff} depend, in turn, on the displacement response u_{code} (refer to Chapter 2, Section 2.1 for more details on the procedure).

Figures 5.18 and 5.19 present probability density functions of the ratios between the peak displacements from nonlinear time history analyses (NLTHA) and peak displacements obtained using the CSA-S6-06 simplified method. Values in the plots are computed for a sample of 1200 responses, that correspond to 60 different isolated bridge structures (5 (R) x 4 (T_e) x 3 (β)) analyzed under 20 time-history records. Accordingly, there are 20 responses from NLTHA that correspond to one response estimate using the CSA-S6-06 simplified method. Each plot is obtained for one site (West *vs* East) and one value of α (0.1, 0.05, 0.01).

It can be noted from these figures that the probability density is close to a normal distribution: the distribution pattern is symmetrical; the highest point is close to the center of the distribution; and the shape of the distribution follows a general "bell" curve. In addition, for the normally

distributed data within a range from -∞ up to a value at one standard deviation above the average, 84% of the response population can be expected to occur while the probability obtained from NLTHA is ranging between 85.2% and 86.5% suggesting that the data can be considered as normally distributed.

Assuming that the data is normally distributed, the cumulative distribution at u_{NLTH} / u_{code}=1, presents the probability of occurrence of a conservative response estimate and describes how many response estimates are likely to occur at a value of the ratio u_{NLTH} / u_{code} that is less than or equal to unity. These values are tabulated and compared in Table 5-2.

For the West, for all three values of α, the code method gives more consistent results while being, on average, slightly conservative given that the probability of obtaining a conservative response estimate is greater than 50%. As expected, for systems with low recentring capability, the lower probability of occurrence is observed for α=0.01: 50.8%. The same tendencies are observed for the code values obtained for the East when using n=0.3. However, these values are characterized by a probability of less than 50% for all three values of α, indicating mostly unconservative response estimates that highlight the need to enhance the accuracy of the CSA-S6-06 simplified method for response estimates in ENA.

Table 5-2 Summary on comparison between individual responses from NLTHA and the corresponding response estimates according to the code provisions (sample of 1200 values)

	α	Mean u_{NLTH} / u_{code}	Probability of $u_{NLTH} / u_{code} = 1$	Standard Deviation	COV
WNA	0.1	0.95	58.3%	0.24	25.6%
Eq.2.8 with	0.05	0.94	57.7%	0.30	31.4%
n=0.3	0.01	0.99	50.8%	0.46	46.5%
ENA	0.1	1.05	43.3%	0.32	30.5%
Eq.2.8 with	0.05	1.15	34.9%	0.37	32.7%
n=0.3	0.01	1.30	26.9%	0.49	37.4%

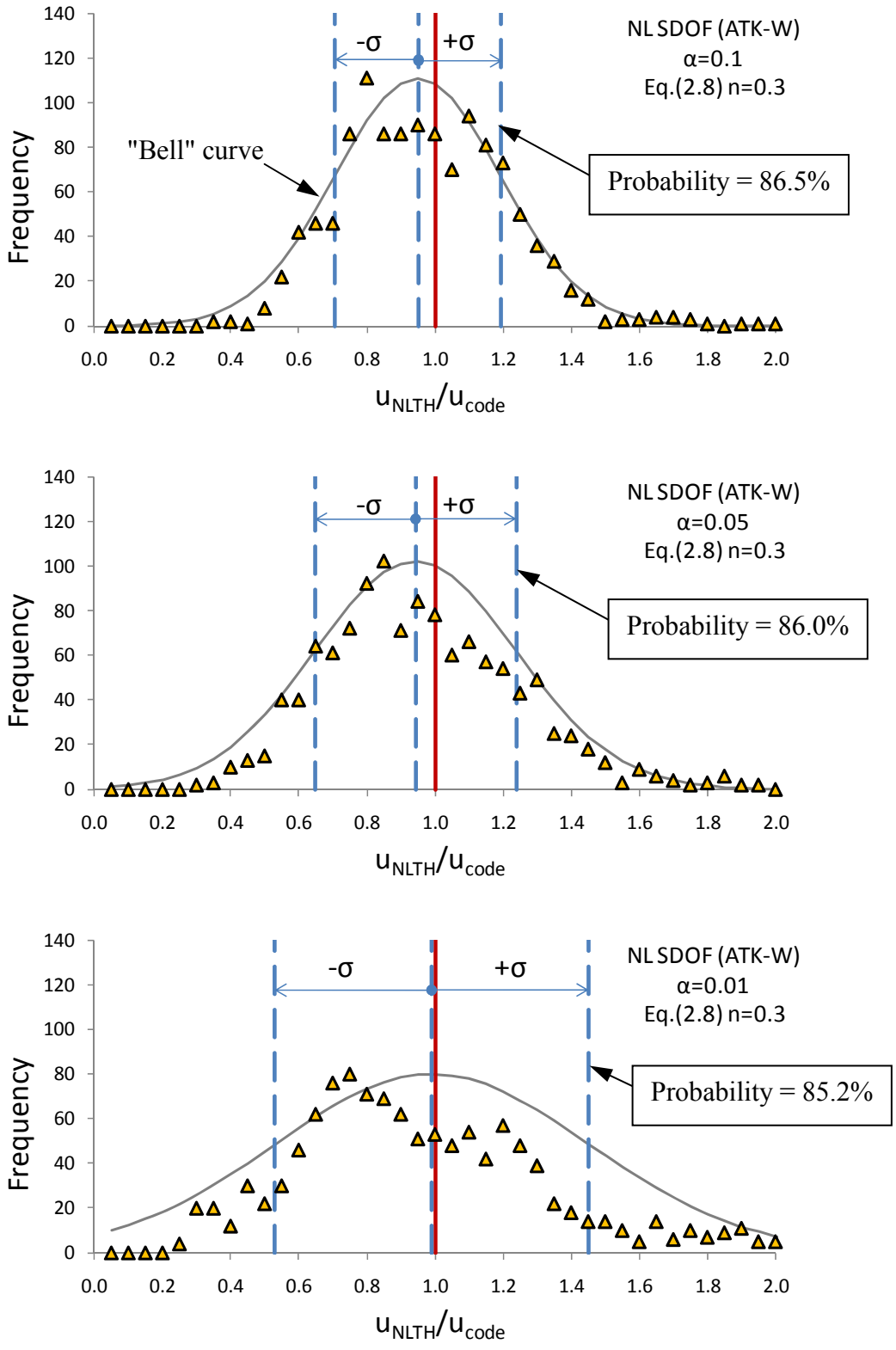

Figure 5.18 Frequency of u_{NLTH}/u_{code} versus normal distribution - WNA Eq.(2.8) with n=0.3

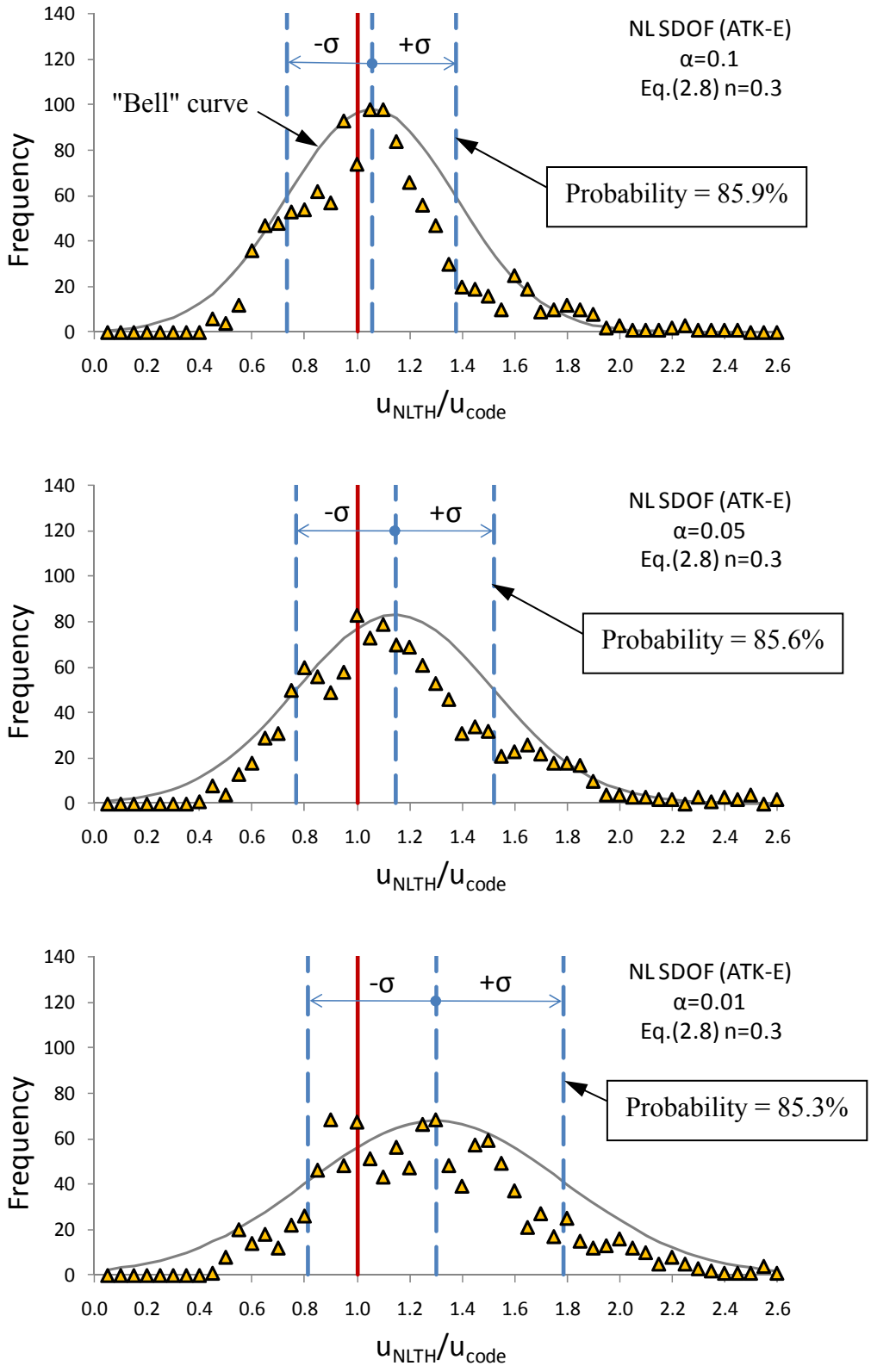

Figure 5.19 Frequency of u_{NLTH}/u_{code} versus normal distribution - ENA Eq.(2.8) with n=0.3

Ratios obtained from individual records are presented in Figures 5.20 to 5.21. As mentioned previously, the observed deviation from the sample mean value is mostly due to the record-to-record variability including the differences observed between the response spectrum from each individual record and the corresponding UHS (as shown in Figure 5.16). It should be recalled that the 20 records (ENA or WNA) are scaled over a certain period range so the mean response spectrum matches closely the UHS (for Montreal and Vancouver respectively) while individual records may deviate significantly from each other.

The variability is measured in terms of the standard deviation, which is compared in Tables 5.2 for samples of 1200. As expected for the systems with low recentring capability, which are easily prone to residual displacements, the variability increases as the value of α decreases. The upper and lower limits of standard deviations observed for α=0.01 are 0.46 for the West and 0.49 for the East. The respective coefficients of variation (COV), which describe the standard deviation as a percentage of the sample mean, are 46.5% and 37.4%. The greater coefficient of variation can be explained by stronger ground-motion intensities in Western Canadian regions.

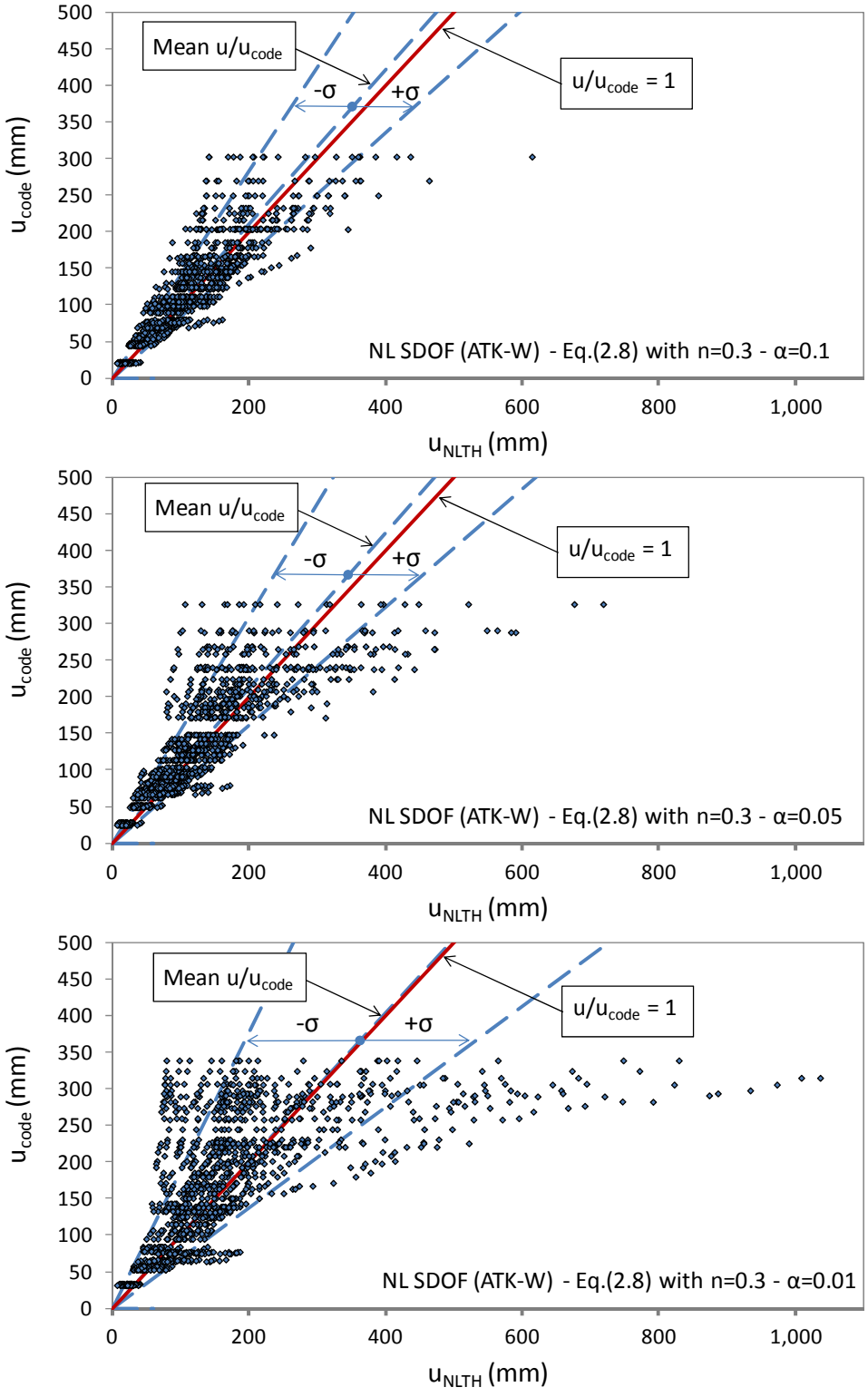

Figure 5.20 Responses from NLTHA versus code estimate - WNA Eq.(2.8) with n=0.3

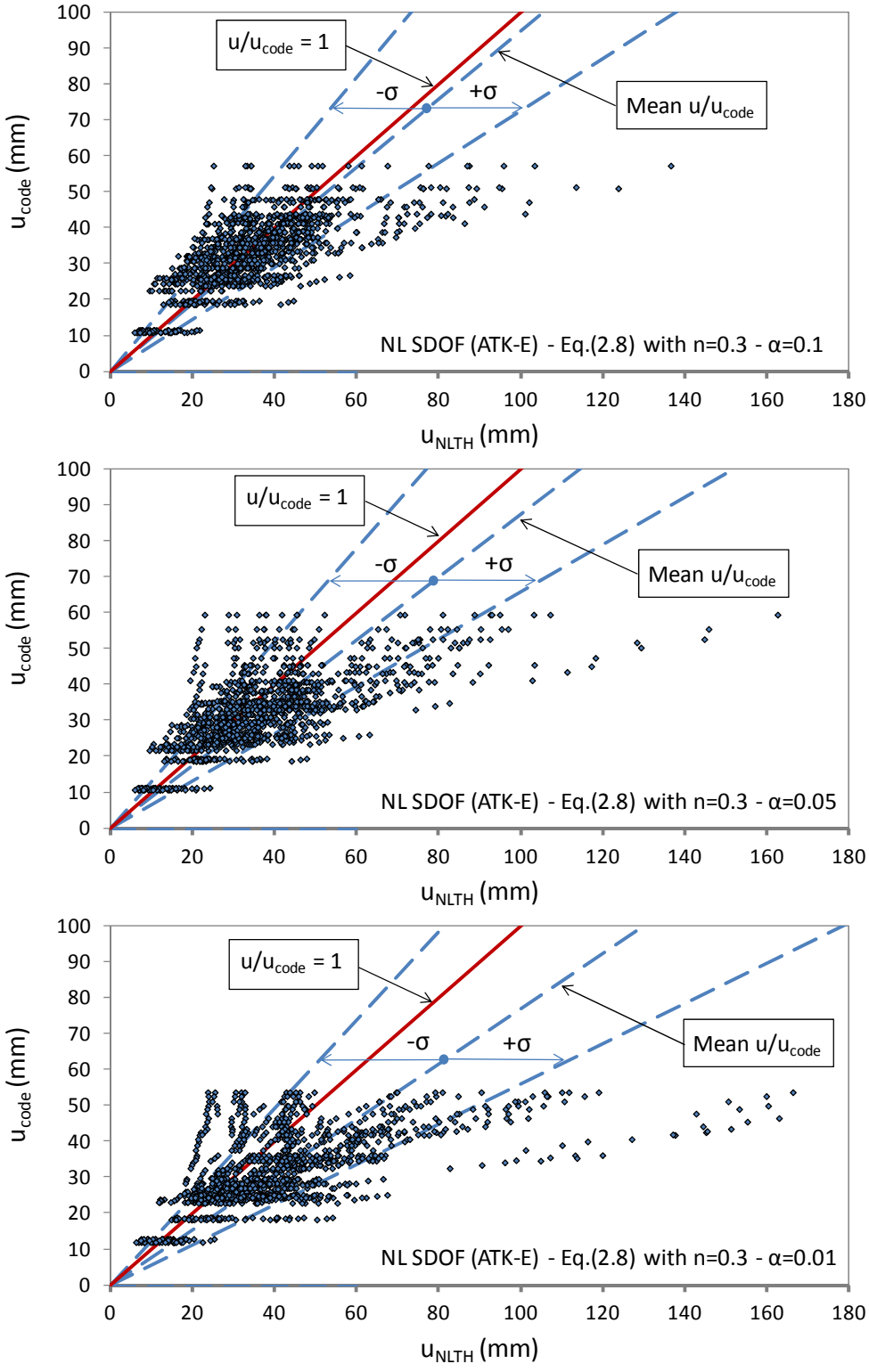

Figure 5.21 Responses from NLTHA versus code estimate - ENA Eq.(2.8) with n=0.3

5.5 Proposed Equation for Damping Coefficients, *B*

The analysis results that were presented earlier in this chapter showed that the damping coefficients specified in NA codes may lead to underestimations of peak isolator displacements in ENA and, therefore, modified damping coefficient values are required to better predict the damping reduction effect.

5.5.1 Calibrating Damping Coefficients, *B*

As previously stated, the most critical value of α for obtaining the conservative response estimates corresponds to $\alpha = 0.01$. To improve the accuracy of the simplified method for estimating the bridge responses in ENA, the damping coefficients were modified so that for ENA and WNA, the levels of statistical significance for the response estimates are similar for isolated bridges having $\alpha = 0.01$. The calibration criteria are based on the confidence interval for a population mean with a 95% confidence level. Two samples of 1200 results were examined. By assuming the one-tailed hypothesis test, the sample mean that is greater than the upper bound of the confidence interval is rejected. As a result, the upper bound for a confidence interval represents the lower-bound damping coefficients and it is determined as:

$$x = \bar{x} + 1.645\frac{\sigma}{\sqrt{1200}} \tag{5.12}$$

where $\bar{x}$ corresponds to a u_{NLTH}/u_{code} mean value obtained for a population with a size of 1200 and a standard deviation σ. The upper critical value for one-tailed standard distribution to accumulate 95% of probability is accordingly 1.645σ. The corresponding test hypothesis adopted for this study is presented in Figure 5.22.

There is a probability of 95% that the u_{NLTH}/u_{code} mean value for a next sample of 1200 results in WNA will occur within a confidence interval defined from $-\infty$ to x.

$$x = 0.99 + 1.645\frac{0.46}{\sqrt{1200}} = 1.01 \tag{5.13}$$

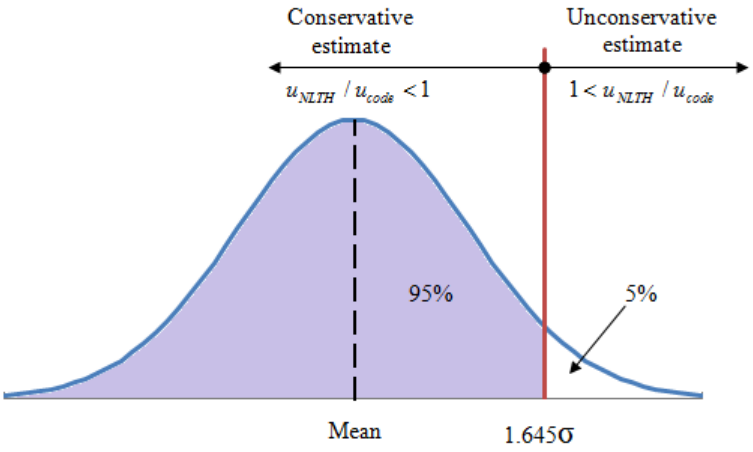

Figure 5.22 One-tailed hypothesis test for the population mean at a 95% confidence level

As it can be stated, for WNA, the resulting confidence interval is defined from $-\infty$ to 1.0 what corresponds to the conservative code use. The same confidence interval is then adopted as a calibration criterion for the ENA damping coefficients. As previously observed, these damping coefficients, determined using Equation (2.8) with n=0.3, result mostly in unconservative response estimates. Based on these results, the upper limit of the corresponding confidence interval yields:

$$x = 1.30 + 1.645\frac{0.49}{\sqrt{1200}} = 1.32 \tag{5.14}$$

The damping coefficients are then modified by decreasing the exponent in Equation (2.8) so that the resulting confidence interval for the u_{NLTH} / u_{code} mean value is defined between $-\infty$ to 1.0 to represent conservative response estimates similar to those obtained for WNA. It is found that a conservative (lower bound) damping coefficient estimate for ENA can be obtained using Equation (2.8) with an exponent n = 0.2. The upper bound of the resulting confidence interval is determined as follows:

$$x = 0.98 + 1.645\frac{0.37}{\sqrt{1200}} = 1.00 \tag{5.15}$$

Table 5-3 summarizes the statistical parameters obtained from the response estimates for bridges in ENA using the modified damping coefficients (Equation (2.8) with n = 0.2).

Table 5-3 Statistical assessment for results obtained for ENA using Eq.(2.8) with n=0.2

	α	Mean u_{NLTH}/u_{code}	Probability of $u_{NLTH}/u_{code}=1$	Standard Deviation	COV
ENA Eq.2.8 with n=0.2	0.1	0.93	60.3%	0.27	29.2%
	0.05	0.95	56.1%	0.31	32.3%
	0.01	0.98	51.8%	0.37	37.6%

5.5.2 Validation of the Proposed Damping Coefficients, *B*

To validate the accuracy of the proposed *B*-coefficients on the seismic response prediction, the same 180 isolated bridge structures (5 (R) x 4 (T_e) x 3 (β) x 3 (α)) were analyzed following the complete iterative procedure prescribed in the CSA-S6-06 simplified method using Equation (2.8) with n=0.2. The results are then validated by comparing the corresponding relative error to that resulting from the use of Equation (2.8) with n = 0.3 for WNA.

The relative errors were computed for individual responses of 180 isolated bridges undergoing each individual ground motion demand. Then individual results were averaged over the 20 records for the two ground-motion suites (ENA and WNA) and the resulting mean values are then compared as a function of the effective period T_{eff} and effective damping β_{eff} both obtained from the displacement estimate.

As shown in Figures 5.23 and 5.24, for most cases associated to the various β_{eff} and T_{eff} values obtained in the parametric study, the error ranges from 5% to -50% when using Equation (2.8) with n = 0.3 for WNA. In the same figures, it is shown that using Equation (2.8) with an exponent n = 0.2 for ENA results in a comparable relative error range. In this way, the same level of accuracy would be reached in both parts of the country.

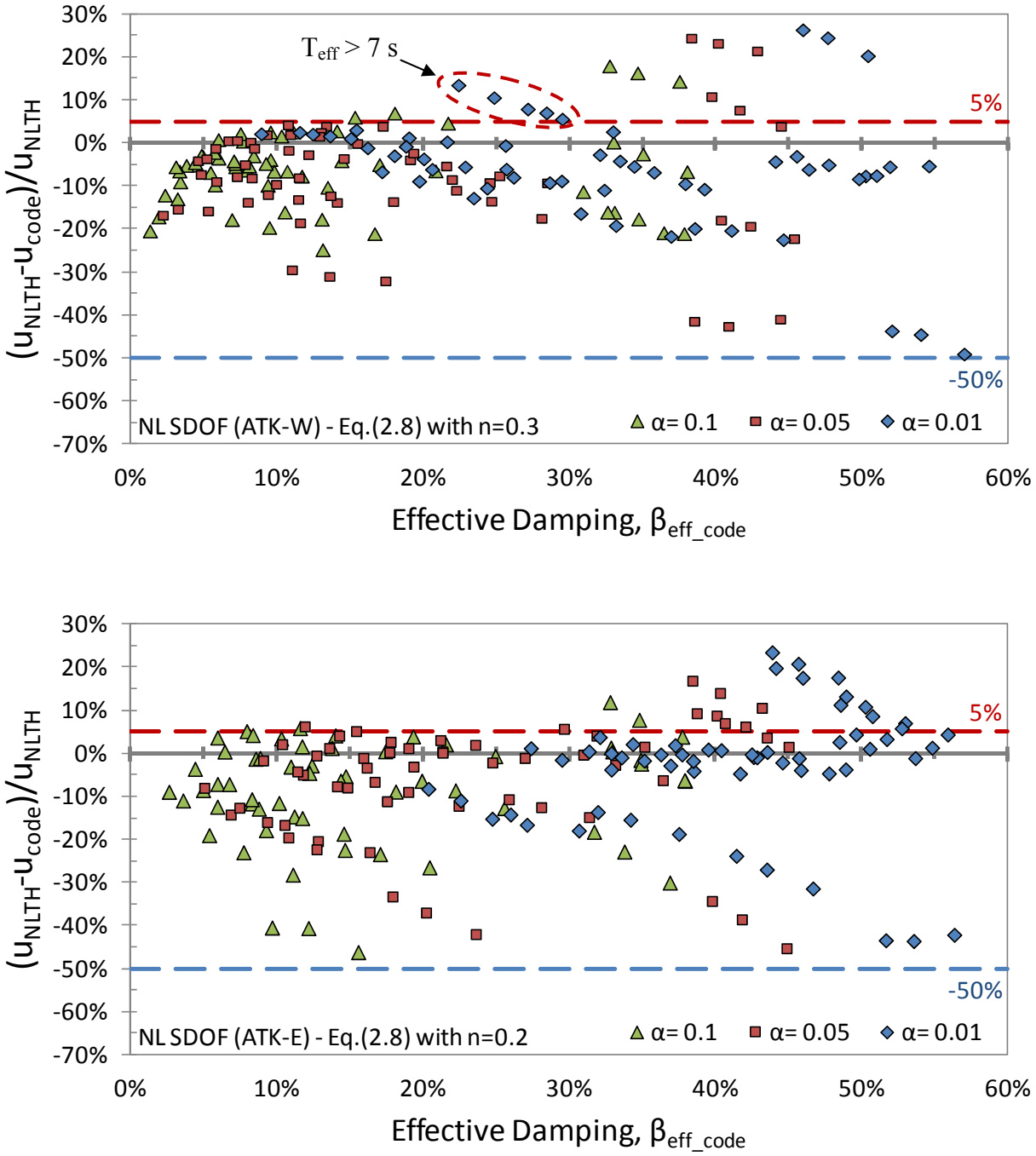

Figure 5.23 Relative errors of the displacement estimate as a function of the effective damping (Equivalent linearization method and coefficients B from Eq.(2.8) with n = 0.3 for WNA and n = 0.2 for ENA)

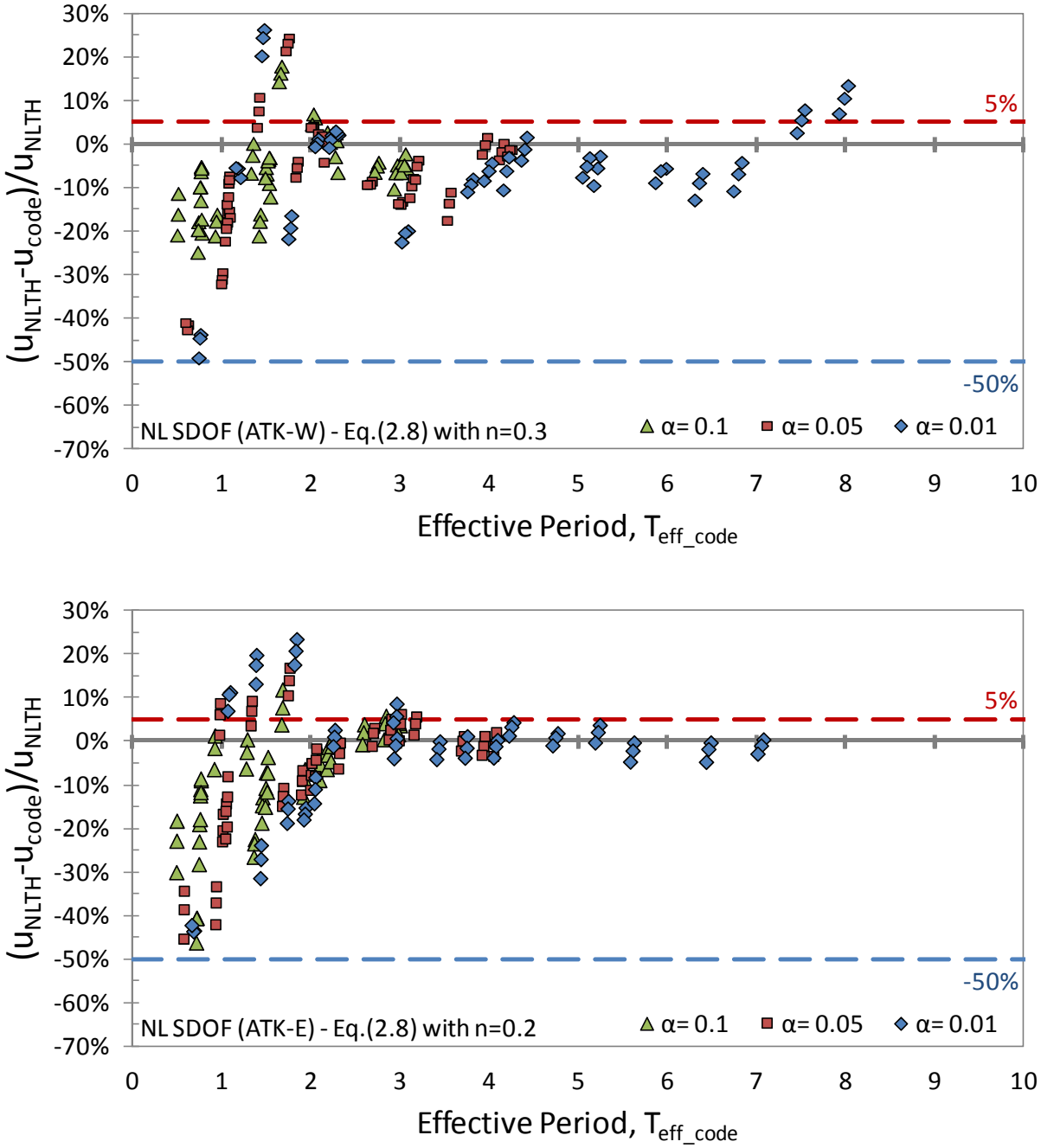

Figure 5.24 Relative errors of the displacement estimate as a function of the effective period (Equivalent linearization method and coefficients B from Eq.(2.8) with n = 0.3 for WNA and n = 0.2 for ENA)

The largest errors corresponding to unconservative response estimates are observed for effective damping ratios $\beta_{eff} > 30\%$ that correspond mostly to the bridge configurations having a low response modification factor ($R = 4$). Such systems experience responses with small inelastic excursions that correspond to a limited period lengthening. The reason for these errors cannot be clearly outlined from these observations and will be further investigated in the next chapter.

It is opportune to mention that for the WNA dataset between β_{eff} =20% and 30%, the largest errors (higher than 5%) correspond to systems exhibiting large displacements. For these systems, the corresponding effective period T_{eff} is longer than 7 s (see Figure 5.24), a period range over which the WNA records posses low power spectrum energy (Figure 5.4). Moreover, these systems are characterized by low recentring capabilities ($\alpha = 0.01$).

Codes indicate that NLTHA is required when β_{eff} exceeds 30% or the maximum value of B corresponding to a $\beta_{eff} = 30\%$ has to be used in the simplified analysis procedure. This study confirms the need for such a limit but the results indicate that the limit could be increased. It can also be noted that the upper damping limit depends on the ratio α and the limit could be extended to values up to approximately 33%, 38%, and 43% for α =0.1, 0.05, and 0.01, respectively. The observed upper limits are also similar for WNA and ENA. Hence, Equation (2.8) could then be used in future editions of CSA-S6 and AASHTO Guide with two different exponent values: n = 0.2 for ENA and n = 0.3 for WNA.

The computed damping coefficients of Figure 5.15(a) are reproduced in Figure 5.25. It can be then noted that the majority of the plotted dots are above the curve representing the damping coefficients obtained by using Equation (2.8) is used with n=0.2 for ENA. It confirms the enhanced reliability of the proposed B-coefficient method that will generally result in conservative (larger) response estimates as in the case when this method is used for bridges in WNA.

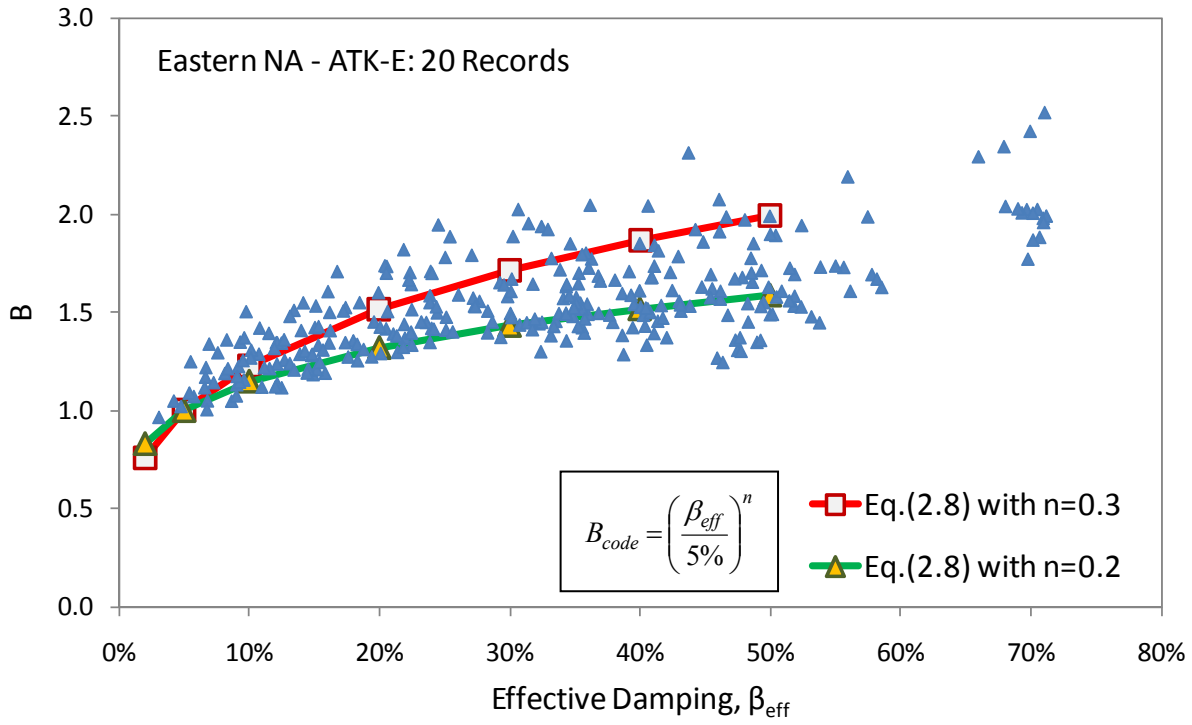

Figure 5.25 Comparison of proposed and computed *B* damping coefficients for ENA

5.6 Conclusions

In this chapter, the appropriateness of damping coefficients *B* currently specified in NA codes (CSA-S6-06 and AASHTO) for the design of isolated bridges in ENA and WNA was investigated.

The *B*-coefficients from LTHA in ENA and WNA were compared to those specified in codes in order to emphasize the influence of the regional seismicity on the reduction damping effect. A lower reduction effect of viscous damping was observed under ENA records when compared to WNA records. The concepts of force transmissibility and response amplification for S_A and S_D were exploited to explain the observed differences that were primarily attributed to different frequency contents distinguishing the ENA and WNA seismicity conditions. The suitability of using the same *B*-coefficient for reducing force and displacement responses was examined based on the LTHA results. It was shown that the coefficients $B(S_A)$ and $B(S_D)$ reflect different aspects of the system response (absolute acceleration and relative displacement) and *B*-coefficients for

reducing force and displacement responses must be independently calibrated. For a more accurate evaluation of the displacement across isolation bearings, the analysis results suggest that for the simplified code method the definition of the *B* coefficients should be based on spectral displacements rather than spectral accelerations. The dependency of the *B*-coefficients on the effective period was also confirmed.

In this study, complementary to most of previous studies performed worldwide in which LTHA was used, an extensive parametric study was carried out using dynamic NLTHA so that a series of nonlinear system parameters was considered to cover a wide range of isolated and damped bridge configurations. A total of 12 000 NLTHA were carried out on 300 isolated bridge configurations under 20 time-history records representatively for the WNA and ENA regional seismicity (40 records in total). Based on the observations made for LTHA, in the parametric study, the damping coefficients were assessed solely for displacement responses. The damping coefficients specified in current CSA-S6 and AASHTO codes were found to result mostly in safe designs for WNA but underestimated the displacement demand of bridges subjected to ENA seismic ground motions.

Based on these results a new value was proposed for the exponent to be used in the equation currently specified in the AASHTO specifications for the damping coefficients so that the same equation can be used with different exponents for WNA and ENA locations. The study also showed that the current upper limit on the effective damping ratio for the application of the simplified methods in North America could be relaxed and defined more accurately as a function of the post-yielding stiffness ratio α.

Despite the improvements made, the simplified method still under predicts the response of isolated bridges for a number of cases. In particular, systems with low *R* factors, low α ratios, with high effective damping ratios or short effective periods were found to be more critical in this regard. This indicates that there is a need to improve our understanding of the sources of the inaccuracy that are inherent to the simplified analysis procedure used in design codes. This aspect is further examined in detail in the following chapters.

Chapter 6: Influence of nonlinear parameters and applicability limits for the code simplified method

6.1 Introduction

In the previous chapter, the appropriateness of damping coefficients B currently specified in NA codes (CSA-S6-06 and AASHTO) for the design of isolated bridges in ENA and WNA was investigated and the limitations inherent to the code simplified analysis method, which rely on these coefficients to account for the effect of damping in the response, was confirmed. It was observed that the inaccuracy of the simplified code method can be associated to certain ranges of nonlinear parameters: low R factors, low α ratios, high effective damping ratios β_{eff} or short effective periods T_{eff}. In this chapter, a more detailed investigation of the nonlinear dynamics of isolated and damped systems is carried out to better characterize the sources of the inaccuracies that are inherent to the simplified analysis procedure used in design codes.

As previously discussed in Chapter 2, the code simplified method is based on the transformation of the actual nonlinear isolated structure into an equivalent linear system (see Figure 2.1(a)) commonly termed *equivalent linearization*. The equivalent damping ratio is defined such that, for a given peak displacement response u_{max}, the equivalent system dissipates the same amount of energy Eh in one cycle as the actual nonlinear system dissipates through hysteretic damping in one cycle at this same amplitude, centred around its origin as illustrated in Figure 6.1. The coefficient B is evaluated as a function of the damping ratio and the response estimate is determined by simply dividing the 5% damped elastic response by the coefficient B. As shown in Chapter 5, the coefficients B are calibrated empirically for a given regional seismicity so the error between NLTH response and the response estimate is reduced to an acceptable level. In this simplified method, the system nonlinear parameters are directly taken into account by the process of *equivalent linearization*, while the effect of regional seismicity is expected to be reflected by applying different coefficients B. The coefficients B are however calibrated so the accuracy of the simplified method is enhanced by reducing errors from both sources, the *equivalent linearization* and the local damping reduction effect.

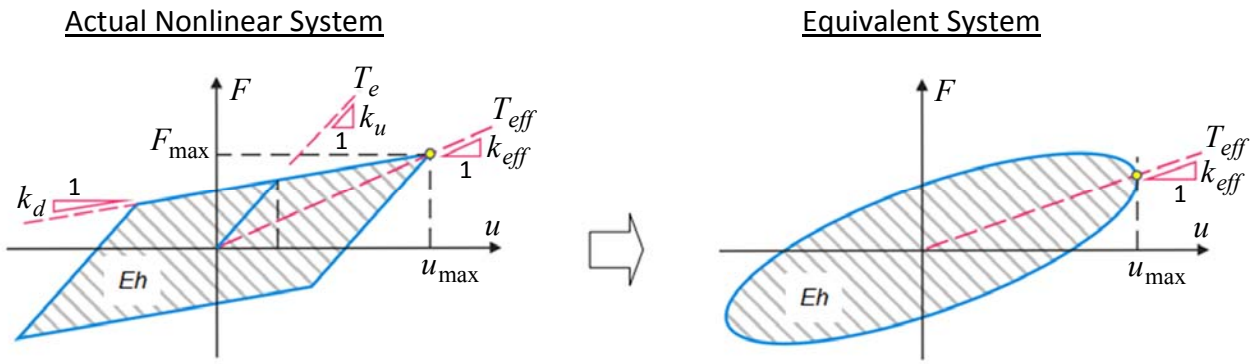

Figure 6.1 Bilinear response and equivalent viscoelastic response

To improve our understanding of the actual sources of inaccuracy that are present in the response estimates, the influence of the nonlinear parameters that were used in the parametric study that was carried out in the previous chapter is first discussed. Then, the accuracy of the *equivalent linearization method* is carefully examined and the influence of the nonlinear parameters is outlined. Recommendations are made on how to define the range of parameters for which the *equivalent linearization method* can provide an accurate response estimate. The need for a new simplified method that takes into account the differences in ground-motion characteristics and isolated bridge design parameters is also outlined in this chapter.

6.2 Influence of System Properties on Damping Coefficients and the Code Simplified Method

Parameters such as the initial period T_e, the post-yield stiffness ratio α, and the response modification factor R make it possible to define the hysteretic properties of the system at the initial design stage. These parameters were adopted for the parametric study carried out in the previous chapter. Their influence on the response of isolated bridges and B coefficients were presented.

Elastic T_e and effective periods T_{eff}

The initial effective period T_e interacts with the predominant earthquake period when the system behaves essentially elastically and is a relevant parameter when using elastic response spectra. In

other words, when the time function of the seismic excitation is decomposed into a Fourier series, the dynamic response amplification may be simply attributed to the resonant interaction between the structure and time functions of the ground motion. Accordingly, for an elastic system, the resonant interaction occurs solely at the elastic period T_e. For such systems, damping coefficients for displacement responses tend to unity for very short periods and very long periods**,** and maximum damping effects are expected for intermediate periods in the velocity-sensitive region of the spectrum, especially for periods close to the predominant ground motion periods (Chopra, 2011). As was discussed in Chapter 5 for harmonic response, the damping effect varies as a function of the ratio T_e / T_g.

For systems responding in the inelastic range, the influence of the effective damping on the response should depend on the ratio T_{eff} / T_g rather than T_e / T_g. However, the initial effective period T_e is a parameter that can be more easily defined at the initial design stage, when the system response is still unknown. It also clearly defines the lower bound and can be used to estimate the extent of the likely range of the effective period T_{eff}. The influence of T_e on the damping coefficients B obtained from NLTHA for ENA ground motions is outlined in Figure 6.2. The reduction effect of damping, represented in terms of B, is the highest for structures with the shortest initial period (T_e = 0.25 s). For these structures, NA code damping coefficients will result in conservative response estimates for most cases. For longer initial periods (T_e = 0.5 s to 1.0 s), damping coefficients are smaller and code-prescribed values are unconservative for β_{eff} greater than the 20-30% range.

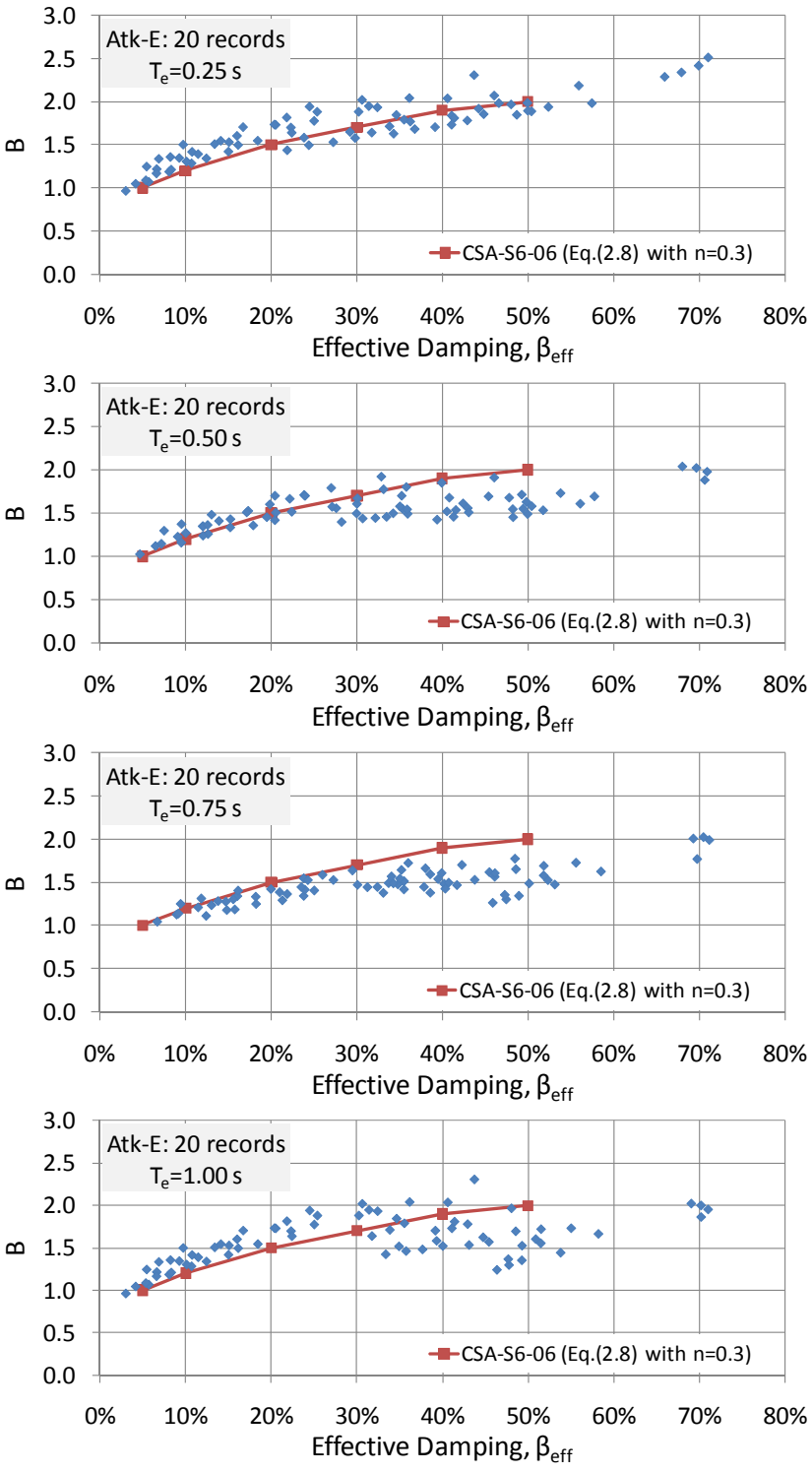

Figure 6.2 Variation of damping coefficients B in ENA with initial period T_e

Response modification factor R

The response modification factor R characterizes the response by relating the isolation activation limit to the elastic demand for a given UHS. Figure 6.3 shows how the system's hysteretic shape is defined based on the response modification factor. It can be noted from this figure that systems designed with low response modification factors *R* exhibit a limited inelastic response and are therefore characterized by the elastic properties of the system while the response of systems with higher *R*-factors is mostly oriented along the post-activation stiffness k_d, resulting in a longer effective period T_{eff} and larger displacements.

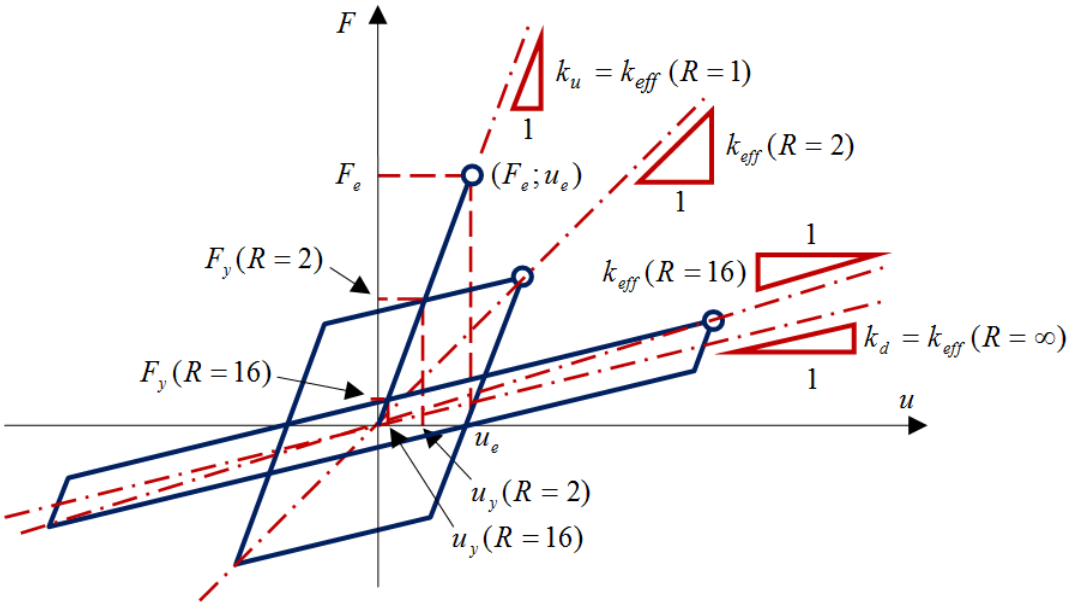

Figure 6.3 Bilinear response - Influence of the R factor on the hysteretic shape

Post-yielding stiffness ratio α

As observed in the previous chapter, larger displacements are observed in systems with a smaller α ratio (small post-activation stiffness) where the peak response is increased as a result of the system's lower recentring capability.

The systems with low recentring capability are also more prone to residual displacements. It is important to take residual displacements into account given that the displacement response to the subsequent ground motion will start from the position corresponding to the residual displacement from the previous motion. Similarly, when the ground motion is represented by a series of single-pulse motions, the initial zero position for each new pulse is the position reached at the end of the previous one.

Accordingly, the initial equilibrium position may drift during an earthquake motion. In other words, during inelastic excursions, the system's oscillation center drifts from its initial zero-displacement position and the system starts vibrating around a new equilibrium position termed the transient oscillation center, after large inelastic cycles. A large or a few consecutive smaller yielding excursions in the same direction produces an inelastic response that is skewed in the direction of these inelastic excursions.

In such cases, the maximum displacement response will not reflect the real damping that is associated with the peak response of the system, and which is defined as a portion of the dissipated hysteretic energy, *Eh* as illustrated in Figure 6.4. For two systems with the same properties as elastic initial period T_e (or elastic stiffness k_u), system activation limit u_y (or response modification factor R), and post-yielding stiffness ratio α (or post-yielding stiffness k_d), the real energy dissipated around a drifted oscillation center may be strongly overestimated by considering an equivalent response around the original center as prescribed in the CSA-S6-06 code (or AASHTO). It could be noted from Figure 6.4 that the effective stiffness k_{eff} (or effective period T_{eff}) of the equivalent response about the original center misrepresents the real system behaviour when the system drifts from its initial equilibrium position.

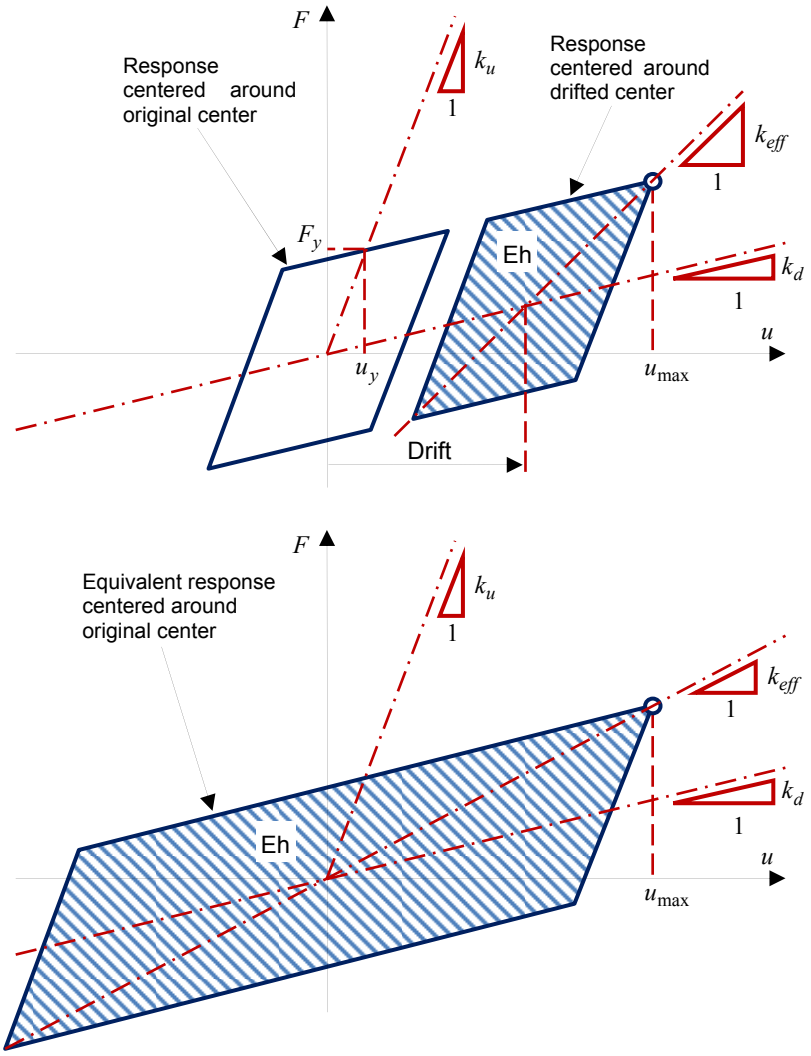

Figure 6.4 Bilinear response - Response around drifted oscillation center and equivalent response around original center as prescribed in the CSA-S6-06 simplified method.

B-coefficients with nonlinear system parameters

The damping coefficients obtained through NLTH in the previous chapter for ENA are presented versus T_{eff} for different R and α parameters in Figure 6.5. Certain trends are outlined by using second degree polynominal trendlines which put in evidence that the same effective damping for different period ranges may be characterized by a different damping reduction effect.

It can be observed that for systems with post-activation stiffness ratio $\alpha = 0.1$ and 0.05, damping coefficients are larger for elastic periods in the range of $T_e = 0.25$ and 1.0 s when compared to those obtained in the range of $T_e = 0.5$ and 0.75 s. For the systems with $\alpha = 0.01$, the largest damping coefficients are observed for $T_e = 0.25$, while for the three longer elastic periods ($T_e = 0.5$, 075 and 1.0), the curves describing B-coefficients are similar and differ generally by the effect of the corresponding period lengthening. As discussed previously, long effective periods are obtained for systems with large R factors and low α factors. For these systems (e.g., $\alpha = 0.01$), the damping coefficients do not vary much with the effective period after approximately $T_{eff} = 3.7$ s.

These observations provide further evidence of the influence of the nonlinear system parameters on the observed damping coefficients. However, a simple physical explanation on the sources of this variability, that may account for the inaccuracies that have been observed in the code simplified methods, has not yet been proposed. This is examined in more detail in the following sections.

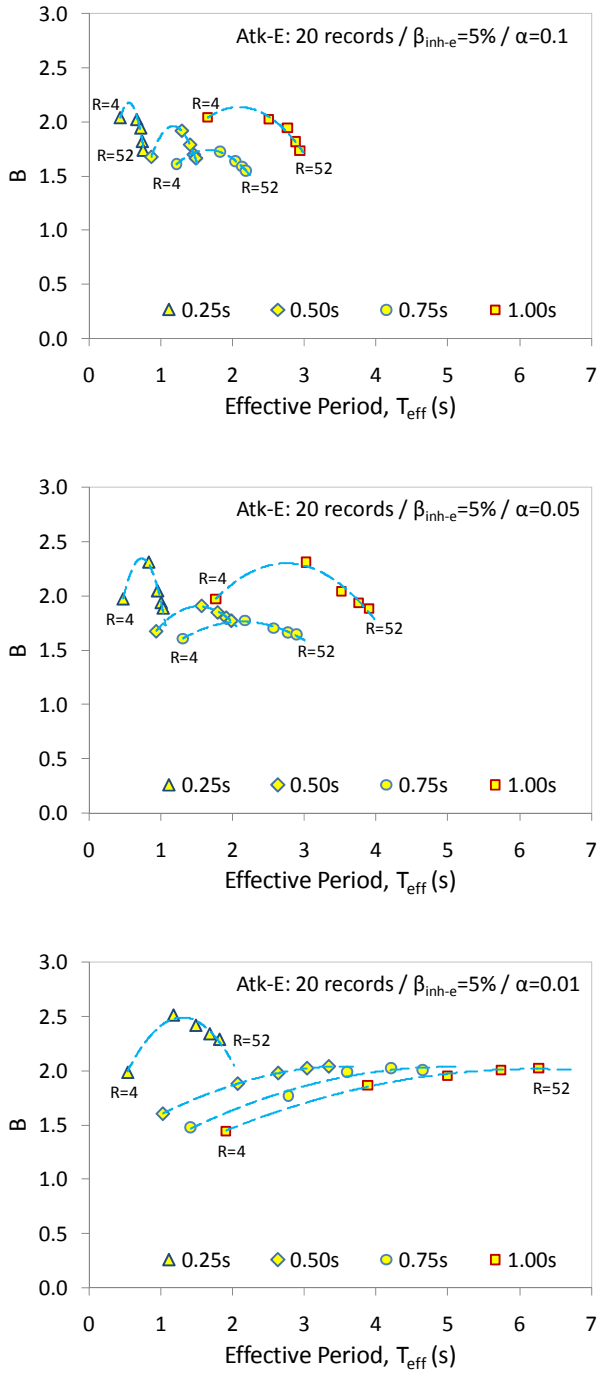

Figure 6.5 Variation of damping coefficients B in ENA with effective period T_{eff} for ratios R = [4, 16, 28, 40, and 52], T_e = [0.25, 0.5, 0.75, and 1.0 s] and α = [0.01, 0.05, and 0.1]

6.3 Limits of the Equivalent Linearization Method

As shown in the previous section, the damping coefficients *B* depend on the system nonlinear parameters that may affect the accuracy of the code simplified method. The relative errors, evaluated in Chapter 5, include the errors from the use of the damping reduction coefficients *B* and from the *equivalent linearization method* which is an intrinsic part of the code method. In this section, a better understanding of the source of these inaccuracies is reached by investigating solely the *equivalent linearization method.* Such an approach factors out the errors that are induced by using the *B*-coefficients to account for the damping effect.

Nonlinear and *linear equivalent* SDOF systems are expected to experience similar displacement responses when subjected to the same time-history demand. The *equivalence ratio* defined as the ratio of the displacements obtained for nonlinear (NL) and linear (L) SDOF systems (u_{NLTH}/u_{LTH}) is adopted to assess the accuracy of the *equivalent linearization method*. The *equivalence ratio* as a function of the effective damping is then examined from a statistical point of view by studying the coefficient of variation.

6.3.1 Evaluation of the Equivalence Ratio

The results obtained in Chapter 5 from the parametric NLTHA were used for this comparative study. The effective parameters T_{eff} and β_{eff} of the systems were determined from the NL displacement response using Equations (2.2), (2.4), and (2.5). The period and the damping ratio of the corresponding equivalent linear SDOF systems were then set equal to the effective properties of the nonlinear systems: $T_e(LTH) = T_{eff}(NLTH)$ and $\xi_e(LTH) = \beta_{eff}(NLTH)$.

A detailed example of an *equivalent transformation* for a bilinear SDOF system (R=4, T_e=0.25 s, and α=0.01) subjected to the artificial ground motion E6C1-42 (ATK-E) is first presented herein to outline the procedure of the *equivalent transformation* used in this study. The elastic limit of the isolation system is first determined from the 5% spectral displacement $u_e=S_D(T_e, 5\%)$ (mean displacement response spectrum - 20 records ATK-E presented in Figure 5.2):

$$u_y = \frac{S_D(T_e, 5\%)}{R} = \frac{9.5}{4} = 2.37\ (mm) \tag{6.1}$$

The peak displacement from the NLTHA is 12.0 mm and the ductility demand μ is then found as:

$$\mu = \frac{u_{NLTH}}{u_y} = \frac{12}{2.37} = 5.06 \tag{6.2}$$

The effective period is determined as a function of the ductility using Equation (2.2):

$$T_{eff} = T_e \sqrt{\frac{\mu}{1+\alpha\mu-\alpha}} = 0.25\sqrt{\frac{5.06}{1+0.01\cdot 5.06-0.01}} = 0.55\ s \tag{6.3}$$

An inherent damping, β_{inh-e}, of 2% is assumed for the system. This damping ratio is based on the elastic period T_e=0.25 s. It is transformed into the inherent damping at T_{eff}=0.55 s as:

$$\beta_{inh-eff} = \beta_{inh-e}\frac{T_{eff}}{T_e} = 2.0\%\cdot\frac{0.55}{0.25} = 4.4\% \tag{6.4}$$

The equivalent damping ratio β_{eq} is determined through the system hysteretic response:

$$\beta_{eq} = \frac{2}{\pi}\cdot\frac{(\mu-1)\cdot(1-\alpha)}{\mu\cdot(1+\alpha\mu-\alpha)} = \frac{2}{\pi}\cdot\frac{(5.06-1)\cdot(1-0.01)}{5.06\cdot(1+0.01\cdot 5.06-0.01)} = 48.6\% \tag{6.5}$$

The combined effective damping ratio of the equivalent linear system can be determined from:

$$\beta_{eff} = \beta_{eq} + \beta_{inh-eff} = 48.6\% + 4.4\% = 53\% \tag{6.6}$$

A linear SDOF system is then defined using the following equivalent effective parameters: T_e=0.55 s and $\xi_e = 53\%$. The peak response of the *equivalent linearized* system under the same ground motion E6C1-42 (ATK-E) results in $u_{LTH} = 8.0\,mm$. The corresponding *equivalence ratio* is determined as:

$$\frac{u_{NLTH}}{u_{LTH}} = \frac{12.0}{8.0} = 1.5 \tag{6.7}$$

An *equivalence ratio* higher than 1.0 indicates that the response obtained using the equivalent linear SDOF system underestimates the "real" displacement demand. The responses from the

NLTHA and equivalent LTHA are presented in Figure 6.6. It can be noted that for the nonlinear (NL-SDOF) and equivalent (L-SDOF) systems, the maximum response amplitudes are reached in opposite directions. The absolute response values are then compared. However, it is opportune to note that if the maximum responses for both NLTH and LTH responses occur in the same direction, the divergence in the peak response is primarily attributed to the drift of the system oscillation center that leads to the underestimation of the "real" displacement response as shown in Figure 6.6.

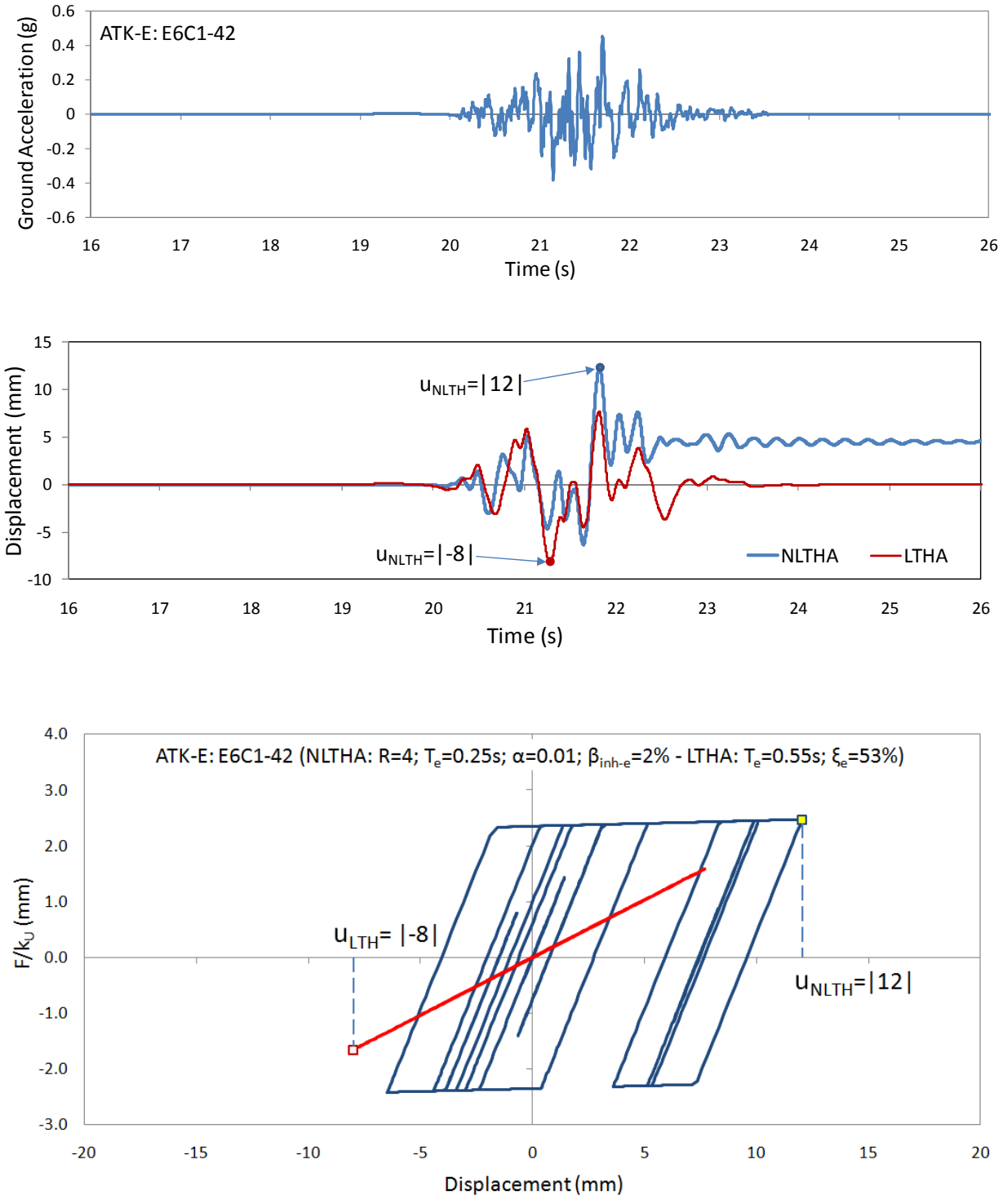

Figure 6.6 Response of SDOF system from NLTHA and equivalent LTHA

Taking into account that the *equivalence ratio* varies from record to record, in this study, this ratio was evaluated separately for each earthquake ground motion. The resulting ratios were averaged over the 20 records for the two ground-motion suites (ENA and WNA). Table 6-1

summarizes the results obtained from the process of *equivalent transformation* for five NL-SDOF systems defined with T_e=0.25 s, α=0.01 and five different R factors: R=[4, 16, 28, 40, 52].

Table 6-1 Examples of equivalent linearization (ATK-E 20 Records, T_e=0.25 s; α=0.01)

Nonlinear Bridge Structure (Bilinear SDOF System)								Equivalent Structure			
R	u_y (mm)	β_{inh-e} (%)	u_{NLTH} (mm)	$\beta_{inh-eff}$ (%)	β_{eq} (%)	β_{eff} (%)	T_{eff} (s)	ξ_e (%)	T_e (s)	u_{LTH} (mm)	$\frac{u_{NLTH}}{u_{LTH}}$
4	2.37	2.0	12.8	4.5	47.9	52.4	0.56	52.4	0.56	8.53	1.54
16	0.59	2.0	20.5	10.1	45.9	56.0	1.26	56.0	1.26	16.0	1.28
28	0.34	2.0	23.4	12.7	37.3	50.0	1.59	50.0	1.59	19.5	1.19
40	0.24	2.0	25.6	14.4	30.5	44.9	1.79	44.9	1.79	22.1	1.16
52	0.18	2.0	26.9	15.4	25.7	41.1	1.92	41.1	1.92	23.8	1.12

6.3.2 Results for Equivalence Ratio as a Function of Effective Damping

In this study, the transformation process is repeated for a total of 300 bridge structures (as defined previously in Table 5.1) subjected to the WNA and ENA 20 record sets. Figures 6.7 to 6.9 and 6.10 to 6.12 present the *equivalence ratios* as a function of the effective damping for WNA and ENA, respectively. The results are presented both for individual responses and for averaged results over 20 records. In addition, individual results were grouped according to the four earthquake scenarios defined in terms of magnitude and distance.

For each of the three stiffness ratios (α=0.1, 0.05, and 0.01), the same general trends are observed for WNA and ENA. It can be noted that the dispersion increases as the stiffness ratio α decreases. As observed in Chapter 5, these results also confirm the need for an upper limit on β_{eff}. The results indicate that these limits would be approximately β_{eff} = 31%, 39%, and 47% for α = 0.10, 0.05, and 0.01, respectively. These damping limits appear to not depend so much on the regional seismicity nor on the magnitude-distance earthquake scenarios.

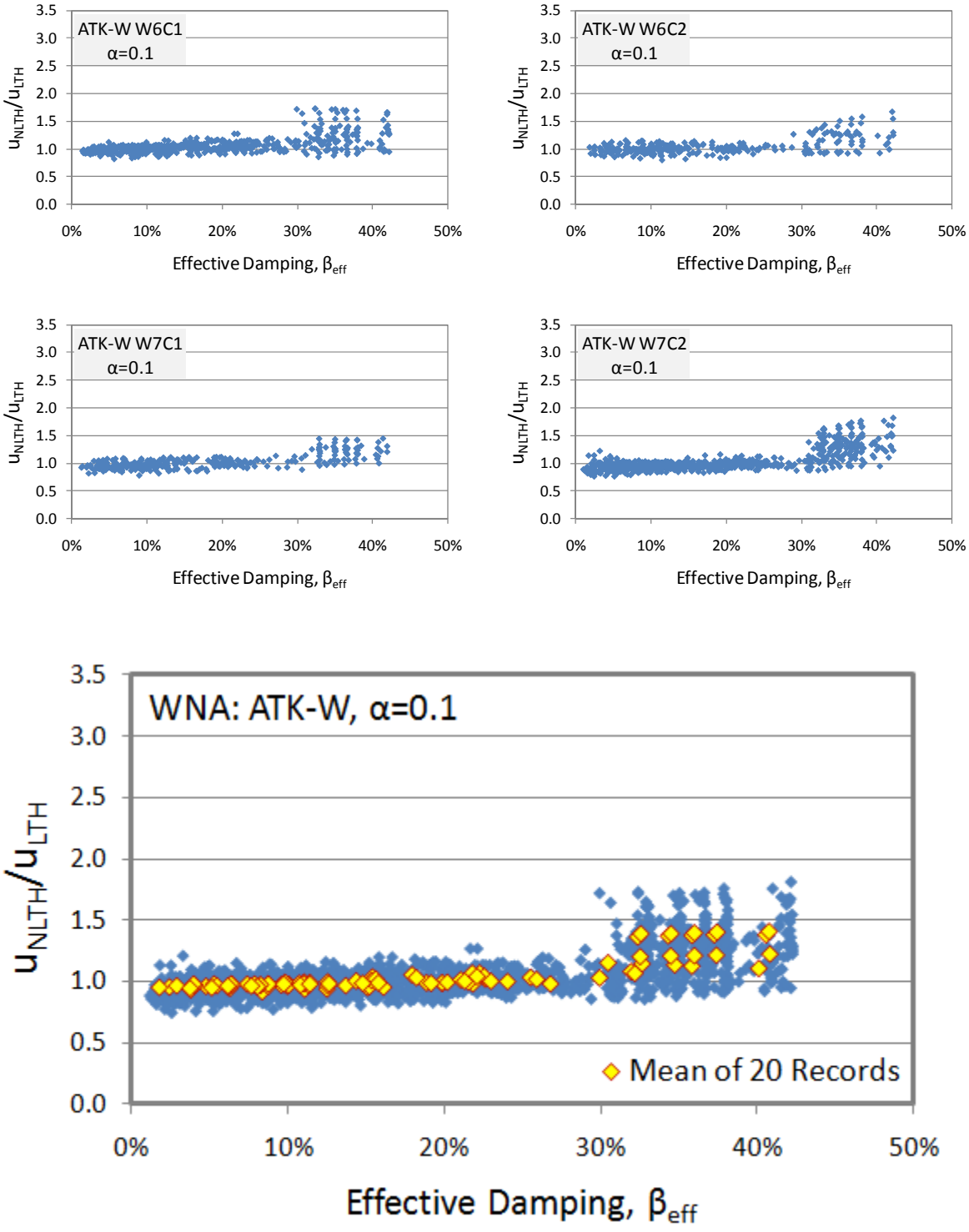

Figure 6.7 Equivalence ratio - WNA ATK-W: α=0.1

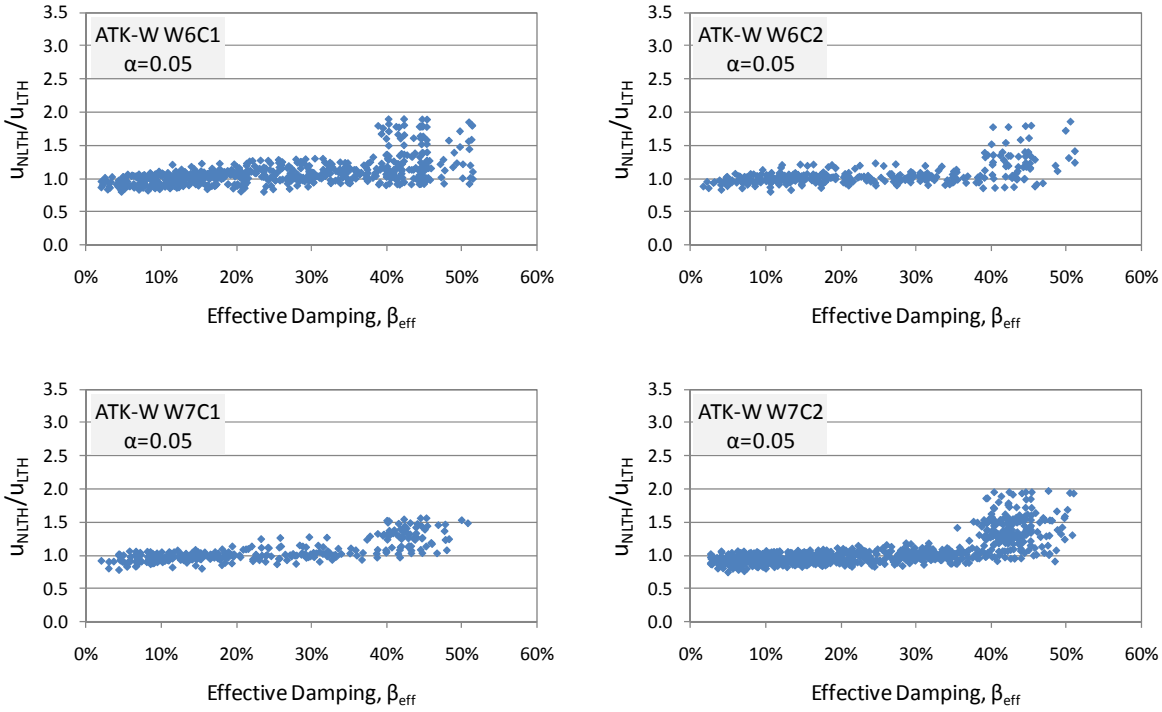

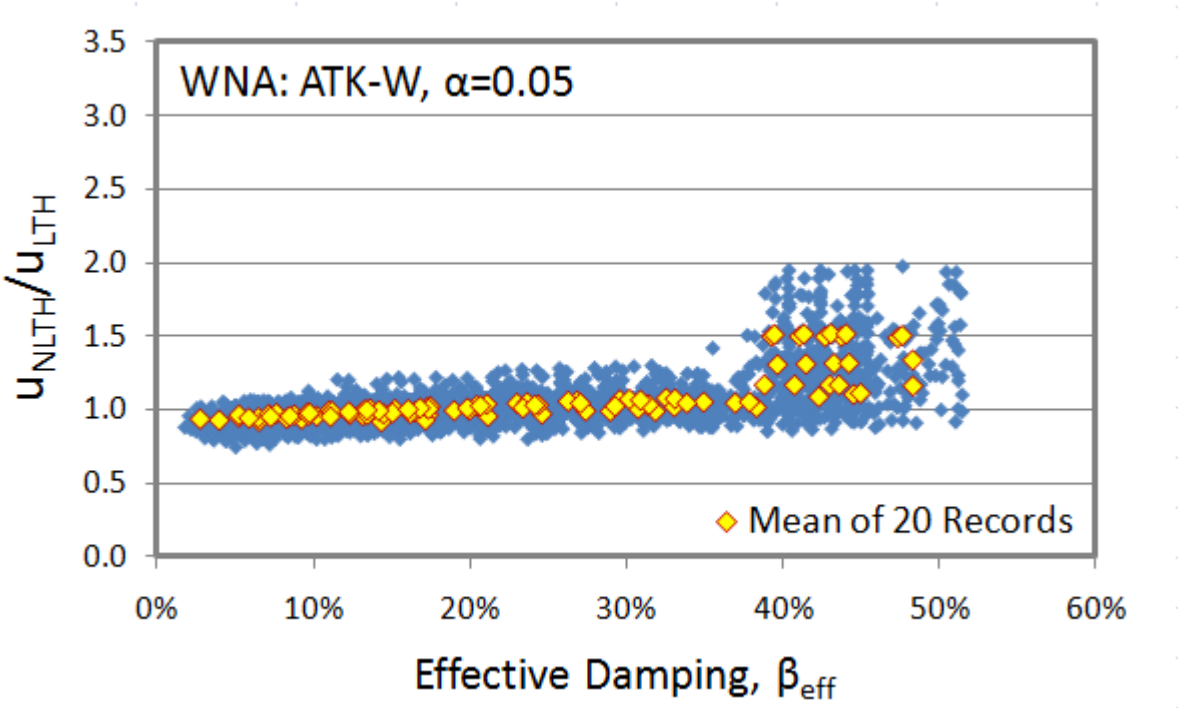

Figure 6.8 Equivalence ratio - WNA ATK-W: α=0.05

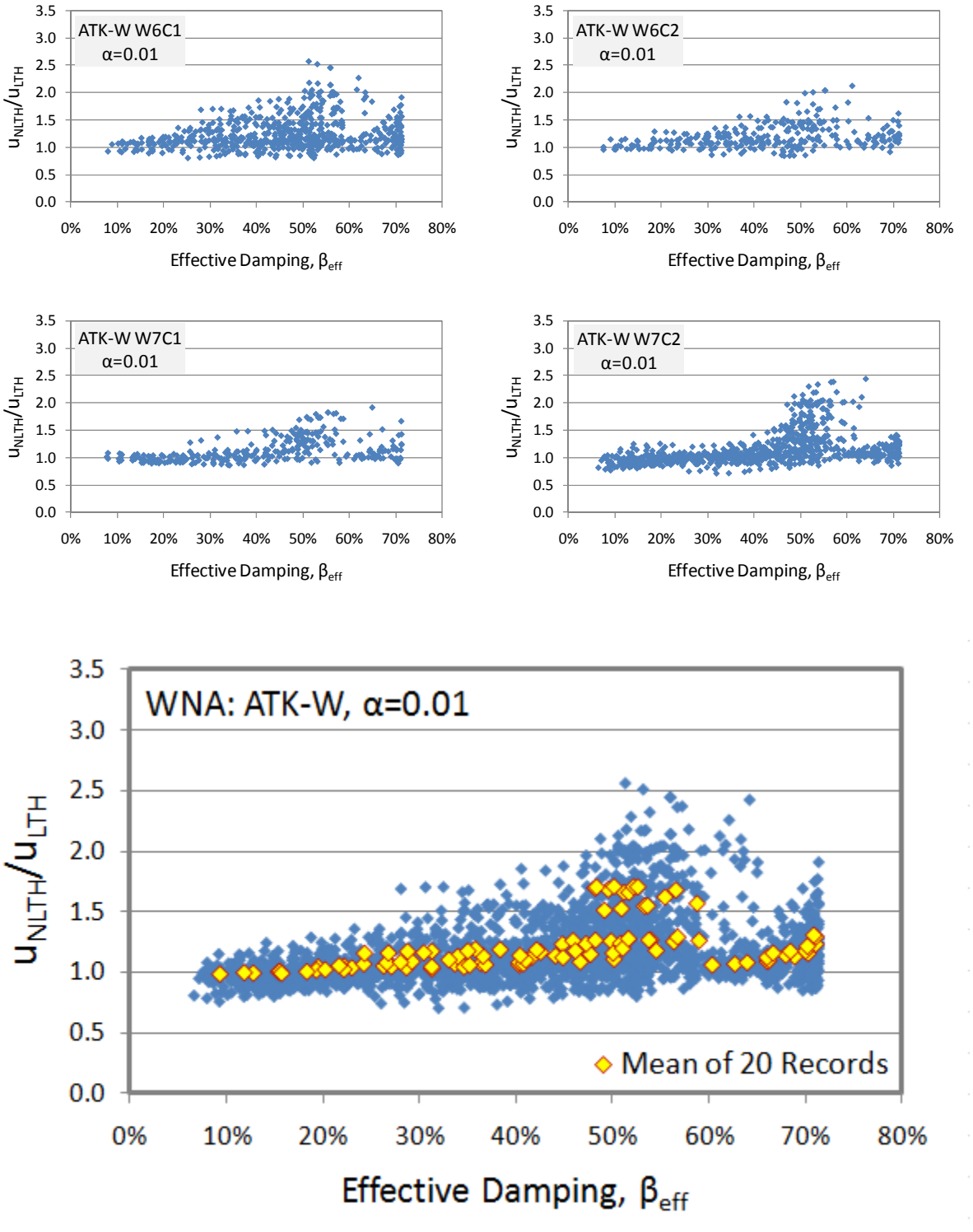

Figure 6.9 Equivalence ratio - WNA ATK-W: α=0.01

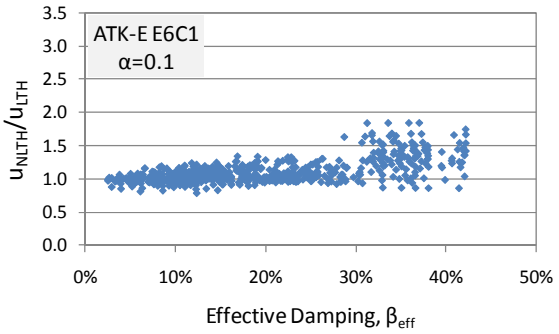

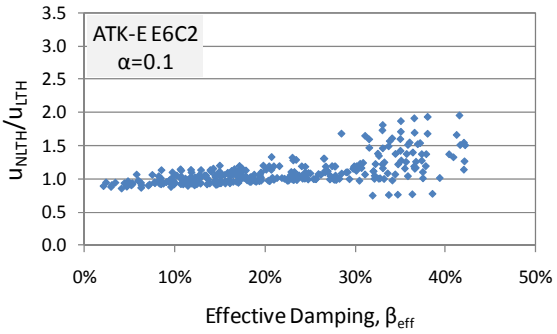

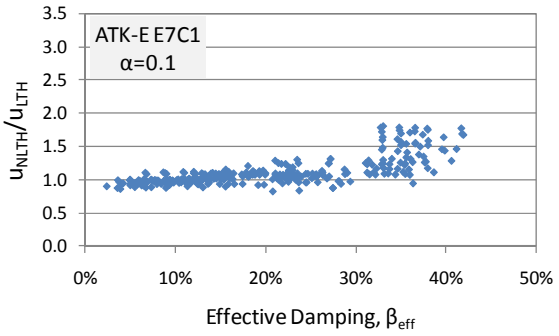

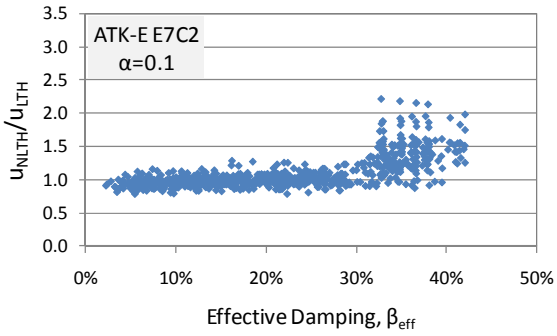

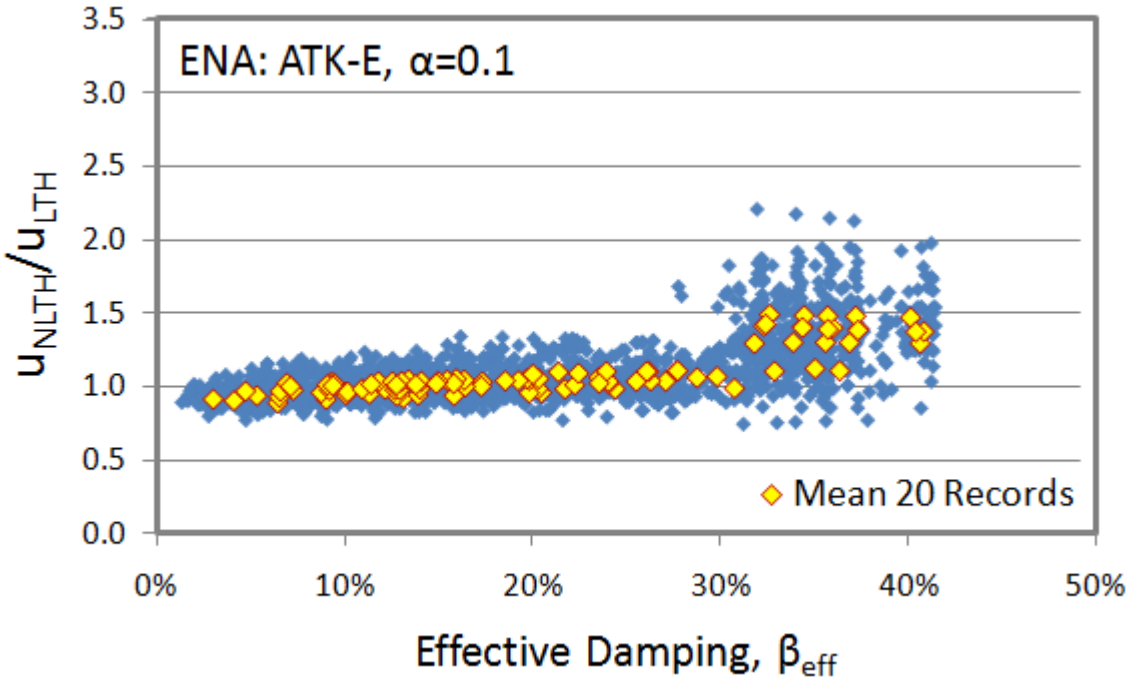

Figure 6.10 Equivalence ratio - ENA ATK-E: α=0.1

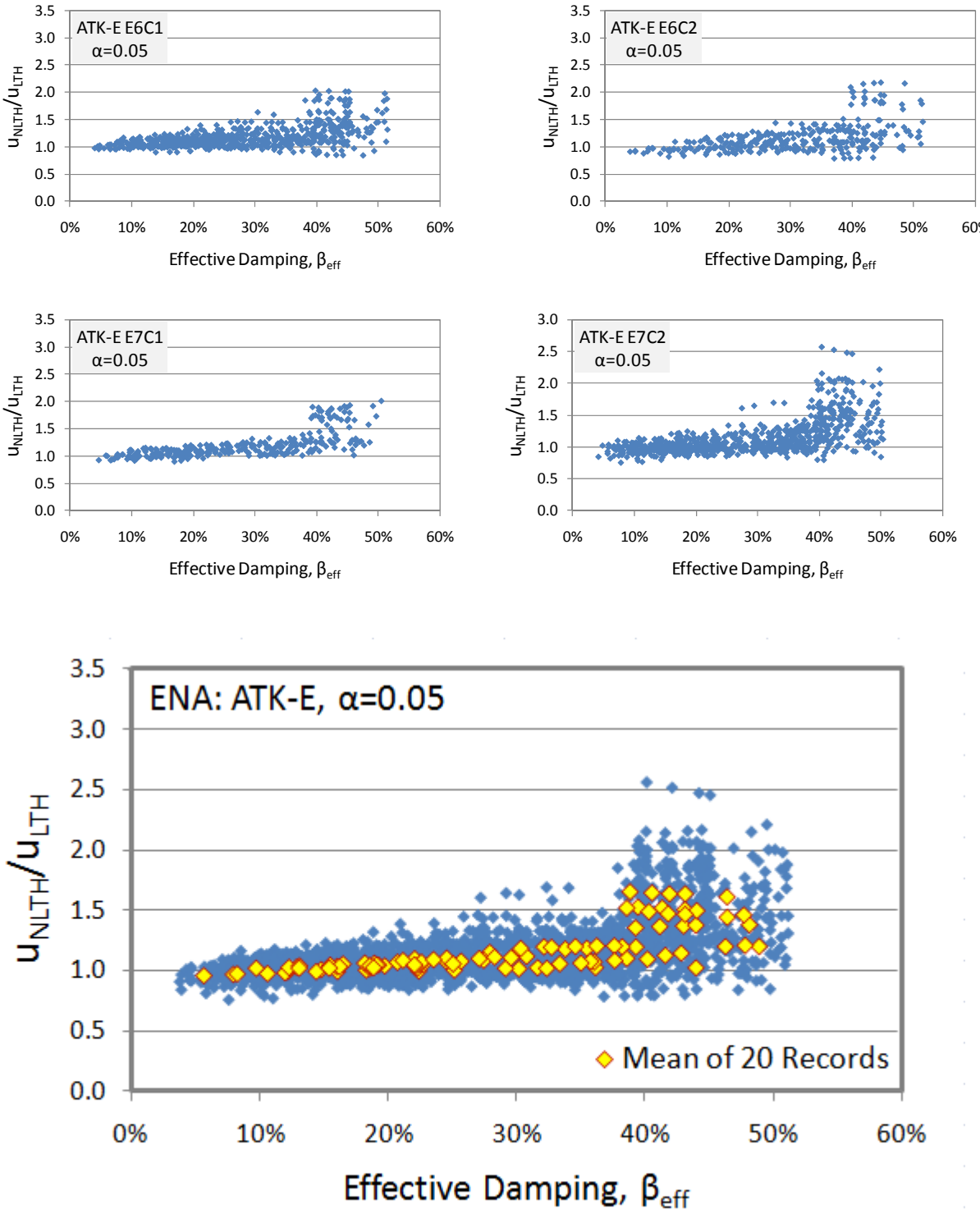

Figure 6.11 Equivalence ratio - ENA ATK-E: α=0.05

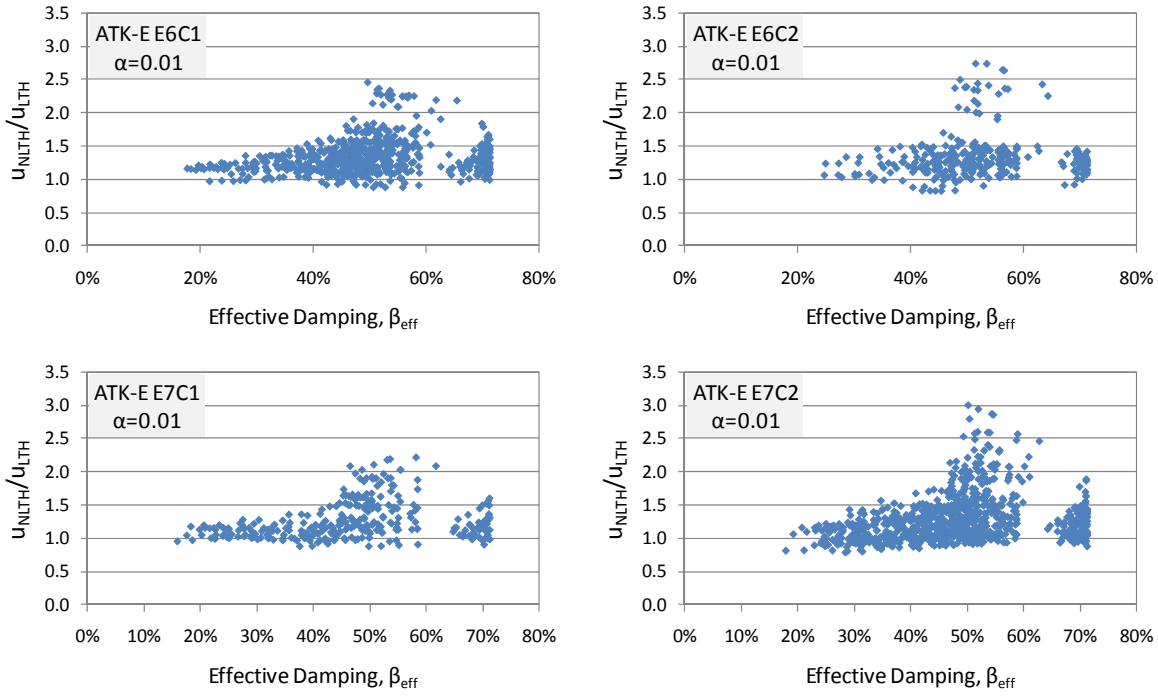

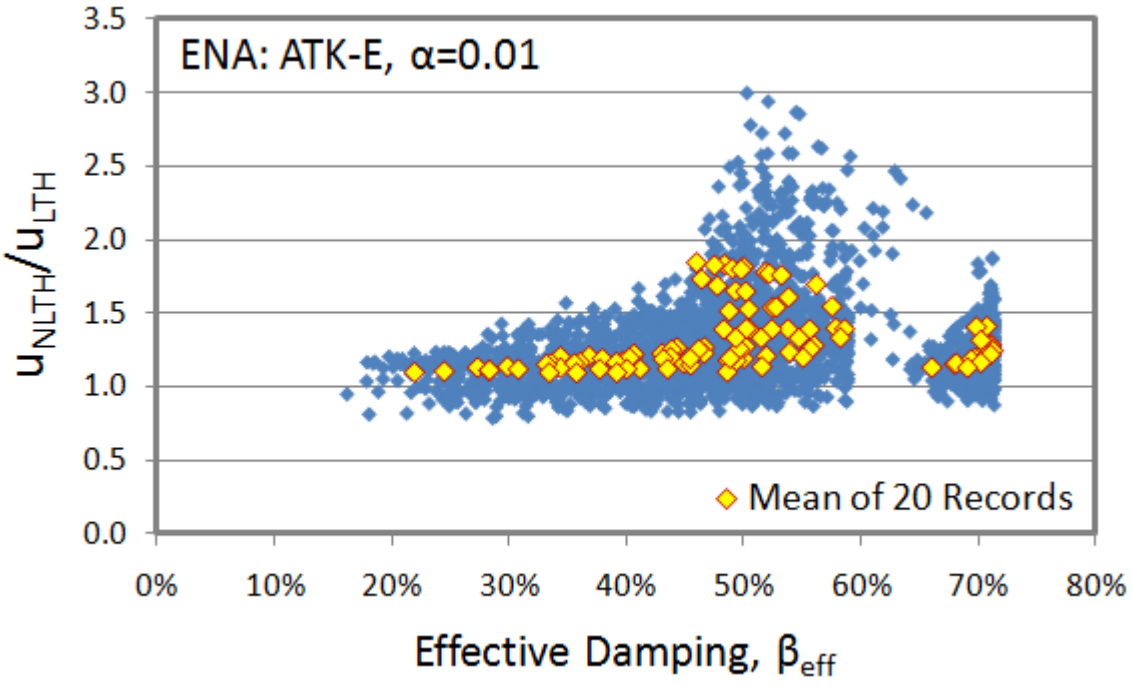

Figure 6.12 Equivalence ratio - ENA ATK-E: α=0.01

The variability in the *equivalence ratio* as a function of the effective damping is characterized in terms of the coefficients of variation (COV), and is compared in Figures 6.13 and 6.14. Each plot is obtained for one site (West *vs* East) and one value of α (0.1, 0.05, 0.01) that correspond, accordingly, to 100 different isolated bridge structures (5 (R) x 4 (T_e) x 5 (β)) analyzed under 20 time-history records.

It can be observed that responses with high effective damping ratios lead to greater coefficients of variation, indicating that less consistent results are obtained in such cases from the linear equivalent systems. As previously mentioned, these observations confirm the need for an upper limit on effective damping defined approximately as $\beta_{eff} = 31\%$, 39%, and 47% for $\alpha = 0.10$, 0.05, and 0.01, respectively.

Accordingly, by inspecting these results, it can be stated that the need for upper effective damping limits to achieve sufficient accuracy originates from limitations of the *equivalent linearization method* rather than from the damping coefficients B.

In addition, a more efficient way to ensure stability for response prediction using the *equivalent linearization method* would be to express these damping limits as a function of the post-yielding stiffness ratio α.

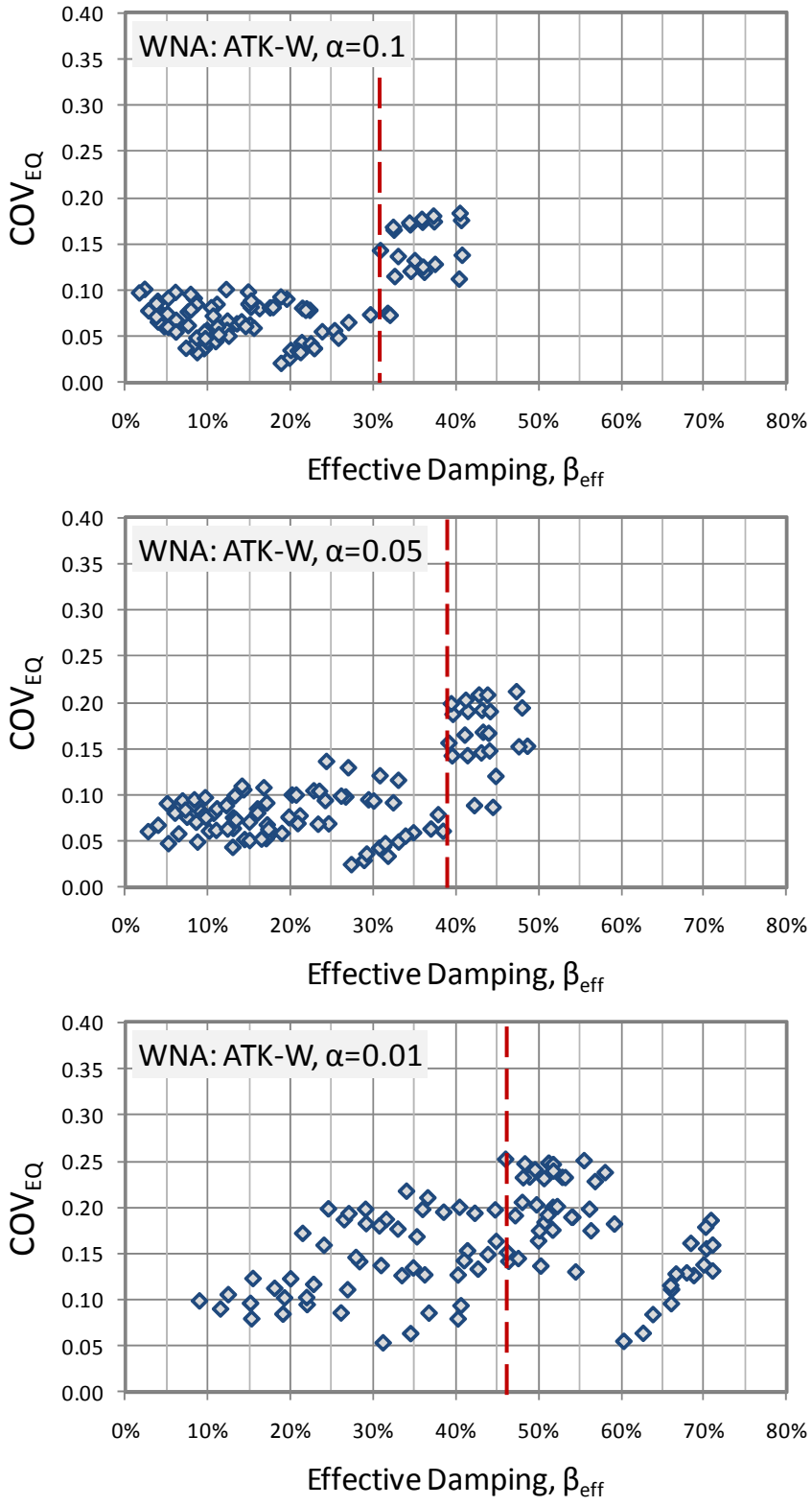

Figure 6.13 Coefficient of variation for equivalence ratio - WNA ATK-W

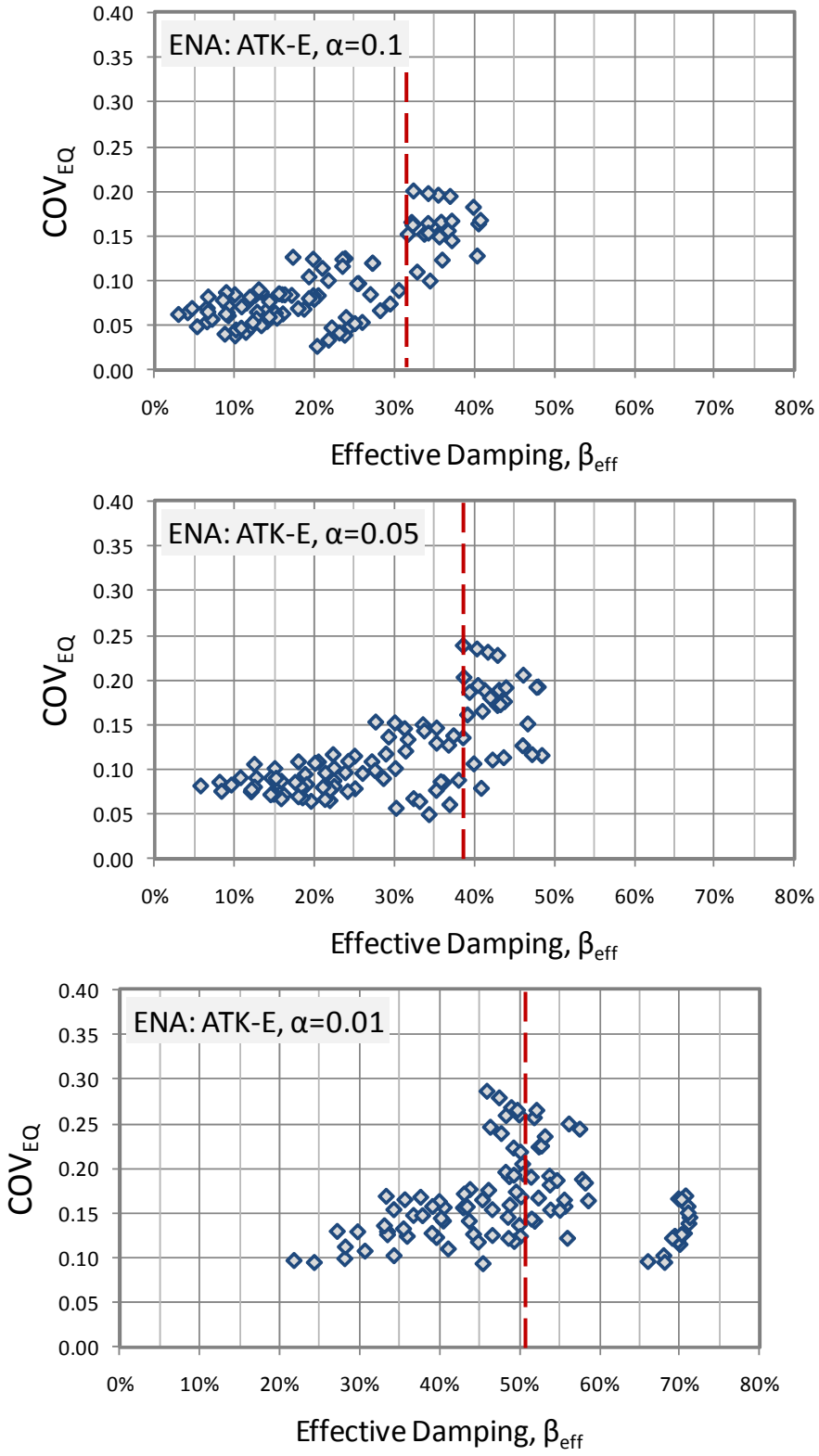

Figure 6.14 Coefficient of variation for equivalence ratio - ENA ATK-E

6.3.3 Influence of the System Parameters on Equivalence Ratio

In the previous subsection, the *equivalence ratio* was exploited to identify the range of the effective damping for which the *equivalent linearization method* can provide an accurate response estimate. In this section, the influence of the three system parameters R, T_e, and α on the *equivalence ratio* is outlined. The *equivalence ratios* averaged over 20 ground-motion records are presented in Figures 6.15 and 6.16 as a function of the response modification factor R and elastic period T_e for ENA and WNA, respectively. Results for one value of α (0.1, 0.05, 0.01) are presented in each three-dimensional bar chart, where each vertical bar corresponds to an *equivalence ratio* value averaged over five levels of inherent damping.

In all cases, the equivalence ratio increases as α decreases. When α is reduced from 0.1 to 0.01, the equivalence ratios may increase by approximately 25% for both WNA and ENA. For all three α-ratios, it was also observed that the variation of the equivalence ratio as a function of R and T_e is consistent.

As for results presented in Chapter 5, systems with low R factors, which correspond to high effective damping ratios or short effective periods, are observed to be more critical given that these systems are characterized by the greatest *equivalence ratio*. The *equivalence ratio* generally decreases when increasing R in the range from R=4 to 28 and then tends to remain constant for the larger R values of 40 and 52. This indicates that the *equivalent linearization method* results in more accurate response estimates for systems with higher R-factors. Such systems mostly experience responses oriented along the post-activation stiffness k_d resulting in larger displacements (ductility ratios) and lower effective damping ratios (see Figure 6.3).

For ENA, the *equivalence ratio* increases with T_e up to 0.75 s and then decreases for T_e = 1.0 s. In the WNA region, for the four elastic periods, the *equivalence ratio* increases with the period T_e. This can be explained by the fact that in contrast to ENA, the WNA ground motions transmit energy to the system at a wider band of frequencies covering longer periods as it was earlier shown in Figure 5.4.

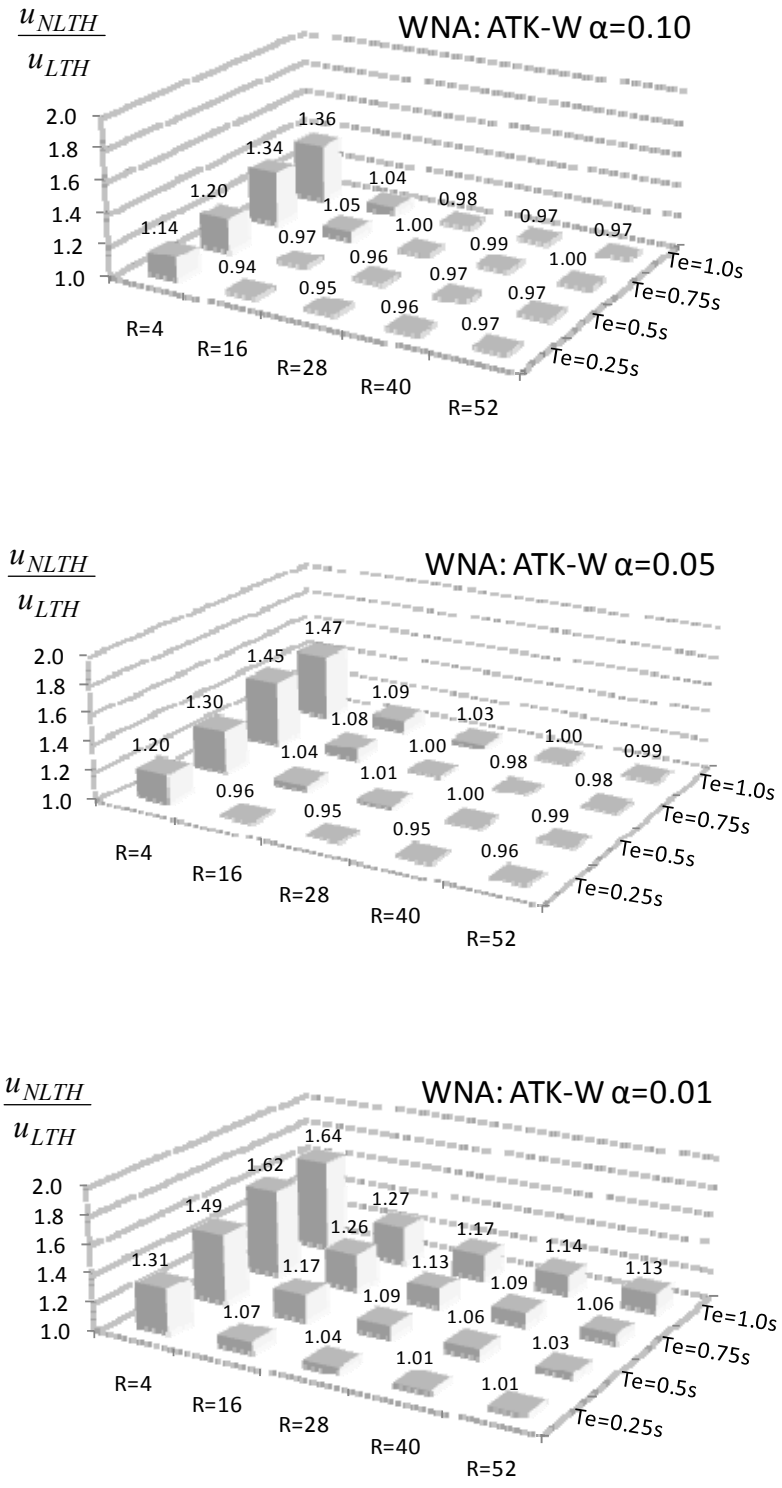

Figure 6.15 Distribution of equivalence ratio by R and T_e (WNA ATK-W)

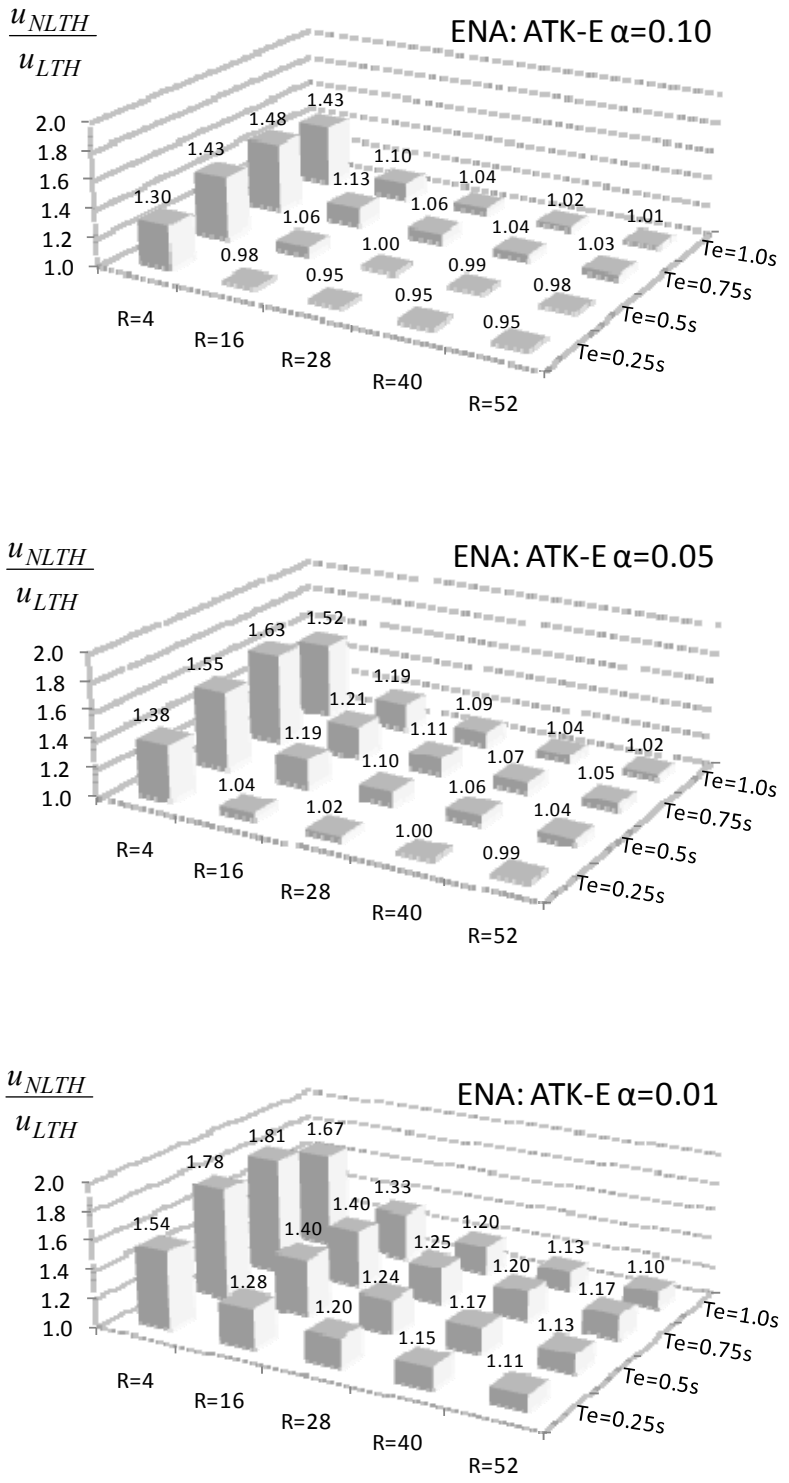

Figure 6.16 Distribution of equivalence ratio by R and T_e (ENA ATK-E)

The overall observations, emerging from the results that were obtained from this study, emphasize the strong dependency of the *equivalence ratios* on the system parameters. These results confirm that the limitation in the use of the code simplified method (CSA-S6-06 and AASHTO) is mostly due to the limited range of system parameters for which the *equivalent linearization method* provides sufficient accuracy. Accordingly, an applicability range for the *equivalent linearization method* can be established for reducing inaccuracy of the code simplified method.

6.4 Applicability Limits for Equivalent Linearization Method

The *equivalent transformation* of the actual nonlinear isolated structure into an equivalent linear system (see Figure 2.1(a)) is obtained by using only two parameters: the effective damping and effective period. Both of these parameters depend on the system response in terms of ductility ratio and they take into account the system's nonlinear parameters α and T_e. The upper limits set as a function of the effective damping β_{eff} and effective period T_{eff} will be accordingly derived in this section as they can provide a realistic insight into the applicability ranges.

6.4.1 Limits on Effective Damping, β_{eff}

As observed previously in this study, the damping limits were found not to depend on the regional seismicity and they are clearly related to the post-yielding stiffness ratio α. Examining the formulation of the *equivalent transformation* for the equivalent damping ratio β_{eq} given by Equation (6.8), the system parameter that defines β_{eq} is the ratio α, with the ductility ratio μ being obtained from the system response.

$$\beta_{eq} = \frac{2}{\pi} \cdot \frac{(\mu - 1) \cdot (1 - \alpha)}{\mu \cdot (1 + \alpha\mu - \alpha)} \tag{6.8}$$

Figure 6.17 shows how the equivalent damping ratio β_{eq} varies with the ductility ratio μ for three different α values: 0.01, 0.05, and 0.1.

From Equation (6.8), the maximum equivalent damping $\beta_{eq-\max}$ can be determined for each value of α. The value of the ductility ratio that corresponds to $\beta_{eq-\max}$ is found by setting the first derivative of Equation (6.8) equal to zero:

$$\mu(\beta_{eq-\max}) = 1 + \frac{1}{\sqrt{\alpha}} \tag{6.9}$$

Then, by substituting Equation (6.9) into Equation (6.8) the formulation for $\beta_{eq-\max}$ is expressed as follows:

$$\beta_{eq-\max} = \frac{2}{\pi} \cdot \frac{1-\alpha}{(1+\sqrt{\alpha})^2} \tag{6.10}$$

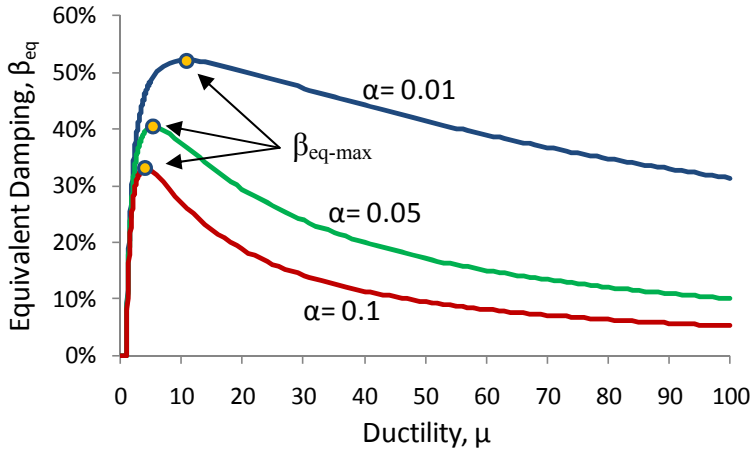

α	μ Eq.(6.9)	β_{eq-max} Eq.(6.10)
0.01	11.0	52.1%
0.05	5.47	40.4%
0.10	4.16	33.1%

Figure 6.17 Equivalent damping ratio with ductility for α =0.01, 0.05, and 0.1

There is a close agreement between the damping that was observed in the previous section by examining the *equivalence ratios* (31%, 39%, and 47%) and the corresponding $\beta_{eq-\max}$ values obtained from Equation (6.9) (33%, 40%, and 52%). The discrepancies between these values may be explained by the fact that the values of the effective damping β_{eff} were averaged over 20 ground motions and the record-to-record variability affects the damping limits observed in this study.

The damping formulations based on Equations (6.8) and (6.10) reflect a relation between the hysteresis shape and dissipated energy and offer a realistic insight into the possible influence of the ratio α on the observed coefficients of variation (see Figures 6.13 and 6.14) and, thereby, the required effective damping limits.

However, there is no obvious physical explanation on why the *equivalent linearization method* does not provide accurate response estimates when approaching and exceeding these damping limits. The drift of the oscillation center was however pointed out as a possible reason for the errors in the response estimates (see Figure 6.6).

6.4.2 Limits on Effective Period, T_{eff}

To determine limits on the effective period, the response-independent relationship between the effective damping and effective period is first established. Then, the relationship of the effective damping as a function of the effective period is derived. Similarly to the limit on the effective damping, the maximum value of the function is assumed to mark a limit for the method's applicability range. These limits are validated with results of the parametric study that was carried-out in Chapter 5.

The formulation for the effective period T_{eff} given by Equation (6.11), is defined by the system's parameters as the elastic period T_e and ratio α, the ductility ratio μ being obtained from the system response.

$$T_{eff} = T_e \cdot \sqrt{\frac{\mu}{1+\alpha\mu-\alpha}} \tag{6.11}$$

The equivalent viscous damping is formulated through the post-yielding stiffness ratio α and ductility ratio μ as:

$$\beta_{eq} = \frac{2}{\pi} \cdot \frac{(\mu-1)\cdot(1-\alpha)}{\mu\cdot(1+\alpha\mu-\alpha)} \tag{6.8}$$

As it can be noted from Equations (6.11) and (6.8), the effective period and effective damping are established as a function of the ductility demand μ. This reflects solely a relationship between the response shape and the maximum displacement response ($u_{\max} = u_y \cdot \mu$).

Solving Equation (6.11) for the ductility ratio results in:

$$\mu = \frac{\alpha - 1}{\alpha - (T_e / T_{eff})^2} \tag{6.12}$$

Then, by substituting Equation (6.12) in Equation (6.8) the formulation for β_{eq} is expressed as follows:

$$\beta_{eq} = \frac{2}{\pi} \cdot \frac{(1 - (T_e / T_{eff})^2) \cdot (\alpha - (T_e / T_{eff})^2)}{(T_e / T_{eff})^2 \cdot (\alpha - 1)} \tag{6.13}$$

The effective damping is given as:

$$\beta_{eff} = \beta_{eq} + \beta_{inh} \tag{6.14}$$

Figure 6.18 shows how the effective damping ratio β_{eff} varies with effective period T_{eff}. The function $\beta_{eff} = f(T_{eff})$ increases up to the maximum equivalent damping $\beta_{eq-\max}$ for the interval from T_e up to T_{eff} (at $\beta_{eq-\max}$). The effective period that corresponds to $\beta_{eq-\max}$ is found by setting the first derivative of Equation (6.6) equal to zero:

$$T_{eff}(\beta_{eq-\max}) = T_e \cdot \alpha^{-0.25} \tag{6.15}$$

For effective periods beyond the peak damping, the damping function decreases and the minimum value is reached when $T_{eff} = T_d = T_e / \sqrt{\alpha}$. Accordingly, a bilinear system can dissipate energy through inelastic behaviour within a range of effective periods defined between T_e and T_d and the system's maximum dissipative capacity is reached when the effective period equals $T_e \cdot \alpha^{-0.25}$ (when $\mu = 1 + 1/\sqrt{\alpha}$). As it can be seen from Figure 6.18, except for the effective periods at the damping function peak, there are two possible values of the effective period, one on the increasing function interval and the other on the decreasing function interval, that correspond to the same value of the effective damping. The system response with effective damping before and after the peak may be characterized by a different damping reduction effect. According to the results observed previously in this study, the method's accuracy is mostly unsatisfactory for those systems for which small inelastic excursions are predicted (low ductility

ratios μ, i.e. low response modification factor R). Such system response estimates correspond to the effective periods before the damping function peak defined by Equation (6.8).

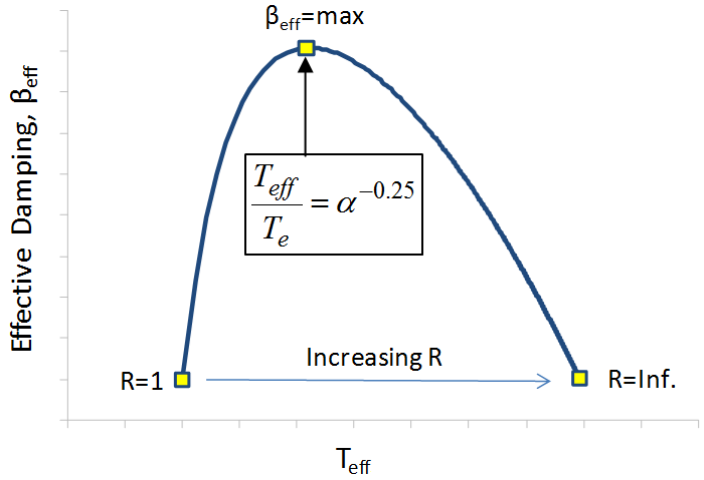

Figure 6.18 Effective damping with effective period: Equations (6.13) and (6.14)

Accordingly, to obtain the responses for damping ratios in the interval where the function increases, the limit on effective damping can be alternatively adopted as the limit of applicability of the effective damping: $T_{\lim} = T_e \cdot \alpha^{-0.25}$.

The coefficients of variation of the *equivalence ratio* as a function of the effective period are presented in Figure 6.19. The limit on the effective damping eliminates the greater coefficients of variation by limiting the use of the method to the decreasing interval of the damping function. It can then be stated that this expression for the limit on the effective period is a consistent means to ensure satisfactory robustness and stability of the *equivalent linearization method*. The limit on the effective period appears to be a more robust way to ensure accuracy given that only values with lower coefficient of variations correspond the proposed range of applicability.

The applicability range established on the effective period is validated on the seismic response prediction following the complete iterative procedure prescribed in the CSA-S6-06 simplified method using Equation (2.8) with n=0.3 for WNA and n=0.2 for ENA. The response estimate and NLTH response are compared in Figures 6.20 and 6.21 for the same 180 isolated bridge structures (5 (R) x 4 (T_e) x 3 (β) x 3 (α)) analyzed in Chapter 5. It can be then noted that the majority of the plotted dots are above the curve representing conservative response estimates while unconservative response estimates with relative errors higher than 5% are generally

occurring beyond the proposed range of applicability. It confirms the enhanced reliability of the proposed applicability limits that could then be used in future editions of CSA-S6 for WNA and ENA.

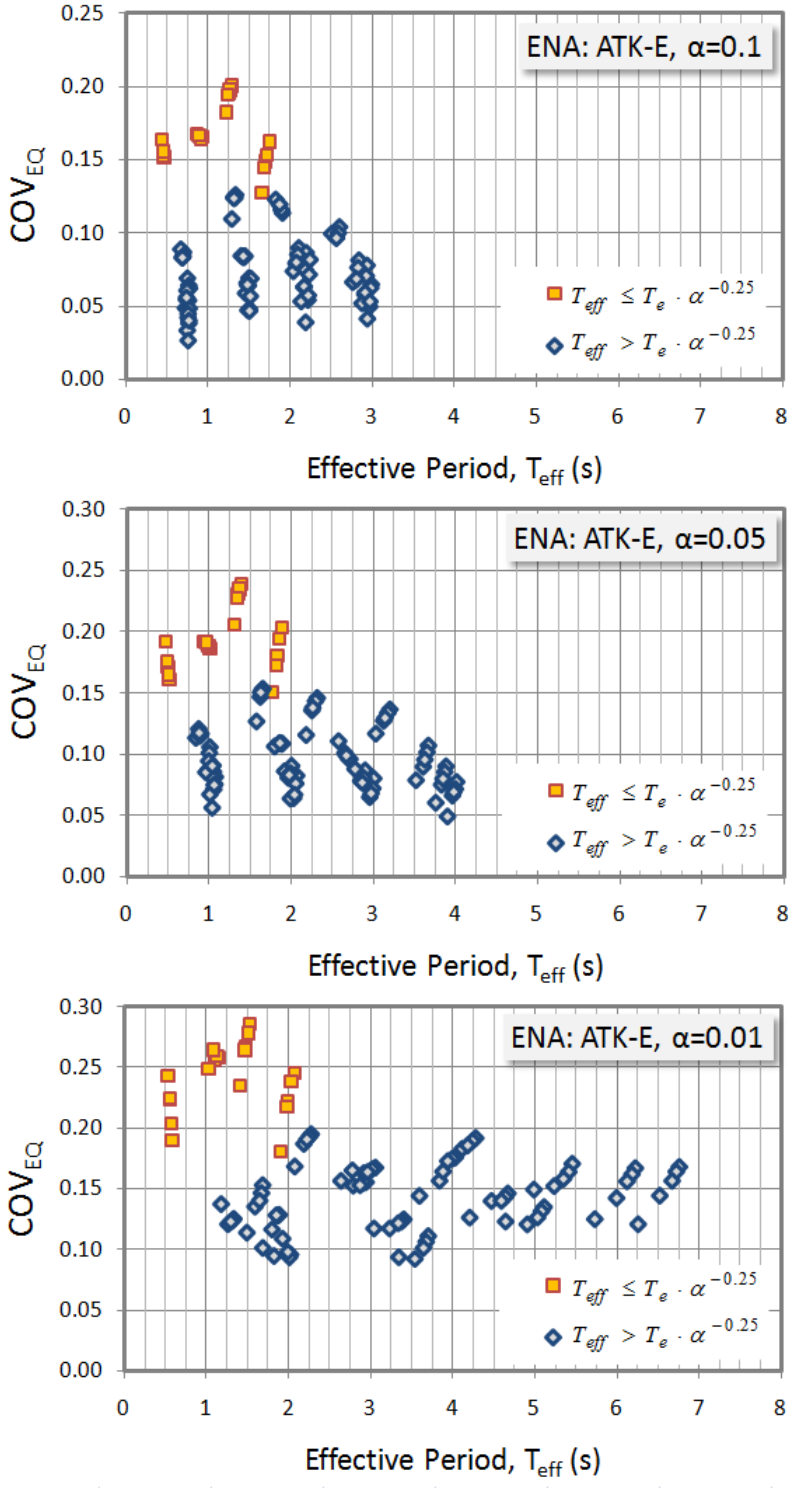

Figure 6.19 Coefficient of variation for equivalence ratio with T_{eff} - ENA ATK-W

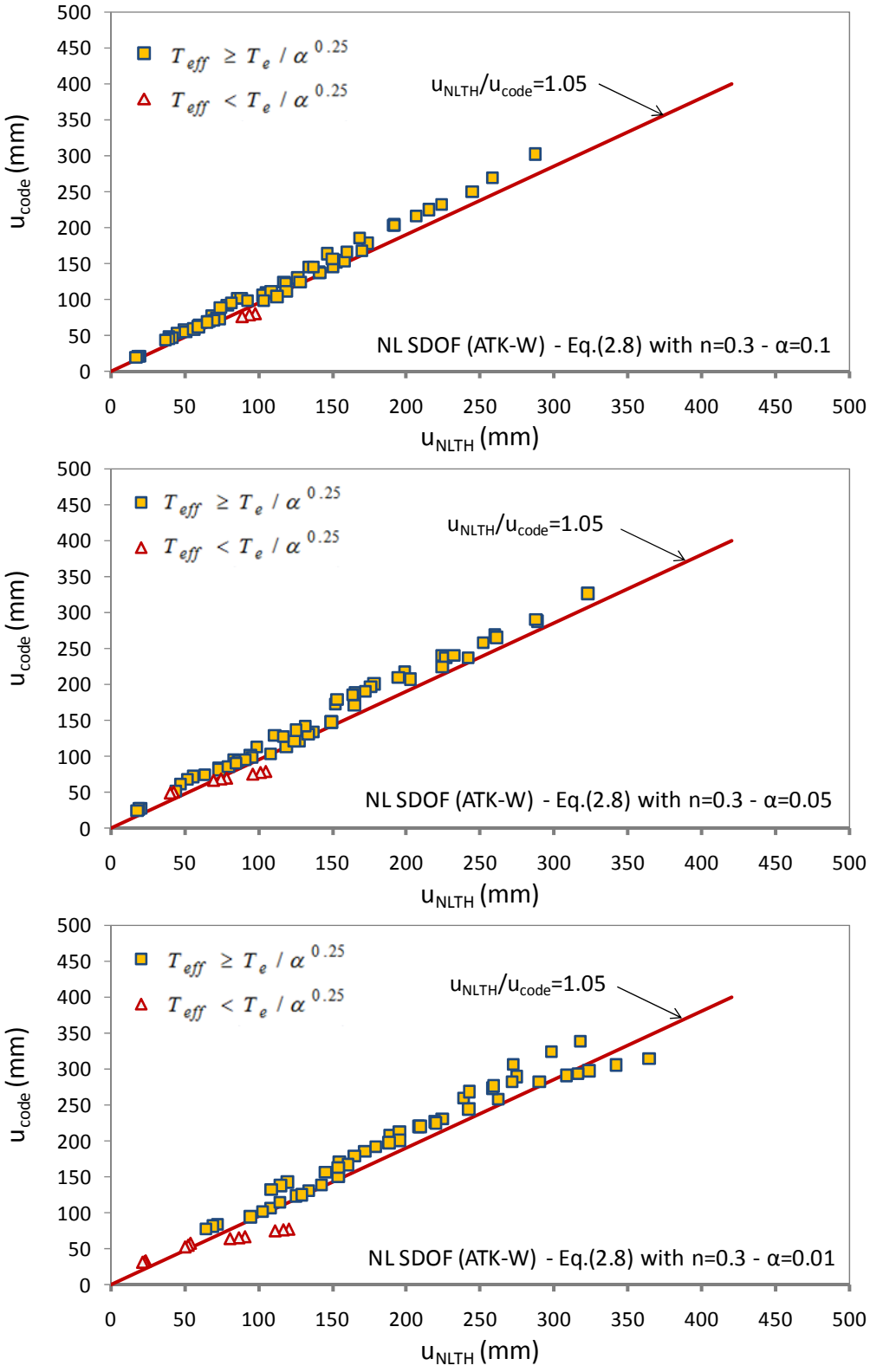

Figure 6.20 20-Records mean responses versus code estimates with proposed limits on effective period - WNA Eq.(2.8) with n=0.3

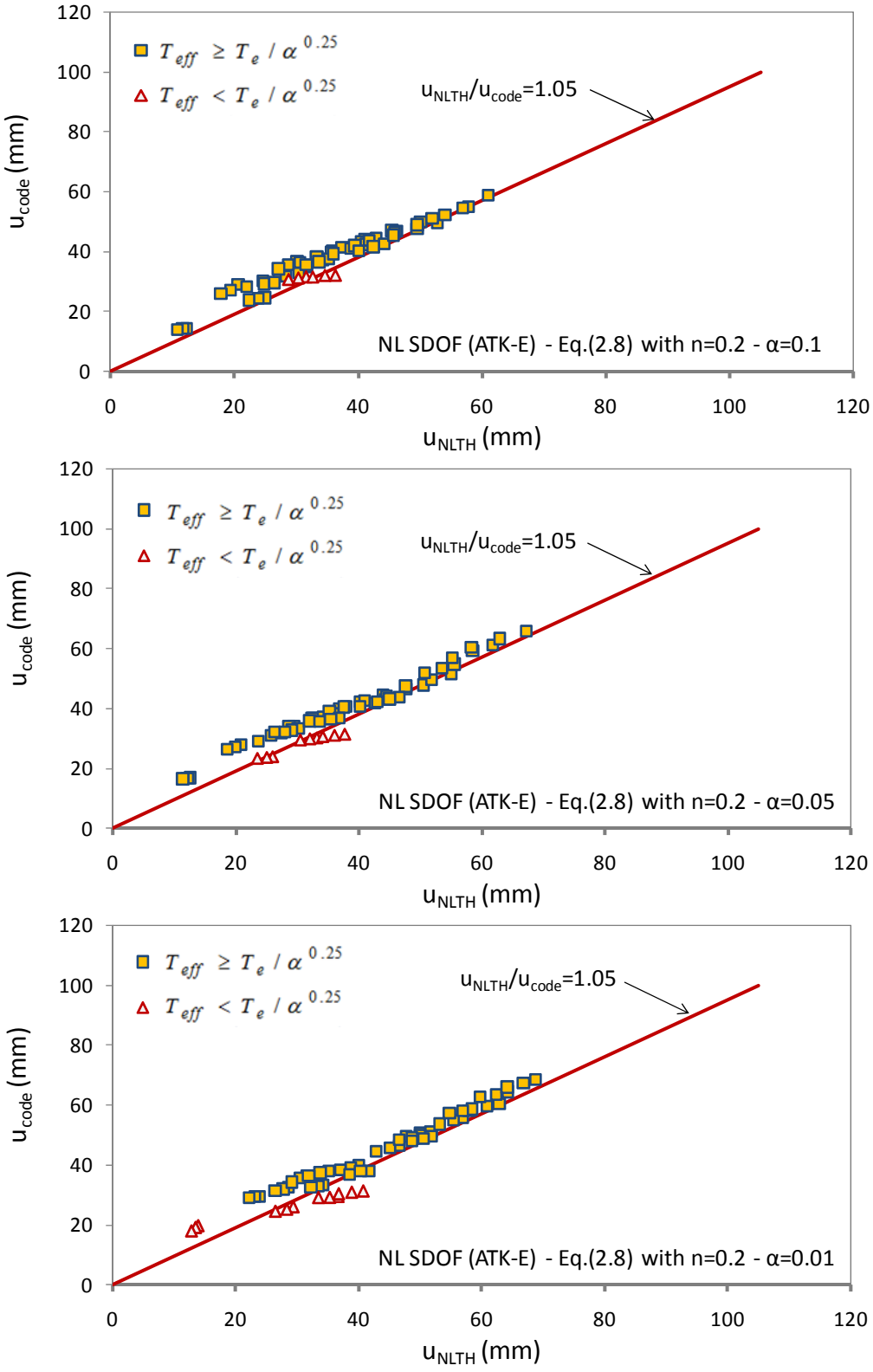

Figure 6.21 20-Records mean responses versus code estimates with proposed limits on effective period - ENA Eq.(2.8) with n=0.2

6.5 Conclusions

In this chapter, the influence of the system nonlinear parameters on the accuracy of the code simplified method (CSA-S6-06 and AASHTO) was carefully examined. It was confirmed that there is a certain range of nonlinear parameters for which the code simplified method can provide an accurate response estimate while inaccuracies are observed outside this range.

It was found that the source of the inaccuracy originates from the *equivalent linearization method* rather than from the definition of the damping coefficients B. By examining in details the process of equivalent linearization, the upper limit for the method applicability range was derived on the effective damping and effective period. In this way, the influence of the nonlinear parameters was taken into account to achieve sufficient accuracy in the seismic response prediction.

The method applicability limits, proposed in this chapter, were validated by comparing NLTH responses, obtained in Chapter 5, to the response estimates obtained during the design process following the complete iterative procedure prescribed in the CSA-S6-06 simplified method using Equation (2.8) with n=0.3 for WNA and n=0.2 for ENA. It was confirmed that the use of the proposed limits makes it possible to reject responses with unsatisfactory accuracy and these limits could then be used in future editions of CSA-S6 for both WNA and ENA.

There is no obvious physical explanation on why the *equivalent linearization method* does not provide accurate response estimates when approaching and exceeding these limits. The drift of the oscillation center was however pointed out as a possible reason for these errors. The real energy dissipated around a drifted oscillation center may be strongly overestimated by considering an equivalent response around the original center as prescribed in the CSA-S6-06 code (or AASHTO).

In addition, it was observed that the effective damping values before (increasing interval) and beyond (decreasing interval) its peak may be characterized by different reduction effects. According to this study, the method accuracy is unsatisfactory mostly for systems that correspond to the increasing interval of the damping function. Such systems experience small inelastic excursions and correspond to low response modification factors R. The response

modification factor R represents the earthquake-structure interaction and its effect cannot be captured by the code simplified method.

In light of these findings and observations, it can be stated that for prediction of the seismic response beyond the limits proposed in this chapter, a new simplified method, which takes into account the differences in ground-motion characteristics and isolated bridge design parameters, appears necessary. Several alternatives for developing the new simplified method are further examined and discussed in the following chapter.

Chapter 7: Basis for Development of New Simplified Method for Estimating the Response of Isolated Bridges

7.1 Introduction

In the previous chapter, it was confirmed that the simplified method, currently specified in the North American codes (CAN/CSA-S6-06 and AASHTO 2009, 2010), is subject to certain limitations that may significantly affect the accuracy in the response estimate for certain ranges of structural properties. The drift of the oscillation center was pointed out as a possible reason for the errors in the response estimates. The real energy dissipated around a drifted oscillation center may be strongly overestimated by considering an equivalent response around the original center as prescribed in the CSA-S6-06 code (or AASHTO). In addition, the current code simplified method (as discussed in Chapter 5 and Chapter 6) does not take into account the complex relation between the structure's properties and the different ground-motion characteristics. As observed in the previous chapters, the parameters as the period ratio T_e / T_g, where T_e is the structure's initial period and T_g is the ground-motion's predominant period, and the response modification factor R make it possible to characterize the effect of the structure-earthquake interaction.

In light of these findings and observations, a new simplified method that takes into account the differences in ground-motion characteristics and isolated bridge design parameters is necessary. This chapter aims at examining the potentiality for developing a new method for predicting isolated bridge response more accurately. The basis for the new method concept and the key elements that may affect the method's accuracy are identified.

In order to establish a basis for the development of this new method, two widely adopted methods in earthquake engineering, the Equal Displacement Approximation (EDA) and the Equal Energy Approximation (EEA) are first briefly reviewed. Then response estimates obtained using these approaches are compared to the nonlinear "real" responses of the bridge isolation systems from a limited series of NLTHA presented in Chapter 5. The accuracy is characterized

in terms of the relative error in order to determine the limitations that are inherent to the EDA and EEA. The energy concept used in the EEA is then considered for further development. In such a way, different system's properties and ground-motion characteristics can then be taken into account for seismic response prediction.

To gain a better understanding of the physical phenomena involved in the response of isolated bridges and how the response is related to the structure's properties and the different ground-motion characteristics, a comprehensive study on the response of SDOF systems under harmonic excitation was carried out in this study.

The harmonic steady-state response of SDOF systems exhibiting bilinear hysteretic rule has been studied in detail by many researchers, as a result, various dynamic aspects of structural response have already been reported (Caughey 1960, Iwan 1961, Masri 1974, Abé 1996). However, the steady-state response of a SDOF system is not necessarily representative of the response of isolated bridges under seismic excitation for all ranges of structural parameters and ground motion characteristics. The nonlinear response to earthquake is not a steady state. In particular, peak displacement response of nonlinear systems is typically observed during short time intervals, ranging from half of a cycle to a maximum of 2 or 3 cycles, each having different amplitudes. In view of that, this chapter will focus on the transient response to sinusoidal excitations, not the steady-state response.

For this reason, to better characterize seismic response in the present study, special attention is drawn to the effect of the transient phase of loading that occurs at the beginning of the excitation. Based on the principle of conservation of energy, the energy flow is examined within the system's motion in the transient phase of the response before reaching peak displacement. This investigation shows that kinetic energy is a possible key element that must be considered in the new simplified method.

Then, a more detailed insight on the energy flow is gained by studying the effect of the response modification factor R and the frequency ratio on the energy allocation. Through this study, it is found that the transition state between *limited-nonlinear* and *highly-nonlinear* responses defines the limit beyond which the kinetic energy has a dominant effect on the response of NL-SDOF systems.

7.2 Equal Displacement and Equal Energy Approximations for Estimating Response of Isolated Bridges

In this section, we examine the appropriateness and limitations of the Equal Displacement Approximation (EDA) and the Equal Energy Approximation (EEA) in assessing the inelastic response of *highly-nonlinear* systems representative of isolated bridge structures responding to strong seismic excitations. Both methods are briefly reviewed first. Then, the method EEA is formulated for application to bilinear SDOF systems having a post-yielding stiffness ratio α higher than zero ($\alpha > 0$).

The results obtained from a limited series of NLTHA in Chapter 5 are compared to those obtained by using EDA and EEA methods. Differences in displacement responses between the NLTHA results and the EEA approximations are then discussed with respect to the concept of kinetic energy deficit.

7.2.1 Background of Inelastic Response Approximation Concepts

EDA and EEA form the basis of the seismic provisions of many design codes worldwide. These empirical approaches have been proposed by Veletsos and Newmark (1960) based on the observations of the inelastic responses of SDOF systems subjected to the 1940 El Centro and 1933 Vernon earthquake records that both occurred in California. The inelastic responses were computed using a numerical integration method for elastic perfectly-plastic systems ($\alpha = 0$) with three levels of ductility: μ = 1.25, 2 and 4. The results were then compared to those of elastic systems (μ = 1) having the same elastic stiffness (same initial period T_e). For relatively small levels of damping, less than 5%, the EDA appeared to be reasonably accurate. For larger levels of damping, an alternative approach was proposed in which the energy absorbed by the inelastic system under monotonic loading is set equal to the energy absorbed by a corresponding elastic system under the earthquake excitation. The elastic system is defined by the elastic stiffness of the inelastic system. The energy absorbed by the inelastic system is equal to the area under the force-displacement curve at maximum displacement. A similar approach was formulated earlier by Housner (1956) who suggested to design inelastic structures so that they can absorb the entire kinetic energy corresponding to an elastic system subjected to the design earthquake. As in EEA, the elastic system is defined by the pre-yielding stiffness of the inelastic system. In fact,

Housner's method relied on an alternative interpretation of the EEA concept. However, Housner noted that such a method will overestimate the absorbed energy if the inelastic excursion has a major effect on the effective stiffness of the structure, i.e., for systems sustaining large ductility demand. Therefore, there is a concern that a similar overestimation might observed when applying EEA to *highly-nonlinear* systems such as isolated bridges, which are intended to experience significant reductions of their effective stiffness during the seismic response. According to Housner, for this approximation, the maximum energy input is equal to the kinetic energy obtained using the damped spectral velocity $S_V(\xi_e, T_e)$ defined at the system's elastic period T_e:

$$E_{in} = \frac{1}{2} m \, S_V{}^2 \tag{7.1}$$

Using the pseudo relationship for a steady-state response, $S_V = S_D \cdot 2\pi / T_e$, the input energy can then be defined in terms of the maximum elastic displacement u_e ($S_D(\xi_e, T_e)$) as follows:

$$E_{in} = \frac{1}{2} m \left(S_D 2\pi / T_e\right)^2 = \frac{1}{2} k_e S_D{}^2 = \frac{1}{2} k_e u_e{}^2 \tag{7.2}$$

If the structure's response exceeds the elastic limit ($T_{eff} > T_e$), the spectral velocity S_V within the period range between T_e and T_{eff} must remain the same in order for the input energy level to be maintained. This is not always the case in nonlinear response and a lower input energy generally characterizes the inelastic response, which results in conservative displacement estimates. In common practice, the energy-equating technique applied for assessing the inelastic displacement is referred to as the EEA. Both of these approaches were proposed for design and can be formulated by means of the response modification factors R defined as:

$$R = \mu \qquad \text{for EDA} \tag{7.3}$$

$$R = \sqrt{2\mu - 1} \quad \text{for EEA} \tag{7.4}$$

Figure 7.1 presents both the EDA and EEA for the elastic perfectly-plastic system (α=0) as initially described by Veletsos and Newmark (1960).

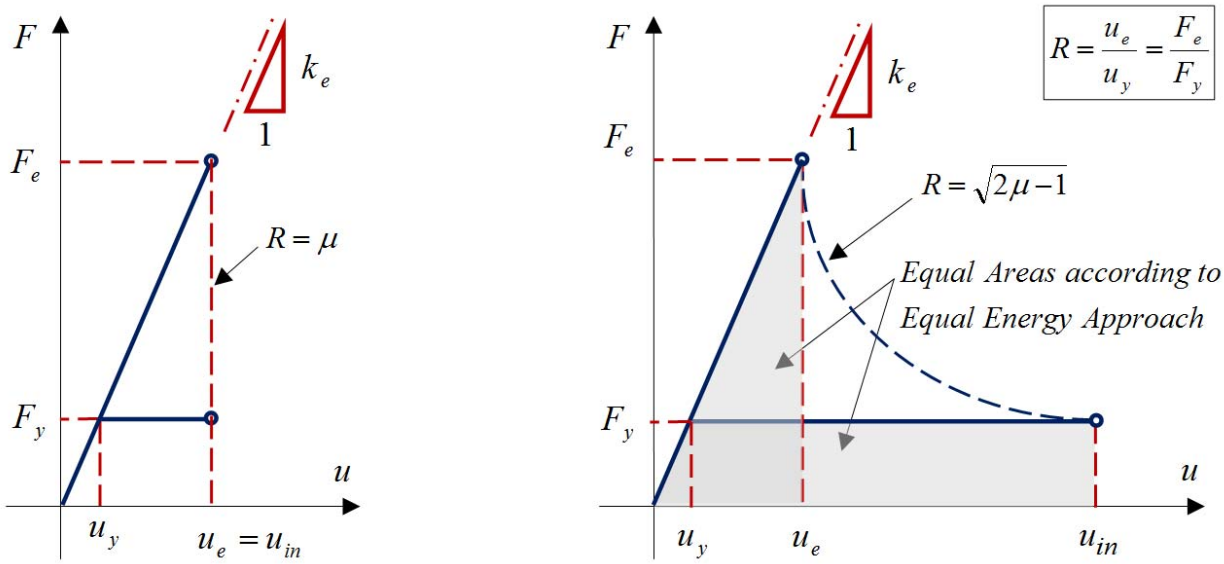

Figure 7.1 EDA and EEA concepts for elastic perfectly-plastic systems: $\alpha = 0$

Using the seismic demand from the 1940 El Centro earthquake, Newmark and Hall (1982) analyzed elasto-plastic SDOF systems with ductility levels up to $\mu = 10$. Their results were presented on the form of tripartite logarithmic plots for acceleration, velocity and displacement responses. Based on the observations, Newmark and Hall divided the frequency scale in three ranges as low, intermediate and high frequencies. They stated that for low frequencies, below about 2 Hz ($T = 0.5$ s), nearly the same maximum displacement is exhibited for all studied ductility ratios ($\mu = 1$ to 10). Meanwhile, for high frequencies greater than about 20 Hz ($T = 0.05$ s), practically the same maximum force is observed. For intermediate frequencies, elastic and inelastic systems display approximately the same amount of energy presented by the area enclosed by the force-displacement hysteretic curve. Those observations had important design implications by suggesting applicability limits for the proposed design methods. Those limits can be summarized as:

1) For very short periods (below about 0.05 s) – use the equal force approximation;

2) For short periods (0.05 s - 0.5 s) – use the equal energy approximation (EEA);

3) Long periods (greater than 0.5 s) – use the equal displacement approximation (EDA).

Typical bridge structures do not fall in the very short period range and in general correspond to longer period ranges as further used in this study (0.25 to 1.0 s).

In light of these observations, Newmark and Hall proposed to incorporate their findings directly in the design process by means of inelastic response spectra as shown in Figure 7.2. The elastic and inelastic response spectra have been presented by the regions of constant displacement, constant velocity and constant acceleration denoted respectively as *D*, *V* and *A*. Accordingly, the elastic response spectra built for the selected level of damping and seismic hazard ($DVAA_0$) is transformed to the inelastic response by using a corresponding aforementioned reduction factor *R* being a function of ductility.

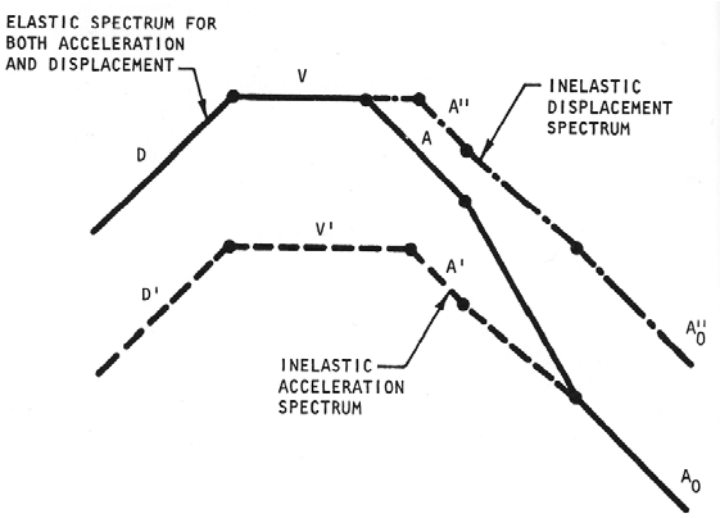

Figure 7.2 Inelastic design spectra for earthquakes (Newmark and Hall, 1960)

In turn, in the same work, in order to construct an elastic response spectrum for different damping levels a series of empirical spectrum amplification factors have been proposed for each of the *D*, *V* and *A* regions of the spectrum. It has to be recognized that these findings have led to the incorporation, by different design codes, of the static equivalent force method which takes into considerations levels of damping greater than 5%. For example, this method is included in the current Canadian Highway Bridge Design Code (CAN/CSA-S6) for a simplified design approach.

7.2.2 EEA Approach for Bilinear Systems with α > 0

As discussed in Chapter 5, the present research is dedicated to the seismic response of seismically isolated bridges, where a certain level of restoring force is required to reduce the system's inelastic excursion and resulting residual displacements. The restoring capabilities of such isolation systems are commonly presented by the non-zero post-yielding stiffness in terms of stiffness ratio α. For bilinear systems with a post-yielding stiffness ratio greater than zero ($\alpha > 0$), the R-μ relationship aforementioned for the equal energy approximation (elastic perfectly-plastic system: $\alpha = 0$) is no longer valid and has to be re-evaluated by equating areas of the corresponding response shapes as shown in Figure 7.3. The energy absorbed by an elastic system (E_{AbL}) and that absorbed by a corresponding nonlinear system (E_{AbNL}) are assumed to be equal and are defined through the area under the force-displacement curve obtained for the first half cycle of the response.

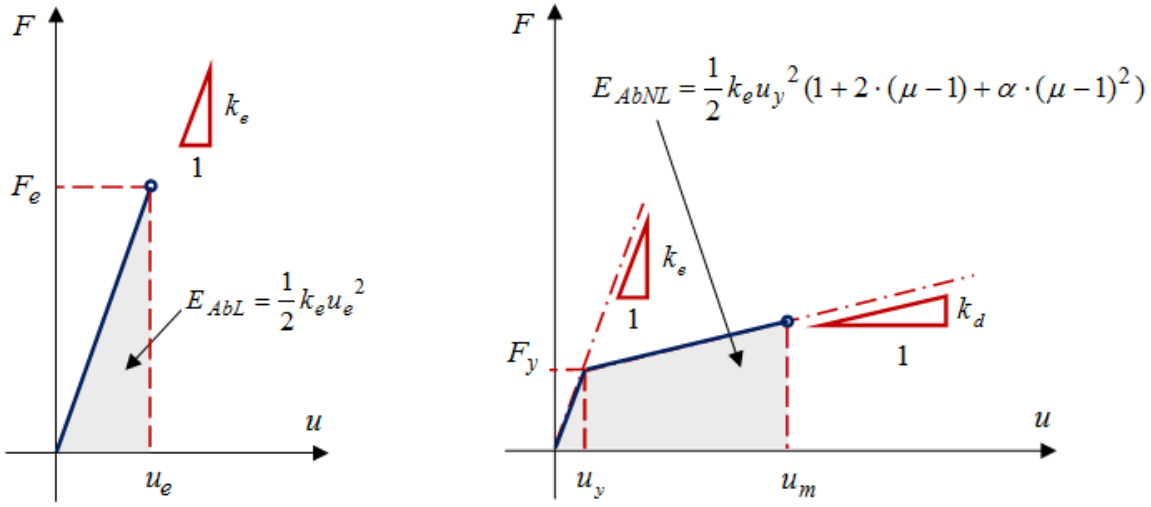

Figure 7.3 Concept of Equal Energy - Energies absorbed by linear and nonlinear systems: : α>0

The energy absorbed by an elastic system is determined as:

$$E_{AbL} = \frac{1}{2} k_e u_e^{\,2} = \frac{1}{2} k_e u_y^{\,2} R^2 \tag{7.5}$$

The energy absorbed by a corresponding bilinear system (the same elastic stiffness k_e) is expressed as follows:

$$E_{AbNL} = \frac{1}{2}k_e u_y{}^2 + k_e u_y{}^2(\mu - 1) + \frac{1}{2}\alpha k_e u_y{}^2(\mu - 1)^2$$
$$= \frac{1}{2}k_e u_y{}^2(1 + 2\cdot(\mu - 1) + \alpha\cdot(\mu - 1)^2) \quad (7.6)$$

Solving both equations for the response modification factor, R results in:

$$R = \sqrt{\alpha\mu^2 + (2\mu - 1)\cdot(1 - \alpha)} \quad (7.7)$$

Consequently the ductility ratio μ can be written as a function of R and α for α>0 as:

$$\mu = 1 - \frac{1}{\alpha} + \sqrt{\frac{1}{\alpha^2} + \frac{R^2 - 1}{\alpha}} \quad (7.8)$$

Equations (7.7) and (7.8) present formulations of the EEA for bilinear SDOF systems with α>0. These expressions are based on the same assumption as the one made by Housner (1956), which states that the input energy remains unchanged for elastic and inelastic systems. It should be clear, however, that this simplified approximation will overestimate the energy absorbed by inelastic systems. In addition, it should be mentioned that the EEA formulation is based on the a steady-state response assumption where the maximum relative velocity, corresponding to the peak kinetic energy, occurs at the zero displacement position. Accordingly, the effect of the oscillation center drift (see Chapter 6) is not accounted for in this approach.

7.2.3 EDA and EEA versus Seismic Response of Nonlinear Systems Responding to Seismic Motions

To better understand the limitations of the EDA and EEA methods in assessing the response of *highly-nonlinear* systems, a limited series of NLTHA presented in Chapter 5 is used here for this comparative study. The nonlinear SDOF systems were subjected to the 20 seismic excitations presented in Chapter 4 (Atkinson's, 2009). The bilinear system configurations are defined by varying the initial fundamental period T_e and response modification factor R, while the post-yielding stiffness ratio $\alpha = 0.05$ remains constant. Four natural periods $T_e = 0.25$, 0.5, 0.75, and

1.0 s were considered for this comparison. The R values are chosen to cover a complete range of nonlinear systems between $R = 1$ (elastic with T_e) and $R = \infty$ (elastic with T_d). The response of a bilinear system with $R = \infty$ corresponds well to the response of an elastic system with its stiffness defined as $k_d = \alpha\, k_e$ (or fundamental period $T_d = T_e / \sqrt{\alpha}$) and damping level of $\xi = 5\%$. The intermediate R-ratios, are then R = [2, 4, 8, 16, 28, 40 and 52].

Figure 7.4 presents the "exact" responses obtained from NLTHA for different R-factors and those obtained through EDA and EEA. Taking into account that EEA overestimates the response of *highly-nonlinear* systems, emphasis is put on the energy deficit observed between the "exact" dynamic response and the corresponding response from EEA (illustrated in the figure for R=4). The difference in absorbed energy (hatched area - Figure 7.4) between these two responses can be attributed to the contribution of the kinetic energy which is ignored when assuming that the input energy is entirely absorbed through monotonic loading. From the perspective of the EEA and for the further developments that are presented in this chapter, this portion of the energy that is ignored by the EEA is termed as an *energy deficit*.

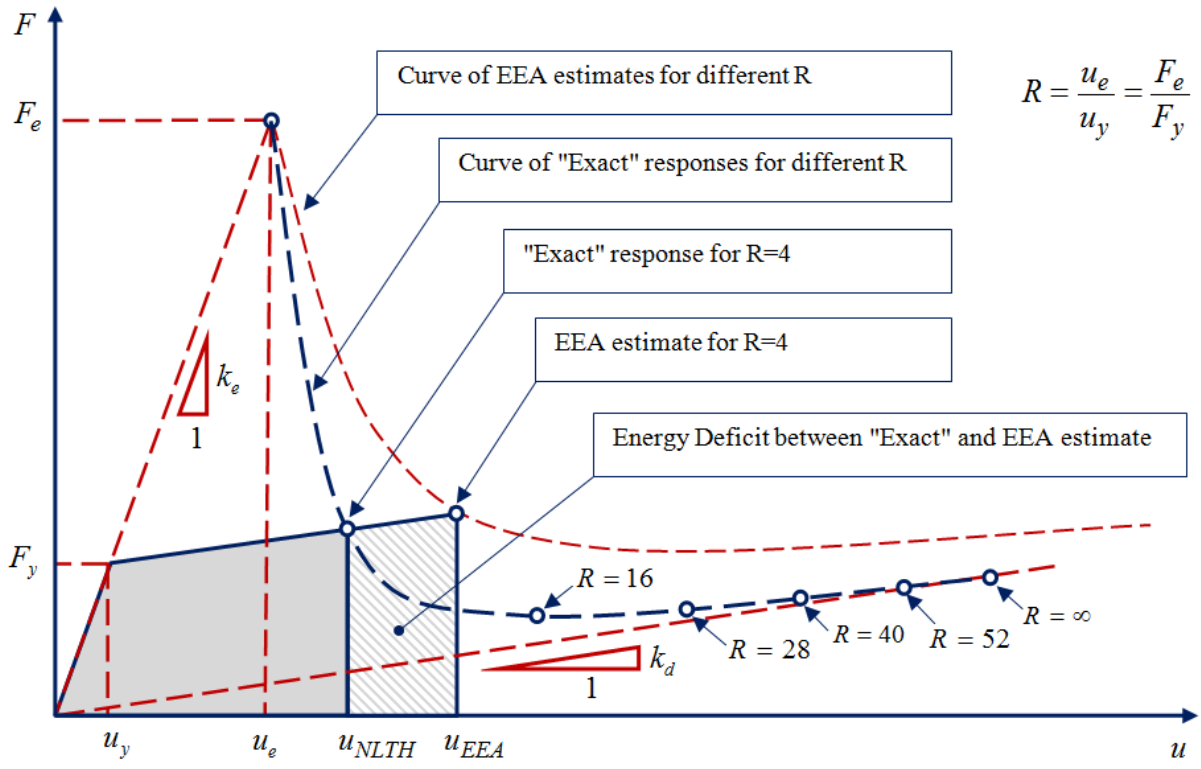

Figure 7.4 Energy deficit between "exact" response and EEA estimate

Figure 7.5 and Figure 7.6 compare the "exact" responses computed for different *R*-ratios to those obtained through EDA and EEA for each of the four elastic periods T_e = 0.25, 0.50, 0.75 and 1.00 s. The comparison is presented on the S_A-PS_D spectrum to show how the ratio *R* influences the systems' responses with respect to the 5% damped elastic response spectra. The responses of the systems characterized by $R = 1$ and $R = \infty$ are given by the intersection between the 5% damped S_A-PS_D spectrum and the lines initiated from the intercept having a system elastic and post-yielding slope. In the graph, the system slopes are presented in terms of the squared frequency of vibration ${\omega_e}^2$ and ${\omega_d}^2$ for the elastic and the post-yielding slopes, respectively. In all cases, the NLTHA "exact" response is situated under the 5% damped spectrum, indicating an equivalent damping level greater than 5%.

For systems with elastic periods of $T_e = 0.25$ s and 0.5 s, the EDA underestimates the peak response of the systems for all values of *R*. When the EDA is applied for the two other systems with longer elastic period ($T_e = 0.75$ s and 1.0 s), the maximum displacements can be approximated with a reasonable degree of accuracy for *R* factors smaller than about $R = 8$. Beyond $R = 16$, the accelerations and, thereby, the forces are nearly the same for systems with $T_e = 0.5$, 0.75 and 1.0 s. For the shorter elastic period (0.25 s), the lowest force level is obtained for $R = 16$ and a slight increase in the force is observed for higher *R*-ratios.

In these figures, the curves representing EEA predictions overestimate the "exact" responses for all four elastic periods studied. However, the EEA values appear to be much closer to the "exact" responses for the shorter elastic period of 0.25 s than for longer periods. This suggests that for elastic periods shorter than 0.25 s, the "exact" response can be reliably approximated using the EEA approach. Given that structures having shorter elastic periods ($T_e < 0.25$ s) represent a small percentage of isolated bridges, this case is of little practical relevance and is therefore not covered later by this study.

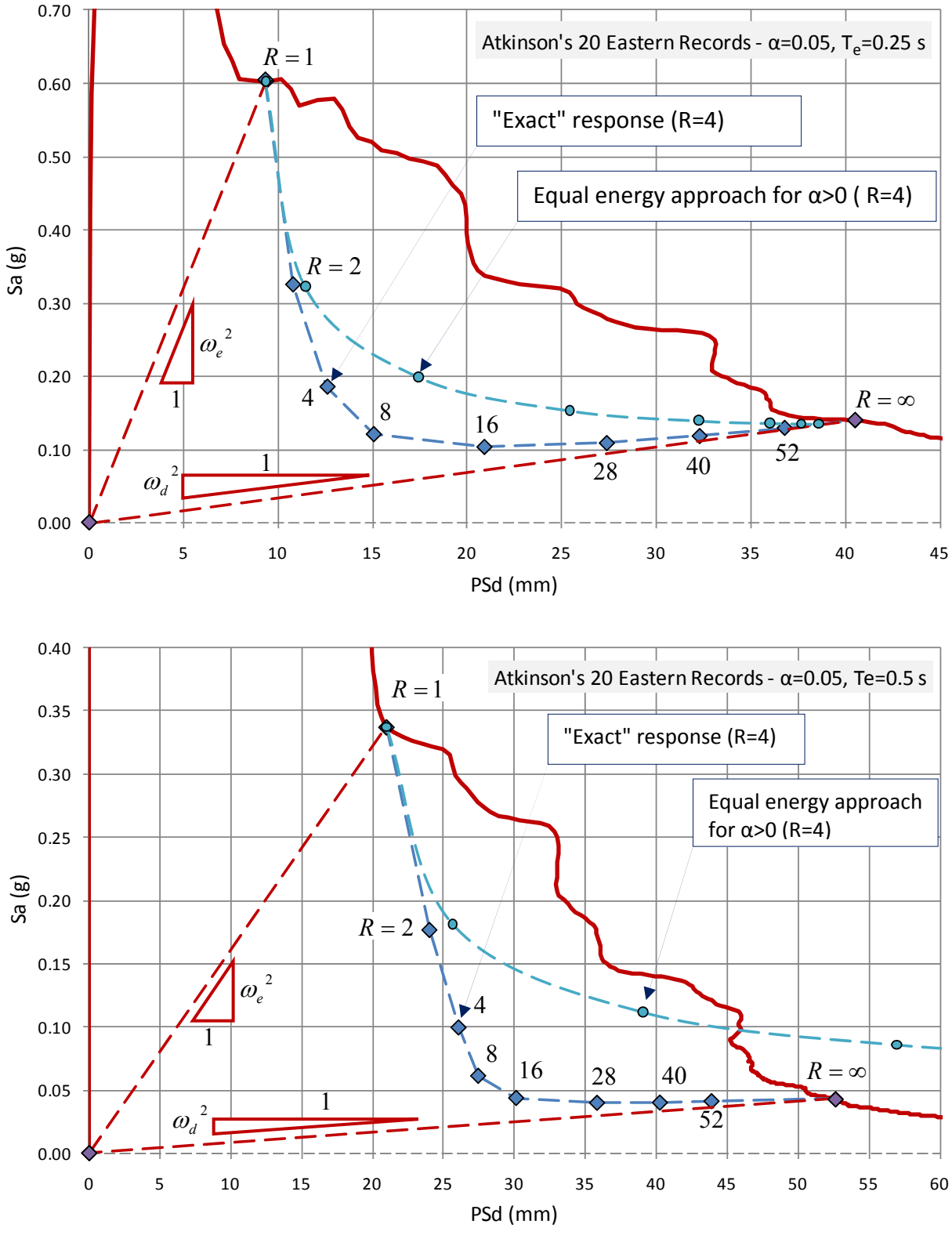

Figure 7.5 "Exact" responses and the 5% damped Sa-PSd spectrum (α=0.05, T_e=0.25 s and 0.5 s)

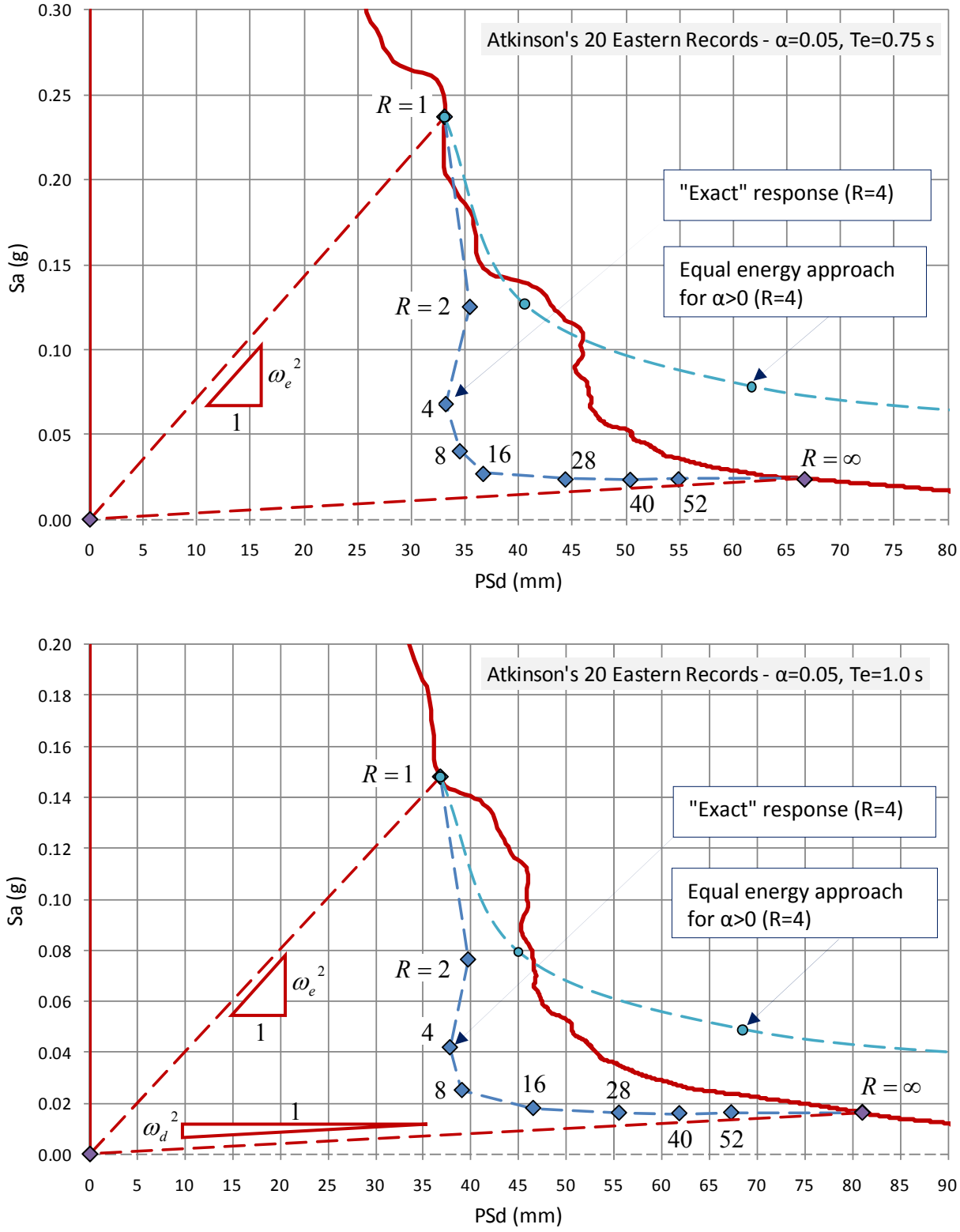

Figure 7.6 "Exact" responses and the 5% damped Sa-PSd spectrum (α=0.05, T_e=0.75 s and 1.0 s)

Figures 7.7 and 7.8 summarize the discrepancies between the "exact" responses and those estimated through EDA and EEA, respectively. The accuracy is evaluated in terms of the relative errors:

$$Error = \frac{u_{NLTH} - u_{EDA}}{u_{NLTH}} \quad \text{and} \quad Error = \frac{u_{NLTH} - u_{EEA}}{u_{NLTH}} \tag{7.9}$$

Positive and negative relative errors correspond respectively to underestimated and overestimated response estimates. For the four examples studied, the EDA (Figure 7.7) consistently underestimates the "exact" responses. A reasonably accurate estimate (*Error* < 10%) is observed for the two systems with longer elastic periods (0.75 and 1.0 s) and for $R \leq 8$, which is in agreement with the observations by Veletsos and Newmark (1960) for ductility levels up to $\mu = 4$ and Newmark and Hall (1982) for ductility up to $\mu = 10$, where $R = \mu$.

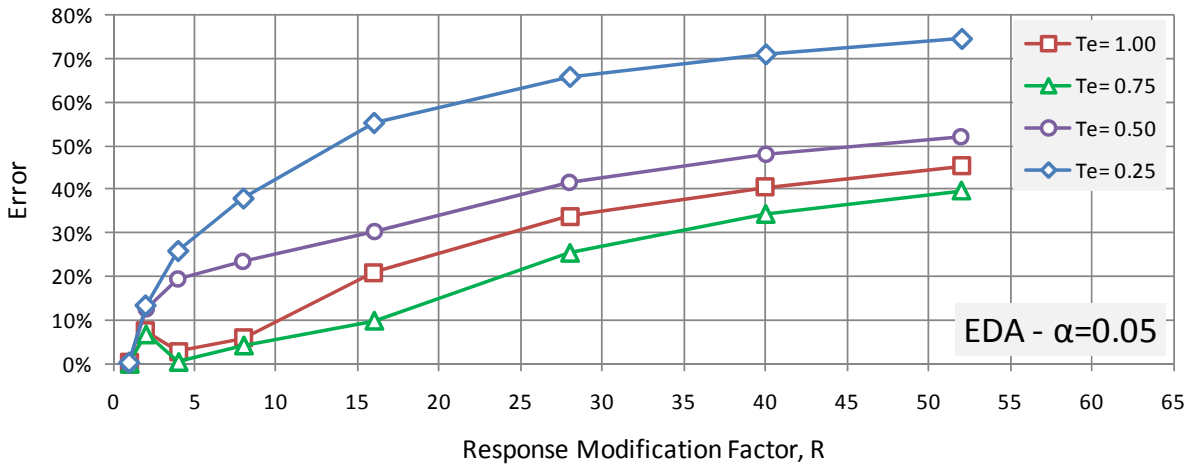

Figure 7.7 Influence of the *R*-factor and period on the error between "exact" response and Equal Displacement Approximation ($\alpha = 0.05$, mean of 20 Atkinson's artificial records - ENA)

Contrary to EDA, the EEA technique (Figure 7.8) overestimates the "exact" responses for all studied cases. As a result, for the four cases studied herein, the "exact" responses are bounded by the EDA and EEA response approximating techniques. Another tendency that can be observed in Figure 7.8 is that the smallest errors for the EEA are obtained for the shortest period of 0.25 s, while the greatest errors are observed for the period of 0.75 s, not for the longest period of 1.0 s. This confirms the dependency of the EEA estimate error on the elastic period, as was the case for the code simplified method observed in Chapter 6 (Figure 6.15).

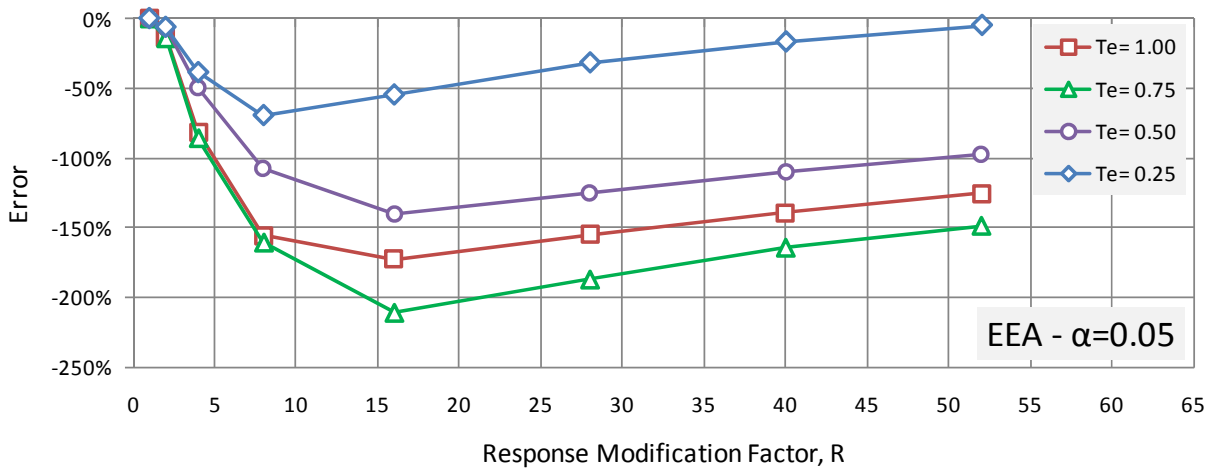

Figure 7.8 Influence of the *R*-factor and period on the error between "exact" response and Equal Energy Approximation (α = 0.05, mean of 20 Atkinson's artificial records - ENA)

To explain the differences observed in response estimates between the EEA and "exact" NLTHA results, the relation between the relative error and the *energy deficit* is presented in Figure 7.9.The *energy deficit* is defined as the difference in the absorbed energy (hatched area - Figure 7.4) between the "exact" dynamic response, E_{NLTHA}, and the absorbed energy assumed in the EEA, E_{EEA}. These energy quantities are determined using Equation (7.6). For the EEA, the error in response estimate generally increases with the energy deficit. By examining Equation (7.6), the *energy deficit* depends on system's parameters such as the post-yield stiffness ratio α, the initial period T_e (in terms of k_e), and the response modification factor R (in terms of u_y).

Given that the "exact" response is overestimated by the EEA, the concept of *energy deficit* due to the kinetic energy contribution to the system's response is kept herein for further developing the concept of energy balance. The concept of energy deficit is proposed and investigated in the following sections.

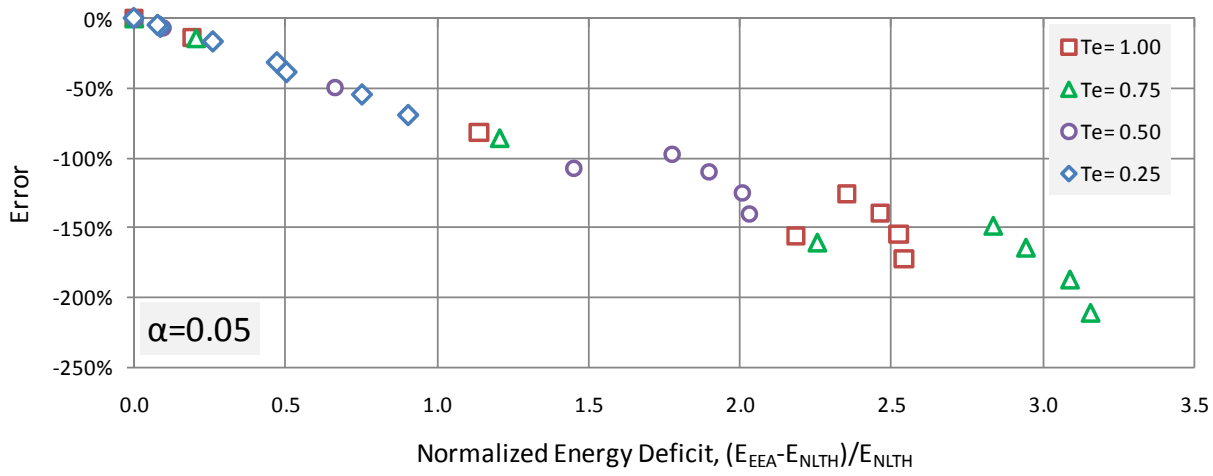

Figure 7.9 Error between "exact" response and Equal Energy Approximation versus normalized energy deficit ($\alpha = 0.05$, mean of 20 Atkinson's artificial records - ENA)

The examples brought here represent only the 5% damped seismic response computed for bilinear systems with a post-yield stiffness of $\alpha = 0.05$. Moreover, the results presented above are mean responses of 20 ground motions and the response of the systems analyzed under each individual earthquake will be affected by the particular characteristics of each ground motions.

However, the main goal of discussing these examples was to show general trends on the limits of applicability for both the EDA and EEA for assessing the response of *highly-nonlinear* seismically isolated bridges. The results obtained from NLTHA suggest that the accuracy of both methods depends on the system parameters R and T_e: the EDA can be applied only for systems with longer elastic periods and *limited-nonlinear* responses ($T_e \geq 0.75$ s *and* $R \leq 8$ in this study) and the accuracy of the EEA generally increases as the elastic periods decrease.

Based on these observations, it can be stated that the accuracy of the EEA depends on the effective period T_{eff}, because T_{eff} depends on both T_e and the R factor through the geometry of the hysteresis loop. In addition, the range of likely T_{eff} is related to a site-specific response spectrum through the elastic period T_e and the post-yielding period $T_d = T_e / \sqrt{\alpha}$. Hence, there is also a possible influence of the characteristics of the ground motions to which the structure is subjected. The influence of the ground motion characteristics depends on the period and can be assessed by determining in which of the two period ranges is the structure period T_e. The period ranges are defined with respect to the ground-motion predominant period T_g (Chopra, 2011):

"slowly varying force" period range ($T < T_g$) and "rapidly varying force" period range ($T > T_g$). As a result, the response can be classified into either one of the three cases:

- "slowly" varying force for $T / T_g < 1$ (or "slow" loading);
- forcing period which is close to the fundamental period $T / T_g \approx 1$;
- "rapidly" varying force for $T / T_g > 1$ (or "rapid" loading).

The system response depends on which of the three cases applies. The energy distribution and *energy deficit* may also vary depending on the period ratio. This is investigated in the following sections.

7.3 NL-SDOF Systems Studied through Response Dynamics and Energy Balance

In the previous section, the *energy deficit* was identified to explain differences in response estimates between the EEA and "exact" NLTHA results. It was observed that the *energy deficit* depends on system parameters (ratio R, elastic period T_e, and post-yielding stiffness ratio α) and the characteristics of the ground motions to which the system is subjected.

A better understanding of the dynamics of nonlinear systems, especially those exhibiting a high ductility response, is however needed before proposing a new approximate method for design. This is done in the following sections by studying the transient response dynamics of L-SDOF and NL-SDOF systems subjected to sinusoidal excitations. Using the principle of conservation of energy, the focus is put on investigating the energy flow within the system. The energy allocation (distribution), corresponding to the maximum system displacement and position of the *transient oscillation center* for L-SDOF and *shifted oscillation center* for NL-SDOF, are of special interest in this study to show how the system's peak response is built and to reveal the source of the *energy deficit*.

The study of L-SDOF systems aims at investigating the influence of the frequency ratio ω_g / ω_e (or period ratio T_e / T_g) on the energy allocation (distribution) when the effects of nonlinear

system's parameters are neglected. Then, further insight on the energy distribution of a transient system's response is gained by including nonlinear system parameters.

7.3.1 Formulation of Energy Balance for Linear and Bilinear SDOF Systems

Two energy formulations can be used to study the seismic response of a structural system: relative energy formulation and absolute energy formulation. In the relative energy formulation, the equivalent external dynamic force acts on the mass of the system that is fixed at its base. The earthquake ground motion at the base of structure is replaced by a "fictitious" dynamic load, $P(t) = -m\,\ddot{u}_g(t)$ acting on the mass. In the absolute energy formulation, the loading is considered through the absolute inertia force acting on the system mass. This "real" inertia force is defined as the product of the system mass and its absolute acceleration. The two energy formulations have been discussed in detail by Filiatrault and al. (1994) and Christopoulos and Filiatrault (2003) for a MDOF system. The researchers compared the relative and absolute formulations proposed by Uang and Bertero (1990) and stated that both formulations are mathematically equivalent and the resulting sums of the kinetic and input energies are equal.

In this study, the relative energy formulation is adopted to investigate the influence of system parameters and ground-motion characteristics on the energy flow. The advantage of this formulation for seismically isolated and damped bridges is that it is directly related to the system relative velocity and displacement, which explicitly characterizes the devices' response. With such an approach, a clear insight can therefore be gained into the seismic performance of bridges.

The energy balance for a nonlinear SDOF system is formulated by using Newton's second law equation of motions which represents the sum of the forces acting on the system mass *m* at the time *t*:

$$Fi\,(t) + Fd\,(t) + Fs\,(t) = P\,(t) \tag{7.10}$$

$$m\,\ddot{u}(t) + c\,\dot{u}\,(t) + k\,u\,(t) = -m\,\ddot{u}_g(t) \tag{7.11}$$

These forces are in equilibrium at every instant of time and the corresponding energy quantities, formulated in terms of the work done by these forces over a distance of the relative displacement

u, will be consequently balanced. The energy flow throughout the ground motion can be tracked by integrating the corresponding contributions to work. When using the relative formulation of the energy for a nonlinear SDOF system subjected to earthquake ground motions, four energy terms must be considered: relative kinetic energy, E_k, energy dissipated by viscous damping, E_d, absorbed energy, E_{Ab}, and relative input energy, E_{in}. The relative formulation of energy balance for an SDOF system is expressed by:

$$E_k(t) + E_d(t) + E_{Ab}(t) = E_{in}(t) \tag{7.12}$$

These energy terms can be further defined as follows::

1) The relative input energy E_{in} is the energy transmitted to the structure during external mechanical excitation (dynamic loading) represented by a "fictitious external" inertia force, $P(t) = -m\,\ddot{u}_g(t)$. It is determined by integrating the inertia force through the relative displacement from the beginning of the ground motion up to the time *t*:

$$E_{in}(t) = -\int m\,\ddot{u}_g(t)\,du \tag{7.13}$$

Note that under the same base excitation, the displacement response varies from one system to another and the resulting quantities of induced energy are different for two systems with different dynamic properties. For the comparative analyses presented in this study, the system mass remains the same, while different dynamic properties are obtained by changing the system parameters as k_e, α, and R. Therefore, the relative energy input will vary from one bridge to the next.

2) The relative kinetic energy E_k is related to the system mass motion (velocity) with respect to its base. When the mass position reaches its maximum relative displacement, the relative velocity becomes equal to zero and the kinetic energy is completely absorbed by the system. In turn, when the system is in motion, the kinetic energy can be expressed for each discrete time as half the product of the oscillator mass and its squared relative velocity at time *t*:

$$E_k(t) = \frac{1}{2}\,m\,\dot{u}(t)^2 \tag{7.14}$$

In this approach, the kinetic energy is determined by integrating the "fictitious internal" force, which is related to the mass acceleration relative to the system base:

$$E_k(t) = \int m\, \ddot{u}(t)\, du \tag{7.15}$$

The relative kinetic energy is an absolute input energy fraction which is stored in the oscillator mass motion. This energy term provides insight into the system capacity to store in motion the part of induced energy before it is completely absorbed or dissipated by the system. For an infinitely stiff system (the fundamental period of vibration tends towards zero), this capacity is null as the system is completely prevented from relative motion. In contrast, a larger amount of relative kinetic energy is expected for more flexible structures with longer fundamental periods of vibration. In this way, the relative kinetic energy may directly reflect the effect of seismic isolation. This concept will be further exploited in this study.

3) The absorbed energy E_{Ab} is the mechanical form of the system energy. It is composed of the elastically stored energy (recoverable) and the energy dissipated during hysteretic behaviour (unrecoverable). At the maximum displacement, the kinetic energy is fully transformed into the energy absorbed by the system. This energy is related to the hysteretic shape (bilinear in this study) and its quantity depends on the relative displacement response. Accordingly, for a response cycle, the peak of the absorbed energy is reached at the maximum displacement when the kinetic energy is fully transformed into the energy absorbed by the system. This energy at time t is determined by integrating the spring force $F_s(t) = k \cdot u(t)$ through the relative displacement. In this formulation, k is the effective stiffness at time *t*.

$$E_{Ab}(t) = \int k\, u(t)\, du \tag{7.16}$$

4.) Part of the induced energy is dissipated through viscous damping. This energy term is determined by integrating the velocity-proportional damping force $F_d(t) = c\, \dot{u}(t)$ through the relative displacement from the beginning of the ground motion up to the time *t*.

$$E_d(t) = \int c\, \dot{u}(t)\, du \tag{7.17}$$

The SDOF system adopted in this study for simulating responses of isolated bridges is represented by the simple Kelvin-Voigt solid model shown in Figure 7.10(a). For the relative energy formulation, the system base remains fixed and the force equilibrium is established using Newton's equation of motions. Figure 7.10(b) presents free-body diagrams of the system subjected to load $P(t) = -m\,\ddot{u}_g(t)$.

Although all interacting forces contribute to the dynamic equilibrium, the inertia force is of special interest when defining and distinguishing the different phases of an oscillatory motion. Changes in motion may by identified using the Newtonian or *inertial reference frame* which relies on the well-known Newton's first law. This law was formulated by Newton in *Principia* in Latin as:

"Lex I: Corpus omne perseverare in statu suo quiescendi vel movendi uniformiter in directum, nisi quatenus a viribus impressis cogitur statum illum mutare."

Being translated to English, the law reads as:

"Law I: Every body persists in its state of being at rest or of moving uniformly straight forward, except insofar as it is compelled to change its state by force impressed." (Isaac Newton (1999) The Principia, A new translation by I.B. Cohen and A. Whitman, University of California press, Berkeley 1999).

Formulating this law for the SDOF system studied, it can be stated that the system's mass will stay at rest so long as no force acts on it or the mass will stay in constant motion until an external force acts on it in its motion's direction. In both cases, the relative velocity is constant when the mass acceleration relative to the system base equals zero that accordingly corresponds to a zero inertia force. In other words, inertia force acts in "resisting" any change in the mass motion. Accordingly, for a system being initially at rest and suddenly subjected to an oscillatory motion, the change between motion phases occurs when the inertia force reduces to zero.

For a steady-state response of an elastic SDOF system, the inertia force equals zero ($F_i = m\,\ddot{u} = 0$) when the system's mass passes through the zero-displacement position ($u = 0$) which is the center of the oscillation motion. At this position, the velocity and the kinetic energy reach their maximum for a given cycle of motion.

For an elastic system within a transient response phase, the kinetic energy does not necessarily reach its peak when the system is at zero displacement. In this case, the system's mass can oscillate about a new oscillation center for where the kinetic energy is maximum (or zero inertia force). The new oscillation center is referred to as a *transient oscillation center (Transient OC)* which is defined for L-SDOF systems as the displacement response that corresponds to the maximum kinetic energy (or maximum relative velocity) during a given cycle of vibration.

The concept of the *transient oscillation center (Transient OC)* of a L-SDOF system is introduced and explained in this section to draw a parallel with the *drifted oscillation center (Drifted OC)* of NL-SDOF systems which was pointed out in Chapter 6 as a likely reason for the limitations of the code simplified method. The *drift of the oscillation center* of NL-SDOF systems are studied further in the following sections of this chapter.

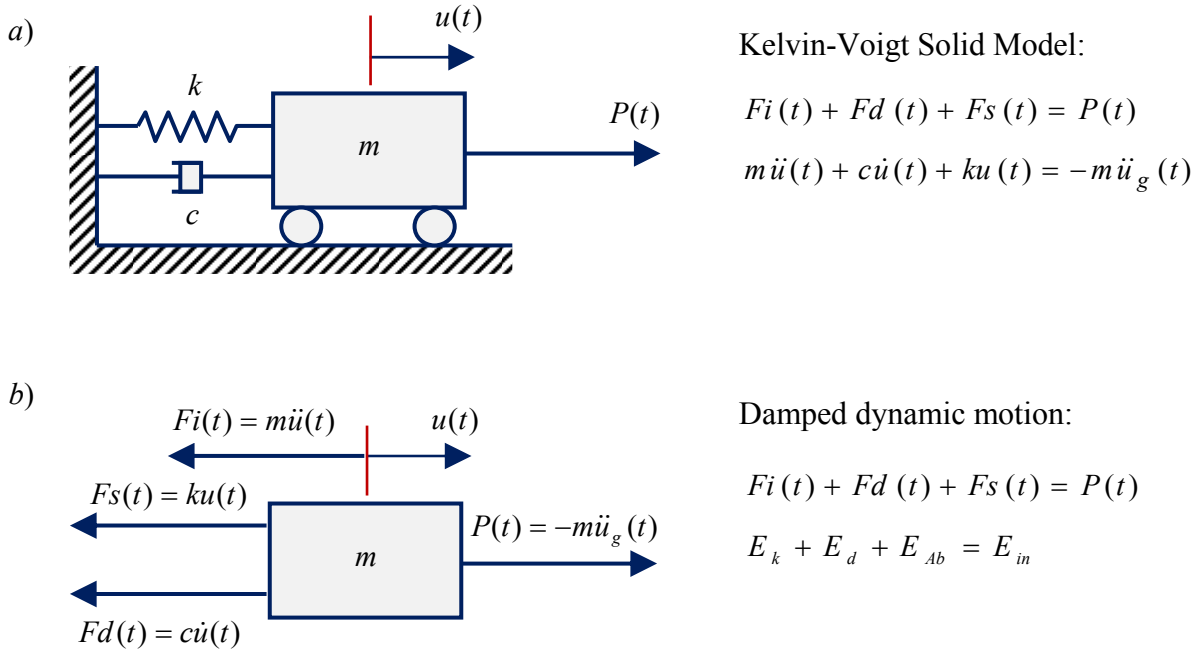

Figure 7.10 SDOF system free-body diagram and energy balance: a) SDOF system model; b) forced damped dynamic motion

7.3.2 Undamped L-SDOF Response Mechanics: Energy Allocation and Transient Oscillation Center

In this section, the response of linear SDOF systems subjected to sinusoidal excitation are presented to emphasize how the energy flow is affected by the frequency ratio representing loading conditions with "slowly" varying ($\omega_g / \omega_e < 1$ or $T_g > T_e$) and "rapidly" varying ($\omega_g / \omega_e > 1$ or $T_g < T_e$) excitation forces. The motivation of this section is to identify the contribution of the kinetic energy to the system response during a transient phase of loading. For simplification, the transient response phase is ignored in the majority of the current simplified analysis methods. As noted in Chapters 5 and 6 and in the previous section, limitations of these simplified methods may result from neglecting the transient response. Special attention is therefore drawn to the *transient oscillation center (Transient OC)* where the maximum kinetic energy (or maximum relative velocity) occurs during a given cycle of vibration. It is opportune to mention that when the system is located at a *transient OC* different from its "at rest" position, the energy absorbed by the system is not zero due to the nonzero relative displacement ($u \neq 0$).

Interaction of the forces acting on a SDOF system during an earthquake may be studied in terms of the energy flow, i.e., the variation of the different energy quantities with time. Monitoring the energy flow when evaluating the nonlinear behaviour of structures has been considered by several researchers for the selection of the optimum properties of seismic protective elements (Housner, 1963; Uang et Bertero, 1990; Filiatrault et al. 1994; Christopoulos et Filiatrault, 2003). In this approach, the force-displacement response is presented as a basis for understanding the energy distribution. Three forces P (t), F_i (t), and F_s (t) were considered to show how the energy input is transformed during the response of an undamped L-SDOF system (see Section 7.3.1 for details). The time histories of velocity and displacement were presented to emphasize the velocity-dependent and displacement-dependent nature of the system response as well as to indicate the maxima of the kinetic and absorbed energies.

Similarities that exist between sinusoidal loading and seismic ground-motion excitations are used in this section to visualize the differences in the energy allocation for ground motions representative of loading with "slowly varying" and "rapidly varying" forces (the existence of these similarities is further justified in the next section). The effect of varying the loading

frequency is therefore examined for an undamped linear elastic system initially at rest and suddenly subjected to a one-cycle sinusoidal loading. Three frequency ratios are considered: $\omega_g / \omega_e = [0.75; 1.0; 1.5]$. These three loading cases are respectively representative of a structure characterized by a fundamental period T_e (ω_e) subjected to three different ground motions ($T_{g1} > T_e, T_{g2} = T_e$, and $T_{g3} < T_e$), or a ground motion with predominant period T_g (ω_g) that excites three different structures ($T_g > T_{e1}, T_g = T_{e2}$, and $T_g < T_{e3}$). This is illustrated in Figures 7.11 and 7.12.

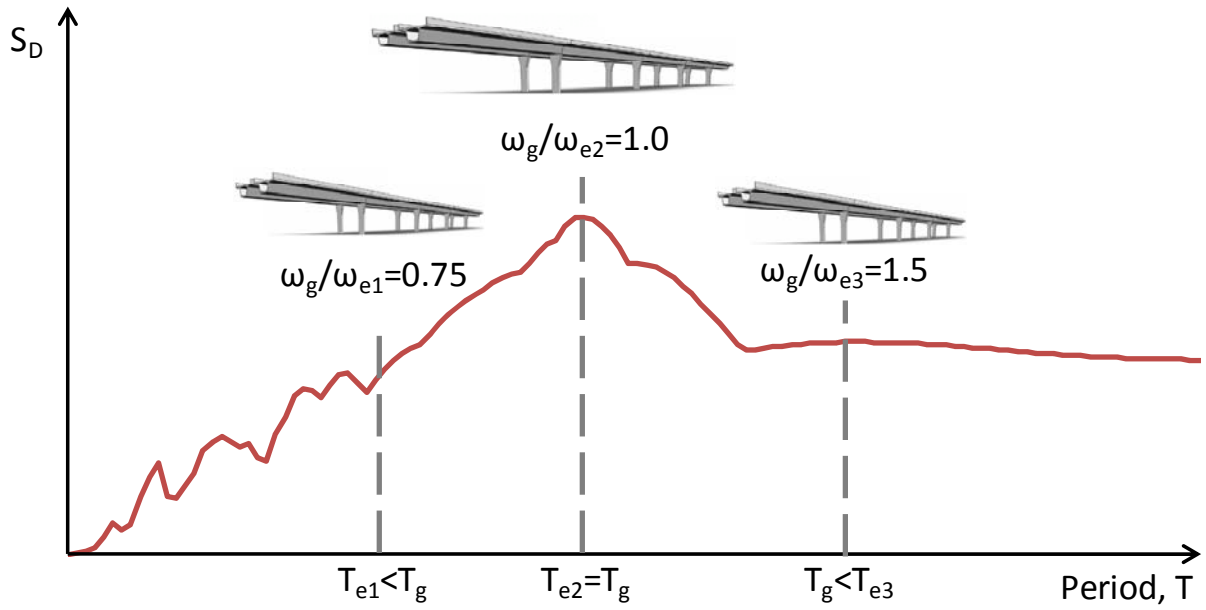

Figure 7.11 Example of loading frequency ratios $\omega_g / \omega_e = [\ 0.75; 1.0; 1.5\ ]$ for three different bridge structures subjected to the same ground motion excitation

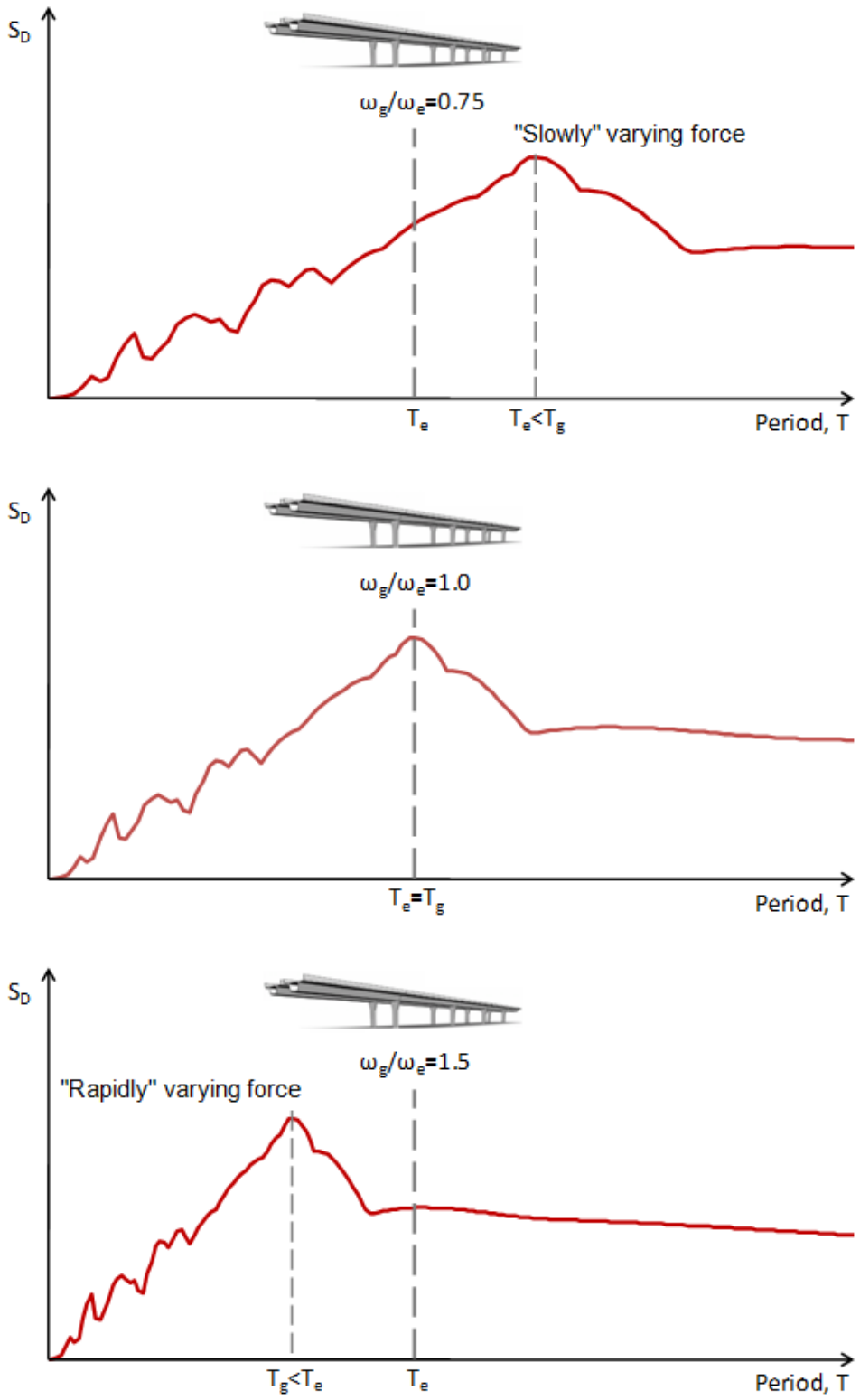

Figure 7.12 Example of loading frequency ratios $\omega_g / \omega_e = [\, 0.75; 1.0; 1.5 \,]$ for a bridge structure subjected to three different ground-motion excitations

The loading function considered for the linear time-history analyses on the undamped L-SDOF systems is given as:

$$P(t) = p_0 \cdot \sin(\omega_g t + \varphi) = -m \cdot \ddot{u}_0 \sin(\omega_g t + \varphi) = -m \cdot u_0 \cdot \omega_g{}^2 \sin(\omega_g t + \varphi) \quad (7.18)$$

Where the phase angle $\varphi = 0°$ corresponds to the system's initial conditions at rest ($u(0) = 0$ and $\dot{u}(0) = 0$).

The energy balance is established through the contribution of the three forces interacting at the level of the mass:

$$E_k(t) + E_{Ab}(t) = E_{in}(t) \quad (7.19)$$

Figures 7.13 and 7.14 compare the responses of the L-SDOF systems undergoing one cycle of sinusoidal loading from the "at rest" state where the transient portion of the response is predominant. The results were normalized with respect to the force excitation amplitude p_0, the base displacement amplitude u_0, and the excitation frequency ω_g (or period T_g). Key system and response parameters are presented in Table 7-1. The calculations are performed for ω_g / ω_e = 0.75, 1.0 and 1.5. The first and third cases are representative of the responses for $\omega_g / \omega_e < 1.0$ and $\omega_g / \omega_e > 1.0$, respectively.

In Figure 7.13, force time-histories and force-displacement responses during the excitation cycle of the L-SDOF system are presented on the left-hand side (LHS) and right-hand side (RHS) of the figure, respectively. In the LHS figure, the time history of the elastic force also represents the relative displacement history as both parameters are proportional to each other. As discussed in the previous section, in each half-cycle, the inertia force passes by zero ($F_i = m\,\ddot{u} = 0$) and the kinetic energy then reaches its maximum at this point. Accordingly, for the entire cycle, there are two *transient OCs*, one in each displacement direction, where kinetic energy is maximum. At these system positions, because the inertia force is zero, the excitation input force is balanced by the spring force ($P = F_s$). From the beginning of the loading, the inertia force F_i was acting in the opposite direction with respect to the excitation force P. At the *transient OC*, the inertia force changes sign and, from this point on, P and F_i act in the same direction, opposite to the direction of the elastic spring force F_s. For all three frequency ratios, F_i is still acting in the direction

opposite to F_s when F_s (and the relative displacement) reaches its maximum. However, the input (excitation) force P is opposite to F_s for $\omega_g / \omega_e < 1.0$ and acts in the same direction as F_s for $\omega_g / \omega_e > 1.0$. For $\omega_g / \omega_e = 1.0$, P=0 when F_s is maximum and, accordingly, $F_s = F_i$ at this point. In the figure, the portion of the inertia force in the overall force balance increases with the frequency ratio. It can also be noted that the L-SDOF system experiences larger displacement responses for higher frequency ratios. This is due to the greater contribution of the inertia force and kinetic energy, as explained next.

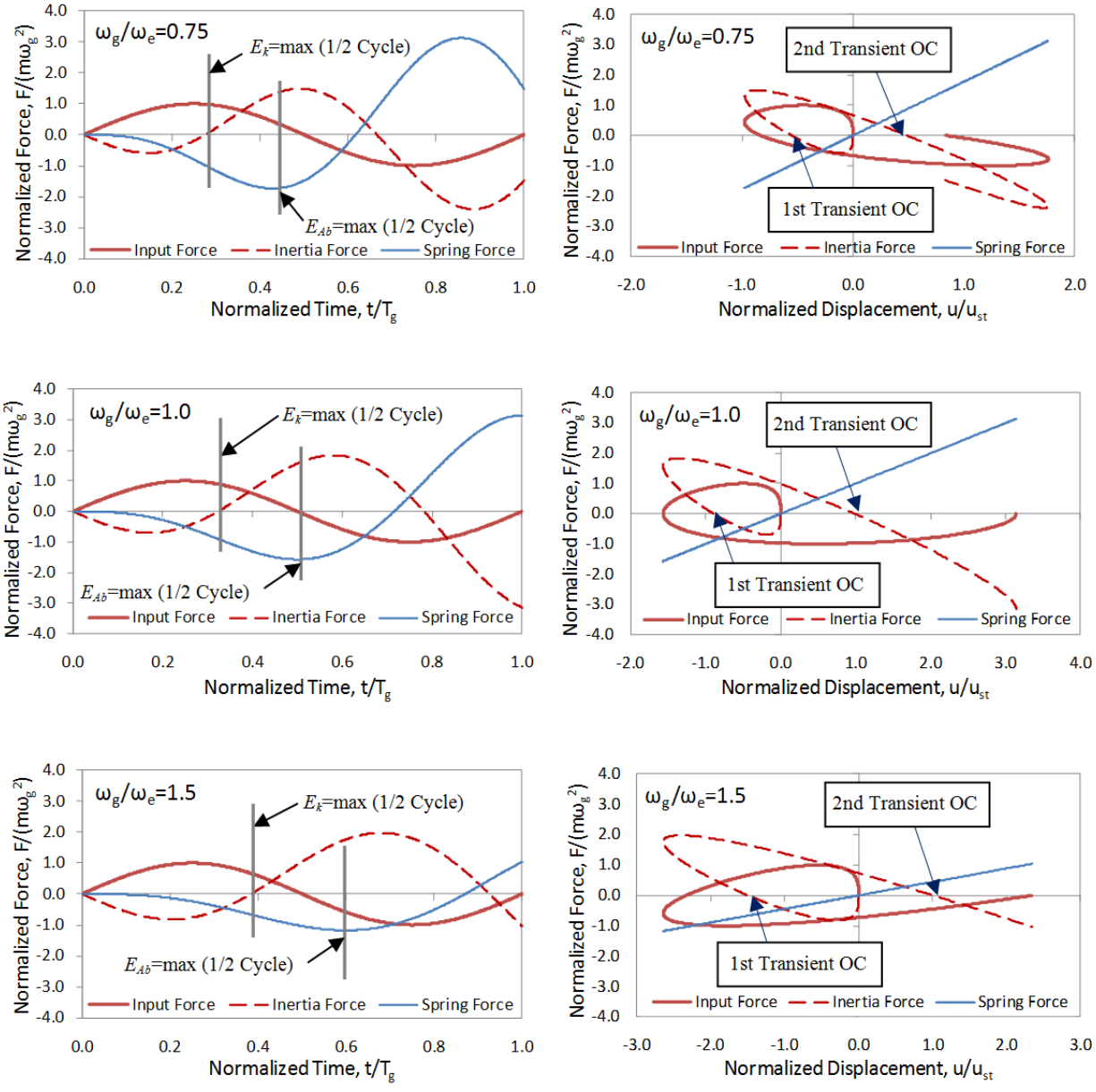

Figure 7.13 Response of elastic SDOF system for $\omega_g / \omega_e = [\,0.75; 1.0; 1.5\,]$

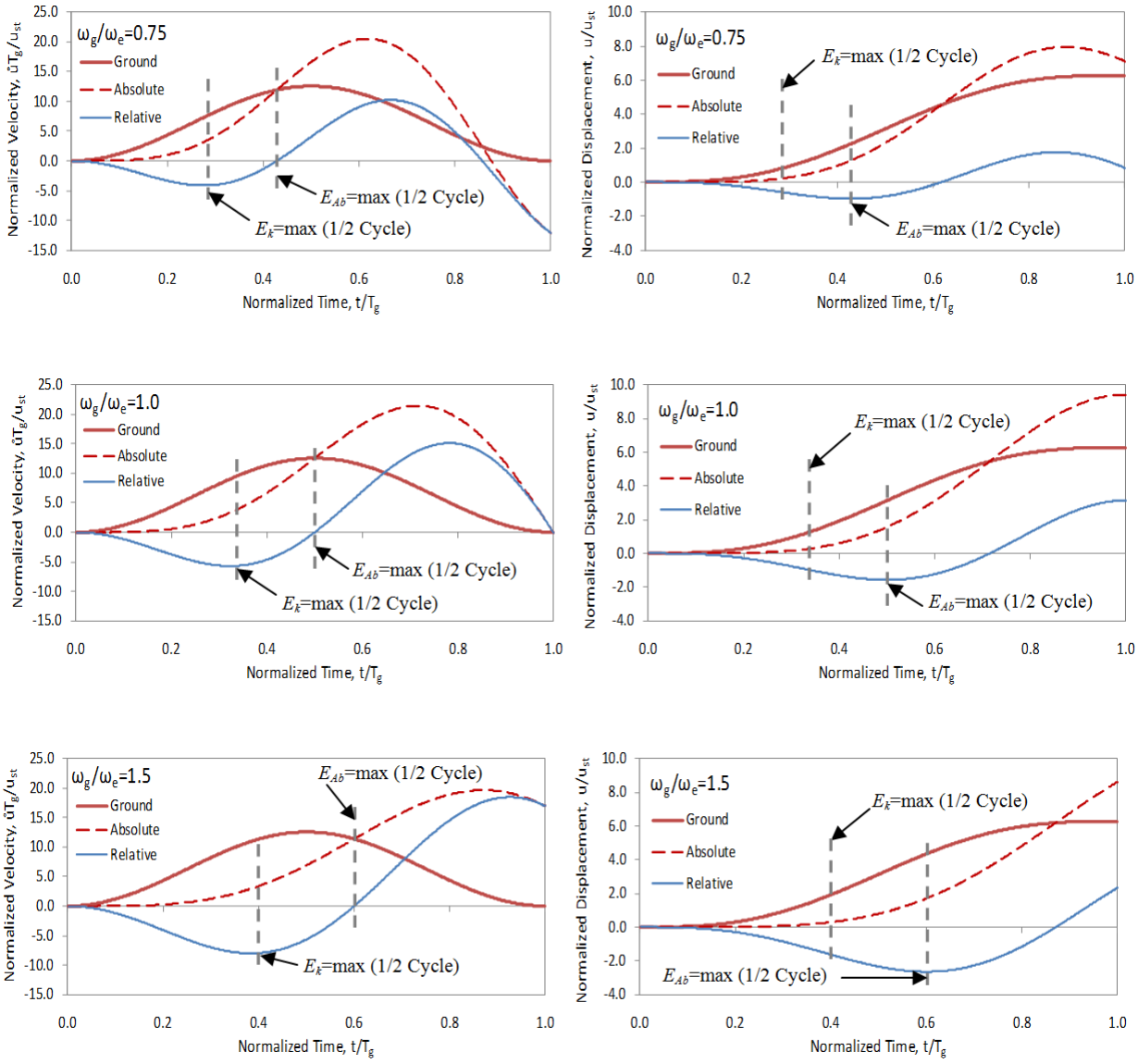

Figure 7.14 Velocity and displacement of elastic SDOF system for $\omega_g / \omega_e = [\,0.75; 1.0; 1.5\,]$

Figure 7.14 presents the time-histories of the normalized velocity (LHS) and displacement (RHS). The ground velocity and displacement are the same for the three cases studied in this example. However, the relative and consequently absolute system responses depend on the frequency ratio. The kinetic and absorbed energies computed from the system relative velocity and displacement are plotted in Figure 7.14. Table 7.1 presents the normalized time, energy and displacement corresponding to the *transient OC* when the kinetic energy reaches its first maximum value.

In Figures 7.14 and 7.15, it can be noted that peak velocity and, thereby, peak kinetic energy, occur first for all three frequency ratios, before peak relative displacement and absorbed energy. For a given frequency ratio, peak kinetic energy and peak absorbed energy have the same amplitude, meaning that the kinetic energy eventually transforms into absorbed energy. In Figure 7.15 and in Table 7-1, the peak kinetic energy and peak absorbed energy have larger magnitudes and occur at a later relative time as the frequency ratio increases, i.e. when the structure is subjected to more rapidly varying ground motions (or when the system's elastic period T_e becomes longer relative to the ground motion period T_g). Higher energies are expected for higher frequency ratios because the capacity to absorb energy of the system is reduced and a larger portion of the energy input in the first half-cycle must transform into kinetic energy. The input energy time history is also shown in Figure 7.14. For all three frequency ratios, the peak absorbed energy at maximum displacement is equal to the input energy input at this time.

In Figure 7.15 and Table 7-1, two differences of significance in energy flows can be observed as a function of the frequency ratio. Firstly, at the *transient OC*, the magnitudes of the kinetic and absorbed energies are close to each other for $\omega_g / \omega_e \leq 1$ whereas the kinetic energy is much larger than the absorbed energy for $\omega_g / \omega_e > 1$. Secondly, from the "at rest" zero position up to the maximum displacement, the input energy always increases with displacement for frequency ratios $\omega_g / \omega_e \leq 1$. In contrast, for ratios $\omega_g / \omega_e > 1$, the input energy peaks before the absorbed energy reaches its maximum. The peak in input energy corresponds to a zero input force and the relatively earlier occurrence of zero input force is confirmed when observing the force time-histories in Figure 7.13.

Table 7-1 Normalized time, kinetic energy, absorbed energy, and displacement at *transient OC* for the first half response cycle

Frequency Ratio ω_g / ω_e	Normalized Time t/T_g at E_{k_max}	Normalized Kinetic Energy E_{k_max}	Normalized Absorbed Energy E_{Ab} at E_{k_max}	Energy Difference E_{k_max} - E_{Ab}	Normalized Displacement u at E_{k_max}
0.75	0.28	0.217	0.277	-0.060	0.559
1.00	0.32	0.414	0.402	0.012	0.897
1.50	0.38	0.813	0.502	0.311	1.430

Based on these observations, it can be stated that for ratios $\omega_g / \omega_e > 1$, the input energy is transmitted into the system at a faster rate than the rate of energy absorption of the system. In other words, the portion of the input energy transformed into the kinetic energy is larger than that can be transformed into absorbed energy. Accordingly, an excessive amount of energy is stored within the system's motion (kinetic energy) that will be absorbed by the system at a later time, leading to a larger displacement response.

When the system is initially at rest, the first half cycle seems to be crucial from an energy allocation point of view, and this energy distribution may affect peak displacement demand. The system response during the transient phase may be represented by the combined effect of the free vibration and forced steady-state responses. These responses may be solved mathematically as the sum of the particular solution, $u_p(t)$, and complementary solution, $u_c(t)$, for steady-state and transient responses, respectively (Chopra, 2011). The complete displacement solution $u(t)$ characterizes the system's mass position with respect to its "at rest" equilibrium position at the time t starting "at rest" initial conditions $u(0) = 0$ and $\dot{u}(0) = 0$. Figures 7.16 and 7.17 show histories of the normalized relative displacement and velocity for transient and steady-state responses for a high frequency ratio ($\omega_g / \omega_e = 1.5$). As shown in the figure, higher displacement demand can occur under this combined effect compared to a steady-state response alone, which can be missed when using simplified analysis methods that rely only on the steady-state response.

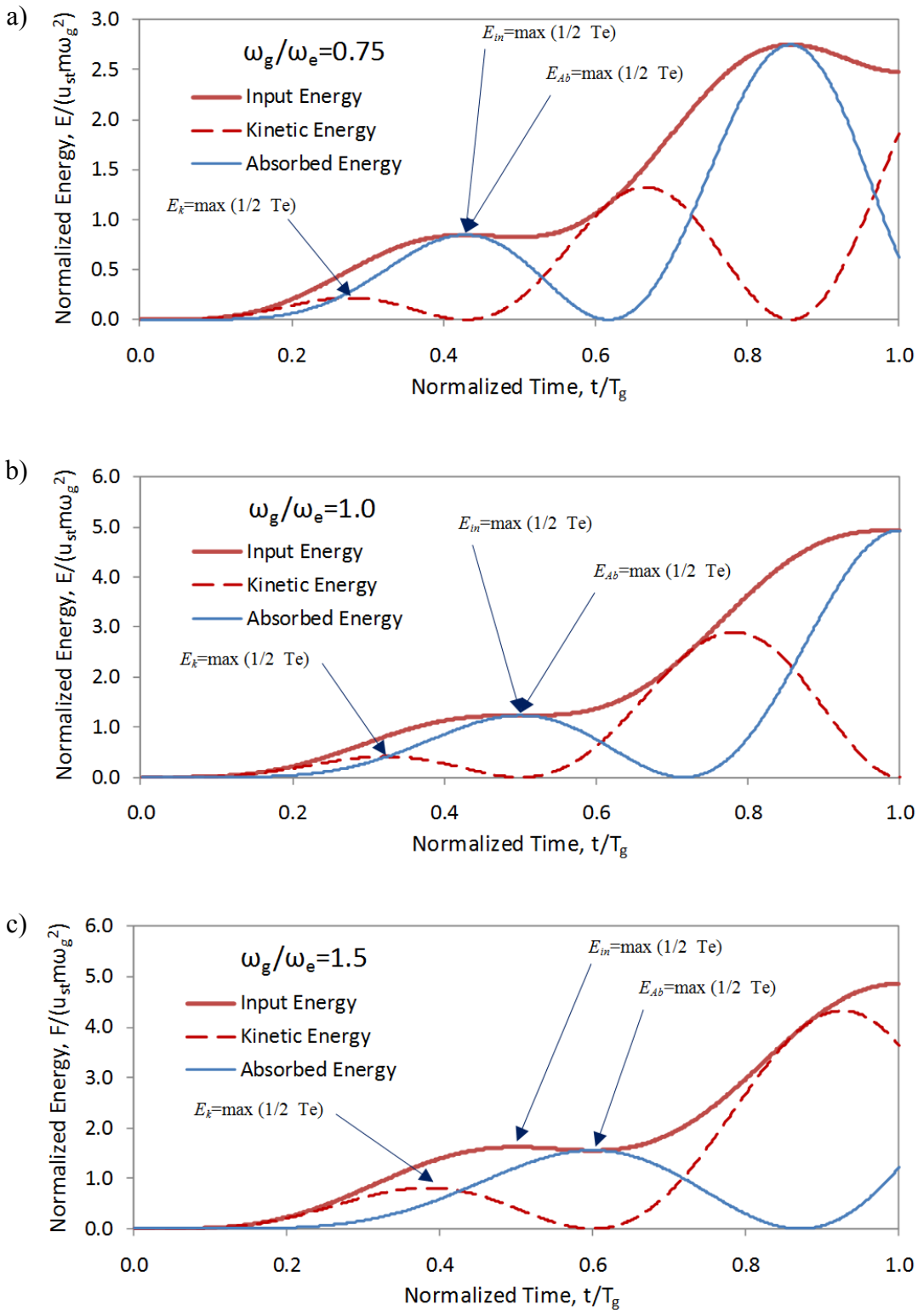

Figure 7.15 Energy flow, elastic SDOF system for: a) $\omega_g / \omega_e = 0.75$; b) $\omega_g / \omega_e = 1.0$ and c) $\omega_g / \omega_e = 1.5$

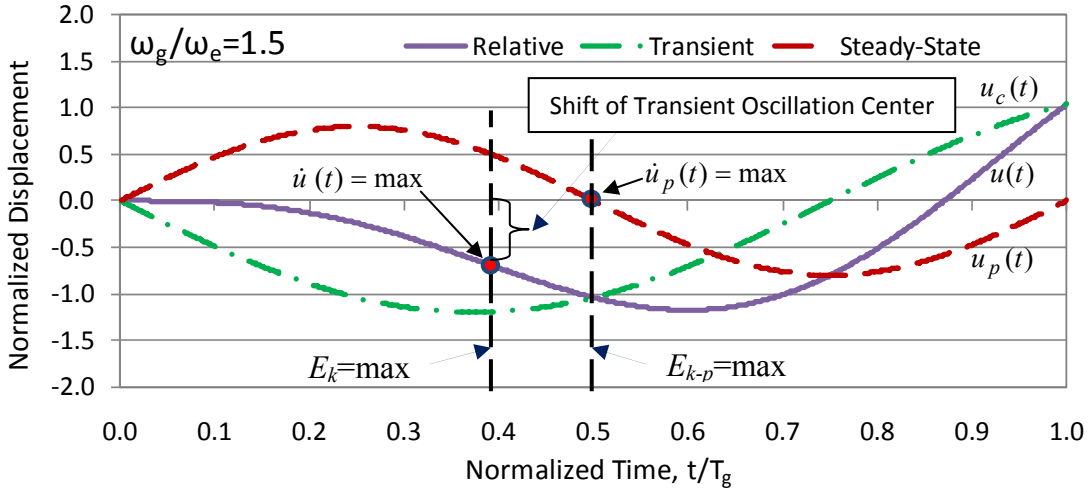

Figure 7.16 Relative complete displacement as a result of transient and steady-state responses

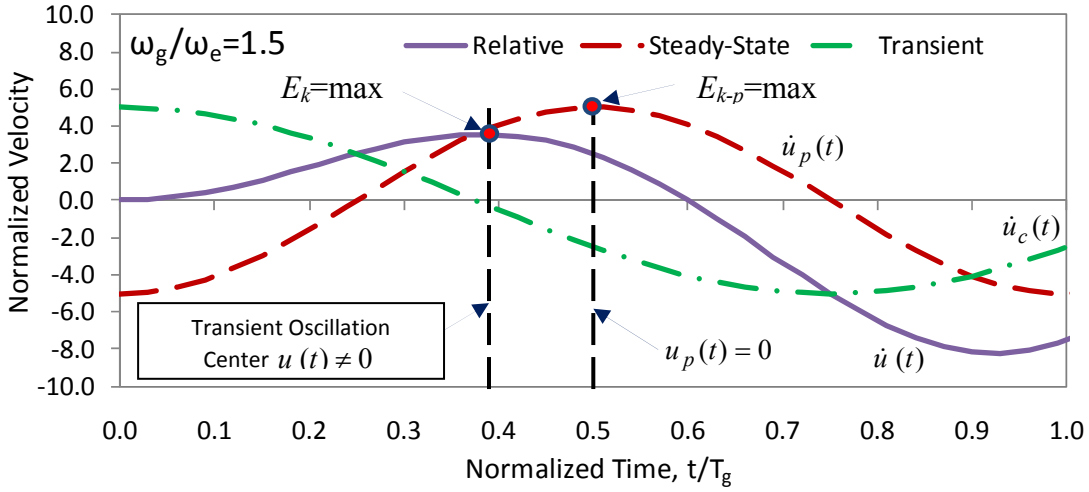

Figure 7.17 Relative complete velocity as a result of transient and steady-state responses

The equation of motion corresponding to the elastic system without damping subjected to harmonic sinusoidal loading is presented as follows (Chopra, 2011):

$$m\ddot{u}(t) + F_s(t) = p_0 \sin \omega_g t \tag{7.20}$$

The particular solution that describes a steady-state motion is given as ($\omega_g \neq \omega_e$):

$$u_p(t) = \frac{p_0}{k_e} \cdot \frac{1}{1 - {\omega_g}^2 / {\omega_e}^2} \cdot \sin \omega_g t \tag{7.21}$$

The complementary solution that represents transient response is given as ($\omega_g \neq \omega_e$):

$$u_c(t) = u(0) \cdot \cos \omega_e t + \frac{\dot{u}(0)}{\omega_e} \cdot \sin \omega_e t - \frac{p_0}{k_e} \cdot \frac{\omega_g / \omega_e}{1 - {\omega_g}^2 / {\omega_e}^2} \cdot \sin \omega_e t \tag{7.22}$$

For the system being at rest at the start of the loading, Equation 7.22 is reduces to:

$$u_c(t) = -\frac{p_0}{k_e} \cdot \frac{\omega_g / \omega_e}{1 - {\omega_g}^2 / {\omega_e}^2} \cdot \sin \omega_e t \tag{7.23}$$

The corresponding complete solution becomes:

$$u(t) = u_c(t) + u_p(t) = \frac{p_0}{k_e} \frac{1}{1 - {\omega_g}^2 / {\omega_e}^2} \cdot \left(\sin \omega_g t - \frac{\omega_g}{\omega_e} \sin \omega_e t \right) \tag{7.24}$$

Differentiating Equations 7.21 and 7.22 with respect to time and rewriting for the initial conditions at rest the velocity particular and complementary solutions are obtained as:

$$\dot{u}_p(t) = \frac{p_0}{k_e} \cdot \frac{\omega_g}{1 - {\omega_g}^2 / {\omega_e}^2} \cdot \cos \omega_g t \tag{7.25}$$

$$\dot{u}_c(t) = -\frac{p_0}{k_e} \cdot \frac{\omega_g}{1 - {\omega_g}^2 / {\omega_e}^2} \cdot \cos \omega_e t \tag{7.26}$$

Similarly, the complete solution for the relative velocity is given as:

$$\dot{u}(t) = \frac{p_0}{k_e} \cdot \frac{\omega_g}{1 - {\omega_g}^2 / {\omega_e}^2} \cdot (\cos \omega_g t - \cos \omega_e t) \tag{7.27}$$

By differentiating Equation 7.27 with respect to time and equating the resulting acceleration to zero, the time at which the relative velocity (and kinetic energy) reaches its maximum is obtained from the following equation:

$$\ddot{u}(t) = \frac{p_0}{k_e} \cdot \frac{\omega_g}{1 - {\omega_g}^2 / {\omega_e}^2} \cdot (\omega_e \sin \omega_e t - \omega_g \sin \omega_g t) = 0 \tag{7.28}$$

Equation 6.23 is satisfied when:

$$\sin \omega_e t - \frac{\omega_g}{\omega_e} \sin \omega_g t = 0 \quad \text{or} \quad \frac{\sin \omega_e t}{\sin \omega_g t} = \frac{\omega_g}{\omega_e} \tag{7.29}$$

Solving Equation 7.29 for time t and substituting it in Equations 7.22 and 7.27 respectively, the relative displacement, $u(\dot{u}_{\max})$ and the maximum relative velocity, $\dot{u}_{\max}$ at the position of the *transient OC* can be calculated. The maximum kinetic energy is then obtained from Equation 7.30 as a function of the relative velocity (complete solution - $\dot{u}(t)$):

$$E_k(t) = \frac{m\,(\dot{u}_p(t) + \dot{u}_c(t))^2}{2} = \frac{m\,\dot{u}^2(t)}{2} \tag{7.30}$$

The corresponding absorbed energy is determined with the system relative displacement as a static strain energy stored in the spring, k_e:

$$E_{Ab}(\dot{u}_{\max}) = \frac{1}{2} u^2 k_e \tag{7.31}$$

The kinetic and absorbed energies at the *transient OC* are plotted in Figure 7.17 for ω_g / ω_e ranging from 0.2 to 2.0. In this figure, the energies are normalized with respect to $u_{st} m \omega_g^2$. It can be noted that for frequency ratios up to the resonant state $\omega_g / \omega_e = 1$, the magnitudes of the two energies are close. Beyond the resonant ratio, the maximum kinetic energy increases with the

frequency ratio, while the corresponding absorbed energy remains nearly constant at a level slightly higher than at resonance. Based on the previous discussion, higher kinetic energy compared to absorbed energy at the *transient OC* produces an unbalanced condition at this point: the system will have to deform to larger peak displacements before it can completely absorb the excess in kinetic energy. In Figure 7.18, the significant increase in the difference between the two energies for frequency ratios higher than unity ($\omega_g / \omega_e > 1$) suggests that larger peak displacements can be expected during the transient phase of the response to ground motions having dominant frequencies higher than that of the bridge structure.

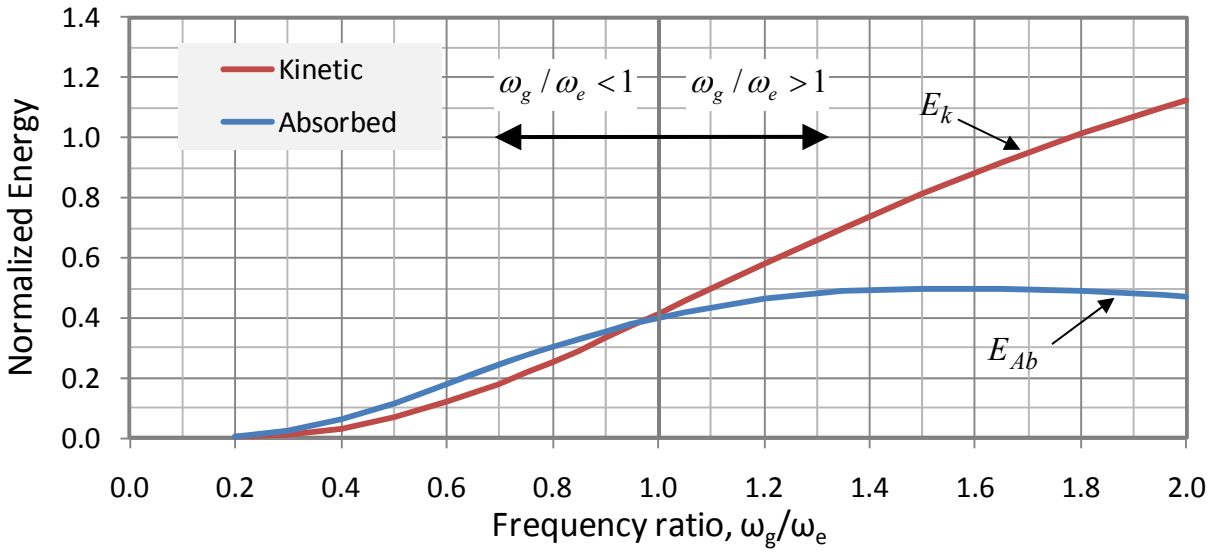

Figure 7.18 Influence of the frequency ration on normalized kinetic E_k and absorbed E_{Ab} energies at the *transient OC* for undamped L-SDOF systems

In the following sections the similarity between the effect of the frequency ratio on the response of L-SDOF systems and the influence of the effective stiffness k_{eff} for NL-SDOF systems will be outlined. Isolated bridge structures are typically designed with low lateral resistance at the activation of the isolation system (high *R*-ratios), which translates into low effective stiffness and, possibly, high frequency ratios. This means that transient response may be of importance for such structures.

Before moving to the response of nonlinear systems, it should be noted that the *transient oscillation center* for L-SDOF systems gradually converges to the system's initial zero deformation position when the transient response gradually diminishes and the system reaches its

steady-state condition. In turn, the *transient oscillation center* for NL-SDOF systems corresponds to a permanent residual displacement when the system experiences inelastic response. It is therefore expected, as will be further investigated in the following sections, that there is a critical value of the response modification factor R (R_{cr}) beyond which an excessive amount of energy amount is allocated to kinetic energy and produces a permanent shift, or drift, of the oscillation center. In such a case, the total displacement of the nonlinear system is equal to the sum of the oscillation center drift and the local system response about this new oscillation center. The effect of the energy excess allocated as kinetic energy and the resulting oscillation center drift on the responses of NL-SDOF systems are therefore further studied in this chapter.

7.3.3 Transient Response of NL-SDOF Systems to Sinusoidal Loading

In the previous section, the *transient oscillation center* and the excess of *kinetic energy* at that point were outlined for the transient response of L-SDOF systems by examining the energy flow in the system. Excess of kinetic energy was found to occur for frequency ratios higher than 1.0, i.e., for "rapidly" varying ($\omega_g / \omega_e > 1$) ground motions with respect to the structure frequency. In this section, the concepts of excess of *kinetic energy* and the *transient oscillation center* are examined for undamped nonlinear (bilinear) systems subjected to harmonic loading.

Contrary to the undamped linear system in which there was no dissipation of energy, the energy in undamped NL-SDOF systems is dissipated through inelastic behaviour of the system. An overview of loading assumptions for reproducing seismic response of structures by using harmonically applied loading is presented first. A sinusoidal function is then defined to excite structures from their rest conditions. The reference structure and system's nonlinear parameters are configured so that a wide range of isolated bridges subjected to different earthquake ground motions are covered.

7.3.3.1 Definition of Loading Function: Assumptions and Parameters

The loading function used for the L-SDOF systems is considered again here for the parametric study on the NL-SDOF systems:

$$P(t) = p_0 \cdot \sin(\omega_g t + \varphi) = -m \cdot \ddot{u}_0 \sin(\omega_g t + \varphi) = -m \cdot u_0 \cdot {\omega_g}^2 \sin(\omega_g t + \varphi) \tag{7.18}$$

where the phase angle $\varphi = 0°$ corresponds to the system's initial conditions at rest ($u(0) = 0$ or $\dot{u}(0) = 0$). These initial conditions were adopted to approximate the system response at the beginning of the few large amplitude cycles of the strong motion portion of a seismic ground motion..

In order to approximate seismic response using theoretical closed form solutions, various forcing functions have been studied by many researchers over the last decades. The response of systems initially at rest subjected to a series of load-time functions has been discussed by Jacobsen and Ayre (1958), Housner (1963), and Biggs (1964). Closed-form solutions have been proposed for the response of linear elastic systems for these loading functions. Iwan (1961) and Masri (1974) proposed "exact" analytical solutions for a steady-state response of bilinear systems. Despite the significant effort in developing "exact" solutions for bilinear systems analytically, there seems to exist no closed-form expression to obtain the transient response of an inelastic bilinear system subjected to sinusoidal loading.

Hall et al. (1995) introduced two types of simple ground pulses to idealize forward only (non-reversing) displacement and forward and back (reversing) displacement denoted as Type A and Type B, respectively. Makris (1997) proposed to approximate pulse-like ground motions with trigonometric functions having a cycloidal front. He highlighted that the use of such a function was preferred to the step-pulse loading previously proposed by Hall et al. (1995) since the possibility of a closed-form solution as well as that the response to this type of loading is not influenced by infinite accelerations or "jerks". Figure 7.19 presents two pulse motions of type A and B studied by Makris to simulate ground motions produced, respectively, by the 17 January 1994 Northridge and the 28 June 1992 Landers earthquakes.

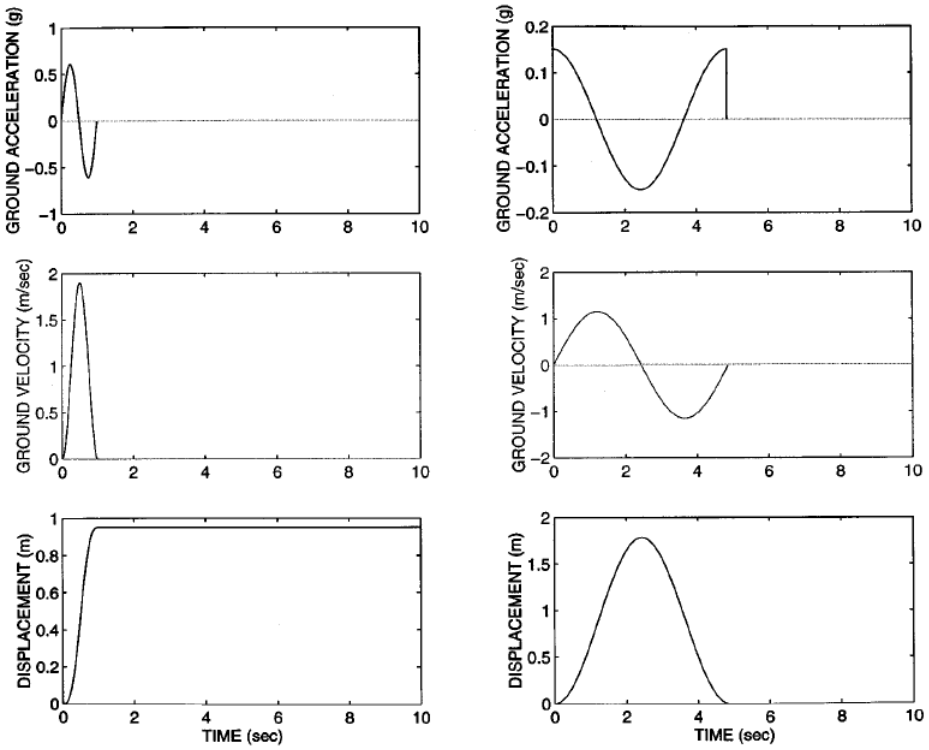

Figure 7.19 Cycloidal front pulses: Type A (left) and Type B (right) used by Makris (1997) to approximate recorded ground motions.

To assign the appropriate pulse amplitude and period, Makris (1997) manipulated the peak ground displacement and the peak ground velocity of the corresponding ground motion, so that the predominant period can be obtained by dividing the maximum ground displacement by the maximum ground velocity. While the maximum pulse displacement and velocity were in good agreement with those of the ground motion, the obtained accelerations underestimated the actual peak accelerations. As a result, to describe the pulse acceleration amplitude, $A_{\max}$, the following expressions have been proposed:

Type A:

$$A_{\max} = \omega_g V_g / 2 \tag{7.31}$$

Type B:

$$A_{\max} = \omega_g V_g \tag{7.32}$$

where ω_g is the pulse angular frequency and V_g is the maximum pulse velocity. The frequency ω_g is given by:

$$\omega_g = A_{\max} / V_g \tag{7.32}$$

In order to idealize the response of an undamped bilinear system subjected to earthquake ground motions, the sine loading function of A-type pulse as denoted by Makris (1997) was adopted in the study presented in this chapter. Such a pulse has the same effect as a suddenly applied force acting on the system initially at rest. After the loading has stopped, the system motion continues as a free vibration response with nonzero initial conditions. When more than one loading cycle is considered for analysis, between the transient state and state of free vibration, the steady-state response with stationary system motion can be obtained. However, during the transient response state, if the system experiences a *drift of the transient oscillation center*, the stationary motion will be occurring about a new shifted position of the *oscillation center* (as discussed in Chapter 6, see Figure 6.3).

Ten cycles of harmonic excitation with constant amplitude was applied to study the oscillation center phenomenon. The loading frequency is defined in terms of the frequency ratio, ω_g / ω_e. The frequency ratio is varied over a range between $\omega_g / \omega_e = 0.1$ and 2.0 with increments $\Delta(\omega_g / \omega_e) = 0.1$. For the frequency ratio $\omega_g / \omega_e = 0.1$, the duration of one loading cycle is equal to 10 times the period T_e of the analyzed SDOF system. Accordingly, the variation of the frequency ratio from ω_g / ω_e from 0.1 to 2.0 represents a loading duration ranging from 100 to 5 times the systems' elastic period T_e.

The range of frequency ratios ω_g / ω_e is chosen so that two resonant frequencies are covered: i) the resonant frequency corresponding to the elastic stiffness k_e and ii) the resonant frequency corresponding to the post-yielding stiffness k_d. When the system behaves essentially elastically, the effect of resonance occurs at the frequency ratio $\omega_g / \omega_e = 1$. The resulting response amplification is however constrained after the elastic limit u_y is reached and exceeded because high displacement response leads to a reduction of the effective stiffness of the system ($k_{eff} < k_e$) and, consequently, an effective frequency $\omega_{eff} < \omega_e = \omega_g$ that no longer corresponds to the

resonance conditions. A sustainable resonance effect can however be anticipated when the effective frequency approaches the frequency corresponding to the post-yield stiffness ($k_{eff} \rightarrow k_d$). The frequency ratio for this condition ($\omega_{eff} \rightarrow \omega_d$) can be determined as a function of the post-yield stiffness ratio α as follows:

System's elastic frequency is determined as:

$$\omega_e = \sqrt{\frac{k_e}{m}} \tag{7.33}$$

Post-yielding frequency related to the second slope stiffness αk_e :

$$\omega_d = \sqrt{\frac{k_d}{m}} = \sqrt{\frac{\alpha \cdot k_e}{m}} = \omega_e \sqrt{\alpha} \tag{7.34}$$

Resonance condition corresponding to the post-yielding stiffness k_d when:

$$\omega_g = \omega_d \tag{7.35}$$

By substituting Equation (7.34) in (7.35), the frequency ratio for post-yielding resonance is then given as:

$$\frac{\omega_g}{\omega_e} = \sqrt{\alpha} \tag{7.36}$$

Using Equation (7.36), the frequency ratios for post-yielding resonance are respectively equal to 0.71, 0.32, 0.22 and 0.1 for the selected values of α = 0.5, 0.1, 0.05, and 0.01 (see below).

7.3.3.2 Definition of the Nonlinear Parameters

The parametric study was performed on SDOF systems exhibiting a bilinear hysteretic response. Viscous damping is not considered in order to isolate the effect of the energy dissipated by a bilinear system through its hysteretic behaviour.

A range of nonlinear systems was considered by varying the response modification factor R and the post-yielding stiffness ratio α. Ten response modification factors R = 1.0, 1.25, 1.5, 2, 4, 8,

16, 28, 40 and 52 and four post-yield stiffness ratios $\alpha = 0.5$, 0.1, 0.05 and 0.01 were considered. While $\alpha = 0.1$, 0.05 and 0.01 are representative of structures equipped with typical isolation systems, the case $\alpha = 0.5$ is used to represent a non-isolated system. As mentioned, the ω_g / ω_e ratio was varied from 0.1 to 2.0.

To establish a common comparison basis, a unique peak elastic displacement u_e was used to determine the activation displacement, $u_y = u_e / R$ of all nonlinear systems. The displacement u_e was taken equal to the maximum elastic response for a frequency ratio $\omega_g / \omega_e = 1.0$. This ratio was selected because it corresponds to resonance and, therefore, leads to the maximum elastic displacement among all frequency ratios. However, peak undamped elastic response at resonance keeps increasing when applying several cycles of loading. For simplicity in this study, the maximum displacement at the end of the first cycle of loading was selected for u_e. The calculation of u_e is discussed next. This elastic displacement u_e corresponds to a ratio $R = 1$ and the activation displacement, $u_y = u_e / R$, of all nonlinear configurations was defined as a function of this elastic response, regardless of the frequency ratio. This represents an ensemble of isolated bridge structures having different activation displacements, each bridge being subjected to a series of harmonic signals exhibiting different frequencies.

The following paragraphs present the response at resonance of an elastic system subjected to a sinusoidal excitation. This information is used to determine the reference displacement u_e. It is also used later when defining the critical value of the R factor, R_{cr}. The equation of motion corresponding to the response of the undamped system is given as:

$$m\ddot{u}(t) + F_s(t) = p_0 \sin \omega_g t \tag{7.20}$$

and the transient and steady-state responses are as follows (Filiatrault, 2008):

$$u(t) = \frac{p_0}{m\omega_e} \int_0^t \sin \omega_g \tau \cdot \sin \omega_e (t - \tau) d\tau \tag{7.37}$$

Evaluating the integral of Equation (7.37), the response solution at an excitation time, t is:

$$u(t) = \frac{p_0}{k_e} \cdot \frac{1}{1 - {\omega_g}^2 / {\omega_e}^2} \cdot (\sin \omega_g t - \frac{\omega_g}{\omega_e} \sin \omega_e t) \tag{7.38}$$

where the first term is the static displacement:

$$u_{st} = \frac{p_0}{m{\omega_e}^2} = \frac{p_0}{k_e} \tag{7.39}$$

and the second term is the dynamic amplification factor, DAF:

$$DAF = \frac{1}{1 - {\omega_g}^2 / {\omega_e}^2} \tag{7.40}$$

From Equation (7.40), the system solution and *DAF* are undefined for the condition of resonance ($\omega_g = \omega_e$). To overcome this difficulty, the response is solved for an excitation frequency slightly smaller than the fundamental frequency of the structure. This assumption introduces a small error whose effect is of small influence and can be neglected.

With the objective of obtaining system responses without the necessity of specifying each parameter of an analyzed structure, displacement and time are normalized with respect to the static displacement and natural period, respectively. The normalized displacement as a function of normalized time is presented in Figure 7.20. It can be seen that for the first cycle, the maximum displacement response happens at a time corresponding to the system natural period. The maximum elastic displacement at this time can be then evaluated as a function of the static displacement, u_{st}:

$$u_e = u_{st} \cdot \pi \tag{7.41}$$

The displacement at the elastic limit is then determined as follows:

$$u_y = \frac{u_e}{R} = \frac{u_{st} \cdot \pi}{R} \tag{7.42}$$

Alternatively, using L'Hôpital's rule, it can be demonstrated that for the resonant condition, the response amplitude of an undamped SDOF system increases linearly at every cycle with an

increment per cycle equal to π for normalized response (Paultre, 2005). This is illustrated in Figure 7-21.

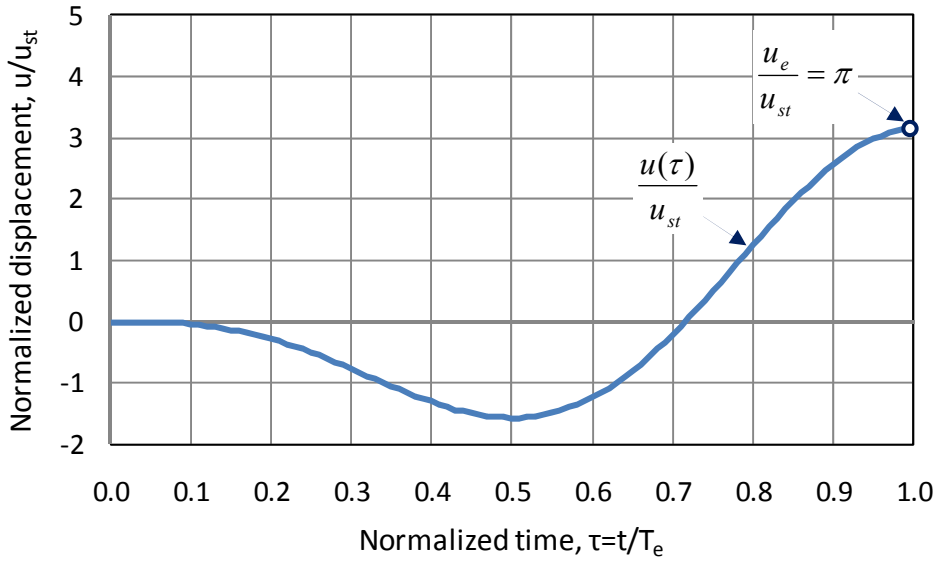

Figure 7.20 Normalized response of an elastic undamped system (1 cycle at $\omega_g / \omega_e = 1$)

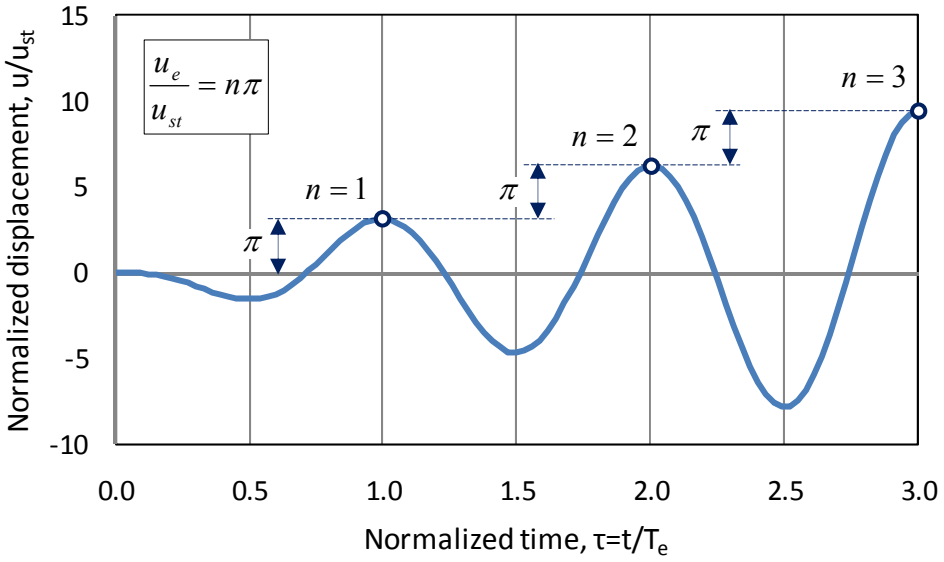

Figure 7.21 Amplitude increase with cycles for an elastic undamped system ($\omega_g / \omega_e = 1$)

It must be understood that the relationships presented by Equations (7.41) and (7.42) are valid only for this comparative analysis where a unique reference u_e is adopted to establish the same comparative basis. For a more general case, u_e has to be redefined for every added n^{th} cycle as:

$$u_e = n \cdot u_{st} \cdot \pi \tag{7.43}$$

7.3.4 NL-SDOF Response Mechanics: Results and Discussions

In this section, the results obtained from the parametric study on NL-SDOF systems subjected to harmonic excitation are presented and discussed. First, the maximum displacement responses obtained when applying one-cycle and ten-cycle sinusoidal loadings are examined and compared. Drift of the transient oscillation center is examined. The concept of a critical value for the response modification factor, R_{cr}, is then proposed and formulated. This critical value is introduced in order to better define NL-SDOF systems for which excessive energy is allocated to kinetic energy and results in *oscillation center drift*.

7.3.4.1 Results and Discussions

Figures 7.22 to 7.25 present normalized peak displacement amplitude (u / u_{st}) as a function of the frequency ratio for the four values of α. As explained in the previous subsection, the same elastic displacement u_e under a single cycle of sinusoidal excitation at a frequency ratio $\omega_g / \omega_e = 1$ was adopted to configure the systems' nonlinear parameters. The resulting activation displacement u_y varies with the R factor but it is kept the same for all frequency ratios and both loading conditions (one-cycle or ten-cycle excitations). For all cases, $R = 1$ correspond to elastic systems.

In Figures 7.22 to 7.25, nonlinear systems with $R = 1.25$, 1.5, and 2 under the single cycle loading exhibit responses close to that of the elastic system ($R = 1$) throughout the entire frequency range from $\omega_g / \omega_e = 0.1$ to 2.0. Systems designed with $R < 4.0$ can be defined as exhibiting a *limited-nonlinear behaviour* and their response will be mostly characterized by their elastic properties.

For systems with $R = 4$ and higher, the inelastic response is larger than the elastic one. This observation leads to the definition of *highly-nonlinear behaviour* more representative of the response of isolated bridges. As observed, the *highly-nonlinear* response becomes more pronounced when the ratio R is increased. As described in Chapter 6 (Figure 6.3), the system inelastic response becomes oriented closer to the post-activation stiffness k_d when R factor is increased. In the figure, this behaviour is reflected by a gradual shifting of the frequency ratio

where maximum response is obtained gradually shifting from the value of 1.0 to the value associated to the post-yielding resonance conditions defined by Equation (6.31) when increasing R. This shift from elastic to post-yield resonance is more pronounced when the system is subjected to the repeated loading of 10 cycles.

Using equations (7.41) and (7.43), the normalized peak displacement amplitude (u / u_{st}) for the elastic systems ($R = 1$) with $\omega_g / \omega_e = 1$ that are subjected to one-cycle or ten-cycle are 3.14 and 31.4, respectively. The response amplification caused by the elastic resonance is primarily due to the increase in energy stored within the system with each consecutive cycle. Such a resonance amplification is unbounded (Iwan, 1961), given that there is an energy excess which is the difference between the input energy and the energy dissipated by the system in each cycle. No amplification is observed for systems exhibiting *limited-nonlinear* responses as those with $R = 1.25$, 1.5, and 2.0. For *limited-nonlinear response*, the energy induced in the system over a loading cycle is dissipated through the system's inelastic response within the same cycle and the system generally oscillates about its original equilibrium position.

In contrast, for *highly-nonlinear* responses (in this study $R \geq 4$), the amplitude increase with the number of cycles is primarily due to the *drift of the oscillation center*. Such a drift results from the excess of energy, as was the case in the elastic resonance. However, when the system is in the *highly-nonlinear response range*, the energy excess is generated during a transient phase of loading and can be dissipated through a few consecutive cycles. This resonance amplification is bounded given that the *transient oscillation center* shifts gradually in each of these cycles until the excess of energy is entirely dissipated (as is further shown in this section). Unbounded resonance is expected, however, when $R \to \infty$ because the system cannot dissipate the input energy completely. Such a system behaves nearly elastically, with $k_{eff} \to k_d$, rather than inelastically. The unbounded inelastic behaviour is outside the scope of this study.

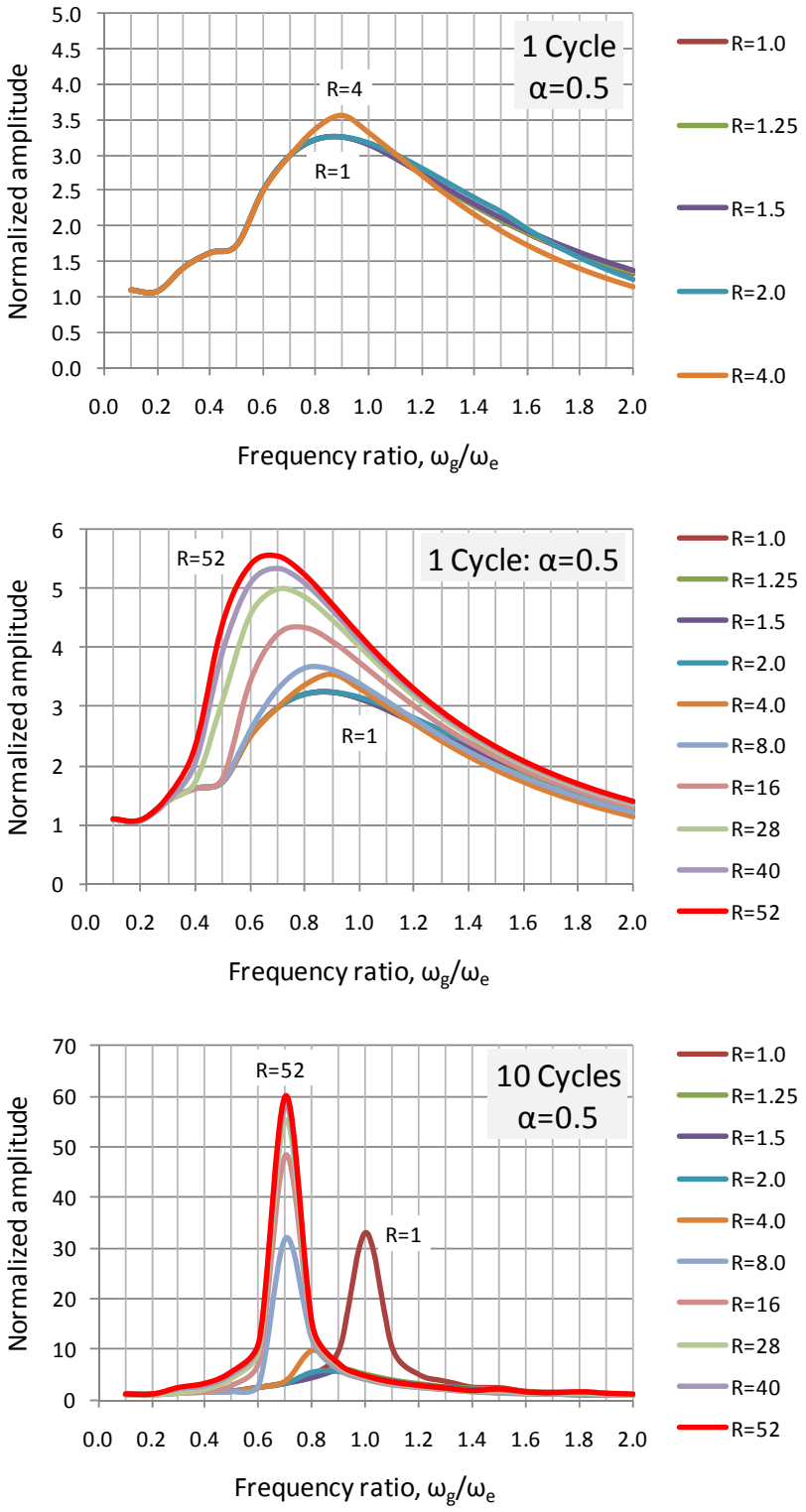

Figure 7.22 Normalized amplitude versus frequency ratio for different R-factors (1 cycle and 10 cycles loadings, $\alpha = 0.5$)

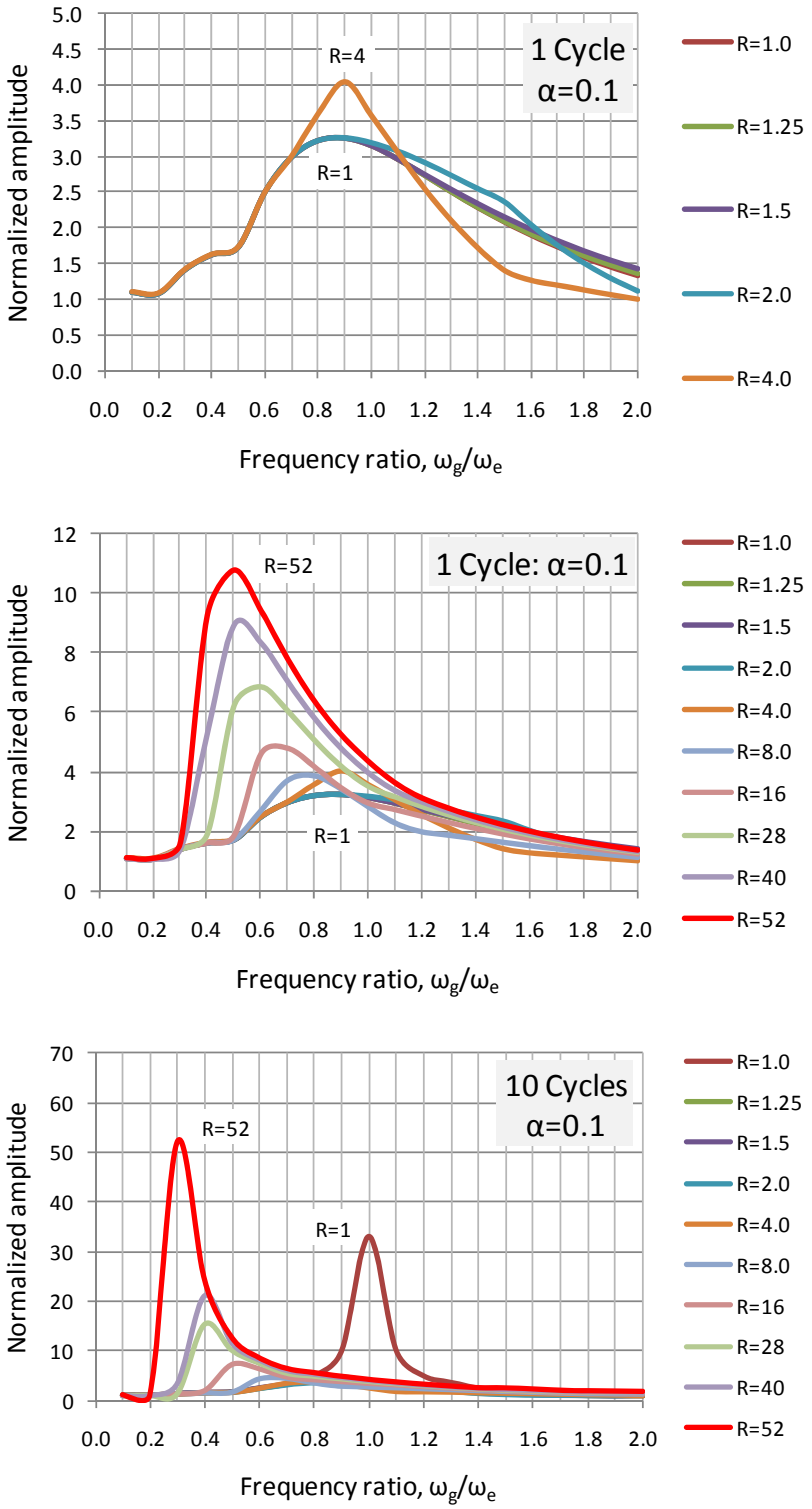

Figure 7.23 Normalized amplitude versus frequency ratio for different R-factors (1 cycle and 10 cycles loading, $\alpha = 0.1$)

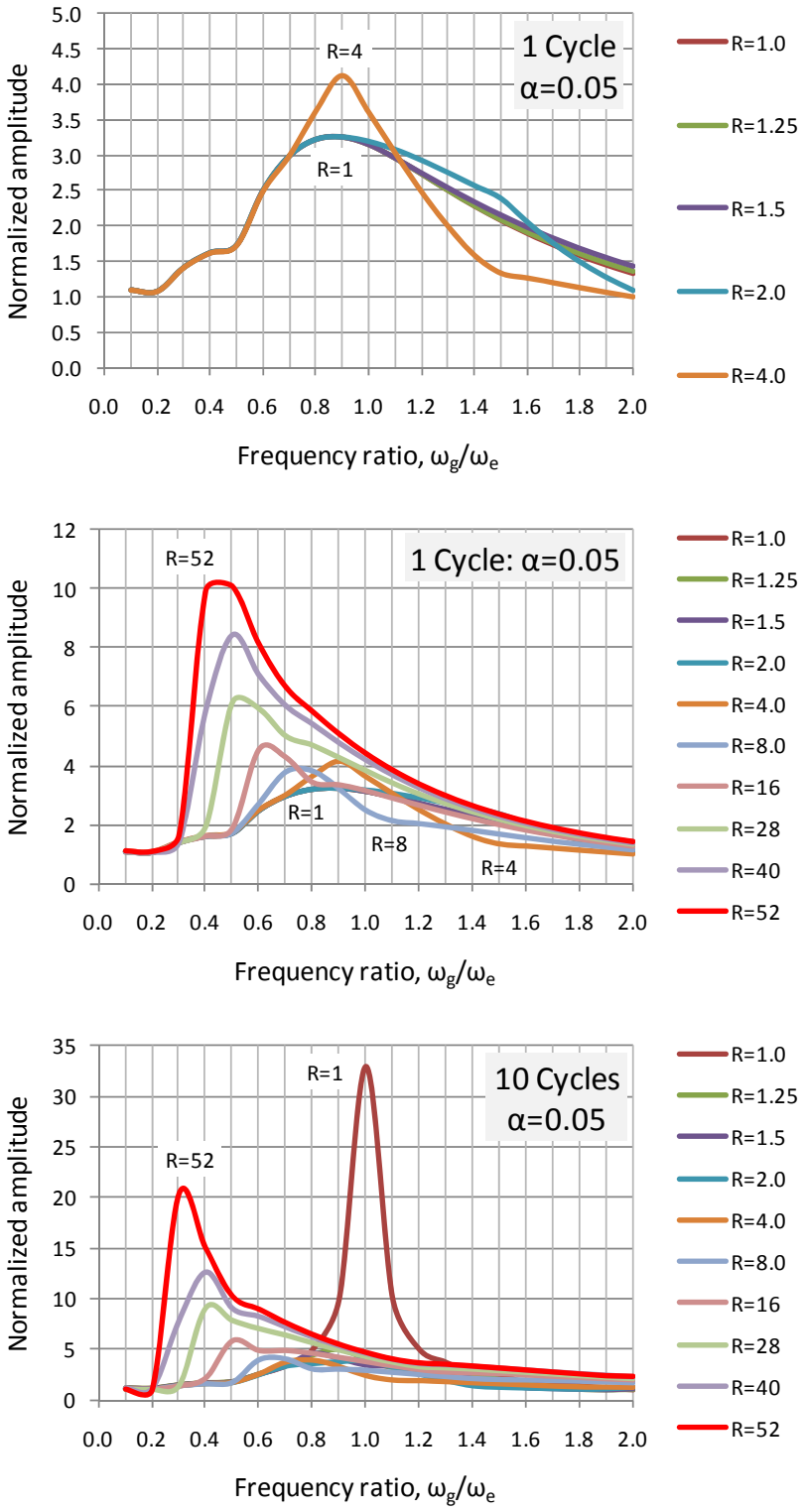

Figure 7.24 Normalized amplitude versus frequency ratio for different R-factors (1 cycle and 10 cycles loading, $\alpha = 0.05$)

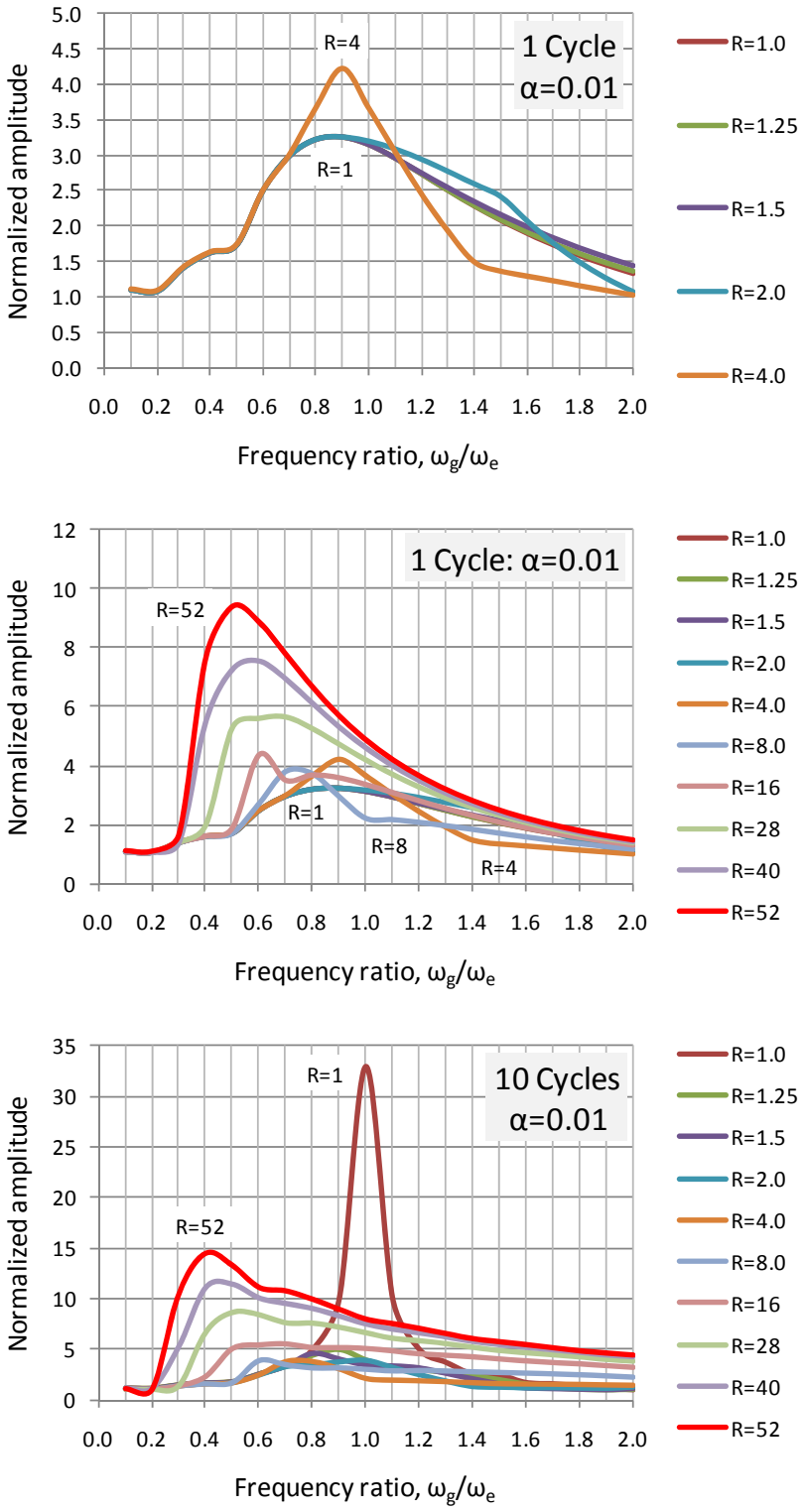

Figure 7.25 Normalized amplitude versus frequency ratio for different R-factors (1 cycle and 10 cycles loading, $\alpha = 0.01$)

To provide more insight into these observations, velocity and displacement response time histories under 10 cycles of sinusoidal loading are presented in Figure 7.25 for $\omega_g / \omega_e = 1$ and $\alpha = 0.01$. For the system with $R = 2$, the velocity response reaches its maximum during the second half of the first cycle. The same maximum positive and minimum negative velocities are observed in all subsequent cycles of loading. This highlights that there is a constant level of kinetic energy that is stored within the system. The peak displacement response is also reached during the second half of the first cycle. During the first half cycle, the system behaves elastically and it starts dissipating energy only in the second half cycle. As shown, the maximum displacement decreases in the subsequent cycles, indicating that the system's capacity to dissipate energy remains higher than the energy input.

The system with $R = 4$ also exhibits the maximum velocity level during the second half of the first cycle. However, lower velocity peaks are observed in the following cycles. The maximum displacement is observed during the first cycle. In the first half cycle, the system experiences inelastic excursions with similar maximum negative and the maximum positive displacements. This represents a *balanced displacement response*, meaning that the same amount of energy is dissipated in both directions during the cycle of loading.

Contrary to the *balanced displacement response* experienced by the system with $R = 4$, the systems with $R = 8$ and 16 exhibit an *unbalanced displacement response* which is skewed in the direction of the inelastic negative excursions. The maximum displacement response is observed during the first and second cycles for the systems with $R = 8$ and $R = 16$, respectively. In these cases, the maximum displacement comprises the oscillation center drift plus the local system response about the new oscillation center. The peak displacements for subsequent cycles are lower. The gradual reduction in displacement is attributed to the *drift of the transient oscillation center* towards the "at rest" equilibrium position. The initial shifting of the *transient oscillation center* results from the transformation of the excess of kinetic energy into the energy absorbed by the system. It can be observed by comparing systems with $R = 8$ and $R = 16$ in Figure 7.26, the system with the higher peak velocity during the first half cycle experiences the larger shift of the *transient oscillation center.*

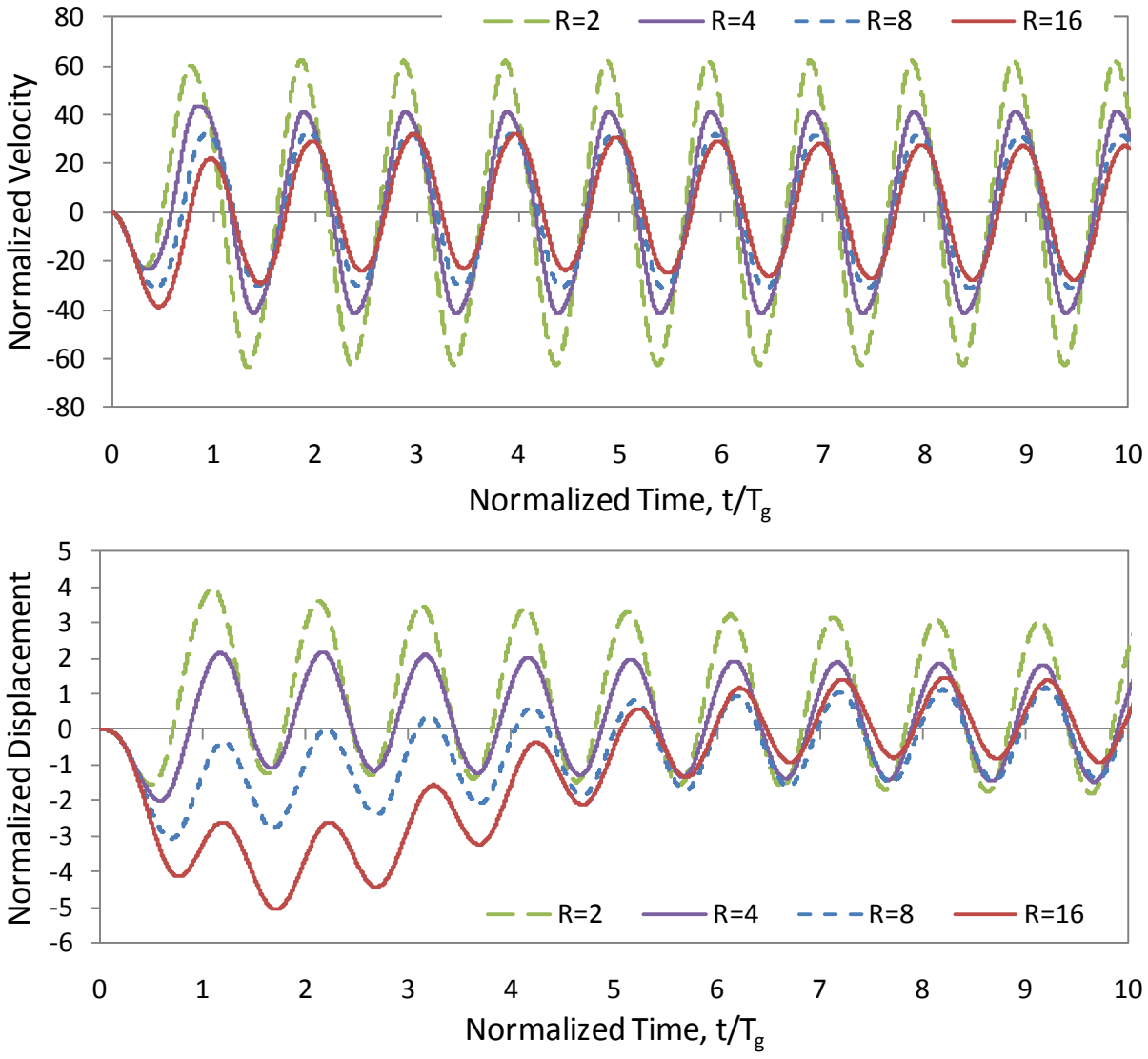

Figure 7.26 Time histories of velocity and displacement responses for NL-SDOF with $\omega_g / \omega_e = 1$, $\alpha = 0.01$ under 10 cycles of sinusoidal loading

The influence of the R factor on the energy flow is illustrated in Figure 7.27 for systems at resonance with $R = 2$, 4, and 16. In the figure the energies are normalized with respect to the common reference $u_{st} m \omega_g^2$ and all energy quantities for the three systems can be directly compared. In this figure, the straight dash-dotted line indicates an idealized input energy rate at which the system will exhibit a *balanced displacement response*. For the system with $R = 4$, the energy input is generally follows the straight line indicating that the amount of input energy induced in the system corresponds well to the system's capacity to absorb and dissipate this

energy completely over the same cycle of loading. For the system with $R = 2$, the energy input is situated under the straight line of the balanced displacement, which means that the system's capacity to store the input energy is underused and the system therefore exhibits *limited-nonlinear response*. For $R = 16$, the input energy is situated above the balanced energy straight line suggesting a *highly-nonlinear response*. In this case, much higher input and kinetic energies are developed over the first cycle.

The capacity to absorb energy of the system is reduced when increasing R, so that a larger portion of the energy input in the first half-cycle must transform into kinetic energy. Higher kinetic energy also means higher velocity in one direction. The system then has to absorb that kinetic energy so that the velocity returns to zero at peak displacement. This takes longer in time because of the limited capacity of the system to absorb energy. The shift in time for the kinetic energy built-up and transformation into absorbed energy up to peak displacement can be seen in Figure 7.27 when R is increased from 4 to 16.

The excessive kinetic energy over the first half response cycle can be confirmed by comparing the peak kinetic energy at the first, second and third *transient oscillation center*s (transient OC). This phenomenon is more pronounced in the first half-cycle, because energy dissipation has not started yet. After peak displacement has been reached, most of the energy stored in the system is dissipated and is no longer in the system to contribute to the response in the opposite direction. Energy dissipation, together with the fact that energy input no longer is in phase with points of system zero velocity, eventually leads to the stabilization of the response in the subsequent cycles.

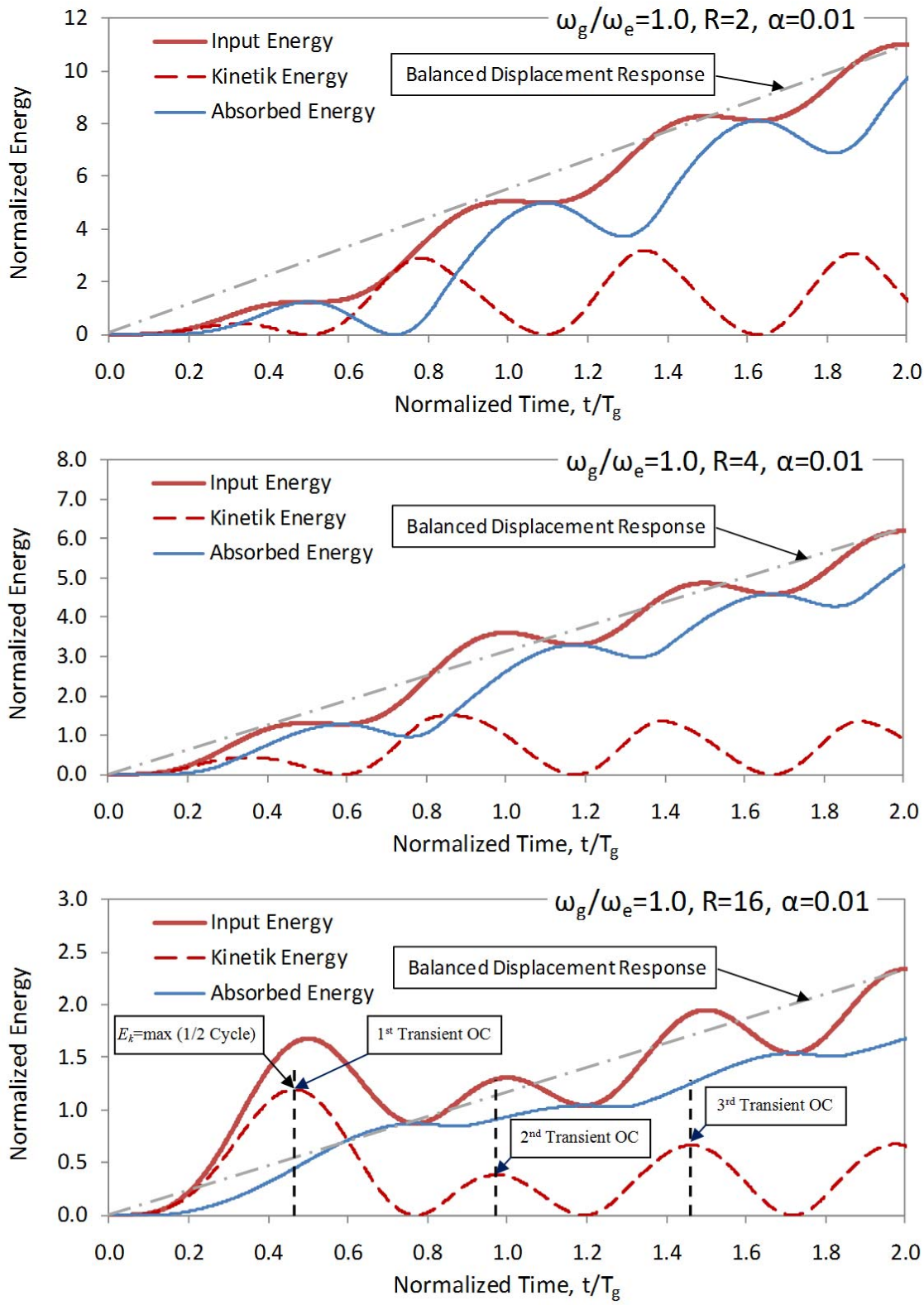

Figure 7.27 Energy allocation for NL-SDOF system with $\omega_g / \omega_e = 1$, $\alpha = 0.01$, $R = 2$, 4 and 16 (input, kinetic, absorbed energies, and power of balanced displacement response)

According to the observations discussed above, the response of the NL-SDOF systems can be classified as exhibiting either a *limited-nonlinear* or a *highly-nonlinear response*, where the transition between these two response types is defined by the *balanced displacement response* (as observed in this study for $R = 4$).

1) During the *limited-nonlinear response*, systems oscillate about its "at rest" equilibrium position and as previously discussed, the energy induced to the system over a loading cycle is dissipated completely through the system's inelastic response over the same cycle.

2) In turn, during the *highly-nonlinear response*, the systems experience the oscillation center drift which results from the kinetic energy excess. In such a case, the maximum displacement response consists of the oscillation center drift and the local system response about the new oscillation center. The energy excess generated during a transient phase of loading can be dissipated through a few consecutive cycles. The transient oscillation center shifts gradually with each of these cycles until the energy excess is entirely dissipated.

These results make it possible to provide a detailed insight into the response mechanics of the *limited-nonlinear* and *highly-nonlinear responses* from the perspective of the energy allocation. There appears to exist a limit between the two states of nonlinear behaviour and it is of interest to express this limit in terms the system's nonlinear parameters. The influence of the R factor on the energy flow explains why shifting of the OC is mainly observed in the first half-cycle, which is kept as the basis for the further developments that are presented in this and subsequent chapters.

7.3.4.2 Definition of Critical Response Modification Factor R_{cr}

As pointed out in the previous discussions, the system inelastic behaviour is characterized as *limited-nonlinear response* for low R or *highly-nonlinear response* for higher R-ratios. The point of transition between these two response states corresponds to the *balanced displacement response* that can be defined by a critical response modification factor R_{cr}. For $R < R_{cr}$, nonlinear systems generally exhibit a limited-nonlinear response with oscillations about their "at rest" equilibrium position. The response is therefore mostly characterized by the elastic properties of the system and. Conversely, for $R > R_{cr}$, *highly-nonlinear response* mostly oriented along the post-activation (or post-yield) stiffness k_d is observed. The systems are prone to oscillation center drifting that may results in relatively larger displacements (see Chapter 6, Figure 6.3).

A system with $R = R_{cr}$ can absorb exactly the entire amount of input energy in each of the two directions of motion. This corresponds well to a particular case of the transient response when the system behaves similarly to the one under a steady-state motion. For such a system, the energy input in the system within a loading cycle is dissipated completely over the same cycle. An energy excess on the form of kinetic energy will be absorbed by the system at a later time and will result in a larger inelastic excursion. Thus, the critical parameter R_{cr} is defined as the value of R that leads to the limit case of a *balanced displacement response* where the energy delivered by the excitation and the energy dissipated during one inelastic response cycle are equal and there is no drifting of the oscillation center.

The input energy for an entire cycle of loading is defined as:

$$E_{in} = \pi \cdot m \cdot \ddot{u}_g \cdot u_y \cdot \mu = \pi \, m \, u_g \, \omega_g{}^2 \, u_y \, \mu \tag{7.43}$$

The energy dissipated by a bilinear system over the entire cycle is determined as:

$$E_{Ab} = 4 \, k_e \, u_y{}^2 \, (1-\alpha) \, (\mu - 1) \tag{7.44}$$

Solving Equations (7.43) and (7.44) simultaneously for ductility response,

$$\mu = \frac{\alpha - 1}{\frac{\pi}{4} \cdot \frac{u_g}{u_y} \cdot \frac{\omega_g{}^2}{\omega_e{}^2} + \alpha - 1} \tag{7.45}$$

This is the solution for *balanced displacement response*, i.e., when the system has sufficient resistance to exactly absorb the kinetic energy within the same cycle, which leads to a stable bounded response, without drifting. If the resistance of the system is slightly reduced, drifting of the oscillation center will occur and the response will be unbounded, eventually resulting in a ductility that will tend to infinity. The value of R_{cr} can therefore be defined for the conditions that lead to $\mu = \infty$, i.e., when the denominator term in Equation (7.45) becomes equal to zero:

$$\frac{\pi}{4} \cdot \frac{u_g}{u_y} \cdot \frac{\omega_g{}^2}{\omega_e{}^2} + \alpha - 1 = 0 \tag{7.46}$$

$$\frac{u_g}{u_y} = \frac{4\,(1-\alpha)}{\pi} \cdot \frac{\omega_e{}^2}{\omega_g{}^2} \tag{7.47}$$

Rewriting Equation (7.47) in terms of the amplitude P_0 of the loading force and the activation force F_y by using $u_g = P_o\,/(m\omega_g{}^2)$ and $u_y = F_y\,/(m\omega_e{}^2)$ leads to:

$$\frac{P_o}{F_y} = \frac{4\,(1-\alpha)}{\pi} \cdot \frac{\omega_e{}^2}{\omega_g{}^2} \cdot \frac{m\omega_g{}^2}{m\omega_e{}^2} = \frac{4\,(1-\alpha)}{\pi} \tag{7.48}$$

This expression is in good agreement with that derived by Caughey (1960) and Iwan (1961) for the stability conditions of unbounded resonance under a steady-state motion at the frequency ratio $\omega_g / \omega_e = \sqrt{\alpha}$ (resonance condition corresponding to the post-yielding stiffness k_d). Contrary to this previous work, Equations (7.47) and (7.48) are derived for a transient phase of loading and may be applied for any frequency ratio.

In this study, the reference elastic displacement used to establish the activation displacements and R factors of the systems is defined as: $u_e = u_y \cdot R = \pi \cdot u_g$. Using this definition, the critical response modification factor R_{cr} is determined by posing $u_g = u_y \cdot R_{cr} / \pi$ in Equation (7.47):

$$R_{cr} = 4\,(1-\alpha) \cdot \frac{\omega_e{}^2}{\omega_g{}^2} \tag{7.49}$$

Balanced displacement response that corresponds to the transition state between *limited-nonlinear* and *highly-nonlinear* responses therefore depends on the post-yielding stiffness ratio and the frequency ratio. For instance, using Equation (7.49), a system with $\alpha = 0.01$ and a frequency ratio $\omega_g / \omega_e = 1.0$, as was examined previously in this section, will exhibit, *highly-nonlinear response* for R values higher than $R_{cr} = 3.96$. This limit is close to the value $R = 4$ for which a nearly *balanced displacement response* was found in the previous section (see Figure 7.27).

Figure 7.28 presents the maximum response and the maximum drift of the *transient oscillation center* as a function of the frequency ratio for the system with $\alpha = 0.01$ and $R = 16$. A large drift

of the *transient oscillation center* is observed for the frequency ratios higher than 0.5. This frequency ratio corresponds to the intersection of the curve R_{cr} and that of $R = 16$. Accordingly, at $\omega_g / \omega_e = 0.5$, $R_{cr} = 16$ indicates *balanced displacement response*. Using Equation (7.49), the critical frequency ratio that corresponds to the transition state between *limited-nonlinear* and *highly-nonlinear* responses for a given R factor may be determined as follows:

$$\left(\frac{\omega_g}{\omega_e}\right)_{cr} = \sqrt{\frac{4(1-\alpha)}{R}} \tag{7.50}$$

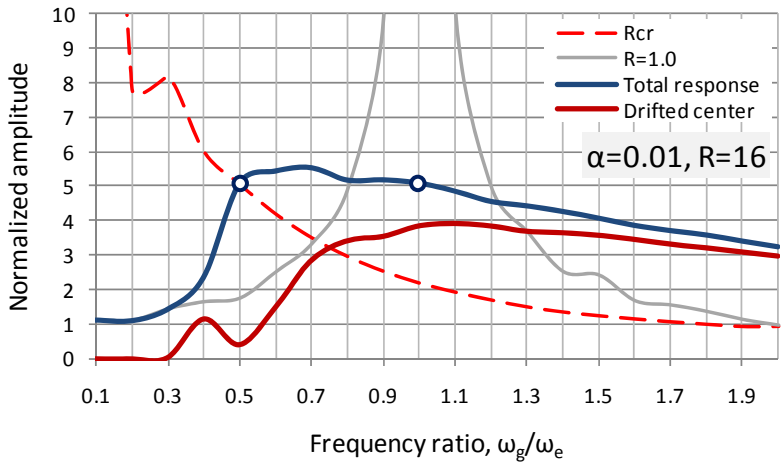

Figure 7.28 Normalized response with frequency ratio: maximum response and drifted oscillation center for $\alpha = 0.01$ and $R = 16$

In Figure 7.29, the computed response of the same system with $\alpha = 0.01$ and $R = 16$ is plotted for $\omega_g / \omega_e = 0.5$ and $\omega_g / \omega_e = 1.0$. In both cases, the maximum response is similar; however, the behaviour of the system is different. During a *balanced displacement response* ($\omega_g / \omega_e = 0.5$, $R_{cr} = 16$), the system oscillates about its original center of equilibrium. For the system with $R = 16$ at $\omega_g / \omega_e = 1.0$, the response is unbalanced and the system oscillates about a transient oscillation center that drifts progressively in each cycle. In such a case, the system experiences a *highly-nonlinear response* and the maximum response consists of the drift and local (about new oscillation center) displacements. These observations confirm that the expressions given by Equations (7.49) and (7.50) can accurately capture the point of transition between *limited-*

nonlinear and *highly-nonlinear* responses in terms of the nonlinear system parameters considered in this study.

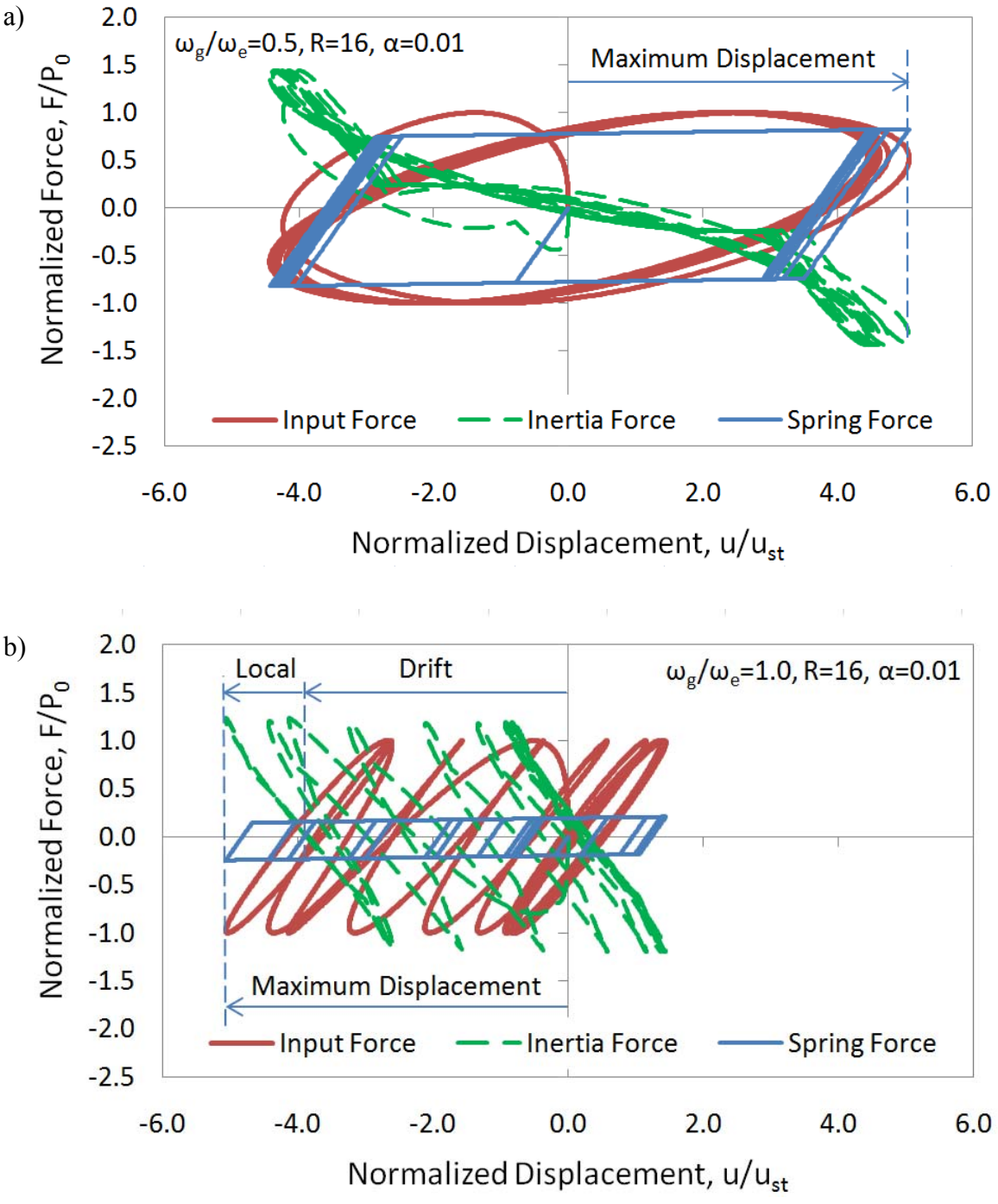

Figure 7.29 Normalized hysteretic response maximum response and drifted oscillation center for $\alpha = 0.01$, $R = 16$, and for: a) $\omega_g / \omega_e = 0.5$; b) $\omega_g / \omega_e = 1.0$.

7.4 Conclusions

In this chapter, the potential for the development of a new energy-based method to predict isolated bridge response more accurately is studied. Two widely adopted methods in earthquake engineering, the Equal Displacement (EDA) and the Equal Energy (EEA) approaches, were briefly reviewed and examined. It was found that the "exact" responses from NLTHA are confined by that obtained from these two response approximating techniques (EDA and EEA). The response estimates obtained by using the EEA were found to be conservative for all studied cases. It was shown that the differences between the response estimates from the EEA and “exact” NLTHA results may be related to the amount of absorbed energy. It was assumed that the difference in absorbed energy between these two responses can be attributed to the kinetic energy which is ignored when assuming that the input energy is absorbed entirely through monotonic loading. This portion of the energy input that is ignored by the EEA was termed as an *energy deficit*.

The energy concept used in the Equal Energy Approach was then considered as a basis for further development given that this approach relies upon the principle of conservation of energy. Then, the energy deficit was identified by studying the response of SDOF systems under harmonic excitation. To better characterize seismic response in the present study, special attention was drawn to the transient phase of loading that occurs at the beginning of the excitation.

According to the observations made in this study, bi-linear NL-SDOF systems were classified as exhibiting either a *limited-nonlinear* or a *highly-nonlinear response*. It was confirmed that during *limited-nonlinear response*, systems oscillate about their "at rest" equilibrium position and the energy induced into the systems over a loading cycle is dissipated completely through the system's inelastic response within the same cycle. In turn, during *highly-nonlinear response*, the systems experience a drift of the oscillation center which results from an excess of kinetic energy compared to the energy absorption capacity of the system. In such a case, the maximum displacement response consists of the drift of the oscillation center plus the local system response about the new oscillation center. The energy excess generated during a transient phase of loading can be dissipated through a few consecutive cycles. The transient oscillation center shifts gradually in each of these cycles until the energy excess is entirely dissipated.

The effect of the kinetic energy on the system behaviour was identified as a key element to be considered in the development of the new simplified method for complementing the assumptions of the original EEA. It is postulated that isolated bridge response can probably be predicted more accurately by using the concept of *energy allocation* under transient excitation, a concept that accounts for the transient response and possible shifting of the *transient oscillation center*, two aspects that are not accounted for in the current code simplified method. Using this approach, it was found that different system properties, including the initial elastic period, the post-activation stiffness and the R factor, as well as ground motion characteristics including amplitude and frequency content will be taken into account in the seismic response prediction.

Finally, the transition state between limited-nonlinear and highly-nonlinear responses was defined as the point beyond which the response of a system starts oscillating about a drifted equilibrium center. The critical parameter R_{cr} was derived to mark this point of transition.

Chapter 8: Proposed Energy-Based Simplified Analytical Method for Predicting the Response of Isolated Bridges

8.1 Introduction

In Chapters 5 and 6, it was shown that the simplified method, currently specified in the North American codes (CAN/CSA-S6-06 and AASHTO 2009, 2010), is subject to limitations that may affect the accuracy in predicting the peak response of isolated bridges. As shown in Chapter 7 these limitations are primarily attributed to the fact that the highly nonlinear response of isolated bridges is better characterized by the nonlinear dynamics of the system's response to transient dynamic loading rather than the steady-state loading and the phenomenon of shifting of the transient oscillation centre during the nonlinear response. These two aspects are not accounted for in current code simplified methods.

In addition, the previous study indicated that the response of isolated systems is dependent on the complex relation between the structure's properties and the ground-motion characteristics. It was also recognized that the use of the response modification factor R and the ratio between the structure's initial period and the ground-motion's predominant period T_e / T_g make it possible to better characterize the response of the structure to seismic loading.

These observations indicate that a new simplified method is needed that could address the limitations of current methods in accurately estimating the highly-nonlinear response of isolated bridges. The development of the new simplified method for predicting isolated bridge response is the main objective of the study presented in this chapter.

As discussed in the previous chapter, the energy concept used in the Equal Energy Approach (EEA) could be used as the basis for the development of a simplified analysis method that can be adopted in design process as an efficient alternative to the currently specified design approach (CSA-S6-06). The transient response and possible shifting of the *transient oscillation centre*, may be taken into account by applying the concept of *energy allocation* under transient excitation.

Based on this, a new simplified method that takes into account the differences in ground-motion characteristics and bridge design parameters is proposed. This method can predict the peak displacement of bilinear systems. This new energy-based *E-R-μ* method was developed purely based on analytical derivations rather than being empirically calibrated on a region-by-region basis to obtain accurate response predictions. The basis on which the predictions are made assumes that a) ground motions are represented by a single sine-wave pulse defined by *PGA* and *PGD* and b) response to that pulse can be predicted using the *E-R-μ* method.

In Section 8.2, the main assumptions and fundamentals of the energy-based *E-R-μ* relationship are presented. In Section 8.3, the new energy-based *E-R-μ* relationship is formulated. Given that this relationship is developed based on an energy formulation, the letter *E* was added to differentiate this proposed *E-R-μ* formulation from a series of existing *R-μ* relationships that have been derived empirically based on nonlinear time history analyses or other methods. The design procedure using this new energy-based *E-R-μ* relationship is proposed in Section 8.4. In order to harmonize the use of the proposed method with the design procedure specified in the CAN/CSA-S6-06, the terms and parameters commonly used in current design practice are adopted in the formulation of the method.

At the end of Section 8.4, the effectiveness and accuracy of the new energy-based method for capturing the response of highly-nonlinear systems is validated by comparing the response estimates against results from dynamic nonlinear time-history analyses (NLTHA) that were presented in Chapter 5. The results from NLTHA are compared to the response estimates made for isolated bridges in WNA and ENA by using the proposed method and the EEA.

8.2 Assumptions of New *E-R-μ* Relationships for the Proposed Energy Formulation for Bilinear Elastoplastic Systems

This section adapts the theoretical results from Chapter 7 to propose a design method for isolated bridges exhibiting a highly nonlinear response. The proposed method can predict the peak displacement of bilinear systems which is defined by structure parameters used in design of isolated bridges (the response modification factor R, elastic period T_e and post-yielding stiffness ratio α as shown in Figure 5.13). The bridge structure, being initially at rest, is assumed to be subjected to the ground motion excitation that are represented by a single sine-wave pulse

defined by *PGA* and *PGD*. To predict the peak displacement response to the pulse loading, an energy-based method is used. The energy method accounts for the excess in kinetic energy and shifting of the oscillation centre (OC).

Based on the results obtained in Chapter 7, the following assumptions are made for developing the new energy-based simplified design method:

1) As discussed in Section 7.3.3, an earthquake loading is not periodic. In order to approximate the seismic response of a system using theoretical solutions, the excitation is assumed to be a sinusoidal force function as was done for analyzing linear and nonlinear SDOF systems in Chapter 7. The same sine loading function (A-type cycloidal pulse) was proposed by Makris (1997) to idealize excitations representing pulse-like ground motions. The effect of such a pulse is similar to the effect of a suddenly applied force acting on a system which is initially at rest. To characterize the acceleration pulse of loading cycle, *PGA* and *PGD* values should be determined. To predict the demand under a specific ground motion, *PGA* is obtained from records; for design, *PGA* is obtained directly from seismic hazard design values provided by GSC (Geological Survey of Canada). For *PGD*, spectral displacement values are used for individual records and for design. The predominant ground-motion period T_g is obtained from *PGA* and *PGD* using Equation 8.1 (based on the assumption that the pulse is a sine wave). This assumption is similar to that made by Jacobsen and Ayre (1958) for transient responses to pulse-type excitations.

$$T_g = 2\pi\sqrt{\frac{PGD}{PGA}} \tag{8.1}$$

2) As confirmed in Chapter 7, an excess of kinetic energy is produced during a transient phase of loading when the system exhibits a highly nonlinear response to seismic loading. Such a response is expected when *R* is high, as in the case of isolated bridges exhibiting limited lateral resistance: the kinetic energy induced by large amplitude ground motion cannot be absorbed and dissipated within the first response cycle. The energy excess generated during a transient phase of loading can be dissipated through a few subsequent cycles. The transient oscillation centre shifts gradually with each of these cycles until the energy excess is entirely dissipated. As shown in Figures 7.26 and 7.29, such a behaviour is characterized by a skewed response which consists of consecutive drifts of the transient oscillation centre and the local

response around new equilibrium position. The sum of consecutive drifts results in a total drift. It is assumed that the total drift can be approximated by transforming the excess kinetic energy directly into energy absorbed during the total drift of the oscillation centre. The maximum displacement is then determined by adding the total drift resulted from this transformation to the local response around the drifted equilibrium positions.

3) As also pointed out in Chapter 7, the kinetic energy allocation corresponding to the maximum system displacement and to the position of the *transient oscillation centre* provides a better insight into the source of the *energy deficit* that marks the difference between the "exact" response and EEA estimate. In the EEA, the energy absorbed by an elastic system and that absorbed by a corresponding nonlinear system are assumed to be equal and are defined through the area under the force-displacement curve obtained for the first half cycle of the response. As a result, the energy absorbed by the nonlinear system under monotonic loading is assumed be equal to the work done by the excitation (P) and inertia (F_i) forces. The energy equilibrium is formulated for the first half cycle of the response.

The assumptions adopted for developing the energy-based E-R-μ relationship imply certain degree of conservatism. The energy transmitted to the isolated system is idealized as being representative of the system response under a sinusoidal excitation with a sole period T_g which relates the peak ground displacement and the peak ground acceleration. The response estimates will correspond to the response of isolated bridges under the most demanding loading conditions from the strong motion portion of a seismic ground motion.

Makris (1997), however, assumed that the acceleration record contains several random spikes that must be neglected in deriving a smooth acceleration function. In this way, the maximum values of Makris' acceleration function are 30% less than the recorded *PGA* value. This technique can be considered in the frame of specialized record-to-record analyses with a more detailed understanding of seismological effects.

The technique that was selected for evaluating *PGA*, *PGD* and T_g, and that was assumed for developing the new energy-based simplified method in the present chapter, is simple enough for its implementation in a new simplified design approach. In addition, because it utilizes the recorded *PGA* value, this new energy-based simplified method will provide engineers mostly with conservative response estimates which is also desirable for a design procedure.

Note that the source of the kinetic energy used to extend the EEA also represents a single excitation pulse. It is clear that being derived for a single loading pulse, this method has an inherent limitation to capture the effect of the loading duration or complex irregularity in the seismic excitation and the structural response. Accordingly, the discrepancies in the response estimate can be attributed to the effect of multiple *oscillation centre* drifts that originate from various loading pulses.

8.3 Development of New *E-R-μ* Relationships for the Proposed Energy Formulation for Bilinear Elastoplastic Systems

In this section, the proposed design procedure using a new energy-based *E-R-μ* relationship is formulated.

8.3.1 Development of New *E-R-μ* Relationships

The idealized force-displacement response and the corresponding input and kinetic energies are presented in Figure 8.1 (a) and (b). The energy that is absorbed during the nonlinear response of the system is formulated in Figure 8.1 (c). To account for the effect of damping, the dissipated portion of the absorbed energy is defined through equivalent damping and viscous damping ratios (β_{eq} and ξ). An equivalent presentation of the energy absorbed by a substitute equivalent structure is shown in Figures 8.1 (d) and (e) in terms of the strain energy and the portion of energy dissipated through viscous damping. In this approach, it is assumed that the system completes a half-cycle between the maximum and minimum displacements. As a result, the first half cycle is defined from the zero displacement to the maximum displacement u_m.

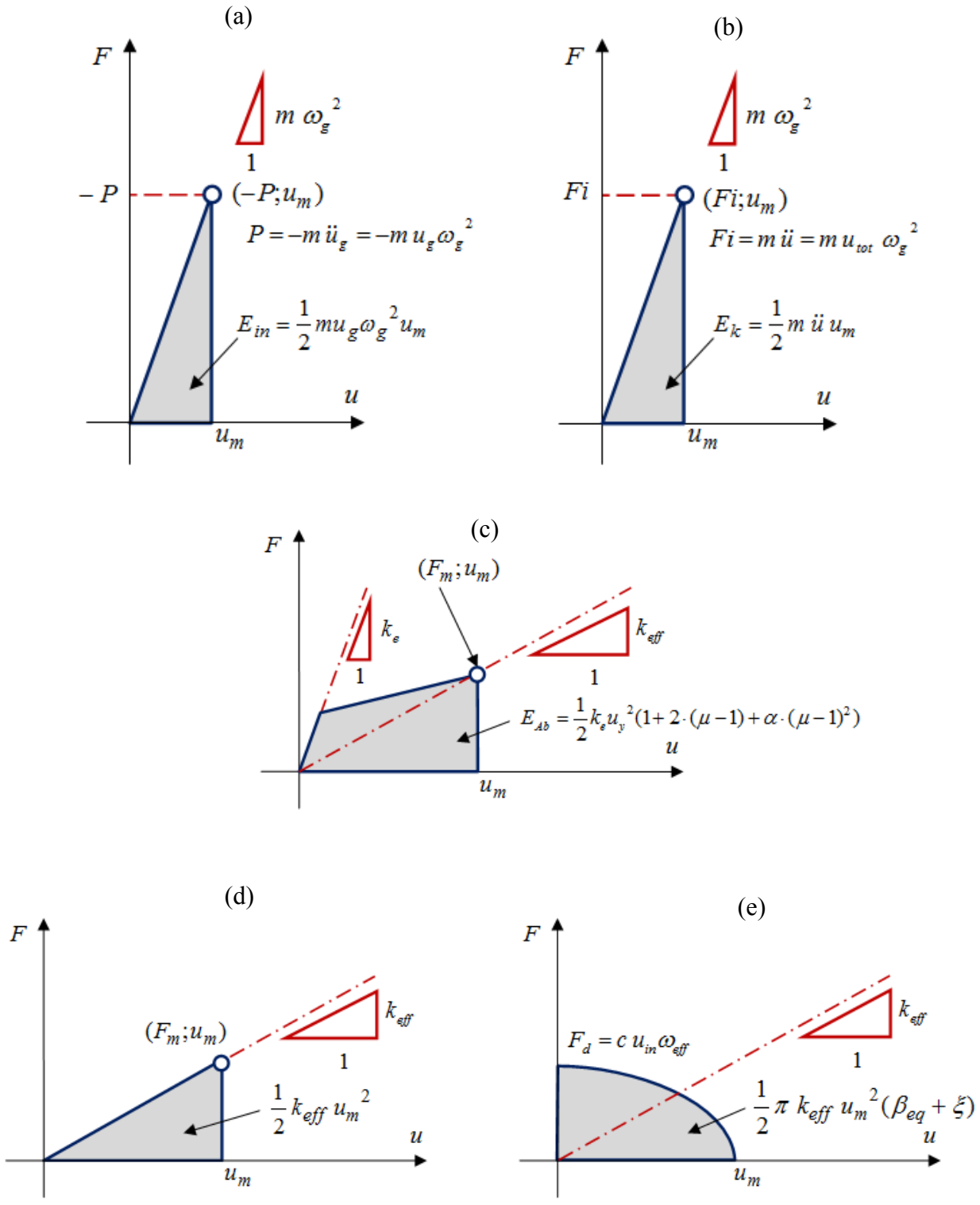

Figure 8.1 Idealized response a) input energy, b) kinetic energy, c) absorbed energy, d) equivalent strain energy as portion of absorbed energy, and e) dissipated portion of absorbed energy

The basis for the development of the new *E-R-μ* relationship is the energy equilibrium of the system, which is defined as follows:

$$E_{in} = E_k + E_{Ab} \tag{8.2}$$

The input energy is defined as a function of the maximum ground acceleration, $\ddot{u}_g$ and the maximum inelastic displacement, u_m:

$$E_{in} = \frac{1}{2} m \ddot{u}_g u_m = \frac{1}{2} m u_g \omega_g{}^2 u_m \tag{8.3}$$

where the maximum base acceleration is related to the maximum base displacement, u_g by:

$$\ddot{u}_g = u_g \omega_g{}^2 \tag{8.4}$$

The kinetic energy at the maximum displacement u_m, which corresponds to a first half cycle, is given by:

$$E_k = \frac{1}{2} m \, \ddot{u} \, u_m = \frac{1}{2} m \, u_{tot} \, \omega_g{}^2 u_m = \frac{1}{2} m \, \omega_g{}^2 u_m \, (u_m + u_g) \tag{8.5}$$

The energy absorbed by the system in a first half cycle under inelastic behaviour:

$$E_{Ab} = \frac{1}{2} k_e u_y{}^2 (1 + 2\,(\mu - 1) + \alpha\,(\mu - 1)^2) \tag{8.6}$$

The energy absorbed by the equivalent substitute system:

$$E_{Ab\,Eq} = \frac{1}{2} k_{eff} u_m{}^2 + \frac{1}{4} \pi \, k_{eff} u_m{}^2 \beta_{eff} \tag{8.7}$$

where β_{eff} represents both, equivalent and viscous damping ratios at k_{eff} ($\beta_{eq} + \xi\,(k_{eff})$).

The maximum inelastic response, u_m is presented in terms of the ductility as $u_m = u_y \, \mu$. The elastic limit, u_y is related to R ($u_y = u_e / R$), where u_e is the maximum elastic response that may

be determined as a 5% damped spectral displacement $u_e = S_D\,(5\%, T_e)$. To make u_g and $\ddot{u}_g$ representative of a generic seismic excitation, the peak ground displacement and acceleration are defined as suggested by Jacobsen and Ayre (1958) for transient responses to pulse-type excitations. The excitation is therefore defined as a sinusoidal force function $P(t) = -m\,\ddot{u}_g \sin(\omega_g t)$ applied to the system that is initially at rest ($\dot{u}(0) = u(0) = 0$).

The normalized ground acceleration, velocity and displacement as a function of time are shown in Figure 8.2. These functions were obtained by integrating the ground acceleration with respect to time and assuming zero initial conditions:

$$\dot{u}_g(t) = \int_0^t \ddot{u}_g \sin(\omega_g t)\,dt = -\frac{\ddot{u}_g}{\omega_g}\cos(\omega_g t) + C_v \tag{8.8}$$

where the arbitrary constant of integration C_v can be found by assuming that the ground velocity at t=0 is zero ($\dot{u}_g(0) = 0$):

$$C_v = \frac{\ddot{u}_g}{\omega_g}\cos(0) = \frac{\ddot{u}_g}{\omega_g} \tag{8.9}$$

Thus the function of the ground velocity starting at rest yields:

$$\dot{u}_g(t) = \frac{\ddot{u}_g}{\omega_g} - \frac{\ddot{u}_g}{\omega_g}\cos(\omega_g t) \tag{8.10}$$

Integrating Equation (8.10) once, the function of the ground displacement is:

$$u_g(t) = \int_0^t \frac{\ddot{u}_g}{\omega_g} - \frac{\ddot{u}_g}{\omega_g}\cos(\omega_g t)\,dt = \frac{\ddot{u}_g t}{\omega_g} - \frac{\ddot{u}_g}{{\omega_g}^2}\sin(\omega_g t) + C_u \tag{8.11}$$

where the integration constant equals zero ($C_u = 0$) to satisfy the zero ground displacement at rest.

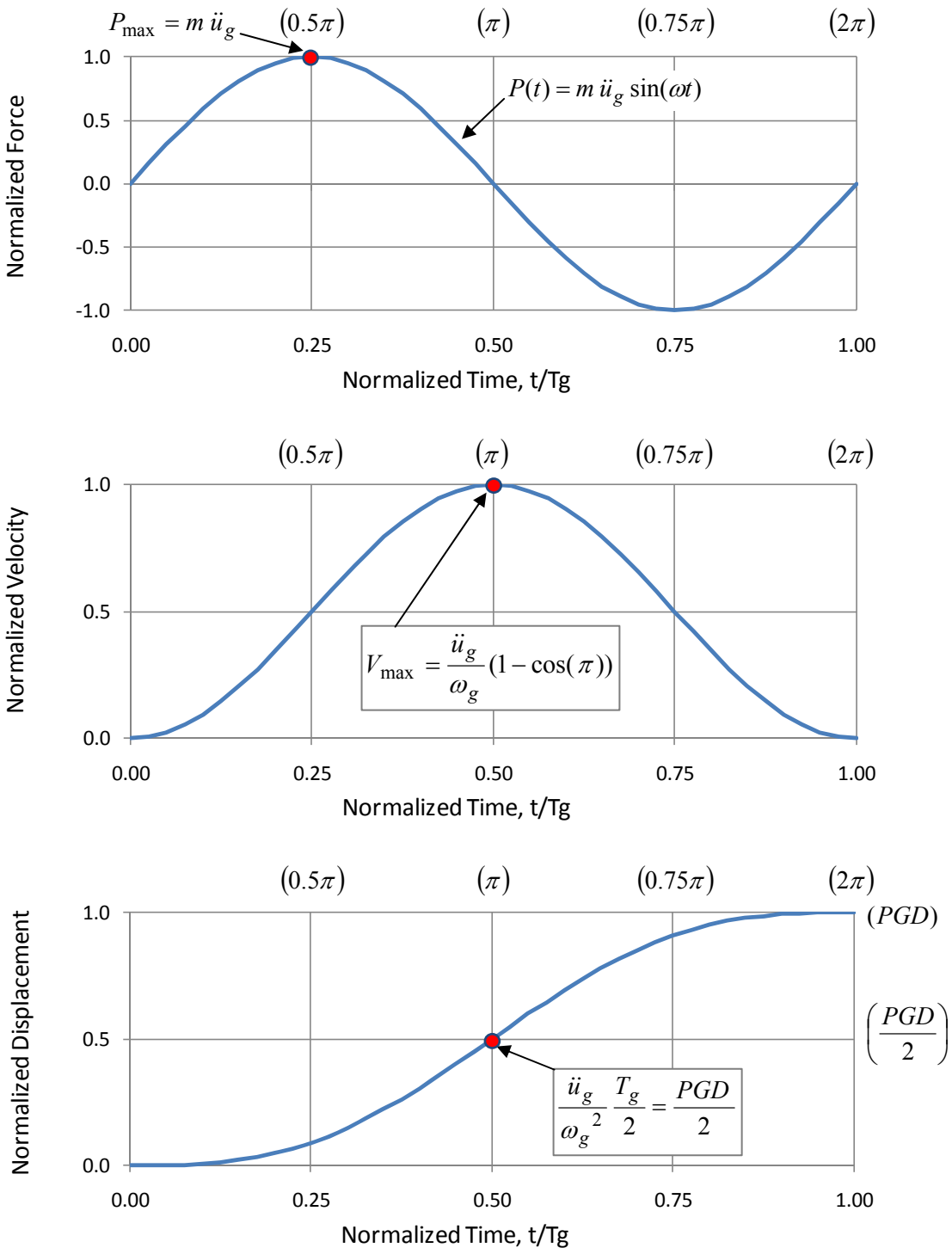

Figure 8.2 Characteristics of the ground forcing function

According to the assumptions in Section 8.2, the maximum ground displacement representative of a seismic peak ground displacement (*PGD*) occurs at the end of an entire cycle ($t = T_g$). However, the energy equilibrium is formulated for the first half cycle. The ground displacements at time T_g (at $w_g t = 2\pi$) and $T_g / 2$ (at $w_g t = \pi$) can be found by using Equation (8.11) with $C_u = 0$:

$$u_g(T_g) = \frac{\ddot{u}_g}{\omega_g} T_g - \frac{\ddot{u}_g}{{\omega_g}^2} \sin(2\pi) = \frac{\ddot{u}_g}{\omega_g} T_g = PGD \tag{8.12}$$

$$u_g(T_g/2) = \frac{\ddot{u}_g}{\omega_g} \frac{T_g}{2} - \frac{\ddot{u}_g}{{\omega_g}^2} \sin(\pi) = \frac{\ddot{u}_g}{\omega_g} \frac{T_g}{2} = \frac{PGD}{2} \tag{8.13}$$

The maximum base displacement u_g and acceleration $\ddot{u}_g$ corresponding to the half cycle that is used in the analytical formulation are defined as follows:

$$u_g = PGD/2 \text{ and } \ddot{u}_g = u_g {\omega_g}^2 = (PGD/2)\, {\omega_g}^2 \tag{8.14}$$

Substituting equations (8.3), (8.5), and (8.6) in the energy balance equations for the system without added damping ($E_{in} = E_k + E_{Ab}$) and solving for *R*, the *E-R-μ* relationship is defined as:

$$R = \frac{u_e\, \mu}{PGD} + \frac{u_e\, {\omega_e}^2}{PGA} \left(\alpha\mu + (\alpha - 1)\,(1/\mu - 2) \right) \tag{8.15}$$

For the system with added damping, instead of using Equation (8.6), *R* may be determined with the equivalent formulation for the absorbed energy (Equation (8.7)):

$$R = \frac{u_e\, \mu}{PGD} + \frac{u_e\, {\omega_e}^2}{PGA} \left(3 + \mu\alpha - 3\alpha - \beta_{eff}\, \pi\, (1 + \mu\alpha - \alpha)/2 + 2\,(\alpha - 1)/\mu \right) \tag{8.16}$$

In Figure 8.3, the interaction of the input and kinetic energies (E_{in}-E_k) as a function of ductility is shown against the corresponding function of the energy absorbed by the system E_{Ab}. The energy E_{in}-E_k represents the amount to be absorbed by the system at the end of loading in the direction of the inelastic excursions. It can be noted that the absorbed energy grows with ductility until the

input equals the kinetic energy. The maximum possible magnitude of the absorbed energy corresponds to the case where the kinetic energy approaches zero (intersection of the curves E_{in} and E_{in}-E_k). This point corresponds to the critical ratio R_{cr} as discussed in Chapter 7. The critical ratio R_{cr} is formulated in Equation (8.17) using the current code parameters. This equation was obtained by substituting Equation (7.42) in Equation (7.47). Given that this expression was derived using the entire loading cycle, the ground displacement amplitude u_g was set equal to the *PGD* rather than obtained using Equation (8.14).

$$R_{cr} = \frac{u_e}{PGD} \cdot \frac{4\,(1-\alpha)}{\pi} \cdot \frac{{\omega_e}^2}{{\omega_g}^2} = \frac{u_e}{PGD} \cdot \frac{4\,(1-\alpha)}{\pi} \cdot \frac{{T_g}^2}{{T_e}^2} \tag{8.17}$$

This expression indicates the transition state between *limited-nonlinear* and *highly-nonlinear responses* and suggests whether the system has sufficient strength to exactly absorb the kinetic energy within the same cycle of loading, which leads to a stable bounded response, without drifting. The system oscillates about its original center of equilibrium as shown in Figure 7.29 (a). This represents a *balanced displacement response*, meaning that the same amount of energy is dissipated in both directions during the cycle of loading.

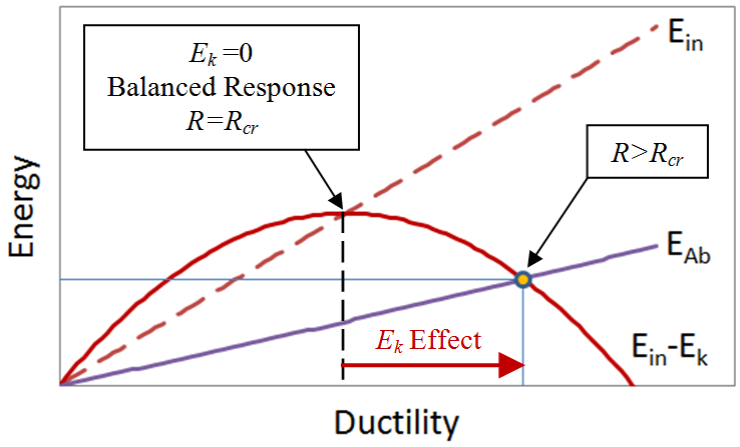

Figure 8.3 Concept of energy balance for transient response

Accordingly, the range of applicability for equations (8.15) and (8.16) corresponds to a *highly-nonlinear response* which is defined within $R_{cr} < R < \infty$. When Equation 8.17 yields $R_{cr} \leq 1.0$, a *balanced displacement response* is not possible and the structure will experience a highly nonlinear response as soon as the structure exceeds its elastic limit. For such a case, R_{cr} is set to 1.0.

For structures with response modification factors greater than R_{cr}, the capacity to absorb energy of the system is reduced when increasing R (reducing strength), so that a larger portion of the energy input E_{in} in the first half-cycle must transform into kinetic energy E_k. In such a case, the transient OC shifts gradually with each of consecutive cycles until the energy excess is entirely dissipated. The energy excess will be absorbed by the system at a later time and will result in a larger ductility demand. This is illustrated in Figure 8.3 as E_k Effect.

8.3.2 Influence of Ground-Motion and Nonlinear System Parameters

To better understand the influence of different ground-motion and nonlinear system parameters on the response estimates obtained through the energy-based *E-R-μ* relationship, Equation (8.15) is rearranged. After substituting the PGA obtained using the pseudo relationship $PGD \cdot \omega_g{}^2$ and by replacing the frequency terms (ω_g and ω_e) by the corresponding periods, the solution becomes:

$$R = \frac{u_e}{PGD}\mu + \frac{u_e}{PGD}\frac{T_g{}^2}{T_e{}^2}\left(\alpha\mu + (1-\alpha)(2-1/\mu)\right) \tag{8.18}$$

The effect of the loading with "slowly" or "rapidly" varying forces which was discussed in detail in Chapter 7 (see Figure 7.12) is captured by the period ratio T_g / T_e in the second term of Equation (8.18). Accordingly, the effect of the kinetic energy excess is taken into account by the second term in this formulation.

The second term can be reorganized to isolate the effect of the kinetic energy on the sytem response within its elastic and inelastic ranges as follows:

$$R = \frac{u_e}{PGD}\mu + \frac{u_e}{PGD}\frac{{T_g}^2}{{T_e}^2}\alpha\mu + \frac{u_e}{PGD}\frac{{T_g}^2}{{T_e}^2}(1-\alpha)(2-1/\mu) \tag{8.19}$$

$$R = \frac{u_e}{PGD}\mu + \frac{u_e}{PGD}\frac{{T_g}^2}{{T_d}^2}\mu + \frac{u_e}{PGD}\frac{{T_g}^2}{{T_e}^2}(1-\alpha)(2-1/\mu) \tag{8.20}$$

For systems with supplemental damping, Equation (8.16) is rearranged to obtain an expression similar to Eq. 8.18):

$$R = \frac{u_e}{PGD}\mu + \frac{u_e}{PGD}\frac{{T_g}^2}{{T_e}^2}\left(3+\mu\alpha-3\alpha-\beta_{eff}\pi(1+\mu\alpha-\alpha)/2+2(\alpha-1)/\mu\right) \tag{8.21}$$

For a given response modification factor R, the maximum response is reached when the second and third terms of Equation (8.20) tend towards zero. As such, the E-R-μ relationship is reduced to the following form:

$$R = \frac{u_e}{PGD}\mu \tag{8.22}$$

and the maximum ductility response is:

$$\mu = \frac{R \cdot PGD}{u_e} = \frac{PGD}{u_y} \tag{8.23}$$

As a result, the maximum displacement of the structure equals the peak ground displacement PGD for a "perfectly" isolated structure for which the motions of the mass and the base of the system are completely uncoupled ($u_m = PGD$). In Equation (8.20), the second and third terms tend to zero when the periods T_d and T_e become very large, i.e. for a structure that has an infinitely small stiffness or an infinitely large mass. When the second and third terms of Equation (8.20) become less significant, the response is dominated by the first term that represents isolation effects. The same effect is attained when the ground-motion predominant period is very short which is representative of a very "rapidly" varying loading force (see Figure 7.12).

The effect of the period ratio T_e / T_g on the response amplitude is presented in Figure 8.4. The

response amplitude in terms of the ductility ratio was calculated using Equation (8.20) for different R and α-ratios. It can be observed that the maximum response amplitude corresponds to the post-yielding resonance defined by Equation (7.36). This resonance condition corresponding to the post-yielding stiffness k_d is met when $T_g = T_d$ and the ratio $T_e / T_g = T_e / T_d = T_e / (T_e / \sqrt{\alpha}) = \sqrt{\alpha}$. It can be noted that for higher period ratios, which correspond to systems with relatively longer elastic periods, the response amplitude decreases and tends to the ground displacement or, in terms of ductility, to $\mu = PGD / u_y$ (see Equation (8.23)). The tendencies observed from Figure 8.4 are in good agreement with those presented in Chapter 7 (see Figures 7.22 to 7.24) for the response of NL-SDOF systems under harmonic excitation. This confirms the ability of the proposed E-R-μ relationship to properly take into account the complex relation between the structure's nonlinear response and the ground-motion characteristics that are not accounted for in the code simplified methods.

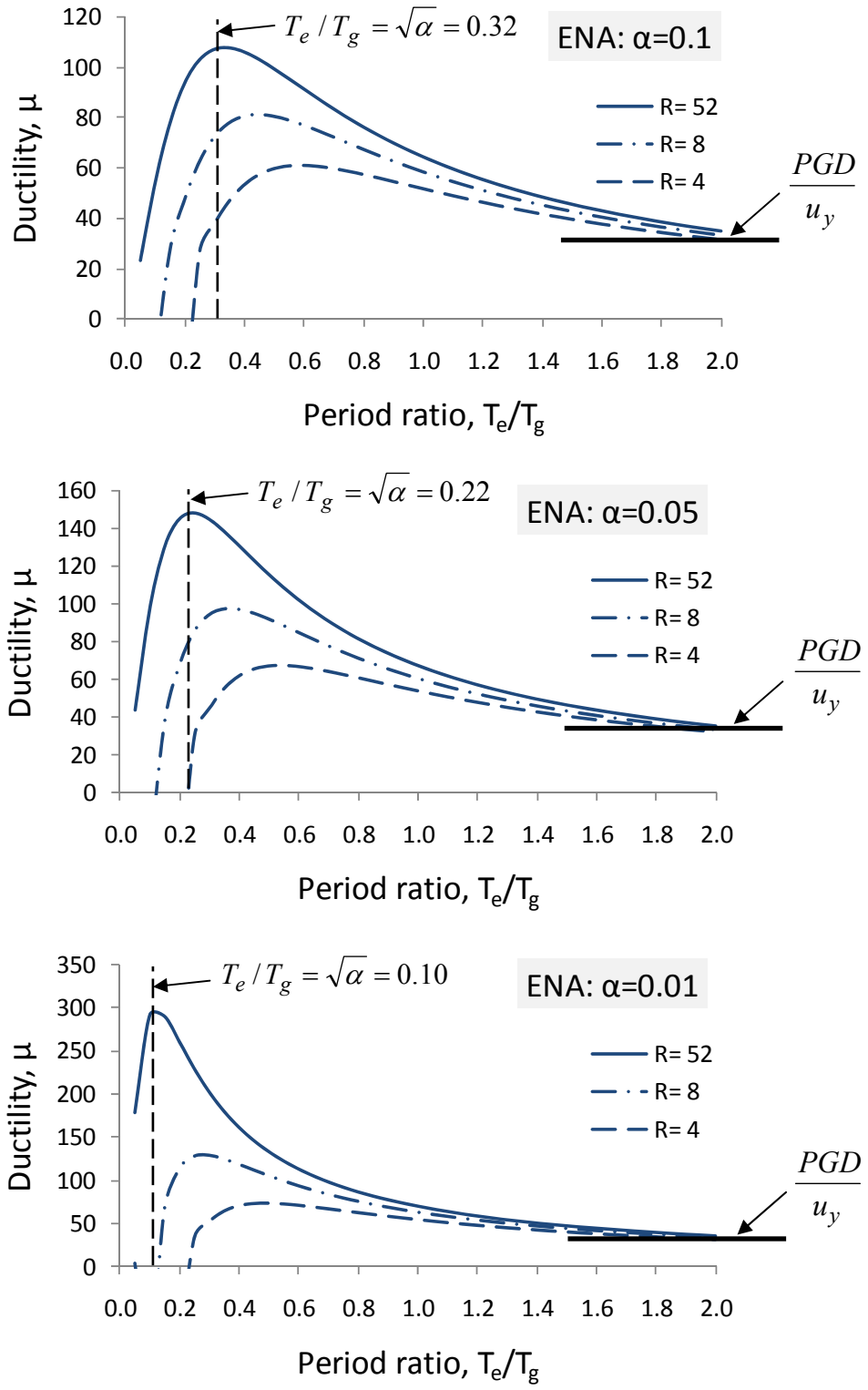

Figure 8.4 Ductility response with ratio T_e / T_g using the *E-R-μ* relationship with *PGD* = 72 mm, T_g = 0.9 s, $u_e(T_e) = 40T_e$ (mean parametres - 20 Atkinson's records)

Figure 8.5 compares *R*-ratios, obtained for ENA ground motions by using the *E-R-μ* relationship (Equation (8.20)), with those from the EEA *E-R-μ* expression given by Equation (7.7) for $\alpha > 0$. The two expressions are in good agreement for the elastic period $T_e = 0.25$ s. However, the *R* ratios diverge for a range of $0.25 \text{ s} < T_e \leq 0.75$ s. In this period range, the ductility responses obtained with the proposed *E-R-μ* relationship are lower than those from the EEA when they are compared for the same *R*-ratios. The *R* ratios from the *E-R-μ* relationship are found to increase with increasing elastic period.

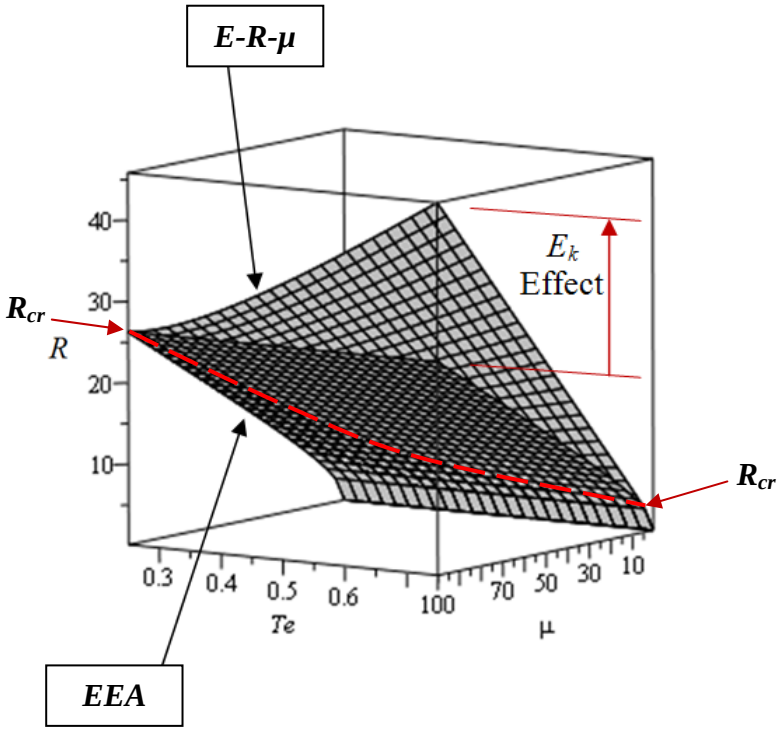

Figure 8.5 *E-R-μ* relationship obtained from Equation (8.20) compared to *R-μ* expression for EEA given by Equation (7.7): ENA for $\alpha = 0.05$

The dashed red curve represents the R_{cr} values and indicates whether the two methods diverge. These observations highlight the capacity of capturing the effect of the kinetic energy excess on the system response with the proposed *E-R-μ* relationship. The same trends resulted from the effect of the kinetic energy are observed in Figure 8.3. Structures with response modification factors greater than R_{cr}, respond with a decrease of the absorbed energy while they experience an increase in their ductility demand. In contrast with the *E-R-μ* relationship, the *EEA* method assumes that the system oscillates about its original center of equilibrium ($E_k = 0$) and the input

energy E_{in} is fully transformed into the energy absorbed by the system E_{Ab} leading to a larger displacement response.

8.4 Design Procedure and Validation

In this section, the proposed energy-based *E-R-μ* relationship is adapted for the design of bridges equipped with seismic isolation systems. First, the *E-R-μ* method is formulated as a direct design procedure. Then, an iterative design procedure is proposed to facilitate the implementation of the method in current North American design practice. The effectiveness and accuracy of the *E-R-μ* method for capturing the response of highly nonlinear systems is validated by comparing the response estimates against results from dynamic NLTHA.

8.4.1 Design Implementation of the Energy-Based *E-R-μ* Method

The steps for the design procedure are outlined in Table 8-1.

The ground-motion characteristics for the actual bridge location, importance category and site are determined first in Step 1. The design response spectrum is selected to represent the earthquake scenarios for the seismic hazard at the site using the uniform hazard spectrum (UHS) currently used in NBCC (NRCC, 2005) for buildings that will be adopted as the design spectrum in the next CSA-S6-14. When a displacement S_D design spectrum is not available, the pseudo displacement PS_D spectrum is used instead for the design process. The S_A spectrum provides the peak ground acceleration *PGA* while the peak ground displacement *PGD* is determined as the pseudo-displacement at the longest available spectral period. Alternatively, the displacement response spectrum S_D and the corresponding *PGD* may be determined using a simple method specified in Eurocode 8 (EC8) as shown in Figure 2.2. The predominant ground-motion period is calculated using Equation (8.1) in Step 2.

In Step 3, the properties of the isolated bridge system are determined as follows:

m - mass of the of the bridge superstructure;

T_e - initial elastic period:

$$T_e = 2\pi \cdot \sqrt{\frac{m}{k_e}} \tag{8.24}$$

where

k_e - lateral elastic stiffness represents the contribution of the substructure elements including piers, abutments, isolation devices and determined using Equations (3.1) to (3.3).

T_d – post-yield period of vibration defined using the post-yielding stiffness $k_d = \alpha\, k_e$ as follows:

$$T_d = 2\pi \cdot \sqrt{\frac{W}{k_d \cdot g}} \text{ or } T_d = T_e / \sqrt{\alpha} \tag{8.25}$$

u_y - deck displacement at activation of the isolation system;

ξ_{inh} - inherent damping which corresponds to the damping level of the design response spectrum;

ξ_{el} - damping ratio of viscous dampers determined at an elastic period T_e.

In Step 4, the maximum elastic displacement u_e is determined using the damped design response spectra as follows:

$$u_e = S_D(T_e; \xi_{inh}) \tag{8.26}$$

In Step 5, the response modification factor R is determined as the ratio between the activation displacement of the isolation system u_y and the maximum elastic displacement u_e.

$$R = \frac{u_e}{u_y} \tag{8.27}$$

Equation (8.20) can be used to determine the response modification factor R for a given set of the isolated structure's properties, ground motion characteristics and a target ductility. Alternatively, the system's response in terms of ductility can be determined from Equation (8.20) for a given R-factor by trials and errors in Step 6. In cases where supplemental damping devices are used, Equation (8.21) can be used instead of Equation (8.20) to determine the system's response.

In Equation (8.21), the effective damping ratio β_{eff} represents both, equivalent and viscous damping ratios determined at the effective period T_{eff}. The equivalent damping ratio β_{eq} and effective period T_{eff} are defined in Chapter 2 using Equations (2.4) and (2.2), respectively. The effective damping can be then determined as a function of ductility as follows:

$$\beta_{eff} = \beta_{eq} + \xi_{el}\frac{T_{eff}}{T_e} = \frac{2}{\pi}\cdot\frac{(\mu-1)\cdot(1-\alpha)}{\mu\cdot(1+\alpha\mu-\alpha)} + \xi_{el}\sqrt{\frac{\mu}{1+\alpha\mu-\alpha}} \tag{8.28}$$

Once the solution for the ductility μ is obtained in Step 6, the displacement response of the bridge deck is calculated in Step 7 using Equation (8.29).

$$d = \frac{u_e}{R}\cdot\mu \tag{8.29}$$

Table 8-1 Direct energy-based *E-R-μ* design method

Direct Energy-Based *E-R-μ* Method
Step 1. Determine ground-motion characteristics for seismic hazard and site: *Design Response Spectra (S_A or S_D) for ξ_{inh};* *PGD - peak ground displacement;* *PGA - peak ground displacement;*
Step 2. Calculate predominant period of the ground motion using Equation (8.1): $T_g = 2\pi\sqrt{\frac{PGD}{PGA}}$
Step 3. Determine properties of the isolated bridge system: *m -mass of the bridge superstructure;* *u_y - deck displacement at activation of the isolation system;* *α - post-yielding stiffness ratio;* *T_e - initial elastic period at elastic stiffness k_e defined as:* $T_e = 2\pi\cdot\sqrt{\frac{m}{k_e}}$ *T_d - period of vibration at the post-yielding stiffness $k_d = \alpha\, k_e$ defined as:* $T_d = T_e/\sqrt{\alpha}$ *ξ_{inh} - inherent damping;*
Step 4. Determine displacement of elastic system using *Design Response Spectra*: $u_e = S_D(T_e;\xi_{inh})$

Step 5. Determine the response modification factor: $R = \frac{u_e}{u_y}$

Step 6. Calculate the ductility μ using *E-R-*μ relationship (Equation (8.20) or Equation (8.21) for supplemental damping):

Step 7. Calculate the displacement: $d = \frac{u_e}{R} \cdot \mu$

In order to harmonize the use of the proposed energy-based *E-R-*μ method with the design procedure specified in the CAN/CSA-S6-06, the procedure summarized in Table 8-1 was rewritten using the terms and variables that are commonly used in current North American design practice. Accordingly, the response modification factor *R* is expressed as:

$$R = \frac{F_e \cdot (1-\alpha)}{Q_d} \tag{8.30}$$

where the parameters Q_d and α are respectively the characteristic strength and post-yielding stiffness ratio of the isolation system. These parameters are commonly determined using technical data specified for a given isolation device by its manufacturer.

The elastic force F_e is determined using the damped design response spectra as follows:

$$F_e = S_A(T_e;\xi_{inh}) \cdot \frac{W}{g} \tag{8.31}$$

where

W - dead load of the structure;

g - acceleration due to gravity;

ξ_{inh} - inherent damping which corresponds to the damping level of the design response spectrum;

T_e - initial elastic period defined at elastic stiffness k_e as:

$$T_e = 2\pi \cdot \sqrt{\frac{W}{k_e \cdot g}} \tag{8.32}$$

T_d – post-yield period of vibration defined using the post-yielding stiffness $k_d = \alpha\, k_e$ as follows:

$$T_d = 2\pi \cdot \sqrt{\frac{W}{k_d \cdot g}} \text{ or } T_d = T_e / \sqrt{\alpha} \tag{8.33}$$

Although the intent of rearranging Equation (8.20) was to solve for the displacement ductility ratio μ, the resulting expression was deemed too long and complex for the purposes of a simplified design method. For this reason, a simpler and more direct expression was derived for the displacement d as follows:

$$d_i = \left(PGD - \frac{249 \cdot Q_d \cdot {T_g}^2}{W} \cdot \left(2 - \frac{1}{\mu_i} \right) \right) / \left(1 + \frac{{T_g}^2}{{T_d}^2} \right) (mm) \tag{8.34}$$

where the ground-motion characteristics are defined in terms of the peak ground displacement PGD (mm) and the predominant period T_g determined from Equation (8.1).

It can be noted that the ductility μ, which depends on the displacement response d, is still in the right side of Equation (8.34). Thus, the solution is obtained through an iterative calculation. The initial estimate of the ductility μ_1 to start the iteration process is given by Equation (8.35) which was obtained by substituting Equation (8.30) in Equation (7.7) which was derived for the EEA:

$$\mu_1 = 1 - \frac{1}{\alpha} + \sqrt{\frac{1}{\alpha^2} + \frac{(F_e \cdot (1-\alpha)/Q_d)^2 - 1}{\alpha}} \tag{8.35}$$

Thus, the initial value of ductility μ_1 corresponds to the response estimate obtained with the EEA. This response estimate will be refined in the next iterative steps using the *E-R-μ* method. The displacement estimate d_i obtained from Equation (8.34) during iterative step i must be compared to the displacement d_{i-1}. For the first iteration ($i = 1$), the displacement d_i is checked against the displacement d_0 which is obtained using the initial estimate of the ductility μ_1.

$$d_0 = \frac{u_e}{R} \cdot \mu_1 = \frac{u_e \cdot Q_d}{F_e \cdot (1-\alpha)} \cdot \mu_1 \tag{8.36}$$

The iterative steps are repeated until an acceptable displacement error is reached (for example 5%). Once the solution for the displacement is obtained, the design seismic forces for the bridge substructure are subsequently determined from the load-displacement response of the actual nonlinear isolation system using Equation (8.37).

$$F = Q_d + 4\frac{W}{T_d{}^2} \cdot d_i \tag{8.37}$$

Table 8-2 provides a summary of the proposed iterative code compatible design procedure for assessing the response of isolated bridges using the energy-based *E-R-μ* method. Being mathematically equivalent, the direct and iterative *E-R-μ* methods provide the same response estimates. For this reason their responses do not need to be compared.

Table 8-2 Procedure for the response estimate using iterative energy-based *E-R-μ* method

Iterative Energy-Based *E-R-μ* Method
Step 1. Determine ground-motion characteristics for seismic hazard and site: ▪ *Design Response Spectra (S_A or S_D) for ξ_{inh};* ▪ *PGD - peak ground displacement;* ▪ *PGA - peak ground displacement;* ***Step 2.*** Calculate predominant period using Equation (8.1): $T_g = 2\pi\sqrt{\frac{PGD}{PGA}}$ ***Step 3.*** Determine properties of the bridge system: ▪ *W - dead load of the superstructure supported by the isolator device (bearing);* ▪ *Q_d - characteristic strength of the isolation system;* ▪ *α - post-yielding stiffness ratio* ▪ *T_e - initial elastic period at elastic stiffness k_e defined as:*

$$T_e = 2\pi \cdot \sqrt{\frac{W}{k_e \cdot g}}$$

- *T_d - period of vibration at the post-yielding stiffness $k_d = \alpha\, k_e$ defined as:*

$$T_d = T_e / \sqrt{\alpha}$$

- *ξ_{inh} - inherent damping,;*

Step 4. Determine displacement and force of elastic system using *Design Response Spectra*:

$$u_e = S_D(T_e; \xi_{inh})$$

$$F_e = S_A(T_e; \xi_{inh}) \cdot \frac{W}{g}$$

Step 5. Calculate initial values of ductility μ_1 to be used in an iterative solution for displacement across the isolation device, Equation (7.7) is rewritten as follows:

$$\mu_1 = 1 - \frac{1}{\alpha} + \sqrt{\frac{1}{\alpha^2} + \frac{(F_e \cdot (1-\alpha)/Q_d)^2 - 1}{\alpha}}$$

Step 6. Calculate the displacement according to the expression derived from the *E-R-μ* relationship (Equation (8.20)):

$$d_i\ (mm) = \left(PGD(mm) - \frac{249 \cdot Q_d \cdot {T_g}^2}{W} \cdot \left(2 - \frac{1}{\mu_i} \right) \right) / \left(1 + \frac{{T_g}^2}{{T_d}^2} \right)$$

check error with respect to d_{i-1}. For $i = 1$, use d_0 determined as:

$$d_0 = \frac{u_e \cdot Q_d}{F_e \cdot (1-\alpha)} \cdot \mu_1$$

Step 7. Calculate the design forces to be resisted by the bridge substructure:

$$F = Q_d + 4\frac{W}{{T_d}^2} \cdot d_i$$

8.4.2 Validation of the New Energy-Based Method against NLTHA

In contrast to the EEA analytical form originally proposed by Newmark and Hall (1982), the method proposed in this study takes into account the nonlinear system parameters (T_e and α) and the ground-motion characteristics (T_g, *PGA*, and *PGD*). The structure-earthquake interaction is therefore explicitly accounted for in the method. To demonstrate the capacity of the proposed energy-based method for capturing the highly-nonlinear response of isolated bridges to different ground motions, the *E-R-*μ relationship (Equation (8.20)) is validated against the responses of isolated bridges located in eastern and western Canada.

The results obtained in Chapter 5 from the parametric NLTHA were used for this comparative study. The nonlinear responses were investigated under site-specific ground motions anticipated in ENA and WNA. Each of these ground-motions sets were comprised of twenty records that were selected according to the site-specific dominant *M-R* earthquake scenarios. Details on these scenarios are presented in Chapter 4 (Sections 4.3 and 4.4). Figure 8.6 presents the ground-motion characteristics and the mean displacement spectra averaged over 20 records and over each of the four *M-R* scenario sets.

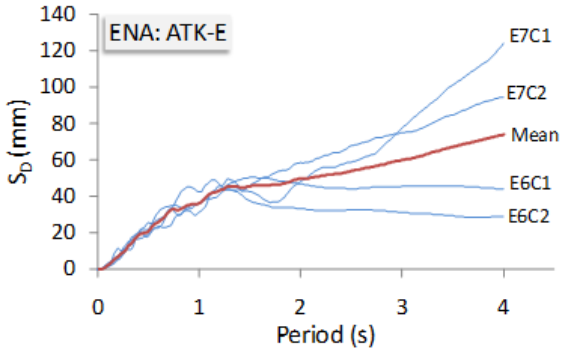

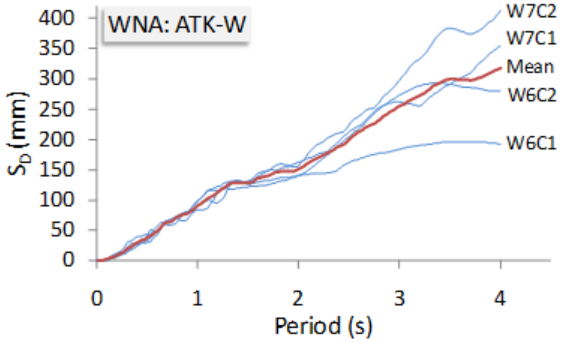

EQ-Set ENA	Number of records	PGD (mm)	PGA (mm/s^2)	Tg (s)
E6C1	6	39	4900	0.56
E6C2	3	23	4313	0.46
E7C1	3	110	3015	1.20
E7C2	8	101	2414	1.29
Mean	**20**	**72**	**3535**	**0.90**

EQ-Set WNA	Number of records	PGD (mm)	PGA (mm/s^2)	Tg (s)
W6C1	6	156	5998	1.01
W6C2	3	198	4306	1.35
W7C1	3	318	3891	1.80
W7C2	8	533	2485	2.91
Mean	**20**	**337**	**4023**	**1.82**

Figure 8.6 Ground-motion characteristics and 5% damped displacement spectra for four *M-R* scenario sets (ATK-ENA and ATK-WNA)

The peak ground displacement *PGD* and peak ground acceleration *PGA* were determined for each individual record: the *PGD* is the spectral displacement ordinate at a very long period while the *PGA* value is the spectral acceleration ordinate at zero period. The predominant ground-motion period T_g is determined using Equation 8.1. The individual record characteristics (*PGD*, *PGA*, T_g) were averaged and the averaged values were used for estimating the displacement response with the direct energy-based *E-R-*μ Method (summarized in Table 8.1) for each of four *M-R* scenario sets.

Figures 8.7 and 8.8 compare the results obtained from nonlinear time-history analyses versus those calculated using the new energy-based method. The curves with dots correspond to the responses from NLTHA. These values were obtained by averaging the responses from the individual records over the respective *M-R* scenario set. The values from the *E-R-*μ relationship (Equation (8.20) are plotted in the form of a surface with gridlines that correspond to the μ and T_e axis units.

The results from Equation (8.20) agree generally well with those obtained from the NLTHA for all ground-motion sets. This demonstrates the capacity of the new energy-based method for capturing the effect of different structural parameters and ground-motion characteristics. The largest discrepancies are mainly observed for structures with an elastic period of $T_e = 0.25$ s, which correspond to frequency ratios $T_e / T_g < 1$, thus representative of "slowly" varying loading forces. For this range of period ratios, the contribution of the kinetic energy to the system behaviour is less significant and the discrepancies can be explained by the effect of multiple *oscillation centre* drifts that originate from various loading pulses.

In spite of the limitations to capture multiple loading pulses, the proposed energy-based method appears to result mostly in conservative response estimates as shown in Figure 8.9. It can be noted that the majority of the markers are above the straight line. These results correspond to conservative response estimates with less than 5% relative error with respect to the responses from NLTHA. Conservative response estimates were obtained for 77% and 93% of the analyzed bridges for the WNA and ENA earthquake suites, respectively.

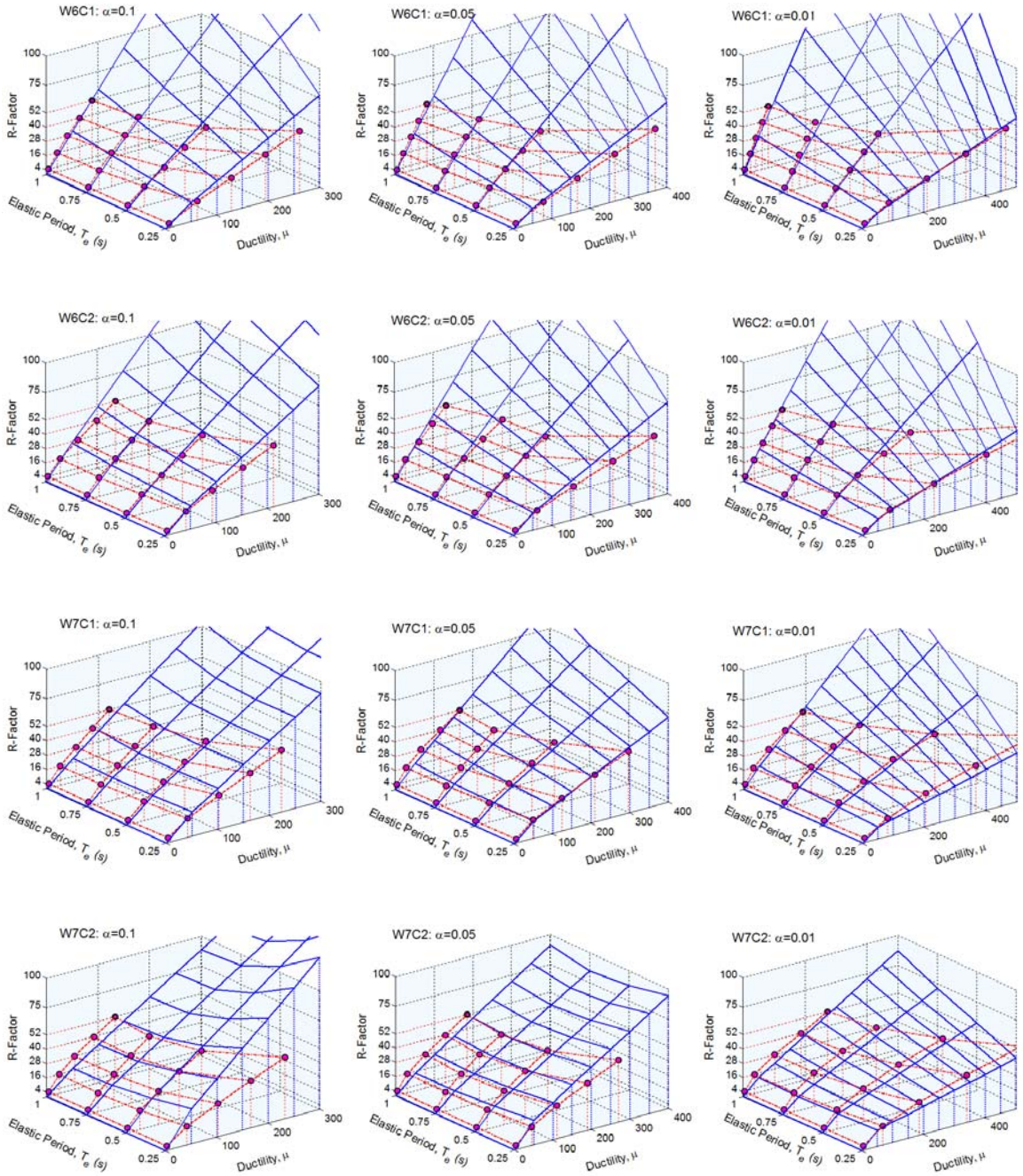

Figure 8.7 WNA *E-R-μ* relationship from analytical estimate and NL SDOF analyses

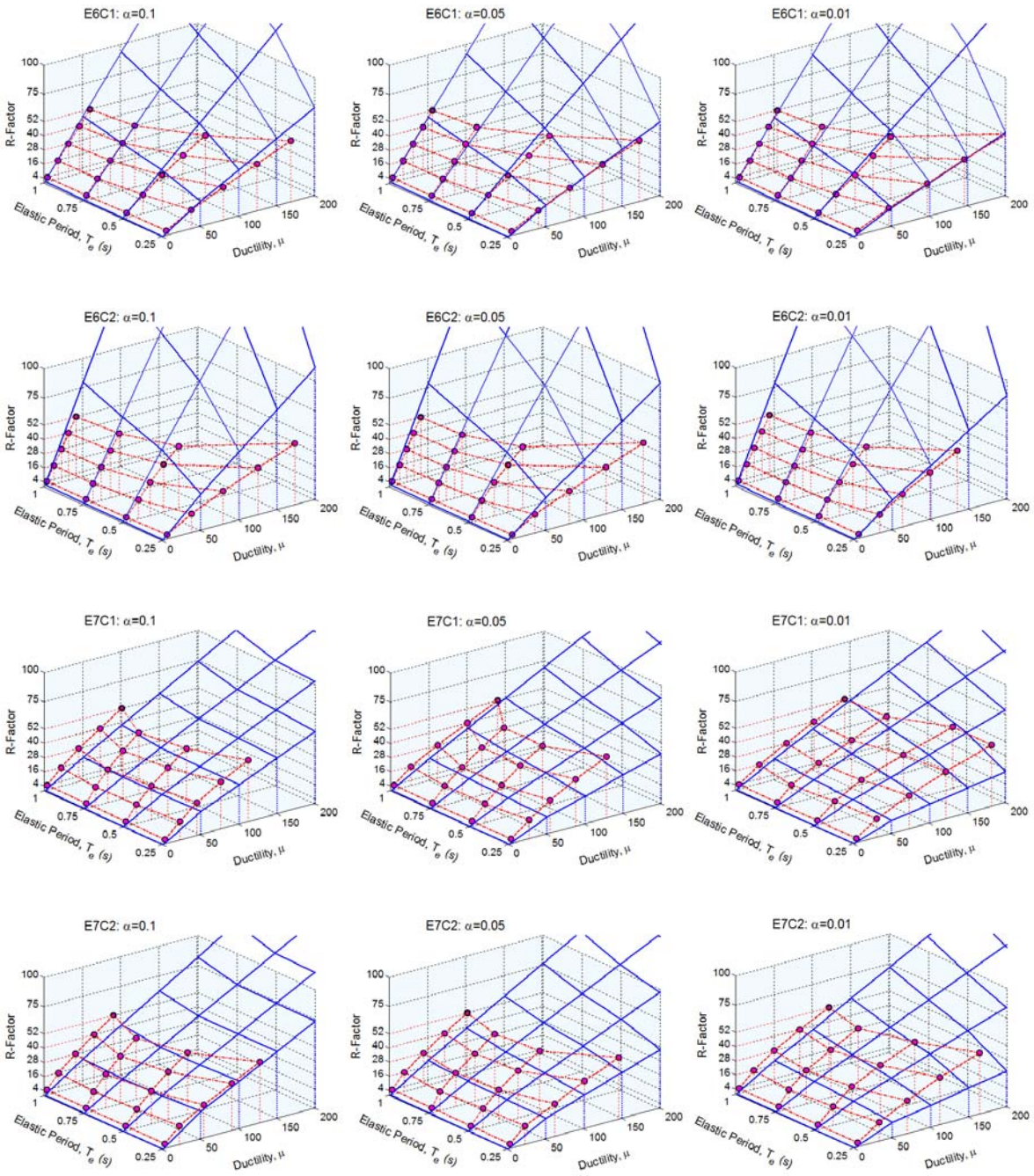

Figure 8.8 ENA *E-R-μ* relationship from analytical estimate and NL SDOF analyses

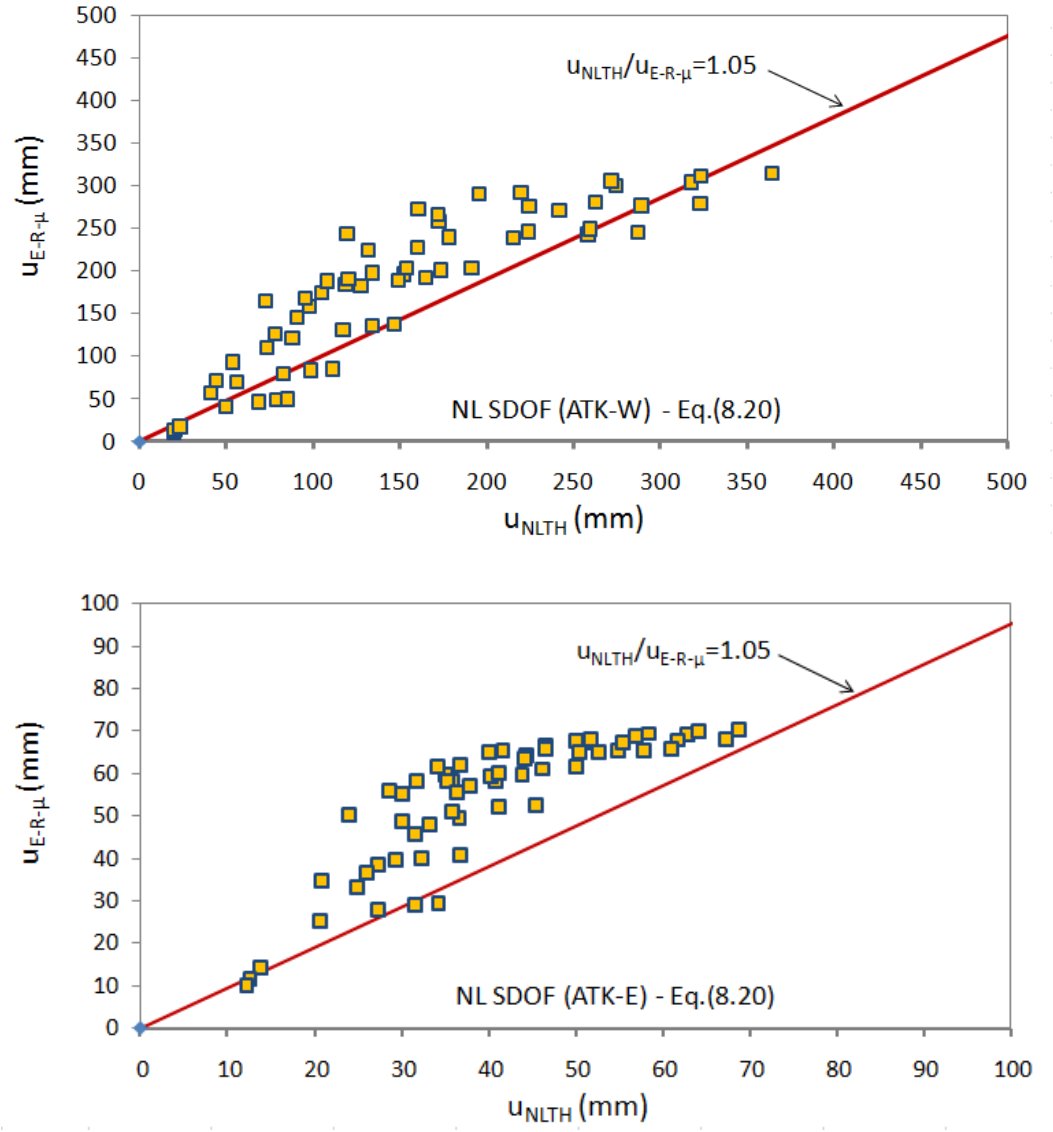

Figure 8.9 NLTHA versus energy-based *E-R-μ* approach using Equation (8.20)

The values presented in Figure 8.9 for the new energy-based *E-R-μ* method are reproduced in Figure 8.10. In the same figure, the response estimates obtained from the EEA are presented versus the responses obtained from NLTHA. By comparing these results, it can be noted that these two methods provide similar response estimates for bridges exhibiting limited nonlinear responses which are characterized by small inelastic displacements as discussed in Chapter 7. For structures sustaining larger inelastic displacements, the response estimates from the EEA are generally much more conservative than those obtained from the proposed *E-R-μ* method. It emphasizes the effect of the kinetic energy that was considered in the development of the

proposed method for better characterizing highly nonlinear behaviour. The same trends in the response reduction effect are observed in Figures 8.5 and 8.10.

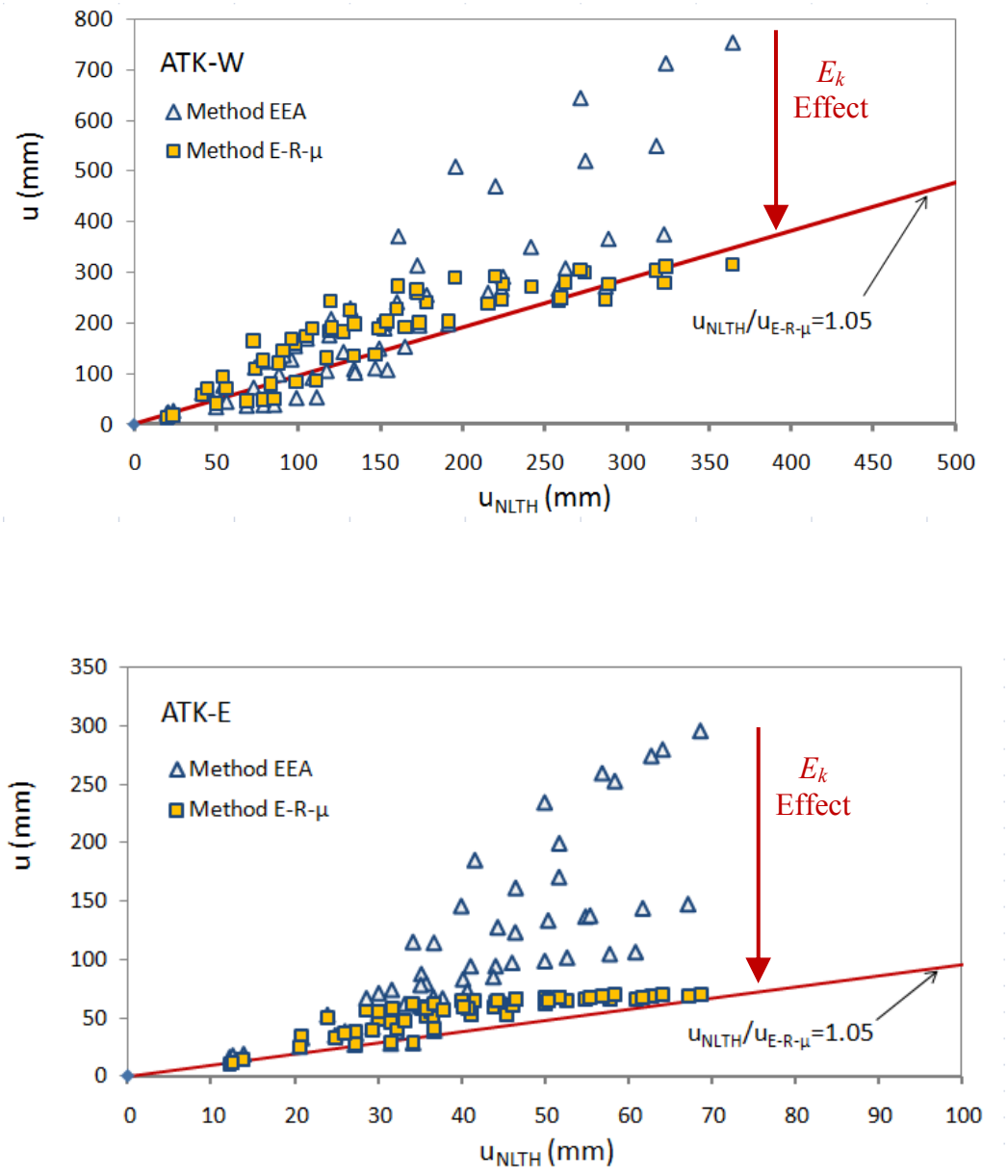

Figure 8.10 NLTHA versus energy-based *E-R-μ* approach using Equation (8.20) and Equal Energy Approach (EEA) using Equation (7.8)

As a result, the use of the energy-based *E-R-μ* method represents a significant accuracy improvement for the design of isolated bridges when compared to the Equal Energy Approach

(EEA) proposed by Newmark and Hall (1982). The energy-based *E-R-μ* method may be incorporated in the current design provisions as an efficient alternative to the currently specified in the North American codes (CAN/CSA-S6-06 and AASHTO 2009, 2010), which is subject to certain limitations. The main advantage of the proposed energy-based *E-R-μ* method with respect to that currently specified in the code (CSA-S6-06) is that the energy-based *E-R-μ* method accounts more explicitly for bilinear response and ground motion properties. The use of the proposed method for developing effective and optimal seismic protection strategies is another attractive point which is further studied in the next chapter.

8.5 Conclusions

In this chapter, a new energy-based *E-R-μ* method was developed for predicting the peak displacement response of isolated bridges. The method assumes that the bridge structure being initially at rest is subjected to the ground motion excitation that is represented by a single sine-wave pulse. The response to the pulse loading is solved by making use of the concept of *energy allocation* under transient excitation that was derived in chapter 7. The energy concept used in the Equal Energy Approach (EEA) was adopted as a basis for the development of the new method. The method's account of the kinetic energy distinguishes it from EEA-based methods derived solely assuming a steady-state response of the nonlinear structure.

This new energy-based *E-R-μ* method, was developed purely based on analytical derivations rather than being empirically calibrated on a region-by-region basis to obtain accurate response predictions. The ground motion characteristics and the system's nonlinear parameters are taken into account by the new simplified method. In order to harmonize the use of the proposed energy-based *E-R-μ* method with the design procedure specified in the CAN/CSA-S6-06, the design procedure was formulated by adopting the seismic and structure parameters commonly used in current design practice.

As was shown in this chapter, the use of the proposed energy-based *E-R-μ* method represents a significant accuracy improvement for the design of isolated bridges over the currently used EEA-based methods (Figure 8.10). The results obtained from NLTHA (Chapter 5) for 120 isolated bridges (60 in WNA and 60 in ENA) were compared to those calculated by the new energy-based *E-R-μ* method. The proposed energy-based *E-R-μ* method appears to result mostly

in conservative response prediction. Conservative response estimates were obtained for 77% and 93% of analyzed bridges in WNA and in ENA, respectively.

Being derived for a single loading pulse, this method has an inherent limitation to capture the effect of the loading duration or irregularity in seismic excitation and structural response that may be very complex.

The energy-based *E-R-μ* method may be incorporated into the current design provisions as an efficient alternative to the currently specified design approach. This method can be applied at a preliminary design stage. Once the protection strategy is defined, more detailed and time-consuming analyses can be used to refine preliminary response estimates. This method can be extended to any SDOF system and it is not limited to bridge applications. The use of the new energy-based *E-R-μ* method for developing optimum cost-effective isolation solutions is further explored in the next chapters.

Chapter 9: Design Implications of the Proposed Methods

9.1 General

This chapter summarizes the improvements proposed in this thesis for designing seismically isolated bridge structures and it also concludes with a discussion of their design implications.

The first part of this chapter presents the modifications that are proposed, based on this research thesis (Chapters 5 and 6), to improve the accuracy and extend the applicability of current code simplified methods. The effect of these modifications is demonstrated for a series of 180 isolated bridge structures that were analyzed in Chapter 5.

The response of the same isolated bridges is then re-assessed by using the new energy-based method that was proposed in Chapter 8 as an alternative design approach to account for the different structural parameters and ground-motion characteristics.

Finally, a bridge retrofit example is presented to compare bridge designs using the current code provisions and those proposed in this research. The focus is set on assessing the possibility of using the new energy-based method as an alternative design approach to address the limitations of the current code methods.

In addition, a detailed insight on the use of the new energy-based E-R-μ method for achieving an optimum isolation solution is gained by studying the effect of the bridge parameters.

9.2 Proposed Improvements to CSA-S6-06 Simplified Method

The observations made in Chapter 5 suggest that the code simplified method results mostly in safe designs for WNA but underestimates the displacement demand of bridges subjected to ENA seismic ground motions. It was also observed that the damping limits of the current code simplified method disqualify a large number of physically achievable and even desirable seismic protection schemes, including cases where the code method results in conservative response predictions.

In addition to the damping limits, current CSA-S6 and AASHTO codes also have minimum lateral restoring force criteria to ensure a minimum recentring capability to the system. CSA-S6-06, clause 4.10.10.2 reads: "… The isolation system shall be configured to produce a lateral restoring force such that the lateral force at the design displacement is greater than the lateral force at 50% of the design displacement by at least 0.025W". In AASHTO (2009, 2010), the minimum restoring force at 50% of the design displacement is 0.0125W, which is less stringent than in CSA S6. Unfortunately, the codes do not provide a clear scientific basis for these criteria although it is speculated that these criteria are intended to result in systems with a non-zero post-elastic stiffness. As a result of the difference between both codes, the design of isolated bridges in Canada may be limited more frequently by this requirement when compared to engineering practice in the US.

To address the limitations inherent to the current seismic code provisions (CSA-S6-06 and AASHTO), the modifications are proposed in this research thesis. These modifications could then be used in future editions of CSA-S6 for both WNA and ENA to improve the accuracy and to extend the applicability of the current simplified method by superseding the original requirements for the maximum damping limit and minimum lateral restoring force.

Table 9.1 summarizes a method that follows the framework of the one presented in clause 4.10.6.2.1 of CAN/CSA-S6-06 but with the following proposed revisions:

1) Improving method's accuracy - Damping coefficients *B*

- Damping coefficients B specified in Table 4.8 can be replaced by an exponential equation between B and β_{eff} (Equation 2.8). Interpolation between tabulated values would therefore no longer be required.

- The same equation can be used with different exponents for WNA and ENA locations to reflect different damping response reduction effects. The exponents $n = 0.3$ and 0.2 are suggested for design of isolated bridges in WNA and ENA, respectively.

2) Extending method's applicability limits

- The damping limits can be relaxed and expressed as a function of the post-yielding stiffness ratio α (Equation (6.10)). This expression reflects a geometrical relation between the

hysteresis shape and dissipated energy and reflects the influence of the ratio α on the accuracy of the *equivalent linearization method* that forms the basis of the code-specified simplified method. The damping limit of 30% currently specified in CAN/CSA-S6-06 has been established for $\alpha = 0.10$, a value which is primarily representative of the lead-rubber bearing (LRB) system. An upper limit greater than $\beta_{eff} = 30\%$ can be adopted for α-ratios lower than 0.10. As further presented in this section, this would allow for a wider range of seismic protection systems with $\alpha \leq 0.1$ such as friction pendulum isolators (FPI) and flat sliding isolators (FSI) to be efficiently used up to their maximum dissipative capacity. maximum allowable effective damping β_{eff} is determined using Equation (6.10) and yields 33%, 40%, and 52% for $\alpha = 0.10$, 0.05, and 0.01, respectively.

- To ensure that the method will lead to conservative results, the method applicability limits can be established in terms of the effective period T_{eff} (Equation (6.15)). This expression takes into account the influence of the initial elastic period T_e and post-yielding stiffness ratio α on the accuracy of the code-specified simplified method. As a result, the damping limits proposed by Equation (6.10) would be automatically satisfied. Responses that are not sufficiently accurate are automatically rejected when using limits that depend on T_{eff}.

Table 9-1 Modified procedure following the *Simplified Equivalent Static Force Method* (CAN/CSA-S6)

CSA-S6 Simplified Method Procedure
Step 1. Ground-motion data required: 5% Damped Response Spectrum *Step 2.* System data required: T_e ; β_{inh} ; α ; R For the first iteration, assume $T_{eff} = T_e$; $\beta_{eff} = \beta_{inh}$ *Step 3.* Determine from spectrum: $PS_D(T_{eff};5\%)$ *Step 4.* Determine damping coefficient *B* using Equation 2.8: $B = \left(\frac{\beta_{eff}}{5\%}\right)^n$ with n=0.3 for WNA and 0.2 for ENA *Step 5.* Calculate: $d_i = PS_D(T_{eff};5\%) / B(\beta_{eff})$ *Step 6.* For iteration 2 and higher, check accuracy: $error = \left\lvert\frac{d_i - d_{i-1}}{d_i}\right\rvert \cdot 100\%$ if error is acceptable, go to Step 8 *Step 7.* Calculate and Return to Step 3: $\mu = \frac{R}{PS_D(T_e;5\%)} \cdot d_i$ $T_{eff} = T_e \cdot \sqrt{\frac{\mu}{1+\alpha\mu-\alpha}}$ $\beta_{eq} = \frac{2\cdot(\mu-1)\cdot(1-\alpha)}{\pi\cdot\mu\cdot(1+\alpha\mu-\alpha)}$ $\beta_{eff} = \beta_{eq} + \beta_{inh}$ *Step 8.* Save and print response: d_i

The effects of the proposed modifications can be examined in Figures 9.1 to 9.6, which present the relative error between the maximum displacements and the isolation level from the code simplified method, u_{code}, and the results from nonlinear time-history analyses (u_{NLTH}). The comparison is performed using the response of 180 isolated bridge structures obtained by varying the following parameters: for T_e = [0.25, 0.5, 0.75, and 1.0 s], R = [4, 16, 28, 40, 52], and α = [0.1, 0.05, and 0.01]. The bridges have been analyzed in Chapter 5. For the improved code method, the displacement estimates were obtained by following the complete iterative procedure shown in Table 9.1. The resulting displacement estimates are the deck displacements which corresponds to the displacements across the isolation devices located at the abutments. The displacements across the isolators on the piers must then be determined from that value in proportion to the relative stiffness of the piers and piers' isolators.

The results are presented in 6 figures (Figures 9.1 to 9.6) to cover the two regions (WNA and ENA) and three values of α. In each figure, three sub-plots are shown. Figures 9.1(a) to 9.6(a) give the errors obtained when applying the current code method, without the suggested modifications. In the plots, the isolated bridges that satisfy the current code applicability limits are identified. Figures 9.1(b) to 9.6(b) shows the improvement in the method's accuracy when using the proposed exponential expression (Equation (2.8)) for the damping coefficient, with the exponents n=0.3 and 0.2 for WNA and ENA, respectively. Figures 9.1(c) to 9.6(c) shows the effects of applying the proposed method applicability limits that are function of T_{eff}.

For WNA, the use of Equation (2.8) for the damping coefficients does not affect the response prediction much because the damping coefficients B from Equation (2.8) with n=0.3 corresponds well to the originally tabulated values of B in the code provisions, as presented in Table 2-1. By respectively comparing Figures 9.4(a), 9.5(a) and 9.6(a) to Figures 9.4(b), 9.5(b), and 9.6(b), a greater improvement is obtained for displacement estimates in ENA. Equation (2.8) with n=0.2 gives more uniform predictions over the possible range of effective damping. The number of bridges satisfying the conservative response estimates in ENA was accordingly increased from 31% to 89%. This number is close in agreement with 90% of satisfactory estimates in WNA. To implement the modifications proposed in this thesis, ENA and WNA seismic regions can be distinguished using the criteria based on the ratio $Sa(0.2) / Sa(2.0) \geq 8.0$ and $Sa(0.2) / Sa(2.0) < 8.0$ (for ENA and WNA, respectively), as currently specified in the NBCC (NRCC, 2010).

In the figures, it is noted that applying the current maximum damping limit (30%) and the minimum lateral restoring force requirement (0.025W at 50% of the design displacement) ensures that the current method, without revisions, gives conservative predictions. More importantly, it is also clear from these figures that these limits are excessively stringent because a large portion of the bridges for which satisfactory (conservative) estimates are obtained are rejected. For WNA, only 60% of the bridges for which a conservative result was obtained meet the current code limits. For ENA, this percentage reduces to 36%.

The second proposed improvement aims at extending the percentage of accepted satisfactory estimates with unconservative relative errors ranging up to 5%. This effect can be outlined by comparing Figures 9.1(b) - 9.6(b) to Figures 9.1(c) - 9.6(b). As shown, the proposed limits can be used to identify and reject responses with unsatisfactory accuracy. A comparison of the response of 180 isolated bridge structures shows that the percentages of cases with satisfactory predictions increase from 60% to 93% and from 36% to 94% for WNA and ENA, respectively, when the structures meet the proposed limit set as a function of the effective period (Equation (6.15)). On this basis, it is believed that the proposed limits could be used in future editions of CSA-S6 for both WNA and ENA.

Based on the above, it can be stated that the implementation of the modifications proposed in this research would significantly improve the current code simplified method for estimating displacement demands, in terms of both the accuracy of the predictions and the number of cases for which the method can be applied. The modified simplified code method will then result in the same level of accuracy in WNA and ENA, with relative errors ranging from 5% (unconservative) to -50% (conservative) in both seismic regions. In addition, a wider choice of market-available seismic protective devices will be covered by the modified seismic provisions.

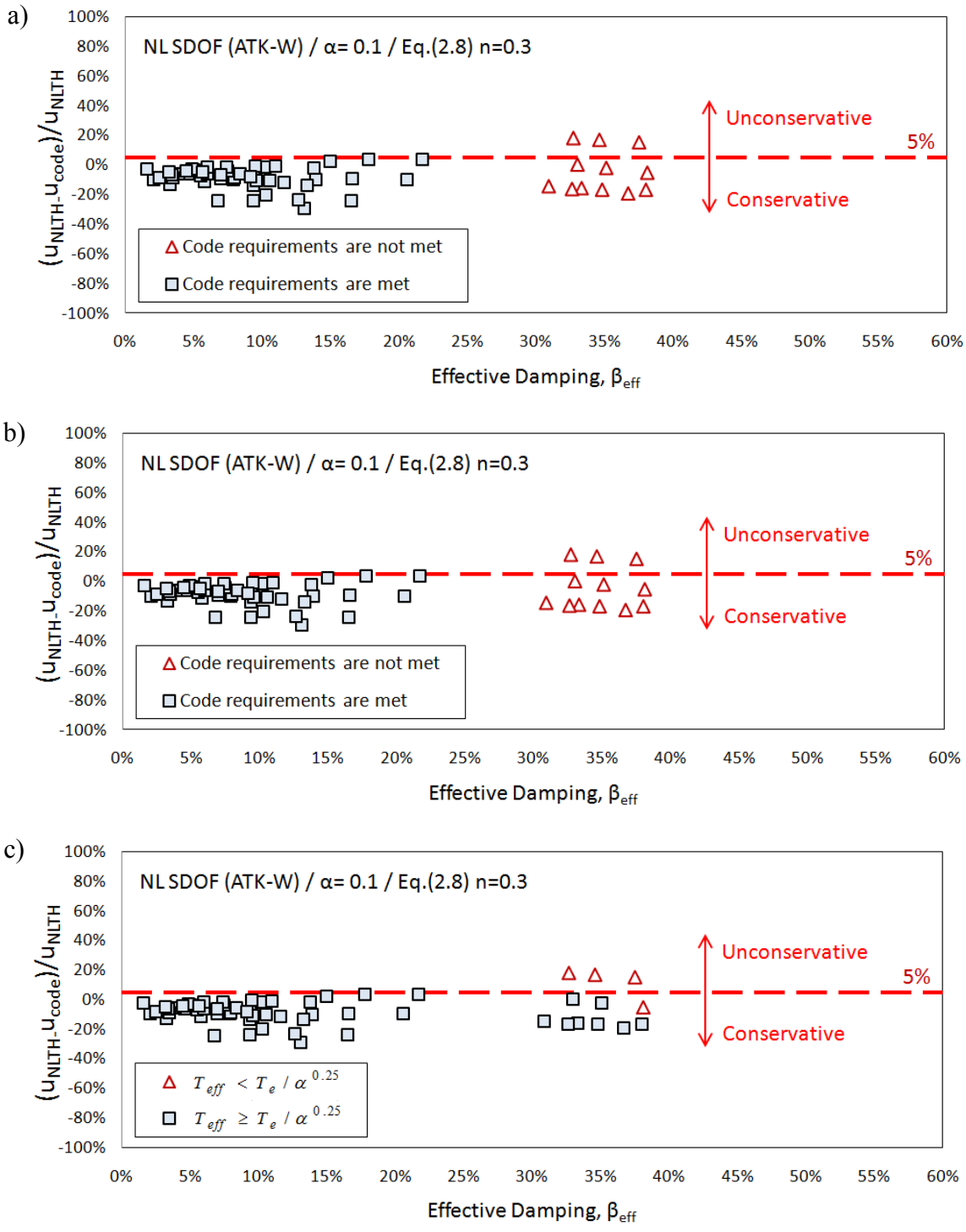

Figure 9.1 Relative errors in maximum displacements at the isolation level using the code simplified method compared to NLTHA for WNA and α = 0.1 (ATK-W): a) current CSA-S6-06 method; b) current method with damping coefficients from Eq.(2.8) applicability limits; c) current method with damping coefficients from Eq.(2.8) and applicability limits based on effective period.

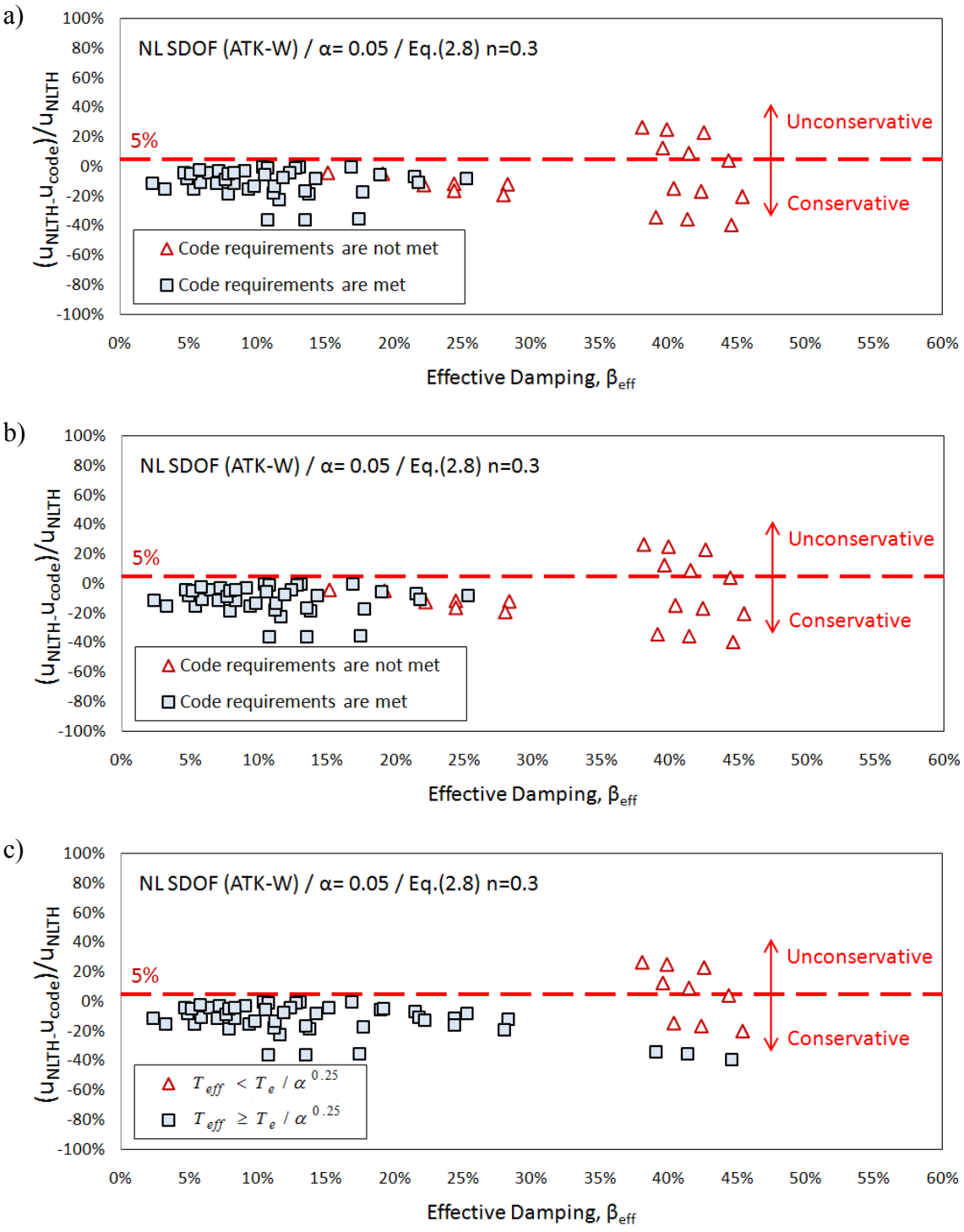

Figure 9.2 Relative errors in maximum displacements at the isolation level using the code simplified method compared to NLTHA for WNA and α = 0.05 (ATK-W): a) current CSA-S6-06 method; b) current method with damping coefficients from Eq.(2.8) applicability limits; c) current method with damping coefficients from Eq.(2.8) and applicability limits based on effective period.

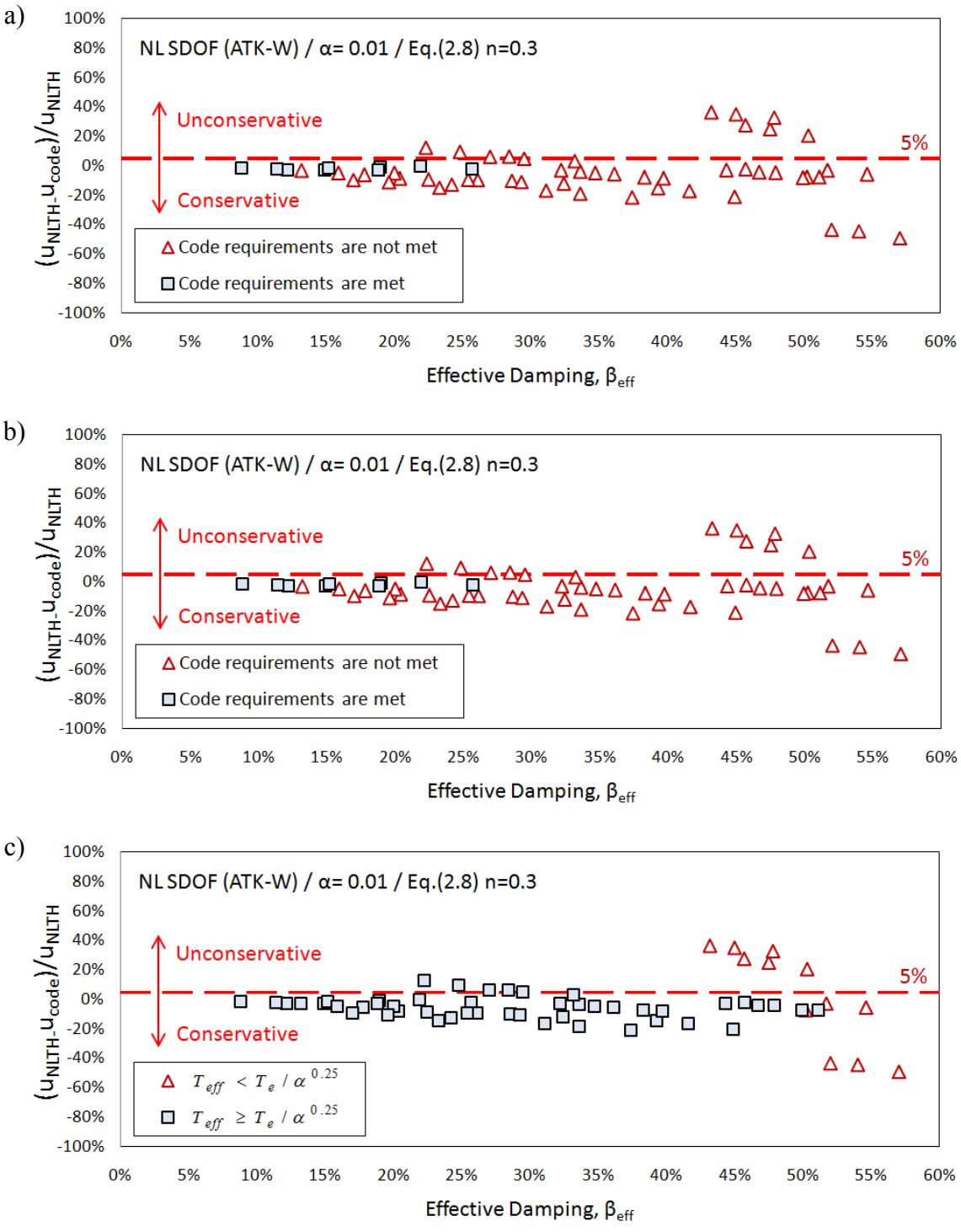

Figure 9.3 Relative errors in maximum displacements at the isolation level using the code simplified method compared to NLTHA for WNA and α = 0.01 (ATK-W): a) current CSA-S6-06 method; b) current method with damping coefficients from Eq.(2.8) applicability limits; c) current method with damping coefficients from Eq.(2.8) and applicability limits based on effective period.

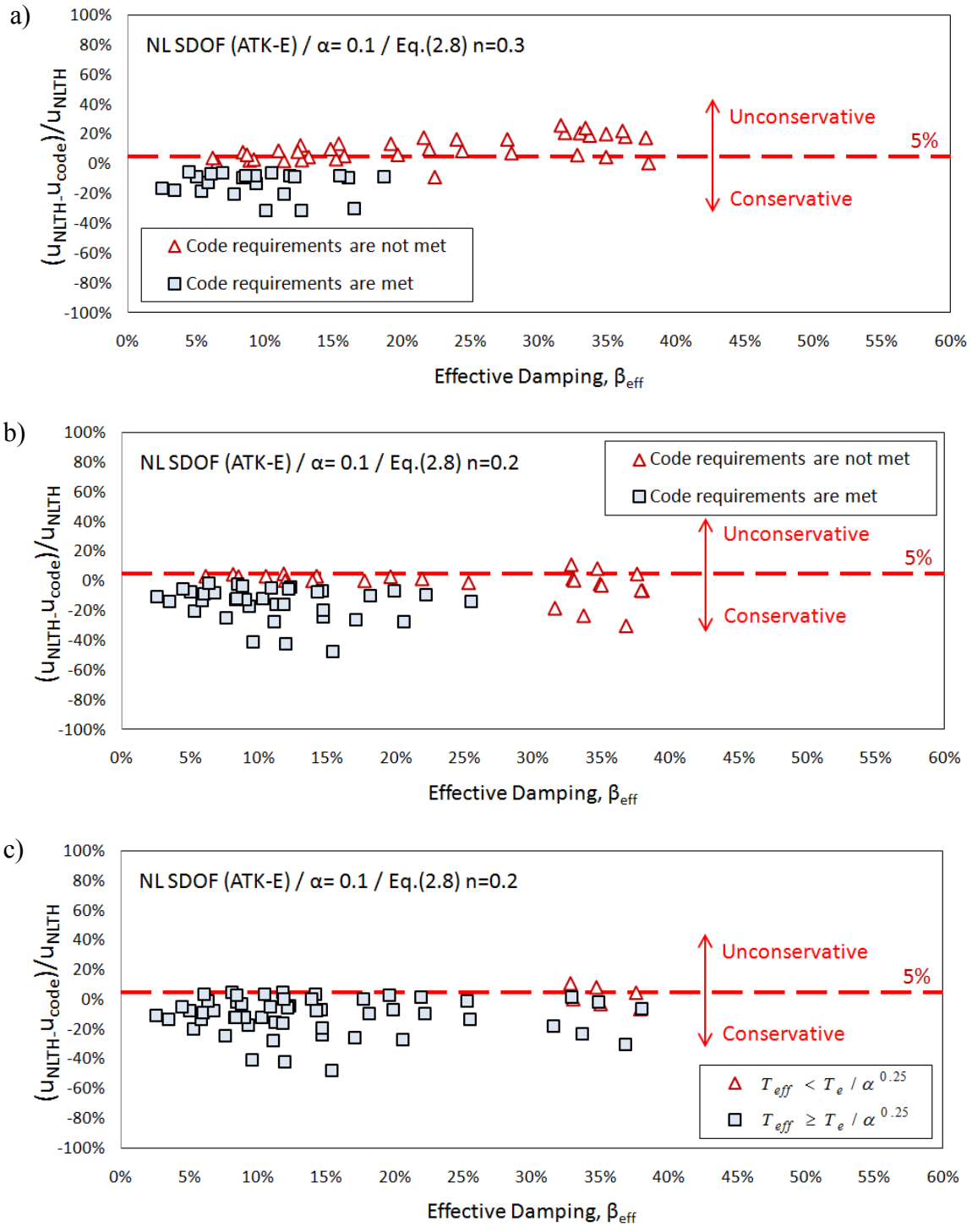

Figure 9.4 Relative errors in maximum displacements at the isolation level using the code simplified method compared to NLTHA for ENA and α = 0.1 (ATK-E): a) current CSA-S6-06 method; b) current method with damping coefficients from Eq.(2.8) applicability limits; c) current method with damping coefficients from Eq.(2.8) and applicability limits based on effective period.

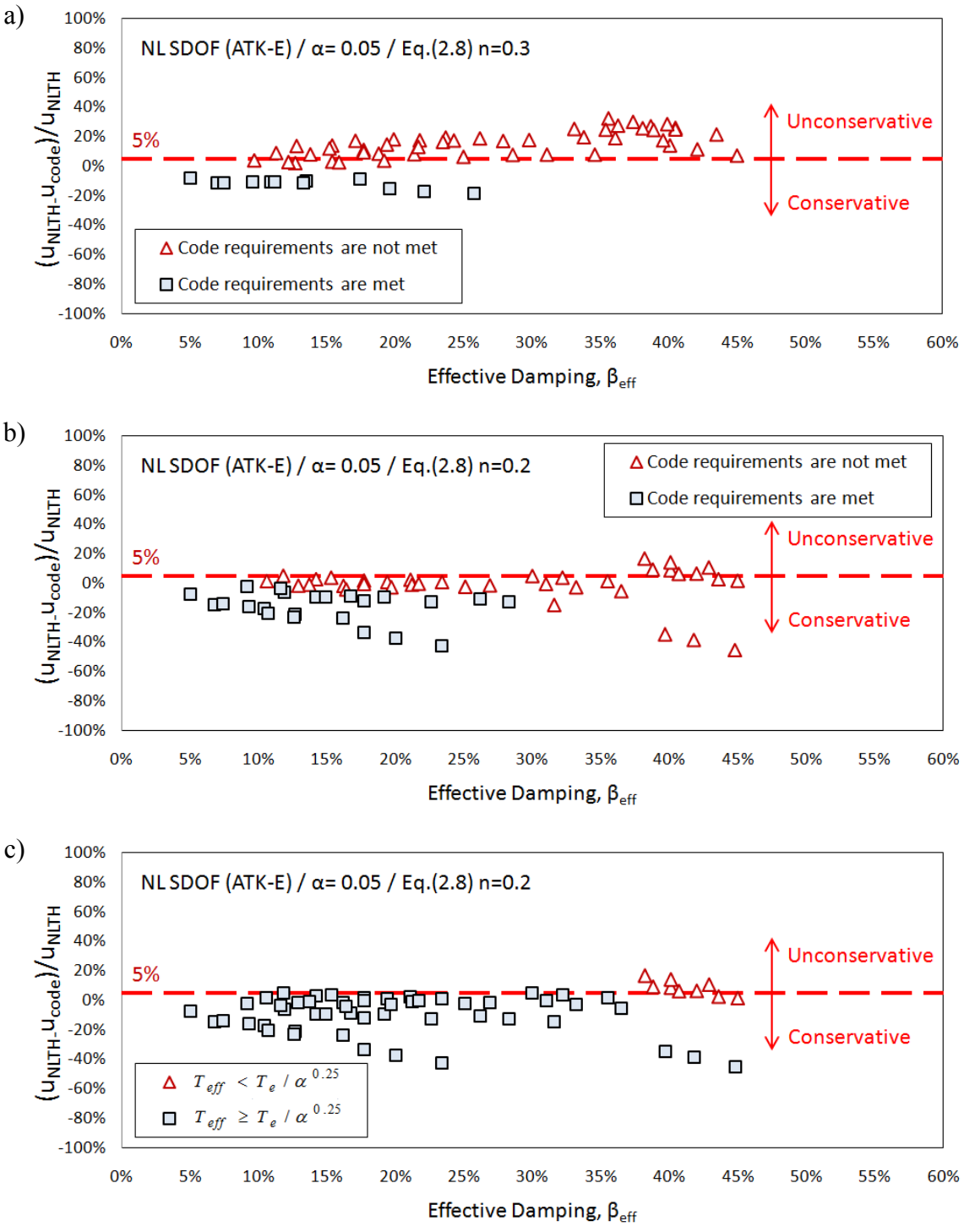

Figure 9.5 Relative errors in maximum displacements at the isolation level using the code simplified method compared to NLTHA for ENA and α = 0.05 (ATK-E): a) current CSA-S6-06 method; b) current method with damping coefficients from Eq.(2.8) applicability limits; c) current method with damping coefficients from Eq.(2.8) and applicability limits based on effective period.

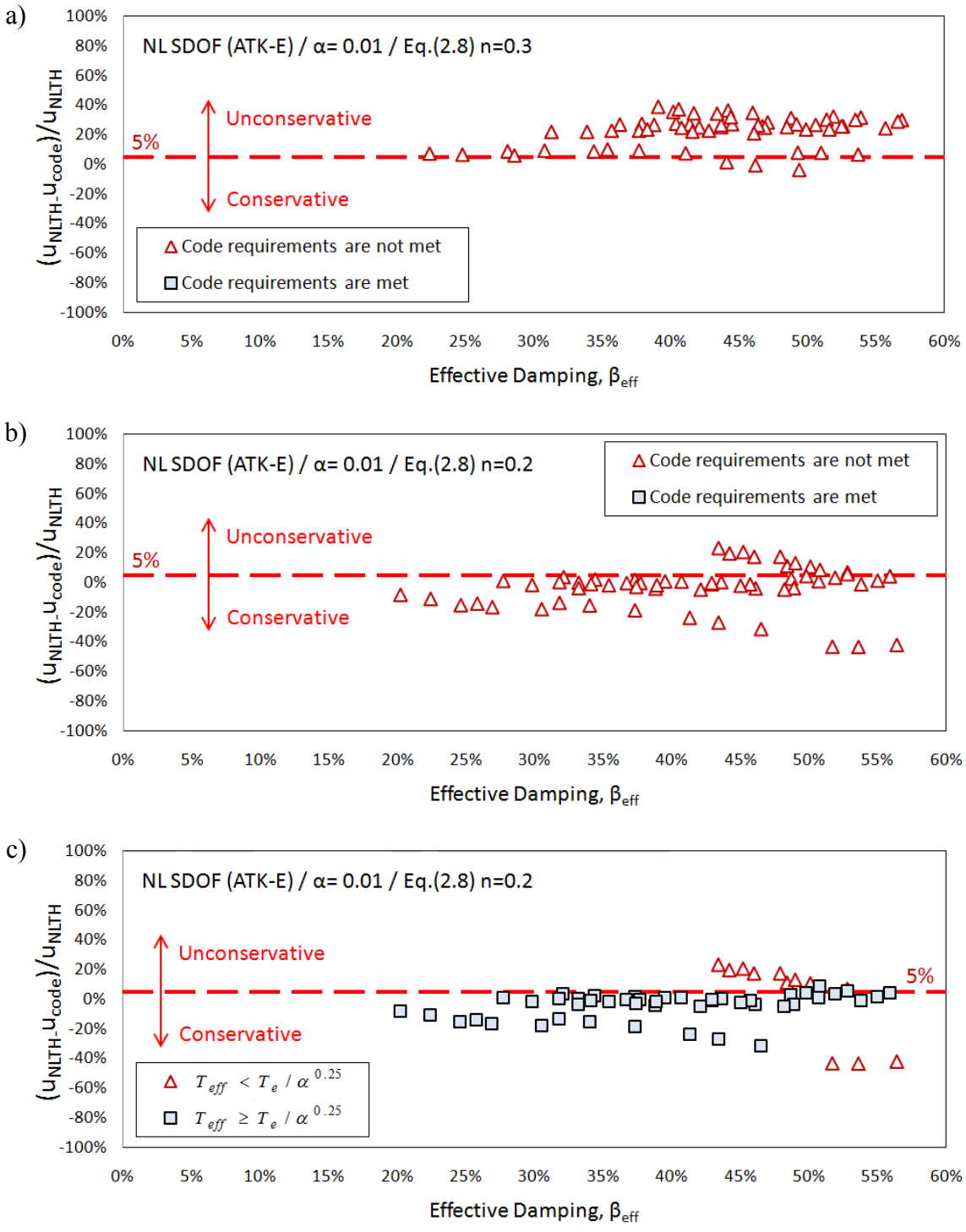

Figure 9.6 Relative errors in maximum displacements at the isolation level using the code simplified method compared to NLTHA for ENA and α = 0.01 (ATK-E): a) current CSA-S6-06 method; b) current method with damping coefficients from Eq.(2.8) applicability limits; c) current method with damping coefficients from Eq.(2.8) and applicability limits based on effective period.

9.3 Proposed New Energy-Based *E-R-μ* Method

The new energy-based simplified method proposed in this research (Chapter 8) is based on the *E-R-μ* relationship. The energy concept used in the Equal Energy Approach (EEA) was adopted as a basis for the development of the new method. The EEA was extended by considering the transient response to pulse type loading, which is deemed to better represent the response of an isolated bridge structure that is subjected to seismic ground motions. The proposed method was derived based on the concept of *energy allocation* under transient response.

The method's capability for directly accounting for the kinetic energy differentiates it from the EEA method derived solely from a steady-state response. The strong ground motion characteristics and the system's nonlinear parameters are both taken into account in the energy-based *E-R-μ* method. This reflects more closely the actual nonlinear response of isolated bridges to strong ground motions. As a result, it is applicable to a broader range of structures and the accuracy of the prediction has generally been improved. With the proposed method, displacement estimates can be obtained directly, without iterations, which represents a significant advantage compared to linearization approach used in current code simplified methods. This direct method has been worked into a design procedure that was outlined in detail in Table 8.1. This design procedure may be used for the preliminary design of isolated bridge structures; it could also be used as a replacement of the simplified method currently specified in CAN/CSA-S6.

Figures 9.7 and 9.8 present the errors in response estimates from the proposed method relative to the results from NLTHA. The response estimates were obtained using mean values of the ground-motion characteristics. The response spectrum, predominant period T_g and peak ground displacement *PGD* were determined by averaging the characteristics of 20 individual time histories as presented in Figure 8.6 for ATK-W and ATK-E. As shown, the proposed method generally results in conservative response estimates. The level of conservatism in the response estimates is comparable to those attained using the different linearization methods that were compared in Figure 2.5 (Mavronicola and Komodromos, 2011) and Figure 2.6 (FEMA 356, ATC-40, and FEMA 440). Taking into account that the linearization methods were empirically calibrated, the level of conservatism from the new energy-based *E-R-μ* method, which was

developed solely on a theoretical basis without any additional calibration, makes this method an interesting alternative in the design process.

Contrary to the current simplified code method, the energy-based *E-R-μ* method is not iterative and a large number of possible solutions can be obtained directly to evaluate the most appropriate scheme complying with the design objectives. The proposed method can provide upper bound displacement predictions that will unlikely be exceeded and will represent useful information for the design engineers.

It can be noted from Figures 9.7 and 9.8 that the level of conservatism mostly decreases as the response modification factor *R* increases. This suggests that the proposed energy-based *E-R-μ* method is better suited for bridge structures that exhibit a response of larger displacement ductility demands (larger *R* factors). It was also found that the errors increase for structures with shorter elastic periods.

The conservatism of the proposed method is inherent to the method's assumptions that were explained in Chapter 8. The energy transmitted to the isolated system is idealized as being the representative of the system response under a sinusoidal excitation with a sole period T_g which relates the peak ground displacement and the peak ground acceleration. The response estimates will correspond to the response of isolated bridges under the most demanding loading conditions form the strong motion portion of a seismic ground motion.

Providing mainly upper bound displacement estimates, the energy-based *E-R-μ* method may also be adopted for complementing the current code method beyond its applicability limits. In this way, the response estimate may be obtained for a given isolated bridge when the simplified code method does not provide engineers with reliable response predictions.

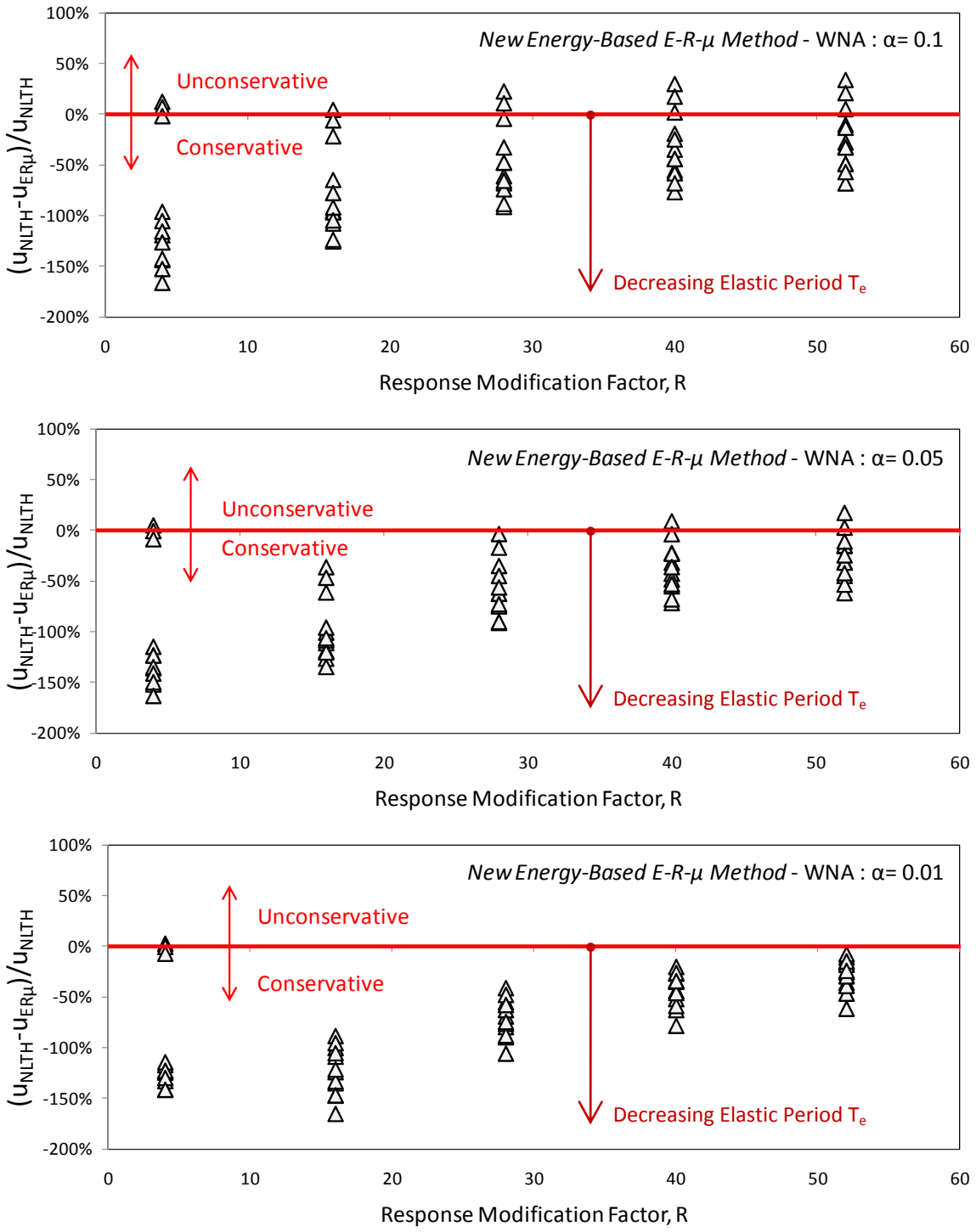

Figure 9.7 Relative error of the maximum displacements at the isolation level using the new energy-based *E-R-μ* method - PGD=337 mm; T_g=1.82 s (mean of 20 Atkinson's records - WNA)

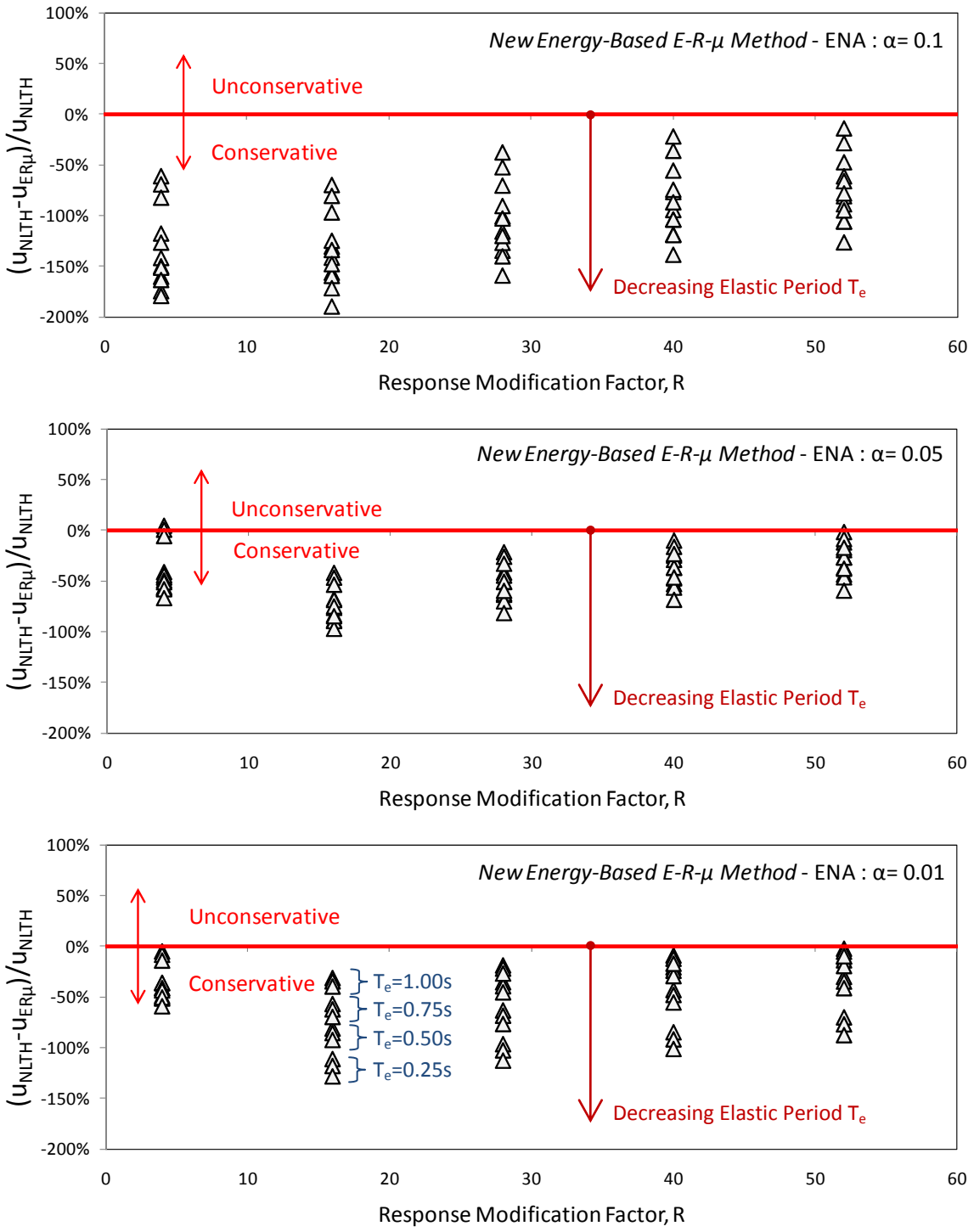

Figure 9.8 Relative error of the maximum displacements at the isolation level using the new energy-based *E-R-μ* method - PGD = 72 mm; T_g=0.89 s (mean of 20 Atkinson's records - ENA)

9.4 Example of Response Prediction Using Simplified Methods

In this section, an example is presented to illustrate the application of the current and modified simplified methods for the prediction of the response of an isolated bridge. The improvements achieved when using the modified simplified method are outlined. A bridge located near Montreal, Quebec, is adopted to represent a typical aging bridge that is seismically upgraded with an isolation system. Figure 9.9 presents the elevation of the bridge. The structure is 78 m long and has three equal spans crossing over a river obstacle.

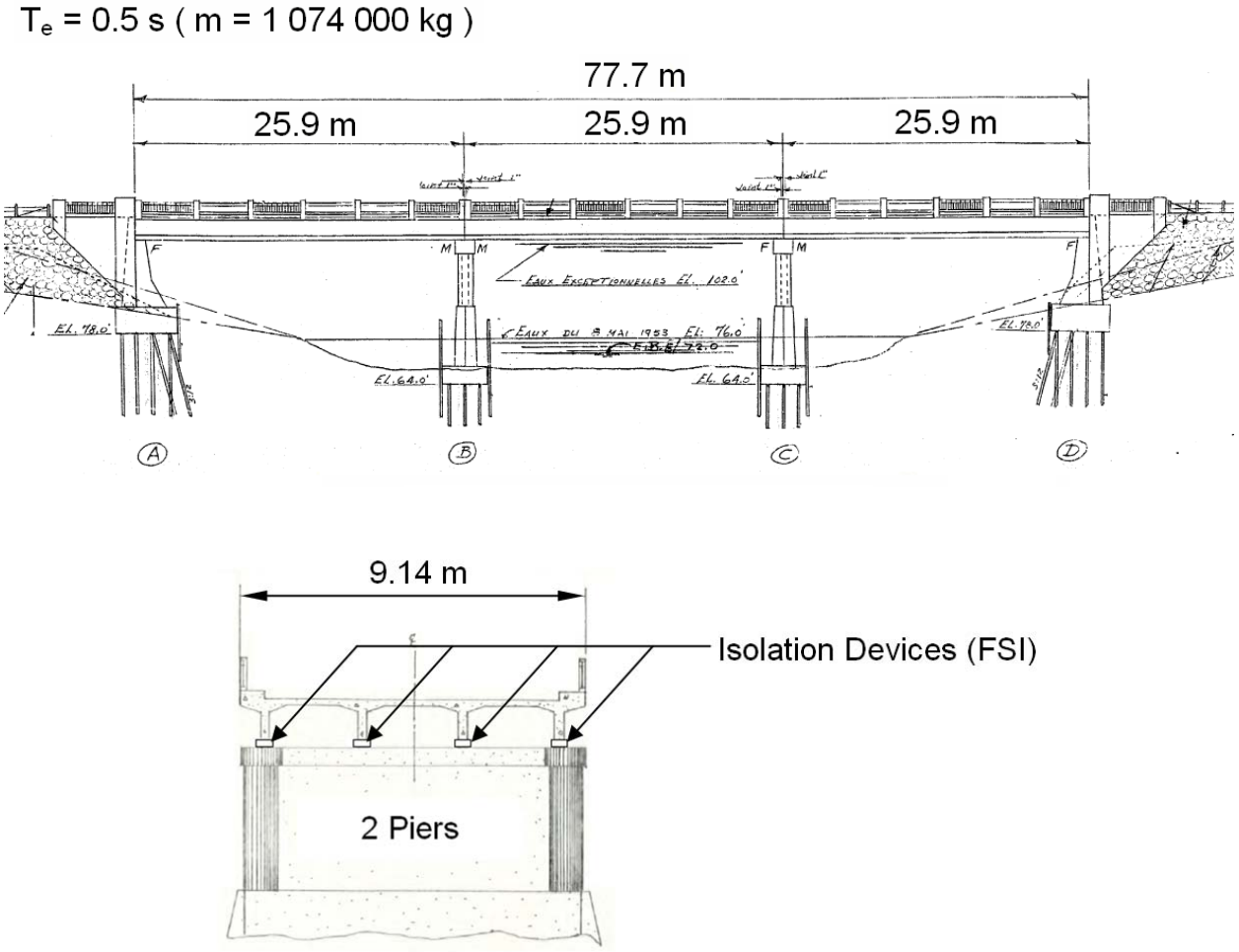

Figure 9.9 Archetype three-span bridge in Montreal

In this example, the bridge is analyzed in the longitudinal direction. In this direction, the bridge retrofit consists of incorporating isolation devices between the superstructure and both piers. Frictionless roller supports are considered at both abutments. A typical friction sliding isolation (FSI) device was adopted to increase the bridge seismic resistance.

The initial elastic period T_e of the bridge isolation system in the longitudinal direction is 0.5 s. The FSI devices have a high initial stiffness before being activated. The activation sliding strength was set equal to the force corresponding to a value of R equal to 4. Upon sliding, the FSI units exhibit elastic restoring force characterized by the post-yielding stiffness ratio $\alpha = 0.01$. The mean damped response spectrum obtained from the suites of 20 eastern records (ATK-E), as presented in Figures 5.2, is adopted for design. This ensures consistency between the demand considered for design and the NLTHA performed later to validate the design. For simplicity, the inherent damping of the structure is assumed to be equal to 5% of critical based on the effective structural properties. This is the same as the damping level considered in the design spectrum. The elastic stiffness of the isolated bridge structure is 169.6 kN/mm and the bridge displacement at activation is 5.2 mm.

In the example, response estimates are determined using three simplified methods:

1) Current CSA-S6-06 method using Equation (2.8) with n=0.3;

2) Modified CSA-S6-06 method using Equation (2.8) with n=0.2;

3) New energy-based E-R-μ method.

The results from these three approaches are summarized in Tables 9-2 to 9-4. The displacements shown are those of the superstructure relative to the ground. For the first two methods, the superstructure displacement is obtained following the iterative code procedure outlined in Table 9-1. For the new energy-based E-R-μ method, the direct method is used as presented in Table 8-1. All three response estimates are compared to the reference response from NLTHA. The relative errors with respect to the NLTHA are presented in Table 9-5. Positive error values correspond to unconservative response estimates. The comparison of the response predictions against the "exact" response from NLTHA is presented in Figure 9.10.

Table 9-2 Iterative approach for response estimate using current Equation (2.8) with n = 0.3 (where for β_{eff} > 30%, B = 1.7)

iteration	Sd_i (mm)	d_i (mm)	Error (%)	μ	T_{eff} (s)	β_{eq} (%)	β_{eff} (%)	B
1	20.8	20.8	-	4.01	0.99	45.9	50.9	1.70
2	36.2	21.3	2.24	4.10	1.00	46.2	51.2	1.70
3	36.5	21.5	0.63	4.13	-	-	-	-

Table 9-3 Iterative approach for response estimate using Equation (2.8) with n = 0.2

iteration	Sd_i (mm)	d_i (mm)	Error (%)	μ	T_{eff} (s)	β_{eq} (%)	β_{eff} (%)	B
1	20.8	20.8	-	4.01	0.99	45.9	50.9	1.59
2	36.2	22.8	8.53	4.38	1.03	47.0	52.0	1.60
3	37.5	23.5	3.02	4.52	1.04	47.4	52.4	1.60
4	38.1	23.8	1.29	4.58	1.05	47.5	52.5	1.60
5	38.6	24.1	1.36	4.64	1.06	47.7	52.7	1.60
6	39.1	24.4	1.15	4.69	1.06	47.8	52.8	1.60
7	39.1	24.4	-0.04	-	-	-	-	-

Table 9-4 Direct approach for response estimate using new energy-based *E-R-μ* method

PGD (mm)	PGA (mm/s^2)	T_g (s)	β_{inh} (%)	R	α	T_e (s)	T_d (s)	u_e (mm)	μ	d (mm)
72	3535	0.89	5	4	0.01	0.5	5	20.8	7.76	40.4

Table 9-5 Relative error for response estimates

Method	d (mm)	error
NLTHA	29.3	0%
CSA-S6-06 (Eq.2.8 with n=0.3)	21.5	27%
CSA-S6-06 (Eq.2.8 with n=0.2)	24.4	17%
New energy based R-mu method	40.4	-38%

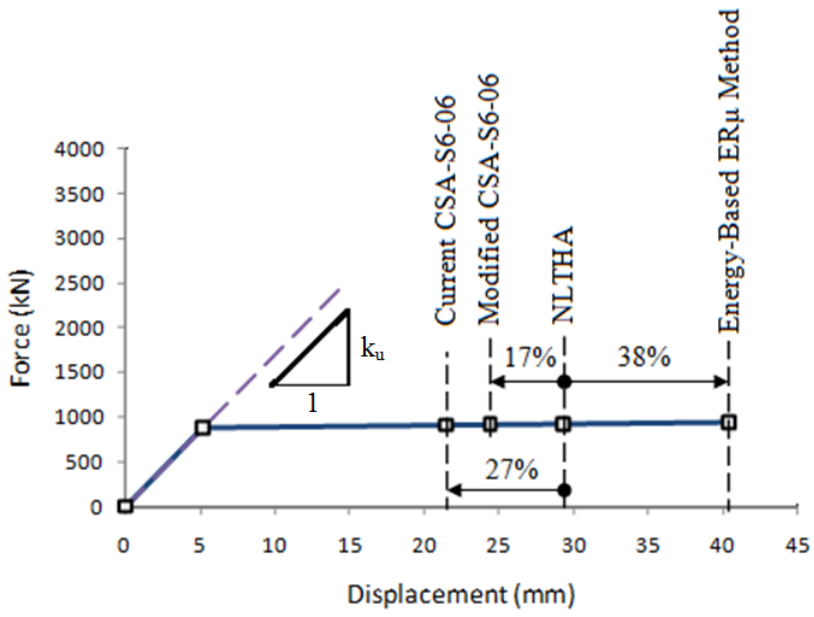

Figure 9.10 Response estimates using different methods (Current simplified CSA-S6-06 method; Modified simplified CSA-S6-06 method; New energy-based *E-R-μ* method; NLTHA)

In this example, both approaches using the simplified code method provide unconservative response estimates. The estimates obtained using the modified code method are more accurate than that from the current code method. However, both estimates are not close enough to the "exact" (NLTHA) response to be considered as satisfactory. Equally important is the fact that this simple structure does not satisfy the limits set in the CSA S6-06 for the current and modified methods:

i) In Table 9.3, the current CSA-S6-06 method using Equation (2.8) with n=0.3 (d=21.5 mm):

i-1) The effective damping ratio is higher than 30% thus B=1.7 is used according to CSA-S6-06, Table 4.8.

i-2) The bridge isolation system does not develop a lateral restoring force at least 0.025W greater than the lateral force at 50% of the design displacement, as required in CSA-S6-06 Clause 4.10.10.2 Lateral restoring force). The lateral force is verified as follows:

The displacement of the elastic system is given as:

$$u_e = S_D(0.5\ s;\ 5\%) = 20.8\ mm \tag{9.1}$$

The elastic limit which corresponds to the displacement at activation is determined using the response modification factor *R* as:

$$u_y = \frac{u_e}{R} = \frac{20.8\ mm}{4} = 5.2\ mm \tag{9.2}$$

The elastic stiffness is given as:

$$k_u = \left(\frac{2\pi}{T_e}\right)^2 m = \left(\frac{2\pi}{0.5\ s}\right)^2 1.074\ \frac{kN \cdot s^2}{mm} = 169.6\ \frac{kN}{mm} \tag{9.3}$$

The ductility demand at 100% of the design displacement d determined in iteration 3 (Table 9.2):

$$\mu_{100\%} = \frac{d}{u_y} = \frac{21.5\ mm}{5.2\ mm} = 4.14 \tag{9.4}$$

The ductility demand at 50% of the design displacement *d* is determined as:

$$\mu_{50\%} = \mu_{100\%} \frac{50\%}{100\%} = 2.07 \tag{9.5}$$

The effective stiffness at 100% of the design displacement using Equation (2.1) is:

$$k_{eff}(\mu_{100\%}) = 169.6\ kN/mm \cdot \frac{1 + 0.01 \cdot 4.14 - 0.01}{4.14} = 42.3\ kN/mm \tag{9.6}$$

The effective stiffness at 50% of the design displacement using Equation (2.1) is:

$$k_{eff}(\mu_{50\%}) = 169.6\ kN/mm \cdot \frac{1 + 0.01 \cdot 2.07 - 0.01}{2.07} = 82.8\ kN/mm \tag{9.7}$$

The system lateral force at 100% of the design displacement is determined as:

$$F(\mu_{100\%}) = 42.3\ kN/mm \cdot 21.5\ mm = 909.5\ kN \tag{9.8}$$

The system lateral force at 50% of the design displacement is determined as:

$$F(\mu_{50\%}) = 82.8\ kN/mm \cdot 5.2\ mm \cdot 2.07 = 891.3\ kN \tag{9.9}$$

The difference between the lateral forces at 50% and 100% of the design displacement is:

$$F(\mu_{100\%}) - F(\mu_{50\%}) = 909.5\ kN - 891.3\ kN = 18.2\ kN \tag{9.10}$$

The minimum force to be verified is found as (CSA-S6-06, Cl.4.10.10.2):

$$0.025W = 0.025 \cdot 1074000\ kg \cdot 9.81 m/s^2 \times 10^{-3} = 263.4\ kN \tag{9.11}$$

Thus, the minimum lateral restoring force requirement is not satisfied given that:

$$F(\mu_{100\%}) - F(\mu_{50\%}) < 0.025W$$

$$18.2\ kN < 263.4\ kN$$

ii) For the modified CSA-S6-06 method using Equation (2.8) with $n = 0.2$, the effective period must be longer than the value given by Equation (6.15):

$$T_{eff}(\beta_{eq-\max}) = T_e \cdot \alpha^{-0.25} = \frac{0.5\ s}{0.01^{0.25}} = 1.58\ s \tag{9.12}$$

The ductility demand at 100% of the design displacement determined at iteration 7 (Table 9.3):

$$\mu = \frac{d}{u_y} = \frac{24.4\ mm}{5.2\ mm} = 4.69 \tag{9.13}$$

The effective period is determined using Equation (2.2) as:

$$T_{eff} = 0.5\ s \cdot \sqrt{\frac{4.69}{1 + 0.01 \cdot 4.69 - 0.01}} = 1.06\ s \tag{9.14}$$

Thus, the minimum effective period requirement is not satisfied given that:

$T_{eff}(\beta_{eq-\max}) > T_{eff}$

$1.58\ s > 1.06\ s$

Hence, the current and modified methods could not be used for this particular example. The example therefore highlights how the new energy-based *E-R-μ* method represents an applicable alternative simplified approach for cases where the desired seismic protection scheme does not meet the code methods' limits.

9.5 Optimizing Bridge Performance with the New Energy-Based *E-R-μ* Method

The use of current seismic code provisions (CSA-S6-06 and AASHTO) for achieving a cost-effective isolation solution implies the use of an elaborate iterative analysis and design approach. The effective properties of a bridge such as the effective period and the effective damping must be redefined for each iteration, which represents a complex, time-consuming and laborious task.

In this section, it is illustrated how the *E-R-μ* method can be efficiently used to optimize the design of bridges with isolation and damping. For the same example presented above, an optimization design process is performed using the energy-based *E-R-μ* method.

Figures 9.11 and 9.12 illustrate how the displacement and force vary with the characteristic strength Q_d. In Figure 9.11, the intersection of the displacement and force curves does not necessary indicate an optimal solution. This point is arbitrary set to represent the bridge configuration previously adopted in this study. In such a way the tendencies in response of a bridge structure are outlined providing information needed to find the response that best meets the performance target.

The optimum displacements and forces can be found by only varying the bridge parameters in Equations (8.28) and (8.31). For the same T_d and α, if the force activation, or characteristic strength Q_d, is reduced, the seismic forces transmitted by the isolators to the bridge substructure decrease. In such a case, the effective period of the structure lengthens, resulting in larger displacement response. Target performance objectives for the bridge structure may be achieved by carefully selecting the activation force of the isolators. For example, in Figure 9.11, it is shown that Q_d = 881 kN is needed to limit the displacement to 40 mm. Using Q_d = 400 kN will result in an increased displacement of 55 mm. For this structure, this would translate in an increase of the response modification factor from R = 4.0 to 8.74.

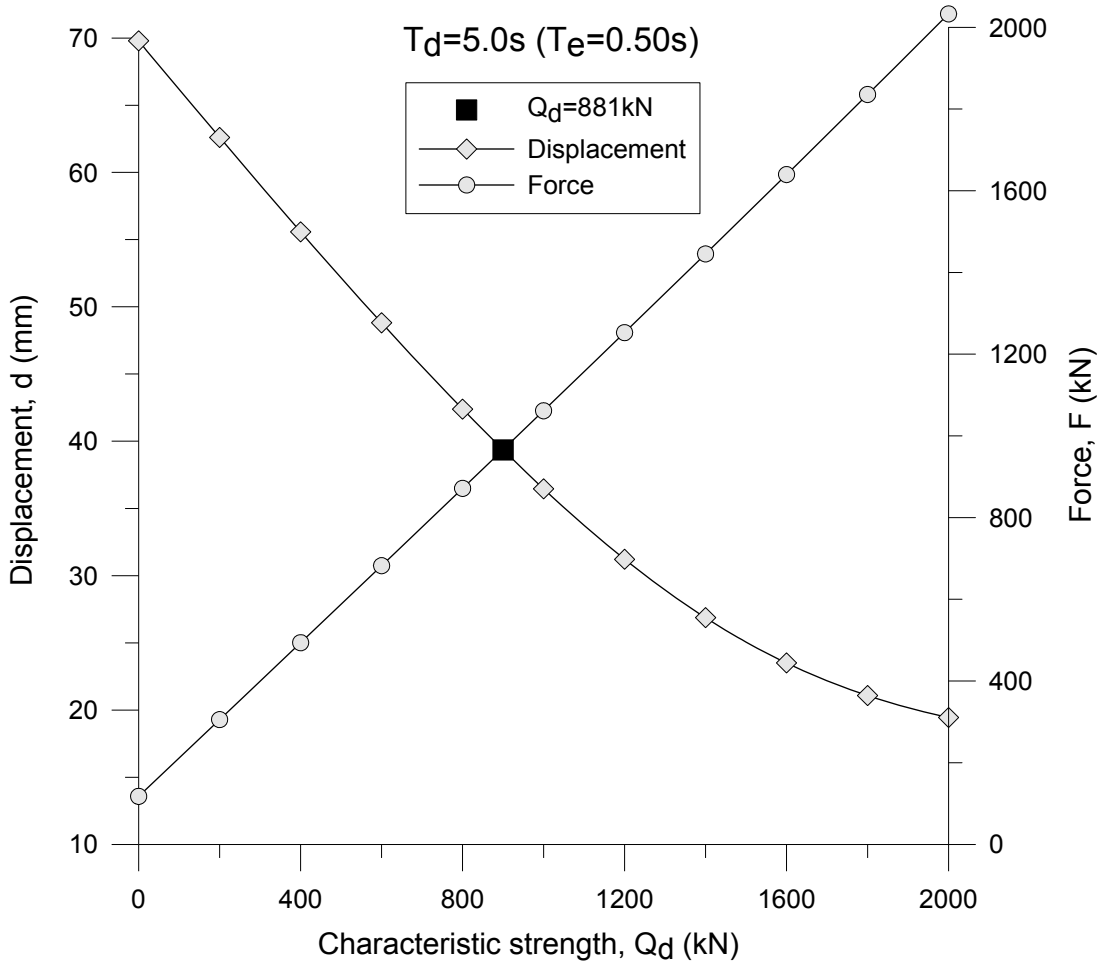

Figure 9.11 Displacement and force responses with characteristic strength Q_d

The results in Figure 9.11 were obtained with T_d = 5 s and α = 0.01. As is shown in Figure 9.12, an additional reduction in the displacement response may be obtained by reducing the period T_d. This can be achieved by increasing α or by reducing the elastic period T_e.

The post-yielding stiffness ratio α for friction sliding isolators (FSI) may be ensured by supplemental lateral spring elements that are installed in parallel with the sliding surface as shown in Figure 2.7. FSIs usually have a very small activation displacement u_y. However, when the sliding interface is combined in series with an elastomeric pad, the elastic period T_e may be adjusted as a function of the height of the elastomeric pad.

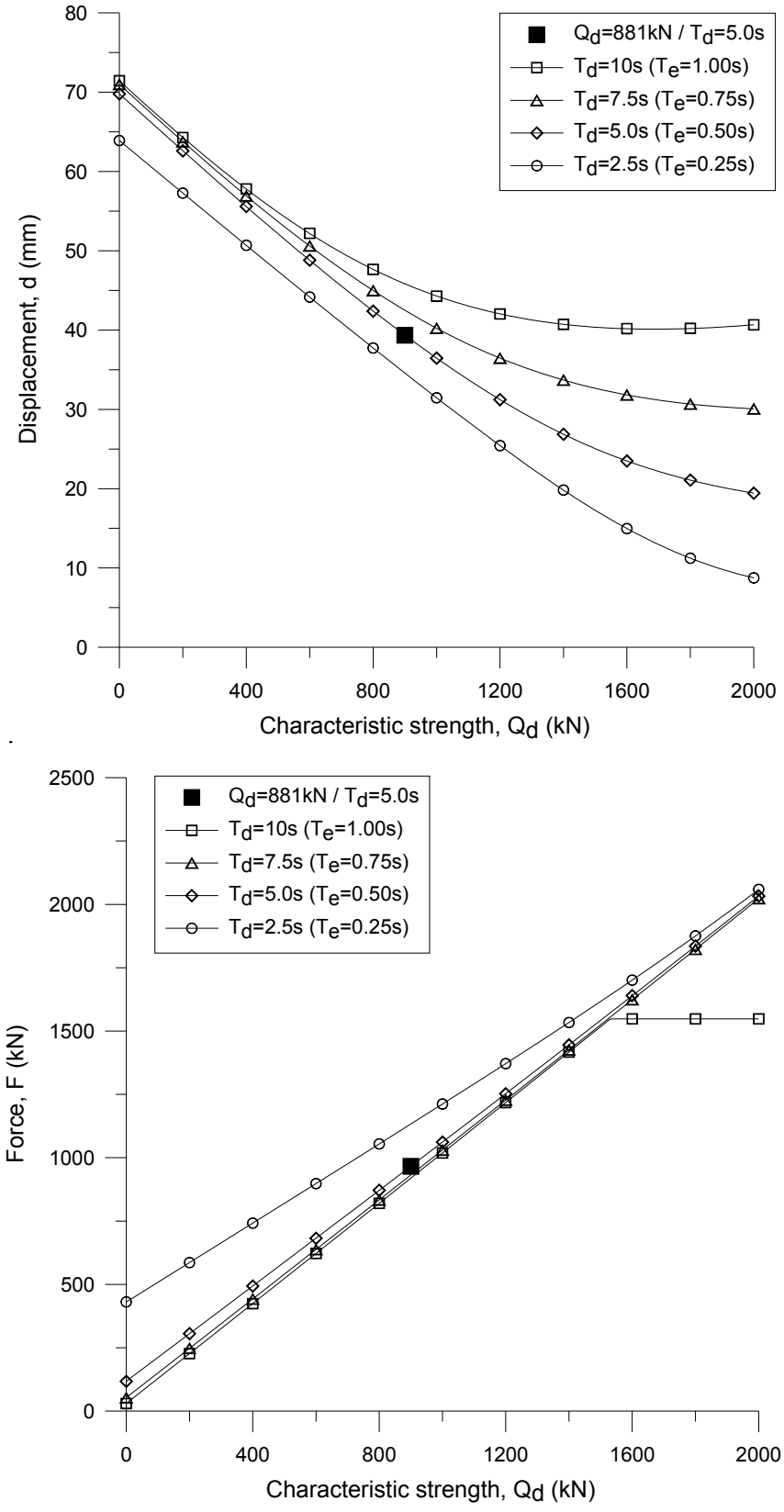

Figure 9.12 Bridge response with characteristic strength Q_d and period T_d

The example discussed below illustrates how the peak seismic force can be reduced while the target displacement of 40 mm is met. The optimization process is performed using the new energy-based *E-R-μ* method. An optimum solution is achieved by varying the period T_d and characteristic strength Q_d.

In Figure 9.12, it is shown that for T_d=10 s, the displacement can be reduced by increasing Q_d up to 1530 kN beyond which the displacement remains at its minimum of 40 mm. For the range of $Q_d \geq$1530 kN, the system behaves elastically and the minimum displacement and maximum force correspond to the system maximum elastic response u_e and F_e, respectively.

To obtain the same displacement of 40 mm when using a shorter period T_d, a reduced Q_d will be needed. The solutions for displacements and forces obtained for this particular problem are summarized in Table 9-5 for four values of T_d. As shown in Figure 9.13, among the four periods considered in this example, the best solution corresponds to T_d =5.0 s and Q_d =881 kN. How the optimum response can be defined as a function of the response modification factor *R* is presented in Figure 9.14. The peak seismic forces will be reduced by 39% when compared to those from the system with T_d =10 s and Q_d =1530 kN. The decrease in forces to be resisted by a structure can provide bridge owners with significant cost saving.

Table 9-6 Direct approach for response estimate using new energy-based *E-R-μ* method

Bridge Parameters					Ground Motion Characteristics		Bridge Response Estimates			
T_e (s)	T_d (s)	Q_d (kN)	W (kN)	R	PGD (mm)	T_g (s)	μ	d (mm) Eq.(8.28)	F (kN) Eq.(8.31)	(%)
1.00	10	1530	10536	1.0	72	0.89	1.00	**40**	1547	100
0.75	7.5	1010	10536	2.5	72	0.89	2.96	**40**	1040	67
0.50	**5.0**	**881**	**10536**	**4.0**	**72**	**0.89**	**7.76**	**40**	**947**	**61**
0.25	2.5	730	10536	8.0	72	0.89	36.8	**40**	1000	65

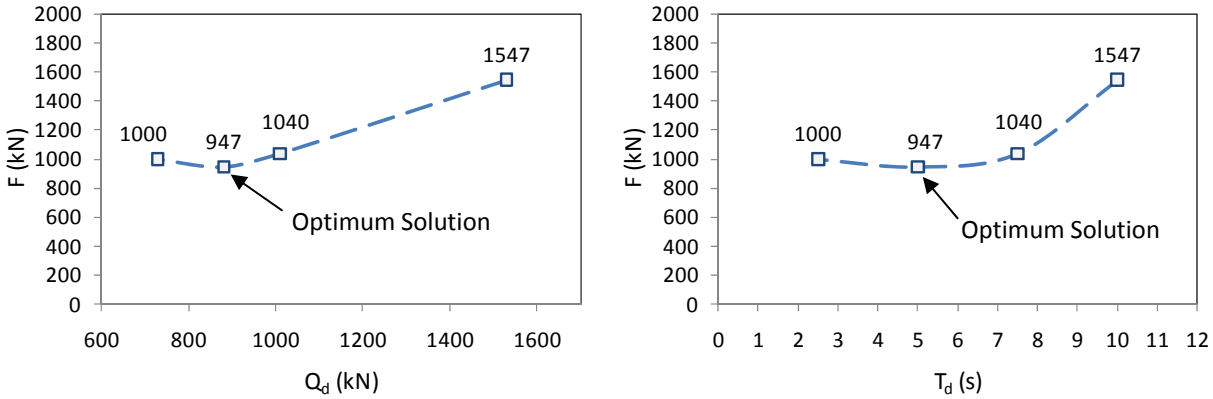

Figure 9.13 Peak seismic forces with characteristic strength Q_d and period T_d

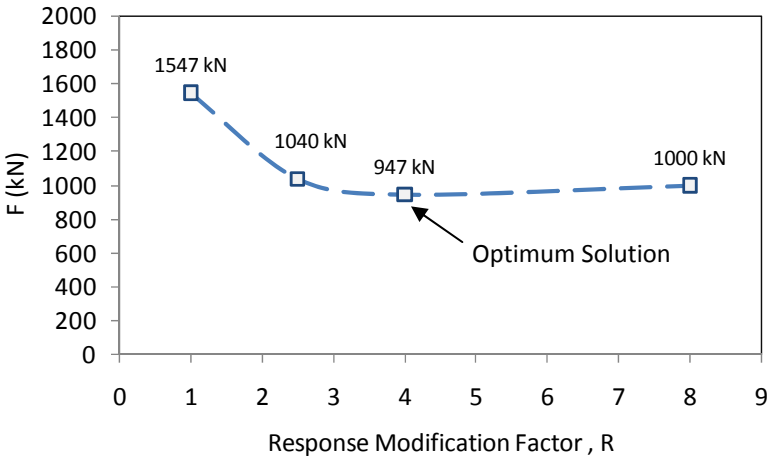

Figure 9.14 Peak seismic forces with response modification factor R

These examples show that the proposed method can be very effective for the selection of an optimum isolation system. The main reason being that the method is not iterative and a large number of possible solutions can be obtained directly to evaluate the most appropriate scheme for the studied structure and design objective.

9.6 Conclusions

In this chapter, the modifications proposed within this research to improve the accuracy and extend the applicability of the current code simplified method (CSA-S6-06) were summarized and discussed. The ability to accurately predict the response of isolated bridges was demonstrated for a series of 180 isolated bridge structures.

It was shown that the modified simplified code method proposed in this thesis for estimating displacement demand result in comparable relative errors ranging from 5% (unconservative) to -50% (conservative) for both WNA and ENA. In addition, a wider choice of the market-available seismic protective devices can be covered by the modified simplified method.

The displacements of the same 180 isolated bridges were determined using the new energy-based method proposed in Chapter 8 as an alternative design approach that accounts for different structure parameters and strong ground motion characteristics. It was confirmed that the proposed energy-based method results consistently in conservative response prediction. The level of conservatism generally decreases as the response modification factor R and elastic periods T_e increase, thus suggesting that the proposed energy-based E-R-μ method is an appropriate approach for designing bridge structures with a high level of isolation.

A bridge retrofit example was presented to compare the current code and proposed simplified methods. The example showed the possibility of using the new energy-based method as an alternative design approach when the code methods' requirements are not satisfied.

This new energy-based E-R-μ method can be adopted for preliminary design as a straight-forward procedure to define an optimum seismic protection strategy. More efficient and reliable seismic protection systems may be designed providing bridge owners with significant cost saving. The use of the new energy-based E-R-μ method in the context of developing optimum cost-effective isolation solutions is further presented in the next chapter.

Chapter 10: Dual-Level Seismic Protection Approach for Isolated and Damped Bridge Structures

10.1 Introduction

The design of isolated brides using current seismic code provisions (CSA-S6-06 and AASHTO) implies the use of an elaborate iterative analysis and design approach. The effective properties of the bridge such as the effective period and the effective damping must be redefined for each iteration. The properties of the seismic isolation devices may vary due to the effects of wear, aging, and temperature, which introduces an additional degree of complexity for the design of isolated bridges. Use of such an iterative approach for achieving a cost-effective isolation solution for different levels of earthquake performance represents for engineers a complex, time-consuming and laborious task.

The current seismic code provisions (CSA-S6-06 and AASHTO) do not provide an explicit optimization procedure that allows engineers to fully benefit from the performance enhancements that can be achieved with isolation and damping. In particular, it is still challenging to meet specific performance objectives under different levels of seismic hazard by using a single isolation scheme when its properties are based on a single seismic hazard level.

The possibility of achieving the multi-level performance goals in seismic protection of isolated buildings has been investigated Morgan and Mahin (2011) using the triple pendulum isolator. The triple pendulum isolator is capable of exhibiting different hysteretic characteristics under different hazard levels. The appropriate hysteretic properties must be established for each design case by carefully selecting the pendulum radii, friction coefficient and dish displacement. As the three pendulum mechanisms are progressively activated, the response becomes stiffer thus limiting isolator displacements under rare earthquakes while allowing increase in force demand. The stiffening effect is particularly efficient for seismic protection of buildings given that the drift demand in the superstructure is limited. However, the researchers stated that this effect may not be general for a wide-class of structural systems and further investigations will be needed. For seismic protection of bridges, the response stiffening is less advantageous given that the

limits in isolator displacement demand may be less stringent than for buildings. It is rather preferred to limit the displacement demand in the bridge substructure thus limiting the forces imposed to the piers and abutments. It is apparent that there is no potential in using the triple pendulum isolators as a force-limiting fuse protection which can be achieved by using conventional isolators without recentring capability. The development of a new multi-hazard protection concept is of significance for achieving optimal designs for the upgrade of existing seismically deficient bridges and for the design of new isolated bridges.

In the previous chapter it was shown that the new energy-based *E-R-μ* method can be very effective for the selection of an optimum isolation system. The main reason being that the method is not iterative when using direct procedure (Table 8-1) and a large number of possible solutions can be obtained directly from the *E-R-μ* relationship. This new energy-based *E-R-μ* method can therefore be adopted for preliminary design, allowing engineers to rapidly identify the most appropriate scheme for the structure for multi-level-hazard design objectives.

To fill the gap in the design of isolated bridges for multi-level-hazard objectives, this chapter introduces a Dual-Level Seismic Protection (DLSP) design method. This method relies on the combination of different isolation and damping systems to achieve a different optimal response for different seismic hazard levels. The proposed methodology makes uses of the new energy-based *E-R-μ* method presented in Chapter 8. In this chapter, the methodology is first described and then applied for the seismic retrofit of existing, seismically deficient bridges. Detailed DLSP designs are carried out for the bridge structures with the primary objective of preventing damage to the substructure under two different seismic hazard levels. An optimization process is then used to identify the properties of the system that best meet the stringent lifeline bridge design objectives at the two hazard levels.

The optimal design process of a DLSP is illustrated by using the energy-based *E-R-μ* method for the retrofit of a bridge in Montreal. Then, an optimization process is shown for a bridge in Vancouver using detailed NLTHA. These two approaches for configuring the DLSP system are presented to illustrate that the DLSP concept is self-contained and independent from the adopted design method. The estimates predicted using the new energy-based *E-R-μ* method are compared to the response obtained from NLTHA to demonstrate the appropriateness of adopting this method for preliminary design to define an optimum seismic protection strategy. To enhance the

multi-level-hazard performance, a further optimization of the system that can be achieved by introducing viscous dampers at the abutments is also investigated through nonlinear time-history analyses.

10.2 Seismic Performance Objectives for Dual-Hazard Level Design of Bridges

The concept of performance-based design is based on the ability to realistically evaluate seismic demands and assess the performance of the structure under such demands. Following the 1989 Loma Prieta and 1994 Northridge earthquakes, performance based design criteria and recommendations were proposed for the seismic design of bridges (ATC 1996a, 1996b). For the first time, a design approach based on two levels of seismic hazard, the functional-evaluation earthquake and the safety-evaluation earthquake, was implemented. This approach was then incorporated in different performance-based specifications for the seismic design of bridges. The primary performance objective is to provide for life-safety under an upper-level design seismic demand that corresponds to ground motion effects with low probabilities of exceedance, typically in the range of 2% to 10% in 50 years (corresponding to 2,475 and 475 year return periods, respectively). The implementation of the lower-level design seismic demand was motivated by the unexpectedly high bridge repair costs resulting from the destructive earthquakes of 1989 and 1994. Even though the intended goal of preventing the loss of life was achieved, the extensive damage to bridges was a disappointing aspect that clearly demarked "the need to consider seismic design in a manner that limits the repair costs and the time needed to complete the repair" (Itani and Malik, 2000). Table 10-1 presents performance objectives in terms of damage for two hazard levels that have been proposed for possible inclusion in the future edition of the CSA-S6 Canadian Highway Bridge Design Code (Huffman et al. 2012). Two hazard levels are considered: the Design (DE: upper-level) and the Service (SE: lower-level) earthquakes with a probability of exceedance of 2% and 10% in 50 years, respectively. The functionality objectives immediately after the DE are summarized in Table 10-2.

Table 10-1 Bridge classification performance levels (Huffman et al. 2012)

Earthquake level	Performance level		
	Other (OR)	Major Route (MR)	Lifeline (LL)
Design (2% - 50 years)	Life Safety	Extensive	Repairable
Service (10% - 50 years)	Extensive	Repairable	Minimal

Table 10-2 Expected bridge functionality levels (summarized from Huffman et al., 2012)

Performance Level	Expected Bridge Functionality
Minimal	Fully serviceable for normal traffic
Repairable	Can be used for emergency traffic, and repair can be made without closing the entire bridge allowing normal service within a short time
Extensive	Can be used for restricted emergency traffic after inspection, and with repair can be restored to full service
Life Safety	May be unusable. Persons on the bridge should be able to exit safely

The use of isolation and damping techniques is an efficient means of achieving the desirable level of earthquake performance and safety. However, it is difficult to achieve the desired design objectives at each of the two seismic hazard levels while taking full advantage of the benefits provided by the isolation and damping systems. In practice, the design is carried out for a single-hazard performance level, usually corresponding to the highest seismic hazard, and the consequences of this design on the performance for lower seismic hazard levels are accepted, without any optimization. Such a design approach usually results in seismic protective solutions that bring no or very limited improvement to the performance of the bridge structure under more frequent, smaller SE events because the isolation system is unlikely to be activated under such earthquakes. Prevention of damage under SE events will require that the bridge be designed to respond elastically for this seismic hazard level. If, in contrast, the protection system is designed to fully engage under the lower-level (SE) event, the bridge is likely to experience excessive deformations across the isolation system and, thereby, extensive damage or even the possibility of collapse under a stronger earthquake (DE). Ideally, a bridge protective system based on isolation and damping should positively impact the seismic performance at both hazard levels.

Such an optimum response can be achieved by using a DLSP design methodology. The approach relies on carefully selecting and establishing an effective hierarchy of activation of different protective devices exhibiting complementary properties.

10.3 DLSP Concept for Seismic Protection Mechanism

The Dual-Level Seismic Protection (DLSP) design implemented in this study is based on the selection, combination and sizing of different isolation and damping systems to develop a predefined hierarchy of activation in order to achieve optimal responses for different seismic hazard levels. Isolation devices are introduced at all supports to act as fuses and to control the seismic input in the substructure.

The combination of isolators and supplemental dampers for the protection of a simple two-span bridge along the longitudinal direction is illustrated in Figure 10.1. This is a simplified protection layout that can also be adopted for bridges with more than two spans as illustrated in Section 10.5. The protection system can be represented by the 2-DOF numerical model that was presented in Chapter 3. This model includes both the mass of the substructure, m_1, and the mass of the superstructure, m_2. The inelastic response of the system is modelled by assigning nonlinear properties to the springs characterizing the bridge piers, k_1, the isolators at the piers, k_2, and the isolators at the abutments, k_3. Linear or nonlinear damping properties c_1, c_2 and c_3 are assigned to dashpots that represent the pier inherent damping, dampers at the piers, and dampers at the abutments, respectively. This model is general and can be simplified for simpler systems by setting the appropriate parameters to zero if they are not present in a particular design.

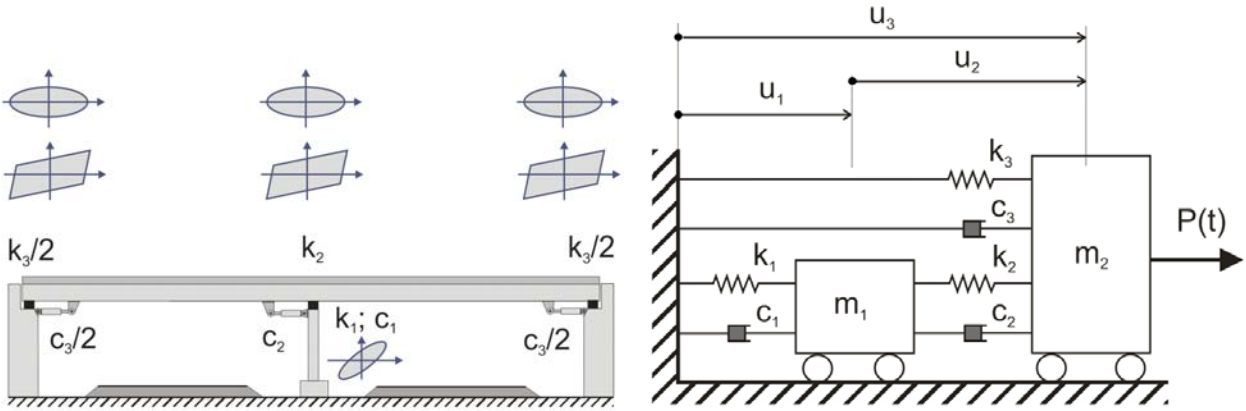

Figure 10.1 Bridge seismic protection along longitudinal direction of a bridge: a) Combination of seismic isolators and supplemental dampers; b) 2-DOF equivalent model (see Chapter 3).

Typically, some properties of the system can be initially selected based on key performance objectives. Other properties are subsequently determined by optimizing the bridge response through a large number of possible solutions obtained directly for each hazard level using the new energy-based *E-R-μ* method.

Using the Dual-Level Seismic Protection (DLSP), the optimum solutions are achieved by defining an effective hierarchy of two activation stages denoted as Stage I and II, respectively. The hierarchy of activation of the individual components is tailored to form a DLSP system that effectively meets design objectives corresponding to both seismic hazard levels defined in Table 10-1 as the Design (DE) and the Service (SE) earthquakes. The DLSP optimization concept for the seismic protection mechanism is summarized in Table 10-3.

Table 10-3 DLSP optimization strategy for seismic protection mechanism

Stage I	Longitudinal displacements are controlled by the energy dissipation mobilized in the isolation and damping devices located at the two abutments without the activation of the isolation system located at the bridge piers. In this case, the forces attracted by the piers are kept low enough to ensure that the piers remain in the elastic range ($F_{2y} > F_{2(10\%\text{-}50y.)}$ or $u_{2y} > u_{2(10\%\text{-}50y.)}$).
Stage II	The isolation systems at the piers are activated, limiting the forces imposed to the piers (by setting $F_{2y} < F_{1y}$). The resulting increase in displacement in Stage II is mitigated through a higher restraint being offered by the isolators and dampers positioned at the abutments.
Optimum solution	Amongst the various solutions satisfying the pre-defined objectives at the two seismic hazard levels, the optimum solution is the one inducing the lowest forces to be resisted by the abutments.

The DLSP system can be configured using different seismic protection devices such as dampers and isolators. The DLSP concept is independent from the type of adopted isolators. However, the concept requires that isolators with recentring capability are installed at the abutments while isolators without recentring capability are installed at the piers. From the capacity perspective, the abutment structures are typically laterally stiffer and more resistant than the piers due to the contribution of the wing walls and backfill. For this reason, it would be more cost effective to concentrate the force restoring capability in a few abutments' isolators. The isolators on the piers would dissipate seismic energy while controlling the forces imposed on the piers.

The design optimization flowchart for the DLSP system is presented in Figure 10.2. The bridge category and corresponding performance objectives are defined in Steps 1 and 2. Then, in Step 3, the inelastic structural response of the bridge substructure is assessed to explicitly relate the resulting structural parameters (u_y and u_u) to the performance objectives. In Steps 4 to 6, the elements of the DLSP system are selected and configured.

The isolators at the piers are simply selected to act as force-limiting fuse protection in Step 4. Then, in Step 5, the post-yielding stiffness, k_{d3} is configured. For the initial design phase, k_{d3} is set so that the elastic displacement response, $S_d(5\%,T_e)$ of the bridge deck, u_3, is lower than the limit $u_{max(10\%\text{-}50y)}$ under SE. As previously studied in Chapter 7, adopting the Equal Displacement Approximation (EDA) for structures with low R-ratios and periods longer than 0.5 s, the inelastic displacement response is assumed to be close to that of an elastic response of the bridge. Thus, the initial parameter k_{d3} is configured to start the optimization process. The parameter k_{d3} can be adjusted in Step 10 if required for the system to meet the target performance objectives.

The optimization process comprises steps from 6 to 11. The activation limits Q_{3d} of the isolators located at the abutments (selected in Step 6) is a critical parameter for the reduction of the maximum force transmitted to the abutments. For convenience in the optimization process, this limit can be defined as a function of the response modification factor R.

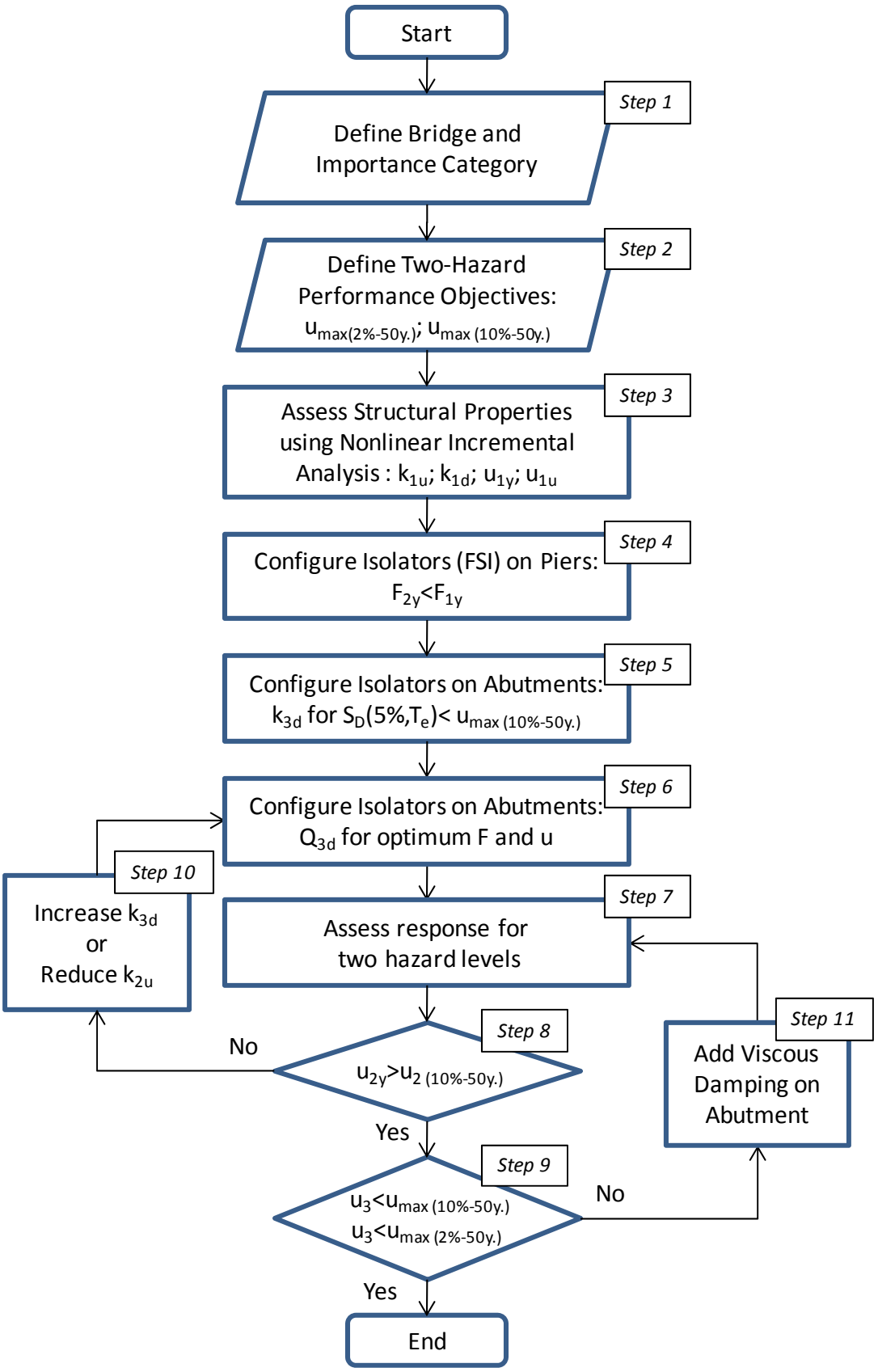

Figure 10.2 Optimization flowchart for DLSP

Figure 10.3 illustrates how the normalized displacement u / u_e and normalized force F / F_e vary with the response modification factor R. The intersection of the displacement and force curves is arbitrary set at the SE intensity to outline the tendencies in the response of a bridge structure when the earthquake intensity increases up to the DE level.

For a given bridge structure, the same activation limit Q_{3d} may correspond to different R-factors being representative of different seismic hazard levels. The response modification factor R increases with the earthquake intensity and, as shown in Figure 10.3, the factors R_{min} and R_{max} correspond to the SE and DE hazard levels, respectively. As the R-factor increases, the normalized forces F / F_e transmitted by the isolators to the substructure decrease and the normalized displacements u / u_e increase. The DE corresponds to larger displacements and higher R-ratios when compared to the SE. As shown for the example in Figure 10.3, this would translate in an increase of the response modification factor from R = 4.0 (SE) to 16 (DE).

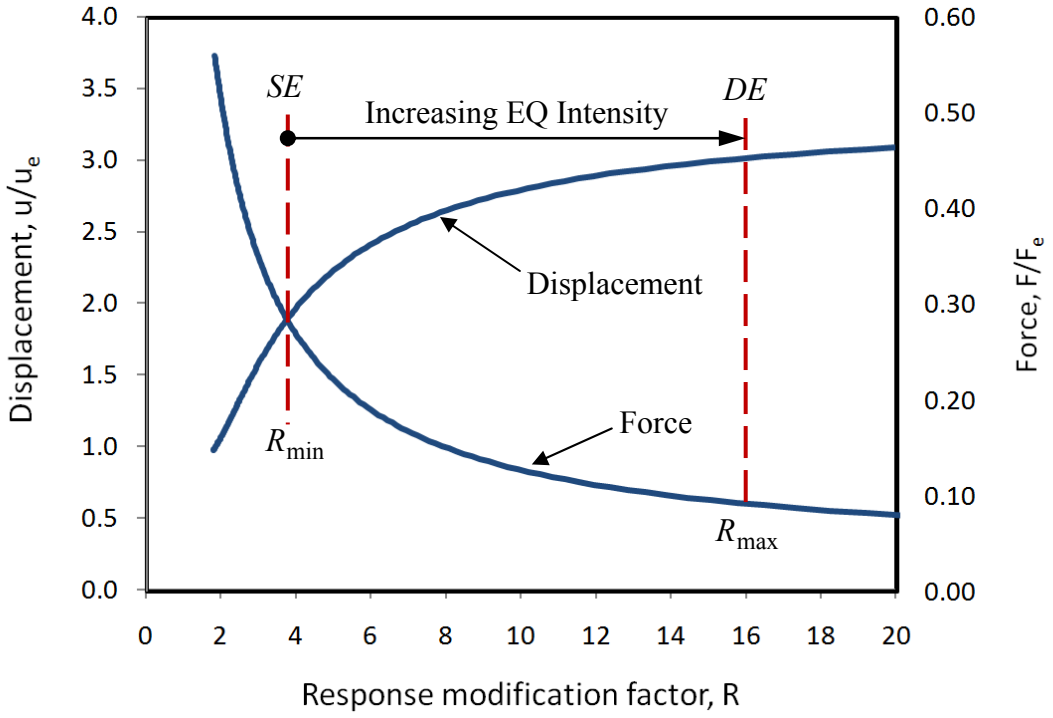

Figure 10.3 Response of isolated bridges with response modification factor R in ENA using Equation (8.20) PGD = 72 mm, T_g = 0.89, T_e = 0.5, α = 0.01

For a given hazard level, different R-factors represent different activation limits, thus providing a range of possible isolation arrangements. The activation limit is selected such that among the

different responses satisfying the target performance objectives, the one optimizing the displacement and force demands would be selected.

In Step 7, the responses are assessed for the bridge piers, the isolators at the piers, and the isolators at the abutments. If the isolators at the piers are activated under SE rather than under DE as suggested in Table 10.3 for Stage II (check in Step 8), the lateral stiffness k_2 can be reduced by adding elastic pads between the pier and the isolators in Step 10 (see discussion in Chapter 2, Figure 2.7). In Step 9, the displacements of the bridge deck u_3 are compared to the limits $u_{max(10\%\text{-}50y)}$ and $u_{max(2\%\text{-}50y)}$ under SE and DE, respectively. If adjustments are necessary to satisfy the target performance objectives, the displacements are controlled by adding velocity-dependent damping elements in Step 11.

The DLSP design methodology presented above must be adjusted to take into account the variability of the system properties due to the effects of wear, aging, and temperature. The exact properties of the isolation devices can be rarely known over the bridge lifespan. Nevertheless, the actual properties of the isolation devices subjected to different loading, environmental, and aging conditions can be evaluated through testing such that maximum and minimum probable values can be established. The properties that are most likely subject to variations are the stiffness and the characteristic strength.

To consider the variation in isolator properties, the well known bounded analysis procedure using lower (LB) and upper (UB) bound property values is considered for every hazard level. The UB values represent higher activation forces which result in lower *R*-factors. Conversely, the LB values result in higher *R*-factors and are characterized by larger displacement demands. For each hazard level, the range of responses between the UB and LB values may be assessed as a function of the response modification factor *R*. Optimum protection solutions can then be found though a bounded analysis.

By considering two hazard levels with specific sets of properties for each level, the response range is defined between the SE-UB (Service Earthquake Upper-Bound) and DE-LB (Design Earthquake Lower-Bound) thus corresponding to R_{min} and R_{max}, respectively. The new energy-based E-R-μ method is applied to evaluate the most appropriate scheme for the studied structure and design objective. Such an approach provides engineers with the information they need to establish a range of design displacements. Then, the SE-LB and DE-UB levels should be

checked more carefully after the design is completed. The forces obtained with this technique correspond to those transmitted to the substructure by the isolation system and, when used, the dampers.

Although not investigated in this study, the same methodology can be applied for a new bridge to reduce construction costs for the main structural members in addition to achieving higher performance at multiple hazard levels.

10.4 Energy-Based *E-R-μ* Method for Designing a Dual-Level Seismic Protection System for a Bridge Retrofit in Montreal

In this section, the optimal design process of a DLSP is illustrated by using the energy-based *E-R-μ* method developed in Chapter 8. The effects of aging and temperature on the isolator sliding resistances will be considered.

A simplified procedure for developing an optimum DLSP system is presented and validated against the results obtained from NLTHA.

The Dual-Level Seismic Protection (DLSP) system developed in this example is based on the DLSP's assumptions and methodology described in Section 10.3. Isolation devices are introduced at all supports to act as fuses and to control the seismic input in the substructure. As suggested by the DLSP's concept (Table 10-3) the isolators without recentring capability are installed at the piers while isolators with recentering capability are installed at the abutments. The hierarchy of activation is predefined so that isolators located on the abutments are activated under SE (Stage I) and isolators on the piers are expected to start sliding under DE (Stage II). An optimization process as specified in Figure 10.2 is then used to identify the properties of the system that best meet the lifeline bridge design objectives at the SE and DE hazard levels defined in Table 10-1.

The protection system considered for this example consists of flat sliding isolators (FSI) as described in Chapter 2. For the FSI isolators, the energy dissipation is provided through sliding friction between a stainless steel interface and a compound slider surface. The restoring force capacity is ensured by supplemental lateral spring elements that are installed in parallel with the sliding surface for FSI devices. The FSI isolators have a very small activation displacement due

to a high pre-activation stiffness. The pre-activation displacement can be increased when the sliding interface is combined in series with an elastomeric pad as illustrated in Figure 2.7.

10.4.1 Defining Bridge and Importance Category

An existing two-span concrete bridge was used to represent a typical overpass bridge that needs to be seismically retrofitted. The superstructure is a continuous two-girder concrete post-tensioned deck spanning a total length of 76 m and being supported at mid-length by a single pier (Figure 10.4).

As part of the seismic retrofit, the bridge is upgraded from the ordinary *Other bridges* category to the *Lifeline* bridge importance category. A target performance to be achieved with the DLSP system is defined for the two hazard levels considered and is based on the recommendations outlined in Table 10-4.

a)

b)

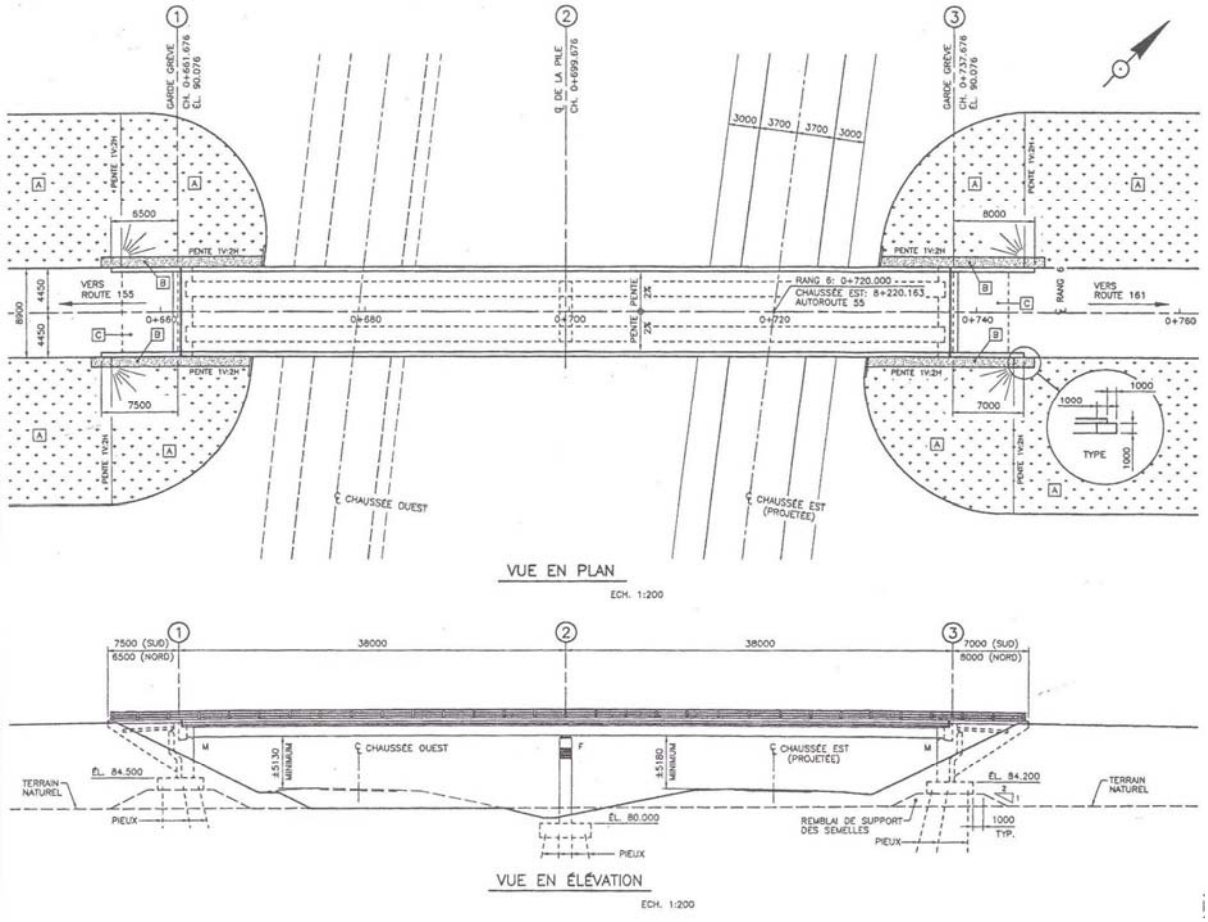

Figure 10.4 Photo (Google Maps- ©2012 Google), plan and elevation of the two-span bridge in Montreal

Table 10-4 Dual-level performance objectives for design of isolated bridges

Stage	Hazard level	Performance objectives		
		Bridge	Abutment	Pier
I	SE (10% - 50 years)	Functional No damage	Isolator activated Elastic response	Isolator not activated Elastic response
II	DE (2% - 50 years)	Functional Minor damage	Isolator activated Elastic response	Isolator activated Elastic response

10.4.2 Defining Dual-Hazard Performance Objectives

The performance objectives are that the bridge structure (superstructure and substructure) responds essentially elastically under both hazard levels ($u_{1max} < u_{1y}$) and is fully serviceable for normal traffic following both DE and SE events. This is referred as Functional in Table 10.4. *Minor Damage* to the bridge is tolerated under DE events as long as it does not impair its normal operation and its repair does not require total closure of the bridge. Examples of *Minor Damage* correspond to the superstructure expansion joints exceeding their displacement limit, cracking or residual displacement during a DE motion. For this example, a damage threshold of 20 mm is adopted for the expansion joints.

The isolation and damping devices, in turn, must exhibit adequate performance under the effects of a main shock and remain functional for possible aftershock motions. The need for explicit performance criteria for aftershocks is based on observations in past earthquakes such as the situation that occurred in 2012 in Italy`s Emilia-Romagna region where a M6 main shock (May, 20) was followed by two damaging aftershocks of M5.8 and M5.4 (May, 29) (EQECAT, 2012)). The total economic losses were greatly increased as a result of the aftershocks. Accordingly, a limit of 50 mm is adopted in this example to represent the maximum allowable displacement for the abutment isolators. Exceeding this limit, isolators on the abutments will be damaged.

10.4.3 Assessing Structural Properties using Nonlinear Incremental Analyses

Figure 10.5 presents the results from an inelastic lateral pushover analysis of the bridge substructure. The axial load acting on the pier is 10 301 kN. The response was obtained through nonlinear incremental static (pushover) analyses using Response 2000 (Bentz, 2000). Three response stages can be distinguished as the load is increased. The first stage corresponds to the uncracked concrete state where the contribution of concrete in tension is assumed to be linear elastic. Immediately after the first cracking, the concrete cracking stage is characterized by a gradual reduction in stiffness. The concrete elements can carry tension between the cracks through the tension stiffening phenomenon (Bentz, 2000). Due to the concrete degradation during a structure's life span, the real stiffness that corresponds to the cracking stage before yielding is not known with certainty. Assuming that elastic response of the pier structure is ensured by the contribution of the steel reinforcement, the tension stiffening effect is neglected in the pier modeling. The pier elastic stiffness is then determined from the linear secant segment as shown below in Figure 10.5 ($k_{1u} = u_y / F_y$). The resulting structural parameters are $k_{1u} = 11\ 273$ kN/m, $F_y = 620$ kN and $u_y = 55$ mm. These parameters are applied herein to configure the DLSP system.

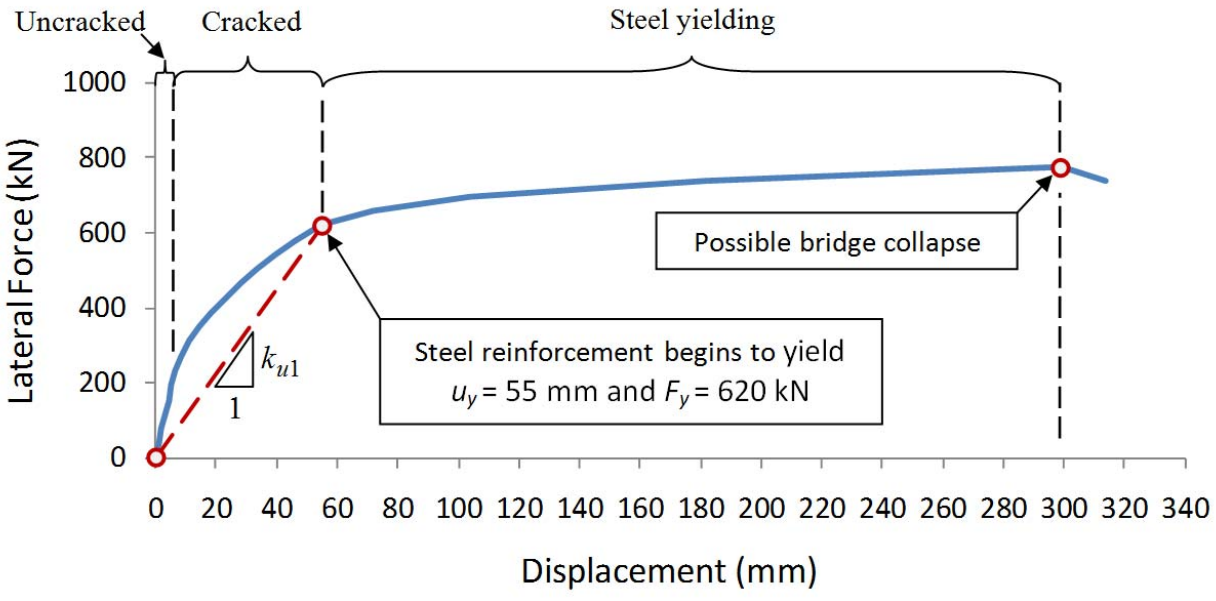

Figure 10.5 Pier pushover analysis - Bridge in Montreal

10.4.4 Defining Low and Upper Bounds for DLSP System

The overall response range in terms of the response modification factors R_{min} and R_{max} is defined between SE-UB (Service Upper-Bound) and DE-LB (Design Lower-Bound).

Effect of two hazard levels on the R-factor for defining the SE-DE range

Two hazard levels are considered in this retrofit example: the Design (DE: upper-level event) and the Service (SE: lower-level event) earthquakes with a probability of exceedance of 2% and 10% in 50 years, respectively. The design spectrum for the DE level is known and is presented in Figure 10.6. As shown in this figure, a factor of 0.426 (1/2.35 - Adams et al., 1999) is applied to the spectral values of the DE event to reduce its intensity linearly down to the SE event. For the same system activation force, the response modification factors corresponding to these two hazards are related in the following manner:

$$R(SE) = R(DE) / 0.426 \text{ or } R(DE) = 2.35 \times R(SE) \quad (10.1)$$

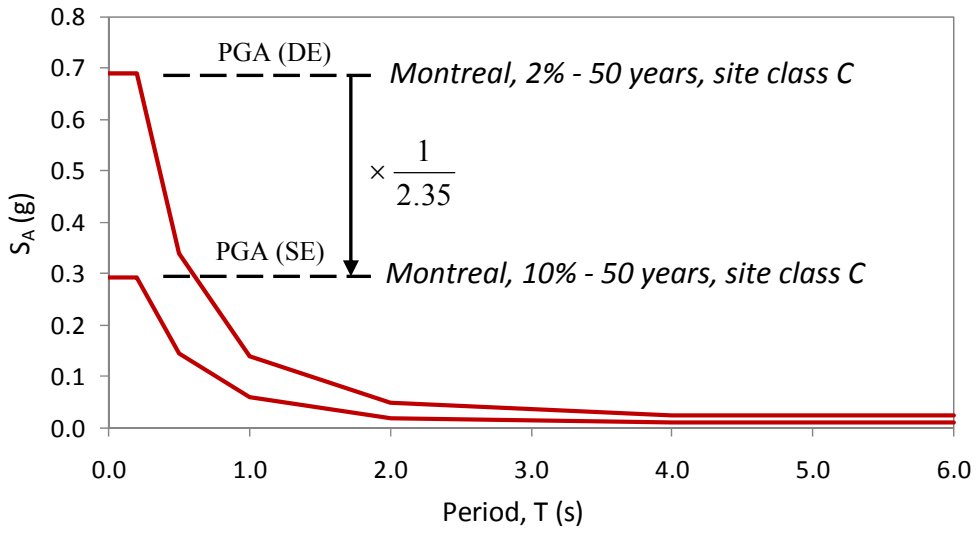

T (s)	0.0	0.2	0.5	1.0	2.0	4.0	6.0
SE - SA (g)	0.2936	0.2936	0.1447	0.0596	0.0204	0.0102	0.0102
DE - SA (g)	0.6900	0.6900	0.3400	0.1400	0.0480	0.0240	0.0240

Figure 10.6 Design spectra for SE (10% in 50 years) and DE (2% in 50 years)

Effect of property modification factors on the R-factor for defining the UB-LB range

The variability of the isolators' properties is quantified by a means of the system property modification factors λ. The nominal device properties are multiplied by λ to reflect the effect of the specific conditions to which the isolation system is subjected. The protection system considered for this example consists of flat sliding isolators (FSI). The FSI isolators with recentring capability are installed at the abutments while the FSI isolators without recentring capability are installed at the piers.

The system property modification factors λ for FSIs having stainless steel surface facing downward and sealed lubricated PTFE (Constantinou et al., 2007) influence the isolators' activation limits and are determined as follows:

1) Effect of temperature at -30°C and 20°C (Tremblay and Koval, 2008):

$$\lambda_{\min,t} = 1.0 \text{ at } 20°\text{C and } \lambda_{\max,t} = 1.3 \text{ at } -30°\text{C} \tag{10.2}$$

2) Effect of aging (Constantinou et al., 2007):

$$\lambda_{\min,a} = 1.0 \text{ new and } \lambda_{\max,a} = 1.3 \text{ under aging effect} \tag{10.3}$$

3) Effect of contamination (Constantinou et al., 2007):

$$\lambda_{\min,c} = 1.0 \text{ new and } \lambda_{\max,c} = 1.0 \text{ under contamination effect} \tag{10.4}$$

4) Effect of cumulative movement or travel (Constantinou et al., 2007):

$$\lambda_{\min,tr} = 1.0 \text{ new and } \lambda_{\max,tr} = 1.0 \text{ cumulative travel of 2000 m} \tag{10.5}$$

The resulting modification factor to be applied to the nominal value of the coefficient of friction:

$$\lambda_{\min} = 1.0 \text{ and } \lambda_{\max} = 1.69 \tag{10.6}$$

The maximum property modification factor λ_{max}=1.69 relates the UB and LB for each EQ event. In Figure 10.7, it is shown that the two hazard levels are related through a factor of 2.35 and this results in a factor of 3.97 between the range limits SE-UB with λ_{max} and R_{min} and DE-LB with λ_{min} and R_{max}. The corresponding system displacements are assessed using the *E-R-μ* relationship. The range of optimum solutions is then determined by selecting responses according to the performance objectives. The response ranges for two hazard levels are illustrated in Figure 10.8. It can be noted from this figure that the deck displacement should

remain under 20 mm and 50 mm for the SE-LB and DE-LB cases, respectively. The maximum force resisted by the abutments may correspond to either the DE-UB or the DE-LB.

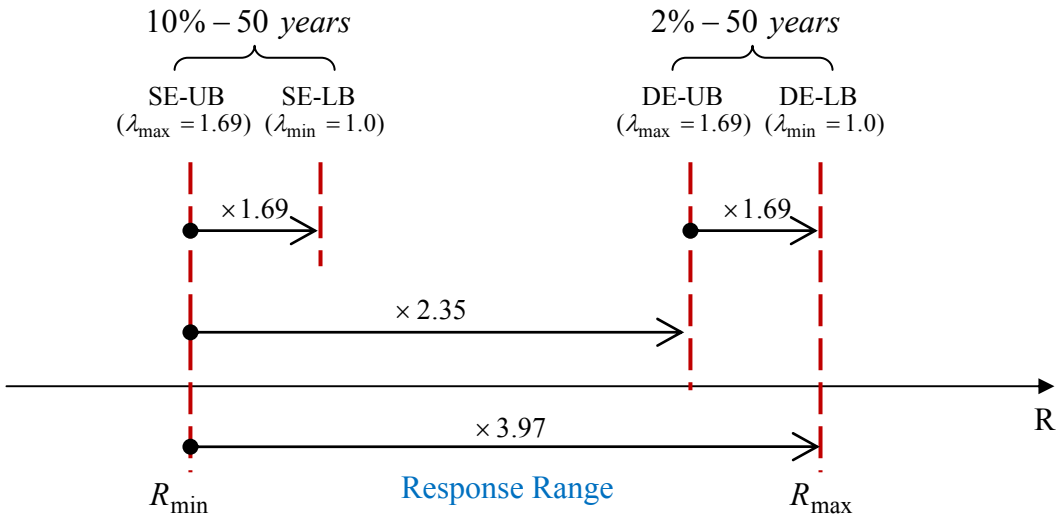

Figure 10.7 Response ranges using factor *R* for bounded analyses

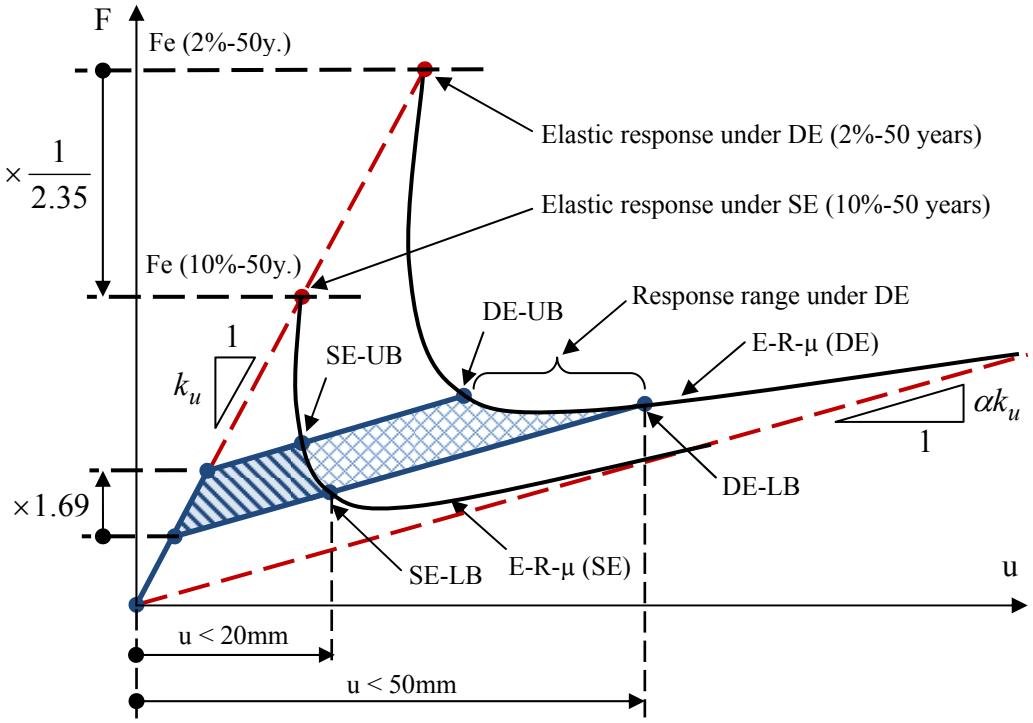

Figure 10.8 Performance objectives and responses ranges using *E-R-μ* relationship for two hazard levels with variation of the isolator's properties

10.4.5 Modeling and Basic System Parameters for DLSP Approach

In order to adequately simulate the structural behaviour of the bridge, the numerical model shown in Figure 10.1 included two main parts, one representing the superstructure and one representing the substructure. Given that most of the bridge mass is located at the level of the deck, the mass of the substructure m_1 was neglected in the dynamic analyses. The total bridge mass in the analysis m_2 was therefore defined using the total dead load situated above the isolation system interface. In the model presented in Figure 10.1, it is assumed that the deck element has infinite axial stiffness such that that displacement of the deck is the same at any point along the bridge length. The parameters of the substructure lateral stiffness (k_1 in Figure 10.1) were obtained using Response 2000 analyses as discussed earlier. The design parameters for the isolator units at the abutments and pier were determined as described in Section 10.3. Once the pier and isolators parameters have been determined, the equivalent system parameters were calculated to represent the global bridge behavior. The entire bridge structure was then represented as a SDOF system.

Table 10-5 summarizes the two sets of design parameters that were considered in this example. The lower bound (LB) with the nominal system properties $\lambda = \lambda_{min} = 1.0$ is representative of an isolated bridge at a temperature of +20°C that was recently retrofitted and its isolators are not yet affected by aging. The upper bound (UB) with $\lambda = \lambda_{max} = 1.69$ corresponds to the behaviour of the aged isolators at -30C°.

Table 10-5 Original bridge - Substructure parameters

Parameters	Lower Bound Recently retrofitted bridge at +20°C $\lambda_{\min} = 1.0$	Upper Bound Bridge with aged isolators at -30°C $\lambda_{\max} = 1.69$
$T_{eq\text{-}e1}$	0.29 s	0.29 s
$T_{eq\text{-}e2}$	1.08 s	1.08 s
$m=m_2$	2 100 000 kg	2 100 000 kg
Piers	1 Pier (fixed-pinned)	1 Pier (fixed-pinned)
m_1	0 kg	0 kg
k_{u1}	11 273 kN/m	11 273 kN/m
F_{y1}	620 kN	620 kN
u_{y1}	55 mm	55 mm
u_{u1}	205 mm	205 mm
β_{inh}	5%	5%
IS on Pier	2 Isolators	2 Isolators
k_{u2}	1 000 000 kN/m	1 000 000 kN/m
$\alpha_2 = k_{d2} / k_{u2}$	0	0
F_{y2}	361 kN (3.5%)	610 kN (5.92%)
Q_{d2}	361 kN	610 kN
IS on Abutment	4 Isolators	4 Isolators
k_{u3}	1 000 000 kN/m	1 000 000 kN/m
$\alpha_3 = k_{d3} / k_{u3}$	0.05	0.05
F_{y3}	515 kN (5%)	870 kN (8.45%)
Q_{d3}	515 kN (1.0 - 0.1)=464 kN	870 kN (1.0 - 0.1)=783 kN

The isolation systems at the piers are configured to act as fuse protection elements by setting the UB activation force to be lower than the pier elastic limit ($1.63\ F_{y2} = 610$ kN $< F_{y1} = 620$ kN). For the isolators at the abutments, the activation force F_{y3} is configured by assuming that the nominal coefficient of friction is 5% ($F_{y3} = 2\,100\,000 \cdot 9.81/1000/2 \cdot 0.05 = 515\ (kN)$. For this

example, the isolators' elastic and post-yielding stiffness values are configured to be representative of the typical nominal properties of the FSI isolators. The nominal stiffness of an FSI isolator is not affected by the property modification factor λ (Constantinou et al., 2007).

The protection systems having isolators on the abutments and piers have different activation levels. As a result, the bridge behaviour will be characterized by three response segments with different stiffness ratios. The first response segment represents the system elastic response when isolators on the abutments and piers are not activated. The second response segment corresponds to the system having activated only the isolation devices located at the abutments. The third response segment represents the system behavior after activating the isolators on the piers. The tri-linear system response is shown in Figure 10.9.

However, to apply the new energy-based *E-R-μ* method, the hysteretic behaviour must be idealized as bilinear for each of two DLSP's stages as presented in Figure 10.9. Within the DLSP's first stage, only the isolation devices located at the abutments are activated. The behaviour of the isolation system before its activation will be characterized by the bridge equivalent period $T_{eq\text{-}e1}$. The $T_{eq\text{-}e1}$ is determined as a function of the equivalent stiffness $k_{eq\text{-}e1}$ resulting from the contribution of all of the system's elements. The equivalent post-yielding stiffness ratio α_{eq1} is used to define the bilinear hysteretic response for the DLSP's Stage I. To facilitate the design when the isolators on the piers are activated, or for the DLSP's Stage II, the equivalent elastic period is redefined as a function of the equivalent stiffness $k_{eq\text{-}e2}$ which is determined as a secant stiffness at the activation force and displacement. The bilinear hysteretic response for the DLSP's Stage II is defined using the equivalent post-yielding stiffness ratio α_{eq2}. Such an idealisation technique does not acount for a portion of the absorbed energy shown as hatched area in Figure 10.9 thus making this approach slightly conservative.

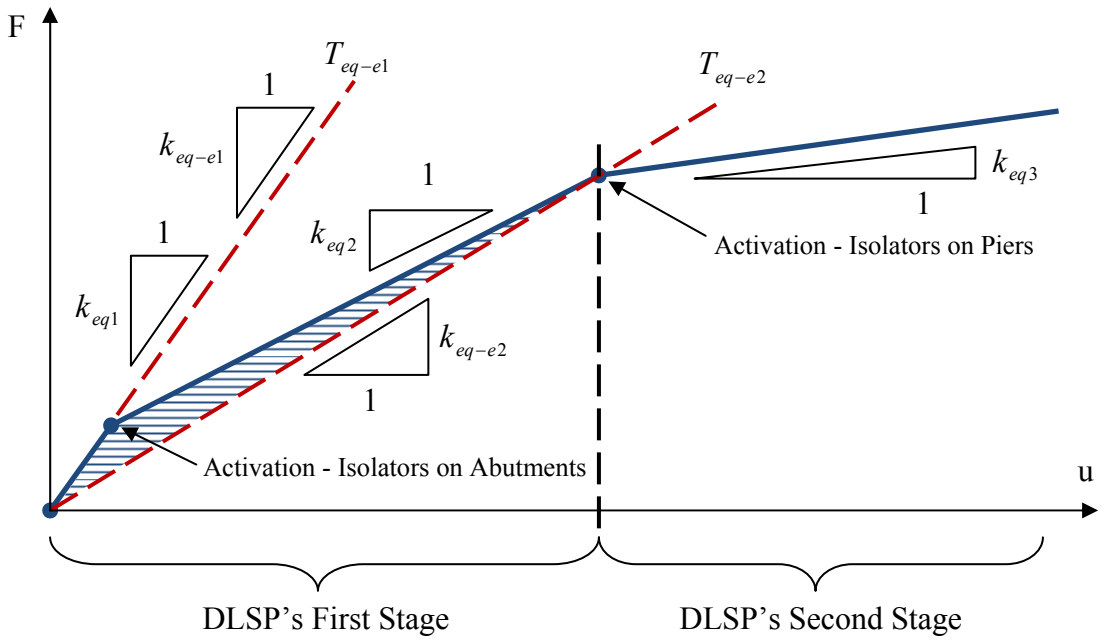

Figure 10.9 Response idealizations for two DLSP's stages

The design process is performed by solving the system responses according to the DLSP's stage being activated at the bridge maximum diplacement. The two DLSP's bilinear systems are characterized by two elastic periods (T_{eq-e1} and T_{eq-e2}) and post-yielding stiffness ratios (α_{eq1} and α_{eq2}). The design parameters given in Table 10-5 individually characterize the pier, isolator units at the abutments and isolator units at the pier. These parameters are transformed in equivalent system parameters to characterize the global bridge behavior. The corresponding system parameters are determined as presented below.

The equivalent system stiffness is calculated for the three response segments as follows:

$$k_{eq} = \frac{k_1 \cdot k_2}{k_1 + k_2} + k_3 \tag{10.7}$$

$$k_{eq1} = \frac{11\,273 \cdot 1\,000\,000}{11\,273 + 1\,000\,000} + 1\,000\,000 = 1\,011\,147\ (kN/m) \tag{10.8}$$

$$k_{eq2} = \frac{11\,273 \cdot 1\,000\,000}{11\,273 + 1\,000\,000} + 0.05 \cdot 1\,000\,000 = 61\,147\ (kN/m) \tag{10.9}$$

$$k_{eq3} = \frac{11\,273 \cdot 0}{11\,273 + 0} + 0.05 \cdot 1\,000\,000 = 50\,000\ (kN/m) \tag{10.10}$$

The deck displacement that is required to activate the isolator at the abutments is determined for the isolators' activation force $F_{y3} = 515\ kN$:

$$u_{y3} = \frac{515}{1\,000\,000} \cdot 10^3 = 0.515\ (mm) \tag{10.11}$$

The system total force resisted by the isolators on the abutments and pier is calculated as:

$$F(u_{y3}) = 1\,011\,147 \cdot 0.515 \cdot 10^{-3} = 520.7\ (kN) \tag{10.12}$$

The deck displacement required to activate isolators on the pier is determined for the isolators' activation force $F_{y2} = 361\ kN$:

$$u_{y2} = 361 \cdot \frac{11\,273 + 1\,000\,000}{11\,273 \cdot 1\,000\,000} \cdot 10^3 = 32.4\ (mm) \tag{10.13}$$

The system total force resisted by the isolators on the abutments and pier is then calculated as:

$$F(u_{y2}) = 520.7 + 61\,147 \cdot (32.4 - 0.515) \cdot 10^{-3} = 2470\ (kN) \tag{10.14}$$

The effective stiffness at activation of the isolators installed at the pier is determined as:

$$k_{eq-e2} = \frac{2470}{32.4} \cdot 10^3 = 76235\ (kN/m) \tag{10.15}$$

The equivalent system elastic period for DLSP's first stage ($k_{eq-e1} = k_{eq1}$):

$$T_{eq-e1} = 2\pi\sqrt{\frac{m}{k_{eq-e1}}} = 2\pi\sqrt{\frac{2\,100\,000}{1\,011\,147\,000}} = 0.29\ (s) \tag{10.16}$$

The equivalent system elastic period for DLSP's second stage:

$$T_{eq-e2} = 2\pi\sqrt{\frac{m}{k_{eq-e2}}} = 2\pi\sqrt{\frac{2\,100\,000}{76\,235\,000}} = 1.04\ (s) \tag{10.17}$$

The post-yielding stiffness ratio for DLSP's first stage:

$$\alpha_{eq1} = \frac{61147}{1\,011147} = 0.06 \tag{10.18}$$

The post-yielding stiffness ratio for DLSP's second stage:

$$\alpha_{eq2} = \frac{50\,000}{76\,235} = 0.656 \tag{10.19}$$

R_{max} (DE-LB) is then evaluated using elastic response of the bridge system without aging at 20°C (DE: 2%-50 years)

- DLSP's Stage I ($T_{eq\text{-}e1}$=0.29s and α_{eq1}=0.06):

$$S_{D1}(5\%; 0.29s) = 12.09\ mm \tag{10.20}$$

$$R_{\max 1} = \frac{12.09}{0.515} = 23.5 \tag{10.21}$$

- DLSP's Stage II - idealized response ($T_{eq\text{-}e2}$=1.04s, α_{eq2}=0.656):

$$S_{D2}(5\%; 1.04s) = 38.3\ mm \tag{10.22}$$

$$R_{\max 2} = \frac{38.3}{32.4} = 1.2 > 1 \tag{10.23}$$

Thus, it is expected that the isolators on the pier will be activated and that the system will behave within the DLSP's Stage II under the DE (Table 10-3). The system response should be calculated with the proposed energy-based *E-R-μ* method using the elastic period $T_{eq\text{-}e2}$ that will result in the greater response with respect to that obtained with $T_{eq\text{-}e1}$.

R_{min} (SE-UB) is evaluated using the elastic response of the bridge system with aged isolators at -30°C (SE: 10%-50 years):

- DLSP's Stage I ($T_{eq\text{-}e1}$=0.29s and α_{eq1}=0.06):

$$R_{\min 1} = \frac{12.09}{0.515} \cdot \frac{1}{3.97} = 5.9 \tag{10.24}$$

- DLSP's Stage II - idealized response ($T_{eq\text{-}e2}$=1.04s, α_{eq2}=0.656):

$$R_{\min 2} = \frac{38.3}{32.4} \cdot \frac{1}{3.97} = 0.30 \leq 1 \tag{10.25}$$

The response modification factor R_{min2} is less than unity. Thus, under the SE, the isolators on the pier are not activated and the system behaves within the DLSP's Stage I. The response is first estimated for the system defined by $T_{eq\text{-}e1}$=0.29s and α_{eq1}=0.06 within the range R_{min1} =5.9 and R_{max1} =23.5. Then the response is calculated for the system defined by $T_{eq\text{-}e2}$=1.04s, α_{eq2}=0.656 and R_{max2} =1.2.

What is shown above is how the system parameters are determined for each trial when the pier and isolators parameters are redefined.

10.4.6 Evaluating the Bridge's Performance Using the New Energy-Based *E-R-μ* Method

The displacement and force responses obtained with the *E-R-μ* relationship are compared to those obtained from NLTH analyses in Figure 10.10. The figure illustrates how the displacement and force vary with the response modification factor *R*. For NLTH analyses, a set of 20 artificial ground motions developed by Atkinson (2009), as presented in Chapter 4, were adopted for the site of Montreal. To facilitate the understanding of these results, the forces and displacements are normalized with respect to the corresponding bridge elastic responses F_e and u_e obtained with the initial elastic period T_e = 0.29 s and β_{inh} = 5%. It can be noted that the new energy-based *E-R-μ* method generally provides conservative response estimates, which represents an upper bound for the system forces and displacements. This observation is in good agreement with those made in Chapters 8 and 9.

Table 10-6 summarizes the results obtained using the *E-R-μ* relationship for each performance level which is represented in terms of the response modification factor *R*. It can be observed that the target performance objectives, as specified in Table 10.4, are achieved for both hazard levels defined in Table 10.1 as the Design (DE) and the Service (SE) earthquakes. The pier behaves within its elastic range during both hazard levels, the DE and SE, as well as for both isolators' states UB and LB.

During the SE motion, the deck displacement will not exceed the 20 mm limit. The bridge is operational with no damage to its elements. During the DE motion, the opening of the superstructure expansion joints will exceed the 20 mm limit while the deck displacement is smaller than the 50 mm limit. Accordingly, after the DE motion, the bridge is expected to be operational with minor damage.

It was also found that the system behaves within the DLSP's first stage for performance levels SE-UB, SE-LB, and DE-UB. For the DE-LB performance level, the bridge response within the DLSP's first stage results in the pier force $F_1 = 448$ kN which is below the pier elastic limit of 620 kN. However, for the DE-LB performance level, the DLSP's second stage is activated limiting the pier forces at $F_1 = 361$ kN. In such a case, the isolators do not provide an increased protection to the pier. The use of the pier protective devices would be justified only for the DE-UB level when the isolators will be limiting the forces imposed to the piers to 610 kN which is just below the pier elastic limit of 620 kN.

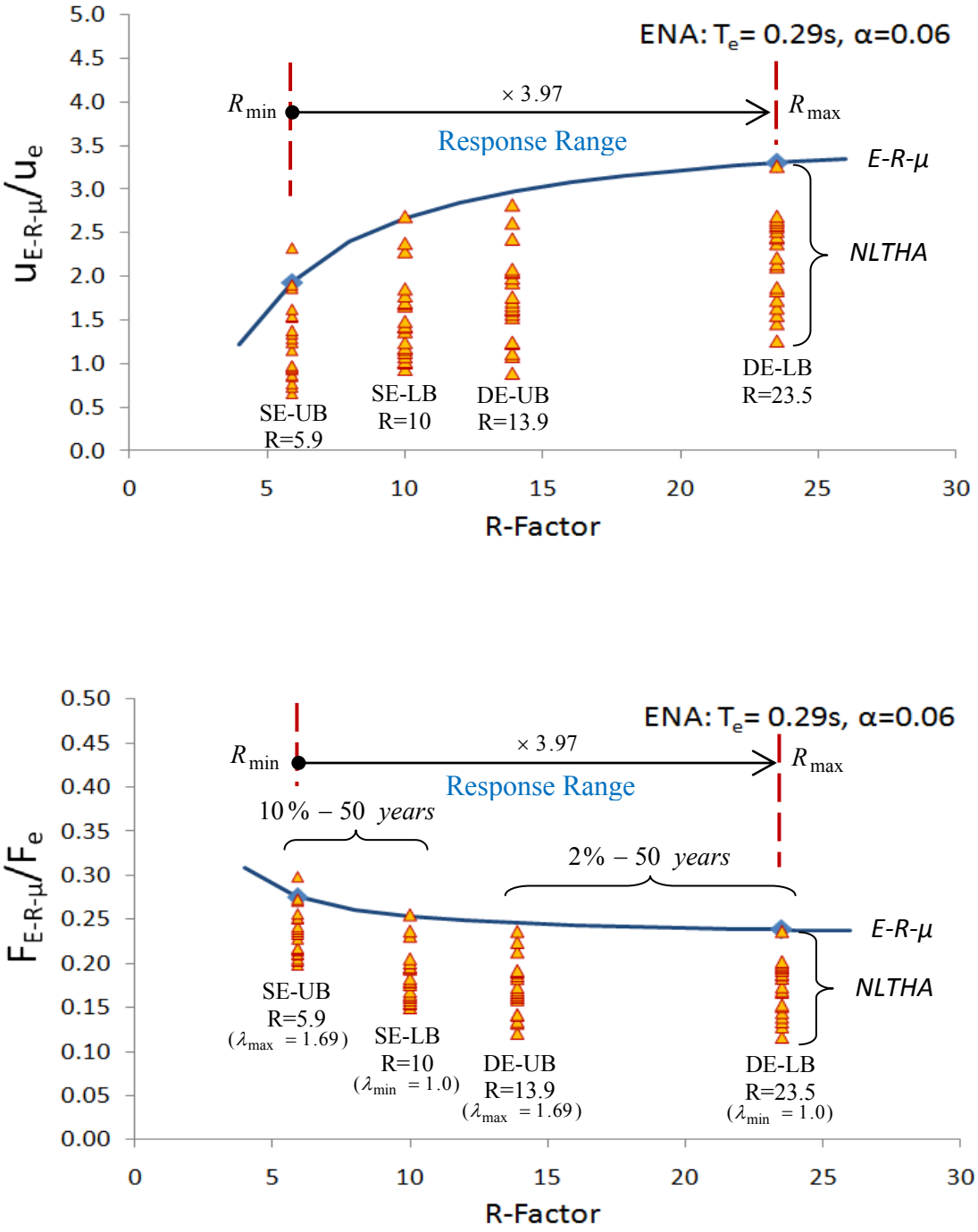

Figure 10.10 Responses normalized to elastic response: curve from *E-R-μ* with respect to NLTHA (20 Atk-E Records, Montreal)

Table 10-6 DLSP's responses obtained using the *E-R-μ* relationship for each performance level

Level	Deck displacement u_3 (mm)	Forces (kN)			Pier Performance	Bridge Performance
		Abutment F_3	Pier F_1*	Total F		
DLSP's Stage I (T_{eq-e1} = 0.29 s and α_{eq1} = 0.06)						
SE-UB R=5.9	10.1	1335	114	1449	F_1* < 620 kN Elastic	u_3 < 20 mm Operational with no damage
SE-LB R=10	13.9	1182	155	1337	F_1* < 620 kN Elastic	u_3 < 20 mm Operational with no damage
DE-UB R=13.9	36.3	2640	405	3045	F_1* < 620 kN Elastic	20 mm < u_3 < 50 mm Operational with minor damage
DE-LB R=23.5	40.2	2500	448	2948	F_1* < 620 kN Elastic	20 mm < u_3 < 50 mm Operational with minor damage
DLSP's Stage II - idealized response (T_{eq-e2} = 1.04 s, α_{eq2} = 0.656)						
DE-LB R=1.2	41.9	2566	361	2927	F_1* < 620 kN Elastic	20 mm < u_3 < 50 mm Operational with minor damage

* F_1- force resisted by the pier (when F_1 < 620 kN, the pier's steel reinforcements are elastic)

Figure 10.11 provides a detailed overview on the bridge's performance obtained in this example. The bridge response curves are shown for both isolators' states UB and LB. The UB state is characterized by the bilinear response where change in stiffness between elastic and post-activation responses corresponds to the activation of isolators on the abutments. For the isolators' LB state, three linear segments represent the bridge elastic and post-activation responses given that isolators located at the abutments and piers are subsequently activated. Three curves obtained using the corresponding *E-R-μ* relationship represent the range of responses corresponding to system's Stage I under SE and DE and system's Stage II under DE. The performance levels correspond to the intersection of the bridge response curves with curves obtained using the corresponding *E-R-μ* relationship.

The two dashed lines correspond to two post-activation stiffness ratios, thus representing the response of systems having relatively small resistance ($R \rightarrow \infty$). These lines bound the maximum displacements for the response range represented by the corresponding E-R-μ curve. For this bridge protection system, the E-R-μ relationship does not provide any solutions for displacements exceeding the limits of 20 mm and 50 mm for SE and DE motions, respectively. This indicates that for any R value within the range from $R = 1.0$ to ∞, the performance objectives will be met. As specified in Table 10.3, amongst the various solutions satisfying the pre-defined objectives at the two seismic hazard levels, the optimum solution is the one inducing the lowest forces to be resisted by the abutments. As shown in Section 9.5, an optimum solution can be achieved by varying simultaneously the isolator's nominal stiffness (or period) and activation force (or characteristic strength).

However, the range of possible solutions is subject to physical limitations as for example, the isolators' minimum activation force. For instance, for a FSI, the minimum activation load is the force needed to overcome the static friction. This force depends on the applied vertical load, the type of sliding interface and its condition. In this example for the FSI isolators at the abutments, the minimum coefficient of friction of 5% is assumed. In practice, the isolator activation force is specified in the manufacturers' product specifications and should be accurately taken into account during the design process. Alternatively, to reduce the isolators' minimum activation force, the vertical force acting on the isolators can be reduced. This can be achieved by distributing vertical forces between isolators and "frictionless" mechanical bearings: rockers and rollers. However, such solutions are not covered by the scope of this chapter and alternative optimization options will be studied in the following subsection.

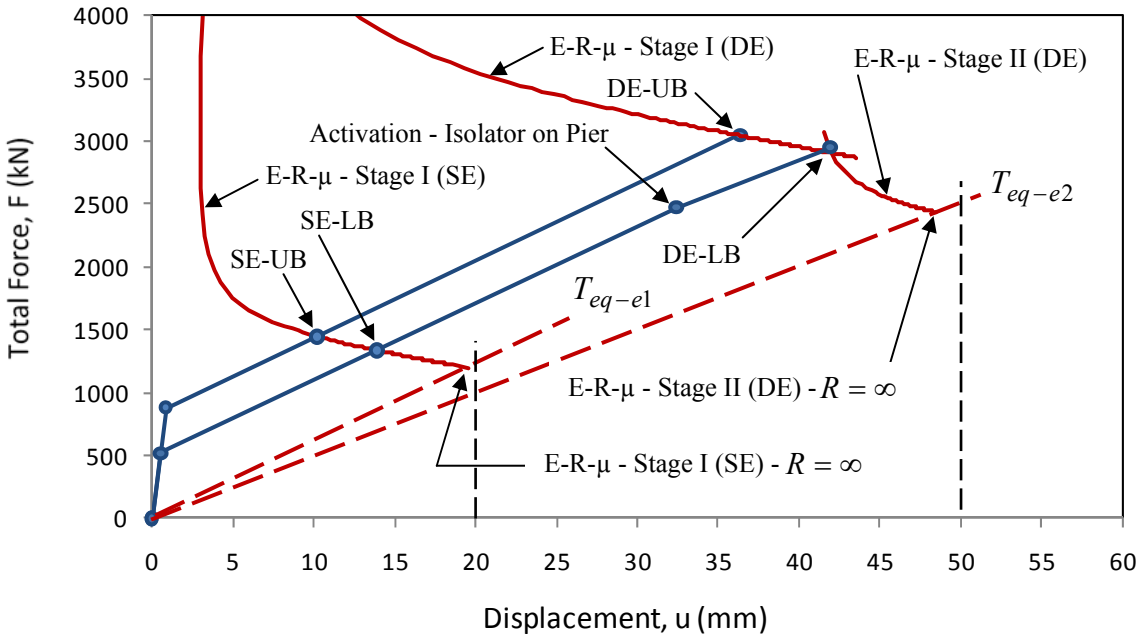

Figure 10.11 Bridge's performance obtained using the new energy-based *E-R-μ* method (ATK-E: PGD=72 mm, Tg=0.89 s)

10.4.7 Improving the Bridge's Performance Using the New Energy-Based *E-R-μ* Method

In the previous subsection, the DLSP system was configured to meet design objectives corresponding to both seismic hazard levels, the DE and SE earthquakes. It was however assumed that for the isolators at the abutments, the activation force was subject to physical limitations and was prevented from further reduction needed to take full advantage of the benefits provided by the isolation system. In this subsection, the optimization process is performed following the design optimization flowchart for the DLSP system as presented in Figure 10.2.

Starting from Step 5 (Figure 10.2) as a first phase, the elastic stiffness of the FSI isolators on the abutments is reduced. By installing an elastomer on top of the sliding interface, the elastic period may be lengthened such that system forces are further decreased. As a counterpart of the period lengthening, the increase in displacement is expected. The second optimization phase consists in

adjusting the displacement response so that the target performance objectives are still met. The damping devices can be then installed at the abutments as suggested in Step 11 (Figure 10.2).

To avoid a complex iterative process, a straightforward approach for selecting k_{u3} is proposed. The parameter k_{u3} is varied such that the corresponding elastic period T_e results in the elastic displacement response $u_{e3}=S_d(5\%,T_e)$ of the bridge deck that is smaller than 20 mm. As mentioned in Section 10.4.2, a damage threshold of 20 mm corresponds to the deformation limit of the expansion joints. As shown in Figure 10.12, a period of T_e = 1.12 s was needed to achieve this objective. The parameter of the post-yield stiffness, k_{d3} is then determined following Equations (10.26) to (10.28). The modified system equivalent parameters are summarized in Table 10.7.

$$k_{u,eq} = \frac{4\pi^2}{T_e^{\,2}} m \tag{10.26}$$

$$k_{u3} = k_{u,eq} - \frac{k_{u1} \cdot k_{u2}}{k_{u1} + k_{u2}} \tag{10.27}$$

$$k_{d3} = \alpha \cdot k_{u3} \tag{10.28}$$

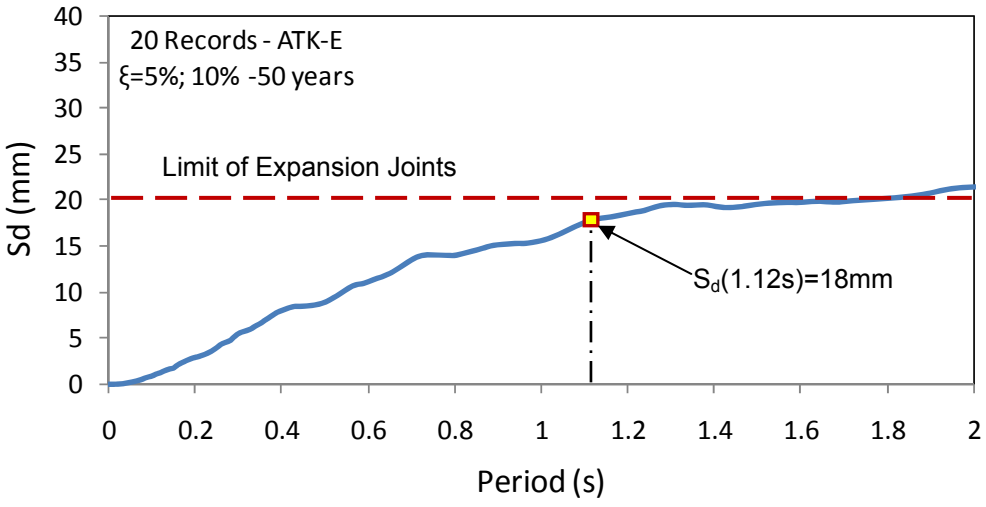

Figure 10.12 Selection of elastic stiffness for isolators at the abutments

Table 10-7 System equivalent parameters for DLSP's stages

k_{u3} (kN/m)	k_{eq1} (kN/m)	k_{eq2} (kN/m)	k_{eq3} (kN/m)	$T_{eq\text{-}e1}$ (s)	$T_{eq\text{-}e1}$ (s)	α_{eq1}	α_{eq2}
54 944	66 091	14 452	2 747	1.12	1.68	0.219	0.093

The performance of the bridge protection system with reduced stiffness is assessed using the new energy-based *E-R-μ* method and is presented in Figure 10.13. By comparing this system's response to that of the previous example (presented in Figure 10.11 and Table 10.6), it can be noted that the maximum force obtained for DE-UB was significantly reduced from 3045 kN to 1545 kN. However, as shown, two pre-defined performance objectives are not satisfied with this design. The displacement under the SE motions exceeds 20 mm for the LB condition, which indicates that the opening of the expansion joints will exceed the targeted limit. In addition, under the DE motions, the deck displacement for the LB condition is larger than the specified limit of 50 mm.

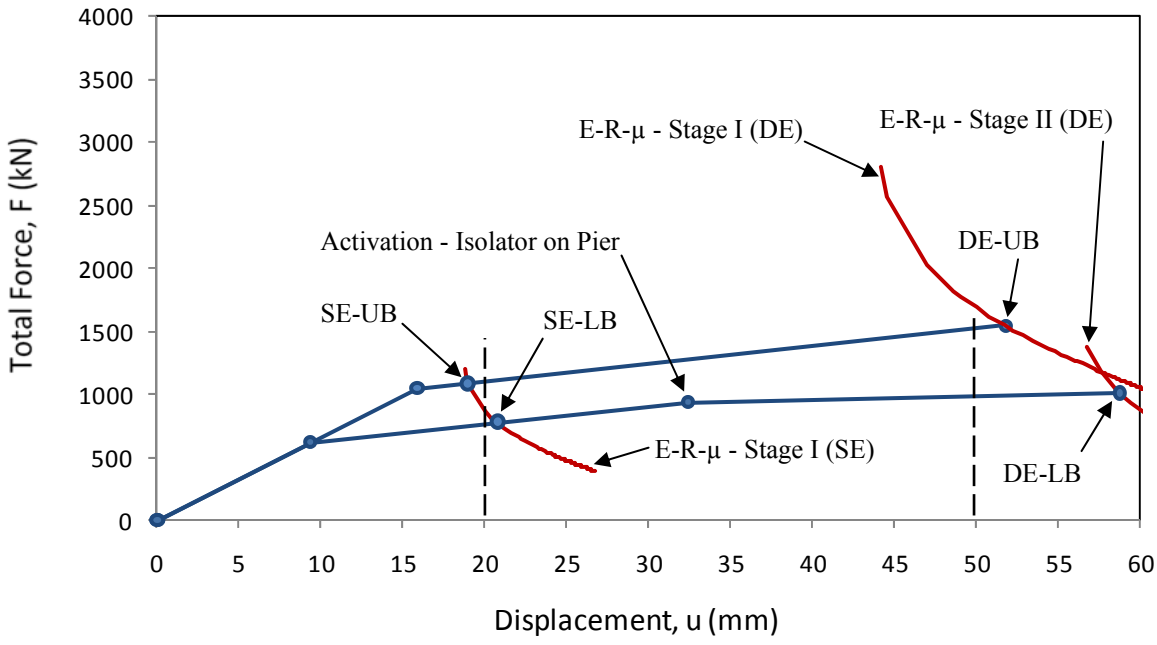

Figure 10.13 Performance of the DLSP with reduced stiffness using the new energy-based *E-R-μ* method (ATK-E: PGD=72 mm, Tg=0.89 s)

To improve the bridge performance, the increase in the deck displacement is mitigated following Steps 9 and 11 as specified in the DLSP optimization flowchart (Figure 10.2). In this example, the displacement is controlled by adding viscous damping. The damping level to be added in addition to the 5% inherent damping is arbitrary set to 5%. Such an approach is representative of the selection of damping devices from the manufacturers' product chart which is tailored at a 5% damping increment. To determine how much damping is needed to comply with the target displacement, the *B*-factor relationships (Equation (2.8)) can be adopted.

Figure 10.14 presents the performance of the DLSP with reduced stiffness and added damping. In this approach, to take into account the added viscous damping, the new energy-based *E-R-μ* method is based on Equation (8.16).

The targeted performance levels are satisfied, resulting in an operational bridge and an elastic substructure after both the SE and DE ground motions. When compared to the performance of the initial DLSP configuration (Figure 10.11), the maximum system force is reduced by 49.2% from 3045 kN to 1497 kN. The maximum force to be resisted by the abutments is reduced from 2640 kN to 958 kN which corresponds to a considerable reduction of 63.7%.

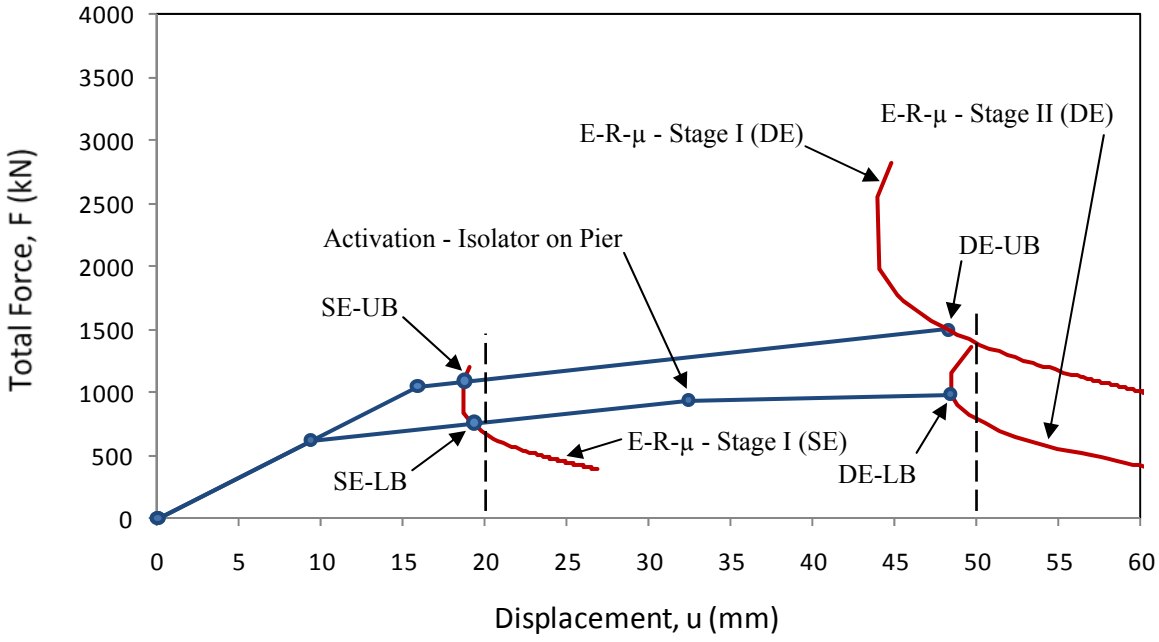

Figure 10.14 Performance of the DLSP with reduced stiffness and adding 5% of viscous damping using the new energy-based *E-R-μ* method (ATK-E: *PGD* = 72 mm, T_g = 0.89 s)

The examples presented above illustrate how the performance of the DLSP system can be improved using a simple and straight-forward procedure based on the proposed energy-based *E-R-μ* method. Although not shown in this section, when using the new energy-based *E-R-μ* method, an optimum solution can be directly achieved by varying simultaneously the system stiffness k_d, characteristic strength Q_d and damping level β_{eff}. Such an improvement represents an interesting and cost-effective solution that can be adopted by engineers during preliminary design to achieve multi-level-hazard design objectives.

10.5 Implementation of a Dual-Level Seismic Protection System for a Bridge Retrofit in Vancouver

In this section, the optimal design process of a DLSP is illustrated for the case of an existing bridge that needs to be upgraded to meet the requirements of current seismic provisions. Such a bridge may be eventually subjected to a seismic demand that is beyond its capacity. A simplified procedure for developing an optimum DLSP system using detailed NLTH analyses is presented and validated using this example. The responses from the NLTHA are compared to the estimates obtained using the energy-based *E-R-μ* method in order to validate the appropriateness of adopting this method for preliminary design in the definition of an optimum seismic protection strategy.

As previously discussed in Section 10.3 for the seismic protection at the pier support, the lateral resistance provided by the isolators must not exceed the lateral force producing yielding of the piers. Supplemental damping devices are combined to the isolation system at the abutments to control the lateral displacement of the superstructure. At the abutments, the isolators are also designed with a minimum recentring capacity to control displacements and prevent progressive drifting of the superstructure. The primary objective of such an implementation is to prevent any damage to the bridge substructure for both seismic hazard levels defined in Table 10-1 as the Design (DE) and the Service (SE) earthquakes.

The protection system considered for this example consists of the flat sliding isolators (FSI) and lead rubber bearings (LRB) that are installed at the piers and abutments, respectively. LRBs inherently exhibit higher restoring forces upon yielding and the system is therefore more suitable at the abutments where greater lateral resistance can be more easily developed. The energy

dissipation capacity is obtained through the inelastic response of the lead core under lateral seismic motion.

10.5.1 Defining Bridge and Importance Category

The structure that is studied is located in Vancouver. The bridge is an existing four-span concrete bridge with a total length of 68 m (Figure 10.15). The bridge is comprised of two independent structures, one servicing east bound traffic and the other servicing west bound traffic. In this example, only the eastbound bridge was examined. The superstructure cross-section includes six AASHTO precast prestressed girders spanning over 18 m. The bridge is skewed but the effects of the skew angle on the seismic response are deemed to be small and are neglected in this preliminary DLSP design.

As part of the retrofit, the bridge is upgraded from the *Other bridges* category to the *Lifeline* bridge importance category. A target performance to be achieved with the DLSP system is defined for the two hazard levels considered and is based on the recommendations outlined in Table 10-4.

a)

b)

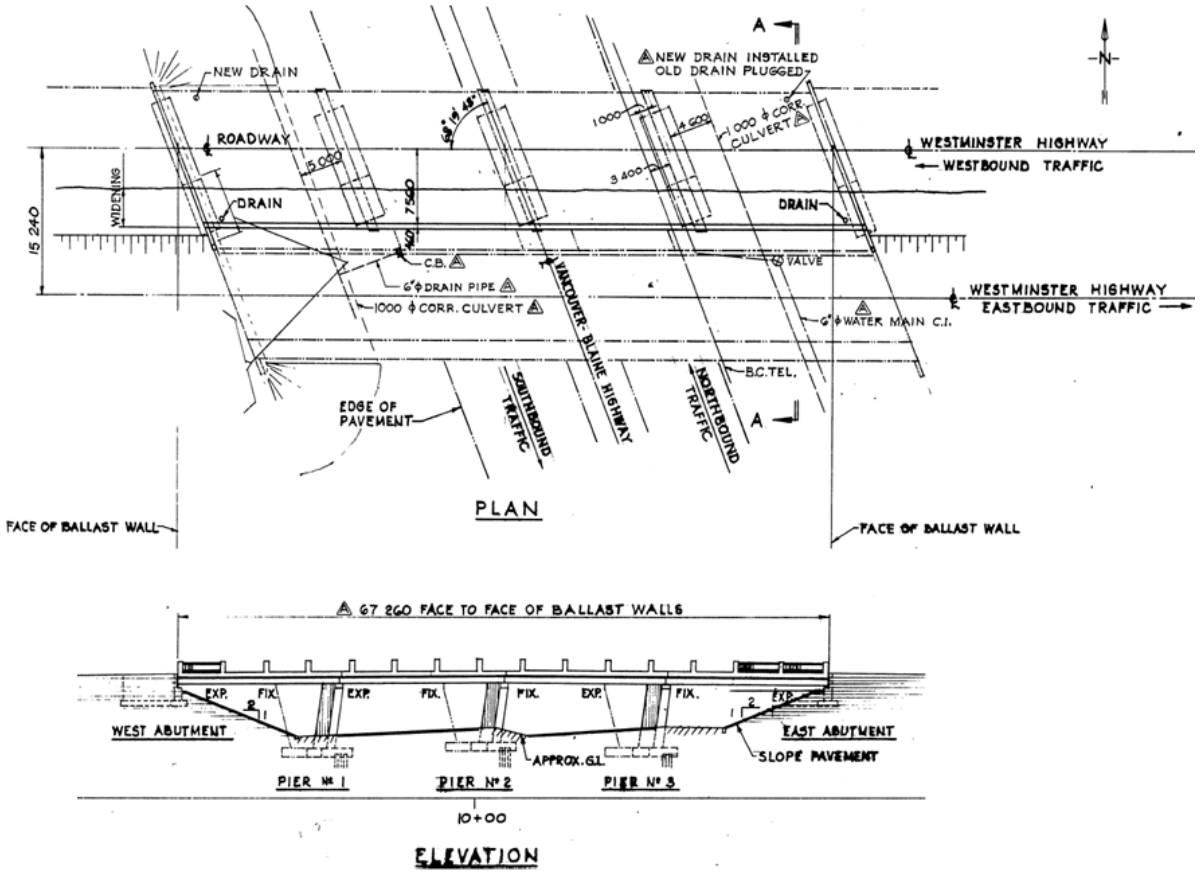

Figure 10.15 Photo (Google Maps- ©2012 Google), plan and elevation of the four-span bridge in Vancouver.

10.5.2 Dual-Hazard Performance Objectives

As in the previous example, the bridge structure is expected to perform elastically under both hazard levels ($u_{1max} < u_{1y}$) and the bridge is to be fully serviceable for normal traffic following

both DE and SE events. A 40 mm limit is defined as the damage threshold for the expansion joints. The deck displacement between this limit and the maximum allowable displacement indicates an allowable *Minor Damage*. The maximum allowable displacement for the abutment isolators is limited to 120 mm.

10.5.3 Assessing Structural Properties Using Nonlinear Incremental Analyses

The structural properties of the as-built bridge were determined through nonlinear incremental static analyses. Sectional analysis of the reinforced concrete piers was performed using Response 2000 (Bentz, 2000) to evaluate their inelastic response and available ductility capacity. Figure 10.16 presents the computed inelastic response for the bridge piers. Similarly as explained in the previous example (see Figure 10.5), the pier elastic stiffness is determined from the linear secant segment as shown below in Figure 10.16 ($k_{u1} = u_y / F_y$). Table 10-8 summarizes the original (non-isolated) bridge properties. In this table, u_{y1} and u_{u1} represent the pier yielding and ultimate displacement levels, respectively.

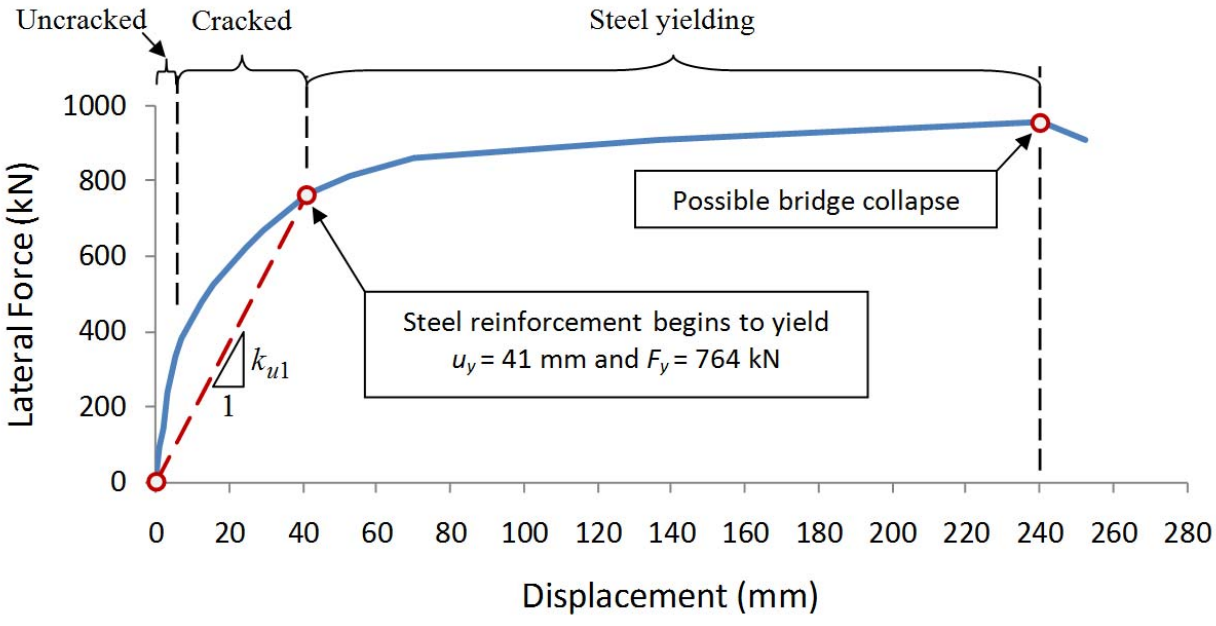

Figure 10.16 Pier pushover analysis - Bridge in Vancouver

Table 10-8 Original bridge (m_2 = 954 000 kg) - Substructure parameters

T_e (s)	k_{u1} (kN/m)	k_{d1} (kN/m)	F_{y1} (kN)	u_{y1} (mm)	u_{u1} (mm)	β_{inh} (%)
0.82	55 814	5 821	2 292	41	240	5

10.5.4 Time-History Ground Motions Considered for Configuring Optimal Protection System

In this example, time-history analyses are used both for configuring and for optimizing the basic system parameters. A set of 20 artificial ground motions developed by Atkinson (2009), as presented in Chapter 4, were adopted for the site of Vancouver. The motions were selected to represent the dominant (DE) magnitude-distance earthquake scenarios as determined from deaggregation of the seismic hazard at the site for a probability of exceedance of 2% in 50 years (Halchuk and Adams, 2004 and Halchuk, 2009). The records were linearly scaled with respect to the NBCC design spectrum (NRCC, 2005). To perform the TH analyses for the 10% in 50 years (SE) hazard level, the same records were used but their intensity was scaled down by a factor of 1.94 according to the hazard curve determined by Adams et al. (1999) for Vancouver.

10.5.5 Basic System Parameters for DLSP Approach

A number of the basic properties of the system can be initially selected to meet specific key performance objectives for the bridge following Steps 3 to 5 in the optimization flowchart presented for DLSP in Figure 10.2. The other properties are subsequently determined by optimizing the bridge response through nonlinear time history analyses using ensembles of earthquake records representative of each hazard level.

As previously mentioned for this structure, flat sliding isolators (FSI) and lead rubber bearings (LRB) are installed at the piers and abutments, respectively. For LRB isolators, the properties that are subject to variations are the stiffness and the characteristic strength. For FSI isolators, only the characteristic strength is affected by the property modification factor λ (Constantinou et al., 2007). For simplicity in this example, the effect of property modification factors is not considered thus assuming $\lambda = 1.0$. Despite the apparent simplicity of such an approach it still

provides useful insight into the response of isolated and damped bridges that can then be used in more comprehensive studies that would include the expected variability of the isolator's properties. Table 10-9 summarizes the retrofitted bridge properties, including the isolation system.

Table 10-9 Isolated bridge - Parameters of isolation on piers and abutments

T_e (s)	k_{u2} (kN/m)	$\alpha_2=k_{d2}/k_{u2}$	Q_{d2} (kN)	k_{u3} (kN/m)	$\alpha_3=k_{d3}/k_{u3}$	Q_{d3} (kN)
0.70	55 814	0	2 106	48 000	0.1 [A]	780 [B]

[A] Post-yielding stiffness ratio for LBR (www.dis-inc.com/pdf_files/DIS_BASE_ISO.pdf)

[B] Maximum available characteristic strength from the isolator design properties

Configuring Pier Isolators

For a set of 18 sliding isolators placed at the piers, a total activation force of 2 106 kN is determined to be lower than the pier elastic limit of 2 292 kN (3 piers). For this example, the activation force was obtained using an assumed Coulomb`s friction with a constant friction coefficient of 30% (personal communication with P. Lapalme, Goodco, 2012).

Configuring Abutment Isolators

The isolators located at the abutments (LRB) are expected to be activated at Stage I. They are configured according to the following two steps:

Step1. The elastic stiffness, k_{u3} is determined by using a post-yielding stiffness ratio, α ($\alpha_3 = 0.1$, Table 10.13). Similar to the previous example, the elastic period T_e is varied such that the resulting elastic displacement response $u_{e3} = S_d(5\%, T_e)$ of the bridge deck is smaller than 40 mm which corresponds to the damage threshold of expansion joints. Once T_e is determined, the parameter of the post-yield stiffness, k_{d3} is determined following Equations (10.26) to (10.28) as illustrated in Figure 10.17. This spectrum corresponds to the SE hazard and represents a mean response of the 20 ground motions adopted for this example. In such a way, for an elastic

response of the bridge, the performance objective consisting of preventing damage to the expansion joints is satisfied for Stage I (SE).

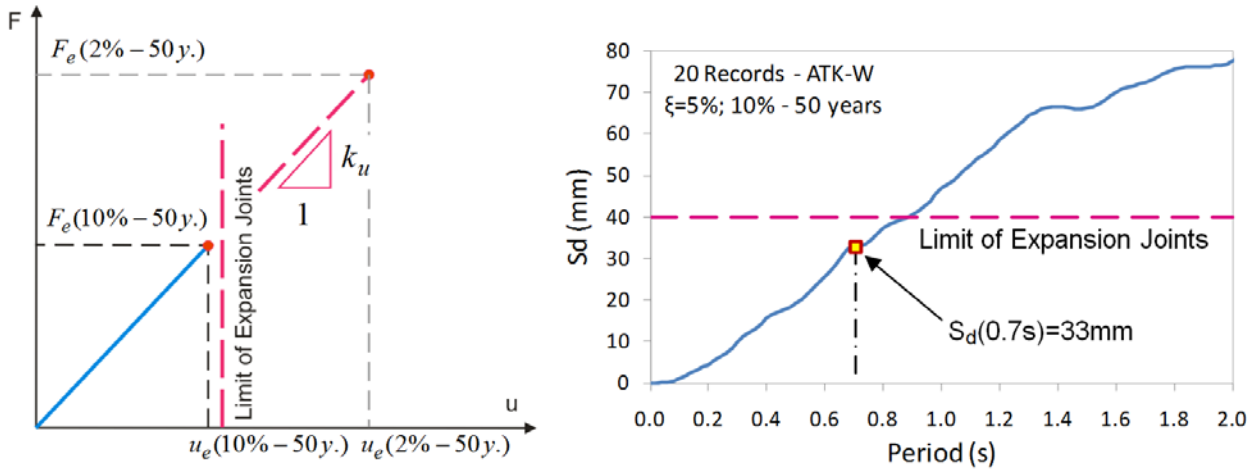

Figure 10.17 Selection of elastic stiffness for isolators at the abutments

Step 2. The characteristic strength, Q_{d3}, of the isolators at the abutments is the second design parameter to be configured. This parameter is defined in terms of the *R*-factor, which, in turn, relates the activation limit u_{y3} to the maximum elastic response, $u_{e3} = S_d(5\%, T_e)$. The maximum available characteristic strength specified by the manufacturer for the isolators used in this example is 65 kN what results for a group of 12 isolators in $Q_{d3} = 65\ kN \cdot 12\ isolators = 780\ kN$ or $F_{y3} = 867$ kN (http://www.dis-inc.com/technical.html). As a result, with respect to the maximum elastic response, the isolator activation force corresponds to the minimum $R = u_{e3} / (F_{y3} / k_{u3}) = 1.85$.

Figure 10.18 illustrates the response of the isolators at the abutments as a function of *R*. Four ground motions were selected to represent general responses characterizing four magnitude-distance events denoted as *E6C1* (M6.5, 10 to 15 km), *E6C2* (M6.5, 20 to 30 km), *E7C1* (M7.5, 15 to 25 km) and *E7C2* (M7.5, 50 to 100 km). The same decreasing trend in force with increasing *R* is observed for all types of events, while each of the displacement curves has a particular shape.

In addition to the responses obtained using NLTHA for each of the four ground motions, Figure 10.18 presents the response estimates obtained using the energy-based *E-R-μ* method. It can be noted that the force curve obtained with the *E-R-μ* relationship is replicating the shape of the

responses very well while overestimating slightly the NLTH responses (Figure 10.18(a)). The displacement curve underestimated the NLTHA responses for $R = 1.85$, provided estimates that were close to the NLTHA average for $R = 3.6$ and mostly overestimated the NLTHA responses for higher R-factors (Figure 10.18(b)). As outlined in the previous section, the straight-forward procedure of the new energy-based E-R-μ method can be very effective for the selection of the most appropriate isolation scheme to achieve multi-level-hazard design objectives. For instance, the NLTH analyses requires certain number of time-history records (20 records in this study, 5 records in CAN/CSA-S6-06 and 11 records in CAN/CSA-S6-14). Previous to carry out the NLTH analyses, the records must be selected and scaled as well as an appropriate nonlinear model must be developed. As a result in engineering practice, the NLTH analyses are much more expensive and time consuming when compared to just a few simple calculations needed to obtain the same trends with the E-R-μ relationship method.

When considering the NLTHA average responses, the minimum displacement occurs for $R = 6.4$ which defines an optimum system configuration for an SE event. However, for a DE event, the R-factor will increase to $R \approx 6.4 \text{ x } 1.94 = 12.4$, and a larger displacement u_3 is expected according to the trends in Figure 10.13. In cases where the limit defining the performance objective of the DLSP's for Stage II is exceeded, this can be remedied by increasing the strength and stiffness of the isolators at the abutments or by adding viscous damping. Both approaches are illustrated in the following sections for protection systems with and without added viscous dampers.

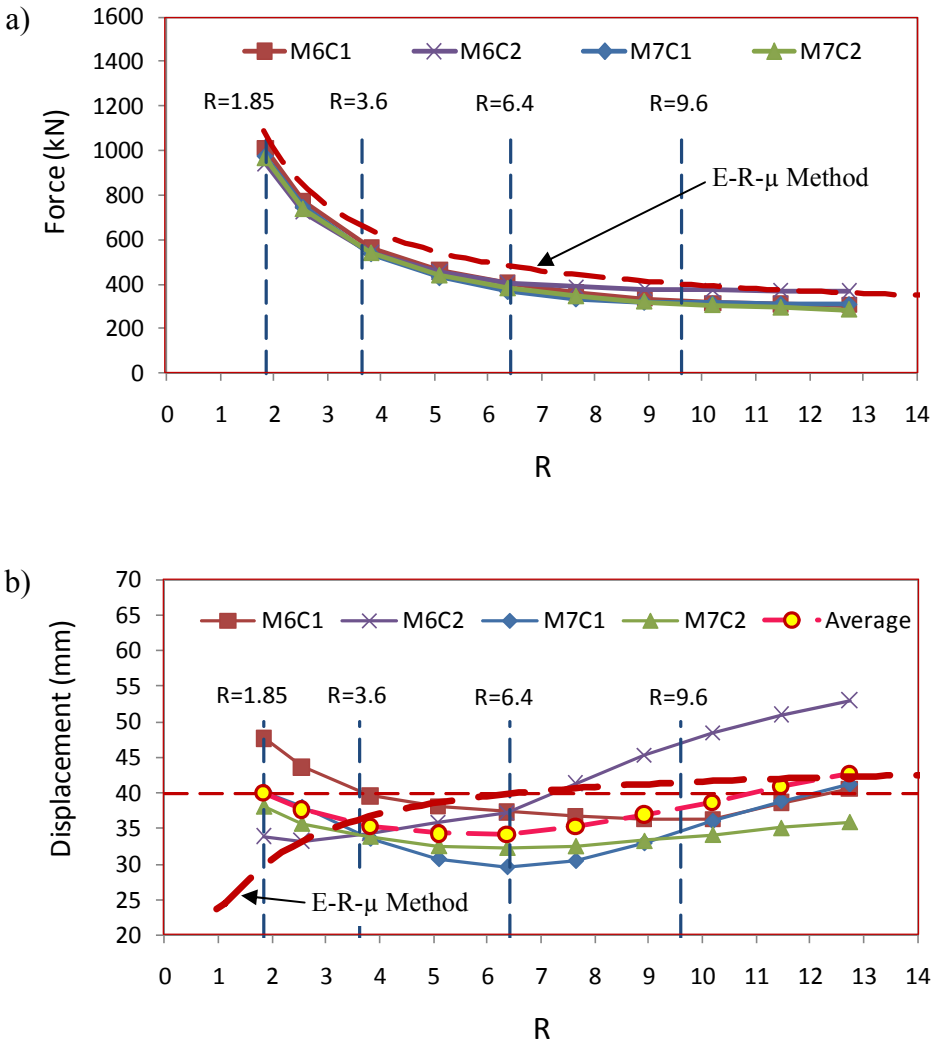

Figure 10.18 Responses of abutment isolators with *R*-factor (10% in 50 years)

10.5.6 Optimization of Isolated Bridges without Added Viscous Dampers

In order to identify the most effective protection system, the responses of four DLSP configurations defined by their force activation levels (F_{3y}), for the isolators at the abutments, were compared under the seismic demand defined by the 20 ground motions. Table 10-10 presents the force levels with the *R*-factors corresponding to their respective hazards. A maximum activation force of F_{3y} = 867 kN, as defined above for the LRB units in terms of the characteristic strength Q_{3d}, corresponds to a reference level of Q_{3d} = 100%.

Table 10-10 Activation levels for isolators at the abutments

Activation Level	Q_{d3} (kN)	10% - 50 years	2% - 50 years
100% Q_{3d_max}	780	R=1.85	R=5.6
51% Q_{3d_max}	398	R=3.6	R=7.0
29% Q_{3d_max}	226	R=6.4	R=12.4
19% Q_{3d_max}	148	R=9.6	R=18.6

Figures 10.19 and 10.20 present the responses from nonlinear time history (NLTH) analysis of the isolated bridges subjected to the SE and DE events, respectively. As noted in Figure 10.19, the deck and the pier experience the same displacements under these lower amplitude ground motions. For the first three configurations (Q_{3d} = 100%, 51% and 29%) the SE performance objective is satisfied. The displacements remain mostly under the 40 mm limit representing the damage threshold for the expansion joints. For the system with Q_{3d} = 19%, however, this performance objective is not satisfied (Figure 10.19(d)). For the DE level (2% in 50 years), the displacements of the pier remain below the pier elastic limit, as intended in the design of the pier isolators. The deck displacement is significantly affected by the increase in the event intensity and exceeds the displacement limit for the expansion joints (accepted minor damage). For the first three configurations (Q_{3d} = 100%, 51% and 29%) under the DE event, the performance objectives are satisfied. The pier remains below the pier elastic limit and the abutment isolator limit (u_{3max} = 120 mm) is not exceeded. Although damage will occur to the expansion joint, the bridge would be expected remain functional, which would be acceptable. As a result, the performance objectives are not satisfied only for the system configuration having Q_{3d} = 19% (Figure 10.20(d)).

The displacements from the NLTHA are compared to the estimate obtained using the energy-based *E-R-*μ method. The method results in comparable response estimates.

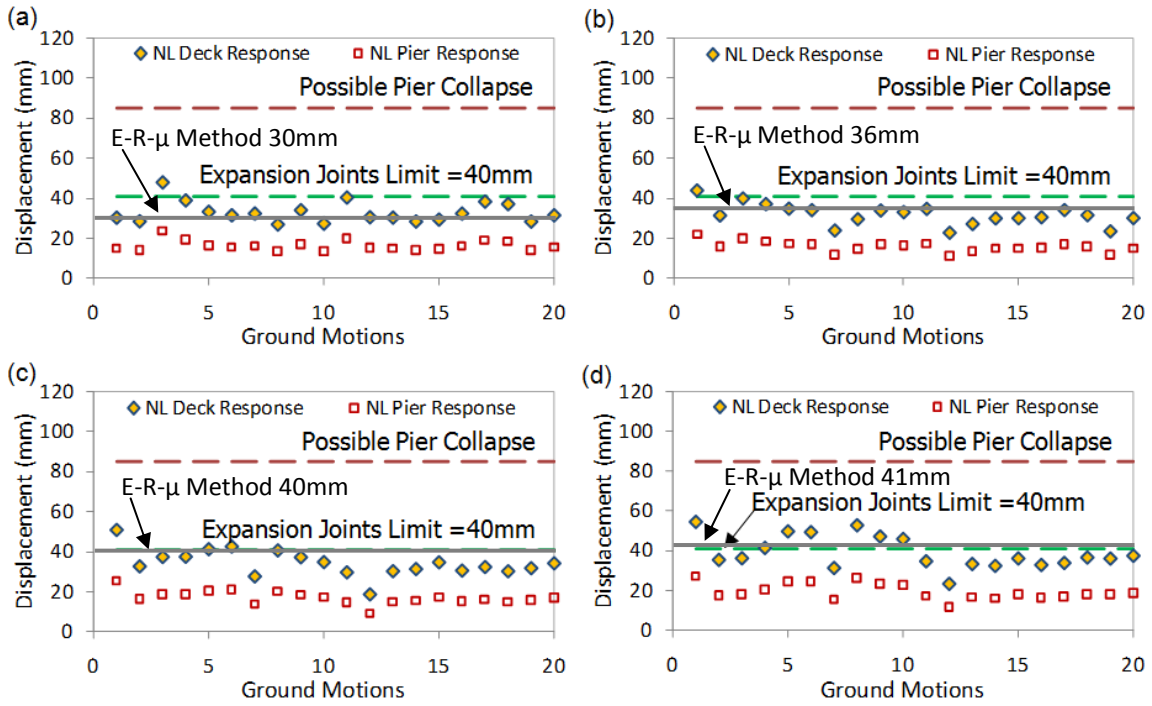

Figure 10.19 Displacement responses for bridge without dampers (20 records - 10%-50 years): (a) Q_{3d} = 100%, (b) Q_{3d} = 51%, (c) Q_{3d} = 29%, and (d) Q_{3d} = 19%

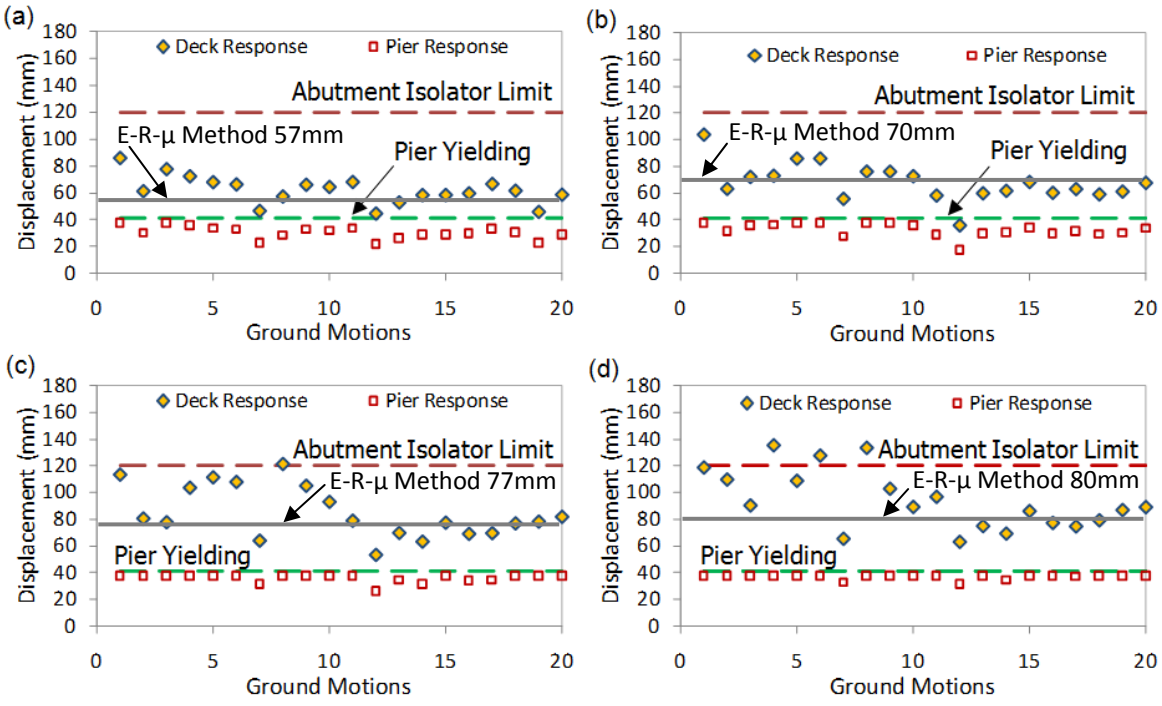

Figure 10.20 Displacement responses for bridge without dampers (20 artificial records - 2%-50 years): (a) Q_{3d} = 100%, (b) Q_{3d} = 51%, (c) Q_{3d} = 29%, and (d) Q_{3d} = 19%

Figure 10.21 presents the maximum forces in the isolators at the piers and at the abutments under earthquakes representing the 2% in 50 years hazard level. As expected, the percentage of ground motions that activate the isolators at the piers increases as the activation force at the abutment isolators decreases (10% for $Q_{d3} = 100\%$, 25% for $Q_{d3} = 51\%$, 70% for $Q_{d3} = 29\%$, and 85% for $Q_{d3} = 19\%$).

These results indicate that among the first three configurations ($Q_{3d} = 100\%$, 51% and 29%) which met the performance objectives, the most effective solution is achieved when the seismic forces are the lowest for $Q_{d3} = 29\%$. This confirms that the response tendency as a function of the *R*-factor represents good indicators for determining the optimal system parameters.

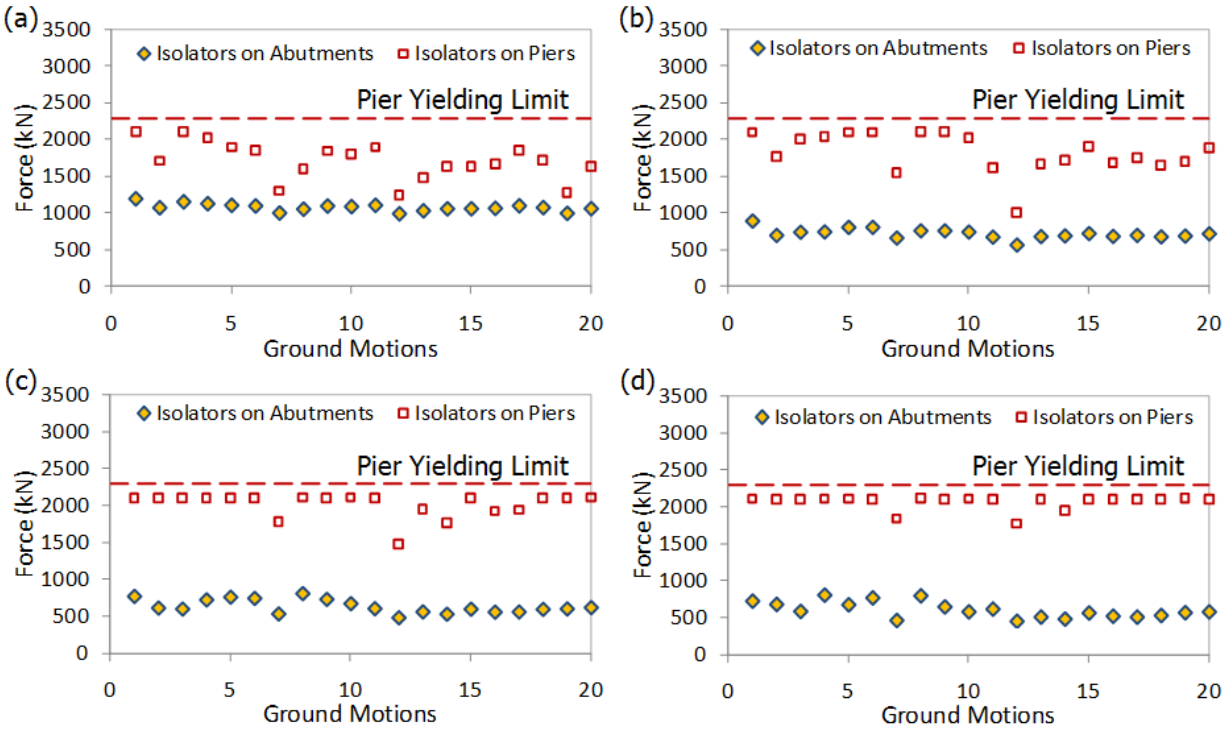

Figure 10.21 Isolator forces for bridge without damper (20 artificial records - 2%-50 years): (a) $Q_{3d} = 100\%$, (b) $Q_{3d} = 51\%$, (c) $Q_{3d} = 29\%$, and (d) $Q_{3d} = 19\%$

10.5.7 Optimization Results for Isolated Bridge with Added Viscous Dampers

In the above examples, an optimization design process was proposed to achieve the target performance levels by tuning the properties of the isolation systems without using supplemental viscous dampers. However, when the available isolation systems cannot achieve the targeted performance, as for the configuration of Q_{d3} = 19% (discussed above), viscous dampers can be used to efficiently control the displacement response. Figure 10.22 illustrates the process used to find the optimum isolation and damping properties for the same bridge with the configuration of Q_{d3} = 19% by varying only the model parameter c_3 characterizing the dampers at the abutments. As can be observed from Figure 10.22, at the abutments, the isolator forces decrease as the damper force increases when increasing c_3. An optimum value of c_3 = 0.6 MN-s/m was found to induce the minimum total lateral force on the abutments while limiting the displacements across the expansion joint to the limit of 40 mm.

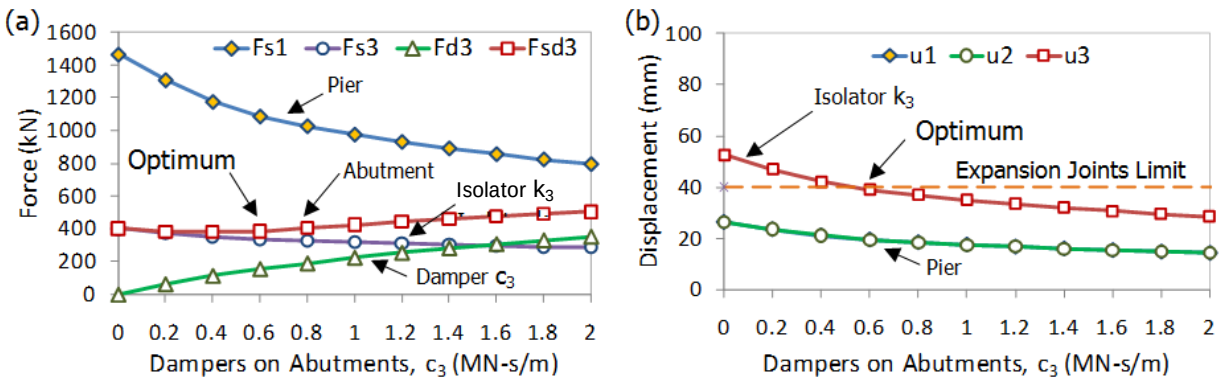

Figure 10.22 Optimizing damper c_3 to expansion joints limit (1 record - 10%-50 years)

Figure 10.23 presents the displacement responses for the bridge retrofitted with the dual-level isolation system having the optimum damping level (0.6 MN-s/m). This figure shows that for all 20 ground motions under both hazard levels, the protection system satisfies the performance objectives: the deck displacements are below the 40 mm expansion joint limit for the 10% in 50 year hazard level (SE) and the 120 mm displacement limit for the isolators at the abutments is not exceeded under the 2% in 50 years excitations (DE). Moreover, the displacements of the pier remain below the pier yield displacements for the both hazard levels, as it was intended.

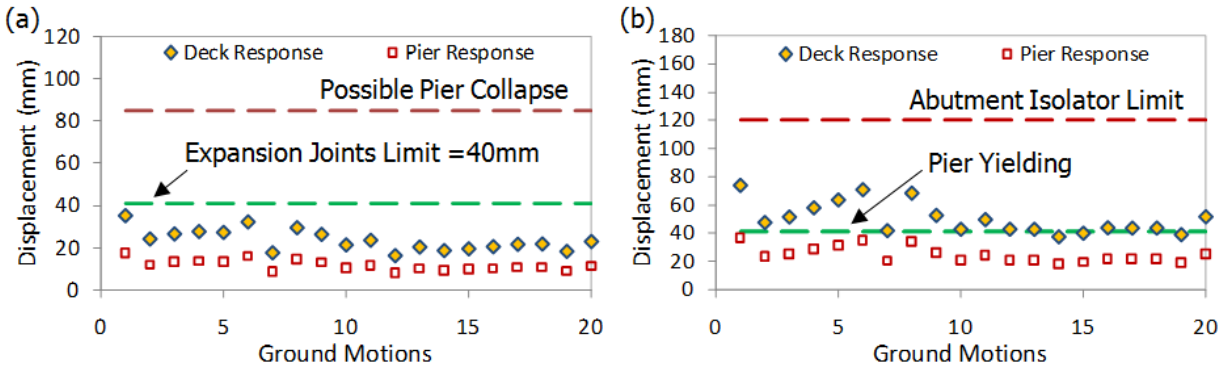

Figure 10.23 Displacement responses for bridge with damper c_3 = 0.6 MN-s/m (20 records)

10.6 Conclusions

The current seismic code provisions (CSA-S6-06 and AASHTO) do not provide an explicit optimization procedure that allows engineers to fully benefit from the performance enhancements at different levels of seismic hazard. To fill the gap in the design of isolated bridges for multi-level-hazard objectives, a dual-level seismic protection (DLSP) system involving sequential activation of isolation and supplemental damping devices was introduced in this chapter.

Through the careful selection of protective devices and the clear definition of a proper hierarchy of activation, which is related to the two-hazard level performance objectives, the concept of a dual-level seismic protection system makes it possible to achieve optimum cost-effective isolation solutions using conventional isolation and damping devices. The ability of the DLSP to control the structural behaviour of isolated bridges equipped with different seismic protective devices was demonstrated through a bridge retrofit example.

The proposed methodology was applied using both NLTHA and the proposed energy-based *E-R-μ* method, for the retrofit of existing, seismically deficient bridges. The optimal design process of a DLSP was illustrated for the retrofit of a bridge in Montreal and a bridge in Vancouver. By comparing the responses from the NLTHA to the estimates obtained using the *E-R-μ* method, the appropriateness of adopting the latter for preliminary design to define an optimum seismic protection strategy was confirmed.

The retrofit designs were further optimized by considering the addition of supplemental viscous dampers at the abutments. Based on the case studies presented in this chapter it was determined that the DLSP concept represents a viable approach for achieving optimal performance-based design of bridges with isolation and damping systems.

Chapter 11: Summary and Conclusions

11.1 Overview and Project Contributions

The code simplified method currently specified in the Canadian seismic design provisions for design of isolated bridges (CAN/CSA-S6-06, Section 4.10 Seismic Base Isolation) has been verified and enhanced. The damping coefficients *B*, on which the CSA-S6 simplified method relies, have been revisited for design of isolated bridges in both eastern and western North American regions. Results of this study incorporate a significant amount of new information that has been generated in the last two decades on the characteristics of the ground motions expected in eastern and western North America. This site-specific seismic data, was not available at the time when the simplified method was developed. Therefore, by addressing concerns about the appropriateness of using the same seismic provisions for ENA and WNA, the study presented in this research will fill a gap in the current design provisions. To improve the accuracy of the simplified method for estimating the bridge responses in ENA, the damping coefficients *B* were modified so that the levels of statistical significance for the response estimates are similar for design of isolated bridges in ENA and WNA.

The limits for the application of the code simplified method have been also examined. It was found that the source of the inaccuracy originates from the *equivalent linearization method* rather than from the definition of the damping coefficients *B*. To ensure that the method will lead to conservative results, the method applicability limits can be established in terms of the effective period. This expression takes into account the influence of the nonlinear parameters. In this way response estimates that are not sufficiently accurate are automatically rejected and the method applicability limits are relaxed with respect to those currently set in the code provisions (CAN/CSA-S6-06). As a result, a much wider choice of the market-available seismic protective devices can be covered by the modified simplified method.

It was shown that these limits are intrinsic to the assumptions made in developing the simplified method which relies on a steady-state response of the equivalent linearized system. The equivalent linearized system oscillates around its original equilibrium position and is naturally

restrained to capture the drift of the oscillation centre that in turn, results in the problem of the method accuracy. To overcome these limitations a new energy-based *E-R-μ* method has been developed. This method can more accurately account for the transient response and the drift of the oscillation centre of isolated bridges, two aspects that are not accounted for in the current code simplified method. The ground motion characteristic and the system's nonlinear parameters are taken into account by the proposed energy-based *E-R-μ* method. The capability of this method to improve, complement and extend the applicability of existing methods is validated against results from NLTHA. The energy-based *E-R-μ* method appears to result mostly in conservative response prediction and may be incorporated into the current design provisions as an efficient alternative to the currently specified design approach.

The current seismic code provisions (CSA-S6-06) do not provide an explicit optimization procedure that allows engineers to fully benefit from the performance enhancements at different levels of seismic hazard. To fill the gap in the design of isolated bridges for multi-level-hazard objectives, a dual-level seismic protection (DLSP) system involving sequential activation of isolation and supplemental damping devices has been developed in the present research. The DLSP system can be configured using different seismic protection devices as dampers and isolators. The DLSP system can be configured such that it can be used for the design of new isolated bridges as well as for the upgrade of existing seismically deficient bridges. More efficient and reliable seismic protection systems may be designed providing bridge owners with significant cost saving.

This research will contribute to the development of next-generation techniques and strategies for the design of isolated and damped bridges in both eastern and western North American regions. The accuracy of the simplified method will be improved and a much wider choice of the market-available seismic protective devices can be covered by the modified simplified method. The new energy-based *E-R-μ* method represents an applicable alternative simplified approach for cases where the desired seismic protection scheme does not meet the code methods' limits. The dual-level seismic protection (DLSP) system will allow engineers to fully benefit from the performance enhancements that can be achieved with isolation and damping to meet specific performance objectives under different levels of seismic hazard.

By implementing these innovative techniques and strategies, bridge owners and designers will be able to determine the optimum bridge protective system in terms of performance and cost-

effectiveness. More realistic response estimates will reduce the impact of the uncertainties related to the decision on the implementation of different isolation and damping devices for seismic protection of bridges. The findings and achievements summarized above put in evidence the significance, originality and contribution to knowledge of this research work.

11.2 Conclusions

Improvement of the CSA-S6-06 code simplified method for design of isolated bridges in ENA and WNA

In this study, the appropriateness of damping coefficients *B* currently specified in the NA codes (CSA-S6-06 and AASHTO) for the design of isolated bridges in ENA and WNA was investigated by using both LTHA and NLTHA.

The *B*-coefficients from LTHA in ENA and WNA were compared to those specified in codes in order to emphasize the influence of the regional seismicity on the reduction damping effect. A lower reduction effect of viscous damping was observed under ENA records when compared to WNA records. The concepts of force transmissibility and response amplification for S_A and S_D were exploited to explain the observed differences that were primarily attributed to different frequency contents distinguishing the ENA and WNA seismicity conditions.

The suitability of using the same *B*-coefficient for reducing force and displacement responses was examined based on the LTHA results. It was shown that the coefficients $B(S_A)$ and $B(S_D)$ reflect different aspects of the system response (absolute acceleration and relative displacement) and *B*-coefficients for reducing force and displacement responses must be independently calibrated. For a more accurate evaluation of the displacement across isolation bearings, the analysis results suggest that for the simplified code method the definition of the *B* coefficients should be based on spectral displacements rather than spectral accelerations. The dependency of the *B*-coefficients on the effective period was also confirmed.

In this research, complementary to most of previous studies performed worldwide in which LTHA was used, an extensive parametric study was carried out using dynamic NLTHA so that a series of nonlinear system parameters was considered to cover a wide range of isolated and damped bridge configurations. A total of 12 000 NLTHA were carried out on 300 isolated bridge

configurations under 20 time-history records representatively for the WNA and ENA regional seismicity (40 records in total). Based on the observations made for LTHA, in the parametric study, the damping coefficients were assessed solely for displacement responses. The damping coefficients specified in current CSA-S6 and AASHTO codes were found to result mostly in safe designs for WNA but underestimated the displacement demand of bridges subjected to ENA seismic ground motions.

Based on these results a new value was proposed for the exponent to be used in the equation currently specified in the AASHTO specifications for the damping coefficients so that the same equation can be used with different exponents for WNA and ENA locations (Chapter 5). The modified simplified code method proposed in this thesis for estimating displacement demand result in comparable relative errors ranging from 5% (unconservative) to -50% (conservative) for both WNA and ENA. The number of bridges satisfying the conservative response estimates in ENA was accordingly increased from 31% to 89%. This number is in close agreement with 90% of satisfactory estimates in WNA. In this way, the same level of accuracy would be reached in both parts of the country.

The study also showed that the simplified method still underpredicts the response of isolated bridges for a number of cases. In particular, systems with low R factors, low α ratios, with high effective damping ratios or short effective periods were found to be more critical in this regard.

The sources of the method inaccuracy may be both the local damping reduction effect and the *equivalent linearization method* which is an intrinsic part of the code method. To improve our understanding of the sources of the method inaccuracy, the accuracy of the *equivalent linearization method* is then carefully examined. It was found that the source of the inaccuracy originates from the *equivalent linearization method* rather than from the definition of the damping coefficients B (Chapter 6). By examining in details the process of equivalent linearization, the upper limit for the method applicability range was derived on the effective damping and effective period. In this way, the influence of the nonlinear parameters was taken into account to achieve sufficient accuracy in the seismic response prediction.

The method applicability limits, proposed in this thesis (Chapter 6), were validated by comparing NLTH responses, obtained in Chapter 5, to the response estimates obtained during the design process following the complete iterative procedure prescribed in the CSA-S6-06 simplified

method using damping coefficients *B* proposed in this thesis for WNA and ENA. It was confirmed that the use of the proposed limits makes it possible to reject responses with unsatisfactory accuracy. When comparing the actual code limits (CSA-S6-06) to those proposed in this thesis, the number of bridges meeting these limits while satisfying the conservative response estimates was increased from 60% to 93% for WNA and from 36% to 94% for ENA (Chapter 9). This represents a major improvement thus ensuring a wider choice of the market-available seismic protective devices that can be covered by the modified simplified method. These limits could then be used in future editions of CSA-S6 for both WNA and ENA.

To overcome these limitations the need for a new simplified method that takes into account the differences in ground-motion characteristics and isolated bridge design parameters is also outlined.

New Energy-Based E-R-μ Simplified Method

In order to establish a basis for the development of a new simplified method, two widely adopted methods in earthquake engineering, the Equal Displacement (EDA) and the Equal Energy (EEA) approaches, were briefly reviewed and examined. It was found that the "exact" responses from NLTHA are confined by that obtained from these two response approximating techniques (EDA and EEA). The response estimates obtained by using the EEA were found to be conservative for all studied cases. It was shown that the differences between the response estimates from the EEA and “exact” NLTHA results may be related to the amount of absorbed energy. It was then shown that the difference in absorbed energy between these two responses is attributed to the kinetic energy which is ignored when assuming that the input energy is absorbed entirely through monotonic loading. This portion of the energy input that is ignored by the EEA was termed as an *energy deficit*.

To better characterize seismic response in the present study, special attention was drawn to the transient phase of loading that occurs at the beginning of the excitation. Through this study, bi-linear NL-SDOF systems were classified as exhibiting either a *limited-nonlinear* or a *highly-nonlinear response*. It was confirmed that during *limited-nonlinear response*, systems oscillate about their "at rest" equilibrium position and the energy induced into the systems over a loading cycle is dissipated completely through the system's inelastic response within the same cycle. In turn, during *highly-nonlinear response*, the systems experience a drift of the oscillation center

which results from an excess of kinetic energy compared to the energy absorption capacity of the system. In such a case, the maximum displacement response consists of the drift of the oscillation center plus the local system response about the new oscillation center. The energy excess generated during a transient phase of loading can be dissipated through a few consecutive cycles. The transient oscillation center shifts gradually in each of these cycles until the energy excess is entirely dissipated.

The transition state between limited-nonlinear and highly-nonlinear responses was defined as the point beyond which the response of a system starts oscillating about a drifted equilibrium center. The critical parameter R_{cr} was derived to mark this point of transition.

The effect of the kinetic energy on the system behaviour was identified as a key element to be considered in the development of the new simplified method. The transient response and possible shifting of the transient oscillation centre, was taken into account by applying the concept of energy allocation under transient excitation. Based on this, a new simplified method was proposed. This method takes into account the differences in ground-motion characteristics and bridge design parameters and can predict the peak displacement of bilinear systems. This new energy-based E-R-μ method was developed purely based on analytical derivations rather than being empirically calibrated. The basis on which the predictions are made assumes that 1) ground motions are represented by a single sine-wave pulse defined by the peak ground acceleration (PGA) and peak ground displacement (PGD) and 2) response to that pulse can be predicted using the E-R-μ method.

New Multi-Level-Hazard Protection Technique

To fill the gap in the design of isolated bridges for multi-level-hazard objectives, a dual-level seismic protection (DLSP) system involving sequential activation of isolation and supplemental damping devices was introduced in this thesis.

Through the careful selection of protective devices and the clear definition of a proper hierarchy of activation, which is related to the two-hazard level performance objectives, the concept of dual-level seismic protection system makes it possible to achieve optimum cost-effective isolation solutions using conventional isolation and damping devices. The ability of the DLSP to control the structural behaviour of isolated bridges equipped with different seismic protective

devices was demonstrated through bridge retrofit examples. It was determined that the DLSP concept represents a viable approach for achieving optimal performance based design of bridges with isolation and damping systems.

11.3 Recommendations for Future Research

Although the code simplified method (CAN/CSA-S6-06) has been extensively examined and the proposed modifications will enhance the method's reliability, there are still certain aspects that can be studied to improve the method accuracy based on the achievements of the present research.

- The damping coefficients B can be derived as a function of the ground motion characteristics and system nonlinear parameters using energy concept for transient phase of loading.

- Different formulations of damping coefficients B can be developed for ranges of the limited-nonlinear and highly-nonlinear responses (defined in Chapter 7).

To improve the accuracy of the energy-based E-R-μ method proposed in this thesis, additional research is suggested on how to capture the effect of the loading duration or complex irregularity in the seismic excitation and the structural response. In this way, the method will take into account the effect of multiple *oscillation centre* drifts that originate from various successive loading pulses.

It is recommended to extend the energy-based E-R-μ method to predict the peak displacement of systems having different hysteresis shapes as for example that flag-shaped or multilinear. As a result, a much wider choice of the market-available seismic protective devices can be covered by the proposed energy-based E-R-μ method.

To extend the dual-level seismic protection concept, research studies can be performed on the development of a number of novel seismic protection devices. Such devices can be designed to have different activation levels to meet specific performance objectives under different levels of seismic hazard. Configuring the multilevel protection device to a proper hierarchy of activation will allow to achieve optimum cost-effective seismic protection.

References

AASHTO (1991). "Guide specifications for seismic isolation design", *American Association of State Highway and Transportation Officials (AASHTO)*, Washington, D.C., US.

AASHTO (1994). "AASHTO LRFD Bridge Design Specifications", *1st Edition including interim revisions for 1996 and 1997, American Association of State Highway and Transportation Officials (AASHTO)*, Washington, D.C., US.

AASHTO (1999). "Guide Specifications for Seismic Isolation Design, 2nd Edition", *American Association State and Highway Transportation Officials (AASHTO),* Washington, D.C., US.

AASHTO (2009). "Guide Specifications for the LRFD Seismic Bridge Design", *American Association of State Highway and Transportation Officials (AASHTO)*, Washington, D.C., US.

AASHTO (2010). "Guide Specifications for Seismic Isolation Design", *3rd Edition, American Association of State Highway and Transportation Officials (AASHTO)*, Washington, D.C., US.

Abé, M. (1996). "Tuned Mass Dampers for Structures with Bilinear Hysteresis", *Journal of Engineering Mechanics*, 122(8), 797-800.

Abrahamson, N.A. and Silva, W.J. (1997). "Empirical response spectral attenuation relations for shallow crustal earthquakes", *Seismological Research Letters*, 68, 94–127.

Abrahamson, N.A. (2000). "Effects of rupture directivity on probabilistic seismic hazard analysis", *Proc. Sixth International Conference on Seismic Zonation*, November 12–15, Palm Springs, California.

Abrahamson, N.A., and Silva, W.J. (2008). "Summary of the Abrahamson & Silva NGA groundmotion relations", *Earthquake Spectra*, 24, 67–97.

Adams, J., Basham, P.W., and Halchuk, S. (1995). "Northeastern North American earthquake potential – new challenges for seismic hazard mapping, In: Current Research 1995-D", *Geological Survey of Canada*, 91–99.

Adams, J., Weichert, D., and Halchuk, S. (1999). "Lowering the probability level - fourth generation seismic hazard results for Canada at the 2% in 50 year probability level", *Proc. of Eighth Canadian Conference on Earthquake Engineering*, Vancouver, 83-88.

Adams, J. and Atkinson, G. (2003). "Development of seismic hazard maps for the 2003 National Building Code of Canada", *Canadian Journal of Civil Engineering*, 30, 255-271.

Adams, J. and Halchuk, S. (2003). "Fourth generation seismic hazard maps of Canada: Values for over 650 Canadian localities intended for the 2005 National Building Code of Canada", *Geological Survey of Canada*, Open File 4459, 150 p.

Adams, J. and Halchuk, S. (2004). "Fourth-generation seismic hazard maps for the 2005 national building code of Canada", *Proceedings of the 13th World Conference on Earthquake Engineering*, Vancouver, Canada. Paper 2502 on CD-ROM.

Adams, J. (2011). "Seismic hazard and seismic risk in Canada perspective for the insurance industry", *Geological Survey of Canada*, Natural Resources Canada, Ottawa, Ontario, ICLR workshop Toronto, ON.

Akkar, S. and Bommer, J.J. (2007). "Prediction of elastic displacement response spectra in Europe and the Middle East", *Earthquake Engineering & Structural Dynamics*, 36, 1275-1301.

Ambraseys, N.N. and Srbulov, M. (1994). "Attenuation of Earthquake-Induced Ground Displacements", *Earthquake Engineering & Structural Dynamics*, 23, 467-487.

Ambraseys, N.N., Simpson, K.A. and Bommer, J. J. (1996), "Prediction of Horizontal Response Spectra in Europe", *Earthquake Engineering & Structural Dynamics*, 25: 371–400.

Ambraseys, N., Smit, P., Sigbjörnsson, R., Suhadolc, P. and Margaris, B. (2001). Internet-Site for European Strong-Motion Data. <http://www.isesd.cv.ic.ac.uk>, *EVR1-CT-1999-40008*, European Commission, Directorate-General XII, Environmental and Climate Programme, Bruxelles, Belgium.

American Society of Civil Engineers (2005). "Minimum Design Loads for Buildings", *ASCE 7-05*, Reston, Virginia, US.

Anderson, J. and Bertero, V. (1987). "Uncertainties in Establishing Design Earthquakes", *Journal of Structural Engineering*, 113(8), 1709–1724.

ASCE (2000a). "Prestandard and Commentary for the Seismic Rehabilitation of Buildings", *FEMA 356 Report*, *American Society of Civil Engineers (ASCE), Federal Emergency Management Agency (FEMA)*, Washington, D.C., US.

ASCE (2000b). "Global Topics Report on the Prestandard and Commentary for the Seismic Rehabilitation of Buildings", *FEMA 357 Report*, *American Society of Civil Engineers (ASCE), Federal Emergency Management Agency (FEMA)*, Washington, D.C., US.

ATC (1996a). "Seismic Design Criteria for Highway Structures: Current and Future", *Report No. ATC-18, Applied Technology Council (ATC)*, Redwood City, California, US.

ATC (1996b). "Improved Seismic Design Criteria for California Bridges: Provisional Recommendations", *Report No. ATC-32, Applied Technology Council (ATC)*, Redwood City, California, US.

ATC (1996c). "Seismic Evaluation and Retrofit of Concrete Buildings", *Report No. ATC-40, Volumes 1 and 2, Applied Technology Council (ATC)*, Redwood City, California, US.

ATC/BSSC (1997). "NEHRP Guidelines for the Seismic Rehabilitation of Buildings", *FEMA 273 Report (Guidelines) and FEMA 274 Report (Commentary), Applied Technology Council (ATC), Federal Emergency Management Agency (FEMA)*, Washington, D.C., US.

Atkinson, G.M. and Beresnev, I., (1998). "Compatible ground-motion time histories for new national seismic hazard maps", *Canadian Journal of Civil Engineering*, 25, 305-318.

Atkinson, G.M. (2004). "An Overview of Developments in Seismic Hazard Analyses", *13th World Conference on Earthquake Engineering*, Vancouver, B.C., Canada

Atkinson, G.M. and Pierre, J.R. (2004). "Ground motion response spectra in Eastern North America for different critical damping values", *Seismological Research Letters*, 75(4), 541–545.

Atkinson, G.M. (2005). "Ground Motions for Earthquakes in southwestern British Columbia and northwestern Washington: Crustal, In-Slab and Offshore Events", *Bulletin of the Seismological Society of America*, 95, 1027-1044.

Atkinson, G.M. and Boore, D. (2006). "Ground motion prediction equations for earthquakes in eastern North America", *Bulletin of the Seismological Society of America*, 96, 2181-2205.

Atkinson, G.M. (2008). "Earthquake time histories compatible with the 2005 NBCC Uniform Hazard Spectrum", *Canadian Journal of Civil Engineering*, Submitted.

Atkinson, G.M. (2009). "Earthquake time histories compatible with the 2005 National Building Code of Canada uniform hazard spectrum", *Canadian Journal of Civil Engineering*, 36(6), 991-1000.

Atkinson, G.M., Assatourians, K., Boore, D.M., Campbell, K., and Motazedian, D. (2009). "A Guide to Differences between Stochastic Point-Source and Stochastic Finite-Fault Simulations", *Bulletin of the Seismological Society of America*, 99(6), 3192–3201

Atkinson, G.M. (2010). "Time History modifications – frequency domain approach", *Presentation*, CSRN Meeting April 2010.

Ben-Menahem, A. (1961). "Radiation of seismic surface-waves from finite moving sources", *Bulletin of the Seismological Society of America*, 51, 401–435.

Ben-Menahem, A. (1962). "Radiation of seismic body-waves from finite moving sources in the earth", *Journal of Geophysical Research*, 67, 345–350.

Beresnev, I. and Atkinson, G.M. (1997). "Modeling finite fault radiation from the ω n spectrum", *Bulletin of the Seismological Society of America*, 87, 67-84.

Beresnev, I. and Atkinson, G.M. (1998). "Stochastic finite-fault modeling of ground motions from the 1994 Northridge, California earthquake. I. Validation on rock sites", *Bulletin of the Seismological Society of America*, 88, 1392-1401.

Bertero, V.V., Mahin, S.A. and Herrera, R.A. (1978). "Aseismic design implications of near-fault San Fernando earthquake records", *Earthquake Engineering & Structural Dynamics* 6, 31-42.

Biggs, J.M. (1964). "Introduction to Structural Dynamics", McGraw-Hill.

Bommer, J.J. and Martinez-Pereira, A. (1999). "The Effective Duration of Earthquake Strong Motion", *Journal of Earthquake Engineering*, 3(2), 127-172

Bommer, J.J., Scott, S.G., and Sarma, S.K. (2000a). "Hazard-consistent earthquake scenarios", *Soil Dynamics and Earthquake Engineering*, 19(4), 219-231.

Bommer, J.J., Elnashai, A.S., and Weir A.G. (2000b). "Compatible acceleration and displacement spectra for seismic design codes", *Proc. 12th World Conference on Earthquake Engineering*, *January 30 - February 4*, Auckland, New Zeland, Paper No. 0207.

Bommer, J.J., Georgallides, G., and Tromans, I.J. (2001). "Is there a near-field for small-to-moderate magnitude earthquakes?", *Journal of Earthquake Engineering* 5(3), 395-423.

Bommer, J.J. and Acevedo, A.B. (2004). "The Use of Real Eathquake Accelerograms as Input to Dynamic Analysis", *Journal of Earthquake Engineering*, 8(1), 43-91.

Bommer, J.J. and Mendis, R. (2005). "Scaling of spectral displacement ordinates with damping ratios", *Earthquake Engineering & Structural Dynamics*, 34(2): 145-165.

Bommer, J.J. and Pinho, R. (2006). "Adapting earthquake actions in Eurocode 8 for performance-based seismic design", *Earthquake Engineering & Structural Dynamics*, 35(1), 39–55.

Bommer, J.J., Stafford, P.J., and Alarcon, J.E. (2009). "Empirical Equations for the Prediction of the Significant, Bracketed, and Uniform Duration of Earthquake Ground Motion", *Bulletin of the Seismological Society of America*, 99, 3217-3233.

Boore, D. and Atkinson, G.M. (2008). "Ground-motion prediction equations for the average horizontal component of PGA, PGV, and 5%-damped SA at spectral periods between 0.01s and 10.0 s", *Earthquake Spectra*, 24(1), 99-138.

Boore, D.M. (2005). SMSIM; Fortran programs for simulating ground motions from earthquakes: Version 2.3 A revision of OFR 96-80-A, U.S. Geol. Surv. Open-File Rept. (a modified version of OFR 00-509, describing the program as of 15 August 2005 [version 2.30]).

Buckle, I., Friedland, I., Mander, J., Martin, G., Nutt, R. and Power, M (2006). "Seismic retrofitting manual for highway structures: Part 1-bridges", *MCEER Publications*, State University of New York, Buffalo, New York, US.

Cameron, W.I., and Green, R. U. (2007). "Damping correction factors for horizontal ground-motion response spectra", *Bulletin of the Seismological Society of America*, 97(3), 934–960.

Cameron, W.I., Green, R.U. (2007). "Damping correction factors for horizontal ground-motion response spectra." *Bulletin of the Seismological Society of America*, 97(3) 934–960.

Campbell, K.W., and Bozorgnia, Y., 2003. Updated near-source ground-motion (attenuation) relations for the horizontal and vertical components of peak ground acceleration and acceleration response spectra, *Bulletin of the Seismological Society of America*, 93, 314–331.

CSA (2006). "Canadian Highway Bridge Design Code", *CAN/CSA-S6-06, Canadian Standards Association (CSA)*, Mississauga, Ontario, Canada.

Caughey, T.K. (1960). "Sinusoidal excitation of a system with bilinear hysteresis", *Journal of Applied Mechanics*, 27(4), 640–643.

CEN. (1996) "Eurocode 8: Design Provisions for Earthquake Resistance of Structures. Part 2: Bridges", *ENV 1998-2:1996, Comité européen de normalisation (CEN)*, Brussels, Belgium.

CEN (2005). "Eurocode 8: Design Provisions for Earthquake Resistance of Structures. Part 2: Bridges", *EN 1998-2:2005, Comité européen de normalisation (CEN)*, Brussels, Belgium.

Chopra, A.K. (1995). "Dynamics of structures: Theory and applications to earthquake engineering", Prentice-Hall, New Jersey, US.

Chopra, A.K. (2011). "Dynamics of structures, theory and applications to earthquake engineering", 4th Edition, Pearson Prentice-Hall, Upper Saddle River, New Jersey, US.

Christopoulos, C. and Filiatrault, A. (2006). “Principles of passive supplemental damping and seismic isolation”, IUSS Press, Pavia, Italy.

Christopoulos, C., Filiatrault, A., and Folz, B. (2002a). "Seismic response of self-centring hysteretic SDOF systems", *Earthquake Engineering & Structural Dynamics*, 31(5), 1131-1150.

Christopoulos, C., Filiatrault, A., Uang, C-M., and Folz, B. (2002b). "Posttensioned Energy Dissipating Connections for Moment-Resisting Steel Frames", *Journal of Structural Engineering,* 128(9), 1111-1120.

Constantinou, M.C., Tsopelas, P., Kim, Y-S., and Okamoto, S. (1993). "NCEER-Taisei Corporation Research Program on Sliding Isolation Systems for Bridges: Experimental and Analytical Study of Friction Pendulum System", *Report No. 93-0020, National Center for Earthquake Engineering*, State University of New York, Buffalo, New York, US.

Constantinou, M.C., Whittaker, A.S., Kalpakidis, Y., Fenz, D.M., and Warn, G.P. (2007). "Performance of Seismic Isolation Hardware under Service and Seismic Loading", Technical Report MCEER-07-0012, Buffalo, New York, US, 469 p.

CSI (2009). SAP2000 [Computer Software] *Computers and Structures Inc.*, Berkeley, California, US.

CSRN (2012). "Topics related to selecting and scaling ground motions", *Workshop related to CSRN activities - Canadian Seismic Research Network (CSRN)*, September 17, Montreal, Quebec, Canada

Den Hartog, J.P. (1930). "Forced Vibrations with Combined Viscous and Coulomb Damping", *The London, Edinbourg, and Dublin Philosophical Magazine*, 9(59) 801-817.

Dicleli, M. (2006). "Supplemental elastic stiffness to reduce isolator displacements for seismic-isolated bridges in near-fault zones", *Engineering Structures*, 29(5) 763–775.

Dicleli, M. and Buddaram, S (2007). "Equivalent linear analysis of seismic-isolated bridges subjected to near-fault ground motions with forward rupture directivity effect", *Engineering Structures*, 29(1), 21-32

Dion, C., Bouaanani, N., Tremblay, R., and Lamarche, C. (2012). ”Real-Time Dynamic Substructuring Testing of a Bridge Equipped with Friction-Based Seismic Isolators”, *Journal of Bridge Engineering*, 17(1) 4–14.

EN1998-2 (2005). "Design of structures for earthquake resistance - Part 2: Bridges", *European Committee for Standardization*, Brussels, Belgium.

EQECAT (2012). http://www.eqecat.com/catwatch/damaging-aftershocks-in-northern-italy-2012-05-29.

Esteva, L. and Rosenblueth, E. (1964). "Espectros de temblores a distancias moderadas y grandes", Sociedad Mexicana de Ingenieria Sismica, Publ. No.1, vol. II, 1–18.

FEMA (1997). "NEHRP commentary on the guidelines for the seismic rehabilitation of buildings", *FEMA-274, Federal Emergency Management Agency (FEMA)*, Washington, D.C., US.

FEMA 273 (1997). "NEHRP Guidelines for the Seismic Rehabilitation of Buildings", *Federal Emergency Management Agency (FEMA)*, Washington, D.C., US.

FEMA 356 (2000). "Prestandard and Commentary for the Seismic Rehabilitation of Buildings", *American Society of Civil Engineers (ASCE), Federal Emergency Management Agency (FEMA)*, Washington, D.C., US.

FEMA 356 (2000). "Prestandard and Commentary for the Seismic Rehabilitation of Buildings", *American Society of Civil Engineers (ASCE), Federal Emergency Management Agency (FEMA)*, Washington, D.C., US.

FEMA 440 (2005). "Improvement of nonlinear static seismic analysis procedures", *American Society of Civil Engineers (ASCE), Federal Emergency Management Agency (FEMA)*, Washington, D.C., US.

Filiatrault, A., Leger, P., and Tinawi, R. (1994). "On the Computation of Seismic Energy in Inelastic Structures", *Engineering Structures*, 16(6), 426-436.

Filiatrault, A. (2008). "Elements of Earthquake Engineering and Structural Dynamics", 2nd Edition, Presses Internationales Polytechnique, Montreal, Quebec, Canada.

Filiatrault, A., Tremblay, R., Christopoulos, C., Folz, B., and Pettigna, D. (2013). "Elements of Earthquake Engineering and Structural Dynamics", 3rd Edition, Presses Internationales Polytechnique, Montreal, Quebec, Canada.

Graizer, V. (2010). "Strong Motion Recordings and Residual Displacements: What Are We Actually Recording in Strong Motion Seismology? ", *Seismological Research Letters*, 81(4), 635-639.

Guilini Charette, K. (2009). "Effets des Mouvements Sismiques sur les Structures en Acier de la Catégorie des Constructions Conventionnelles", *M.Sc. Thesis, Departement of Civil, Geological and Mining Engineering, École Polytechnique de Montréal*, Montreal, Quebec, Canada.

Gulkan P, Sozen M. (1974). "Inelastic response of reinforced concrete structures to earthquakes motions", *ACI Journal*, 71(12) 604-610.

Halchuk, S. and Adams, J. (2004). "Deaggregation of seismic hazard for selected Canadian cities", *Proc. 13th World Conference on Earthquake Engineering*, Vancouver, Canada, August 1-6, Paper No. 2470.

Halchuk, S. (2009-2010). Personal Communication.

Hall, J.F., Heaton, T.H., Halling, M.W., and Wald, D.J. (1995) "Near-source ground motions and its effects on flexible buildings", *Earthquake Spectra* 11(4), 569-605.

Hancock, J. (2006). "The Influence of Duration and the Selection and Scaling of Accelerograms in Engineering Design and Assessment", *Ph.D. Dissertation, Department of Civil and Environmental Engineering, University of London*, London, UK, 442 p.

Hatzigeorgiou, G.D. (2010). "Damping modification factors for SDOF systems subjected to near-fault, far-fault and artificial earthquakes", *Earthquake Eng. Dyn.,* 39 (11), 1239–1258.

Heidebrecht , A.C. (2003)."Overview of seismic provisions of the proposed 2005 edition of the National Building Code of Canada", *Canadian Journal of Civil Engineering*, 30, 241-254.

Housner G.W. (1956). "Limit design of structures to resist earthquakes", *Proceedings of the 1st World Conference on Earthquake Engineering*, California, US, 5, 5-1 to 5-13.

Housner, G.W. (1963). "The behavior of inverted pendulum structures during earthquakes", *Bulletin of the Seismological Society of America*, 53(2), 403-417.

Huang, Y.N., Whittaker, A., and Luco, N. (2008). "Maximum spectral demands in the near-fault region, Earthquake Engineering Research Institute", *Earthquake Spectra*, 24(1), 319-341.

Huffman, S., Gillespie, D.G., and Anderson, D.L. (2012). "Performance-based Design (PBD) of British Columbia Bridges", *Proc. of 15th World Conference on Earthquake Engineering*, Lisbon, Portugal, Paper No. 898.

Hwang, J.S. and Chiou, J.M. (1996). "An equivalent linear model of lead-rubber seismic isolation bearings", *Engineering Structures*, 18(7), 528-536

Hwang, J.S. and Sheng, L.H. (1994). "Equivalent elastic seismic analysis of base-isolated bridges with lead-rubber bearings", *Engineering Structures*, 16(3), 201-209

ICBO (1991). "Uniform Building Code", *International Conference of Building Officials*, California, US.

Iervolino, I., Maddaloni, G., Cosenza, E., and Manfredi, G. (2007). "Selection of Time-Histories for Bridge Design in Eurocode 8", *Proc. of 1st US-Italy Seismic Bridge Workshop*, 18 - 20 April, EUCENTRE, Pavia, Italy.

Itani, A.M., and Malik, A.H. (2000). "Enhancing Seismic Design Criteria for Our Nation's Vulnerable Bridges", CD-ROM, Transportation in the New Millennium: State of the Art and Future Directions, Perspectives from the Transportation Research Board Standing Committees, Retrieved from http://onlinepubs.trb.org/onlinepubs/millennium/00034.pdf.

Iwan, W.D. (1961), "The Dynamic Response of Bilinear Hysteretic Systems", *Ph.D. dissertation, Earthquake Engineering Research Laboratory, California Institute of Technology*, California, US, 152 p.

Iwan, W.D. and Gates, N.C. (1979). "Estimating Earthquake Response of Simple Hysteretic Structures", *Journal of Engineering Mechanics Division*, ASCE, 105(EM3) 391-405.

Iwan, W.D. (1980). "Estimating inelastic response spectra from elastic spectra", *Earthquake Engineering & Structural Dynamics*, 8, 375–388.

Jacobsen, L.S. (1930). "Steady Forced Vibrations as Influenced by Damping", *ASME Transactions*, 52, 169-181.

Jacobsen, L.S. (1960). "Damping in Composite Structures", *Proc. of 2nd World Conference on Earthquake Engineering*, Tokyo and Kyoto, Japan, 1029-1044.

Jacobsen, L.S. and Ayre, R.S. (1958). "Engineering vibrations", McGraw-Hill, New York, New York, US.

Jara, M. and Casas, J.R. (2006). "A direct displacement-based method for the seismic design of bridges on bi-linear isolation devices", *Engineering Structures*, 28(6), 869-879.

Jeong, G.D. and Iwan, W.D. (1988), "The effect of earthquake duration on the damage of structures", *Earthquake Engineering Structural Dynamics*, 16, 1201–1211.

Kalkan, E. and Chopra, A.K. (2010). "Practical guidelines to select and scale earthquake records for nonlinear response history analysis of structures: U.S", *Geological Survey Open-File Report* 2010-1068, 124 p.

Kawashima, K., MacRae, G.A., Hoshikuma, J., and Nagaya, K. (1998). "Residual Displacement Response Spectrum", *Journal of Structural Engineering*, 124(5), 523-530.

Koval, V., Christopoulos, C., and Tremblay, R. (2012a). "Analytical Model for Optimizing the Design of Isolated and Damped Bridge Structures", *Proc. of 29th International Bridge Conference, June 10-13*, Pittsburgh, Pennsylvania, US, Paper IBC-12-106.

Koval, V., Tremblay, R., and Christopoulos, C. (2012b). "Isolation and Damping Mitigation Strategies for Bridges in Western and Eastern North America", *Proc. of 15th World Conference on Earthquake Engineering*, Lisbon, Portugal, Paper No. 898.

Lapalme, P. (2012). Personal communication. Engineer, Goodco Z-Tech.

Lee Marsh, M., Mayes, R.L., and Friedland, I.M (2001). "Recommended LRFD Guidelines for the Seismic Design of Highway Bridges", *Proceedings of the 17th U.S.-Japan Bridge Engineering Workshop, November 12,13 and 14*, Public Works Research Institute, 14 p.

Leger, P. and Tremblay, R. (2009). "Earthquake Ground Motions for Seismic Damage Assessment and Re-Evaluation of Existing Buildings and Critical Facilities", *Damage Assessment and Reconstruction After War and Natural Disaster, NATO Science for Peace and Security Series C: Environmental Security*, 193-219.

Lin, Y.Y. and Chang, K.C. (2003). " Study on Damping Reduction Factor for Buildings under Earthquake Ground Motions", *Journal of Structural Engineering*, 129(2), 206-214.

Liu, A, Stewart, J.P., Abrahamson, N., Moriwaki, Y. (2001). "Equivalent number of uniform stress cycles for liquefaction analysis". *Journal of Geotechnical and Geoenvironmental Engineering (ASCE)*, 127(12):1017–1026.

Makris, N. (1997). "Rigidity-plasticity-viscosity: Can electrorheological dampers protect base-isolated structures from near-source ground motions?", *Earthquake Engineering & Structural Dynamics*, 26(5), 571-591.

Makris, N. and Chang, S. P. (1998), "Effect of Damping Mechanisms on the Response of Seismically Isolated Structures", *Technical Report PEER-98/06*, University of California, Berkeley, California, US.

Masri, S.F. (1975). "Forced vibration of the damped bilinear hysteretic oscillator", *Journal of the Acoustical Society of America*, 57(1), 106–112.

MATLAB. (2009) MATLAB Version 7.8, The MathWorks, Inc.

Mavronicola, E. and Komodromos, P. (2011). "Assessing the suitability of equivalent linear elastic analysis of seismically isolated multi-storey buildings", *Computers and Structures*, 89(21-22), 1920-1231.

MCEER/ATC-49 (2003). "Recommended LRFD guidelines for the seismic design of highway bridges. Part II: Commentary and Appendices", *NCHRP Project 12-49*, FY 98. ATC/MCEER Joint Venture.

McGuire, R.K. (1995). "Probabilistic seismic hazard analysis and design earthquakes: closing the loop", *Bulletin of the Seismological Society of America,* 85(5), 1275-1284.

McGuire, R.K., Silva, W.J., and Kenneally, R (2001a). "New seismic design spectra for nuclear power plants", *Nuclear Engineering and Design*, 203 (2001) 249–257.

McGuire, R.K., Silva, W.J., and Constantino, C.J. (2001b). "Technical Basis for Revision of Regulatory Guidance on Design Ground Motions: Hazard- and Risk-consistent Ground

Motion Spectra Guidelines", *Report No. NUREG/CR-6728 prepared for the U.S. Nuclear Regulatory Commission*, Risk Engineering, Inc., Boulder, CO, 213 p.

McGuire, R.K., Silva, W.J., and Constantino, C.J. (2002). "Technical Basis for Revision of Regulatory Guidance on Design Ground Motions: Development of Hazard- and Risk-consistent Seismic Spectra for Two Sites", *Report No. NUREG/CR-6769 prepared for the U.S. Nuclear Regulatory Commission*, Risk Engineering, Inc., Boulder, CO, 168 p.

Medeot, R. (2004) "Re-Centring Capability Evaluation of Seismic Isolation Systems Based on Energy Concepts", *13th World Conference on Earthquake Engineering*, Vancouver, B.C., Canada.

Medeot, R. (2012). "Re-centring Capability of Seismic Isolation Systems: A controversial matter moving scarcely towards its settlement", *Proc. of 15th World Conference on Earthquake Engineering*, Lisbon, Portugal, Paper No.878.

Monzon, E.V, Wei, C, Buckle, I.G, and Itani, A. (2012). "Seismic Response of Full and Hybrid Isolated Curved Bridges", *Structures Congress 2012, March 29-31*, 2012, Chicago, Illinois, US, 603-612.

Morgan, T.A. and Mahin S.A. (2011). "The Use of Base Isolation Systems to Achieve Complex Seismic Performance Objectives", *PEER Report 2011/06, Pacific Earthquake Engineering Research Center, College of Engineering, University of California*, Berkeley, California, US, 326 p.

Motazedian, D. and Atkinson, G.M. (2005). "Stochastic finite-fault model based on dynamic corner frequency", *Bulletin of the Seismological Society of America*, 95, 995-1010.

Naeim, F., and Kelly, J. M. (1999). "Design of seismic isolated structures: From theory to practice", Wiley, New York, US.

Naeim, F. and Kircher, C.A. (2001). "On the damping adjustment factors for earthquake response spectra", *The Structural Design of Tall Buildings,* 10(5), 361-369.

Nassar, A.A. and Krawinkler, H. (1991). "Seismic Deands or SDOF and MDOF Systems", *Report No.95, Department of Civil and Environmental Engineering, Stanford University*, Stanford, California, US, 218 p.

Naumoski, N.; Tso, W.K. and Heidebrecht, A.C. (1988). "A selection of representative strong mtion earthquake records having different A/V ratios". *Report No.88-01, Earthquake Research Group*, *McMaster University*, Hamilton, Ontario, Canada.

Naumoski, N., Cheung, M.S., and Foo, S. (2000). "Evaluation of the seismic response coefficient introduced in the Canadian Highway Bridge Design Code", *Canadian Journal of Civil Engineering*, 27(6), 1183–1191.

Newmark, N.M. (1959). "A method of computation for structural dynamics", *Journal of Engineering Mechanic.*, 85(3) 67-94.

Newmark, N.M. and Hall, W.J. (1982). "Earthquake spectra and design", *Earthquake Engineering Research Institute*, Oakland, California, US.

Newton, I. (1999). "The Principia", A new translation by I.B. Cohen and A. Whitman, *University of California press*, Berkeley, California, US.

NRCC. (2005). "National Building Code of Canada, 12th ed., and Commentary", *National Research Council of Canada*, Ottawa, Ontario, Canada.

NRCC. (2010). "National Building Code of Canada, 13th ed., and Commentary", *National Research Council of Canada*, Ottawa, Ontario, Canada.

Paultre, P. (2005). "Dynamique des structures", Editions Hermes Lavoisier, Paris, France.

Popov, E.P. (1994). "Development of US Seismic Codes", *Journal of Constructional Steel Research*, 29(1-3), 191-207

Priestley, M.J.N., Calvi, G.M., and Kowalsky, M.J. (2007). "Displacement-Based Seismic Design of Structures", IUSS Press, Pavia, Italy.

Reiter L. (1990). "Earthquake hazard analysis: issues and insights", New York: Columbia University Press.

RESPONSE 2000, Bentz, E.C. (2000). "Sectional analysis of reinforced concrete members", *Ph.D. dissertation*, *University of Toronto*, Toronto, Ontario, Canada.

Rowshandel, B. (2010). "Directivity Correction for the Next Generation Attenuation (NGA) Relations", *Earthquake Engineering Research Institute*, *Earthquake Spectra*, 26(2), 525–559.

SEAOC (1995). "Performance Based Seismic Engineering of Buildings, Vision 2000 Report, Volumes I and II", *Structural Engineers Association of California (SEAOC)*, Sacramento, California, US.

SEAONC. (1986). "Tentative Seismic Isolation Design Requirements", *Structural Engineers Association of Northern California (SEAONC)*, San Francisco, California, US.

Skinner, R.I., Robinson, W.H., and McVerry, G.H. (1991). "Seismic isolation in New Zealand", *Nuclear Engineering and Design*, 127(3), 281-289.

Skinner, R.I., Robinson, W.H., and McVerry, G.H. (1993). "An introduction to seismic isolation", Wiley, Chichester, UK.

Somerville, P.G and Yoshimura, J. (1990). "The influence of critical Moho reflections on strong ground motions recorded in San Francisco and Oakland during the 1989 Loma Prieta earthquake", *Geophysical Research Letters*, 17, 1203-1206.

Somerville, P.G. (1996). "Strong ground motion of the Kobe, Japan earthquake of Jan. 17, 1995, and development of a model of forward rupture directivity effects applicable in California", *Proceedings of Western Regional Technical Seminar on Earthquake Engineering for Dams*, April 11-12, Association of State Dam Safety Officials, Sacramento, California, US.

Somerville, P.G., Smith, N.F., Graves, R.W, and Abrahamson, N.A. (1997a). "Modification of empirical strong ground motion attenuation relations to include the amplitude and duration effects of rupture directivity", *Seismological Research Letters*, 68(1), 199-222.

Somerville, P., Smith, H., Puriyamurthala, S., and Sun. J. (1997b). "Development of Ground Motion Time Histories for Phase 2 of the FEMA/SAC Steel Project", SAC Joint Venture Report SAC/BD 97/04, Sacramento, California, US.

Somerville, P. (2000). "New developments in seismic hazard estimation", *Proceedings of the Sixth International Conference on Seismic Zonation*, Palm Springs, California, US.

Spudich, P., Chiou, B. S-J., Graves, R., Collins, N., and Somerville, P. G. (2004). "A formulation of directivity for earthquake sources using isochrone theory", U.S. Geological Survey *Open File Report 2004-1268*, http://pubs.usgs.gov/of/2004/1268/.

Spudich, P. and Chiou, B. S-J. (2006). "Directivity in preliminary NGA residuals", *Final Project Report for PEER Lifelines Program Task 1M01*, 49 pp.

Stafford, P.J., Mendis, R. and Bommer J.J. (2008). "Dependence of damping correction factors for response spectra on duration and numbers of cycles", *Journal of Structural Engineering*, ASCE, 134(8), 1364-1373.

Stein, S., and Wysession, M. (2003). "An Introduction to Seismology, Earthquakes and Earth Structures", Wiley-Blackwell Publishers, 498 p.

Taylor, P.R. (1999). "Some thoughts on seismic engineering for bridges seen from a Canadian perspective", *Proc. 8th Canadian Conference on Earthquake Engineering*, Vancouver, BC, Canada, 29–41.

Tolis, S.V. and Faccioli, E. (1999). "Displacement design spectra", *Journal of Earthquake Engineering,* 3(1), 107-125.

Tremblay, R. (1998). "Development of design spectra for long-duration ground motions from Cascadia subduction earthquakes", *Canadian Journal of Civil Engineering*, 25, 1078-1090.

Tremblay, R. and Atkinson, G.M. (2001). "Comparative Study of the Inelastic Seismic Demand of Eastern and Western Sites", *Earthquake Spectra*, 17(2), 333-358.

Tremblay, R. (2003). "Analytical Prediction of the nonlinear Seismic Response of a Two-Storey Semi-Rigid Steel-Concrete Composite Frame", European Commission Joint Research Centre, 72 p.

Tremblay, R. and Koval, V. (2008). "Essais de qualification de prototypes d'isolateurs sismiques IS-1 Goodco Z-Tech - Pont P-05328 sur la rivière Nicolet, Autoroute 20, Saint-Léonard-D'Aston, QC", *Rapport No. ST08-15, Département des génies civil, géologique et des mines, Groupe de recherche en génie des structures*, *École Polytechnique*, Montreal, Quebec, Canada, 89 p.

Trifunac, M.D. and Novikova, E.I. (1995). "Duration of Earthquake Fault Motion in California", *Earthquake Engineering & Structural Dynamics*, 24, 781-799.

Tso, W.K., Zhu, T.J., and Heidebrecht, A.C. (1992). "Engineering implications of ground motion A/V ratio", *Soil Dynamics & Earthquake Engineering*, 11(3), 133-144.

Tsopelas P.C., Constantinou M.C., Okamota S., Fujii S, and Ozaki D. (1996). "Experimental study of bridge seismic sliding isolation systems", *Engineering Structures*; 18(4) 301–10.

Tsopelas, P., Constantinou, M.C., Kircher, C.A., and Wittaker, A.S. (1997). "Evaluation of Symplified Methods of Analysis for Yielding Structures", *Technical Report NCEER-97-0012*, *State University of New York*, Buffalo, New York, US, 48 p.

Tsopelas, T., Constantinou, M.C. (1994). "Experimental and Analytical Study of a System Consisting of Sliding Bearings and Fluid Restoring Force/Damping Devices", *Report NCEER-94-0014, Dept. of Civ. Eng., State University of New York*, Buffalo, New York, US.

Uang, C.-M. and Bertero, V. V. (1990). "Evaluation of seismic energy in structures", *Earthquake Engineering & Structural Dynamics*, 19, 77–90.

Veletsos, A.S. and Newmark, N.M. (1960). "Effect of Inelastic Behaviour in the Response of Simple Systems to Earthquake Motions", *Proc. of 2nd World Conference on Earthquake Engineering*, Tokyo, Japan, 895–912.

Yamada, M., Kawamura, H., Tani, A., Katsunobu, I., Sakai, Y., Nishikawa, H., Masui, A., and Yamada, M. (1988). "Fracture ductility of structural elements and of structures", *Proceedings of the 9th World Conference on Earthquake Engineering,* IV*,* Tokyo, Japan, 219-224.

Zhang, J. and Huo, Y. (2009). "Evaluating Effectiveness and Optimum Design of Isolation Devices for Highway Bridges Using the fragility function method", *Engineering Structures*, 31(8), 1648-1660.

Zhang, J., Makris, N., and Delis, T. (2004). "Structural Characterization of Modern Highway Overcrossings—Case Study", *Journal of Structural Engineering*, 130(6), 846–860.

Appendix A

Directivity Effects on the Inelastic Structural Responses

Appendix A presents details and results on the assessment of the fault rupture directivity effects. Using artificial time histories (Atkinson, 2008), the effect of seismic directivity was investigated to outline its effect on response variability.

A1: Presents the characterization of the earthquake records with respect to the ground motion azimuthal direction.

A2: Presents the assessment of the effect of directivity on the inelastic structural responses. The effects of the rupture directivity was outlined herein by using different response parameters.

A1 Ground Motion Record Characterization

The parameters chosen for this study aimed to put in evidence possible trends of the seismic directivity effects on the structural behaviour. Four ground motion parameters adopted for this assessment are as follows:

1) *Arias Duration:*

   Interval of time corresponding to the accumulation of the total ground motion arias intensity between 5% and 95%.

2) *Arias Intensity, I_A:*

$$I_A = \frac{\pi}{g}\int_0^t a^2(t)dt \tag{A.1}$$

3) *Number of Zero Crossing, NZC;*

4) *Ratio of Peak Acceleration to Peak Ground Velocity, PGA/ PGV.*

   PGA/ PGV characterizes the ground motion frequency content (when *PGA/ PGV* is high, the frequency content is high) (Naumoski et al., 1988; Leger and Tremblay, 2009).

The characteristics of the time histories were evaluated for each of the 8 azimuth directions: 0°, 45°, 90°, 135°, 180°, 225°, 270° and 315°. The results are presented in Figures B.1 and B.2. To highlight the effect of directivity, the results are presented on the form of an ratio, $\alpha_{var}(\theta)$, which is defined as the ratio between the ground motion parameter for a given azimuth Θ to the ground motion parameter for an azimuth of 0°:

$$\alpha_{\text{var}}(\theta) = \frac{\text{Parameter}(\theta)}{\text{Parameter}(0°)} \tag{A.2}$$

The trends are outlined by using the polynomial trendline of degree 6. However, the variation is not clearly defined to distinguish predominant effect of the azimuthal positions between the forward or backward directivities. The largest variation of the *Arias Duration* is observed at $\theta = 270°$ for the ENA short-period event at close fault-to-site distance (M6 at 10 km), while the same event for WNA at the same azimuth shows the shortest *Arias Duration*. Large variability of the *Arias Intensity* is primarily due to the record-to-record differences in the peak ground acceleration (not shown). The effect of the normal-to-fault rupture directivity ($\theta = 90°$ and $\theta = 270°$) is more explicitly prevailing for NZC parameter. There is relatively small variation observed between PGA/PGV ratios. It can be stated from these results that the effect of the lateral rupture directivity ($45° \le \theta \le 135°$ and $225° \le \theta \le 315°$) mostly dominate the response variability. This indicates that a larger damage potential may be expected for inelastic response of structures to those ground motions.

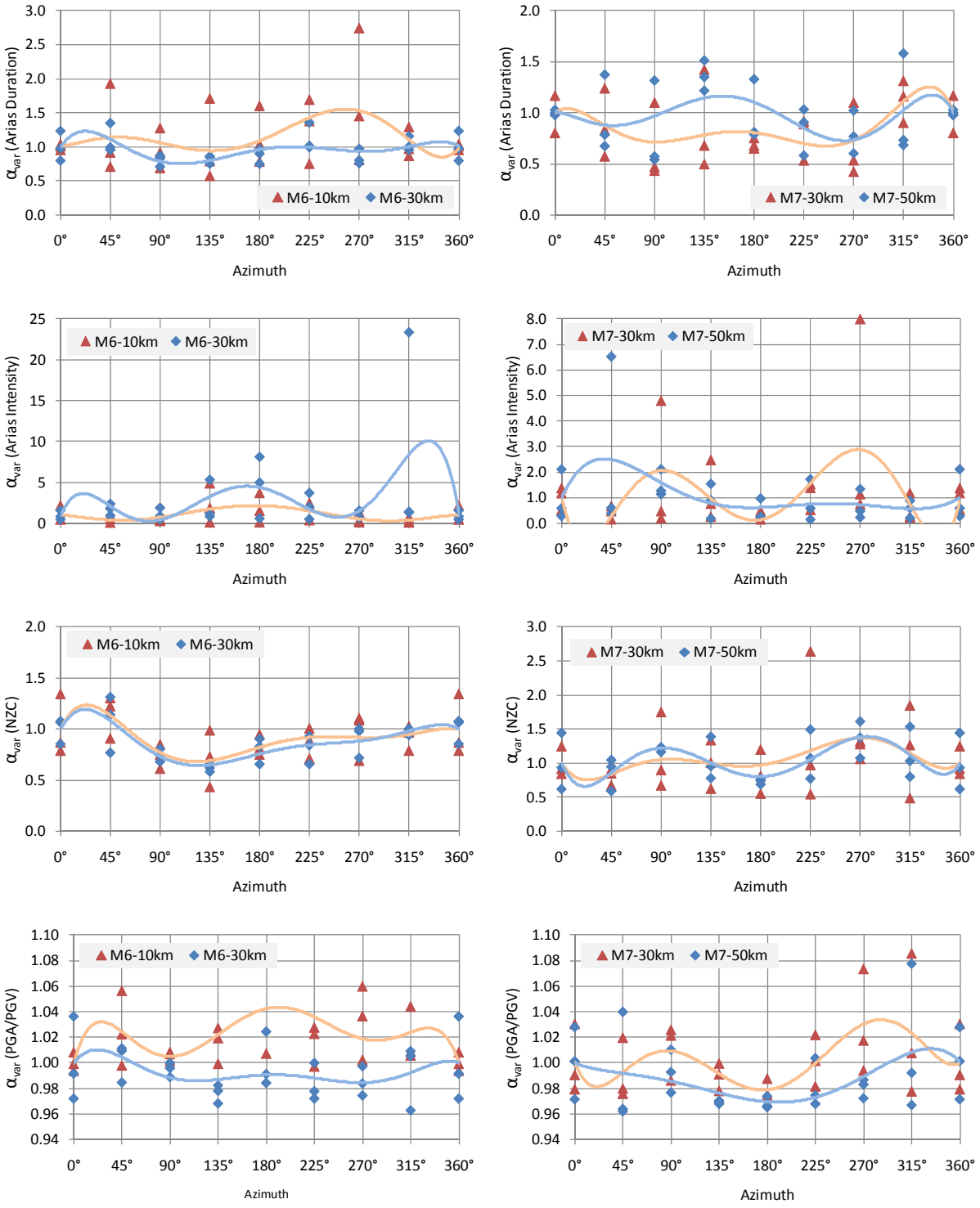

Figure A.1 ENA Normalized seismic parameters for M7.0 and M6.0 events at 30 and 50 km

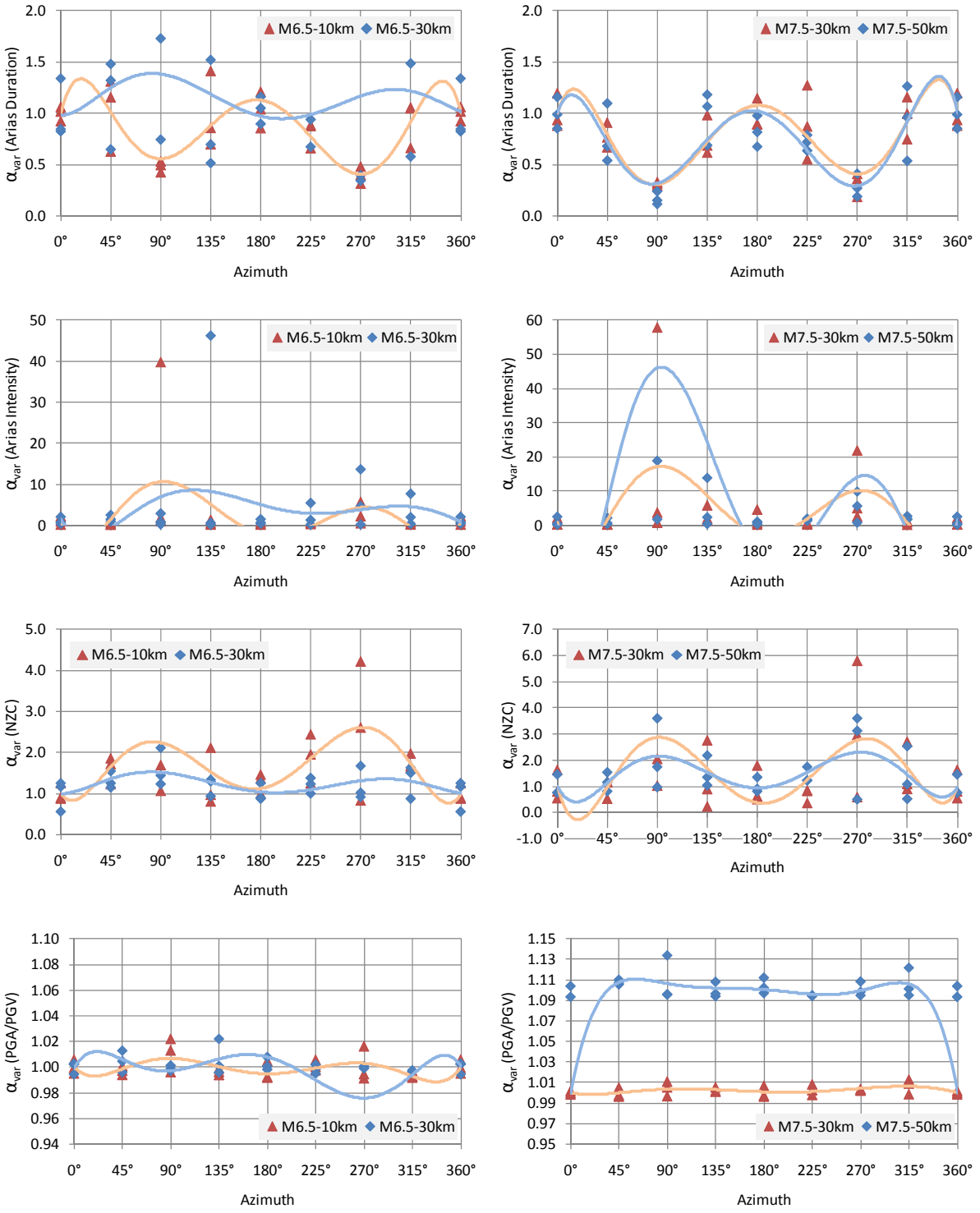

Figure A.2 WNA Normalized seismic parameters for M7.5 and M6.5 events at 30 and 50 km

A2 Effect of Directivity on Inelastic Responses

The effects of the rupture directivity was outlined herein by using different response parameters. The use of damage indices are commonly adopted to evaluate a structure failure potential. The potential damage as a function of azimuth is determined by using a *number of yielding occurrences* as well as the *kinematic*, *hysteretic*, and *low-cycle fatigue damage indices* that are defined in terms of the ductility ratio μ. Note that no limit was defined for these parameters; only the values obtained are compared to indicate the failure occurrence in this assessment. These parameters are explained in details as follows:

1) *Number of Yielding Occurrences* is determined by counting the number of times the state of the structure changes from linear elastic to inelastic. The number of yielding occurrences is an important parameter to emphasize ground motion demand on structure in terms of cumulative damage. This damage indicator may be of significance for seismic protection systems such as elastomeric (rubber or lead-rubber) isolation devices or hysteretic energy dissipation devices made from steel and shape memory alloys.

2) *Kinematic Damage Index* is critical for any isolation system since it reflects the maximum displacement demand. It is determined as:

$$D_{\mu} = \frac{\mu - 1}{\mu_{u,mon} - 1} \tag{A.3}$$

where $\mu = \frac{\Delta_{\max}}{\Delta_y}$;

$\mu_{u,mon}$ = maximum ductility capacity under monotonic loading

For this study, only relative values of D_{μ} are needed for the various azimuth values and $\mu_{u,mon}$ was arbitrarily set equal to 12.

3) *Hysteretic Damage Index* is related to the dissipative capacity of isolation systems and it is defined as:

$$D_{\mu h} = \frac{\mu_h - 1}{\mu_{u,mon} - 1} \tag{A.4}$$

where μ_h is the hysteretic ductility defined by:

$$\mu_h = \frac{E_h}{V_y \cdot u_y} + 1 \tag{A.5}$$

E_h is the total plastic dissipated energy;

F_y and Δ_y are the force and displacement at yield.

4) *Low-Cycle Fatigue Resistance Damage Index* (Kravinkler and Zohrei, 1983) reflects the damage potential related fatigue resistance and may be critical for any isolation system. This parameter is defined as:

$$D_F = \frac{\mu_F}{(\mu_{u,mon} - 1)^b} \tag{A.6}$$

where the fatigue ductility:

$$\mu_F = \sum_{i=1}^{n} (\mu_i - 1)^b \tag{A.7}$$

and the cyclic ductility:

$$\mu_i = \frac{\max\left|\Delta_{p,i}\right|}{\Delta_y} + 1 \tag{A.8}$$

n is a number of cycles and $b=2$

The b factor reflects the rate of degradation and varies depending on the material or detail studied. For this investigation, b was set equal to 2.0. To preserve the intensity intrinsic of the azimuthal directions, the unscaled time histories were considered. A bilinear SDOF system was adopted to examine the directivity effect on the inelastic response. A ratio of initial to post-yielding stiffness $k_d / k_u = 0.01$ was assigned to represent isolation systems with low restoring

force capability as they are more sensitive to the effect of residual displacements. Other system nonlinear parameters were defined with respect to the maximum elastic response to the ground motions with azimuth $\theta = 0°$. The maximum elastic responses $F_{e,i}$ and $\Delta_{e,i}$ from analyses with three (i=1:3) time-history trials at $\theta = 0°$ were averaged. The system strength level F_y was accordingly set as a function of the averaged over 8 records elastic responses ($\overline{F}_e$) using strength reduction factor R=12. Using *Equal displacement rule* (Newmark and Hall, 1982), this level of strength aimed to represent the ductility ratio μ=12 assumed herein as the maximum monotonic response ($\mu_{u,mon}$). Consequently, the force and displacement at elastic limit (at yield) were found as $F_y = \overline{F}_e / 12$ and $\Delta_y = \overline{\Delta}_e / 12$ for each system fundamental period T_e (elastic period). The analyses were carried out for three period ranges defined as 0.5 to 1.0 s, 2.0 to 4.0 s and 5.0 to 6.0 s. The period step used for the analyses was set to 0.5 s resulting in 10 bridge structures defined in terms of elastic period. As a result, the response of the 10 nonlinear systems were studied under 192 ground motions (3 trials x 8 azimuth x 4 *M-R* suites x 2 Canadian regions) resulting in a total of 1920 nonlinear time-history analyses.

The responses computed for different *response indices* were first averaged for each of three trials for the same azimuth, *M-R* suites and region. Then a mean response was calculated for each of three period ranges. These responses from different azimuthal directions were compared with respect that having azimuth $\theta = 0°$ (forward directivity) using Equation (B.2).

Table B.1 presents a general insight into variability of the response indices by presenting α_{var} ranges (minimum and maximum) obtained across both Canadian regions (ENA and WNA). For the 100$^{\text{th}}$ percentile evaluation, the maximum damage potential belongs to the short-period structures (0.5-1.0 s). For 50$^{\text{th}}$ percentile (median), the long-period structures (5.0 - 6.0 s) exhibit the maximum damage potential, while for two shorter period ranges, the same damage potential is found. It emphasizes the importance of considering directivity effects for responses of isolated bridges that may experience large inelastic excursions (or long effective periods).

The maximum variability of the damage response indices for different period ranges are presented in Figure B.3. More detailed variability distribution are summarized in Tables B.2 and presented in Figures B.4 and B.5. It can noted that each of four *M-R* suites of records analyzed for both, ENA and WNA has a particular shape for the variability of the damage response

indices. The forward directivity effect ($\theta = 0°$) on the amplification of damage potential appears to be the least frequent, while the amplification of the damage potential observed at $\theta = 90°$ is the most recurrent among the analyzed directions. The azimuth of 90° controls the maximum damage ($\alpha_{var} = \max$) in 50% and 58% of the cases analyzed for ENA and WNA, respectively. The backward directivity ($\theta = 180°$) appears to be decisive in 25% of the cases for the ENA events and it has no critical incidence in the WNA analysis.

Table A.1 Range for the response indices studied (ENA and WNA)

Measures of Position	Period Range	Variation
50th Percentile	0.5 - 1.0	0.98 - 1.07
	2.0 - 4.0	0.95 - 1.06
	5.0 - 6.0	1.00 - 1.24
84th Percentile	0.5 - 1.0	1.00 - 1.54
	2.0 - 4.0	1.03 - 1.35
	5.0 - 6.0	1.05 - 2.26
100th Percentile	0.5 - 1.0	1.03 – 3.87
	2.0 - 4.0	1.27 – 2.79
	5.0 - 6.0	1.24 – 2.45

The shorter-period structures (0.5 - 1.0 s) subjected to the short-period distant events (M6 - 30 km - ENA and M6.5 - 30 km - WNA) presented the larger damage potential (ENA: $\alpha_{var} = 2.90$ and WNA: $\alpha_{var} = 3.87$). For median responses (50th percentile), the maximum damage potentials are observed from a longer period range (5.0 - 6.0 s) for both ENA and WNA (ENA - M7 - 30 km: $\alpha_{var} = 1.24$ and WNA - M7 - 50 km: $\alpha_{var} = 1.09$). In this case, the damage potential is by 15% larger in ENA with respect to WNA. These observations put in evidence the importance of considering for NLTHA different M-R suites that take into account the rupture directivity effects.

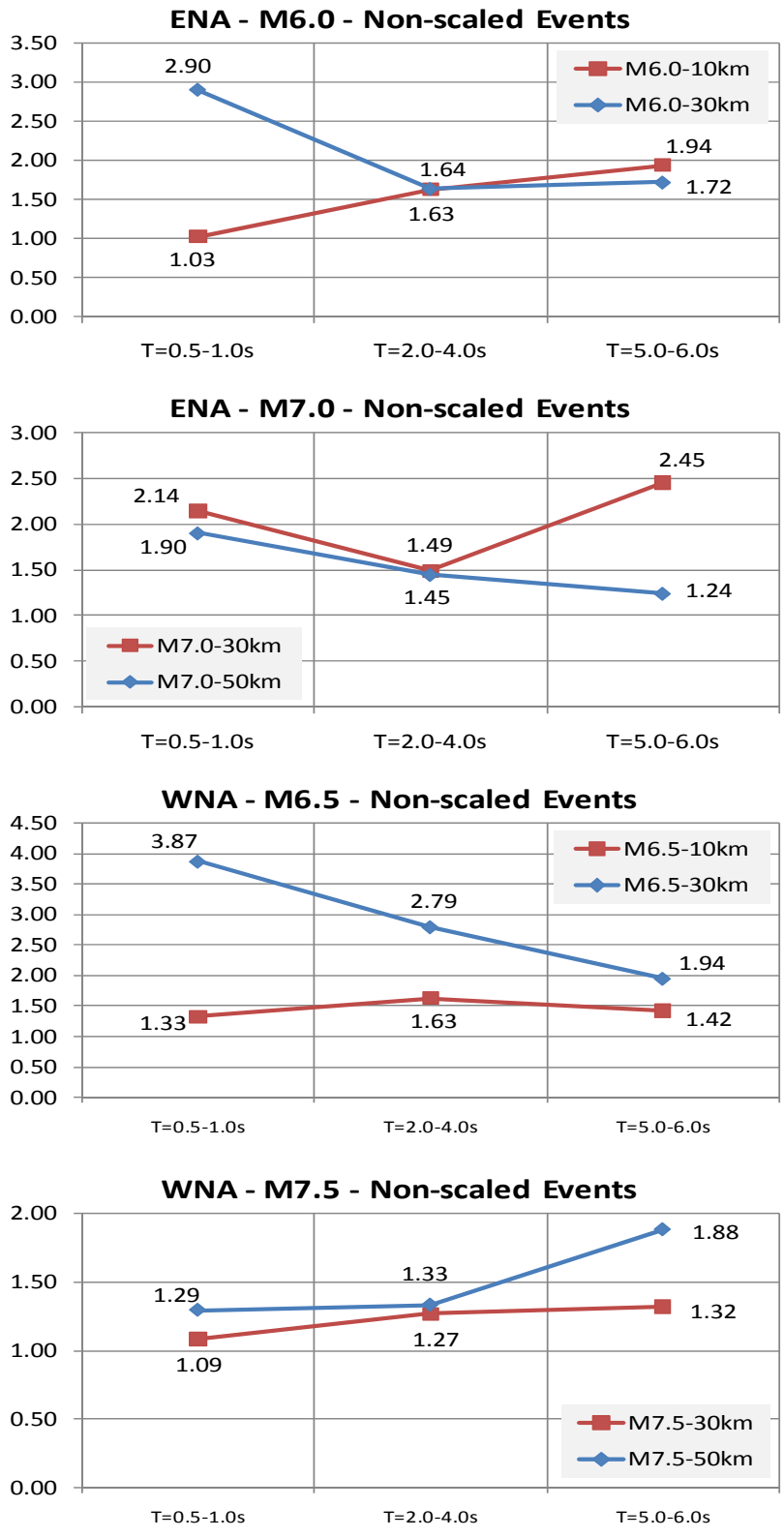

Figure A.3 Maximum (100th Percentile) variability of the damage response indices

Table A.2 Variability of the damage response indices

Region	Events	Period Range T (s)	Response Variation Index (α_{var})		
			50^{th}	84^{th}	100^{th}
ENA	M6.0-10 km	0.5 - 1.0	0.98	1.00	1.03
		2.0 - 4.0	1.06	1.33	1.63
		5.0 - 6.0	1.06	1.35	1.94
	M6.0-30 km	0.5 - 1.0	1.02	1.53	2.90
		2.0 - 4.0	1.04	1.28	1.64
		5.0 - 6.0	1.00	1.26	1.72
	M7.0-30 km	0.5 - 1.0	1.07	1.39	2.14
		2.0 - 4.0	1.00	1.14	1.49
		5.0 - 6.0	1.24	2.26	2.45
	M7.0-50 km	0.5 - 1.0	1.05	1.54	1.90
		2.0 - 4.0	1.00	1.35	1.45
		5.0 - 6.0	1.00	1.13	1.24
WNA	M6.5-10 km	0.5 - 1.0	0.98	1.07	1.33
		2.0 - 4.0	1.04	1.26	1.63
		5.0 - 6.0	1.00	1.05	1.42
	M6.5-30 km	0.5 - 1.0	1.00	1.27	3.87
		2.0 - 4.0	1.00	1.30	2.79
		5.0 - 6.0	1.00	1.22	1.94
	M7.5-30 km	0.5 - 1.0	1.00	1.01	1.09
		2.0 - 4.0	0.95	1.03	1.27
		5.0 - 6.0	1.00	1.27	1.32
	M7.5-50 km	0.5 - 1.0	1.00	1.13	1.29
		2.0 - 4.0	1.00	1.28	1.33
		5.0 - 6.0	1.09	1.52	1.88

Despite these observations, there is no definitive evidence that directivity effect is increasing with period and magnitude as well as it is decreasing with distance such as it has been reported by many researchers. This kind of discrepancy could not be explained by a simple effect of the proximity to fault since the tendencies observed for the long-period distant events are simply inversed for ENA and WNA.

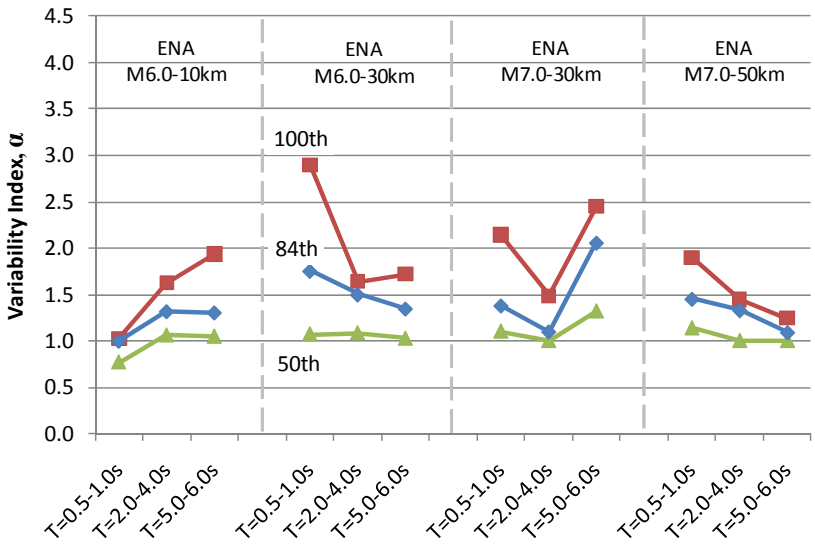

Figure A.4 ENA - Response Variability Index (α_{var})

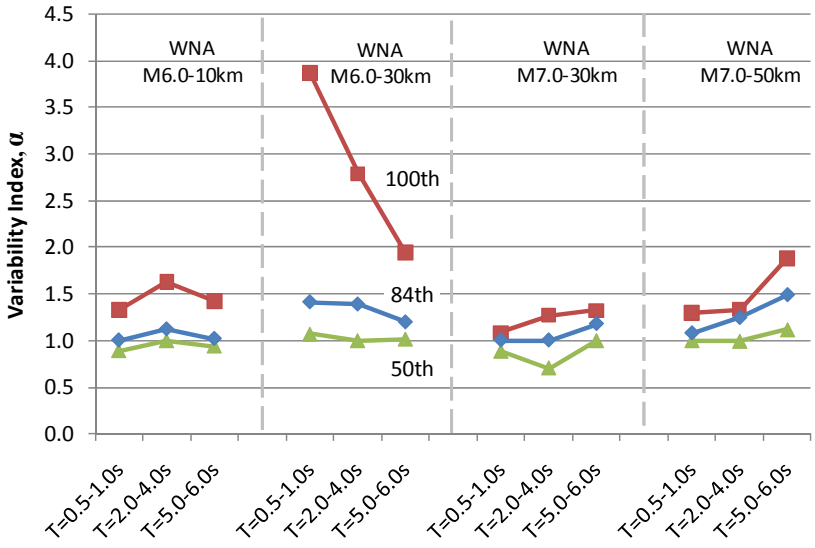

Figure A.5 WNA - Response Variability Index (α_{var})

Figure B.6 presents mean values of the amplification of different damage potential indices as a function of azimuthal direction. The responses from symmetrical pairs as 45° and 315°, 90° and 270°, and 135° and 225° are coupled to facilitate response interpretation. It can be seen from this figure that the response amplification observed at azimuth directions 90° and 135° are dominant with respect to other azimuths. In this case, for both 90° and 135°, the *low-cycle fatigue resistance damage index* appears the most critical and is followed by *kinematic* and *hysteretic damage indices*. The least critical directivity effect is noted for a *number of yielding occurrence*. The largest amplifications correspond to the period range 0.5 - 1.0 s at $\theta = 90°$: $\alpha_{\text{var}}(ENA) = 1.70$ and $\alpha_{\text{var}}(WNA) = 1.67$. The maximum amplification averaged over the three period ranges are $\alpha_{\text{var}}(ENA) = 1.45$ and $\alpha_{\text{var}}(WNA) = 1.41$. These results are in good agreement with those observed from the ground motion characterization and accentuate the importance of considering ground motions with normal directivity ($\theta = 90°$) in addition to those having $\theta = 0°$ and $\theta = 180°$.

Figure A.6 Mean values of the amplification of different damage potential indices